Bulletin 35
Part 5
(of 7 Parts)

THE
SHOCK AND VIBRATION
BULLETIN

FEBRUARY 1966

AD631234

D D C
APR 2 2 1966
D

Office of
The Director of Defense
Research and Engineering

THE
SHOCK AND VIBRATION
BULLETIN

FEBRUARY 1966

A Publication of
**THE SHOCK AND VIBRATION
INFORMATION CENTER**
U.S. Naval Research Laboratory, Washington, D.C.

Office of
The Director of Defense
Research and Engineering

CONTENTS

PART 5

Transportation

Shock and Vibration Isolation

PAPERS APPEARING IN PART 1
Part 1 - Confidential
(Titles Unclassified)

BLAST LOADING OF MODEL ANTENNA STRUCTURES
R. Kirk Gregory, Southwest Research Institute, San Antonio, Texas

ANALYSIS OF RESPONSE OF EQUIPMENT ON A DROPTEST SHOCK MACHINE
Robert L. Bort, David Taylor Model Basin, Washington, D.C.

BACKGROUND AND CURRENT STATUS OF UNDERWATER EXPLOSION SHOCK
SPECIFICATIONS AND TESTING
Gerald M. Mayer, U.S. Navy Underwater Sound Laboratory, New London, Connecticut

A SIMULATED 25-30 CPS DECK FOR SHOCK TESTING
Culver J. Floyd, Raytheon Submarine Signal Division, Portsmouth, Rhode Island

MAGNETIC TAPE RECORDING IN A SEVERE MISSILE ENVIRONMENT—A CASE HISTORY
J. P. White and J. Montsma, Bell Telephone Laboratories, Whippany, New Jersey

LONGITUDINAL VIBRATIONS PRODUCED BY INTERACTION OF THE STRUCTURE
PROPELLANT FLOW, A COMBUSTION PROCESS IN THE LANCE PROPULSION SYSTEM
Ernest King Bramblett, II, Rocketdyne, Canoga Park, California

SIMULATION OF IMPULSIVE ENVIRONMENTS BY USE OF PYROTECHNIC DEVICES
F. A. Ottati, Avco Corporation, Research and Advanced Development Division,
Wilmington, Massachusetts

PAPERS APPEARING IN PART 2

Vibration Testing

PAPERS APPEARING IN PART 3

Structural Analysis

PYROTECHNIC SHOCK ANALYSIS AND TESTING METHODS
Allan R. Hoffman and James E. Randolph, Jet Propulsion Laboratory, Pasadena, California

SHAPED CHARGE SHOCK ENVIRONMENT FOR CENTAUR VEHICLE COMPONENTS
E. C. Noble, Jr., and R. L. Batten, General Dynamics/Convair, San Diego, California

VIBRATION AND SHOCK DATA FROM THE ATHENA BOOSTER
C. J. Moening and F. J. Benedetti, Aerospace Corporation, San Bernardino, California

TRANSPORTATION

A SURVEY OF SHOCK AND VIBRATION ENVIRONMENTS
IN THE FOUR MAJOR MODES OF TRANSPORTATION*

R. W. Schock
Marshall Space Flight Center, NASA
and
W. E. Paulson
Brown Engineering Company
Huntsville, Alabama

An investigation has been conducted, the purpose of which was a review of all available information and test data describing shock and vibration environments in the four major modes of transportation. This information has been collated, analyzed, and combined, to provide a unified reference source of transportation environments for use by the packaging and/or design engineer. A portion of the results of this investigation are presented in this paper.

INTRODUCTION

Over three hundred reports were reviewed and contacts were made with fifty-five agencies and organizations active in the transportation field. Based on the data collected, acceleration versus frequency envelopes were constructed for each of the four major transportation modes. These envelopes facilitate the comparison of transportation environments in the different modes. Where applicable, the information and data are also presented to show the effect of various operating parameters on the transportation environment.

Although many programs have been conducted to collect transportation shock and vibration data, only a portion of the collected data is applicable for use in a general transportation criteria. The lack of applicability is summarized as follows:

1. Few programs dealt solely with cargo environments.

2. The data are not segregated and include measurements from locations such as vehicle appendages, aircraft wing tips, etc.

3. Many studies have been conducted on military vehicles operating under the most severe conditions, which, although setting an upper limit, are not representative of normal commercial carrier environments.

4. Many programs, although providing meaningful information for the purpose for which they were conducted, have no general application.

5. Measurements were made on vehicles that are obsolete or of limited interest.

6. Measurements were made over unknown or restricted frequency ranges, or other factors of importance to general criteria were not recorded.

7. The original data existed in a variety of forms.

In order to correlate the data, a requirement of the review was to edit all reports and include only response measurements of the cargo floor (i.e., input to the cargo). No attempt has been made to define transfer functions or cargo response relationships. In addition to

---

the constraint that data be included which are descriptive only of the cargo floor, unless otherwise noted, the data have been further restricted to standard commercial vehicles traveling normal routes. Data obtained from (a) military vehicles, (b) cross-country terrain operations, (c) special road course operations, and (d) special transporters, have been omitted from the study. Exceptions to the above are (a) data for ships which describe the environment at the aft perpendicular (the area of severest vibrational environment), and (b) results of tests with the 377PG (Pregnant Guppy Aircraft), a special transporter.

In the subsequent figures defining the environments, instrumentation and/or interest limits define the frequency ranges from which the data were taken. A lack of definition in some frequency ranges should not be construed as a lack of environment, but merely a lack of available data to define that environment.

DATA PRESENTATION

The data used to develop the graphs summarizing the shock and vibration environments were extracted from numerous reports. The original data existed in a variety of forms. Some data were in the form of peak acceleration versus frequency, other data were given in peak acceleration versus duration. For the latter, unless otherwise specified, a half sinusoidal shape was assumed and a frequency computed.

An acceleration versus frequency format was chosen for the graph to utilize as much of the available data as possible. The selection of the format was based on two principal factors: (a) it is the only one which will accept all useful data, and (b) it permits data originally presented in terms of power spectral density to be transformed to its original form by merely noting the bandwidth used in the original analysis. G (rms) versus frequency is used for the format when the original data were reduced by a Spectrum Analyzer. G zero-to-peak versus frequency is used for the format when original data were recorded with oscillographs and visually analyzed.

Vibrations which occur in the cargo area have dominant frequencies for particular vehicles, loads, locations, and speeds. Even though conditions and circumstances vary, the graphs show that the vibration levels are fairly constant over wide frequency ranges. In some instances, particularly with aircraft, a noticeable

lack of significant levels may occur in certain frequency bands.

Aircraft

Extensive shock and vibration measurements on aircraft have been performed by the Wright Air Development Division (WADD). Their most recent test programs cover the following aircraft:

1. (C-123), Medium assault cargo airplane, high wing, twin engine (reciprocating), three-bladed propellers.

2. (C-130), Medium range cargo airplane, high wing, four engine (turboprop), three-bladed propellers.

3. (C-133), Long range cargo airplane, high wing, four engine (turboprop), three-bladed propellers.

4. (H-37), Cargo helicopter, single main rotor plus torque compensating tail rotor, twin engine (reciprocating), five main rotor blades and four tail rotor blades.

The measurements were taken during all of the normal service conditions, such as taxi, ground run-up, take-off, straight and level flight (at various altitudes and speeds, and power settings), turns, descents, landing, and landing roll. The effects of cargo load, speed brakes, and other control surfaces were also investigated on some of the aircraft.

These aircraft were instrumented with velocity pickups, and the vibration data were recorded on magnetic tape. Data reduction was performed with a Davies Automatic Analyzer employing a variable-frequency, narrow-band (10 cps) filter.

Vibration data from the Pregnant Guppy (377PG), a low wing, four-engine (reciprocating), four-bladed propeller cargo airplane, were also reviewed. This aircraft is used in transporting space rockets and their allied equipment. A considerable number of vibration measurements have been taken on the cargo floor during transportation of this special cargo.

The environment in these tests was monitored with accelerometers, and the data were recorded on magnetic tape. A variable frequency, one-half cycle, bandwidth filter was used in the analysis of the data. Frequency

2

bands having relatively high vibration levels were analyzed further. A distribution of the accelerations was determined at these frequencies. Data are available for a number of locations, for a number of flight conditions, and for various loads. These data represent one of the most complete descriptions of the shock and vibration environment for any transport vehicle.

Vibration data for the KC-135, a military version of the Boeing 707 jet aircraft, has been obtained from tests by Boeing. The data cover ground run-up, taxi, take-off and cruise conditions. The original report presents the vibration data in power spectral density (g^2/cps versus frequency). The data were converted to g (rms) versus frequency for presentation in this paper. The vibrations were monitored with accelerometers and recorded on magnetic tape. Analyses were performed with a Davies analyzer with the following filters being used for different frequency ranges:

Frequency Range (cps)	Filter Bandwidth (cps)
0-30	0.80
30-50	1.33
50-100	2.64
100-200	5.41
200-400	10.1
400-800	18.7
800-1000	35.3
1000-2000	43.5

Figure 1 is composed of acceleration envelopes depicting the environment for propeller, helicopter, and jet aircraft. These envelopes were obtained by encompassing the maximum vibration levels for the respective classification. Data for the C-123, C-130, C-133, and 377PG were used in developing the plot for propeller aircraft, while the H-37 and KC-135 were used to describe the environment for the helicopter and jet, respectively. The plots show that the vibration levels are highest for the helicopter, and lowest for the jet.

Figure 2 shows the maximum acceleration envelopes for several individual aircraft. These plots were constructed by encompassing the highest recorded vibration levels for all flight conditions. The plots are presented in terms of g (rms) versus frequency.

Railroad

Data descriptive of the railroad shock and vibration environment have been categorized into two major classifications: (a) over-the-road operation, and (b) coupling. The over-the-road environment includes all data except the shock motions associated with coupling or humping operations.

Acceleration versus frequency envelopes of the shock and vibration environment of railroad cars have been compiled from many sources. Because of the high amplitude transient vibrations which occur during starts, stops, slack run-outs, and run-ins, these data have been segregated, when specified, from the vibration data describing normal running conditions. These high amplitude vibrations in Fig. 3 are labeled "transient," whereas the normal running conditions are labeled "continuous." Both of these plots have been constructed by enveloping all reliable data for all types of trucks, rail conditions, directions, and speeds. Therefore, the transient and continuous plots in Fig. 3 represent the highest vibration levels which would be encountered during over-the-road operations.

The two plots appearing in the lower half of Fig. 3 show the effect that soft ride equipment has on the over-the-road vibration environment. These plots were formed by enveloping the maximum accelerations recorded on the floor of a Minuteman transporter railroad car during cross-country operation. The data were reduced by averaging the 4-6 maximum acceleration values within each frequency bandwidth. The truck suspension system for this missile car consisted of a combination air and coil spring system in the vertical direction, and a pendulum system with snubbers in the lateral direction. Damping is provided in both directions of motion. In the longitudinal direction isolation is provided by a sliding center sill and a hydraulic cushioning device.

The effect of train speed on vibration levels is shown in Fig. 4 for a number of train speeds (20, 40, 73, 80 mph). The curves depicting the environment at 40, 73, and 80 mph are a result of tests conducted by the U.S. Army Signal Corps. The data were taken with different types of trucks. The vibrations on the cargo floor were monitored with barium-titanate accelerometers and recorded on magnetic tape. The frequency range of interest in these tests was 20-10,000 cps. The recorded data were analyzed by passing them through a series of octal band pass filters. The results of the

3
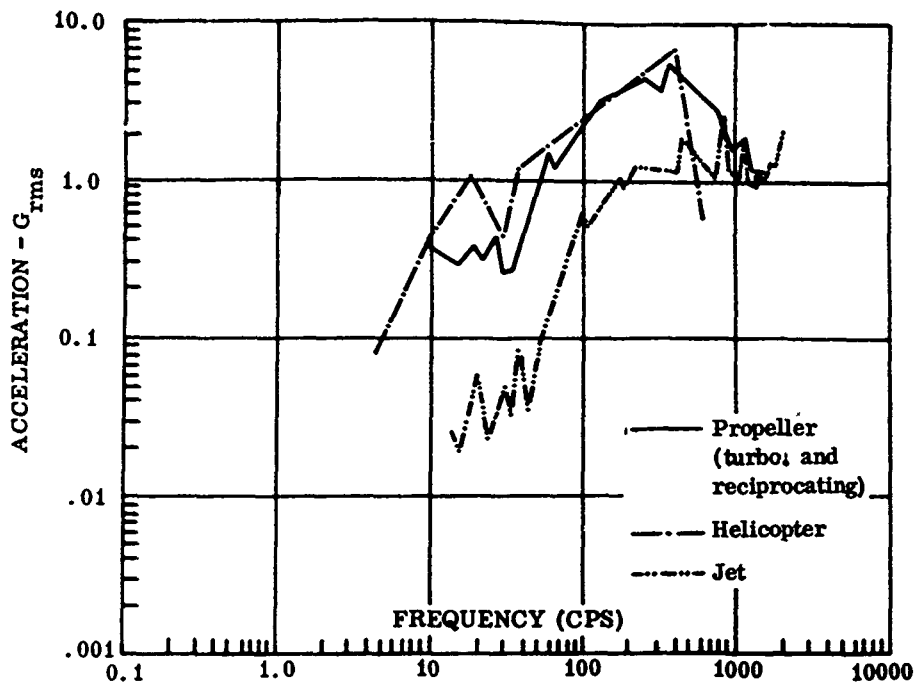
Fig. 1. Aircraft acceleration envelopes (overall composites)
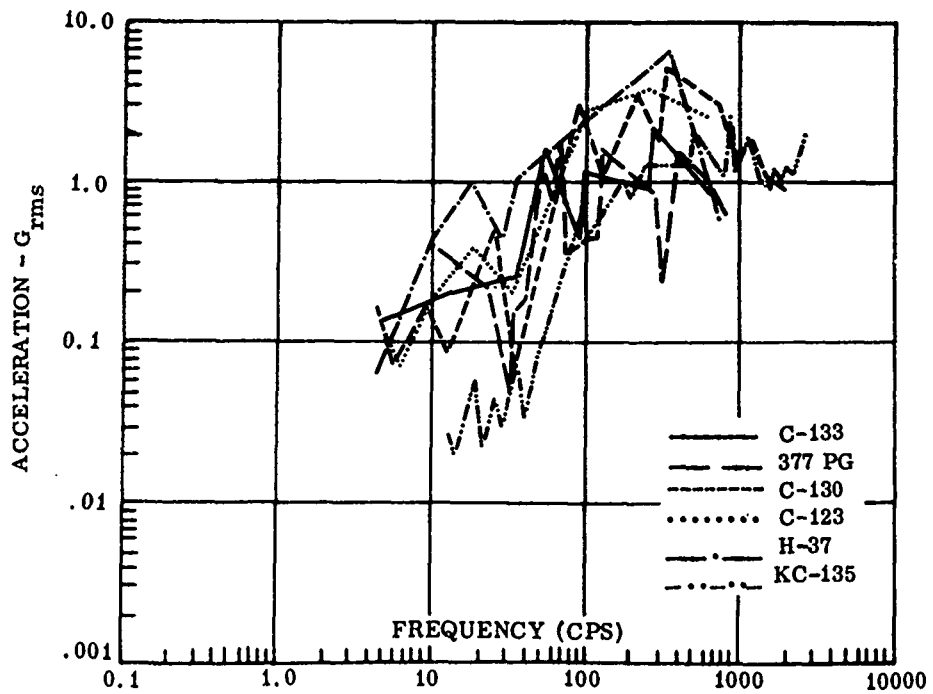
Fig. 2. Aircraft acceleration envelopes (individual composites)

4
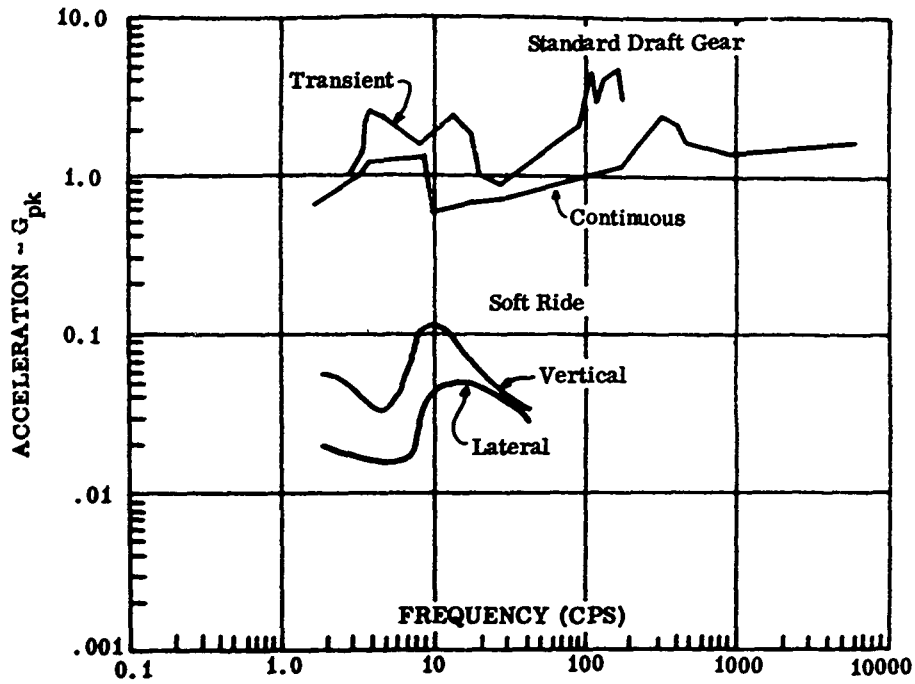
Fig. 3. Railroad acceleration envelopes (over-the-road)
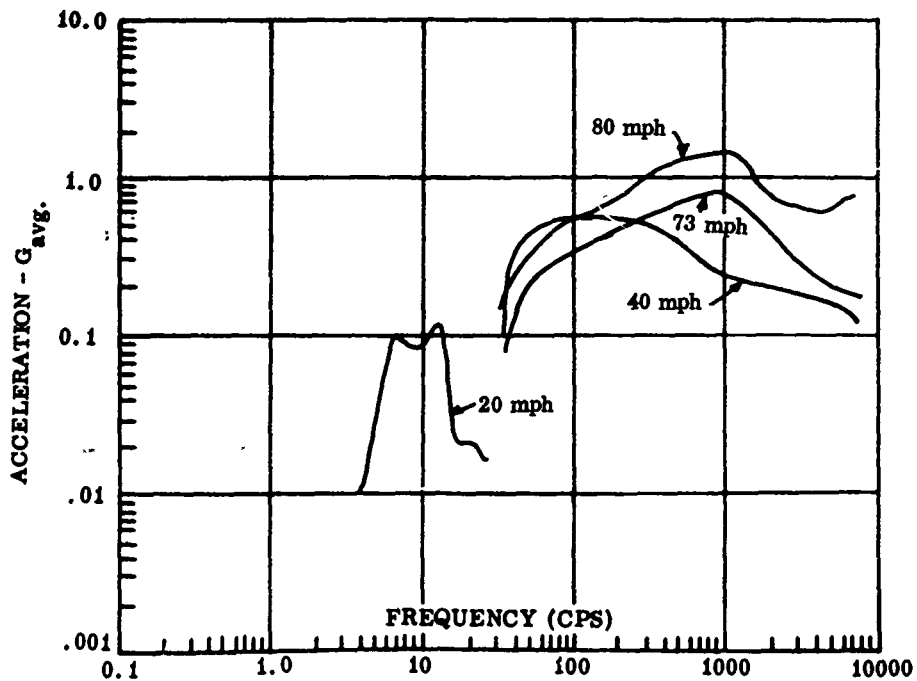
Fig. 4. Railroad acceleration envelopes (over-the-road)

5

analysis are presented in terms of average acceleration versus frequency (cps).

The data presented for 20 mph speed may be misleading because of the different frequency range. These data are a result of a separate program in which frequencies greater than 25 cps were not of interest. The data were analyzed with a frequency analyzer having a continuous band-scan device, with a frequency resolution less than one-half cycle. These data were also presented in terms of average acceleration versus frequency.

Figure 5 consists of plots that show the effect of orientation (direction). These plots are restricted to include only the data descriptive of the continuous vibration environment (i.e., data for transient vibration have been omitted). The plot shows that the vertical is the most severe environment over wide frequency ranges.

Railroad Coupling

Curves describing the shock and vibration environment for railroad coupling and/or humping operations are presented as shock spectra. A shock spectrum is defined as the maximum acceleration of a series of single degree-of-freedom systems resulting from a specific shock excitation. This method of data presentation has been chosen because it provides information on all frequency components.

Data are presented for both standard and shock-absorbing draft gears. These shock spectra were constructed by enveloping the peaks of shock spectra given in the original report. Figures 6-14 show shock spectra for standard draft gear at coupling speeds of 3.4, 6.0, 8.0, and 10 mph. The data used in Figs. 6-14 were obtained from tests conducted by Sandia Corporation. The tests were conducted by impacting a lightly loaded test car with a hammer car.

Figures 15-18 present additional shock spectra for a Miner draft gear at various impact speeds. The Miner draft gear is a high capacity shock absorbing draft gear.

Railroad Distribution of Coupling
   Speeds

Figure 19 shows the distribution of coupling speeds based on 3369 measured impacts. This plot has been constructed by averaging the results of a number of independent investigations. Data are presented in terms of percent of total impacts versus coupling speed (mph).
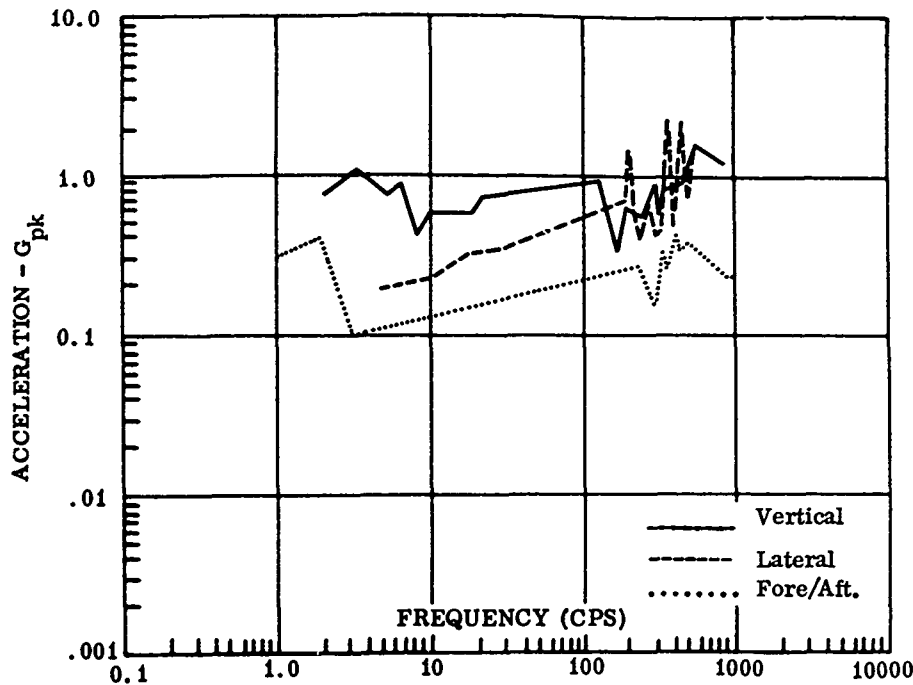
Fig. 5. Railroad acceleration envelopes
(directional composites)

6
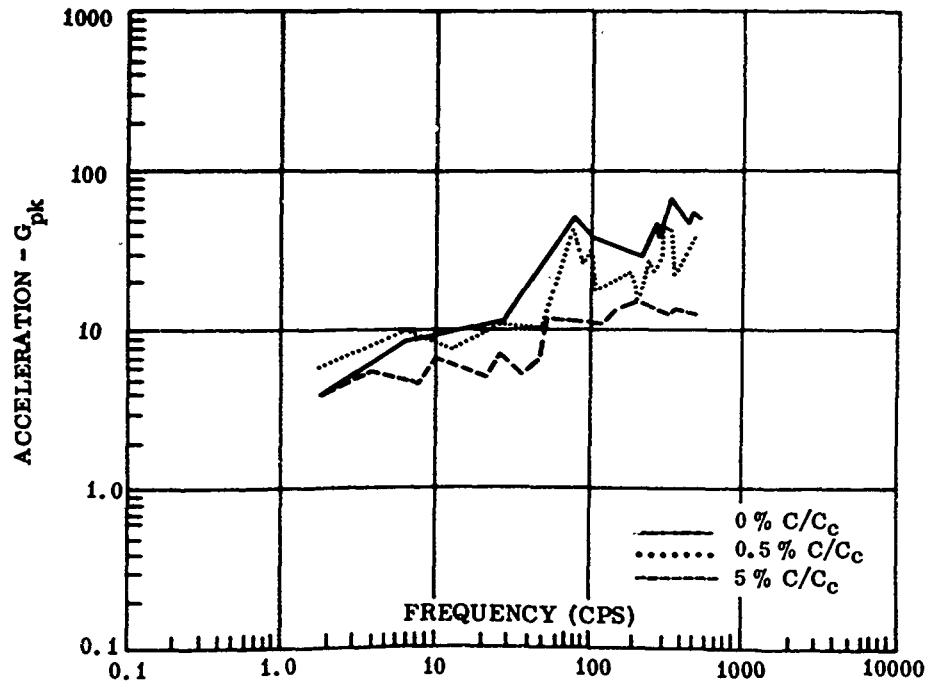
Fig. 6. Railroad coupling shock spectrum (3.4 mph,
fore/aft) standard draft gear
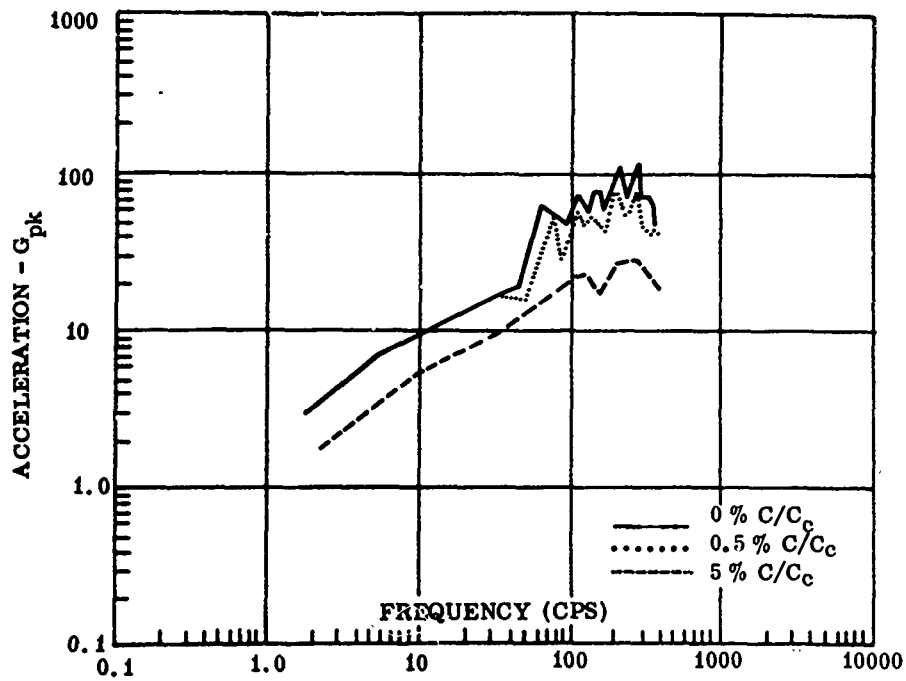
Fig. 7. Railroad coupling shock spectrum (3.4 mph,
vertical) standard draft gear

7
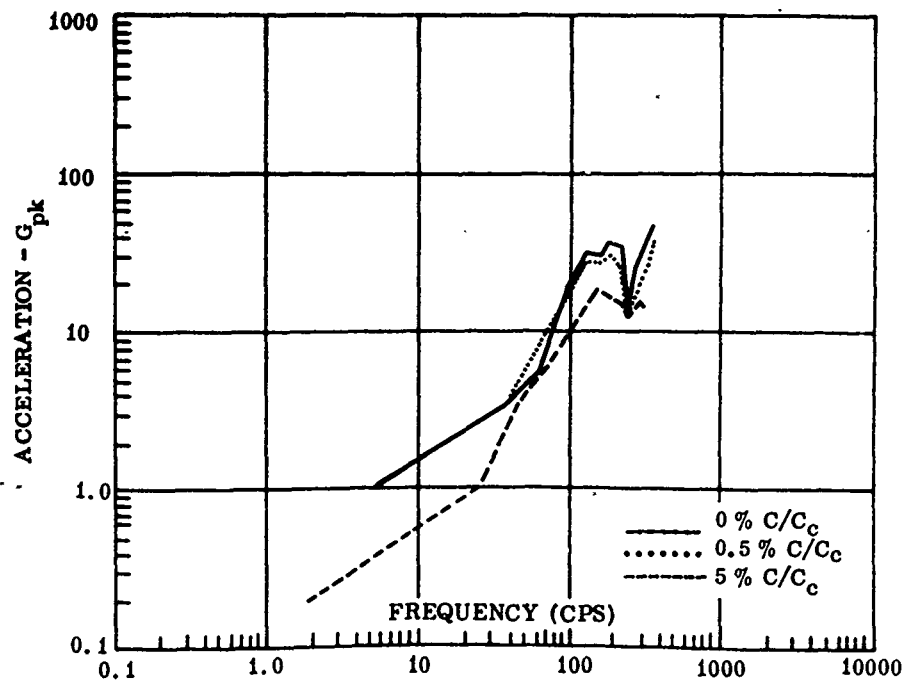
Fig. 8. Railroad coupling shock spectrum (3.4 mph,
lateral) standard draft gear
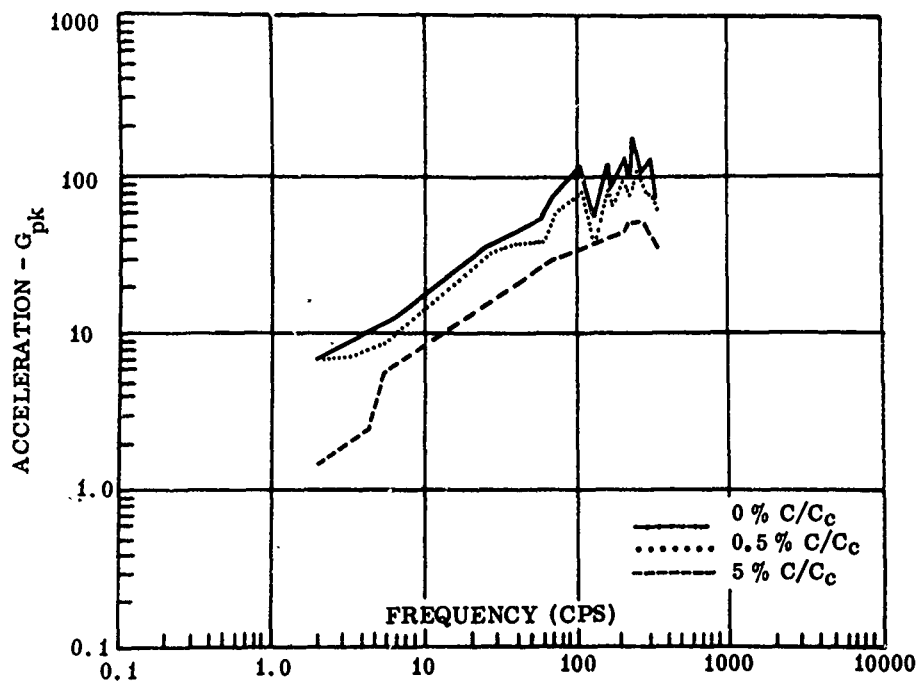
Fig. 9. Railroad coupling shock spectrum (6.0 mph,
fore/aft) standard draft gear

8
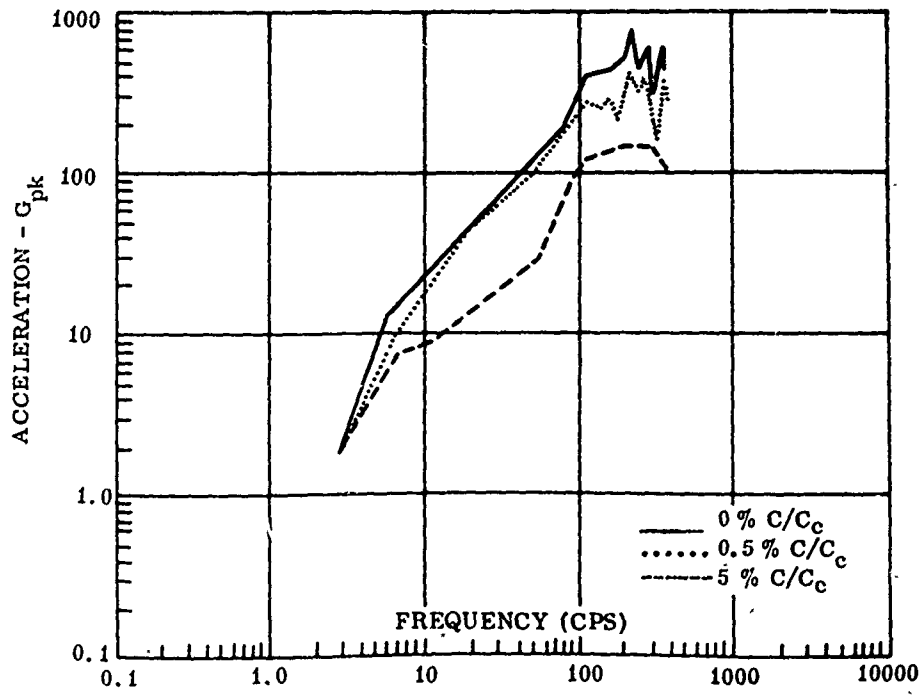
Fig. 10. Railroad coupling shock spectrum (6.0 mph, vertical) standard draft gear
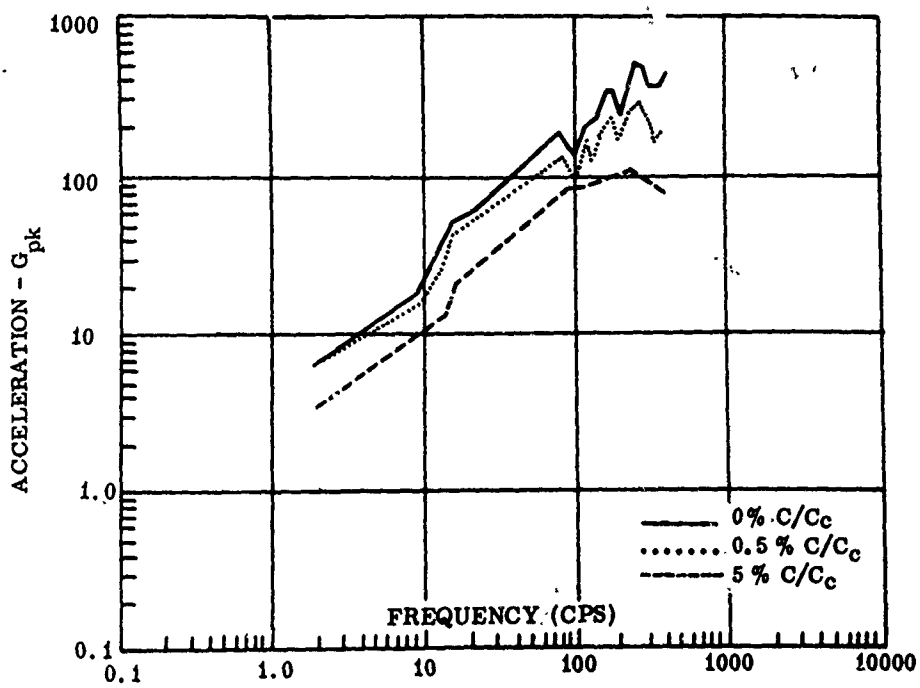
Fig. 11. Railroad coupling shock spectrum (8.0 mph, vertical) standard draft gear
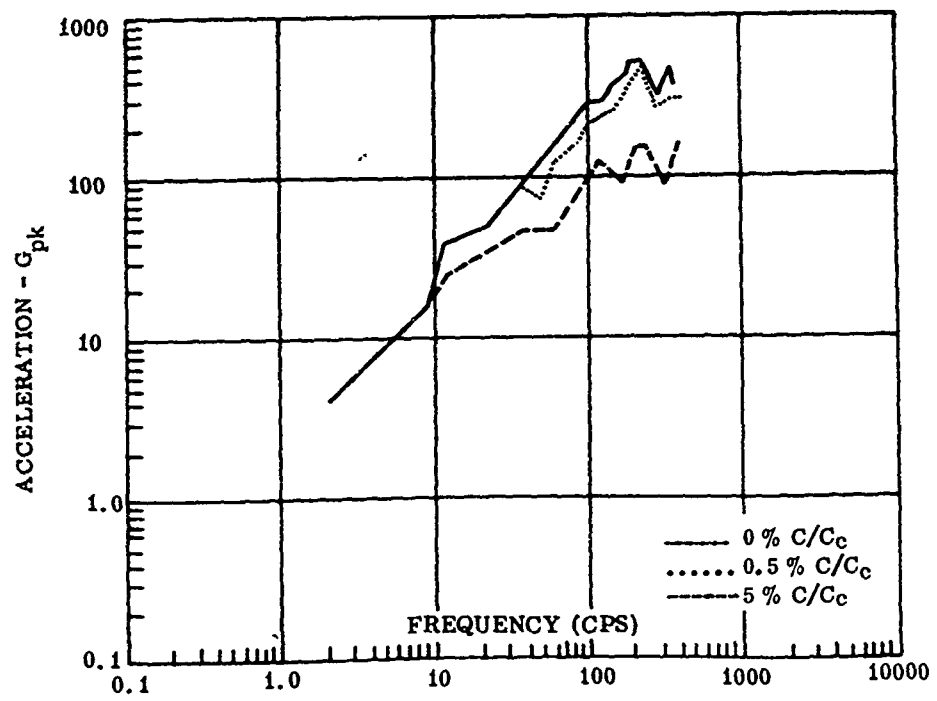
Fig. 12. Railroad coupling shock spectrum (10.0 mph, vertical) standard draft gear
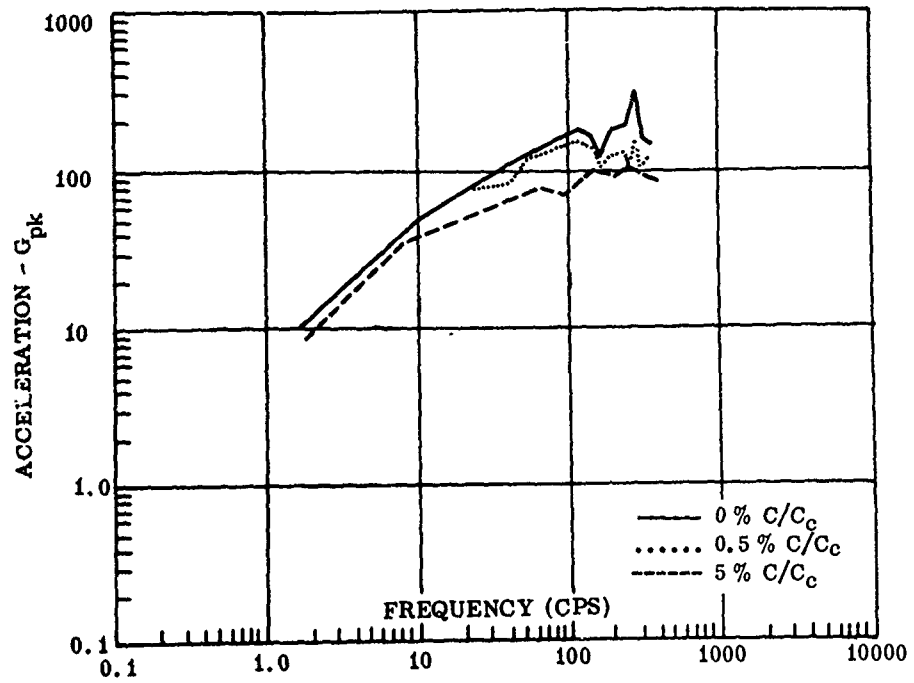
Fig. 13. Railroad coupling shock spectrum (10.0 mph, fore/aft) standard draft gear

10
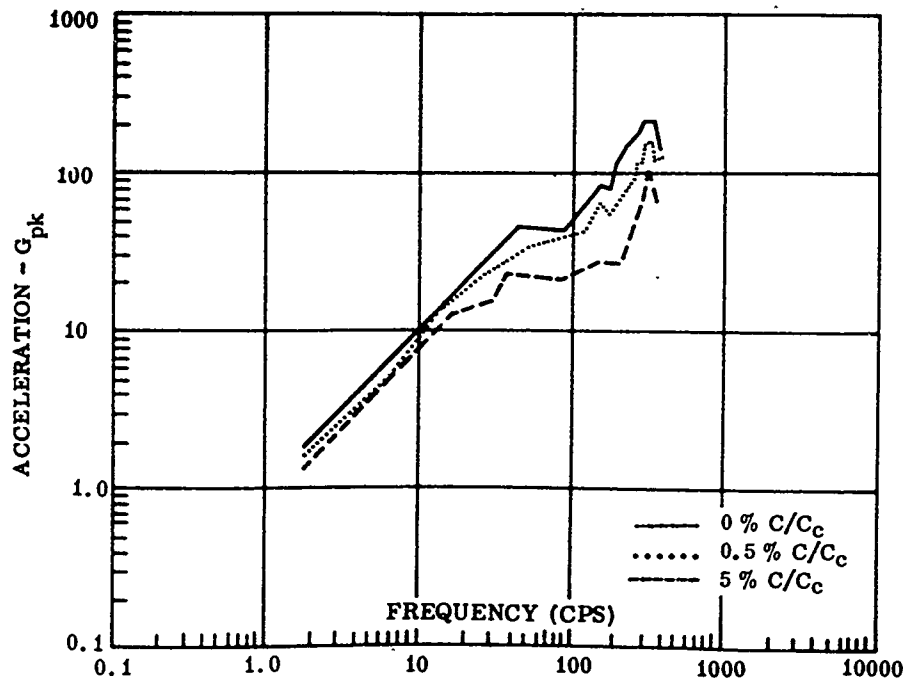
Fig. 14. Railroad coupling shock spectrum (10.0 mph,
lateral) standard draft gear
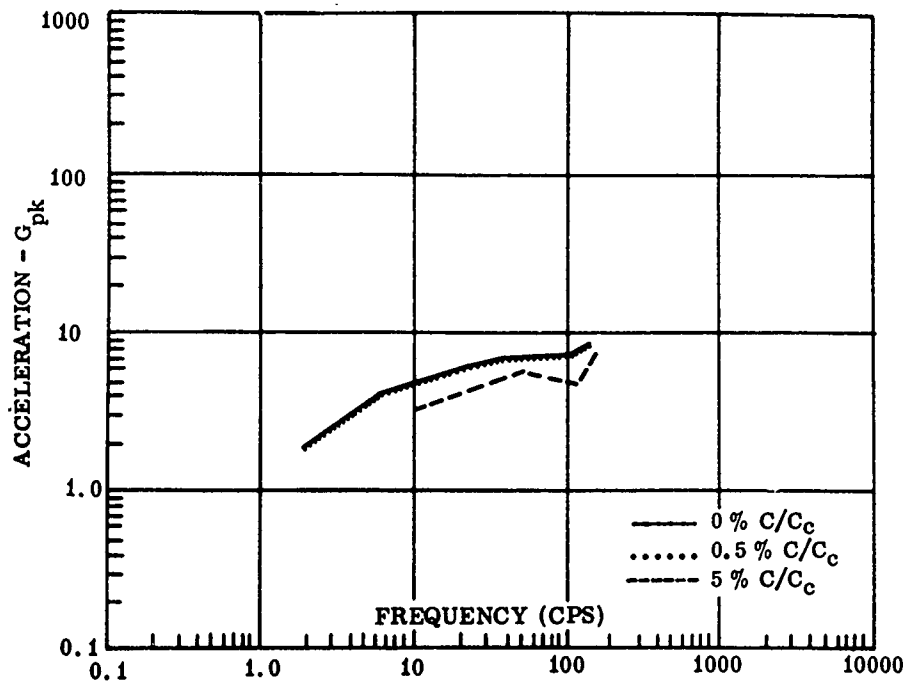
Fig. 15. Railroad coupling shock spectrum (3.7 mph,
fore/aft) cushioned draft gear

11
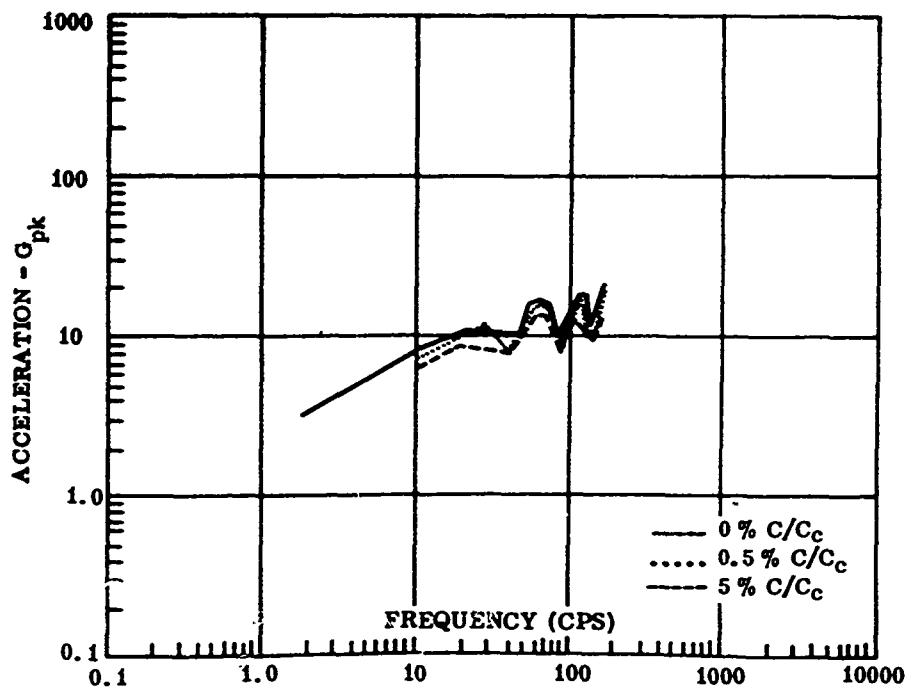
Fig. 16. Railroad coupling shock spectrum (6.8 mph, fore/aft) cushioned draft gear
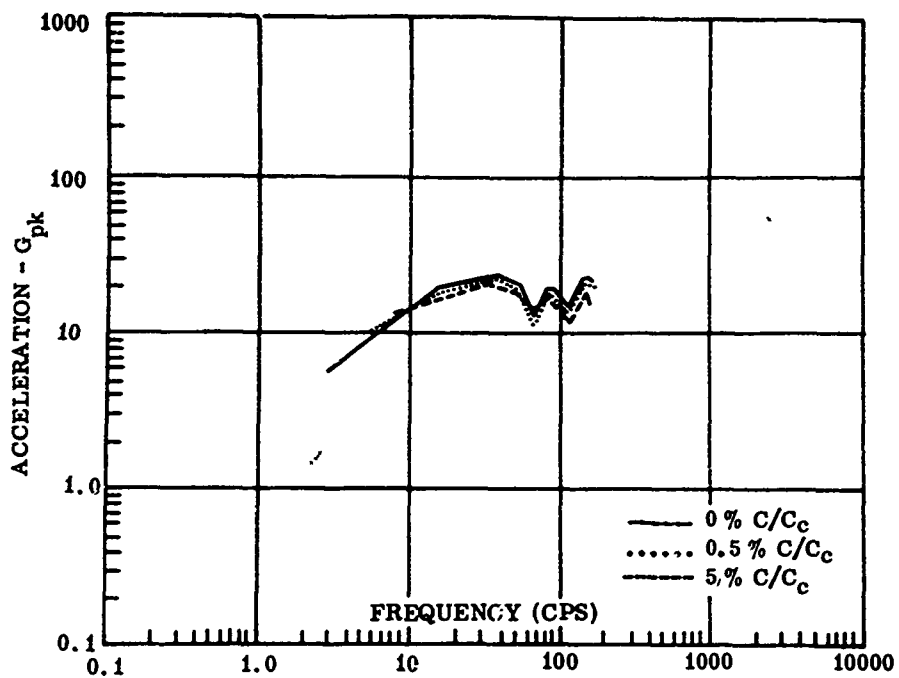
Fig. 17. Railroad coupling shock spectrum (9.8 mph, fore/aft) cushioned draft gear

12
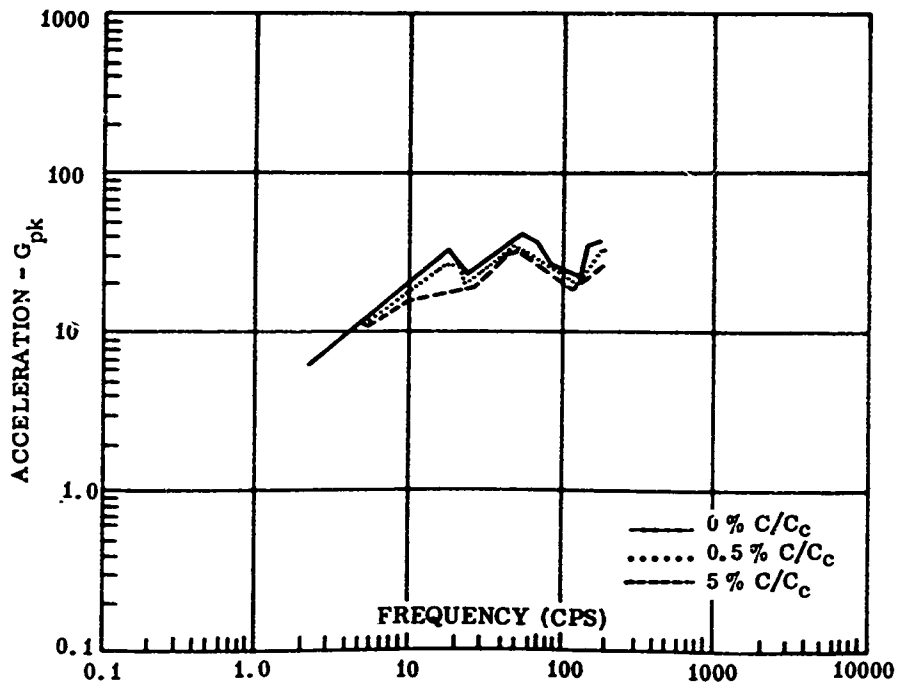
Fig. 18. Railroad coupling shock spectrum (12.0 mph, fore/aft) cushioned draft gear
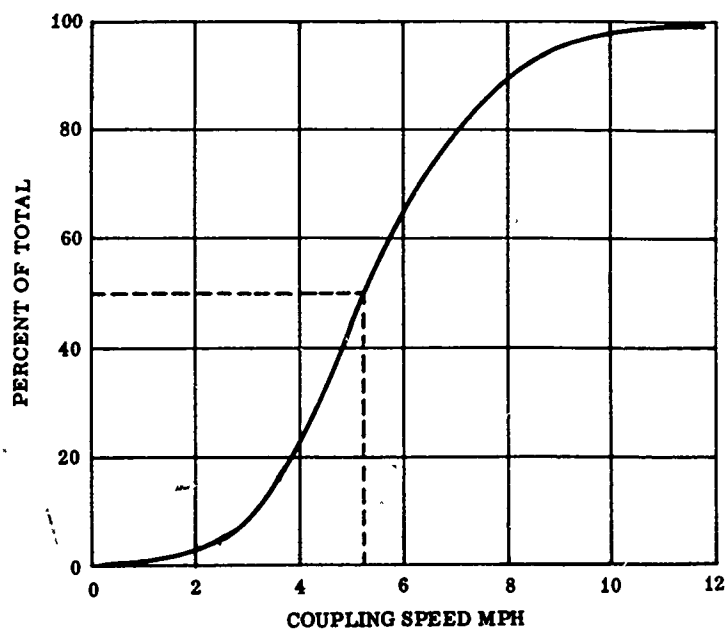
Fig. 19. Railroad distribution of coupling speeds

13

Ship

The data used in plotting the overall composite curves for ships have been separated into continuous and transient vibrations. Transient vibrations are defined as those which occur during emergency maneuvers and slamming (the impacting of the ship with water after the bow has left the water). This separation of data is made because transient vibrations can usually be eliminated from the environment. Slamming, for example, can be avoided if the ship avoids storm areas. Continuous vibrations are defined as those which occur during normal operations, including operations in rough seas.

Most of the data for the shipboard shock and vibration environment were collected by the David Taylor Model Basin. The major portion of their data, however, have been recorded near the aft perpendicular (a line perpendicular to the water line at the stern). This area experiences the highest vibrational levels on a ship. The levels of vibration for the cargo area will always be lower. However, since meager information is available for the cargo area, data for the stern location can serve as an upper bound of the environment.

The upper two curves in Fig. 20 have been constructed by enveloping all data applying to continuous vibration on one diagram, and all data referring to slamming and emergency on another. The continuous vibration composite envelope includes data recorded under extremely rough sea conditions.

The third and lowest plot in Fig. 20 is constructed from data taken on a 572-ft, single screw ship. Measurements were taken with velocity pick-ups mounted at the main thrust bearing foundation and to an angle welded to the deck over the main transverse member at the aft perpendicular. The data were recorded on straight runs and maneuvers during operations in calm seas, and at various propeller speeds.

Figure 21 shows the effect of orientation (i.e., the effect of direction). The data used to construct this figure were obtained from the tests conducted on the 572-ft single screw ship mentioned above. The curves show that the vertical vibration environment is the highest, followed by the lateral and fore-and-aft directions.

Figures 22 and 23 show the effect of sea state for two different ship lengths (L = 820 ft and L = 380 ft). The curves show that the acceleration levels increase with increasing frequency from 4 to 10 cps, and are constant at higher frequencies. The accelerations for the small ship (L = 380 ft) are almost twice as large as those for the larger ship (L = 820 ft). For each ship class, the acceleration increases by a factor of two, when the ship operates in a rough rather than in a smooth sea.
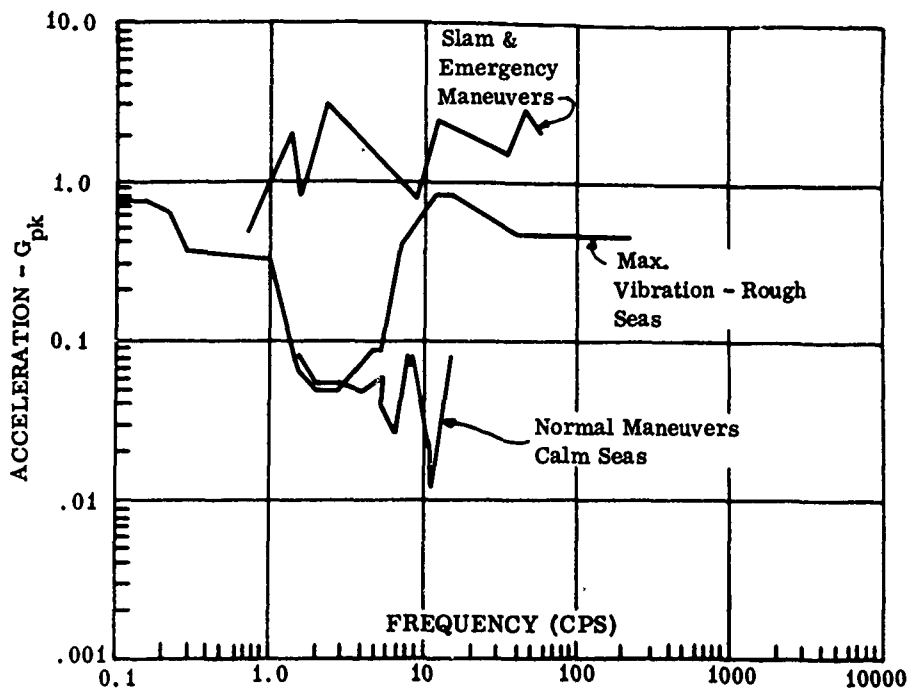
Fig. 20.   Ship acceleration envelopes
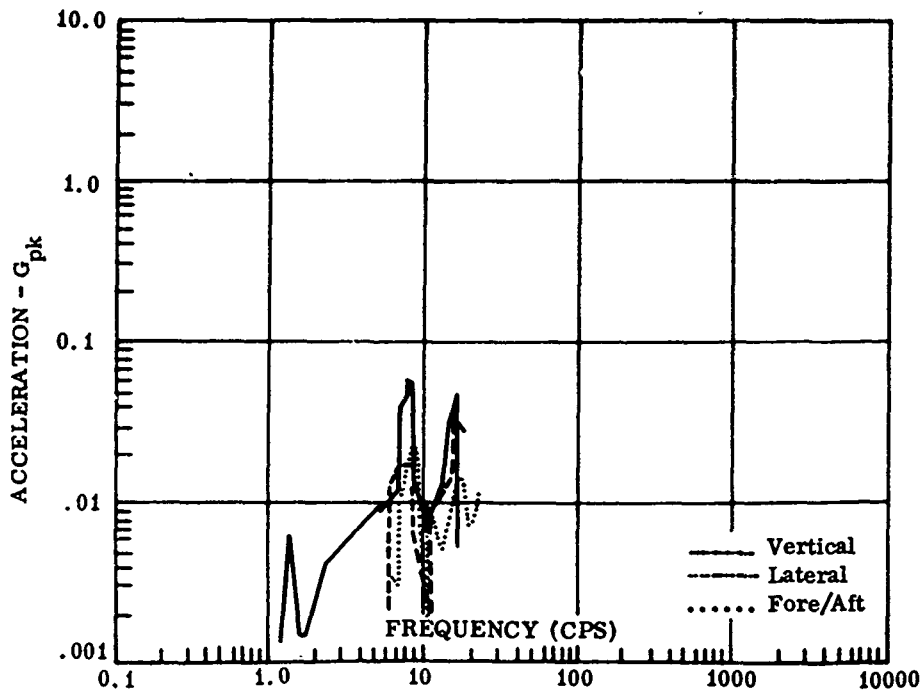
Fig. 21. Ship acceleration envelopes (straight runs)
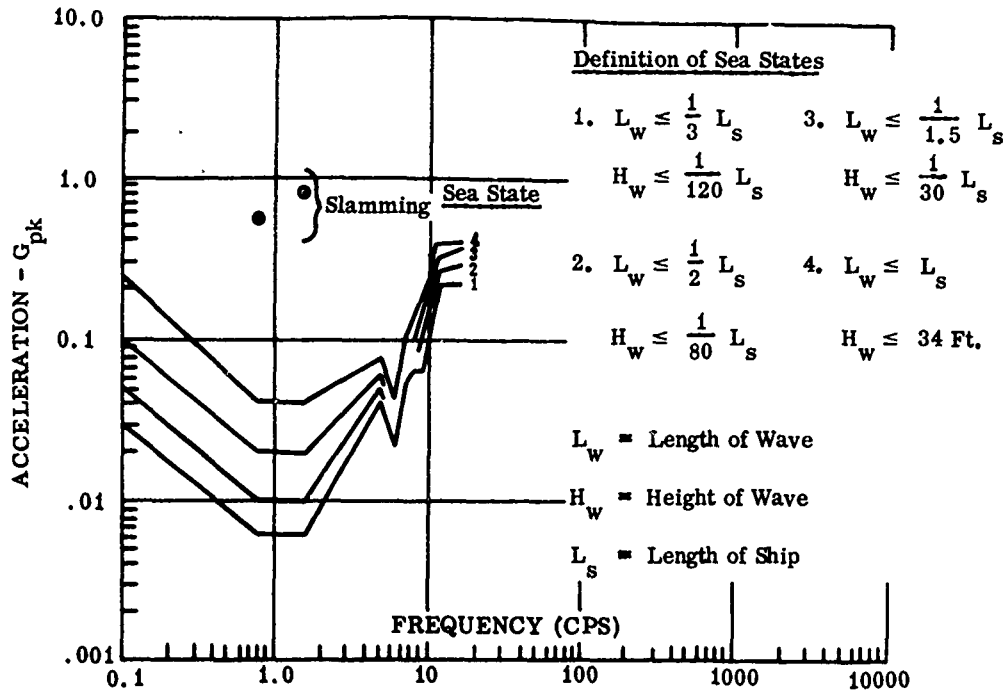
Fig. 22. Ship acceleration envelopes (L_s = 820 ft)

15
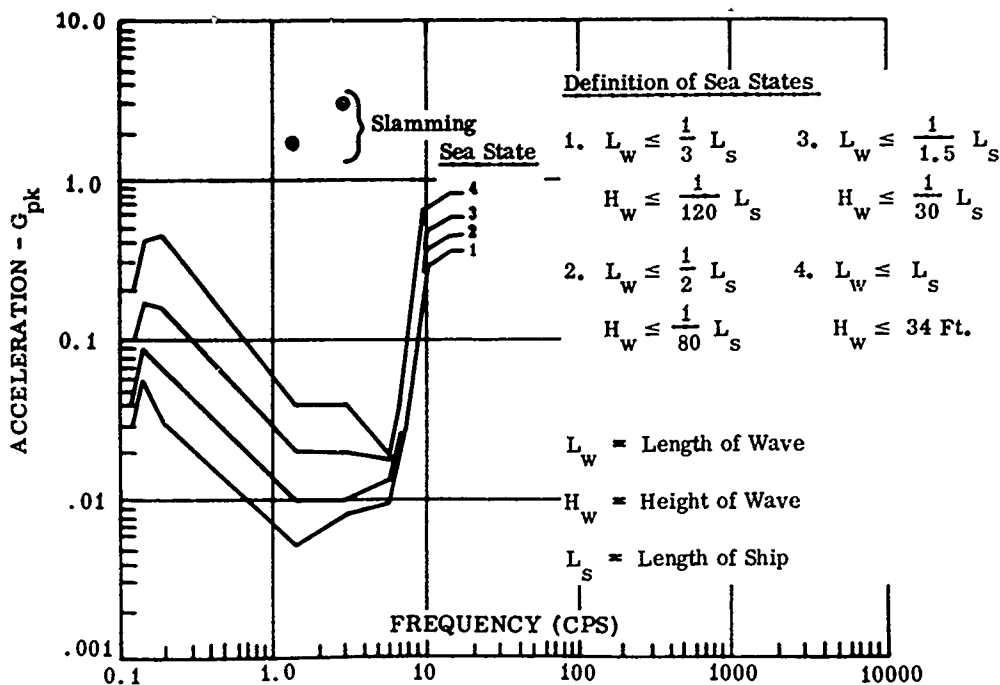
Fig. 23. Ship acceleration envelopes (L_s = 380 ft)

The higher vibration frequencies (>10 cps) are due to machinery vibration, and are less a function of sea state than the lower frequency rigid body motions.

Truck

Figure 24 shows the effect of road condition on the vibration environment.

The upper curve in Fig. 24 has been obtained by enveloping data from a number of individual test programs. This curve includes peak values representing the environment experienced in traversing rough roads, ditches, potholes, railroad crossings, and bridges. Data reduction procedures vary from one report to another, but in most cases the method used was to record the data oscillographically, and visually determine the peak (zero-to-peak) acceleration and predominant frequency. This method has been used extensively in transportation studies, since it requires little auxiliary equipment, and since the magnitude of the significant predominant frequencies can be conveniently and immediately determined.

The lower curve in Fig. 24 has been obtained by enveloping paved road data. The combination of these two curves show the differences in vibration levels between vibrations which occur while traversing potholes, ditches, railroad crossings, etc., and the maximum vibration environment occurring during operation on paved roads.

Figure 25 shows the effects of cargo load on the vibration environment. These curves are the result of a single measurement program. The tests were conducted with three standard commercial semitrailers, each having one of three basic types of suspension (air-ride tandem suspension, stable-ride single suspension and single-axle spring suspension). Tests were run at two load conditions, empty and full, over a first-class asphalt road. Vertical accelerations were monitored at three locations on the cargo floor (over the fifth wheel, the center of the van floor, and over the rear axle). These curves show that the vibration levels are practically unaffected by load in the lower frequency ranges. Higher frequency components, however, are reduced on loaded trucks.

CONCLUSIONS AND
RECOMMENDATIONS

The most severe transient environment associated with transport vehicles occurs during railroad car coupling or humping operations, whereas the most severe steady-state environment occurs during phases of aircraft transportation. Railroad, truck, and ship follow aircraft in order of decreasing levels of environment.

16
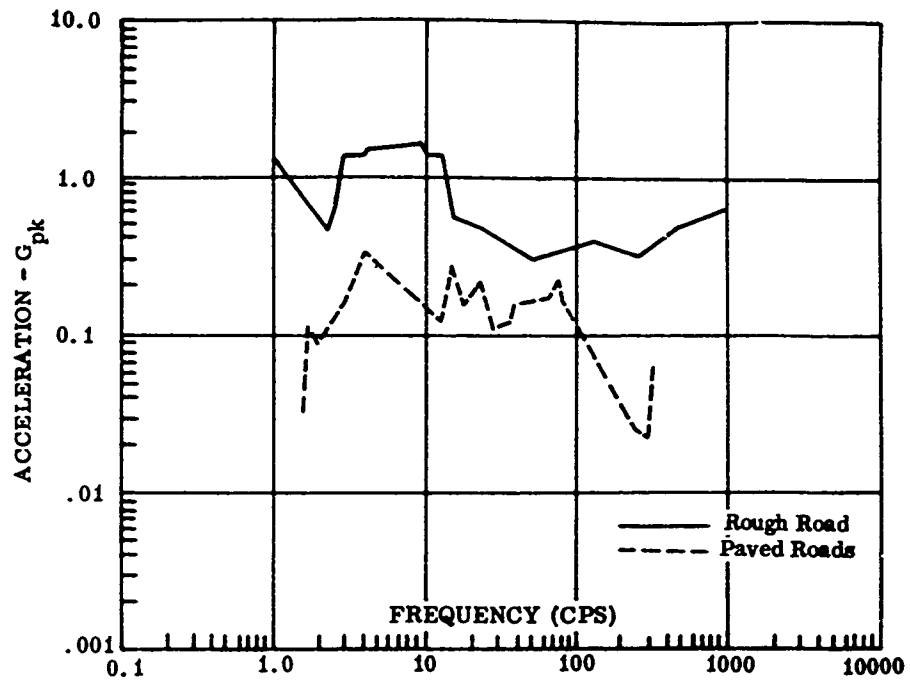
Fig. 24. Truck acceleration envelopes
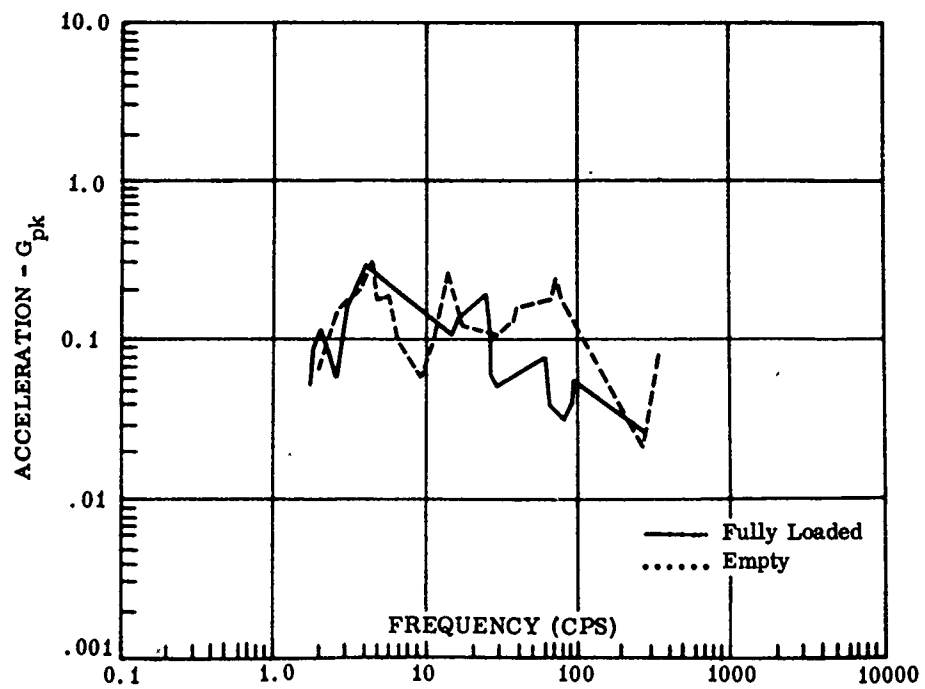
Fig. 25. Truck acceleration envelopes

17

The levels of vibration presented in this paper are considered reliable, even though they are derived from data analyzed by diverse reduction methods. This conclusion is based on the relatively close correlation between data from various reports (for similar test vehicles and conditions).

Data are sufficient at the present time to define adequately the transportation environment in terms of maximum acceleration versus frequency; however, the term maximum should be emphasized. For example, because of the paucity of data describing the environment in the cargo area of ships, data from the extensively monitored fantail area were utilized. Since this is the highest encountered shipboard environment, it does not represent the cargo hold, but does set an upper bound on the expected cargo hold environment. The philosophy of enveloping all data lends itself to a conservative environmental definition with a very high (99 percent) statistical confidence level.

Future studies of interest that would greatly enhance and supplement this investigation could include (a) correlation of fantail to cargo hold shipboard environments, (b) a more extensive breakdown of transportation modes, (c) a statistical processing of accumulated data, (d) a continuing effort of environmental definition, particularly in the truck mode, and (e) an investigation of terminal handling environments.

Due to the increased nationwide interest in transportation environments, many programs are currently being conducted in the previously outlined areas, and should go far to supplement the basic criteria contained herein.

ACKNOWLEDGMENT

DISCUSSION

Mr. Markson (E.R.A. Inc.): The set of ship acceleration curves appears to be a combination of vibration accelerations and shock accelerations. Is that correct?

Mr. Schock: Yes, the impact vibrations are transient in nature although they are of rather long duration. It could be termed a shock vibration. It is a response, but over a longer duration than one would normally consider a shock response.

Mr. Markson: What kind of instruments did you use to pick up the two different types of accelerations?

Mr. Schock: We used accelerometers, mounted in the fantail area.

Mr. Markson: Did you use the same accelerometers for reading vibration at 100 cps on the ship as you did for reading the low frequency shock impact?

Mr. Schock: No, there were two different studies. One was for vibration, and the other was specifically to pick up the slam modes. Different accelerometers were used in each study.

Mr. Markson: This is a summary of several different reports?

Mr. Schock: Yes, over 300 reports were reviewed.

Mr. Fitzgibbon (Mechanics Research): Why did you not present your vibration data in terms of the power spectral densities rather than g's rms? In this manner you could show an envelope of all of the power spectral densities from the various environments which would be a criterion for all environments.

Mr. Schock: We had spectral analyses in some cases during the course of the study, while others presented only data from peak detection meters or oscillograph records. Most of the data on aircraft were in spectral analyses and given in psd. We reduced these to g-rms to get them in a form comparable with the other data.

Mr. Fitzgibbon: Are you suggesting that the rms g's be taken from your curves and converted to psd to arrive at specifications for shock and design?

Mr. Schock: No, I would not use these curves in specifications. The paper itself breaks these curves down in much more detail with more detailed parameters, such as the direction of measurements, and individual aircraft measurements. This will greatly facilitate the definition of a better specification.

18

I would not try to envelope curves such as these for use in a specification. It gives the designer a feel for what the maximum levels will be and what to design for.

Voice: Could you classify the helicopter and the propeller excitation as being one of the most severely characterized as steady state?

Mr. Schock: Yes, the helicopter data was characterized as steady state. It is caused by the response of the structure to the steady state prop wash.

Mr. Krachman (TRW Systems): That truck data seems to be a little low. Was this on any special type of truck?

Mr. Schock: The maximum environment was on trucks that had standard truck gear. Some of them did have air-ride and some had only coil springs and single axles. The data in the lower environment were taken over very good first class asphalt roads, whereas the data in the upper environments were taken on a typical rough road which had pot holes, railway crossings, and bumps. It was not as rough as the Munson course.

*　　*　　*

19

THE DYNAMIC ENVIRONMENT OF SPACECRAFT
SURFACE TRANSPORTATION*

J. W. Schlue
Jet Propulsion Laboratory
Pasadena, California

The data presented in this report include shock and vibration measure-
ments over rough irregular roads, plus vibration measurements over
smooth highways. Comparisons are made between different vans,
smooth and rough roads, and three different locations within the same
van. Data plots envelop the maximum, 95 and 50 percentile levels of
shock spectra and power spectral densities.

A discussion of instrumentation applicable to measurements of trans-
portation dynamic environments is contained in the appendix. Electri-
cal and mechanical instrumentation are included.

INTRODUCTION

The shock and vibration environment im-
posed on spacecraft during surface transporta-
tion was determined by the Jet Propulsion Lab-
oratory in evaluation tests and instrumented
spacecraft shipments. All flight spacecraft
built by JPL have been transported by air sus-
pension vans to the launch site at Cape Kennedy.

The decision to instrument spacecraft ship-
ments was made primarily for the following
reasons:

1. Limited information was available on the
dynamic environment of surface transportation.

2. It is desirable to have shock and vibra-
tion measurements in the event of an accident.
Once the normal environment is determined,
this becomes the underlying reason for continu-
ance of instrumentation.

It is hoped the statistical study presented
in this paper will aid in predicting transporta-
tion environments.

DESCRIPTION OF TRANS-
   PORTATION STUDIES

The data measurements for this study were
made during a van evaluation test and two

spacecraft shipments to Cape Kennedy. The
evaluation test is referred to as the Ranger
Block III test, since it was performed in sup-
port of Block III configuration Ranger ship-
ments. The trips to the Cape involved the
Ranger 8 spacecraft that recently photographed
the moon, and a structural model of the Sur-
veyor spacecraft.

The load distribution of the evaluation test
included the Ranger TV tower at the aft posi-
tion, the Ranger bus structure and electronics
at the middle, and a solar panel trailer at the
front. Steel plates were located in the middle,
also, as ballast. The ballast was intended to
load the van suspension system to its nominal
loading for improved dynamic characteristics.
The Ranger 8 van was loaded in approximately
the same manner except that no ballast was in-
cluded. A structural model constituted the pay-
load of the Surveyor shipment.

The Ranger equipment was installed in
transportation structures secured to the van
floor with no shock or vibration isolators.
Structural integrity between the van floor and
the spacecraft equipment was assumed, so that
measurements at the van floor were considered
the input to the equipment itself. The Surveyor
model, however, was installed on an isolated
trailer that did not linearly transmit the vibra-
tion and shock of the van floor to the spacecraft.

Consequently, the spacecraft structure and transport trailer were instrumented in depth to determine the transfer functions and resonant frequencies of the system. Only one data channel was determined applicable to this report. The Ranger vertical axis measurements used piezoelectric accelerometers located midway between the sides of the van, in the locations depicted in Fig. 1. Two accelerometers were also installed in the longitudinal and horizontal axes.

The Surveyor measurements were made only at the aft position. The accelerometers were mounted on aluminum plates secured to the van floor with lag bolts.

Mechanical accelerometers were also employed. These units were also mounted on metal blocks secured to the floor.

DISCUSSION OF DATA

The data to be discussed were measured with piezoelectric accelerometers and recorded with a magnetic tape recorder. The analyses were performed with digital computer programs.

During the trips to Cape Kennedy from Pasadena, California, about 85 percent of travel time involved smooth highways in good repair. However, the greatest percentage of vibration and shock analyses was with rough road measurements. The data analyses were performed sequentially as follows:

1. The magnetic tapes were coded with the NASA 36 bit time code.

2. Oscillograph records of the data channels, reference channel, and time code were produced. The reference channel recorded only the standard FM carrier frequency. The demodulated signal from the channel was recorded on the oscillograph records. (This channel is discussed in the instrumentation section.)

3. Data were selected from the "O" graphs for power spectral density (PSD) and shock spectrum analysis. These data selections were identified on the tapes with the time code. The quality of data selected was determined by the reference channels.

4. Preliminary PSD and shock spectra were evaluated for required resolution and frequency content.

5. The final PSD and shock spectrum analysis plots were programmed and computed.

6. Selected PSD's were analyzed for amplitude statistics. (The method of analysis was determined by evidence of noise content in the data.) The existence of apparent noise dictated a statistical analysis to estimate the energy distribution.

Shock Analysis

The analyses of all shocks were performed in the sequence listed above. Figure 2 contains an amplitude-time history of a transient measured at the aft position of the van during the RA-8 shipment. The transient was located on the tape via the time code, digitized, and run through the shock analysis program, producing Figs. 2 and 3. Figure 3 contains the shock spectra calculated with an assumed damping ratio of 0.050 or a Q of 10. The spectrum represents the response of a single degree of freedom oscillator to the shock measured. The
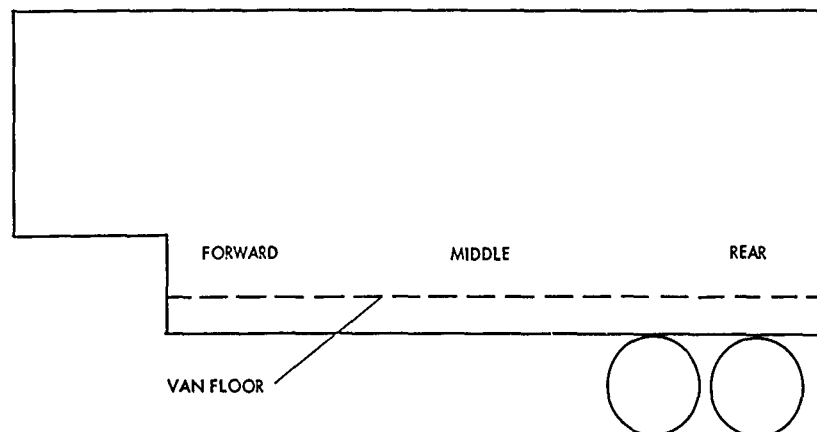
Fig. 1. Accelerometer locations
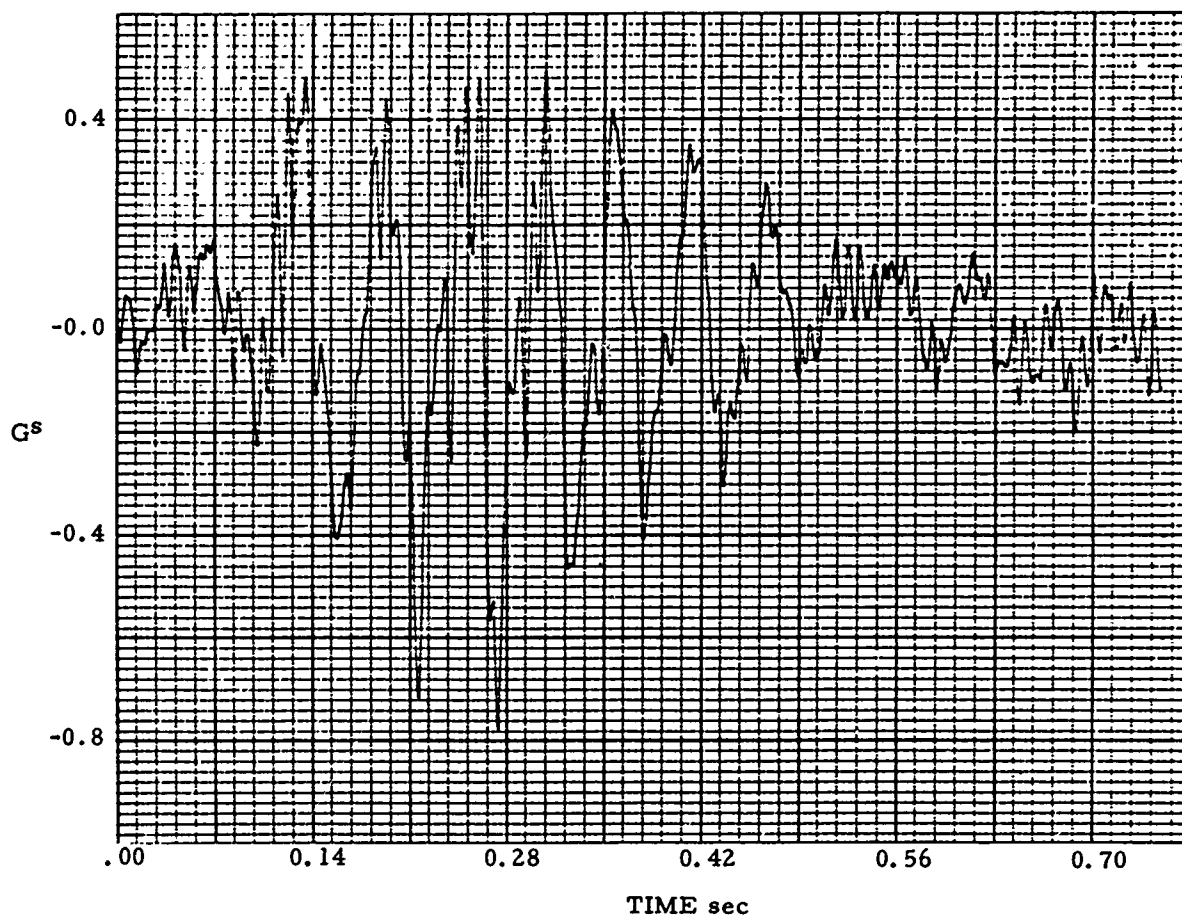
Fig. 2. Observed transient RA8 aft position

assumed Q of 10 represents the Q of the hypothetical oscillator. The theoretical steady state sine equivalent of the shock may be calculated simply by dividing the spectrum by the value of Q. The data were low pass filtered at 200 cps. Although not well defined, the spacecraft fragility at low frequencies was of greatest concern.

Although low pass filtered at 200 cps, the analyzed data are plotted to 100 cps only. It was determined that little energy existed above 100 cps. The reader should bear in mind that at frequencies below 5 cps the frequency response rolls off somewhat. The general trend of the data below 5 cps is probably valid, however.

The observed transient plot is useful as a cursory check of the shock amplitude envelope, but does not readily associate energy levels with frequencies. The shock spectrum plots must be referred to for frequency information, and will, therefore, be the basis of discussion in this report. A Q of 10 will be assumed to limit the quantity of data plots. Damping ratios of 0 and 0.025 were also used to compute shock spectra, but are not discussed in this report.

Three shocks measured by each vertical axis accelerometer in the Ranger 8 van were selected as data to compare the response of the three channels to a given excitation. The maximum envelope of the three shock spectra is plotted for each of the three locations in Fig. 4. The aft position response contains a peak at 18 cps, a notch at 25 cps, and a second major peak at 75 cps. The center and forward position responses peak at about 14 cps and decrease in level to a minimum at 25 cps, similar to the aft response. Below 40 cps the van center indicates the lowest level response. Above 40 cps, however, the center position becomes more severe than the forward section and approaches the amplitude of the aft response at 60 and 88 cps. It is apparent from the figure that the environment at all van locations produces a similar response below 40 cps, but is dominated by local dynamic characteristics above this frequency. The g response levels are quite low, with a maximum of 3.8 g pk. The equivalent sine input at this frequency would be 0.38 g pk.

Figure 5 compares the maximum shock spectra of 9 Ranger shocks, measured at the aft section, and 12 Surveyor shocks. The spread in

23

* ACCELERATION RESPONSE PEAK DURING EVENT
o ACCELERATION RESPONSE PEAK AFTER EVENT
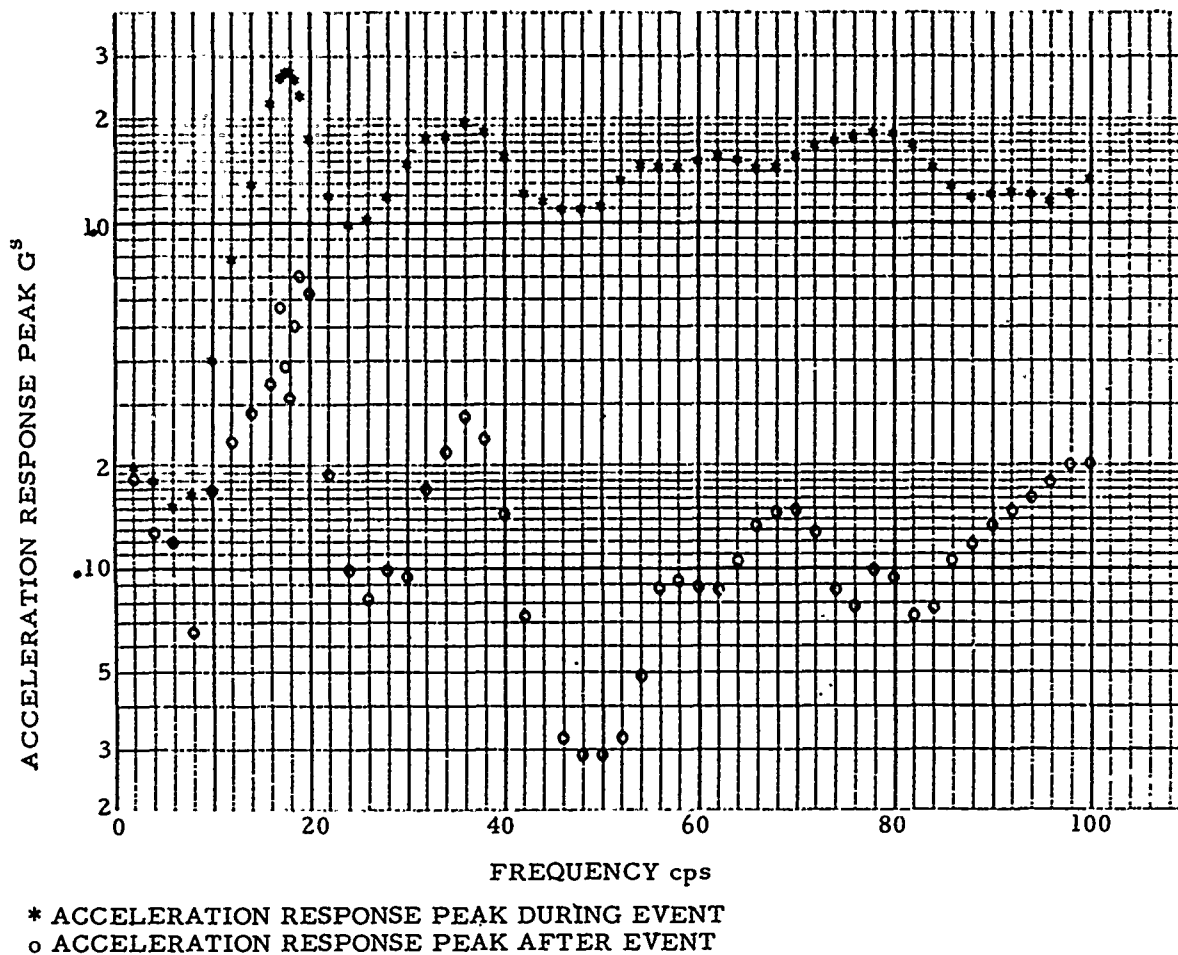
Fig. 3. Shock spectra RA8 aft position

response levels varies with frequency, although some consistency in the responses is apparent. An important similarity is the peak response at 13 cps in spite of the differences in vans, load weights, and distribution. This peak may result from phenomena such as wheel bounce. The Surveyor response is generally between 2 and 4 g pk, whereas the RA-8 response is primarily between 2 and 3 g pk. In both cases the energy levels of the response as a function of frequency generally increase above 25 cps.

Perhaps the most significant data yet presented are contained in Fig. 6. The shock spectra plotted in this figure present the maximum, 95 and 50 percentile levels of a data sample of 21 shock spectra, including 9 from Ranger 8, and 12 from Surveyor. The spectra were computed with an assumed normal distribution. The 21 spectra were all van aft position data. As in previous plots, peak amplitudes are very prominent at 18 cps, indicating a common van characteristic based on a significant sample of data.

The maximum peak amplitude of response is 6 g pk at 95 cps. The maximum amplitude at 18 cps is 4 g pk. The 95 percentile and maximum spectra have generally the same shape, with a maximum dispersion of about 1.5 g pk. The 50 percentile or average spectrum plot is also similar in shape, and often 2 g less than the maximum curve at various frequencies. This indicates that the spread or variation in shock levels is rather small. It is apparent from the spectra that shock-mounted equipment should have a system resonant frequency well below 18 cps.

The spectra presented in Fig. 6 could be used to establish transportation tests for equipment to be transported by air suspension van. The relatively large data sample provides confidence that the spectra envelop typical road shocks. Equipment degradation resulting from shock loading should be insignificant. The maximum equivalent sinusoidal input would be 0.6 g pk at 95 cps, if derived from maximum spectra of Fig. 6, or 0.4 g pk at 18 cps.
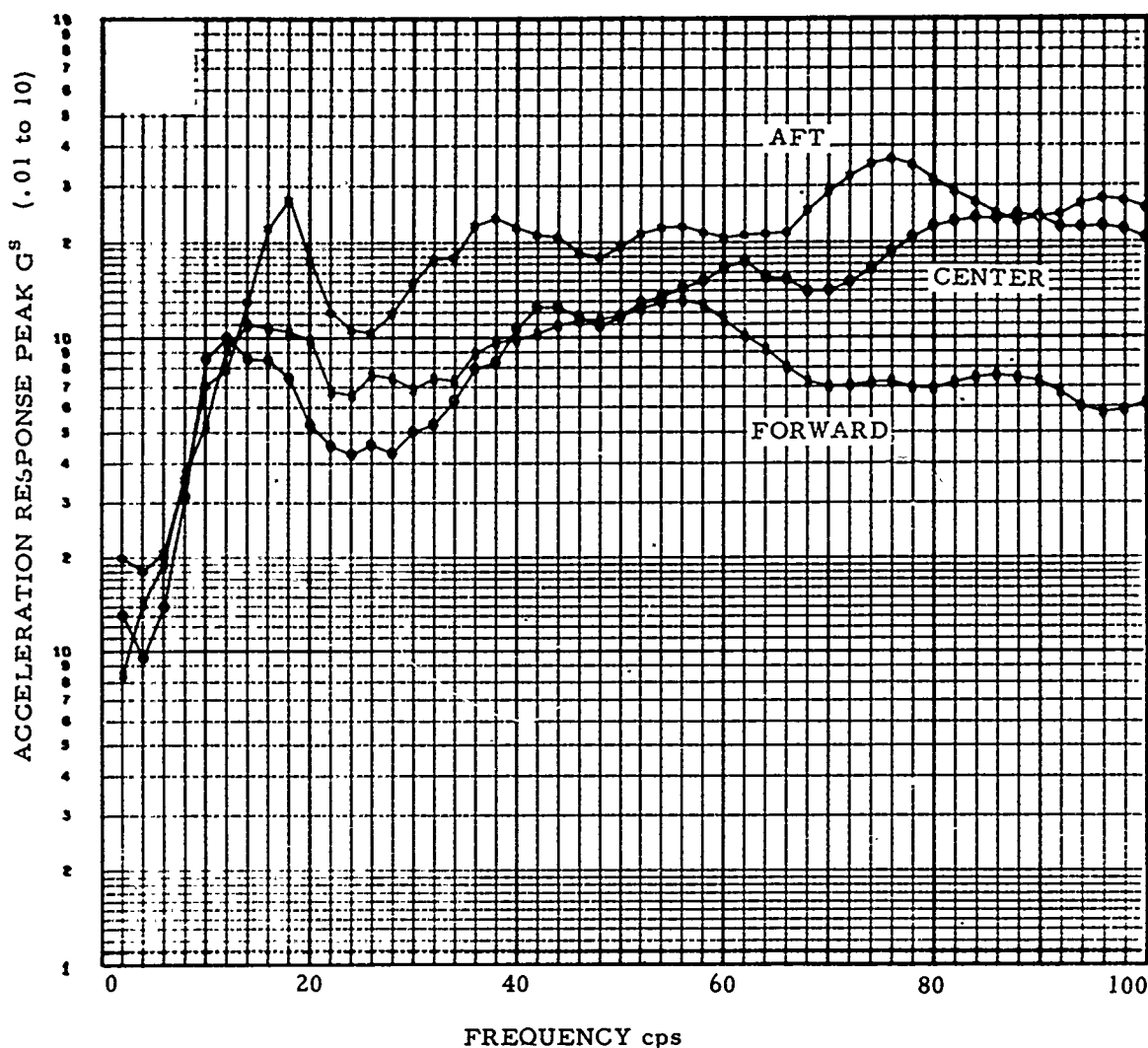
Fig. 4.   Maximum shock spectra RA8 aft, center, forward positions

Vibration Data Analysis

The results of vibration data analysis are contained in power spectral density (PSD) plots. The data selected for PSD analyses were low pass filtered at 180 cps. The accuracy of data below 5 cps is somewhat impared by frequency response roll off. Each plot contains the spectral density in db with a reference of 1 g^2/cps. The frequency scales start at 1 cps, and often include frequencies beyond 180 cps. Data beyond 100 cps are usually of little significance.

PSD's were computed from data measured in the Ranger Block III test, Ranger 8 shipment, and Surveyor model shipment. Both rough and smooth road data are presented. Data measurements during the Ranger Block III test are from rough or detour road surfaces only. The vibration data represent the same accelerometer locations as the shock spectra.

The maximum, 95 and 50 percentile level spectral densities of Surveyor shipment vibration data are shown in Fig. 7 for a normal distribution. The data measurements were made during rough road travel. The maximum and 95 percentile curves are very consistent and show little difference in amplitude. Below 9 cps, the average energy levels deviate from the maximum by 3 to 4 db. This difference decreases to about 2 db above 9 cps. An energy peak at 18 cps appears in the PSD's as it did in the shock spectra. However, a lower frequency peak at 12 to 13 cps is also contained in the PSD. All data samples used in this statistical analysis display the two peaks prominently, indicating a characteristic response of the van to road vibration. The spectrum shapes between 1 and 5 cps may be evidence of a van resonance in contrast to assumed wheel bounce excitation between 10 and 20 cps. The explanation for data characteristics cannot be made definitely at this time.
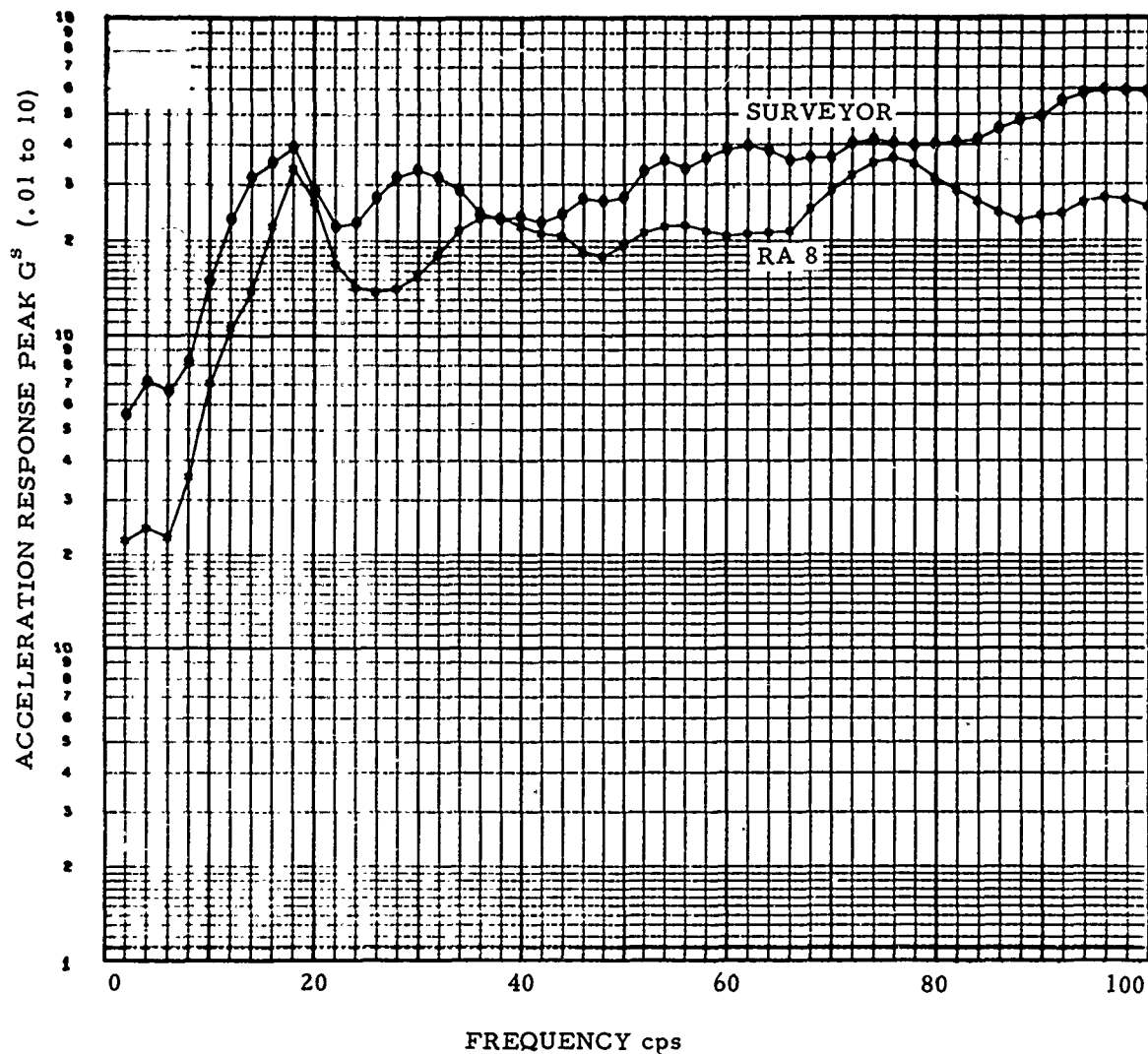
Fig. 5. Maximum shock spectra RA8 and Surveyor aft positions

Figure 8 compares the maximum PSD of rough road Surveyor data with smooth road Surveyor data. Both plots contain the characteristic peak at 18 cps and are very similar in spectral shape, with the exception of the frequency band 6 to 15 cps. In this region more peaks are displayed by the smooth road data. Amplitude differences between the plots substantiate a significant difference in road conditions. Energy differences of 4 to 5 db are common and often far exceed this. It is interesting to note that the greatest margin occurs at 12 cps. Low level excitation does not seem to excite this frequency, perhaps indicating a nonlinearity in the van.

Although not shown in the figures, the spread between the maximum density plot and the 50 percentile remained quite consistent between rough and smooth road data.

Figure 9 contains a composite of the maximum PSD envelopes at the three accelerometer locations in the Ranger Block III van. Each envelope was derived from a total of seven vibration data samples. As previously noted in the shock spectra, the measurements indicate both consistencies and inconsistencies between channels. Measurements at the van rear and middle positions contain a peak at 2 cps. The corresponding peak at the forward position occurs at 4 cps with an amplitude of -21 db. These peaks are probably van resonance frequencies. The second peak occurs at approximately 12 cps at all three locations, and may result from wheel bounce excitation. At 12 cps the spectral density amplitudes are close to -20 db at both the rear and middle positions. The level is greater at the front, however, and reaches a maximum of -15 db. Beyond 12 cps the rear and middle measurements roll off in amplitude, whereas the forward measurements indicate a peak at 35 cps.

It is apparent that the environment of the forward position was most severe during the

26
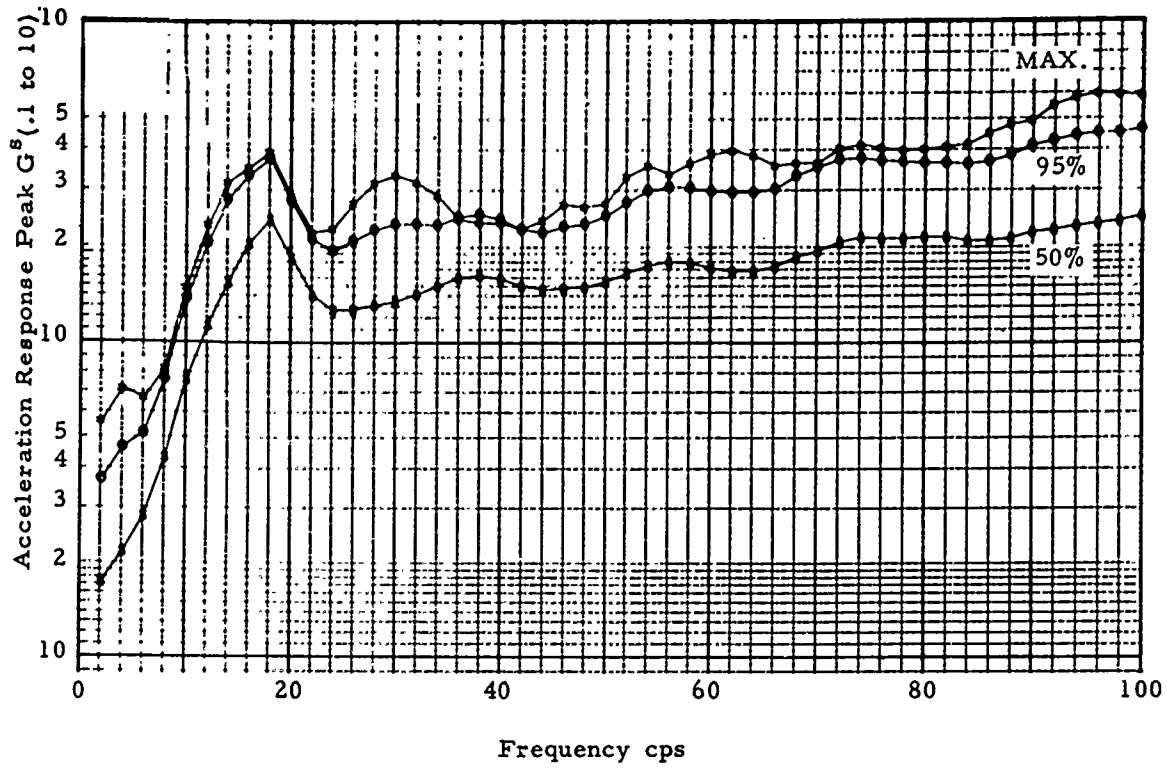
Fig. 6. Maximum, 95%, 50% level shock spectra RA8 and surveyor aft positions
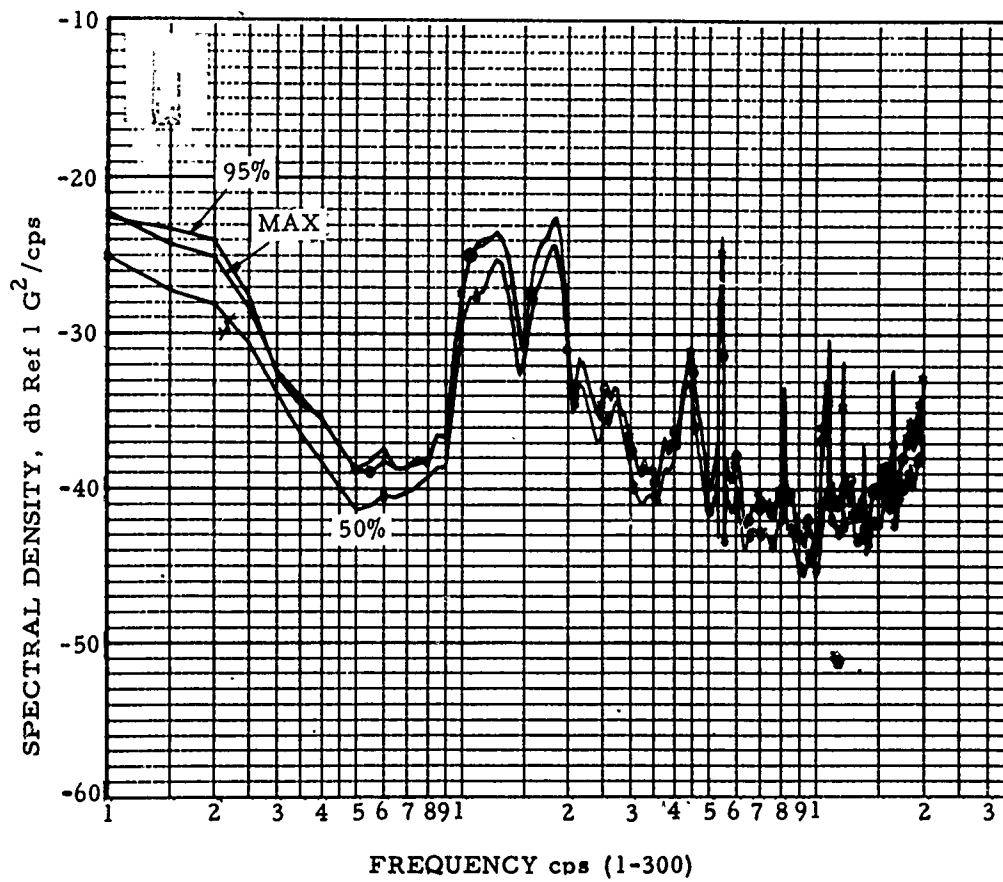
Fig. 7. Surveyor spectral density, maximum, 95%, 50%, rough road

27
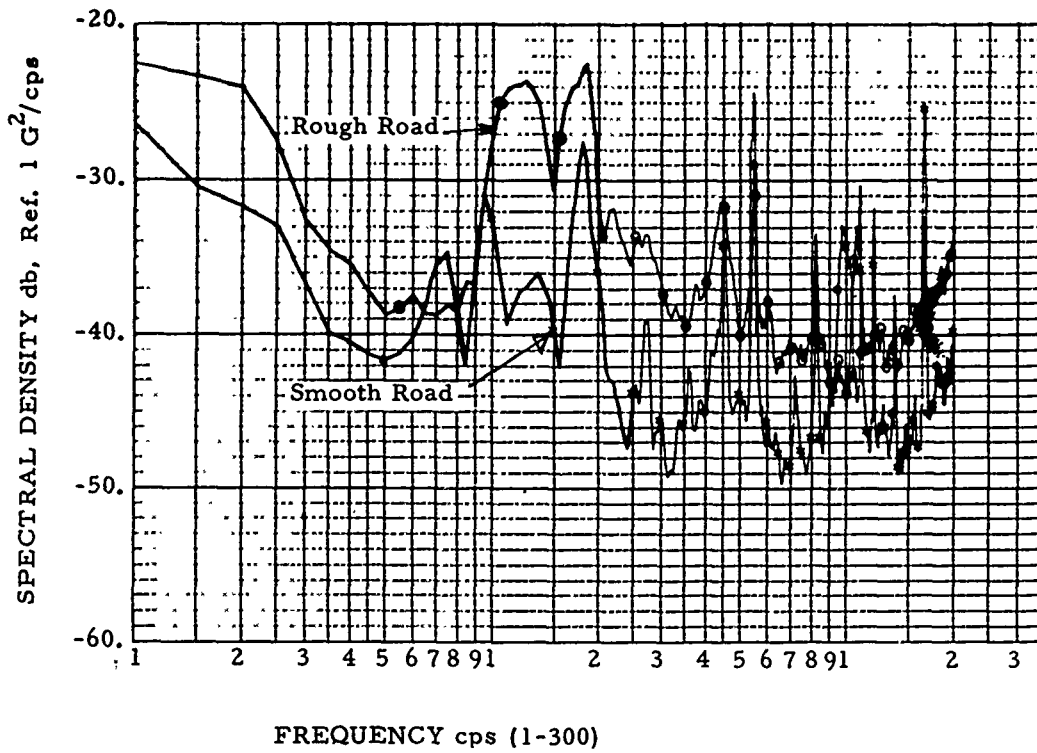
Fig. 8. Surveyor maximum PSD envelope — rough vs smooth road

SPECTRAL DENSITY db, Ref. 1 G²/cps

Rough Road

Smooth Road

FREQUENCY cps (1-300)
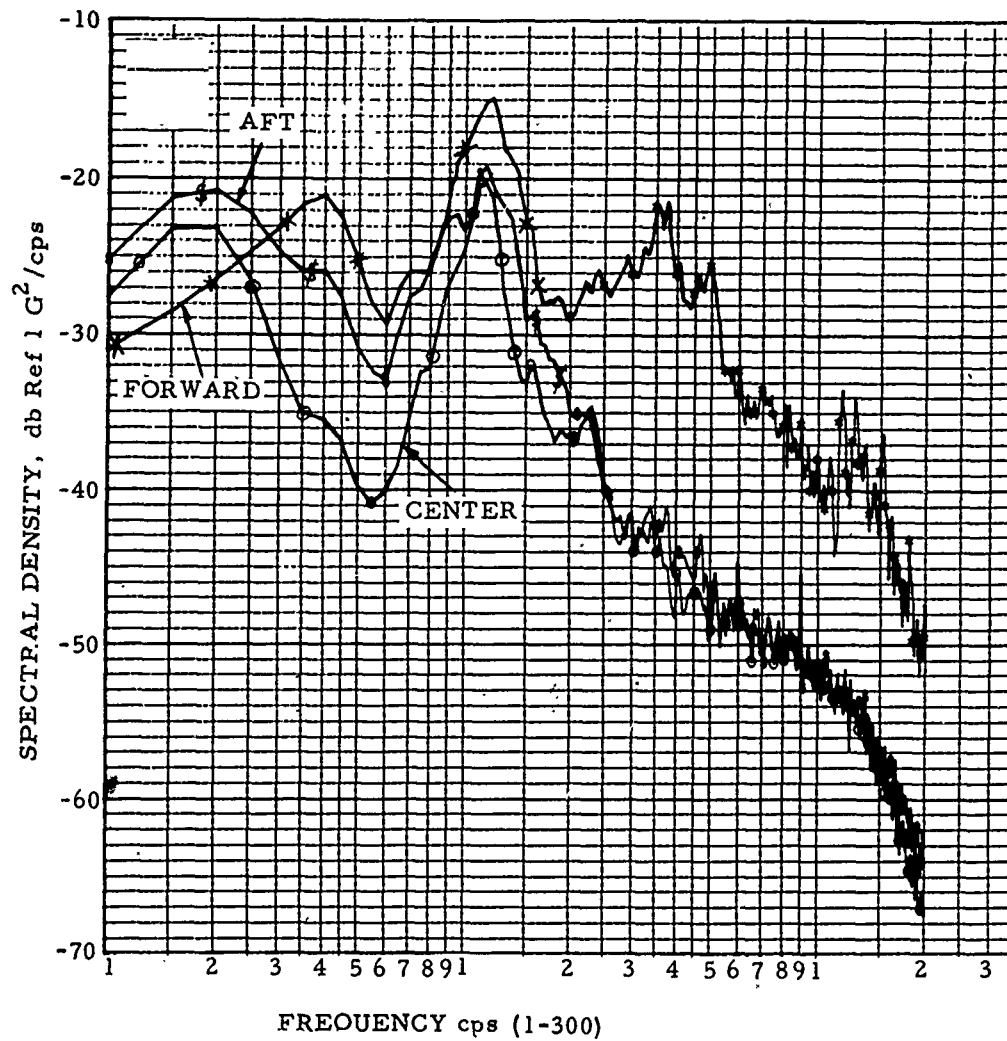
Fig. 9. Test — RA BLK III rough road — aft, center, forward position — maximum envelope PSD

SPECTRAL DENSITY, db Ref 1 G²/cps

AFT

FORWARD

CENTER

FREQUENCY cps (1-300)

28

RA Block III tests. At the 3-db down points of the forward position 12 cps peak, the spectral density value is -18 db, and is about 3 cps in bandwidth, producing a level of 0.22 g rms.

Figure 10 indicates a different comparison between the locations for RA-8. The aft spectral density has the greatest envelope with a few exceptional frequencies. The forward position is less severe below 2 cps, but exceeds the center measurements at higher frequencies. The comparison of amplitudes for the three locations varies with frequency, so that a maximum level position may become the minimum level position at a different frequency.

Figure 11 compares the maximum spectral densities of the aft position of the three van measurements. The important comparison to be made from this figure is the relative shape of plots. RA-8 and Surveyor vans indicate an energy peak at 18 cps. Ranger Block III data do not show a peak in amplitudes at 18 cps, but do peak at 12 cps, similar to the first peak of the Surveyor data. Both these peak frequencies should be considered if shock mounts are used.

The spread in amplitudes is of little significance, since the road conditions were different.

A plot of the maximum, 95 and 50 percent PSD levels computed from all PSD analyses is contained in Fig. 12. Normal distribution was assumed. Thirty-seven data samples are included in this statistical analysis. It is apparent in the figure that a considerable difference in amplitude exists between the curves because of the varied surface conditions represented. The RA Block III measurements were made over a very rough detour road, whereas RA-8 and Surveyor measurements are from highway driving. These energy levels, therefore, cover severe, rough highway and normal surface conditions and should envelop the vibration environment of any eventuality in a cross-country trip (barring accidents). Again the peak frequencies of 12 and 18 cps are prominent. An energy amplification is also indicated at 2 cps.

In general, the vibration data presented indicate low energy levels at all frequencies within the 1 to 180-cps band of analysis. Approximately 56 PSD's were included in the data
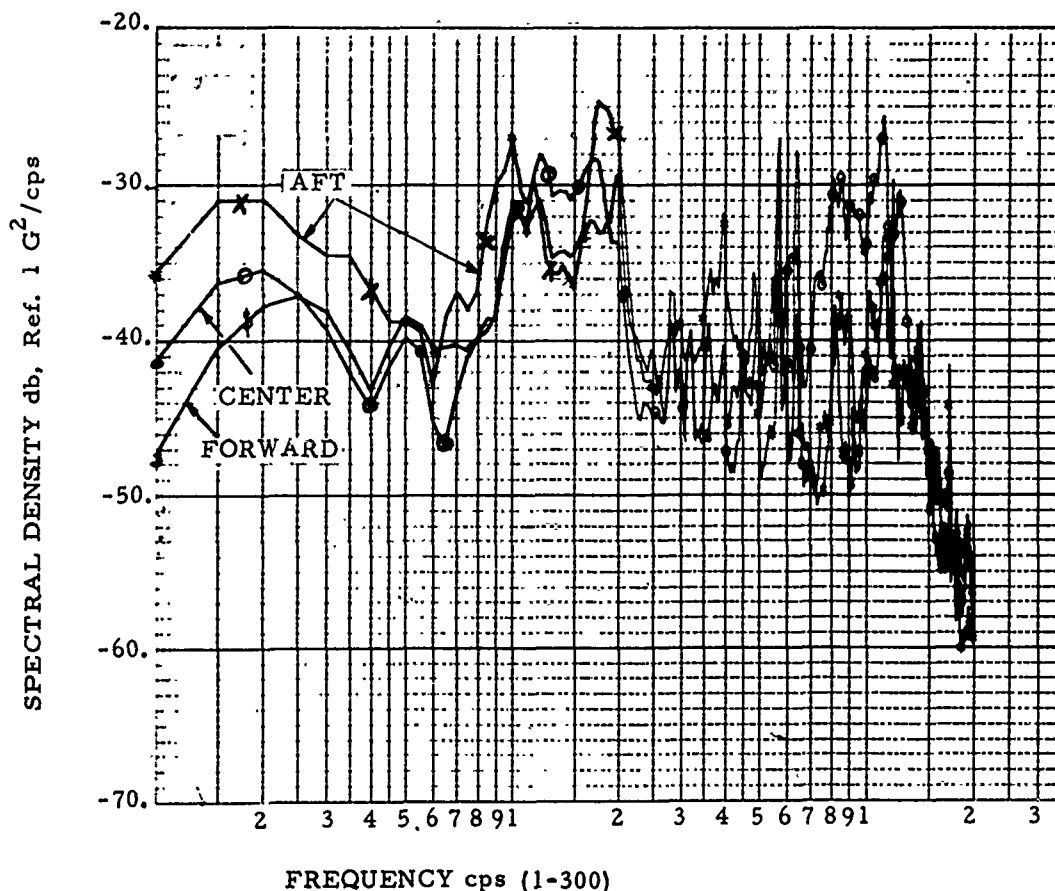
Fig. 10. Test — RA8 power spectral density — smooth road — maximum envelope aft, center, forward positions

29
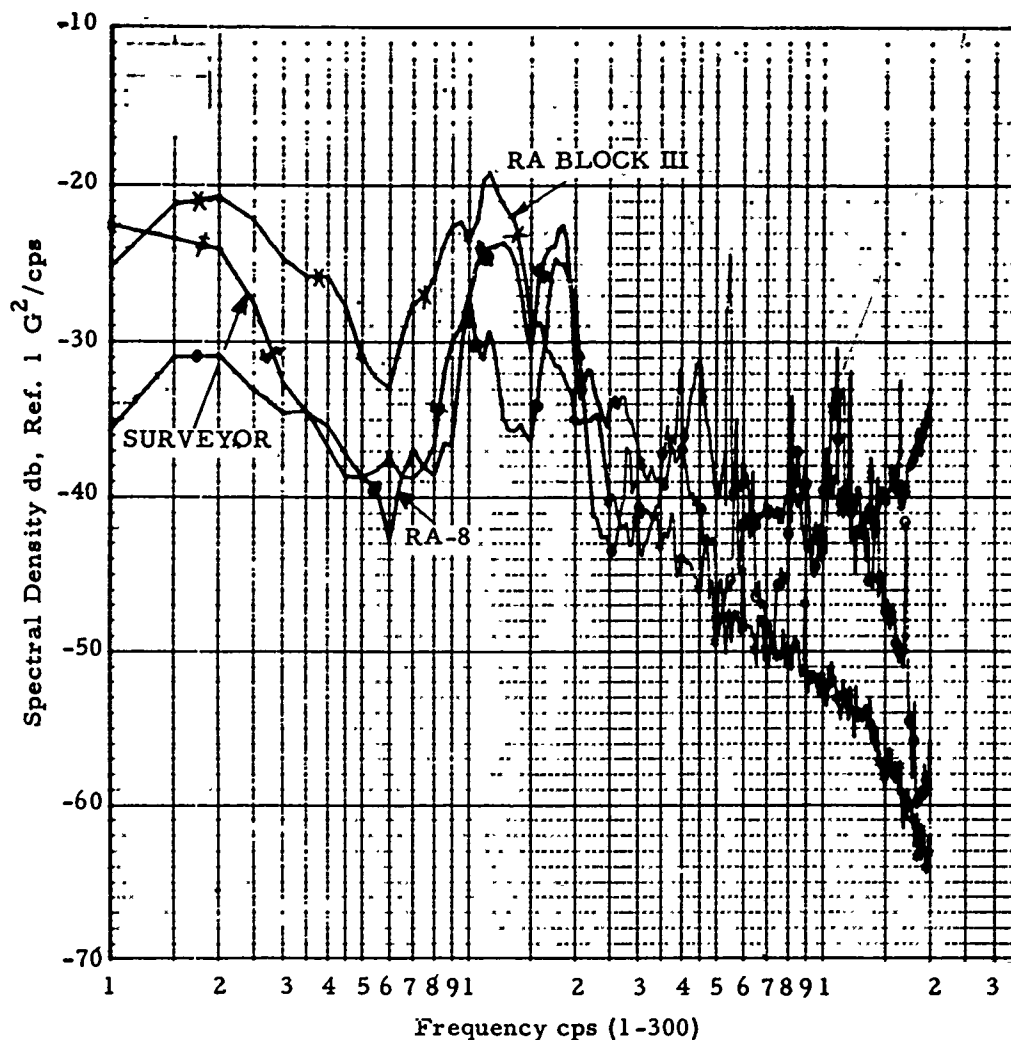
Fig. 11. Maximum PSD levels — RA Block III, RA8, Surveyor aft position

presented. The maximum amplitude of vibration contained in the plots is -19 db at 12 cps. The attenuation of this amplitude depends on the frequency, but is usually significant. It should be noted here that Fig. 9 contains a -15-db peak at 12 cps. This peak energy was measured at the forward position of the van, however, and is not contained in the plots of Fig. 12, which cover only the center and aft positions. Figure 12 does envelop, therefore, the vibration energy at the recommended van locations for installing payload equipment.

No discussion of the longitudinal and horizontal axis data is included in the report. The measurements in these axes were as much as 40 percent less than the vertical axis measurements.

CONCLUSIONS

Based on JPL's experience with the measurement and analysis of transportation data, the following conclusions can be drawn from the data presented, and from the instrumentation discussion in the appendix (the appendix on instrumentation was warranted by significant problems in this area):

1. The shock and vibration environment of an air suspension van should present no degradation problems if safe driving regulations are imposed on the truck operator and no accidents occur. Speed limits and periodic truck inspections should be imposed regulations.

2. Equipment should be hard-mounted to the floor of the van if the dynamic characteristics of a support structure or shock mount have not been accurately determined. The mount or structure dynamics may be coincidentally "tuned" to the input and amplify the response. The amplitudes measured at the van floor are rarely greater than 1 g pk. At low frequencies the center of the van floor, lengthwise and width, has the less severe environment.

30
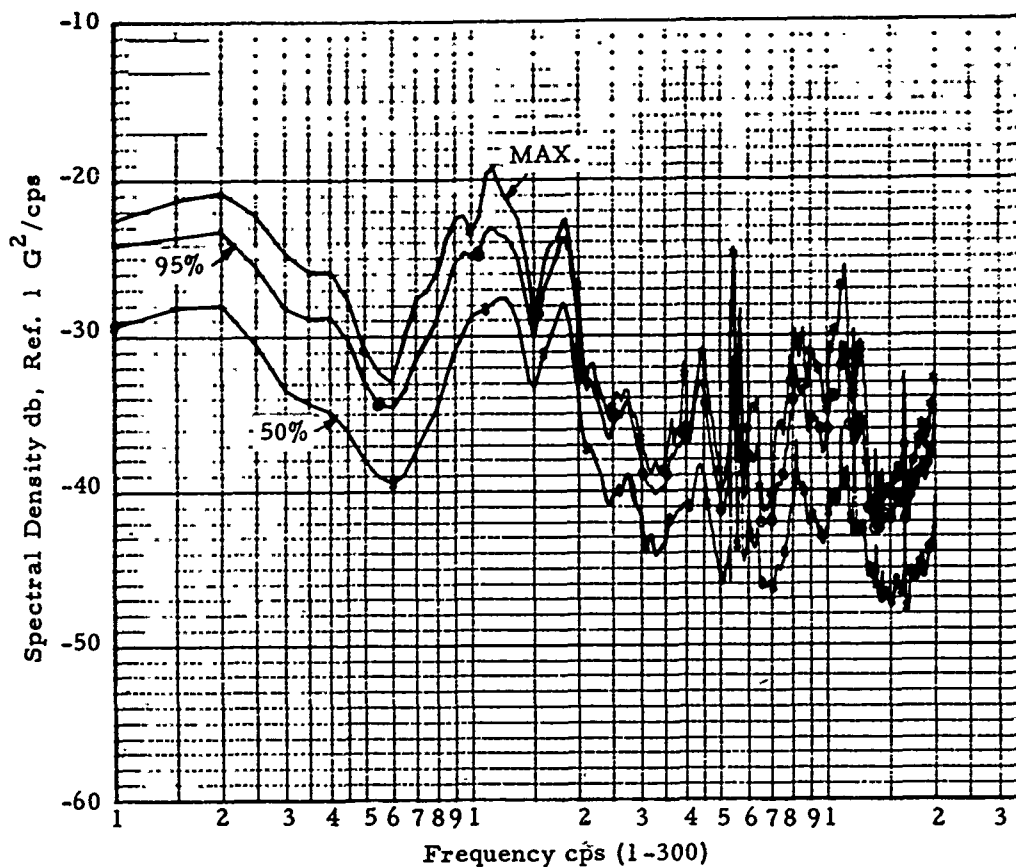
Fig. 12. Maximum, 95%, 50% PSD levels — RA Block III, RA8, Surveyor
aft and center positions

3. The position of least vibration or shock severity in a van is dependent on the frequency, the individual van characteristics, and to some extent the amplitude of excitation. The aft and center positions seem most consistent, although their amplitudes often exceed those in the forward position. For this reason, it may be desirable to design shock mounts for the aft or center positions if mounts are required. The center and aft positions are most predictable.

4. When selecting the mode of instrumentation for a van shipment, forethought should be given to the purpose of the instrumentation. The underlying reason for data acquisition should influence the sophistication of the instrumentation, the location of transducers, the mechanical recorders, the sampling of data required, and the final data analysis.

5. Magnetic tape recorders should be selected with caution for this application. The

tape transport definitely should be a closed loop design (as discussed in the appendix).

6. A method should be developed to code the magnetic tapes if a tape recorder is used. Time coding is required for identification/ computer control for shock or PSD analysis, and correlates events with road conditions.

7. A reference channel should be included with data channels as a means for cursory evaluation of data quality and for identification of microphonics.

8. The requirement for shock and vibration measurements aboard an air suspension van is important primarily to record the loading that may occur in the event of an accident. Normal surface transportation should produce little concern.

31

APPRAISAL OF INSTRUMENTATION TECHNIQUES

The effort involved in acquiring transportation vibration data has resulted in considerable revision of instrumentation techniques. Since the final data quality is dependent on the instrumentation, a brief appraisal of instrumentation techniques is warranted.

PIEZOELECTRIC ACCELEROMETERS

The data discussed previously were measured with piezoelectric or crystal accelerometers. These accelerometers, or other electrical accelerometers with the same capabilities, must be used to record data signals adaptable to detailed analysis.

The accelerometers used in the JPL studies were 1-oz instruments with a frequency response of 2 to 7000 cps. An advantage realized with these accelerometers is their minute size, which facilitates installation. Charge amplifiers were used to amplify the input to the tape recorder. They were set at 3 g pk full scale. The full-scale voltage output of the amplifier was attenuated with a series resistor, making the amplifier output compatible with the recorder full-scale deviation, but yet maintaining low frequency response.

Associated with the use of electrical accelerometers is the tape recorder. Two different tape recorders were used in the JPL data acquisition. Both recorders were made by the same manufacturer but differed in the number of channels available. The recorder used in the evaluation tests was a 14-channel recorder, whereas the other used for the S/C shipment was a 7-channel machine. A motor generator set powered the recorders, since van power was not available.

In each application, the data were acquired in the FM mode. The standard FM carrier frequency related to the record speed was direct-recorded on the reference channel. No transducer outputs were recorded on this channel.

The primary function of the reference channel was to identify data distorted by recorder wow and flutter. This provided further assurance that data selected for analysis were valid and not recorder microphonics. As was expected, the channel did indicate periods of spurious noise, most commonly during the RA-8 shipment when a record speed of 1-7/8 ips was

used. Wow and flutter were problems in spite of an attempt to shock isolate the recorder. In vibration tests conducted prior to shipment, the shock mount system demonstrated a resonant frequency of 4 cps, which was acceptable, assuming the dominant van excitation would be from wheel bounce at approximately 12 cps. The attenuation of the isolation mount was approximately 50 percent at 12 cps. The maximum gain or amplification was 2.5 at 4 cps. The recorder was operational during the shake test and recorded a 10-cps sine wave as a reference input. The point to be made here is that the recorder was the weak link in the instrumentation chain and caused some loss of data. Recorder deficiencies are avoided, however, if the recommendations below can be followed:

1. A recorder with a closed loop tape transport should be used. The JPL recorder was an open loop machine and was not designed for the application. Figure A-1 depicts a closed loop transport as compared to the open loop in Fig. A-2. The closed loop transport is designed to maintain a constant tape velocity over the record head, regardless of transient changes in the tape reel speeds. It also maintains contact between the tape and record head.

2. As high a record speed as possible should be used if the recorder does exhibit susceptibility to shock and vibration. The record speed seemed to influence the recorder's susceptibility to its dynamic environment. Data recorded at 7-1/2 and 30 ips showed much less evidence of distortion than the 1-7/8-ips data. Data recorded at 30 ips was "cleaner" than those at 7-1/2 ips. Since the data channels were FM recorded, the record speed did not affect the low frequency response, which would indicate that a steadier tape velocity across the record head must exist at higher speeds because of tape reel inertia.

3. Arrangements far in advance of the shipment should be made to perform an evaluation of the recorder's ability to operate in the service environment. If necessary, corrective measures can be taken to improve the probability of quality data acquisition.

"Off the shelf" recorders are available that have been designed for operation in a dynamic environment. If the application requires sophisticated instrumentation, these recorders should certainly be considered.
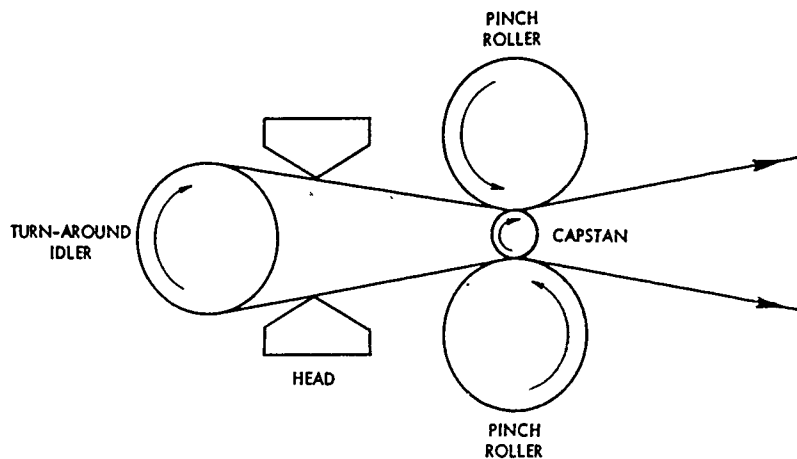
Fig. A-1. Closed-loop tape drive
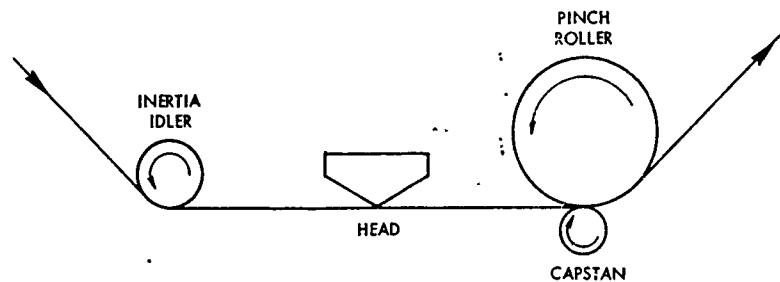
Fig. A-2. Open-loop tape drive

MECHANICAL SHOCK RECORDERS

An immediate appraisal of the amplitudes of shock and vibration occurring during transportation of delicate equipment is often requested by cognizant personnel. An instrument applicable to this requirement is the mechanical shock recorder. These devices simply count the occurrence of amplitudes of shock and vibration that exceed calibrated g levels. No frequency information or time correlation can be obtained from the shock recorder. Typical g level calibrations on a 4-channel recorder are 1, 2, 3, 4 g.

A number of these recorders have been used by JPL in parallel with the accelerometer instrumentation for checks of amplitudes enroute. Most of the devices were 4-channel accelerometers calibrated at 1, 2, 3 and 5 g.

Prior to use, these recorders were tested on a shaker for calibration data. A set of sample calibration curves is shown in Fig. A-3. The vibration input consisted of narrow band noise at selected center frequencies. A noise source was routed through a tracking filter to obtain the 1.5- to 5-cps narrow band noise. Center frequencies were 15, 20, 25, 30, 40 and 50 cps and the noise duration in each test was 60 sec.

The rms amplitude of the noise was limited by the shaker displacement at the lower frequencies, but at 25 cps and above, all 4 channels including the 5-g channel were actuated. The curves in Fig. A-3 were derived from amplitude density plots of the input vibration. Figure A-4 contains a density plot of 1.5-cycle bandwidth noise. With the noise duration and the center frequency known, the number of peaks with amplitudes corresponding to the recorder channels were calculated. The percent deviation in the calibration curves is the percent difference between the recorder channels and the actual number of input peaks at each center frequency. Negative percentages indicate the recorder count was below the actual number of peaks. A sample calculation is shown below for clarification. The plot of Fig. A-4 contains the distribution of peaks at the center frequency of 25 cps, with a noise bandwidth of 1.5 cps. The calculations are performed for the 1 g channel:

33
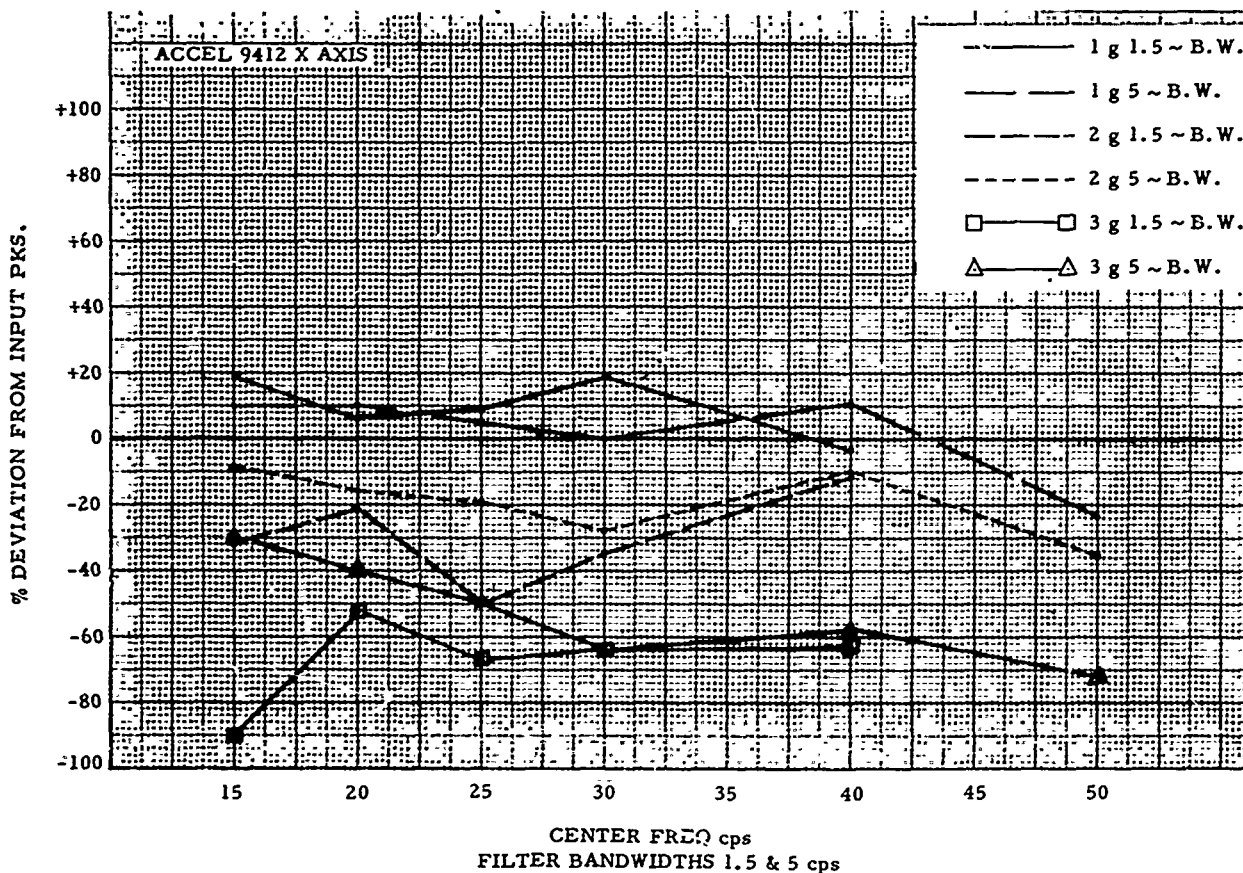
Fig. A-3. Mechanical accelerometer calibrations

1. Plot indicates 65 percent of peaks are less than 1 g; therefore, 35 percent are equal to or greater than 1 g.

2. Total number of input peaks = center frequency × duration × 2 = 25 × 60 × 2 = 3000.

3. Total number of peaks exceeding 1 g = percent from step 1 above × total peaks = 0.35 × 3000 = 1050.

4. Mechanical recorder 1 g counts = 1166.

5. Percent deviation = 116/1050 = 11 percent.

The plots of Figs. A-3 and A-5 indicate the following mechanical recorder characteristics:

1. The percent deviation between actual number of peaks and the recorder counts is quite high for most channels. These percentages are, of course, affected by the tolerances in time duration of the noise and by the reading of the density plot data.

2. The recorders demonstrate a lack of consistency in side by side tests. This is demonstrated by Figure A-5, which is a composite plot of two accelerometer calibrations performed with the units mounted side by side. The curves have different values for comparative channels.

One probable cause for recorder "readings" being below the input values is the tendency noted of some channels to stick when the counter contains an arrangement of digits such as 999. This seems to be a deficiency in the mechanism.

The use of mechanical recorders should not be discounted, however, in spite of the problems noted above. The JPL data curves indicate that the devices are useful tools for convenient shock and vibration amplitude measurements at the most predominant levels of 2 g or less. In general, the suitability of instrumentation techniques is dependent on the data parameters required, the sensitivity of the payload to the environment, and the funding and manpower available to support the project. In many applications, adequately calibrated mechanical accelerometers cr recorders are most practical.

Calibration of the mechanical recorder can require considerable effort and planning.

TEST RA STAT ACCEL EVAL	STANDARD DEVIATION = 2.3418	NO. OF DATA PTS = 0.1600E05
LOCATION REF BLOCK XAXIS	TIME = 25 CY CF 1.5 CY BW	SC = -0.5652E-01
MEAN = 0.2304E-00	SAMPS/SEC = 800.0000	KC = 0.3235E-01
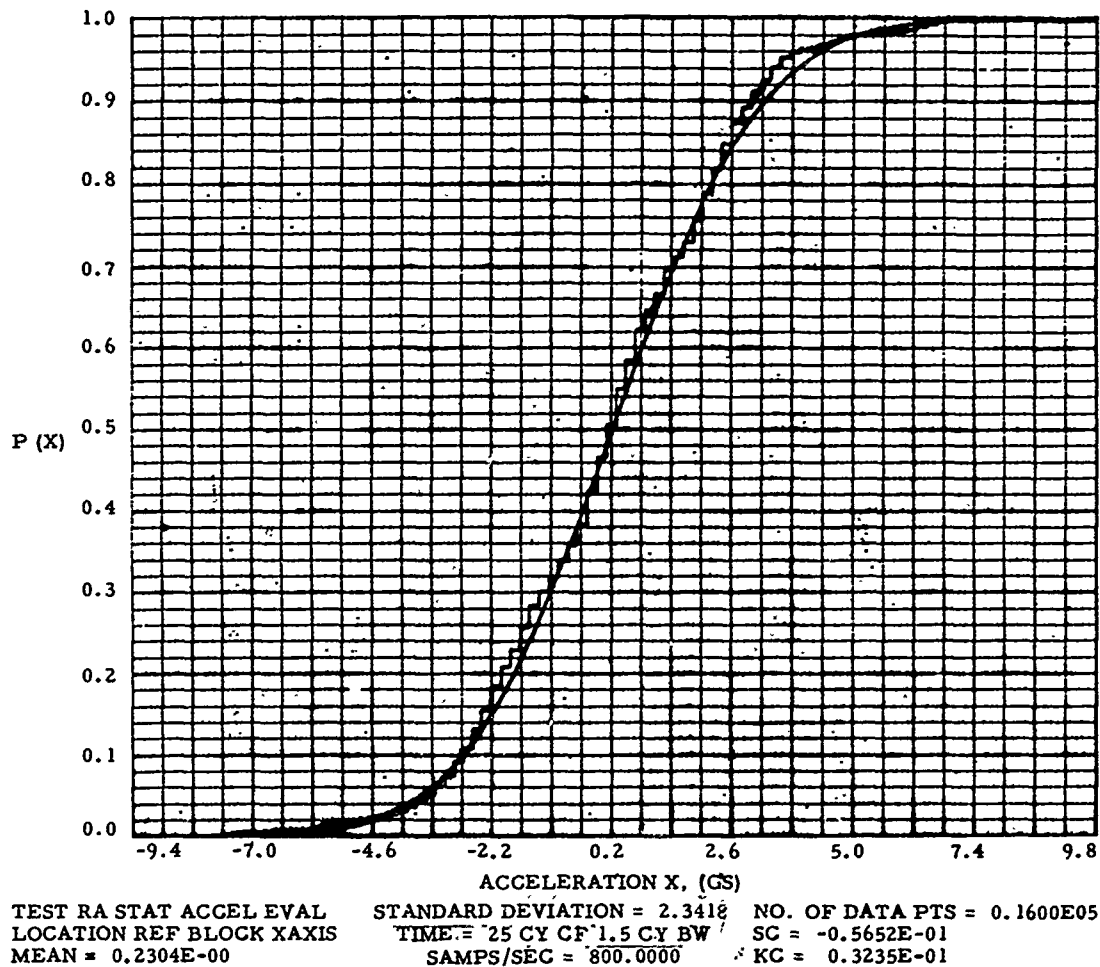
Fig. A-4. Probability distribution function peak acceleration

Figure A-3 indicates that the recorder response varies with noise bandwidth and frequency. Figure A-5 gives evidence the recorders are inconsistent from one unit to another. These limitations require each channel of each unit to be calibrated, and to be calibrated for the predicted service environments, if reasonable accuracy of measurements is required.

In the case of the recorders evaluated by JPL, narrow band noise of 1.5- and 5-cps bandwidths was used to simulate the service environment excitation. Shaker displacement limitations eliminated center frequencies less than 15 cps, which is unfortunate since the calibration data proves that the accuracy increases as the frequency decreases. However, the calibrations are adequate in that the minimum center frequency of 15 cps does put the prominent peak at 18 cps within the calibration frequency range. These peaks are generally 3 to 4 cps at the 3-db down points, which is compatible with the calibration bandwidths of 1.5 and 5 cps. The JPL calibration should be adequate for an "in the ball park" idea of the vibration and shock maximum amplitudes. If transients or significant vibration amplitudes are noted in a sampling of data from a trip, the shock recorders provide useful information in estimating the number of these amplitudes that occurred.
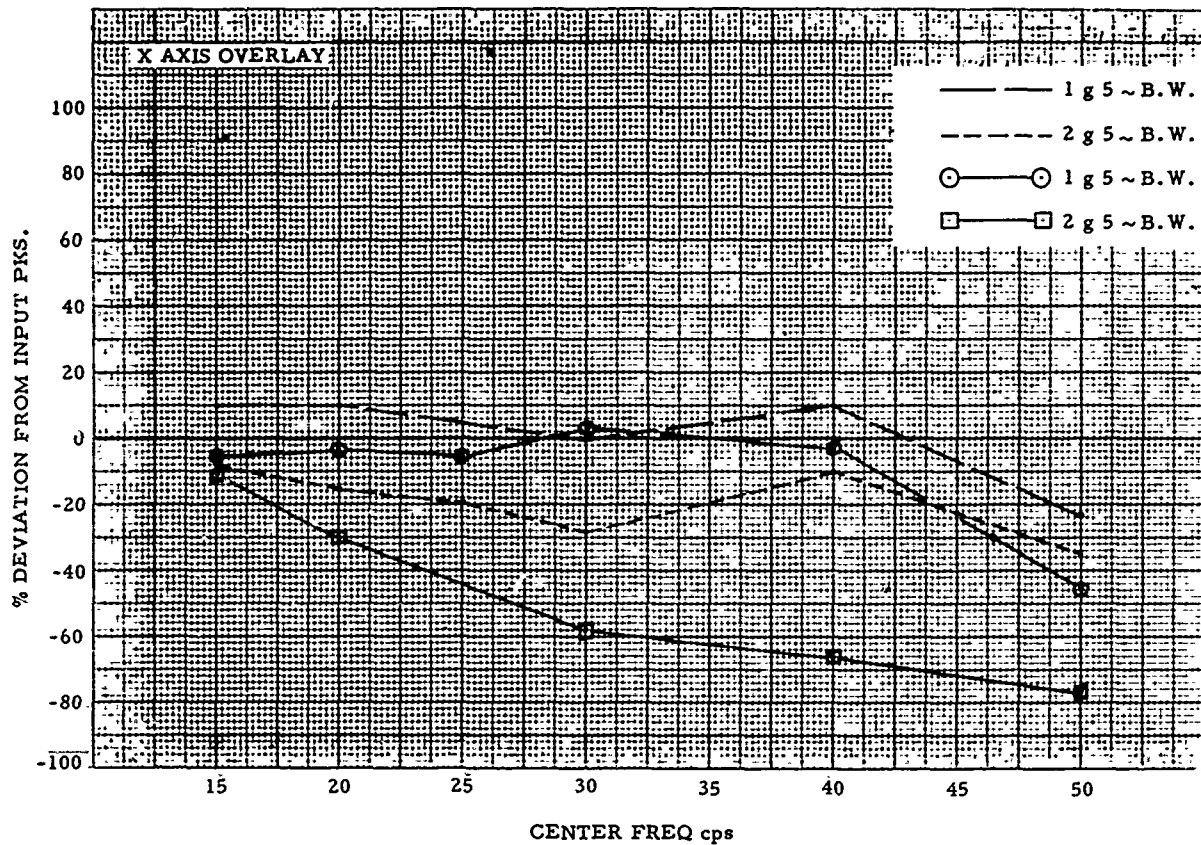
Fig. A-5. Comparison of two mechanical accelerometer calibrations

DISCUSSION

Mr. Clevenson (Langley Research Center): In the first set of shock spectrum slides you show several responses. Would you tell us what value of Q you are assuming, and give your reasons for using that particular value?

Mr. Schlue: We are using a Q of 10. We use our shock program and compute the response with a Q of 10, a Q of 20, and damping ratios of 0.025, 0.05 and 0. In this case we are using an 0.05 damping ratio. Another reason that we are using a Q of 10 is that this is a conservative approach in terms of the equivalent sine. The spectral amplitudes are not proportional to the ratio of the Q's.

*   *   *

A REALISTIC DERIVATION OF A LABORATORY
VIBRATION TEST TO SIMULATE THE OVERLAND
TRANSPORTATION ENVIRONMENT

John A. Kasuba
Aberdeen Proving Ground, Maryland

This paper treats the problem of deriving a vibration schedule for securely tied down vehicle cargo. The derivation is based on the principle of equivalent damage which relates the severity of the field and laboratory environments. This principle was applied in deriving an automotive test schedule to simulate the overland cross-country and paved road transportation environments of truck, tracklayer, and trailer-type vehicles. The automotive test schedule was combined with the existing aircraft test schedule to present a more complete transportation environment.

INTRODUCTION

The primary objective of this paper is to present the techniques used to develop a laboratory vibration test schedule having damage potential equivalent to that encountered in actual overland transportation environments.

The initial test schedule was developed at Aberdeen Proving Ground in 1963 (1-3). It was derived from data gathered on several representative vehicles operating on fixed profile courses. In the opinion of Development and Proof Services personnel, the Belgian block and paved road courses for wheeled and tracked vehicles, respectively, were adequately severe to simulate cross-country behavior. However, it was felt that testing on cross-country courses would have been desirable. This was not possible because course selection was dictated by a landline data acquisition system.

The acquisition of a radio telemetry system removed the restriction on course selection; thus, the derivation of a new standard was undertaken to incorporate cross-country operation, to gather data on vehicles previously not tested, and generally to make a more extensive study of vehicle behavior. The automotive test schedule so derived was combined with the existing aircraft test schedule to present a more complete transportation environment.

THEORY OF SCHEDULE DERIVATION

Description of Cargo

It will be assumed for the present that vehicle cargo can be represented by a one-degree of freedom mechanical system with known characteristic constants. Consequently, the natural frequency, the Q and the bandwidth of the system can be calculated. The first two quantities indicate where, in the frequency spectrum, resonance will occur and how much damping is present to prevent violent vibration. The bandwidth spans the frequency region between the half-power points of the amplification factor and indicates the region of high amplitude response.

The inputs to the mechanical system are obtained by recording cargo-bed accelerations on magnetic tape in analog form. The signals from the tapes are then filtered with a pass-band filter whose center frequency and bandwidth correspond to the natural frequency and bandwidth of the mechanical system. The filtered data represent that portion of the entire frequency spectrum which could cause the mechanical system to fail by fatigue failure.

Fatigue Failure and Damage Potential

The degree to which a material is able to withstand repeated stress reversals is indicated by S-N curves. The general equation for these curves, which are straight lines on log-log coordinates, is given by

$$SN^A = R, \qquad (1)$$

where S is the stress level, N the number of reversals at S to cause failure, A the slope of the line, and R a constant.

When a material is subjected to several levels of alternating stresses, failure cannot be predicted by S-N curves alone. In this case, a theory of cumulative damage such as Miner's criterion must be used. The mathematical expression for this theory is

$$\sum_{i=1}^{z} \frac{n_i}{N_i} = C \qquad (2)$$

where

Z = number of different stress levels,

n_i = number of stress reversals experienced at a stress level S_i,

N_i = life at stress level S_i as indicated by the S-N curve, and

$\dot{C}$ = indicator of damage accumulation.

According to the theory, failure occurs when C = 1; however, experiments indicate that C varies to some extent. Assigning a value of C can be avoided by requiring that an item subjected to a multiplicity of stress cycles at many stress levels experience the same damage potential at a single stress level. Under these requirements Eq. (2) becomes:

$$\sum_{i=1}^{z} \frac{n_i}{N_i} = \frac{n_e}{N_e}, \qquad (3)$$

where

n_e = number of stress reversals at a stress level of S_e, and

N_e = stress reversal life of the item at a stress level S_e.

A combination of Eqs. (1) and (3) yields:

$$\sum_{i=1}^{z} n_i(S_i)^{1/A} = n_e(S_e)^{1/A}. \qquad (4)$$

Furthermore, since the stress level is directly proportional to acceleration, Eq. (4) becomes:

$$\sum_{i=1}^{z} n_i(g_i)^{1/A} = n_e(g_e)^{1/A}. \qquad (5)$$

The combination of n_e and g_e thus describes the time and amplitude of a sinusoid which has the same damage potential as several sinusoids of different amplitudes. Furthermore, if the unknown quantities, that is, n_i, g_i, and $1/A$ of Eq. (5) could be determined, then a simulation schedule for the mechanical system could be established.

The results of the one-degree of freedom mechanical system example can now be summarized. It was assumed that both the description of the cargo and the excitation to which this cargo was subjected in the field were available. A simulation schedule had to be obtained which would expose the cargo to the same damage or damage potential to which it would be exposed in the field. This could have been done by obtaining the number of times, n_e, a single level of sinusoidal acceleration, g_e, would be applied to meet the necessary requirements. It is important to note that this procedure did not exclude any levels of acceleration; it considered the frequencies which are expected to cause damage, and it applied the principle of equivalent damage.

Independence of Material Proof

The distribution of positive or negative peaks within the bandwidth of filtered data was nearly Gaussian. The distribution is expressed by

$$n = \frac{2N}{\sqrt{2\pi}\,\sigma} e^{-\frac{g^2}{2\sigma^2}}, \qquad (6)$$

where

n = frequency of occurrence of peaks,

N = number of cycles in the data sample,

σ = rms value of acceleration within the passband, and

g = peak values.

38

The substitution of this equation into Eq. (5) after the summation is taken to the limit yields:

$$n_e(g_e)^{1/A} = \frac{2N}{\sqrt{2\pi}\,\sigma} \int_0^\infty (g)^{1/A}\, e^{-\frac{g^2}{2\sigma^2}}\, dg. \quad (7)$$

In the absence of excessive shock, it is highly unlikely that a peak acceleration of either infinity or in excess of 3.5 times the standard deviation is possible. Introduction of these limits and a new variable defined by

$$u = \frac{g^2}{2\sigma^2} \quad (8)$$

yields

$$n_e(g_e)^{1/A} = \frac{2^{1/A}\sigma^{1/A}N}{\sqrt{\pi}} \int_0^{\frac{(3.5)^2}{2}} u^{\left(\frac{1}{2A}-\frac{1}{2}\right)} e^{-u}\, du. \quad (9)$$

The solution of this equation is given by an incomplete gamma function which, after rearrangement of terms, becomes:

$$\frac{n_e}{N}\left(\frac{g_e}{\sigma}\right)^{1/A} = \frac{2^{1/2A}}{\sqrt{\pi}}\, \Gamma\left(\frac{1}{2A}+\frac{1}{2},\, \frac{(3.5)^2}{2}\right), \quad (10)$$

where n_e/N is the time-scaling factor and g_e/σ is the amplitude-severity scaling factor. The solution is shown graphically in Fig. 1. A relatively limited range of amplitude scaling factors is shown since it is undesirable to increase the level of simulation acceleration beyond that actually present in the field environment.

The figure indicates that when the severity and time scaling factors are approximately equal to 3 and 0.02, respectively, the test schedule applies for any material having a 1/A value between 5 and 20. This range is so wide that it includes most materials; thus, the limitation imposed by selection of A is removed and the test schedule may be applied to any material.

Generalization

Initially, it was assumed that vehicle cargo could be represented by a one-degree of freedom mechanical system with known characteristic constants. Generally, this is not true; such an accurate description of cargo is not available. A more realistic assumption is that cargo can be represented by many one-degree of freedom subassemblies, all having different characteristic constants. In this case, the amount of data filtering must be based on a
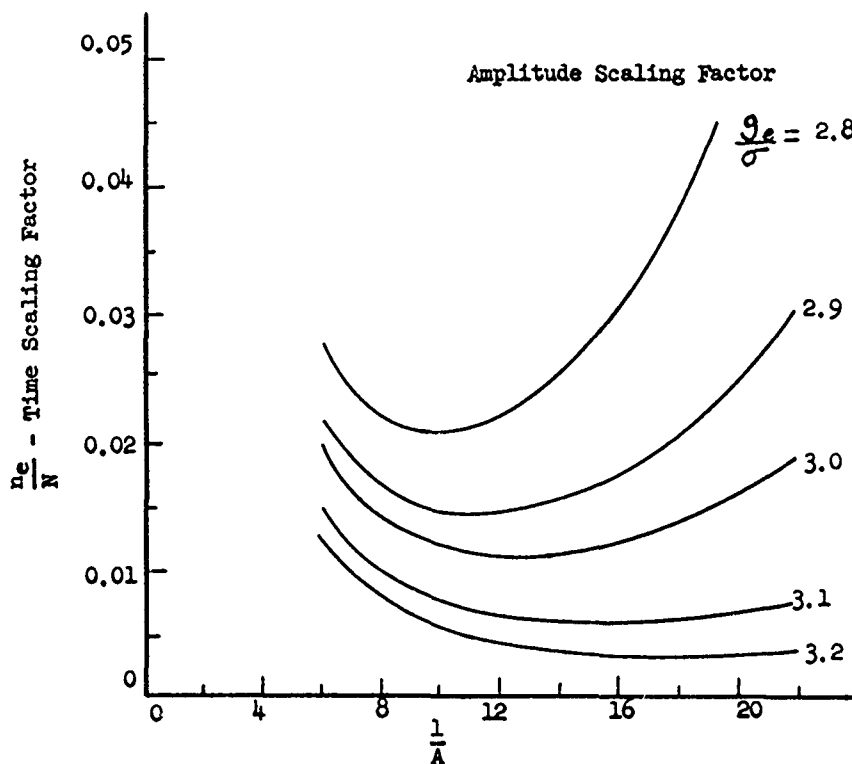
Fig. 1. Time scaling factors vs amplitude scaling factors

39

value of Q, which is representative of all the subassemblies.

If the selection of the pass-band filter is based on a subassembly with a small Q, then the filter bandwidth is wide and the amount of energy in the filtered data is large, resulting in an overtest of subassemblies with large Q values. Exactly the opposite is true if the selection of the filter is based on a large Q. Since an overtest produces an acceptable item and undertest does not, the filter must be selected on the basis of a small Q. Furthermore, an overtest of high Q subassemblies is justifiable because they do not represent the best design practice. Therefore, a conservative value of 2.8 was selected to provide a margin of safety in the final result. With this value, the entire frequency spectrum can be subdivided into frequency intervals by placing electrical filter bandwidths next to each other as shown in Fig. 2. The filtered acceleration data within each bandwidth include acceleration components which cause most of the damage to the associated mechanical subassemblies.

SCHEDULE DERIVATION

Data Acquisition

The data acquisition system consisted of a test vehicle and an instrumentation system.

Acceleration data were gathered on wheeled and tracked vehicles as they were operated over various cross-country and fixed profile test courses. The vehicles were loaded at their rated capacities with either dummy loads or inert ammunition. Selection of vehicles was based on the frequency of use and expected use in the future. Course selection was dictated by the courses which are used for type-classifying particular vehicles. Testing was conducted over courses in a frozen or hard condition. In each case, accelerometer outputs were recorded on magnetic tape after they were suitably transmitted and time indexed. A schematic diagram illustrating the data acquisition system is shown in Fig. 3.

Data Reduction

The initial step in data reduction was to determine if data recorded on one portion of a course were similar to data recorded on another portion of the course. Mathematically, this equivalence is referred to as a stationary process, that is, a process that does not vary with time. The existence of such a process would permit data gathering runs of shorter duration and equally short data reduction runs. The establishment of this process was based on the root mean square value of acceleration. The rms values were determined for various
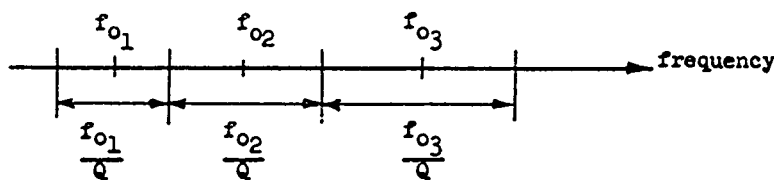
Fig. 2. Successive electrical filter bandwidths
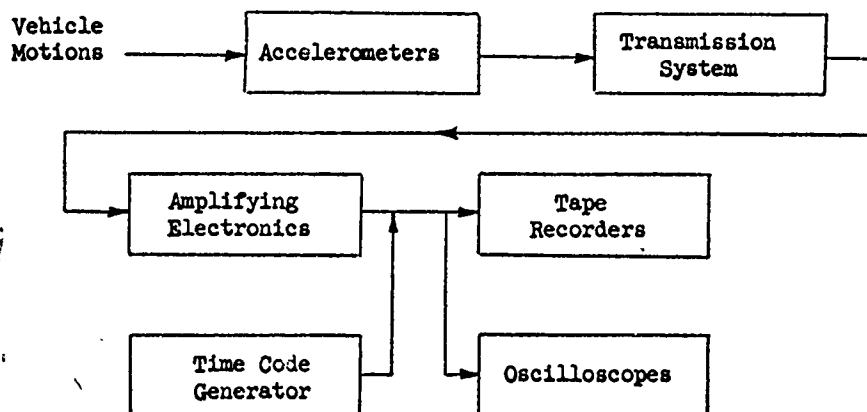
Fig. 3. Data acquisition system

40

segments of an entire data record and compared. Such an investigation indicated that a stationary process existed on the fixed profile courses, but not on the cross-country courses. Consequently, short-duration data runs on the fixed profile courses were adequate, while maximum possible time runs on the cross-country courses were necessary.

The data were passed through a set of half-octave filters having a Q of 2.8 into an axis-crossing analyzer. This analyzer detects the number of times the amplitude of a signal exceeds each of ten preset, linearly separated, positive or negative levels of amplitude. The data from this analyzer can then be used to evaluate the summation quantity of Eq. (5). The data reduction system is shown in Fig. 4.

Data Evaluation

Data from the axis-crossing analyzer were scanned to determine which filter center frequency contained significant levels of acceleration. A sample axis-crossing data sheet is shown in Fig. 5. In this case, the center frequency of interest is 5.6 cps. The mechanics of calculating a test schedule from these data are illustrated in Table 1.

The axis-crossing analyzer is constructed to indicate only that an acceleration signal fell between two successive acceleration levels. Therefore, it is assumed that the level fell midway between two successive levels of acceleration. The number of crossovers in each amplitude level are then converted to the

number of reversals by subtracting the number of crossings between successive amplitude levels.

In the calculation of the original schedule, it was necessary to select a $1/A$ value for the material which was most likely to fail in the system. In that case, aluminum was the predominant material with $1/A$ equal to 19.6. Subsequently, it was shown that the schedule was nearly independent of material. Since the data for the new schedule fall within the previously mentioned restrictions, $1/A$ was picked as 20 for convenience and for consistency with the original derivation.

Data for this example came from vehicle operation on a cross-country course for which a stationary process does not exist. However, it is reasonable to expect that the maximum data run of 1.96 miles, on that particular course, is representative of any other distance which could be traveled on the same course. Such a data run is at least ten times greater than is necessary for a data run on a fixed profile course. For convenience, the results are extrapolated to 1000 miles of vehicle operation.

In the process of calculating the schedule, it is possible first to pick g_e the equivalent acceleration level, and then to calculate t_e, the time of test equivalent to 1000 miles of vehicle operation, or to do the reverse, that is, pick t_e and calculate g_e. The results of such an approach are shown in Fig. 6 which illustrates the original, and presently used, schedule and in Fig. 7 which illustrates the tentative new schedule.

Fig. 4. Data reduction system

41

Number of Times Level Was Exceeded

Filter Band No.	Time Base Ratio	Effective Bandwidth-fc	Value of 100% Level	10	20	30	40	50	60	70	80	90	100	Direction
		1.0												
		1.4												
		2.0	1.0	389	111	34	11	3	2	2	0			+
				401	113	35	9	3	3	1	0			-
		2.8	1.0	654	177	27	4	0						+
				658	179	30	2	0						-
		3.9	1.0	732	159	19	3							+
				808	164	25	2	1	0					-
		5.6	2.0	1583	736	345	151	68	31	6	0			+
				1501	702	332	151	68	28	8	0			-
		7.9	2.0	1130	293	60	15	0						+
				1130	284	58	14	0		0				-
		11.2	1.0	1414	301	60	19	8	3	1				+
				1410	291	66	17	8	4	0				-
		15.7	1.0	3817	1213	318	102	43	16	11	6	2	0	+
				3798	1224	316	94	43	25	8	3	1	0	-
		22.5	2.0	4980	1782	399	70	16	3	1	0			+
				5073	1780	407	76	18	2	1	0			-
		31.5	2.0	2868	372	50	8	3	2	1	0			+
				2910	377	52	11	2	1	0	0			-
		45	1.0	3521	450	126	30	7	3	0				+
				3515	480	111	31	7	2	0				-
		62.5	1.0	1843	175	54	20	7	0					+
				1831	169	51	17	5	1	1	0			-
		90	1.0	451	28	5	0							+
				452	29	5	1	0						-
		125	1.0	3	1	0								+
				3	1	0								-
		178	1.0	0										+
				0										-
		All Pass												

Amplitude Level - Per Cent

STEAP-DS Form 191, 18 Dec 64

Fig. 5. Axis-crossing data sheet

42

TABLE 1
Sample Calculation

Vehicle: Truck, cargo, 2-1/2 ton, 6×6, M35.
Course: Cross-country No. 1.
Transducer Location: 2 vertical, front of cargo bed.
Average Road Speed: 19.7 mph.
Data Sample Time: 360 sec.
Equivalent Length
   of Data Sample: 1.96 miles.
Filter Center Frequency: 5.6 cps.

Amplitude setting of axis-crossing analyzer	0.2 g	0.4 g	0.6 g	0.8 g	1.0 g	1.2 g	1.4 g	1.6 g
No. of crossovers	1501	702	332	151	68	28	8	0
No. of reversals n_i	799	370	181	83	40	20	8	
Average amplitude g_i	0.3 g	0.5 g	0.7 g	0.9 g	1.1 g	1.3 g	1.5 g ·	

$$\Sigma n_i(g_i)^{1/A} = 799\,(0.3)^{20} + 370\,(0.5)^{20} + \ldots = 30,680 = n_e(g_e)^{1/A}$$

where

$\dfrac{1}{A} = 20$. The equivalent acceleration test level g_e is picked as 1.5 g,

$$n_e = \frac{30,680}{(1.5)^{20}} = 9.23\ \frac{\text{cycles}}{1.96\ \text{miles}} = 4708\ \frac{\text{cycles}}{1000\ \text{miles}}, \text{ and}$$

$$t_e = \frac{n_e}{60\,f_o} = \frac{4708}{60(5.6)} = 14.0\ \text{min.}$$

The validity of the approach used to derive the original test schedule was established by conducting a test to compare the actual transportation environment of artillery projectiles with that of the laboratory vibration test. The amount of damage to the high-explosive fillers resulting from road and laboratory tests was about the same (4).

SCHEDULE APPLICATION

Automotive Transportation Phase

The schedule is set up to represent 1000 miles of vehicle operation. Therefore, the user of the schedule must first determine what type of vehicle will transport the item and what distance or equivalent damage-inducing distance this item will be transported. For example, if it is determined that an item will be transported 1500 miles on a tracklayer vehicle, this item would have to be tested for 20×1.5 or 30 minutes.

If the item does not have a clearly defined resonant condition, the frequency spectra would have to be covered by using a sweeping rate outlined in MIL-STD-810 (5) which specifies that for cycling tests of less than 500 cps maximum frequency, the frequency range shall be cycled logarithmically from minimum to maximum in 7.5 minutes for the total test time specified. If the item has reasonably distinct resonances, it would have to be vibrated at the principal resonant frequencies (not more than 4) with a dwell time at each resonant frequency equal to 1/6 of the total test time. The rest of the frequencies would have to be cycled logarithmically as previously mentioned.

Combined Automotive and Aircraft Transportation Phase

Although this paper deals with the automotive environment, cargo has a great probability of being subjected to other transportation
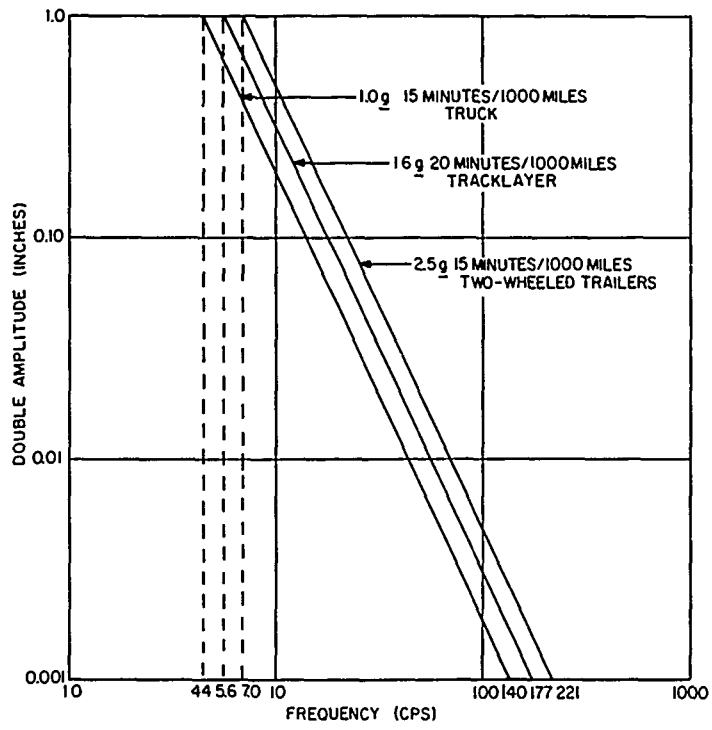
Fig. 6. Original automotive test schedule
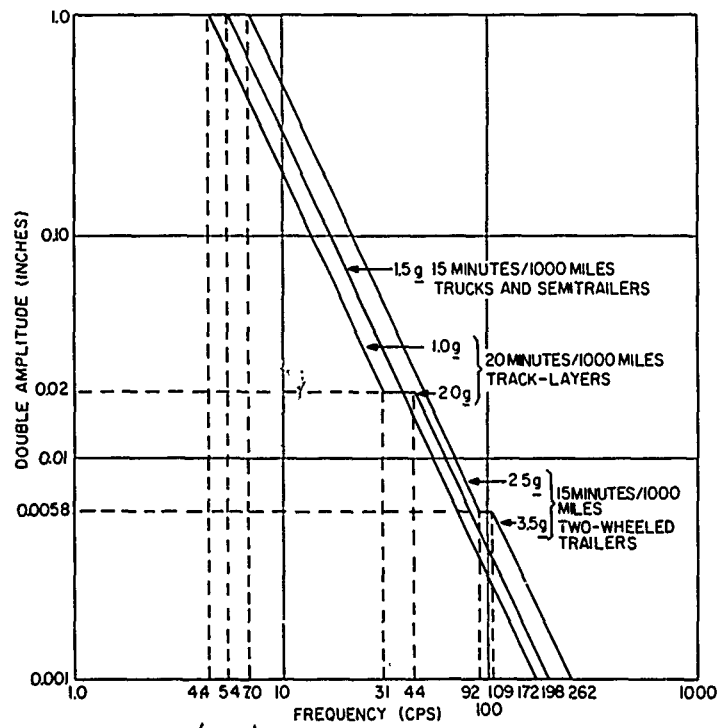
Fig. 7. Revised automotive test schedule

44

environments as well. It has been established that the aircraft and automotive vibration environments are more severe than the railroad and ship vibration environments; thus, the latter two environments can be neglected (2). The aircraft portion of the test schedule was obtained from MIL-STD-810 (5) which depends on the weight of the cargo. For test items weighing more than 50 lb, the acceleration amplitude can be reduced by 1.0 g for each 10-lb increment of weight over 50 lb. However, the level will not be reduced by more than 50 percent of the originally specified test level. This derating has been incorporated in the aircraft portion of the combined automotive and aircraft environment test curves shown in Figs. 8 through 12. Furthermore, the upper frequency levels for these curves are also weight-dependent. The derating of the frequency is shown in Fig. 13.

The application of the combined test schedule requires that for the automotive portion, the test time be computed on the basis of 15 or 20 minutes of exposure per 1000 miles of vehicle operation. For the aircraft portion of the test schedule, the test time is equal to either the actual flying time or to 3 hours, whichever is less. The rate of cycling is as outlined in the previous section.

SUMMARY

A test schedule was derived for cargo transported by truck, tracklayer, and trailer-type vehicles. The schedule is restricted to cargo which must be securely fastened to the cargo bed; otherwise, the validity of the test schedule will be in doubt. This restriction is required because the schedule is representative of a vibratory environment and not of a shock environment. The automotive test schedule was combined with the existing aircraft schedule to present a more complete transportation environment.

The derivation of the test schedule was based on the principle of equivalent damage. This principle requires that when vehicle cargo is exposed to a certain degree of possible damage under field conditions, cargo must also be exposed to the same degree of possible damage in the laboratory. Such conditions relate the severity of the test with distances that the cargo will be transported.

In the process of deriving the schedule, the following safety factors were incorporated:

1. Maximum summation quantities for each vehicle irrespective of acceleration direction were used;
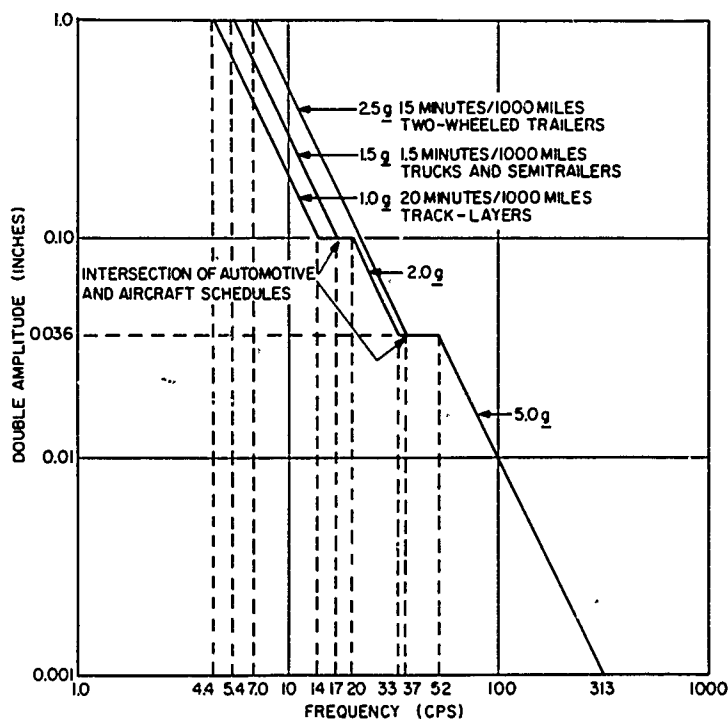
Fig. 8. Combined automotive and aircraft test schedule, item weight, less than 60 lb
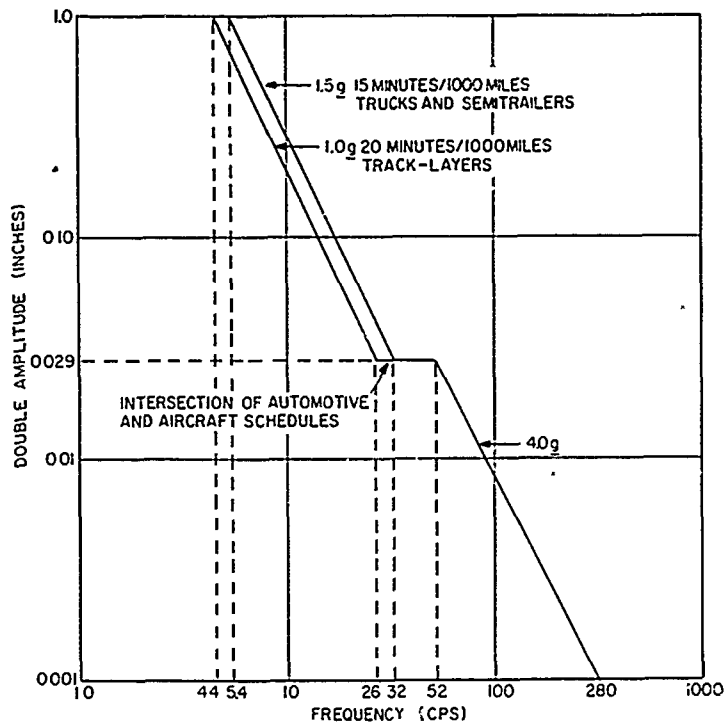
Fig. 9. Combined automotive and aircraft
test schedule, item weight, 60 to 70 lb
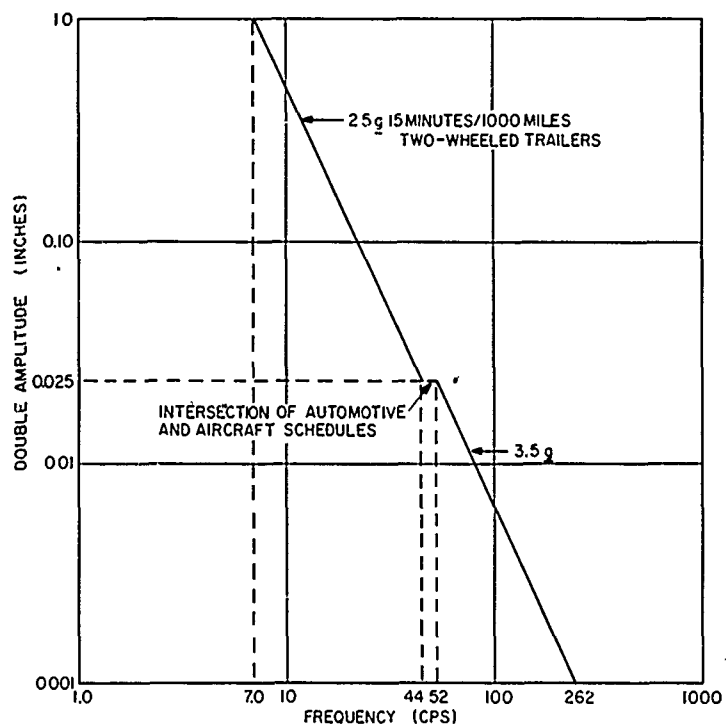
Fig. 10. Combined automotive and aircraft
test schedule, item weight, above 60 lb

46
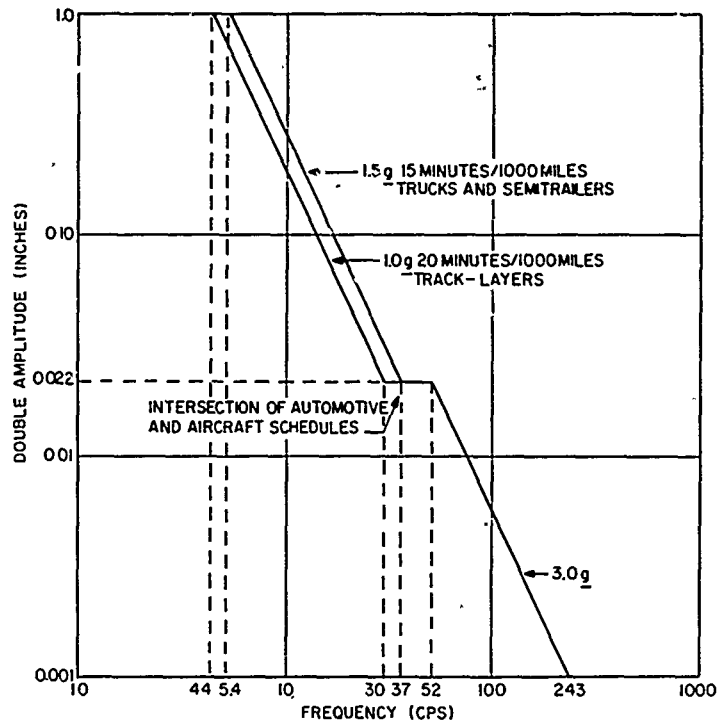
Fig. 11. Combined automotive and aircraft
test schedule, item weight, 70 to 80 lb
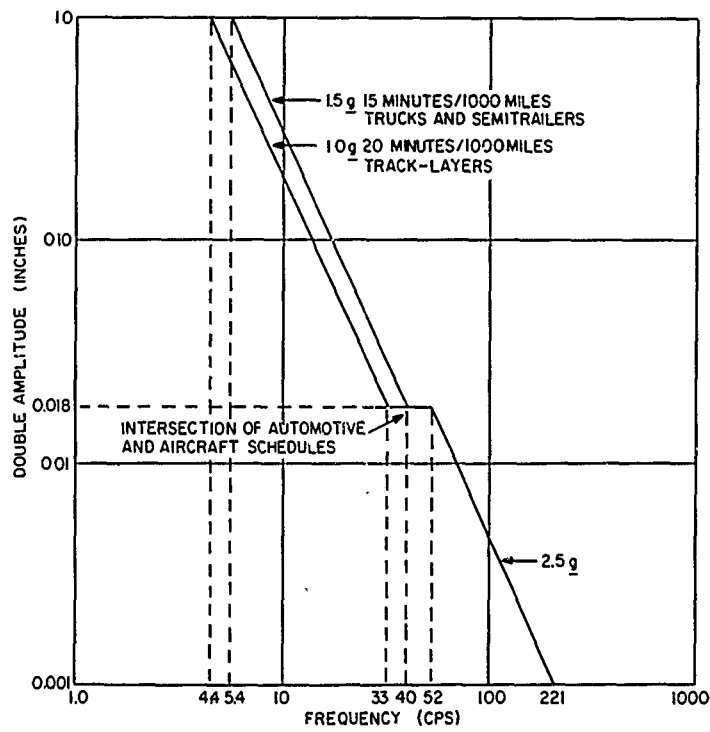
Fig. 12. Combined automotive and aircraft
test schedule, item weight, above 80 lb

47
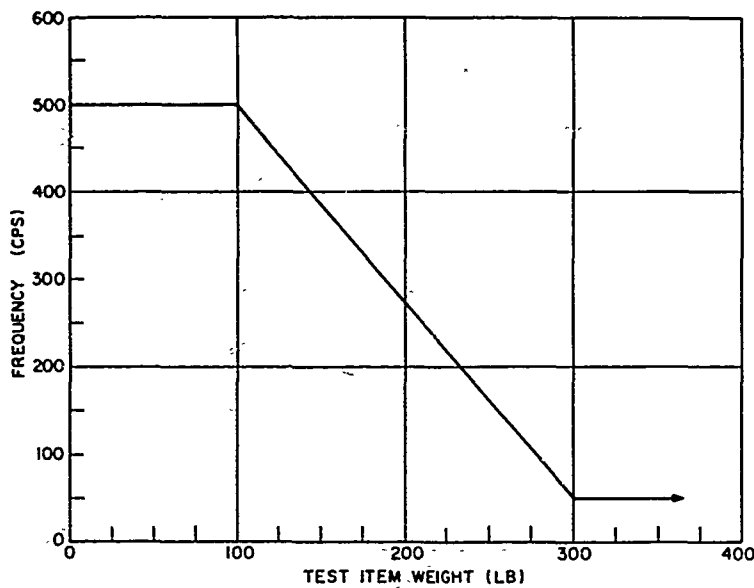
Fig. 13. Weight vs frequency for aircraft cargo

2. The filter bandwidths were based on a low Q;

3. High acceleration values were extrapolated to 1000 miles of vehicle operation; and

4. A sinusoidal forcing function was specified which, unlike a random forcing function, permits the test item to achieve maximum response.

CONCLUSIONS

The technique of deriving the test schedule is based on sound principles and results in a realistic automotive test schedule for securely tied-down vehicle cargo.

REFERENCES

1. J. A. Tolen, "The Development of an Engineering Test Standard Covering the Automotive Transportation Environment," Aberdeen Proving Ground Report No. DPS-1127, November 1963

2. J. A. Tolen, "The Development of an Engineering Test Standard Covering the Transportation Environment of Material," Aberdeen Proving Ground Report No. DPS-1190, December 1963

3. J. A. Kasuba, "An Analysis of the Methods and Criteria Utilized in the Development of an Engineering Test Standard Covering the Automotive Transportation Environment," Aberdeen Proving Ground Report No. DPS-1633, April 1965

4. H. Graves, "Final Report of Research Test of Cross-Country Transportation-Vibration Test of Ammunition," Aberdeen Proving Ground Report No. DPS-1519, January 1965

5. MIL-STD-810 (USAF), Military Standard Environmental Test Methods for Aerospace and Ground Equipment, June 1962

DISCUSSION

Mr. Forkois (U.S. Naval Research Laboratory): What was the maximum g level that you attained in these cross-country runs? Was it as high as 10 g?

Lt. Kasuba: No. It went up to perhaps 3 g, certainly not more than 4 g.

Mr. Forkois: This would indicate that you did not have any hard spring bottoming.

Lt. Kasuba: We tried to eliminate this from our data by screening the readings through oscillographs and so on. We tried to avoid unusual conditions of accelerometer ringing.

*   *   *

48

A METHOD FOR ESTIMATING ACCELERATIONS
OF SHIPPING CONTAINERS MOUNTED ON AN
IMPACTING RAILROAD CAR

John J. Scialdone*
Goddard Space Flight Center
Greenbelt, Maryland

A method is presented for estimating the response of a container and
its contents, when a railroad car on which they are mounted impacts a
group of braked cars standing in a classification railroad yard. Equa-
tions are derived for the container car impact equivalent velocity, con-
tainer car acceleration, car body transmissibility, and container trans-
missibility. By applying characteristic data of the car and its coupler,
the natural frequency of the car is calculated, and the equivalent impact
velocity to the container car is obtained from the actual impact speed
and the car weights. Then, input accelerations of the car and shipping
container are calculated over a 1- to 14-mph range of input velocities,
for bottoming and non-bottoming of the coupler during impact. From
these results, the container transmissibility is obtained, since we know
the inner container design natural frequency, its damping characteris-
tics, and the forcing frequencies resulting from the impact at the car
coupler. The resultant accelerations at the inner container are obtained
for 0 and 10 percent coupler viscous damping ratios. The calculated
values are compared with the upper bound values of the accelerations
obtained from impact tests. The results indicate that if a 10 percent
value for equivalent viscous damping of the car coupler is used, for car
impact speeds above 7.5 mph, accelerations at the inner container and
at the car bed adjacent to the outer container will exceed 1.8 g and 20 g,
respectively.

INTRODUCTION

Railroad impact tests were conducted to
confirm the suitability of a shipping container
rigidly attached to the floor of a railroad car.
The container consisted of an outer steel shell
supporting internally a spring- and damper-
mounted inner container to which was firmly
attached a dummy weight. These tests con-
sisted of impacting the container transport car
traveling at a speed of 7 mph against three
standing braked freight cars. The tests were
intended to simulate the majority of impacts
experienced during normal railroad switching
operations in railroad classification yards.

The tests indicated that for the 8-mph im-
pact, the shipping container attenuated the lat-
eral accelerations to the inner container to
1.8 g. The results of these tests at impact
speeds between 5 and 7.5 mph are shown super-
imposed on Fig. 1 of this report. Because
these impact speeds may be exceeded (1), the
analysis which follows was performed to:

1. Correlate the rests results and deter-
mine the responses of the components of the
system during impact;

2. Obtain the accelerations at the outer
container and inner container for impact speeds
other than those of the tests; and

3. Establish the limiting impact speed for the
acceptable specified inner container acceleration.

METHOD OF ANALYSIS

The method used here for estimating car
impact accelerations is intended to avoid the
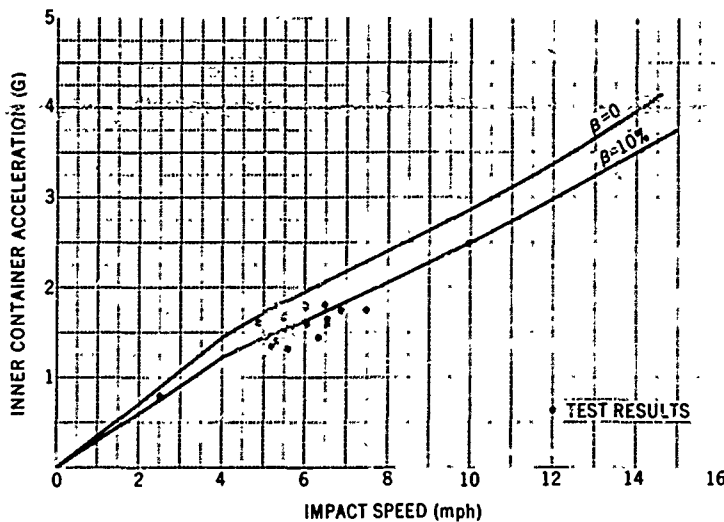
Fig. 1. Inner container acceleration
vs car impact speed

solution of nonlinear differential equations and the use of analog and digital computers. It employs the momentum and energy equations to establish a velocity change applied to a single degree of freedom system. The response of this system including the excited frequencies is used to calculate the response of the container. Since the momentum and energy equations are not applicable for impacts during which sliding of wheels may occur, i.e., for nonconservative systems, the results obtained by this analysis for the car accelerations can be modified to include, if necessary, an empirical coefficient. The coefficient is obtained by comparing the calculated results with experimental data reported in the literature for humping tests.

Container Car Input Velocity Change
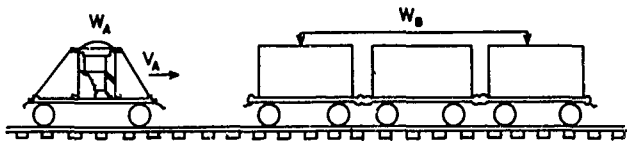
The kinetic energy of the impacting car will be used to impart a kinetic energy to the standing cars and compress the impacting couplers. The following balance of energy equation for the strain energy, the initial kinetic energy, and the kinetic energy of the entire system after impact can be written:

$$\frac{Fd}{2} = \frac{W_A V_A^2}{2g} - \frac{(W_A + W_B) V_{AB}^2}{2g}. \tag{1}$$

Also, a mass momentum transfer equation can be written expressing the balance of momentum between the impacting car and standing cars:

$$\frac{W_A V_A}{g} = \frac{W_A + W_B}{g} V_{AB}. \tag{2}$$

By solving this equation for V_{AB}, we get

$$V_{AB} = \frac{W_A}{W_A + W_B} V_A. \tag{3}$$

By substituting Eq. (3) into Eq. (1), replacing the deflection, d, by F/K, where K is the coupler spring constant, and dividing both sides of the equation by W_A^2, we obtain

$$\frac{F^2}{W_A^2} = \frac{K V_A^2}{W_A g} \left(1 - \frac{W_A}{W_A + W_B}\right). \tag{4}$$

Multiplying the numerator and denominator of the right side of Eq. (4) by g and extracting the square root yields the acceleration, G_o in units of acceleration of gravity, experienced by W_A, as follows:

$$G_o = \frac{F}{W_A} = \frac{V_A}{g} \sqrt{1 - \frac{W_A}{W_A + W_B}} \sqrt{\frac{Kg}{W_A}}. \tag{5}$$

In the above expression, $(Kg/W_A) = \omega_N^2$; i.e., the natural frequency of the impacting car consists of a lumped mass W_A and the spring constant k, provided by the coupler spring attached to the mass. The other square root term can be considered as the fraction representing the amount of the initial velocity returned to the

50

impacting car. The velocity change applied to the container transportation car can then be given by

$$V_E = V_A \sqrt{1 - \frac{W_A}{W_A + W_B}} \quad . \qquad (6)$$

This equivalent velocity will be used in estimating the acceleration provided by the impact to the container car.

Container Car Acceleration

Impact With No Bottoming of Coupler — Equation (5) provides the acceleration felt by the car on impact if coupler damping is assumed not to be present and coupler bottoming has not occurred. Equation (5) can be expressed simply in terms of velocity and natural frequency:

$$G_o = \frac{V_E \, \omega_N}{g} \quad . \qquad (7)$$

If an amount β of the critical damping is present at the coupler, the acceleration felt by the car will be (2):

$$G = \frac{V_E \, \omega_N}{g} e^{-\beta \omega_N t_p} = G_o e^{-\beta \omega_N t_p} , \qquad (8)$$

where the time, t_p, corresponding to maximum acceleration is:

$$t_p = \frac{1}{\omega_N \sqrt{1 - \beta^2}} \tan^{-1} \frac{(1 - 4\beta^2)(1 - \beta^2)^{1/2}}{\beta(3 - 4\beta^2)} \quad .$$

The coupler deflection corresponding to these accelerations will be given by

$$d_o = \frac{G W}{K} \quad . \qquad (9)$$

The frequency of oscillation under this type of impact will be obtained by the lumped car weight and the coupler spring constant.

Impact With Bottoming of Coupler — When the coupler bottoms, the behavior of the car coupler system will be the same as that of a system possessing a bilinear elasticity. The spring will deflect up to a closure deflection d_s with a spring rate K_o, and beyond this deflection with a much higher spring rate K_B. It is shown (2) that for the case of bottoming impact, the acceleration can be obtained in terms of the acceleration and deflection which would be

experienced if bottoming had not occurred. The equation is:

$$G = G_o \sqrt{\frac{K_B}{K_o} + \left[\frac{d_s}{d_o}\right]^2 \left[1 - \frac{K_B}{K_o}\right]} , \qquad (10)$$

where G_o and d_o are given by either Eq. (7), or Eqs. (8) and (9).

In this type of impact, the excitation felt by the car will consist of a low and a high frequency acceleration. These two frequencies will be related to the spring constants of the coupler (K_o) and that of car bed frame (K_B), and the bottoming deflection of the coupler (d_s) and the deflection (d_o), which would exist if bottoming had not occurred. The relations providing these frequencies are given in terms of the frequency which would exist if bottoming had not occurred, as follows (2):

$$\frac{\omega_o}{\omega_L} = \frac{2}{\pi} \sin^{-1} \frac{d_s}{d_o}$$

$$+ \sqrt{\frac{K_o}{K_B}} \left[1 - \frac{2}{\pi} \tan^{-1} \sqrt{\frac{K_o}{K_B \left(\frac{d_o^2}{d_s^2} - 1\right)}}\right] , \qquad (11)$$

and

$$\frac{\omega_o}{\omega_H} = \sqrt{\frac{K_o}{K_B}} \left[1 - \frac{2}{\pi} \tan^{-1} \sqrt{\frac{K_o}{K_B \left(\frac{d_o^2}{d_s^2} - 1\right)}}\right] , \qquad (12)$$

where ω_H is the high frequency, ω_L is the low frequency, and ω_o the frequency which would exist without bottoming.

Car Body Transmissibility

It will be assumed, conservatively, that the impact load experienced by the car frame at the coupler will be transmitted undiminished to the container mounting. This assumption is based on a conclusion that no significant difference in g loading was noted at different locations of the test car during impacts (3).

Container Transmissibility and
Inner Container Acceleration

Impact With No Bottoming of Coupler — The inner container accelerations will be calculated

51

by modifying the accelerations to the outer container, Eq. (7) or (8), by the transmissibility for a viscous damped system. The transmissibility is given by

$$T = \sqrt{\frac{1 + \left(2\beta\frac{\omega}{\omega_n}\right)^2}{\left[1 - \left(\frac{\omega}{\omega_n}\right)^2\right]^2 + \left[2\beta\frac{\omega}{\omega_n}\right]^2}} \quad . \quad (13)$$

In this expression, ω is the forcing frequency of the excitation, which in this case is the natural frequency of the car considered as a single degree of freedom lumped mass attached to a spring. The other parameters, β and ω_n, are characteristics of the container design.

Impact With Bottoming — For this case, the transmissibility will be calculated also by the use of Eq. (13). This relation will be employed to find two transmissibilities, (a) one for the low frequency acceleration, obtained from Eq. (7) or (8), and (b) the other for the high frequency acceleration, obtained from Eq. (10). To obtain these transmissibilities, the forcing frequency, ω, to be used, will be: (a) ω_L, obtained from Eq. (11) for the low frequency excitation, and (b) ω_H, obtained from Eq. (12) for high frequency excitation. The magnitude of the resultant acceleration R produced by the two excitations A_L and A_H will be obtained by the use of the cosine law for the addition of two harmonic functions. Thus,

$$R = \sqrt{A_L^2 + A_H^2 + A_L A_H \cos\theta} \quad , \quad (14)$$

where the angle θ will be the difference between the phase angles θ_H and θ_L of the high and low frequencies accelerations; i.e.,

$$\theta = \tan^{-1}\left|\frac{\left[2\beta\frac{\omega_H}{\omega_N}\right]}{\left[1 - \frac{\omega_H^2}{\omega_N}\right]} - \frac{\left[2\beta\frac{\omega_L}{\omega_N}\right]}{\left[1 - \frac{\omega_L^2}{\omega_N}\right]}\right| \quad . \quad (15)$$

CALCULATIONS

Car Weights

The weight of the container car W_A, including the container, was 71,200 lb. The weights of the three stationary cars were 51,200, 52,000, and 50,400 lb, respectively, providing a stationary total weight W_B of 153,600 lb. With the

relations previously indicated in the section entitled "Method of Analysis," it is possible now to calculate the acceleration at the system. However, the parameter to be used must first be established. These are the car weights, spring constants, natural frequencies, and equivalent impact speeds.

The total weight of the cars will be $W_A + W_B = 71,200 + 153,600 = 224,800$ lb.

Equivalent Impact Velocity

The equivalent impact velocity to the container car is, from Eq. (6),

$$V_E = V_A \sqrt{1 - \frac{71.2}{224.8}} = 0.826 \, V_A. \quad (16)$$

Spring Constant and Natural Frequencies

The spring constant on impact is provided by two couplers in series. The spring constant for the coupler will be estimated from data given for the energy absorption and travel of the coupler during impact, as specified by AAR (4). The draft gear must have a minimum capacity of 18,000 ft-lb, and the travel of the gear must be not less than 2.5 in. From this data, the spring constant of a single coupler being deflected is

$$K_o = \frac{2E}{d^2} = \frac{18,000 \times 12 \times 2}{(2.5)^2} = 75 \times 10^3 \text{ lb/in.} \quad (17)$$

For two couplers in series the spring constant will be

$$K = \frac{K_o}{2} = \frac{2E}{2d^2} = \frac{18,000 \times 12}{2.5^2} = 35 \times 10^3 \text{ lb/in.,} \quad (18)$$

and their relative displacement before bottoming is

$$d_s = 2 \times 2.5 = 5 \text{ in.} \quad (19)$$

The natural frequency for the car acting on a single coupler can then be calculated as

$$\omega_o = \sqrt{\frac{Kg}{W_A}} = \sqrt{\frac{75 \times 10^3 \times 386}{71,200}} = 20.2 \text{ rad/sec,} \quad (20)$$

corresponding to 3.2 cps. For the car acting on two couplers,

$$\omega_N = \sqrt{\frac{Kg}{W_A}} = \sqrt{\frac{35 \times 10^3 \times 386}{71,200}} = 13.75 \text{ rad/sec}, \quad (21)$$

corresponding to 2.2 cps.

Car and Outer Container Input
Acceleration

Input With No Bottoming of Coupler — The
magnitude of the acceleration experienced by
the container and car, where no bottoming of
the coupler occurs, will be obtained by the use
of Eq. (7) or (8), together with Eqs. (11) and
(21). For no damping present at the coupler,
Eq. (7) will reduce to

$$G_o = \frac{V_E \omega_N}{g} = \frac{0.826(13.75) V_A}{32.2}$$

$$= \frac{0.826 \times 13.75 \times \frac{5280}{3600} V_A}{32.2} = 0.518 V_A, \quad (22)$$

where V_A is expressed in mph.

For a 10 percent critical damping present
in the system, Eq. (8), plus the relation for the
time for peak magnitude, reduces to

$$G = 0.82 G_o = 0.443 V_A. \quad (23)$$

The deflections corresponding to Eqs. (22)
and (23) will be from Eq. (9),

$$d_o = \frac{G_o W}{K} = 0.518 V_A \frac{71.2 \times 10^3}{35 \times 10^3} = 1.058 V_A, \quad (24)$$

and

$$d_o = \frac{GW}{K} = 0.443 V_A \frac{71.2 \times 10^3}{35 \times 10^3} = 0.902 V_A. \quad (25)$$

The results of these equations for several
impact speeds have been shown in Fig. 2.

Input With Bottoming of Coupler — To apply
Eq. (9), it is necessary to estimate the spring
constant K_B of the car body. From a graph (5)
of applied force versus body yield, it can be
estimated that the car body spring constant is
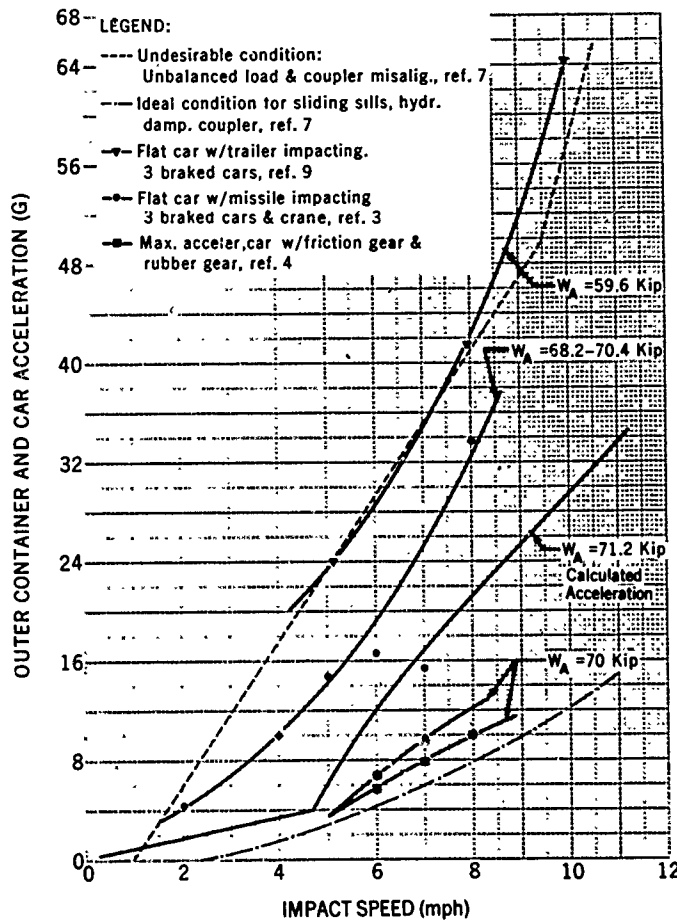
Fig. 2. Car and outer container acceleration
vs car impact speed with zero coupler vis-
cous critical damping

53

$$K_B = 1310 \times 10^3 \text{ lb/in.} \qquad (26)$$

By substituting Eqs. (16), (18), (19), (22) or (23), (24), and (26) into Eq. (10), the following equations are obtained for acceleration with bottoming:

1. For no damping at the coupler,

$$G_o = 0.518 \, V_A \sqrt{\frac{1310 \times 10^3}{35 \times 10^3} + \left|\frac{5}{1.058 \, V_A}\right|^2 \left|1 - \frac{1310 \times 10^3}{35 \times 10^3}\right|}$$

$$= 0.518 \times 6.12 \, V_A \sqrt{1 - \frac{21.7}{V_A^2}}$$

$$= 3.16 \, V_A \sqrt{1 - \frac{21.7}{V_A^2}} = 3.16 \sqrt{V_A^2 - 21.7} \, . \qquad (27)$$

2. For 10 percent critical damping at the coupler,

$$G = 2.72 \sqrt{V_A^2 - 21.7} \, . \qquad (28)$$

Equations (27) and (28), applicable when bottoming has occurred, will be valid for velocities producing $d_o > d_s$. From Eqs. (19) and (24), the velocity corresponding to these deflections will be

$$V_A > \frac{d_s}{1.058} > \frac{5}{1.1} > 4.73 \text{ mph} \, ,$$

and when 10 percent damping is included,

$$V_A > \frac{d_s}{0.902} = 5.5 \text{ mph} \, .$$

The values from Eq. (27) are shown in Fig. 2.

Superimposed on Fig. 2 are the results of several investigators (3,4,7,9), shown together with the envelope of maximum acceleration determined by combining the data of separate tests (7).

The wide range of results in these tests can be explained if one considers the effects of car weights and design, the type of friction gear, the status of maintenance, and the instrumentation and other factors on the response of a car to impact. Comparison of the results of this analysis with the test data indicates that these results fall within expected results and represent an average value of possible results. In view of this, the use of an empirical coefficient to account for the braking of the cars was

not used for the range of impact speeds being considered.

Container Transmissibility —
Accelerations at Inner Container

Impact With No Bottoming of Coupler — The transmissibility for impact speeds less than $V = 4.55$ mph for no coupler damping, and $V = 5.5$ with 10 percent coupler damping will be obtained from Eq. (13), where the following substitutions have been made:

1. $\omega_N = 11.9$, the design natural frequency of the inner container with its content.

2. $\beta = 0.35$, the fraction of critical viscous damping included in the suspension. This is also a design value.

3. $\omega = 20.2$ rad/sec, the excitation frequency resulting from the oscillation of the car when a force is applied to the car coupler. This value was obtained from Eq. (20).

With these values, the transmissibility for impact speeds lower than those indicated above will be

$$T = \sqrt{\frac{1 + \left|2\,(0.35)\,\frac{20.2}{11.9}\right|^2}{\left[1 - \left|\frac{20.2}{11.9}\right|^2\right]^2 + \left|2 \times 0.35 \times \frac{20.2}{11.9}\right|^2}} = 0.70. \qquad (29)$$

The accelerations to the inner container resulting from this transmission are plotted in Fig. 1.

Impact With Bottoming of Coupler — Since during this impact, low and high frequency accelerations as obtained from Eqs. (22) or (23) and (27) or (28), respectively, are present at the outer container and the transmissibility is a function of the forcing frequency, the high and low frequencies during this impact have to be found. The frequencies are indicated in Fig. 3. The equations used are Eqs. (11) and (12), which, with the substitution for $K_o = 35 \times 10^3$ lb/in., $K_B = 1310 \times 10^3$ lb/in. and $\omega_o = 20.2$, reduce to

$$\frac{20.2}{\omega_H} = 0.1634 - 0.1041 \, \tan^{-1} \sqrt{\frac{2.67 \times 10^{-2}}{\frac{d_o^2}{25} - 1}} , \qquad (30)$$

and

$$\frac{20.2}{\omega_L} = 0.637 \, \sin \frac{5}{d_o} + \frac{20.2}{\omega_H} . \qquad (31)$$
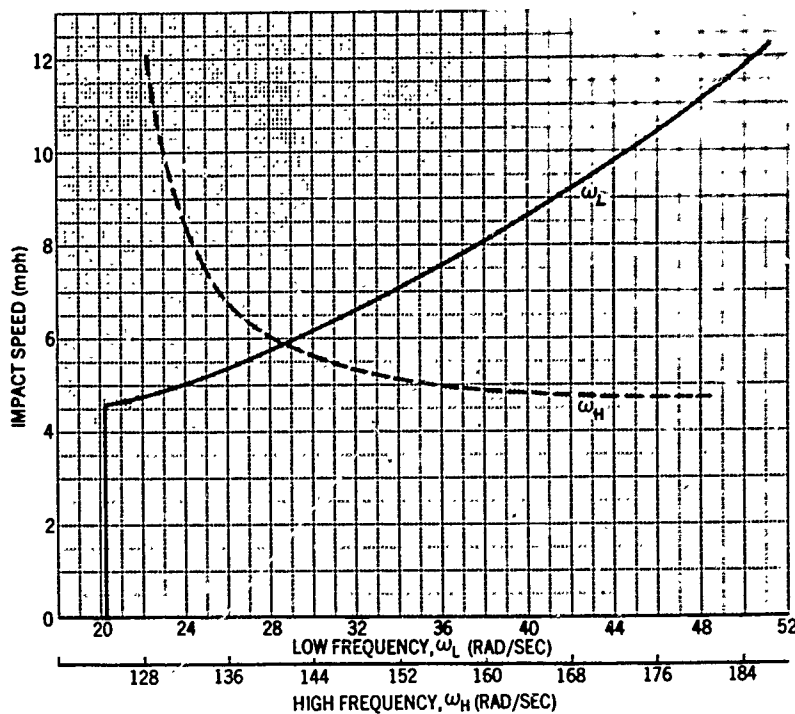
Fig. 3. Car and outer container
frequencies vs car impact speed

Having obtained ω_L and ω_H as in Fig. 3, the transmissibilities are obtained by using Eq. (13) with the design parameters of the container and with the forcing frequency $\omega = \omega_H$ and ω_L. Also the relative transmitted accelerations A_H and A_L and the phase angles are obtained from Eq. (15). The resultant accelerations at the inner container obtained from Eq. (14) are shown plotted in Fig. 1.

RESULTS AND CONCLUSIONS

Figure 2 shows the acceleration loads felt by the car bed and by the outer container at various impact speeds. The graph shows also the test results reported in the pertinent literature. The discontinuity in the curves indicates the speed at which the coupler bottoms. This change in the slope of the acceleration is confirmed by test results reported in the literature (6,8).

Figure 1 shows the accelerations at the inner container resulting from the attenuation of the accelerations of Fig. 2 through the container suspension. The effect of the coupler

damping on the magnitude of the resultant acceleration at the inner container is also shown. Superimposed as data points on these curves are the results of impact tests performed by the container designer. The comparison indicates that the calculated values agree with the upper bound values obtained from the tests. The comparison also suggests that a 10 percent viscous damping at the coupler would have represented the condition of the test container car coupler.

The following conclusions can be drawn from the analysis:

1. The accelerations to be expected at the inner container for various impact speeds can be predicted by this type of analysis. A 10 percent viscous damping should be taken as a representative value of the damping provided by a railroad car coupler.

2. Impact speeds higher than about 7.5 mph will produce inner container accelerations greater than 1.8 g and car bed acceleration above 20 g.

55

REFERENCES

1. "Fundamentals of Guided Missile Packaging," Naval Research Laboratory, Department of Defense, Ch. 6, p. 5

2. R. D. Mindlin, "Dynamics of Package Cushioning," Bell System Technical Journal, Vol. 24, Jul.-Oct. (1945)

3. R. Eustace, "Railroad Humping Testing on Units of the Pershing Weapon System," Institute of Environmental Science, Proceedings, 1962

4. C. M. Harris and C. E. Crede, Shock and Vibration Handbook (McGraw-Hill, New York), Vol. 3, Ch. 3, 1961

5. L. K. Sillcox, Mastering Momentum (Simmons-Boardman Publishing Corp., New York), 1955

6. J. M. Roehm, "Dynamic Testing of Freight Cars," ASME Paper, June 15, 1962

7. J. H. Farrow, "Shock and Vibration Transportation Environmental Criteria," Memorandum to NASA Environmental Data Subcommittee

8. R. E. Barbiere and W. Hall, "Electronic Designer's Shock and Vibration Guide for Airborne Applications," WADC Tech. Rept. 58-363-ASTIA AD 20-1095

9. E. J. Kirchman, "Rough Road and Railroad Humping Spec. Testing," Environment Quarterly, Vol. 4, No. 3, Third Quarter (1958)

* * *

PRELIMINARY ANALYSIS OF DATA OBTAINED IN

THE JOINT ARMY/AEC/SANDIA

TEST OF TRUCK TRANSPORT ENVIRONMENT*

J. T. Foley
Sandia Corporation
Albuquerque, New Mexico

This paper describes the manner in which the data obtained during the joint Army/AEC/Sandia test of truck transport environment was evaluated to arrive at the "best means" for reduction, presentation, and analysis. Four systems of data reduction and presentation were used on experimental portions of the truck test data, and the resultant outputs of each reduction system were evaluated to arrive at the best means of describing the environment.

INTRODUCTION

The truck transportation environment test referred to in this paper was a joint effort to obtain measurements of the transportation dynamic environment. Participants in this effort were the US Army Transportation Engineering Agency (USTEA), Ft. Eustis, Virginia; the AEC Division of Reactor Development, Germantown, Maryland; and Sandia Corporation's Environmental Operations Analysis group, Albuquerque, New Mexico.

The test vehicle was a flatbed tractor-trailer on which was mounted a 15-ton radioactive materials cask (Figs. 1 and 2). The truck and cask were instrumented to measure inputs to and responses of the 15-ton load.

Data were obtained from the unloaded truck during travel from Ft. Eustis, Virginia, to Wilmington, Delaware, and from the loaded truck during travel from Wilmington, Delaware, to Albuquerque, New Mexico (Fig. 3). Upon arrival at Albuquerque, "apparent weight" measurements of the truck, with and without the load, were made (Fig. 4).

The Sandia instrumentation system used an Ampex Corporation Model CP-100, 14-channel tape recorder to record the outputs of Endevco Corporation Model 2235C, Statham Model A737C-4-350 and A46C-15-350 accelerometers. A block diagram of the system is shown in Fig. 5; pickup locations are shown in Fig. 6.

AMOUNT OF DATA

Data were recorded continuously throughout the trip with the exception of short intervals of time between Ft. Eustis and Wilmington and during about 15 minutes of travel in Texas. This yielded thirteen 2500-ft. rolls of recorded magnetic tape data covering 55 hours of moving truck transportation environment. Voice commentary, recorded on the average of every 5 minutes throughout the trip, describe road types encountered, weather conditions, speed, time of day, and correlation information concerning parallel instrumentation being operated by USTEA personnel.

PRELIMINARY ANALYSIS OF DATA

The ultimate repository for the data obtained by Sandia in this joint test is the Sandia Corporation Environmental Data Bank. The users of this bank are primarily designers, dynamicists, and laboratory test engineers. They use such data to determine what to design against and what to test to with respect to the expected environment. In addition, the Environmental Operations

---
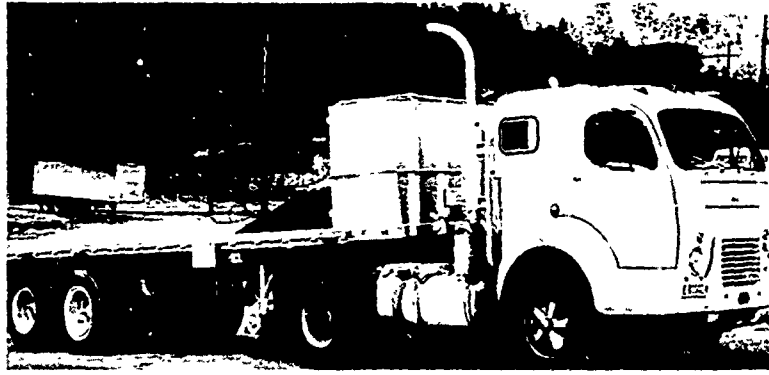
Fig. 1. Semitractor and trailer used for test (1)
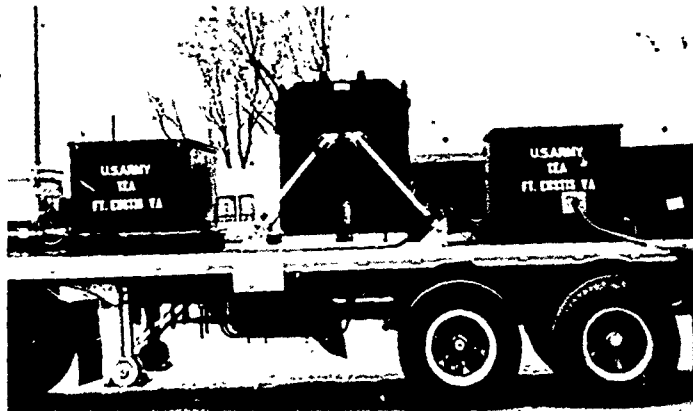
Fig. 2. Loaded and instrumented truck (1)

Analysis group, which operates the data bank, will use the results of this and other similar tests to derive standard transportation environmental test levels for Sandia Corporation products.

The results of a user survey of environmental data requirements within Sandia Corporation about three years ago indicated that environmental data ideally should meet the following four criteria:

1. Data should be statistical;

2. Data should be graphical;

3. Data should present those parameters that can be measured in the test laboratory as well as in the field; and

4. Data should lend themselves to various means of "combination" by numerical or graphical means; or both.

In an attempt to fulfill these requirements, four methods of reducing and presenting vibration data were evaluated to determine which

method would provide data from these truck tests that could best meet these requirements. The four methods evaluated were:

1. Oscillograph records;

2. Power spectral density versus frequency plots;

3. Cumulative instantaneous amplitude distribution plots; and

4. Peak amplitude distribution versus frequency plots.

The data used for illustrating the evaluations in this paper were taken from the truck test under the following conditions:

1. Concrete highway (high speed, unloaded);

2. Blacktop highway (low speed, unloaded);

3. Concrete highway (low speed, loaded); and

4. Blacktop highway (high speed, loaded).
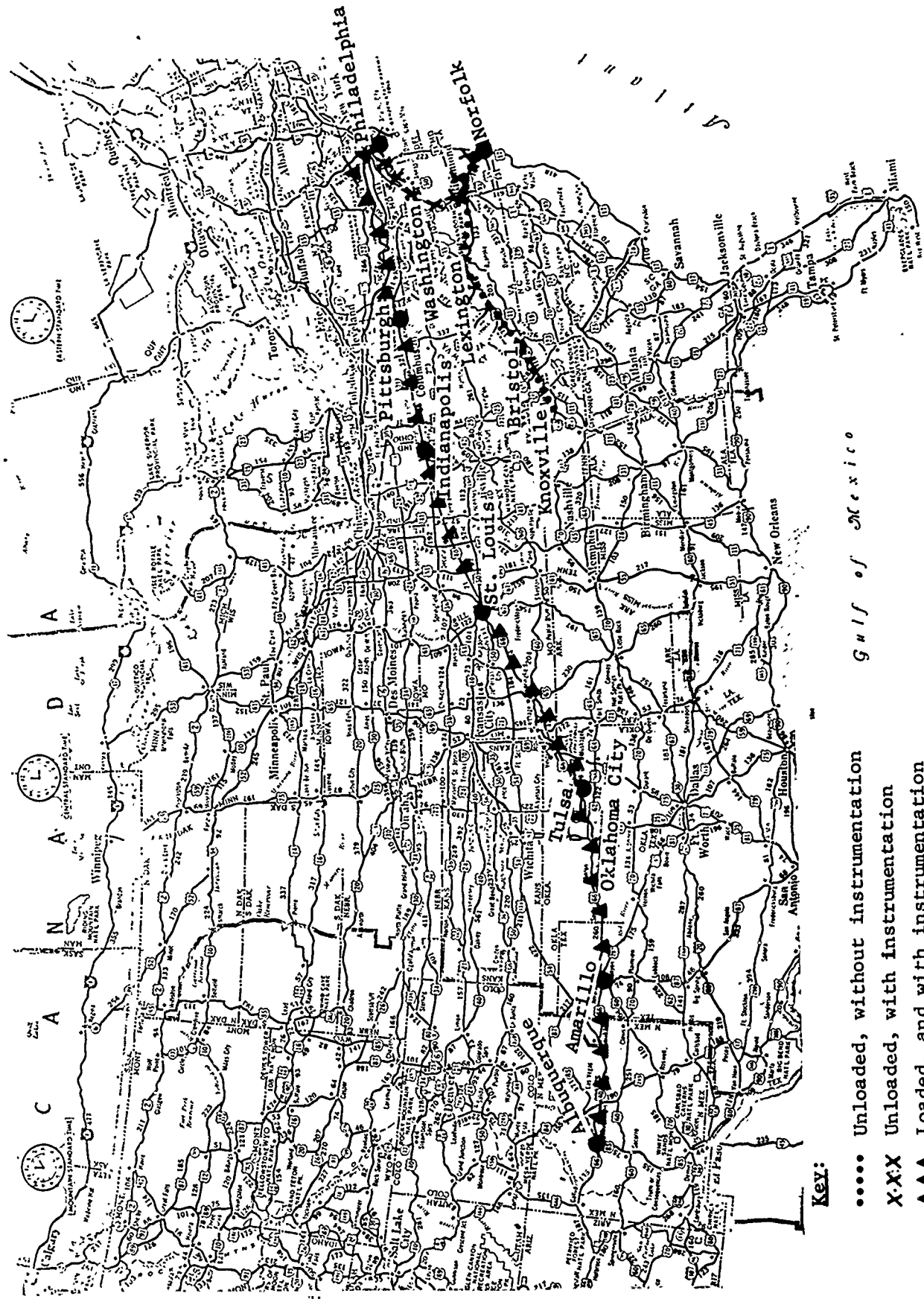
Fig. 3. Routes followed in test of truck transport environment (1)

Key:

..... Unloaded, without instrumentation

x·x·x Unloaded, with instrumentation

▲▲▲ Loaded, and with instrumentation

● Night stopovers
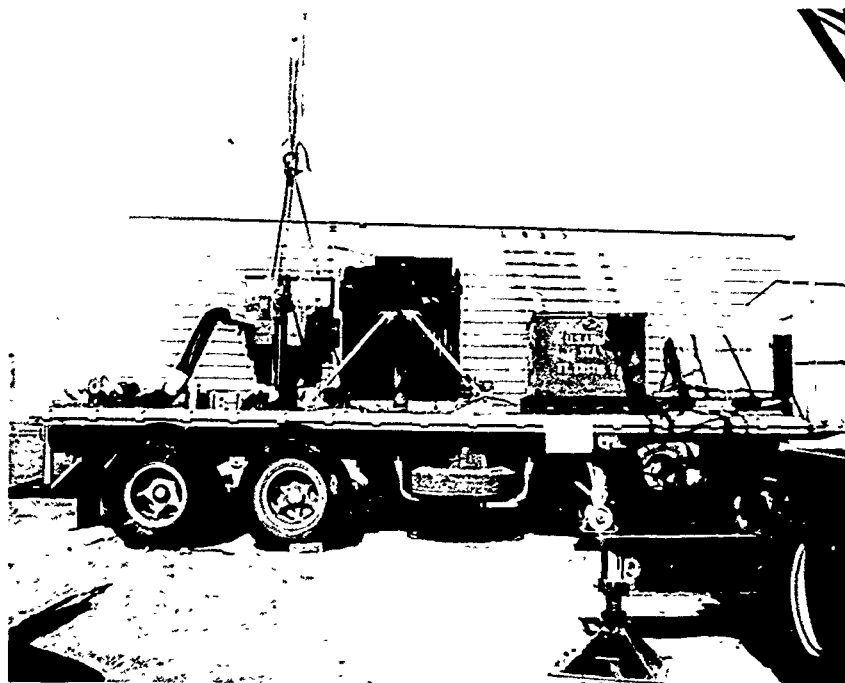
Fig. 4. Test setup for measuring system
"apparent weight" (1)

OSCILLOGRAPH RECORDS

The pickup location illustrated in this paper is in all cases the "input to load" measured on the truck bed to the rear of the cask location.

Figure 7 shows representative traces obtained from the input location near the load. These representations are graphical and present parameters (amplitudes and times) which can be measured in the laboratory and in the field. They are neither statistical in nature, nor do they lend themselves to combination by numerical or graphical means. By choosing a faster playback rate (expanding the record), some estimates of frequency could be made as well as measuring amplitude; however, these would not be only time-consuming and tedious but would be subject to human error.

An alternative method of data presentation by oscillograph trace was also considered. This method consists of playing back the data through fixed bandpass filters. This presentation "separates" the amplitudes encountered into regions or bands of frequency. This was considered an improvement over use of simple amplitude/time presentations, but still would require a considerable amount of hand reduction and interpretation with respect to the amplitude magnitudes encountered. This presentation is illustrated in Fig. 8.

It was considered, therefore, that as a "quick-look" method of reduction/presentation, the oscillograph traces and bandpass analyses were useful tools but would not be an adequate means of final presentation. Any tabulations of amplitude values as hand-read from such records would not be accurate enough or provide a sufficient description of the environment.

POWER SPECTRAL DENSITY VERSUS FREQUENCY PLOTS

Data samples were then reduced and presented in power spectral density (PSD) form (Figs. 9 through 12). Since the data in the test were obtained continuously, it was possible to use a tape loop for PSD analysis that was of long duration. The filter bandwidth selected for good amplitude resolution was 5 cps; the minimum time length of record using this bandwidth to approach stationarity was estimated to be 20 seconds. The time length of record used initially for loop analysis was approximately 300 seconds.

It immediately became apparent that a problem existed in using a PSD presentation format.

60
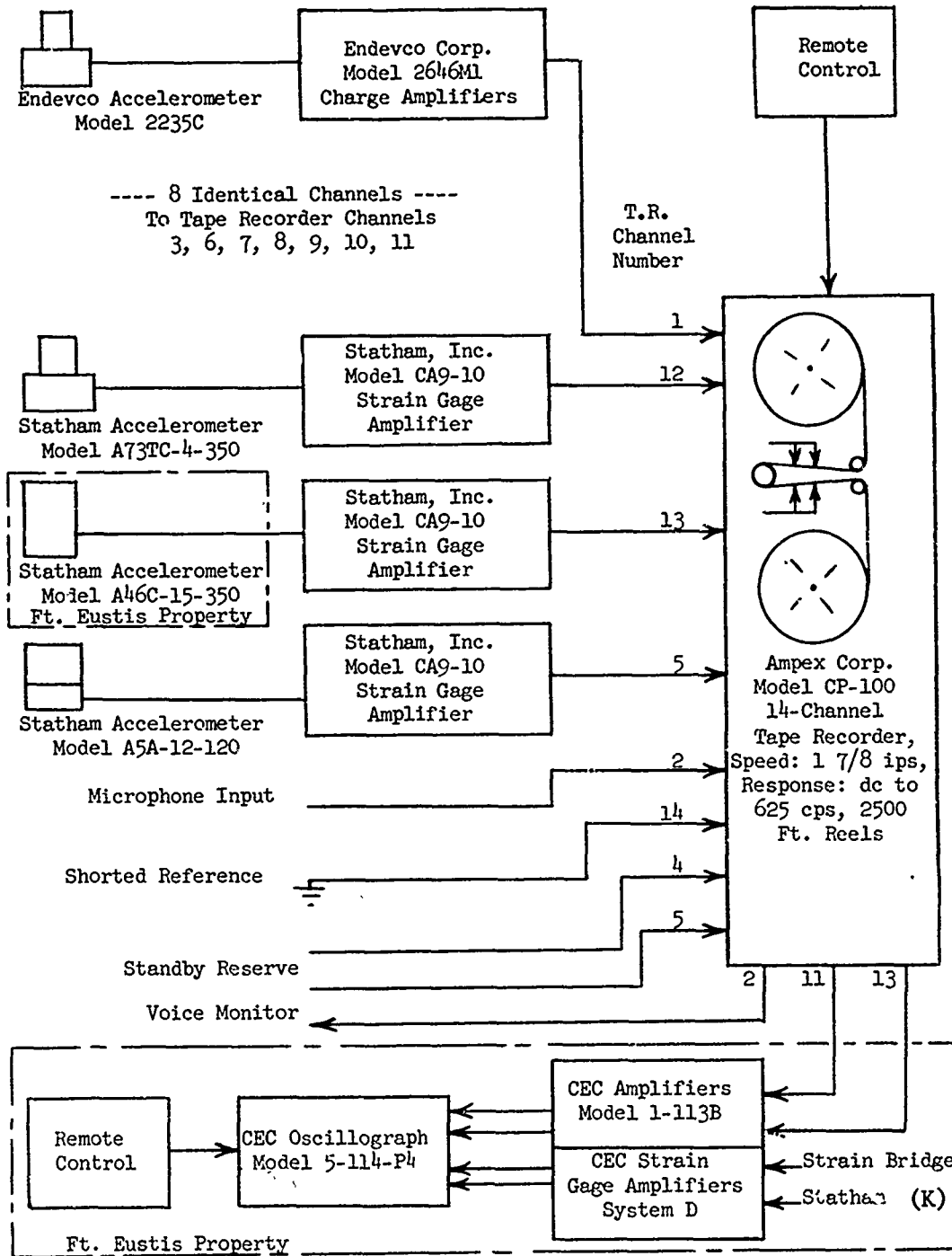
Fig. 5. Block diagram of transportation test instrumentation (1)

The root-mean-square (rms) signal from the record of Condition A varied so that it was impossible to obtain a PSD plot over this time length of record. It was necessary to use one-third of this tape loop length (160 seconds) to obtain a PSD versus frequency plot. It appeared that we would be involved in analysis of a non-stationary process during some road/load conditions.

Subsequent comparisons of PSD plots obtained under varying truck speed, road, and load

conditions indicated that not only amplitude magnitudes changed, but that the shape of the power spectrum changed with respect to truck speed, load, and road condition. Although the PSD format gave a good graphical data description and the parameters could be reproduced in the test laboratory, a disadvantage was that, statistically, any one of the PSD analyses might not be characteristically a reasonable picture of the environment.

An alternative considered was to make up a composite tape composed of samples from many

61

T.R. Channel Number	Order of Priority	Mfgr [*]	Type [**]	Model	Serial No.	Sensitivity	Calibrate	Sensitive Axis	Amplifier Reference No.	Location [*****]
1	7	1	A	2235C	FA-68	27.71 p-q/p-g	180 p-q$_{p-p}$	Vertical	4	Cask trunnion, driver's side (E)
2	.	-	-	-	-	-	-	-	-	Voice logging channel
3	5	1	A	2235C	FA-83	29.46 p-q/p-g	180 p-q$_{p-p}$	Vertical	5	Cask trunnion, right side (C)
4[***]	9	2	B	A5A-12-120	1258	16.8 puv/v/g	±3.43 g	Longitudinal	B-1	Truck bed over rear axle (M)
5[****]	8	2	B	A5A-12-120	1658	22.5 puv/v/g	±2.88 g	Vertical	B-3	Inside T.R. box at right rear mounting bolt(S)
6	1	1	A	2235C	FA-24	29.73 p-q/p-g	180 p-g$_{p-p}$	Longitudinal	6	Truck bed over 5th wheel (E)
7	3	1	A	2235C	FA-21	27.03 p-q/p-g	180 p-q$_{p-p}$	Vertical	7	Truck bed cross-member 2 feet forward of cask(R)
8	5	1	A	2235C	FA-62	28.88 p-q/p-g	180 p-q$_{p-p}$	Longitudinal	8	Cask trunnion, left (driver's) side (D)
9	4	1	A	2235C	FA-18	29.29 p-q/p-g	180 p-q$_{p-p}$	Vertical	3	Truck bed cross-member 2 feet aft of cask (P)
10	7	1	A	2235C	FB-28	29.49 p-q/p-g	180 p-g$_{p-p}$	Longitudinal	10	Cask trunnion, right side (B)
11	1	1	A	2235C	EA-52	27.88 p-q/p-g	180 p-q$_{p-p}$	Vertical	2	Truck bed over 5th wheel (J)
12	6	2	B	A73TC-4-350	178	118.7 puv/v/g	±0.918 g	Transverse	B-3	Top geometrical center of the cask (A)
13	2	2	B	A46C-15-350	624	Unknown	±2.97 g	Vertical	B-2	Truck bed over 5th wheel; transducer supplied by Ft. Eustis (L)
14	-	-	-	-	-	-	-	-	-	Shorted reference channel

[*] - 1 = Endevco Corporation Pasadena, Calif.

  2 = Statham Instruments, Inc. Los Angeles 64, Calif.

[**] - A = Barium Titanate Crystal

  B = Strain Gage

[***] - Removed at Wilmington, Delaware due to excessive noise and crosstalk to other strain gage transducer systems; probably due to excessive input cable length.

[****]- Used to monitor the Ft. Eustis shock isolation mount from Ft. Eustis, Virginia to Wilmington, Delaware; removed at Knapp-Mills Corporation, channel held in reserve for balance of trip.

[*****]- See Figure 3 for exact transducer locations by letter.

Fig. 6. Magnetic tape directory (1)

CONDITION A
UNLOADED TRUCK TRAVEL ON CONCRETE HIGHWAY AT HIGH SPEED

CONDITION B
UNLOADED TRUCK TRAVEL ON BLACKTOP HIGHWAY AT LOW SPEED
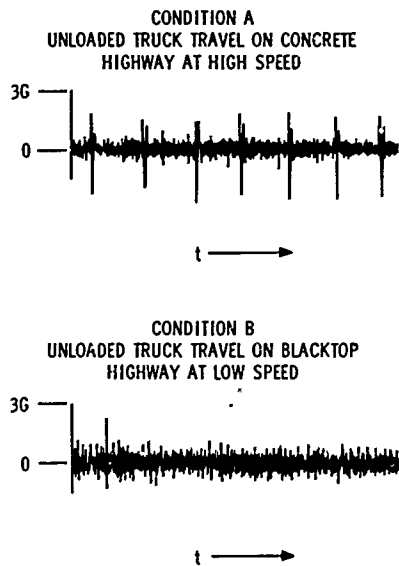
Fig. 7. Examples of oscillograph traces

sections of the continuous recording, i.e., to analyze an ensemble of records. This could be done, and a composite PSD versus frequency plot obtained that contained contributions of all road types, speeds, and/or the variation in load to give a composite summary description of the environment which would be statistically appropriate. The major disadvantage to this alternative approach was that the contribution of individual characteristics such as concrete road versus blacktop would be lost in such a composite. If a future user of the data wished to exclude, for his purposes, some conditions

encountered and then derive a new composite, there would be no way to do this from the data as presented. He would have to obtain the original data tapes and reprocess them to obtain the new result. The feeling, then, was that users would find that the PSD format, although offering many good advantages, would be unsatisfactory for alternative analyses. Further, due to the indications of nonstationarity encountered, it was felt that PSD presentations of some individual conditions could be misleading.

CUMULATIVE INSTANTANEOUS AMPLITUDE DISTRIBUTION PLOTS

Figure 13 illustrates the third means of analysis and presentation which was investigated. This system presents the data on the ordinate in terms of its time-cumulative instantaneous amplitude density in a selected bandwidth. Figure 13 presents "A" conditions using a 5-cps bandwidth. The abscissa is the variation of the signal from a normalized reference (rms) (σ/σ) value. The solid line superimposed on this plot is the result of a Gaussian random (white noise) signal input to this reduction system, to illustrate the deviation of the measured data from the theoretical statistical normal distribution.

This system of analysis/presentation approached the criteria for "good" presentation, in that it is both statistical and graphical in nature. But it offers difficulties in that the parameters are not normally those controlled in the laboratory or measured in the field.

62

NOTES: 1. FIRST LISTING OF FILTER BANDWIDTH IS REAL TIME PLAYBACK
2. BRACKETED VALUE IS "EFFECTIVE" BANDWIDTH @ 8 x REAL TIME PLAYBACK
3. THIS RECORD IS A PLAYBACK @ 8 x REAL TIME OF TRUCK TRAVEL OVER A ROUGH CONCRETE HIGHWAY @ 50 MPH

Fig. 8. Bandpass oscillograph playback
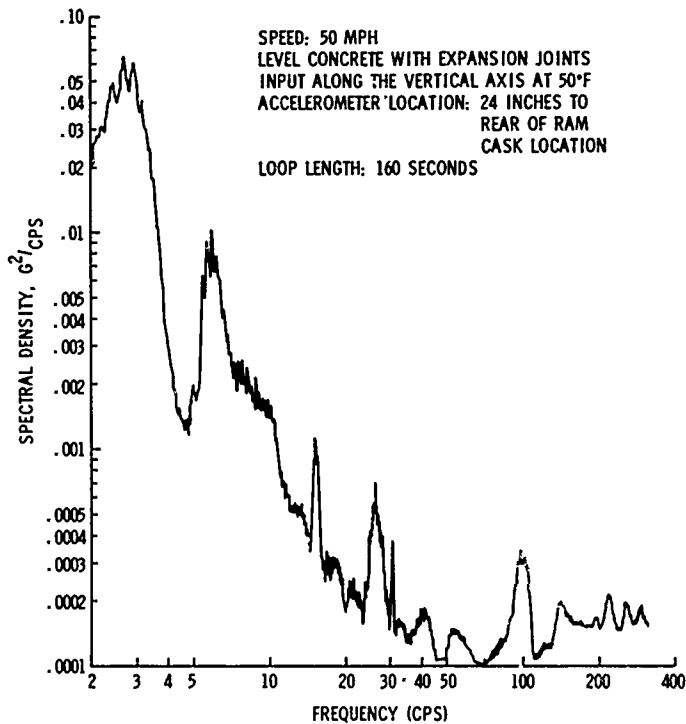
Fig. 9. Vibration test of tractor-trailer, unloaded

Further, the combination of individual increments of data from the truck test would pose similar problems as those which would be encountered in obtaining a composite PSD plot; i.e., one would have to obtain the original tape records to perform additional analyses. This data presentation, however, gives further information concerning the nature of the amplitude distribution. From these data plots, non-Gaussian distributed phenomena were inferred. It was

63
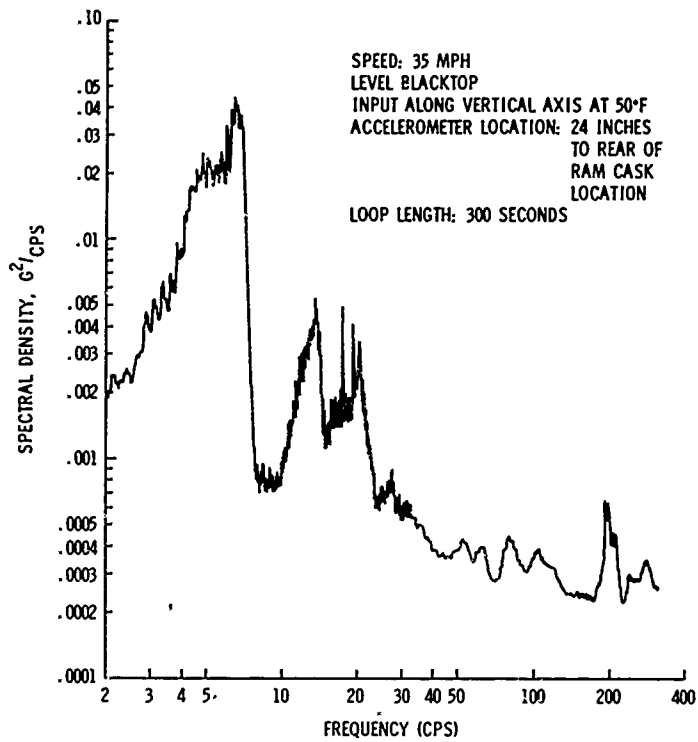
Fig. 10. Vibration test of tractor-
trailer, unloaded
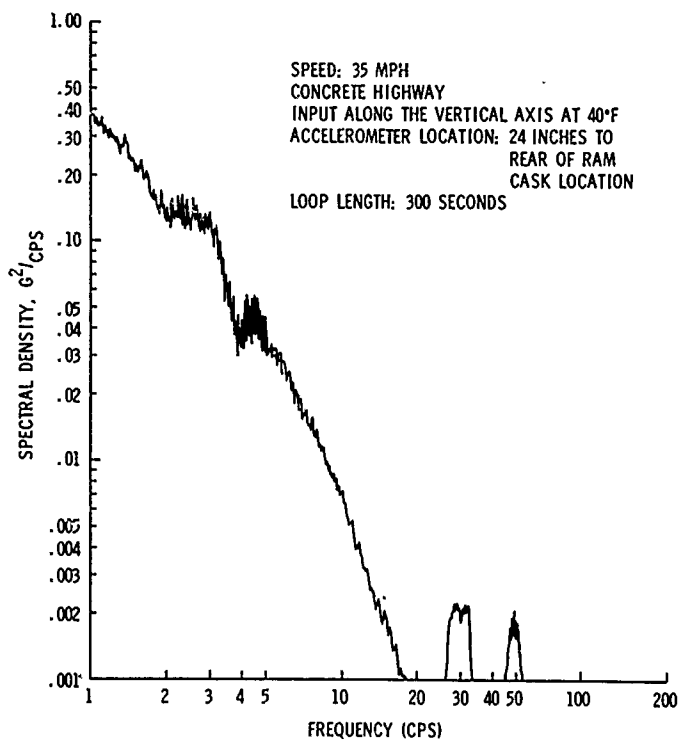
Fig. 11. Vibration test of tractor-
trailer, loaded

64

SPEED: 50 MPH
LEVEL BLACKTOP
INPUT ALONG THE VERTICAL AXIS AT 40°F
ACCELEROMETER LOCATION: 24 INCHES TO
                        REAR OF RAM
                        CASK LOCATION
LOOP LENGTH: 300 SECONDS

Fig. 12. Vibration test of tractor-
trailer, loaded

SPEED 50 MPH, LEVEL CONCRETE
VERTICAL AXIS
LOCATION: 24 INCHES TO REAR OF
          RAM CASK LOCATION
FILTER BAND WIDTH: 5 CPS
TIME LENGTH OF SAMPLE: 160 SECONDS
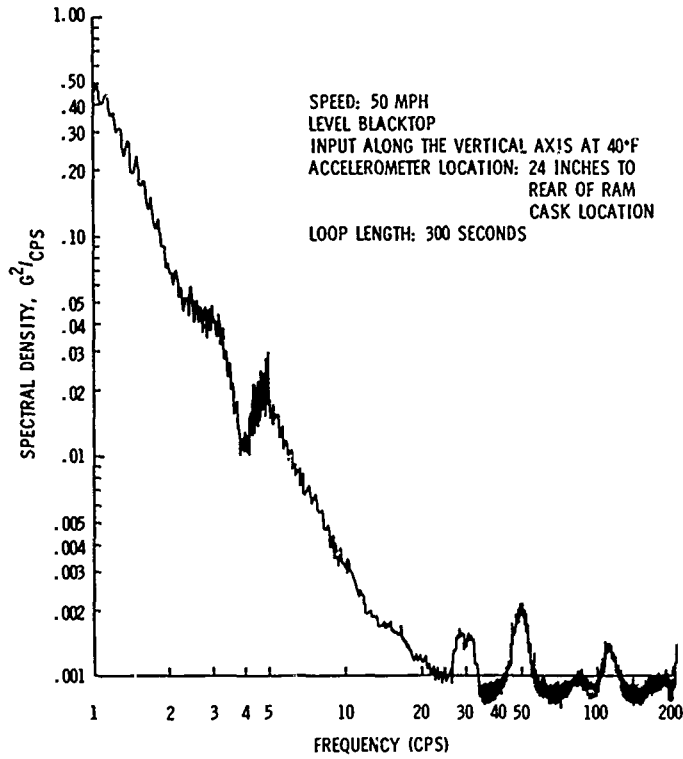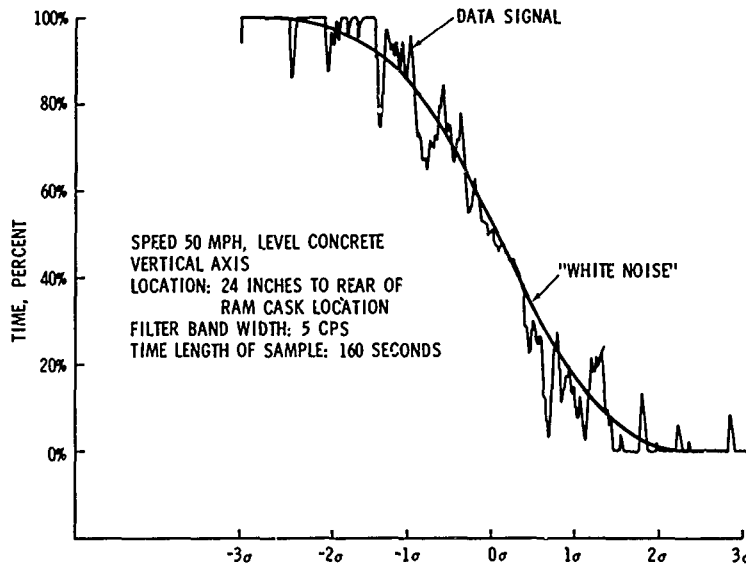
Fig. 13. Vibration test of tractor-
trailer, unloaded

deduced from the data characteristics exhibited that the environment over most roads consisted of a low-level complex vibration on which were superimposed a great number of repetitive shock pulses.

PEAK AMPLITUDE PROBABILITY DISTRIBUTION VERSUS FREQUENCY

A fourth system of data presentation, peak amplitude probability distribution versus

65

frequency, was then employed. The format of presentation is shown in Figs. 14 and 15. This system is an automated extension of the fixed bandpass filter oscillograph record system that was illustrated in Fig. 8. The data are presented as the number and magnitude of the acceleration peaks encountered in each pass band. In essence, then, it is a probability distribution of acceleration peaks, the total number of peaks encountered, and the number of peaks encountered in each bandpass so measured.

This analysis/presentation system best satisfied requirements, for it was statistical in nature, yet graphical in format; the parameters measured (g versus frequency) could be measured in the test laboratory as well as in the field, and the format of the data lends itself to a number of means of comparison by numerical or graphical methods.

As one may see in the illustrated format of Fig. 14, however, the bandwidth is rather wide for the purpose of describing the environment encountered in truck transportation. Our prior evaluations, as well as this data presentation, indicate that the area of interest lies primarily in the 0-20-cps band. Further, it would be

Vibration,File(1),Count(352260)   Tape 72430053

(ACCELERATION DISTRIBUTION IN PERCENT*)

ACCELERATION, 0-PK G

TRK 9
TRUCK BED CROSS-MEMBER
2 FEET TO REAR OF CASK
CONCRETE HIGHWAY, HIGH
SPEED, UNLOADED

ACCELERATION, 0-PK G	0-20	20-40	40-80	80-120	120-180	180-240	240-350
140.0							
100.0							
72.0							
52.0							
37.0							
27.0							
19.0							
14.0							
10.0							
7.2							
5.2							
3.7							
2.7	14.32					0.00	0.01
1.9	0.43	0.02	0.01				
1.4	0.22	0.01	0.02	0.01			0.00
1.0	0.22	0.03	0.01	0.01	0.01		0.00
	84.82	99.94	99.95	99.98	99.99	100.00	99.99

FREQUENCY(CPS)

0-20	20-40	40-80	80-120	120-180	180-240	240-350

SAMPLES PER CHANNEL

| 461 | 12567 | 23493 | 39386 | 45522 | 89546 | 141285 |

*VALUES IN THE TABLE SHOW THE PERCENTAGE OF ACCELERATIONS AT THE CORRESPONDING MAGNITUDE

Fig. 14. Vibran data presentation

66

desirable to measure at least one more amplitude increment between 0 and 1 g.

We are currently investigating two procedures to improve this format. The first is to obtain peak counts at the 0.5-g level. The second is to drive the data tape into the fixed filter system at a multiple of real time to produce effectively a narrow band analysis. Our goal, then, is to obtain the final format in the form as illustrated in Fig. 15.

A third modification indicated on this format is presently being promulgated. This is the inclusion of the rms value obtained in each pass band (and/or its range of variation). With this value included, the amplitude probability distribution obtained in each pass band can be normalized and then tested to determine how closely it approaches the Rayleigh distribution of acceleration peaks predicted for narrow band random vibration. With the addition of this modification, we feel that the environment so described will

Vibration, File(   ), <u>Count (   )</u>   Tape

(ACCELERATION DISTRIBUTION IN PERCENT[*])

Acceleration, 0-Pk G

140.0
100.0
 72.0
 52.0
 37.0
 27.0
 19.0
 14.0
 10.0
  7.2
  5.2
  3.7
  2.7
  1.9
  1.4
  1.0
   .5

FREQUENCY(CPS)

0	2½	5	10	15	22½
2½	5	10	15	22½	30

RMS G

High

Low

SAMPLES PER CHANNEL

[*]Values in the table show the percentage of accelerations at the corresponding magnitude

Fig. 15. Modified vibran

ble to measure at least one more ampli-
ncrement between 0 and 1 g.

/e are currently investigating two pro-
es to improve this format. The first is
ain peak counts at the 0.5-g level. The
d is to drive the data tape into the fixed
system at a multiple of real time to pro-
effectively a narrow band analysis. Our
then, is to obtain the final format in the
as illustrated in Fig. 15.

A third modification indicated on this format is presently being promulgated. This is the inclusion of the rms value obtained in each pass band (and/or its range of variation). With this value included, the amplitude probability distribution obtained in each pass band can be normalized and then tested to determine how closely it approaches the Rayleigh distribution of acceleration peaks predicted for narrow band random vibration. With the addition of this modification, we feel that the environment so described will

Vibration, File(   ), Count (   )   Tape

(ACCELERATION DISTRIBUTION IN PERCENT*)

Acceleration, 0-Pk G
140.0
100.0
 72.0
 52.0
 37.0
 27.0
 19.0
 14.0
 10.0
  7.2
  5.2
  3.7
  2.7
  1.9
  1.4
  1.0
   .5

FREQUENCY(CPS)

0	$2\frac{1}{2}$	5	10	15	$22\frac{1}{2}$
$2\frac{1}{2}$	5	10	15	$22\frac{1}{2}$	30

RMS G

High

Low

SAMPLES PER CHANNEL

*Values in the table show the percentage of accelerations
 at the corresponding magnitude

Fig. 15. Modified vibran

67

offer a direct means of determining the randomness of the amplitude distribution of the environment sample — a feature not presently directly available from other data presentation formats.

CONSTRUCTION OF A COMPOSITE DESCRIPTION OF ENVIRONMENT

As described to this point, we arrived at a method of obtaining and describing a statistical sample of the dynamic environment in terms of its peak acceleration probability density versus frequency. The determination of the length of time during which to take this sample is now not necessarily the length of time estimated to approach stationarity as with PSD-type analyses; it is more appropriately a sufficient period of sampling time to obtain a statistically representative number of peaks counted in a bandpass of interest.

For a general guideline, we have adopted the rule that at least 30 peaks must be counted in a given pass band for the sample distribution to be considered representative. Thirty peaks counted provides 99 percent confidence that the maximum deviation of a measured g value from the true population distribution is 29 percent. By way of illustration as to the degree of confidence to be placed on measurements where greater numbers of peaks are counted, a bandpass where 10,000 peaks were counted provides 99 percent confidence that the maximum deviation of a measured g value from the true population distribution is 0.16 percent. This statistical probability description is nonparametric— i.e., it does not presuppose a normal (Gaussian) distribution, or any other. Preliminary samples taken over a 60-second real time period appear to more than fulfill the 30-count minimum requirement for the truck transportation environment data.

Our next problem was how to relate, in a composite picture of the environment, the effects of road type, truck speed, and load. This is to be done in the following manner:

1. A composite peak amplitude probability density will be obtained for (a) the unloaded and (b) the loaded truck. These composites used in conjunction with the appropriate "apparent weight" measurements which were obtained at these two load conditions can be used to obtain estimates of the input force versus frequency conditions. These estimates can be used for derivation of force-controlled laboratory

vibration tests or to estimate the probable force magnitudes being delivered to the cargo. Since acceleration amplitudes will be in terms of probability of occurrence, it permits the use of analytical techniques to determine what amplitude values should be selected as being appropriate in each pass band for a vibration test, and what amplitude values may be more appropriately accounted for in shock tests.

2. Within each of these two load condition composites, the number of samples taken will be based on the frequency of occurrence of each road type as encountered during the trip and the frequency of occurrence of road speeds achieved. These frequencies of occurrence are presently being obtained from the voice transcript and activity logs recorded throughout the trip.

SUMMARY

It has been determined that the environment description that will be provided as a result of this truck test will be composed of:

1. Individual acceleration amplitude probability distribution versus frequency presentations representative of the various road types and speeds encountered for the (a) unloaded and (b) loaded truck;

2. A composite amplitude probability distribution for the two load conditions based on probability of occurrence of road type and vehicle speed; and

3. Plots of apparent weight of the loaded and unloaded truck versus frequency.

It is believed that the method of environmental measurement and description outlined here is one which, at the present state-of-the-art of environmental analysis, will be most useful for customers of the Sandia Corporation Environmental Data Bank. We hope to extend this approach of combining measurement and activity analysis to other types of truck, train, aircraft, and missile applications, and perhaps to apply this method of analysis to direct force measurements obtained during operational activities.

It is further believed that replications of this method in other tests provide a consistent basis for comparison and/or combination of environmental measurements in a manner superior to that of just "enveloping" data taken from a number of tests.

BIBLIOGRAPHY

Bendat, J. S., "Random Process Theory and Application," Measurement Analysis Corporation, Los Angeles, Cal., May 1964

Harris and Crede, Shock and Vibration Handbook, Vol. 2 (McGraw-Hill, New York), 1961, pp. 22-1 to 22-26

Mortley, J. L., "Joint Army/AEC/Sandia Test of Truck Transport Environment, December 7-17, 1964 (Test No. T-10767)," Sandia Corporation Report SC-DR-65-278, August 1965

Otts, J. V., "Impedance Measurement of a Flatbed Truck," Sandia Corporation Test Report No. T-10768, March 31, 1965

Otts, J. V., "Force-Controlled Vibration Testing," Sandia Corporation Report SC-TM-31, February 1965

Piersol, Allan, "The Measurement and Interpretation of Ordinary Power Spectra for Vibration Problems," Measurement Analysis Corporation, Los Angeles, Cal., June 1963

Sandia Corporation Vibration Analysis Committee, "Vibration Analysis for Weapon Development Test Programs," Sandia Corporation Report SC-DR-321-61, April 1962

Sandia Corporation Environmental Operations Analysis Group, "Weapon Development Test Data," Sandia Laboratory Engineering Manual Procedure S-49, August 6, 1965

Thrall, G. P., "An Analysis of Amplitude Probability Measurements," Measurement Analysis Corporation, Technical Documentary Report No. FDL-7DR-64-116, March 1965

DISCUSSION

Voice (TRW Systems): What kind of accelerometers did you use?

Mr. Foley: There were quite a number of them; primarily we used unbonded strain gage accelerometers in parallel with piezoelectric accelerometers. In some spots strain gages were used as backup for cross-monitoring.

Mr. Zell (Picatinny Arsenal): What is the procedure to get access to the data bank?

Mr. Foley: Just write and ask us. We will be glad to send anything in the way of unclassified data.

Mr. Zell: Were the bandwidths variable with the frequency in this vibran format which you showed?

Mr. Foley: In the system the bandwidth is fixed in the sense that the bandpass filters are fixed. We are, however, using playback speeds faster than real time to produce effectively a narrower analysis with the system. This was found to be necessary, particularly in this transportation situation, since the great majority of the acceleration peaks encountered were below 20 cycles. We felt we had to get narrow in the low frequency region to take a better look at it.

Mr. Zell: What were the statistical levels used in the presentation in each frequency bandwidth?

Mr. Foley: The statistical levels are not preset. An actual counting was made of the peaks

at these various levels. The levels shown started at 1 g, then went to about 1.2, 1.4, 1.8 and so on. Our modification will be to get another count below 1 g.

Mr. Zell: Then they were not in terms of a percentage of occurrences?

Mr. Foley: Yes, they were. They were the actual counts of peaks, and in terms of percentage at each of these levels.

Mr. Rhodes (Endevco Corp.): What was the full-scale acceleration, generally, in the raw data channels?

Mr. Foley: We set up full scale as plus or minus 3 g. The data in the paper indicate this at the low frequencies, from 0 to 20 cps, in the one vibran format shown. Eighty-five percent of the peaks counted in a data sample are below 1 g. Then there is a gap with no peaks up to 3 g. It gives a pretty good indication of what might be called steady state versus transient data superimposed on a low level steady state.

Mr. Edgington (White Sands Missile Range): Did the data on both the loaded truck and the unloaded truck show 3 g as a composite waveform?

Mr. Foley: Yes. The 3 g showed as the peaks and at about the same place. The interesting thing is in the apparent weight measurements of the vehicle itself between the loaded and the unloaded situation. The apparent weight plots indicate that the truck is effectively

decoupled from the load above 10 cps. There is not a great deal of difference between the loaded and the unloaded truck in terms of forces delivered in the range of 10 to about 200 cps, where most of the vibration tests are operating.

Mr. Levin (Bureau of Ships): What was the duration of the impulses at the 3-g level compared with that at the lower g levels?

Mr. Foley: Well that is difficult to answer. On the basis of the vibran, the duration would be equivalent to something between 0 and 20 cps. Fifteen percent of the counts down in this area were at 3 g and the rest of them were about 1 g.

* * *

70

ROUGHNESS MEASUREMENT AND SYSTEM RESPONSE
EVALUATION FOR HIGHWAY ENVIRONMENT

J. R. Harvey and R. A. Wursche
Goodyear Aerospace Corporation
Litchfield Park, Arizona

The paper presents analytical procedures to evaluate the shock and vibration environment of highway mobile transport vehicles. The road roughness measurement technique was used to obtain the road profiles and power spectral density estimates of a large number of road samples in West Germany and Central Arizona. The generated roughness data were used as input to a representative highway mobile weapons system to obtain the statistically average and peak system response. The calculated response data are then summarized to predict the dynamic environment of the payload and the transport vehicle.

INTRODUCTION

In October 1962, Goodyear Aerospace Corporation began an intensive program to develop a technique for analyzing the ride dynamics of a complex vehicle traveling over a road with a known profile. The objective of this program was to provide a design tool for optimizing the suspension system of the vehicle before its final fabrication and test.

The problem was to provide both an acceptable maximum and root-mean-square (rms) acceleration environment to the payload and its associated equipments.

The problem was approached using two techniques:

1. The actual road profiles in the area of planned deployment were obtained and using a transient response mathematical model of the vehicle, maximum payload response was calculated.

2. The displacement power spectral density (PSD), computed from the road profiles, was used as a forcing function to a harmonic response mathematical model of the vehicle to calculate the displacement and acceleration rms response.

Figure 1 is a simplified block diagram of the suspension system analytical techniques.

Road profiles measured in West Germany and in Arizona have been used to calculate the
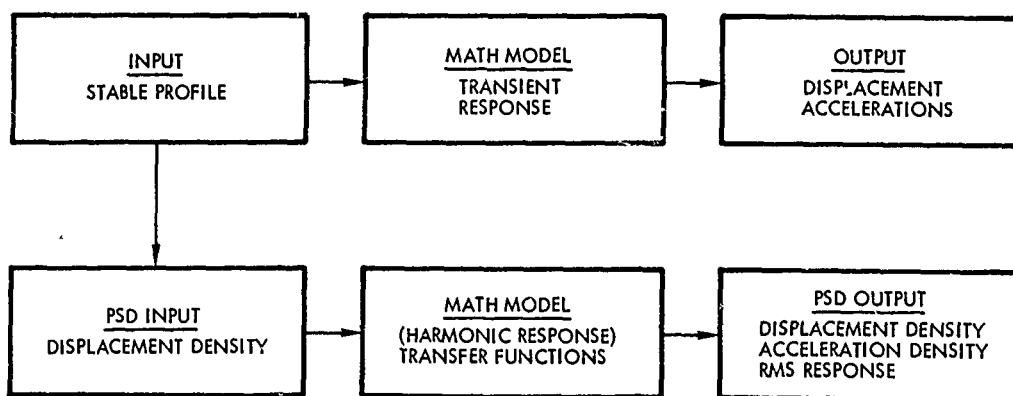
Fig. 1. Simplified diagram of suspension system analytical techniques

acceleration environment envelopes presented in this paper.

This paper presents, in an abbreviated form, the total method for analyzing the ride dynamics from the road surface to the calculated accelerations on the payload.

PROFILE MEASUREMENT TECHNIQUES

The instrument used for measuring the profile was of the slope variance type (1). It was selected because it is very rugged and easily transported.

The instrument consists of a trailing arm assembly that extends, in the deployed position, outward and in the right-hand track of the towing vehicle. A horizontal reference line is established by a gyro mounted on the upper portion of the trailing arm (Fig. 2). A synchronous motor, located at the pivot point of the wheel frame assembly, provides a voltage that is proportional to the slope of the wheel frame with respect to the gyro-established horizontal reference line. The voltage is recorded in analog form on a 7-channel, FM tape recorder.

A square-wave voltage trace is recorded on a second channel. This square wave is generated by interrupting a relay located on the odometer assembly. The distance between voltage rises is 5.01 in.

A third channel was used to record the audio description of the road sample being measured. The recording equipment used in the survey is shown adjacent to the profilometer instrument panel in Fig. 3.

Approximately 200 samples, covering all types of paved roads, were recorded in West Germany, and 55 samples on Arizona roads. All of the sample lengths were 1000 ft.

DATA REDUCTION OF PROFILES

The data reduction of the profiles was accomplished by first amplifying the raw data on the magnetic tape in an analog computer. It was then fed into an analog-to-digital converter, where the slope voltage was digitized and recorded at each voltage pulse from the odometer. The digitized data are then fed into an IBM 7094 digital computer for profile calculations.

Analog-to-digital conversion was accomplished by using a special purpose converter connected directly to the IBM 7094 digital computer, as shown in Fig. 4. To facilitate
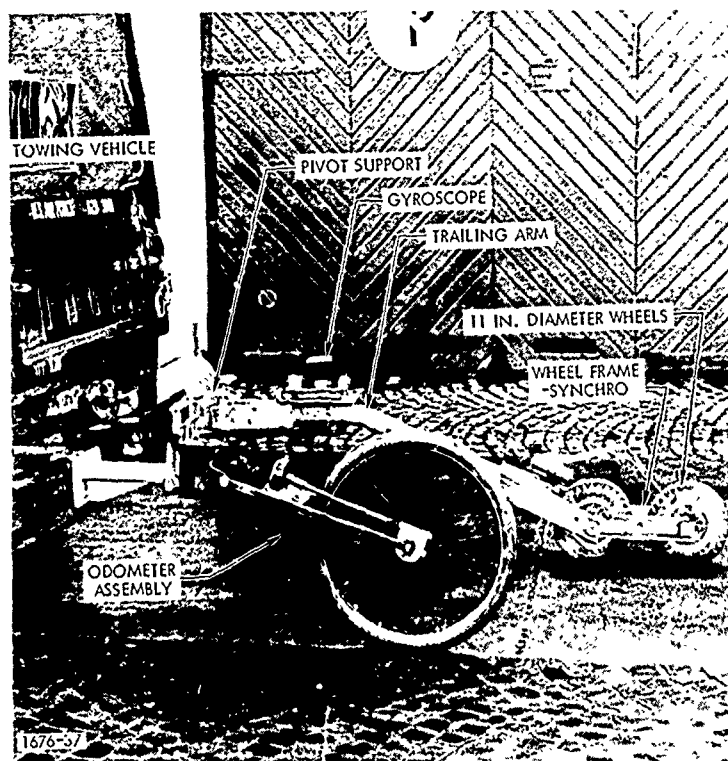
Fig. 2. Profilometer in displayed position
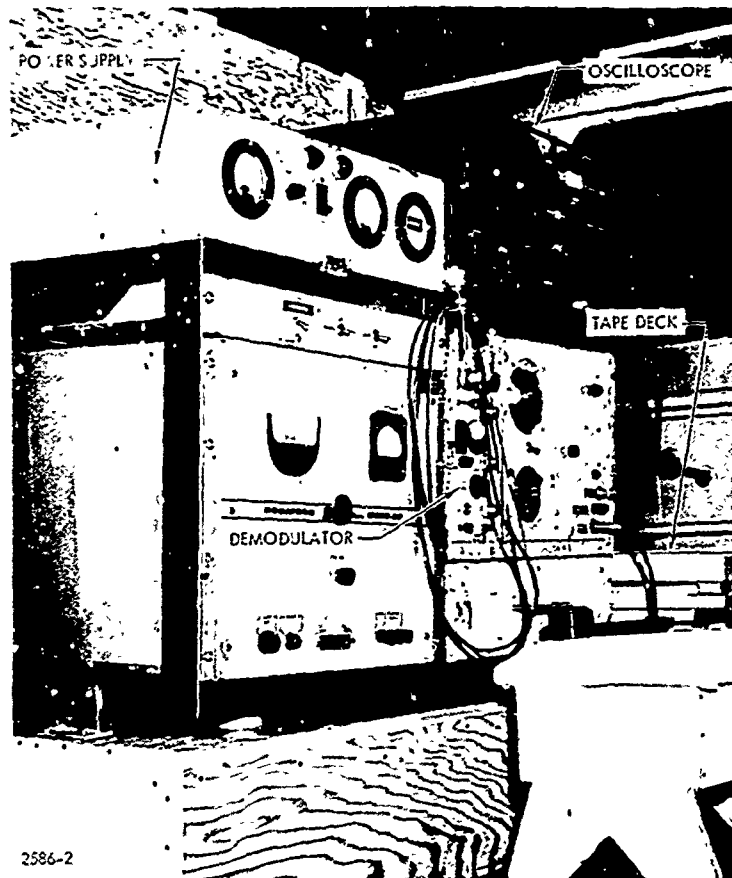
72

Fig. 3. Profilometer instrument panel,
Arizona road roughness study
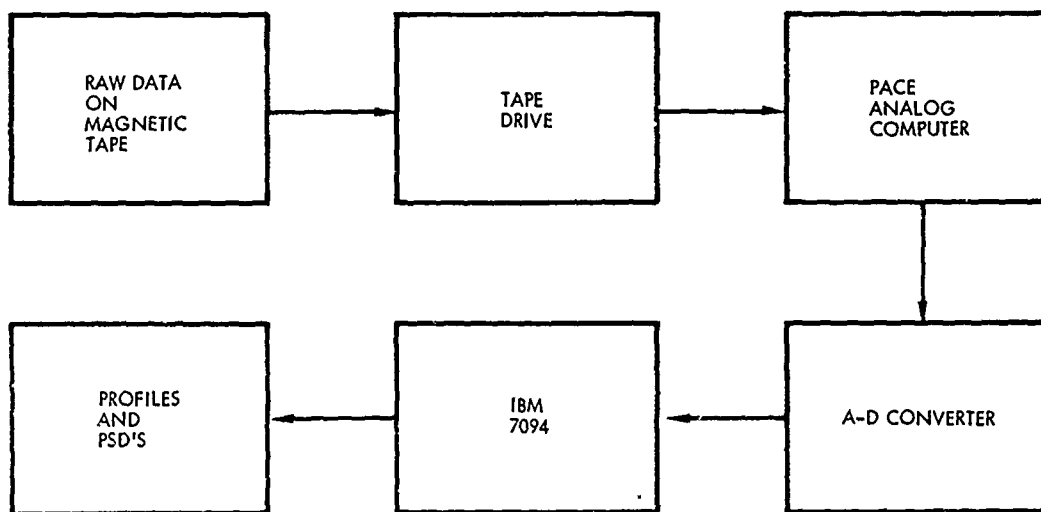
Fig. 4. Block diagram of data reduction procedure

analog-to-digital conversion and to eliminate unwanted and superfluous signals, all data were filtered prior to conversion to eliminate wavelengths less than 1.5 ft.

TERRAIN PROFILE CALCULATIONS

The rectangular coordinates of points along the profile were calculated by the relationships:

$$y_i = \Delta S \sum_{j=1}^{i} (\sin \theta)_j , \qquad (1)$$

and

$$x_i = \Delta S \sum_{j=1}^{i} (\cos \theta) , \qquad (2)$$

where

$(\sin \theta)$ = sine of terrain slope angle at increment j,

ΔS = distance along the terrain between odometer pulses (5.1051),

x_i = horizontal distance in inches,

y_i = elevation at x_i in inches, and

j = the number of an individual increment.

As the profile was calculated, a tape was prepared which ultimately contained all the profiles. This master tape can be used for listing and plotting any or all the profiles. The profile coordinates were moved within the IBM 7094 computer core to make way for the next set of data as it came from the analog-to-digital converter. The discrete sampling of the continuous data signal (sine of the slope angle) was performed at equal increments in space (along the terrain), which were represented by the odometer pulses. When the slope data were converted to profile data, the horizontal increments were considered equivalent. The slope angles are small enough in all tests to make this approximation acceptable.

POWER SPECTRAL DENSITY COMPUTATIONS

Preliminary analysis of the terrain profiles and some of the corresponding PSD's indicated that the power produced by general terrain slopes was several orders of magnitude greater than that for the roughness

characteristics. It was necessary, therefore, to remove the general profile characteristics from the data. Approximately half of the profiles are linear, and most of the remainder can be effectively approximated by a linear form. The "ramp effect" of linear profile trends can be removed by subtracting from the data a line fitted to the data.

It is also desirable to prewhiten the data before calculating the PSD's. A standard technique of proved adequacy for this type of data is

$$Y'_i = Y_i - Y_{i-1} . \qquad (3)$$

Because of the method of integrating the original slope data to obtain the profile, Eq. (1), and in view of the small angles encountered, Eq. (3) can be taken as the terrain slope times ΔS. The linear approximation to the profile can effectively be made and removed by subtracting the average slope from the slope data, i.e.,

$$Y''_i = Y'_i - \frac{1}{n} \sum_{i=1}^{n} Y'_i . \qquad (4)$$

The PSD function of Y'' differs from the desired PSD of Y as a result of the integration required to obtain the profile from the slope and the factor of ΔS contained in Y''. The corresponding Fourier transform produces a function, $\omega \Delta S$ (2), where ω is frequency in radians per inch. The computed spectrum must consequently be divided by this function to convert it to the spectrum of Y.

A surveyed strip of highway 1000 ft long was used to check the profilometer accuracy. In the length of the course, the maximum deviation between the calculated and surveyed profile was 2.8 in. (Fig. 5).

The PSD function associated with each profile (slope) is computed by the techniques of Refs. 2 and 3. Each PSD is calculated from the normalized profile slopes defined by Eq. (4). The ΔS associated with Eq. (4) is used to determine the PSD estimates as functions of spatial frequency. The digital computer program is a modified SHARE Subroutine (No. 13236), "CS TUKS" or "Tukey Spectrum Estimation." The computational procedures are defined below.

The autocorrelation function was calculated by
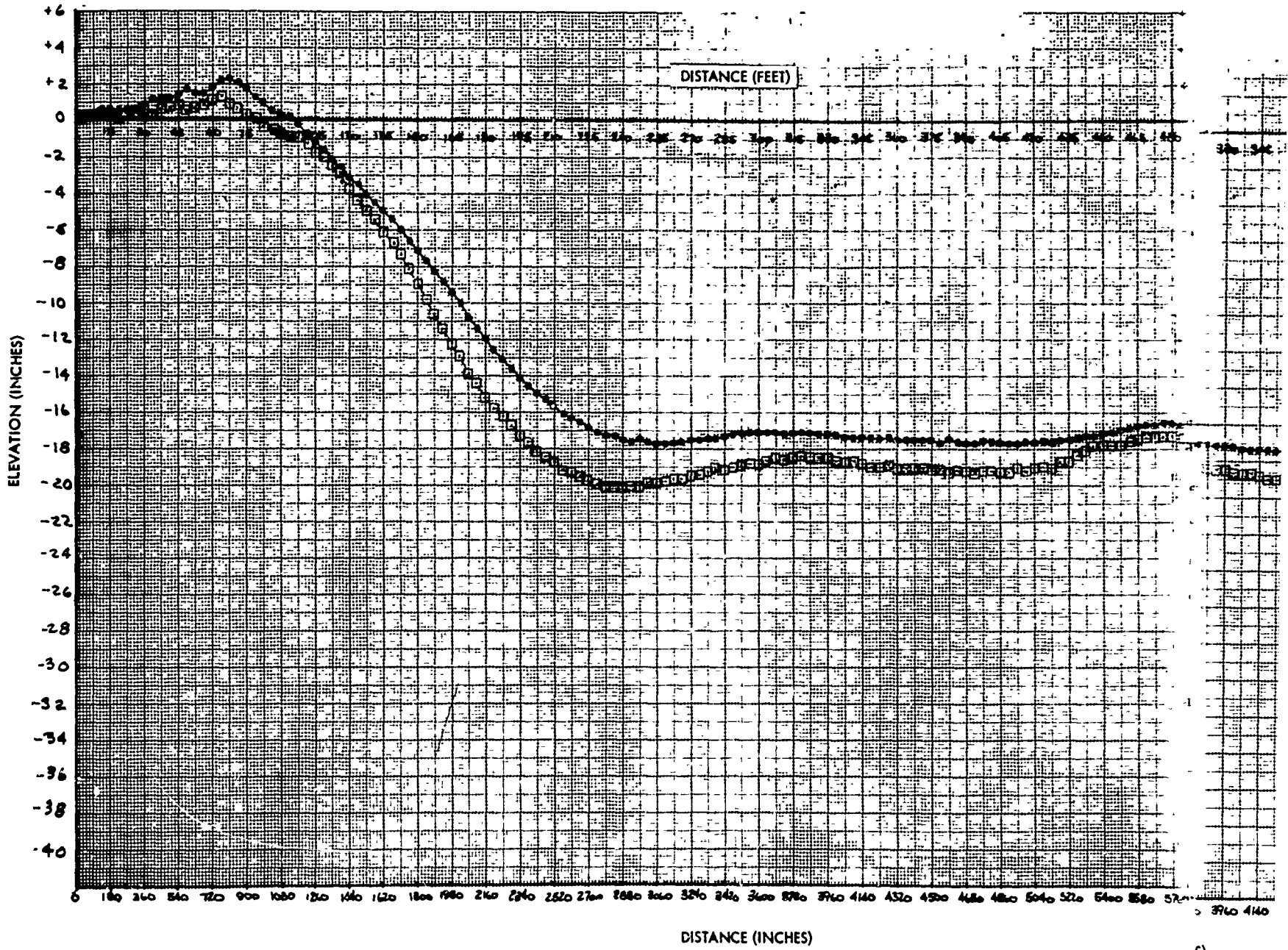
Fig. 5. Calculated and surveyed profiles o

A
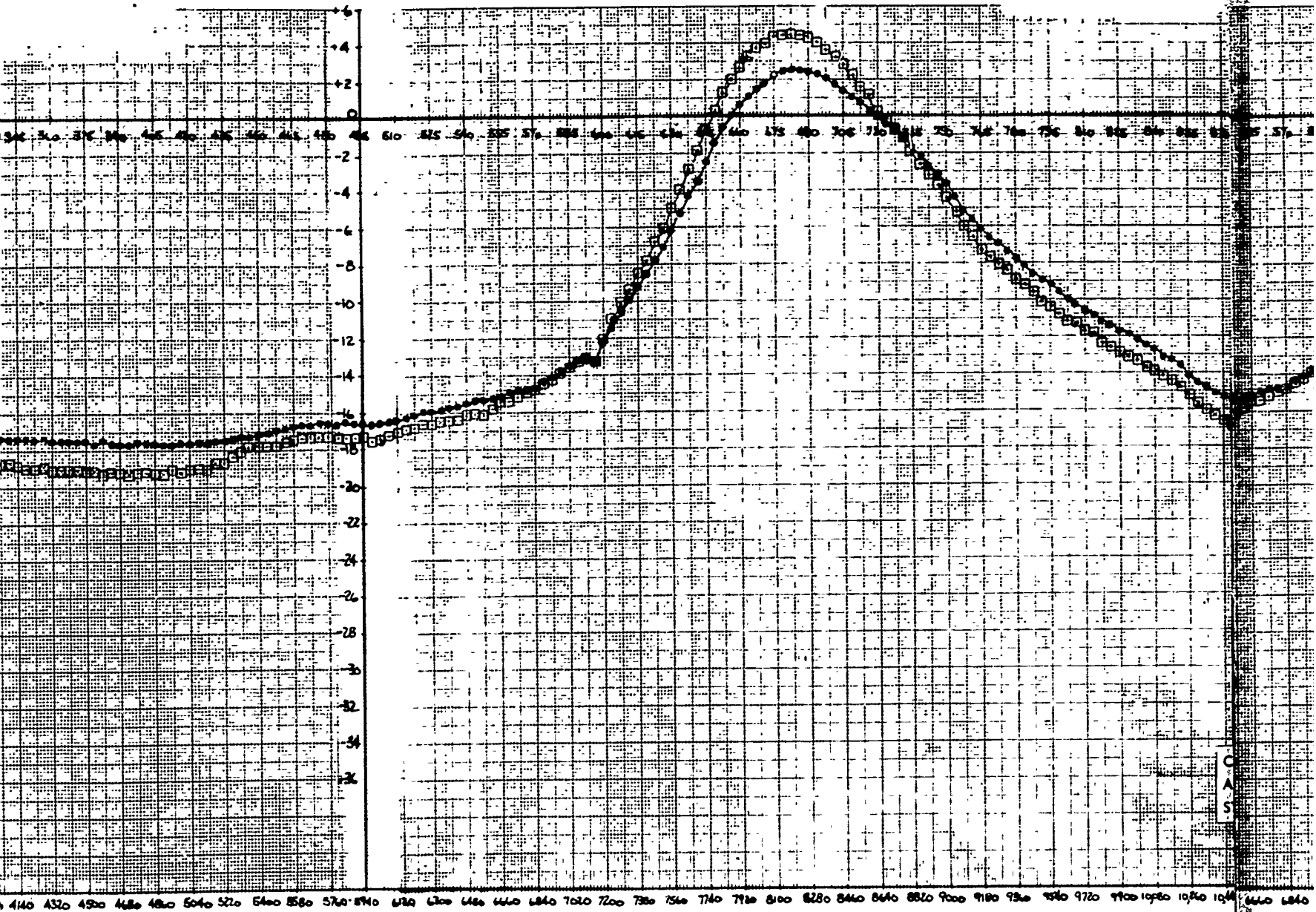
Calculated and surveyed profiles of calibration strips, Arizona road roughness study

B
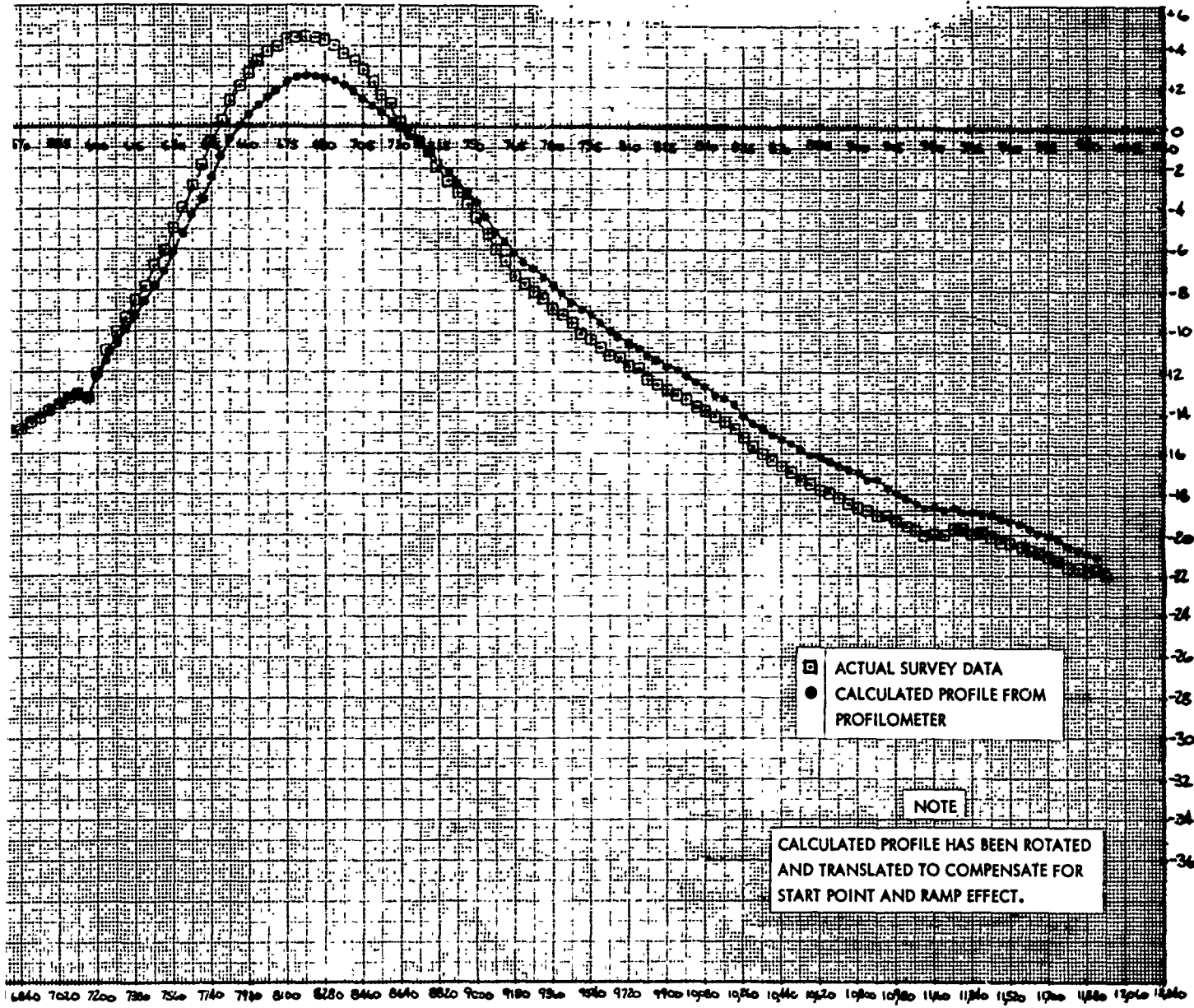
, Arizona road roughness study

$$A(L) = \frac{1}{(n-L)} \sum_{i=L+1}^{N} Y_{i-L}'' Y_i''$$

$$- \left(\frac{1}{n-L}\right)^2 \sum_{i=L+1}^{n} Y_{i-L}'' \sum_{i=L+1}^{n} Y_i'' , \quad (5)$$

where

$L = 0, 1, 2, \ldots 99$, and

n = total number of data points.

The second term in Eq. (4) removes the mean.

Next, the PSD estimates were found by

$$X(K) = \frac{\delta_K}{m} \sum_{L-1}^{m-1} 2e(L) \cos \frac{KL\pi}{m} A(L) + A(0) , \quad (6)$$

where

$K = 0, 1, 2, \ldots 99,$

$\delta_K = 1/2$ for $K = 0$ or $K = m,$

$\delta_K = 1$ for all other values of $K,$

m = number of spectral estimates, and

$2e(L) = 1 + \cos (L\pi/m).$

The latter function is termed a lag window by Tukey (3) and serves to concentrate the principal maximum or main lobe of the PSD near zero frequency. $X(K)$ is an estimate of energy per unit interval of F centered on $F = K$, for values of K equal to $1, 2, \ldots 99$, where F equals frequency (cycles per inch) times m times ΔS.

The number of spectral estimates was chosen to be 100. Using an approximate number of data points equal to 2500 gave 50 degrees of freedom. This was considered a practical minimum and would have been further reduced if more spectral estimates had been taken. Each PSD was stored on a master tape which finally contained all PSD's. This tape was used for listing and plotting purposes, and also can be used, like the profile master tape, for further processing.

RESULTS OF PSD COMPUTATIONS

The results of all PSD samples calculated for West German roads (4) are summarized in Fig. 6. The power spectral density (displacement density = sq in./cycles/in.) is plotted versus the spatial frequency (Ω = cycles/in.). All PSD samples fall within the envelope established by the upper and lower boundaries of the plotted envelope.

The variation of the power content is more pronounced in the low-frequency range (long-wave formation) which indicates the long-term trends of the profile but does not describe its actual roughness content.

The same envelope was also determined for all Arizona road samples, resulting in a slightly lower power content which was caused by the inclusion of some recently completed Interstate highway sections (5). A comparison of the two road PSD envelopes with previously determined aircraft runway data (6) is shown in Fig. 7.

The presented summary envelope of hard surfaced profiles (Fig. 7) establishes the preliminary displacement density input envelope that can be expected for road mobile systems.

MATHEMATICAL MODELS

The generated road profile and PSD data were then used as input to a highway mobile transport vehicle to perform an extensive suspension system analysis. The actual transporter-launcher configuration shown in Fig. 8 was represented by the dynamic model in Fig. 9, simulating the vertical plane motion of the rigid and elastic body modes of the dynamic system.

The mathematical models developed to describe the time-dependent and frequency-dependent system response were formulated by using Lagrange's equations of motion:

$$\frac{d}{dt} \frac{\partial T}{\partial \dot{q}_r} - \frac{\partial T}{\partial q_r} + \frac{\partial Fd}{\partial \dot{q}_r} + \frac{\partial U}{\partial q_r} = 0 . \quad (7)$$

For oscillations about the equilibrium positions of the dynamic system, the kinetic energy (T) is independent of the system displacements, and Eq. (7) can be reduced as shown by Eq. (8):

$$\frac{d}{dt} \frac{\partial T}{\partial \dot{q}_r} + \frac{\partial Fd}{\partial \dot{q}_r} + \frac{\partial U}{\partial q_r} = 0 . \quad (8)$$

Differentiation of Eq. (8) using matrix operations results in the standard (coupled) equations of motion shown in matrix notation by Eq. (9):

$$[m]\{\ddot{q}\} + [c]\{\dot{q}\} + [k]\{q\} = \{Q\} . \quad (9)$$

77
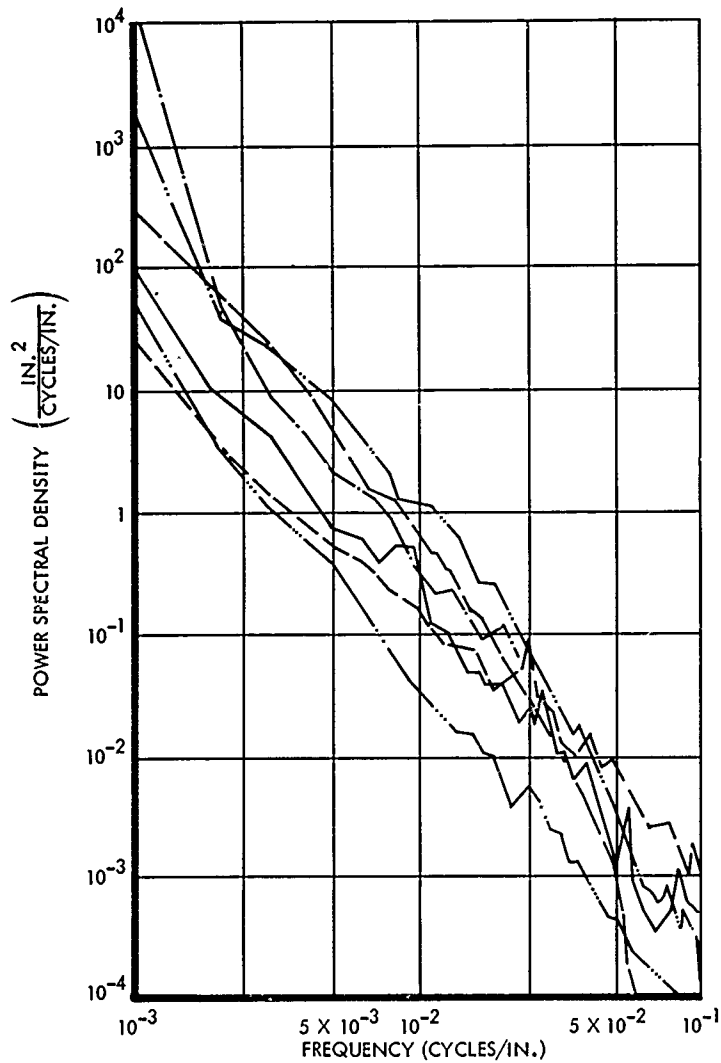
PSD ------ PSD 1-7 – CONCRETE GOOD 3/4° UPGRADE AT START, LEVEL END

PSD 1-72 – CONCRETE GOOD LEVEL SMOOTH NEW

PSD 2-8 AR – BITUMINOUS LOW FAIR, SLIGHT DOWNGRADE

PSD 2-13 – BITUMINOUS INTERMEDIATE POOR; 3/4° UPGRADE, QUITE ROUGH

PSD 2-23 – BITUMINOUS LOW FAIR; 1-1/4° DOWNGRADE, WAVY

PSD 2-5 – BITUMINOUS HIGH FAIR; 1° DOWN FOR 3/4 WAY, THEN 4° UP.

Fig. 6. PSD envelope of West German roads
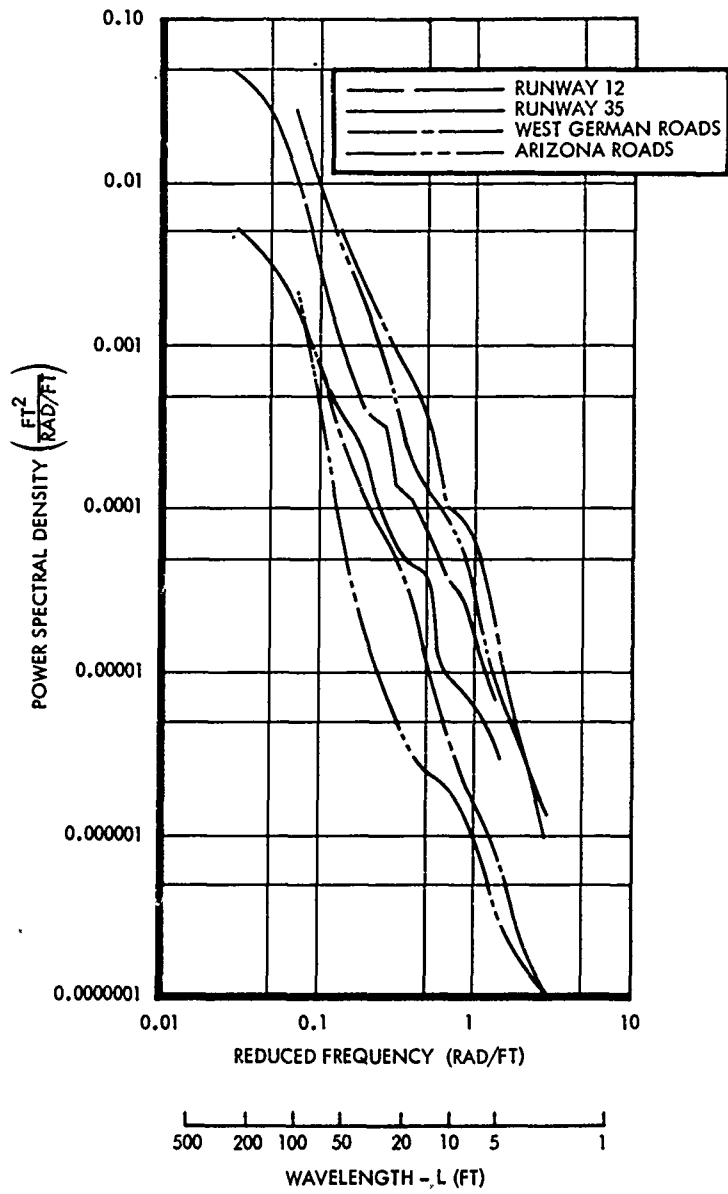
Fig. 7. Summary envelope of road PSD's
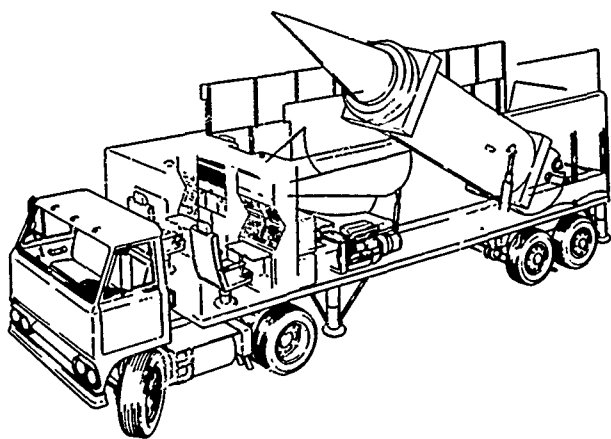
Fig. 8. Transporter-launcher configuration

By use of the superposition principle and the orthogonality relationship of the modes (eigen-vectors), the equations can be uncoupled as indicated by Eq. (10):

$$[u]^{TR}[m][u]\{\ddot{\eta}\} + [u]^{TR}[c][u]\{\dot{\eta}\}$$
$$+ [u]^{TR}[k][u]\{\eta\} = [u]^{TR}\{Q\}. \quad (10)$$

From performance of the indicated matrix operations, the uncoupled equations of motion are obtained as shown in matrix notation by Eq. (11) and expressed individually by Eq. (12):

$$[M]\{\ddot{\eta}\} + [C]\{\dot{\eta}\} + [K]\{\eta\} = \{N\}, \quad (11)$$
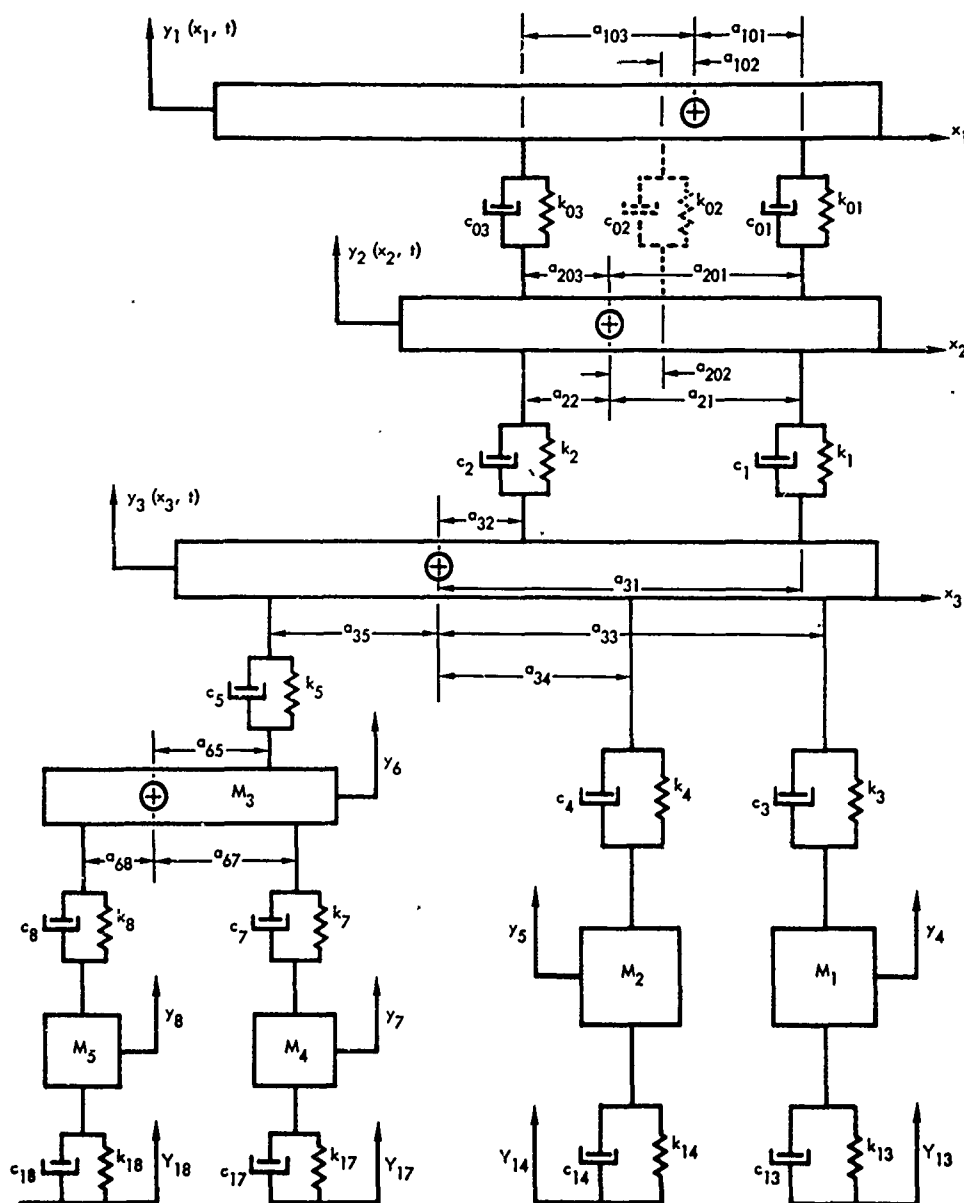
Fig. 9. Mathematical model -- 18 degrees of freedom

$$M_{rr}\ddot{\eta}_r + C_{rr}\dot{\eta}_r + K_{rr}\eta_r = N_r(t) . \qquad (12)$$

The complete discussion of the mathematical models is given in Ref. 7. Figure 10 shows only the sequence of operations that were performed to analyze the dynamic system by both digital and analog computers. The coupled equations of motion were used directly in the analog program to obtain the harmonic system response. In the digital computer programs, they were first uncoupled before proceeding to solve for either the time- or frequency-dependent response. The transient model solves for the instantaneous system response, giving the physical motion of the system (accelerations, velocities, and displacements). The

harmonic model solves for the harmonic response caused by a harmonic input and uses the calculated transfer functions to determine the PSD response for a given road PSD input. The program also determines the mean square (ms) value of the response by the summation process of Eq. (13):

$$\sigma^2 = \int_0^\infty PSD(\omega) \, d\omega . \qquad (13)$$

The rms value represents the statistical average system response resulting with a given road PSD input.
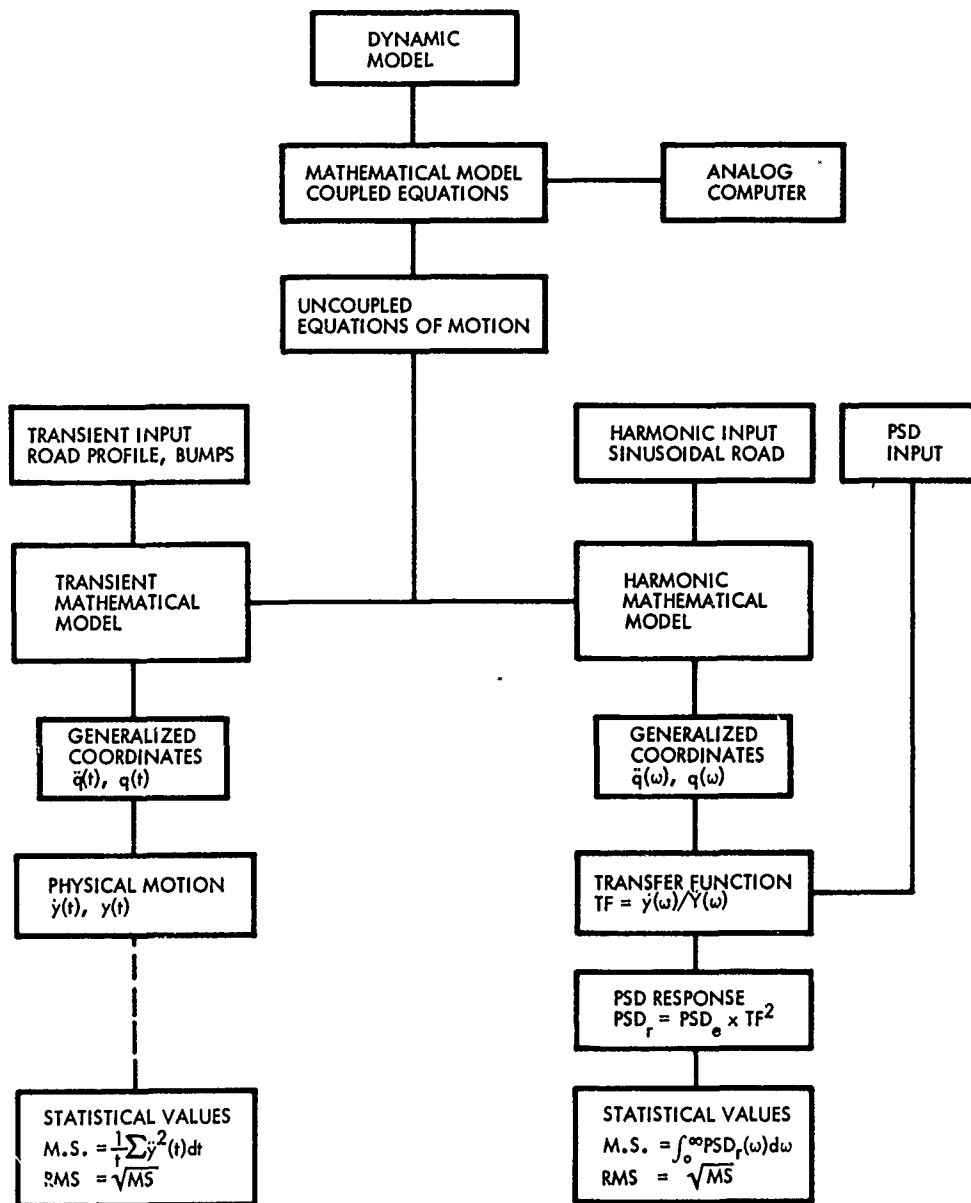
Fig. 10. Outline of mathematical model solution

STATISTICAL SYSTEM RESPONSE

Acceleration density calculations were made for the complete transporter-launcher using the PSD data of all the road samples of West Germany. Sample rms acceleration envelopes for vehicle velocities of 30 and 50 mph are shown in Figs. 11 and 12. The rms accelerations along the length of the payload are presented in Fig. 11. The corresponding rms envelope of the trailer is shown in Fig. 12. The influence of the vehicle velocity on the system response is indicated in Fig. 13.
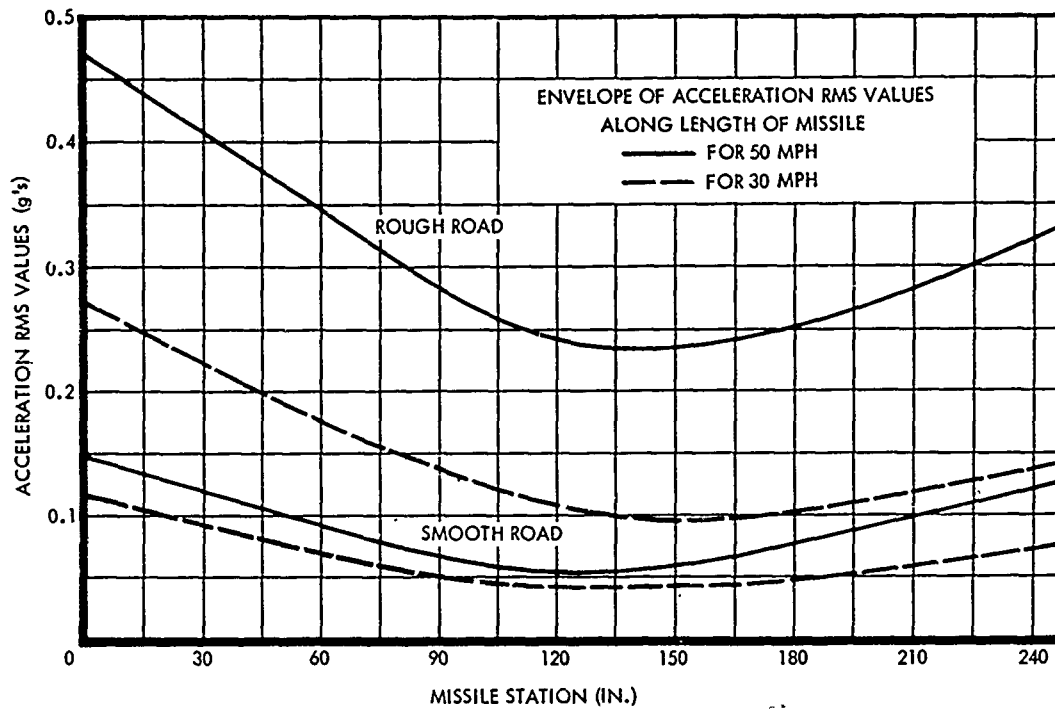
Fig. 11. Transporter-launcher system response envelope — payload
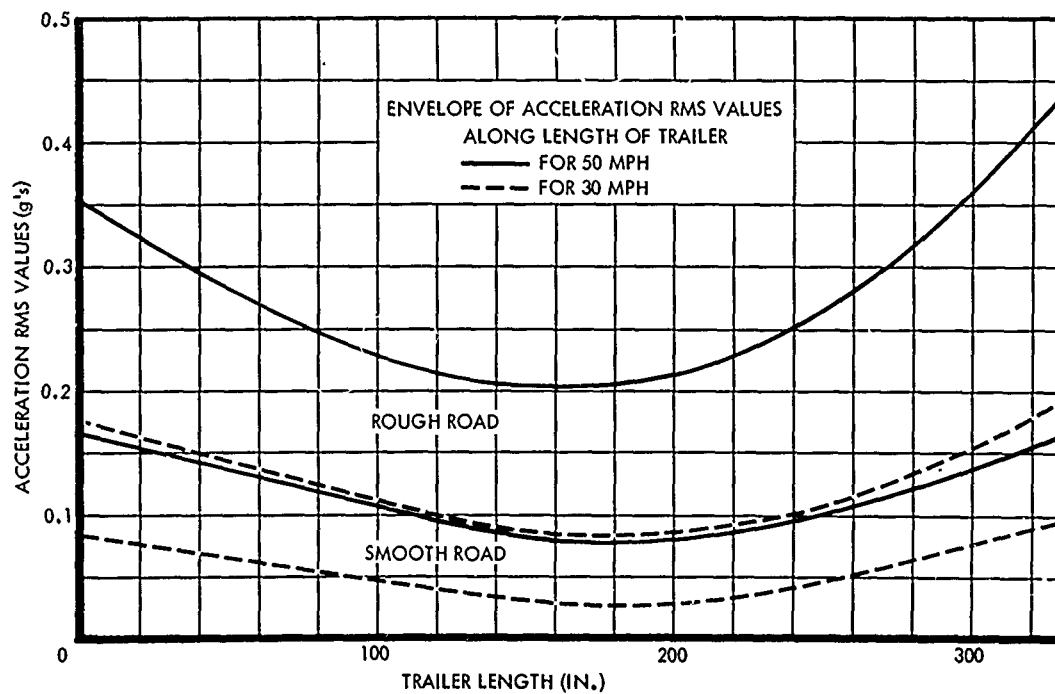
Fig. 12. Transporter-launcher system response envelope — trailer

82
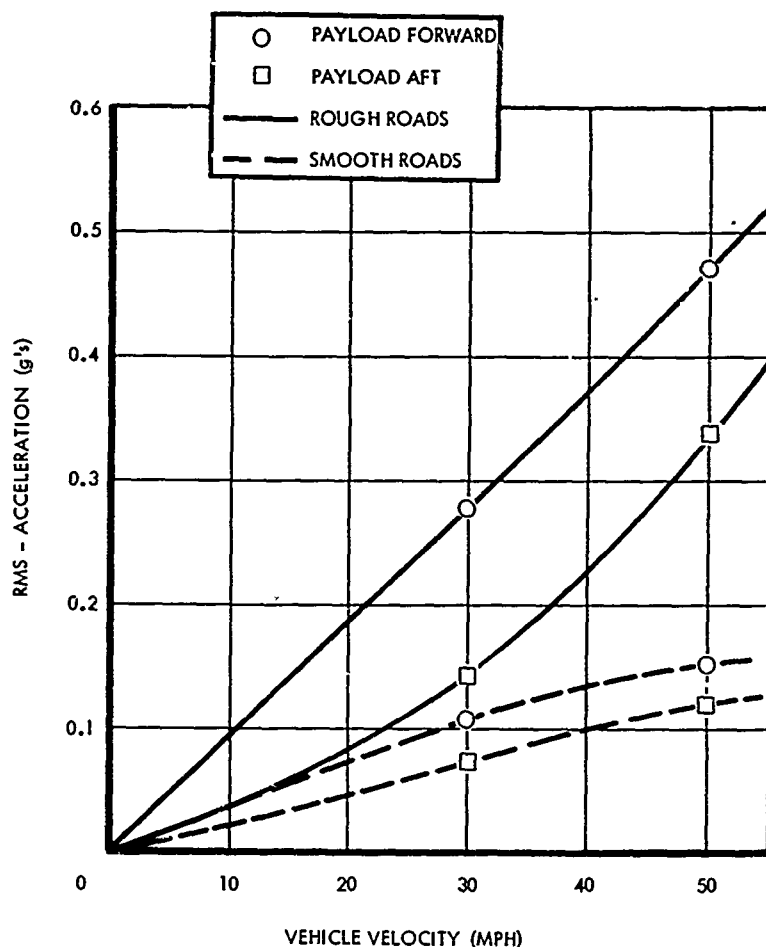
Fig. 13. System response vs vehicle velocity

The results of the statistical solution (PSD response) were then compared with the results obtained by the deterministic solution (transient response), and good correlation was obtained. The peak response determined from the transient solution was, in general, from two to four times the rms value, determined from the ms value of the instantaneous response. This is in good agreement with the statistically expected peak values for narrow and broad band vibrations.

CONCLUSIONS

A roughness measurement technique and its subsequent application to the statistical evaluation of the system response of a highway mobile transport vehicle has been presented.

The plotted displacement density envelopes of hard-surfaced profiles provide a good statistical description of the roughness content of hard-surfaced roads. They can be used as a preliminary input envelope in the fatigue analysis of road mobile vehicles.

The generated system response for a highway mobile weapons system shows a sample solution of the analytical procedure formulated by Goodyear Aerospace Corporation. Both the input and system response analyses can be used very effectively to determine the expected dynamic environment of any road mobile vehicle. Since the mathematical models (computer programs) are written in the most general form, employing mostly matrix operations, they can be used with any dynamic system.

Optimization of the raw data processing technique makes it possible to record large numbers of test strips and convert them to actual profiles and PSD input data. These can be used with either a statistical or deterministic solution.

83

REFERENCES

1. J. Sattinger and S. Sternick, "An Instrumentation System for the Measurement of Terrain Profile," U. of Michigan, Tech. Rept., December 1961

2. R. B. Blackman and J. W. Tukey, "The Measurement of Power Spectra from the Point of View of Communications Engineering," The Bell System Technical Journal, (January and March 1958)

3. J. W. Tukey, "The Sampling Theory of Power Spectrum Estimates," Symposium on Applications of Auto Correlation Analysis to Physical Problems (Woods Hole, Massachusetts, ONR, 1949), pp. 47-67

4. GER-11092, "Reduction of Highway Profile Data for MMRBM Transporter-Launcher Structural Analysis," Supplement 1

(Goodyear Aerospace Corporation, Akron, Ohio), July 1963

5. GERA-868, "Road Roughness Study of Arizona Highways Transporter-Launcher Subsystem," Revision A (Goodyear Aerospace Corporation, Litchfield Park, Arizona), August 1964

6. J. H. Walls, J. C. Houbolt, and H. Press, "Some Measurements and Power Spectra of Runway Roughness," NACA T.N. No. 3305 (Langley Aeronautical Laboratory, Langley Field, Virginia), 1954

7. GERA-693, "Phase I - Final Technical Report, Transporter-Launcher Subsystem (WS 325A), Part B - Volume 10 - Suspension System" (Goodyear Aerospace Corporation, Litchfield Park, Arizona), March 1963

DISCUSSION

Mr. Fitzgibbon (Mechanics Research): It would appear that this type of mathematical model would be most useful for design purposes when one is studying various suspension systems, namely, various shock absorbers. Apparently you have used a modal analysis technique which leads to some very serious deficiencies. One must have particular constraints on the damping properties that go along with the spring constants, primarily the c matrix. The damping matrix has to be proportional to the k matrix. How do you intend to handle this problem?

Mr. Wursche: It is true that the analysis is limited to damping less than 30 to 40 percent critical, which is slightly above most of the damping factors used in commercial vehicles. They usually run about 15 to 20 percent critical. Most of the missile system damping coefficients are around 40 percent critical (Minuteman), and for some of the others it is slightly less. Beyond 40 percent critical damping there is a problem in the coupling of your matrices. So it is true that this analysis is limited in that sense. There is no suitable means, however, of going to a very highly nonlinear system unless a nonlinear or a transient analysis is performed. There is no harmonic solution possible.

Mr. Fitzgibbon: I was not concerned about the magnitude of the damping but the formation of it. If consistency between the stiffness

matrix and the damping matrix is not observed, the modes are coupled, even for very low damping.

Mr. Wursche: This is true. In some cases when the off-diagonal elements are neglected, adjustments for them are made when the equations are coupled.

Mr. Fitzgibbon: There is an approach using a complex eigenvalue solution where one can, in fact, handle arbitrary damping.

Mr. Wursche: Yes, we also have used this approach, but it usually cuts down the number of degrees of freedom to about 12. If one tries to run 18 degrees of freedom, some simplifying assumptions must be made, because more than twice the computer storage is needed to get a complex eigenvalue solution. In a PSD analysis the effects are smoothed out and one gets just statistical values.

Mr. Scott (Sandia Corp.): The profilometer seems to depend a great deal on the wheel diameter, on the tire pressures, and on the fact that the vehicle is rolling along in a straight line and there are four wheels on the truck. How did you decide what tire pressure and what wheel diameter to use?

Mr. Harvey: We did not decide this because the profilometer was already in existence.

We tried different pressures in the tires but the tires are so large and the pressure is so low that there was no sensitivity due to that. Because of the diameter of the tires we could not measure wavelengths accurately under 1-1/2 feet, but the response of our vehicle was not sensitive to these so all the wavelengths under 1-1/2 feet were filtered out.

Mr. Forkois (U.S. Naval Research Laboratory): Did you consider using a machine to simulate the road profile so that you would have a means for actual testing of the vehicle and the transportable item?

Mr. Harvey: I think you have to have the road profile to simulate it using a machine. What did you have in mind?

Mr. Forkois: Rotating drums with some sort of an axis-moving device to change the profile.

Mr. Harvey: If one had a profile and the vehicle, that could be done, but we did not have either. We decided on this approach.

Mr. Forkois: It might be valuable in laboratory testing. One would not have to go out in bad weather.

Mr. Harvey: I think that the tapes we have now would be very useful in laboratory tests. For example, there is a ride simulator in the land locomotion laboratory. These tapes could be used to force the ride simulator, and one could probably get very useful human engineering information.

Mr. Rice (Goodyear Aerospace Corp.): What did the power spectral response look like on the missile itself? What was the upper limit of the frequencies recorded?

Mr. Wursche: The upper frequency limit was about 40 cps. Most of the response was below 10 cps, either due to the natural frequencies of the missile's suspension system or the coupling and the intereffect of the main trailer suspension and the wheel hop frequency. Above 10 or 12 cps the response dropped off very fast.

Mr. Rice: Was there much power in the 40-cps response above 1 g or 1/2 g? What kind of levels did you get on the missile?

Mr. Wursche: The peak acceleration was slightly below 0.5 g and there were a few isolated peaks near 0.5 g.

Mr. Zell (Picatinny Arsenal): What were the relative suspension frequencies of the basic vehicle itself and the secondary suspension of the missile? Do you feel that the frequencies chosen would have any bearing on the overall approach for designing secondary suspension frequencies for equipment to be transported by wheeled vehicles?

Mr. Wursche: The predominant suspension frequency of the trailer was slightly over 1.2 cps and the frequency of the missile suspension was about 3 cps. We tried to stay above the very lowest frequency of the trailer suspension as much as we could so that we would not have interaction. We could not make it too stiff because we had to meet our 1/2-g rms acceleration to the payload during the continuous deployment. We tried to make it at least twice as high to get away from the basic frequency of the trailer suspension. The next frequency of missile rotation was about 3-1/2 to 4 cps. The next predominant one was the wheel hop frequency, about 10 cps.

*   *   *

PROGRAM 624A—TITAN III-C

TRANSPORTATION TESTS

Louis A. Molinari
United Technology Center
Sunnyvale, California

and

Jack R. Reynolds
Space Systems Division
Los Angeles, California

This paper reports on the development of Program 624A transportation systems, and in particular, the major tests contributing to their development.

INTRODUCTION

Award of the Air Force contract for Program 624A (Titan III-C) presented United Technology Center (UTC) with some very new and interesting transportability problems. Transport of Program 624A Solid Rocket Motor (SRM) components, many of which would be of excess weight and dimension, by truck and rail mode over long distances in substantial volume would be required. In addition, special transport equipment and systems would have to be developed for protection of shipments against environmental extremes of shock, vibration, and climate to insure that each components' operating reliability would not be jeopardized during transit.

BACKGROUND

The following descriptions of shipment characteristics, container system, and Program 624A environment requirements are provided as a background for test particulars contained in the body of this paper.

Shipment Characteristics

Physical characteristics of the SRM components and contractual/environmental requirements for specific components and aerospace ground equipment (AGE) is reflected in Table 1.

Container Systems

Containers engineered to protect Titan III-C components during shipment or storage consist of three major assemblies: cover assembly, side enclosure, and base. Base and side closure are equipped with ports for connection of air conditioner discharge and supply hoses. Protection caps cover the openings when not in use. Lifting eyes provided on the cover base and side closure are used when assembling and lifting the empty container.

The loaded container is lifted by use of a hoisting fixture attached to the packaged motor component. Seals at the interfaces between major assemblies and on access doors assure a leak-tight enclosure when assembled. Four machine pads are provided on the container base to index the container to transporter deck interfacing hardware and resist shear loads.

Enclosures are provided on the outside of the base for mounting and protecting temperature, humidity, and shock recording instrumentation. Interfaces for attachment of shock accelerometers are provided on the outside of the base.

Environment

Climate and humidity controls are required during transit to assure the technical integrity of segments, closures, and nozzles. The

TABLE I

⊕ = Shipped on Trailer with Hard Cover

Component	Physical Configuration	UTC Drawing No. and Part No.	Component Shipping Weight (Approximate) In Pounds	Total Shipping Weight With Related AGE & Instrumentation (Approx.) In Pounds	Component Dimensions (Approximate) In Inches		Shipping Container Dimensions (Approximate) In Inches	Explosive Classification
Loaded Segment	Hollow Cylinder Heavy Wall	4M2401	79,000	92,800	122 dia.	126 lg.	136 dia. / 164 ht.	B
Loaded Forward Closure	Hemispheric	4M1402	38,500	58,390	122 dia.	93 lg.	136 dia. / 164 ht.	B
Insulated Case, Igniter (2)	Hollow Cylinder One End Closed Hemispherically	4M1620-2	260	Packaged With Loaded Forward Closure	22 dia.	24 lg.	Packaged With Loaded Forward Closure	
Cartridge, Igniter (2)	Hollow Cylinder Heavy Wall	4M1617			14 dia.	32 lg.		B
Insulated Closure, Igniter (2)	Dished Disc	4M1633	90		22.5 dia.	6.5 lg.		
Cartridge, Initiator (2)	Hollow Cylinder Heavy Wall	4M1630	10		4.5 dia.	9.5 lg.		B
Insulated Case, Initiator (2)	Hollow Cyl, one end Closed Hemispherically	4M1625			22.5 dia.	6.5 lg.		
Loaded Aft Closure	Hemispheric	4M3402	26,500	44,750	122 dia.	54 lg.	136 dia. / 164 ht.	B
Nozzle Assembly	Conical	4M4002	7,700	15,925	106 dia.	80 lg.	121 dia. / 117 ht.	
Nozzle Extension	Conical	4M4001	2,300	10,440	113 dia.	58 lg.	121 dia. / 117 ht.	
TVC Tank Assembly	Hollow Cyl. thin wall both ends closed	4T5001	7,300	17,420	42 dia.	576 lg.	⊕	

temperature range of 60° to 90° F, with a maximum of 50 percent humidity which must be maintained, is provided by temperature control units (TCU) powered by diesel engine generators (DEGS) which accompany the shipments. Since the repair and maintenance of DEGS and TCU's require special in-transit services to be performed by the railroad or trucking firm transporting the shipments, special pamphlets of instructions have been issued for carrier guidance.

Shock limitations for segments, closures, and nozzles will be restricted to a maximum of 3 g on either the longitudinal, transverse, or vertical axis. Accordingly, shock mitigating protection is required. To provide special shock protection required on transcontinental rail runs, specially built cars were fabricated by the Western Pacific and Southern Pacific Railroads. The car features a 20-in. travel hydracushion underframe and a 200,000-lb payload capacity.

Sensing devices and recorders installed on containers housing each component provide a continuous record of conditions encountered in transit. If any prescribed limits are exceeded, the component is subject to special inspection procedures at destination to insure technical integrity and acceptability.

TEST PROGRAMS

Transportation test programs related to shock and vibration environment consist of:

1. Normal handling acceleration and strain test,

2. Highway transportation test — 400 miles,

3. Railcar impact test, and

4. Transcontinental rail test.

Normal Handling Acceleration and Strain Test

The purpose of the test was to demonstrate the effects of normal handling and movement by highway transporter in preparation for an actual 400-mile road test. In this case, transportation conditions were simulated by artificial means. The primary objectives were (a) to demonstrate the normal strains and accelerations to which a thermal gradient (TPGR) segment would be subjected during packaging, loading and transport; (b) to demonstrate the normal strains to

which the AGE and tooling would be subjected during packaging, loading and transport; and (c) to test the engineering calculations and predictions governing the developing and handling of transportation procedures and techniques.

The test configuration consisted of the TPGR segment, a shipping and storage container-base assembly, and the transporter. The transporter consisted of a low-bed trailer (60-ton capacity) 11 ft. wide, a 16-wheel jeep dolly, and a standard truck tractor. The jeep dolly was equipped with a universal fifth wheel, and the tractor was equipped with a standard fifth wheel.

Test instrumentation on the TPGR segment consisted of 24 strain gages placed in the vertical axis and 8 strain gage accelerometers mounted as shown in Figs. 1 and 2. Container base instrumentation consisted of 8 strain gages located as shown in Fig. 3. Another set of 8 strain gages was located on the trailer, as shown in Fig. 4; 4 gages were mounted on the trailer beam in the vertical axis, and 4 on the trailer-beam flange in the horizontal axis.

Test activities consisted of: (a) lifting the segment clear of the ground and positioning it on blocks, (b) lifting the segment off the blocks and installing it on a container-base assembly, (c) installing the segment package on the trailer, (d) measuring transporter trailer bed deflections before and after loading with segment, and (e) simulating highway movements.

Results

Segment Package Build-Up — Oscillogram data indicated that the strain on the segment case during package build-up was insignificant. Maximum strain was estimated at 0.00030 in./in., as compared to the allowable 0.00420 in./in. As the segment/ring assembly was lowered onto the container base, oscillogram data indicated a maximum acceleration of approximately 0.4 g in the X axis, 0.3 g in the Y axis, and 0.26 g in the Z axis.

Maximum accelerations and strains recorded during installation of the segment package on the trailer occurred in lowering the package onto trailer bed; g readings were X axis, 0.22; Y axis, 0.10; and Z axis, 0.20.

Deflection Measurements — Maximum trailer bed deflections with the segment package installed were 1.64 in. with trailer in line with jeep dolly and 0.94 in. with the jeep dolly at a 45-degree angle to the trailer centerline.

THERMAL GRADIENT SEGMENT

CABLE ASSEMBLY

CABLE LEAD TO DATA
ACQUISITION EQUIPMENT

BLH FAB 50-35-56 STRAIN GAGES EQUALLY
SPACED WITH 12 NEAR THE TOP WELD AND
12 NEAR THE BOTTOM WELD

ARROW INDICATES TOP DEAD CENTER

STRAIN GAGE PLACEMENT
APPROXIMATELY 1 INCH
FROM TOP AND BOTTOM
WELDS

TOP WELD

PROPELLANT

SYMBOL   INDICATES STRAIN GAGE

BOTTOM WELD

105°
75°
135°
45°
165°
15°
195°
345°
225°
315°
255°
285°

Fig. 1. Location of strain gages on TPGR segment

90
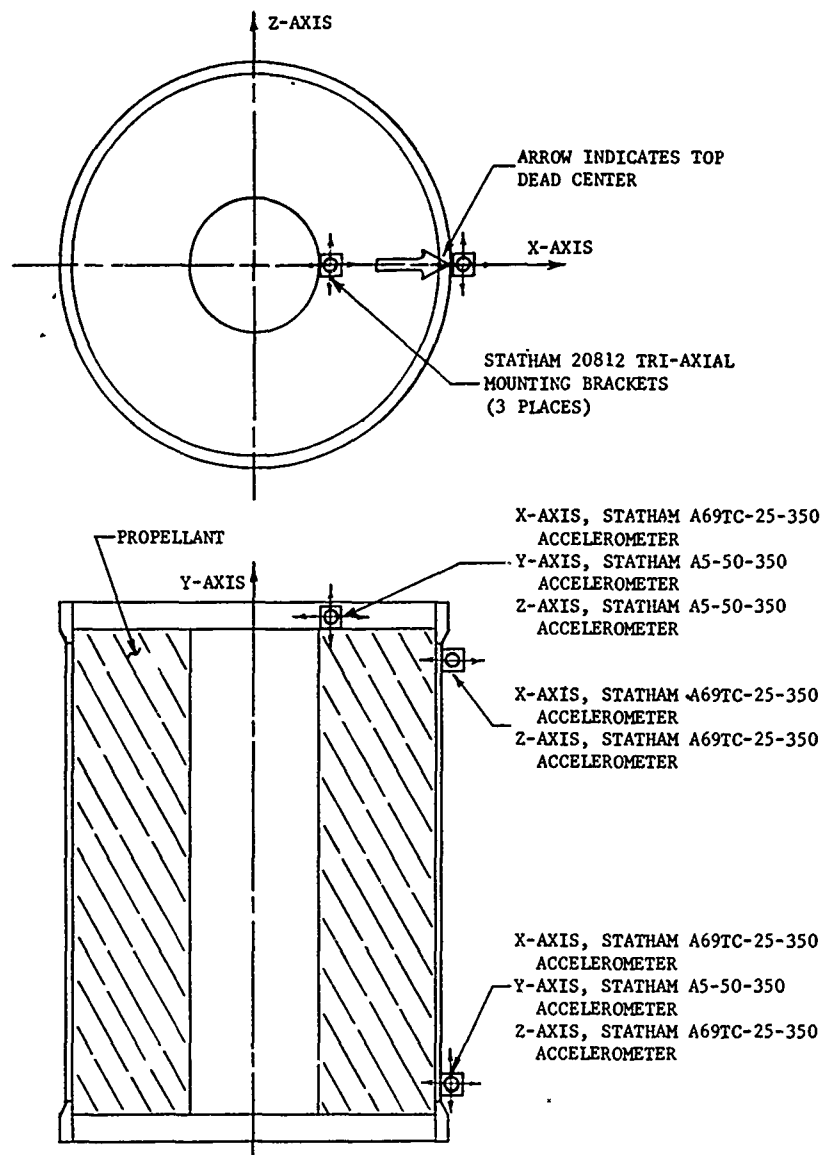
Fig. 2. Location of accelerometers on TPGR segment

Figure 5 plots trailer bed deflections with the jeep dolly at a 45-degree angle to the trailer. A point by point breakdown of the deflection measurements is given in Table 2.

Simulated Highway Movements — Simulation consisted of: (a) lifting right rear corner of trailer bed to 5 in. (jeep dolly in line with trailer), (b) lifting corner of trailer bed to 4 1/2 in. (jeep dolly at 45-degree angle to trailer), (c) lifting corner of trailer bed 5 in. (tractor equipped with standard fifth wheel in line with trailer), (d) lifting corner of trailer bed to 4 1/2 in. (trailer at 45-degree angle to tractor), (e) pulling trailer off 2-in. blocks with braking on impact, and (f) pulling trailer off 2-in. blocks with no braking on impact.

During the lifting tests, it was found that the trailer would not continue to twist beyond a

certain point. This point was reached when the right rear corner of the trailer bed had jacked up to a height of 4 in. At this point, the left front corner of the trailer bed began to drop as the right rear corner lifted. The drop and resulting tilt of the segment package were greater with the universal fifth wheel than with the standard fifth wheel.

The overall maximum acceleration occurred when the trailer was pulled off the blocks and brakes were applied. This acceleration was 0.21 g in the X axis, 0.14 g in the Y axis, and 0.13 g in the Z axis. The overall maximum strain on the trailer bed also occurred when the trailer was pulled off the blocks and the brakes were applied. This reading was 0.00901 in./in.

Overall maximum strains on the segment case and the container base were recorded

91

225°

315°

135°

45°

ARROW INDICATES TOP
DEAD CENTER

BLH FAB-50-35-56 STRAIN GAGES
EQUALLY SPACED WITH 4 ON THE
TOP RIM AND 4 ON THE BOTTOM RIM

SYMBOL ▮ INDICATES STRAIN GAGE
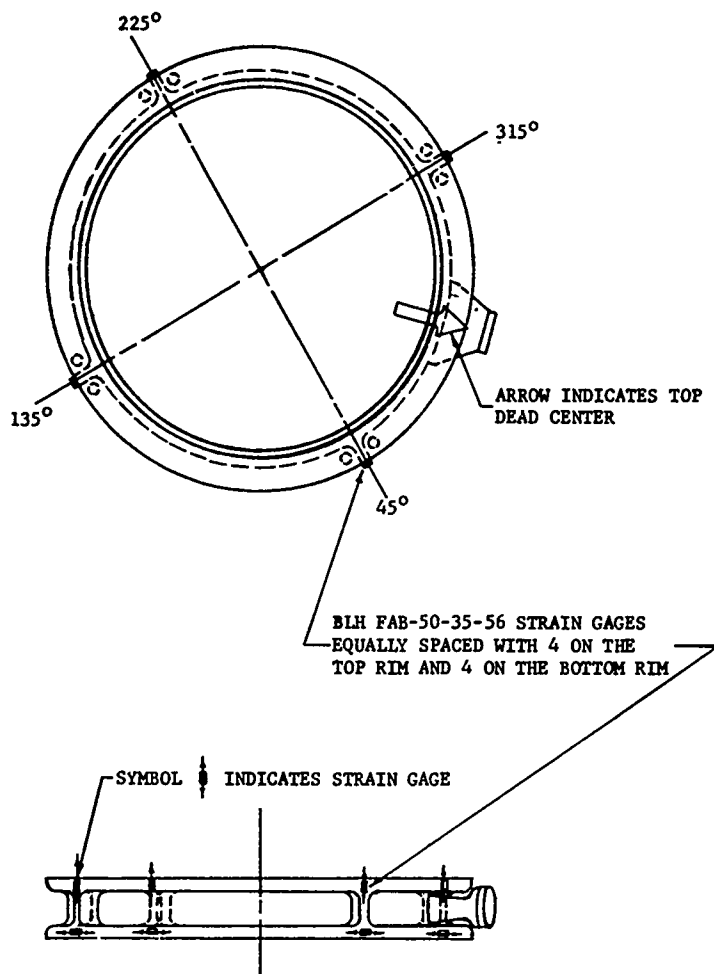
Fig. 3. Location of strain gages on
container base

CONTAINER BASE ADAPTERS

SYMBOL ➤ INDICATES
STRAIN GAGE

BLH FAB-50-35-56 STRAIN GAGES (8 PLACES)
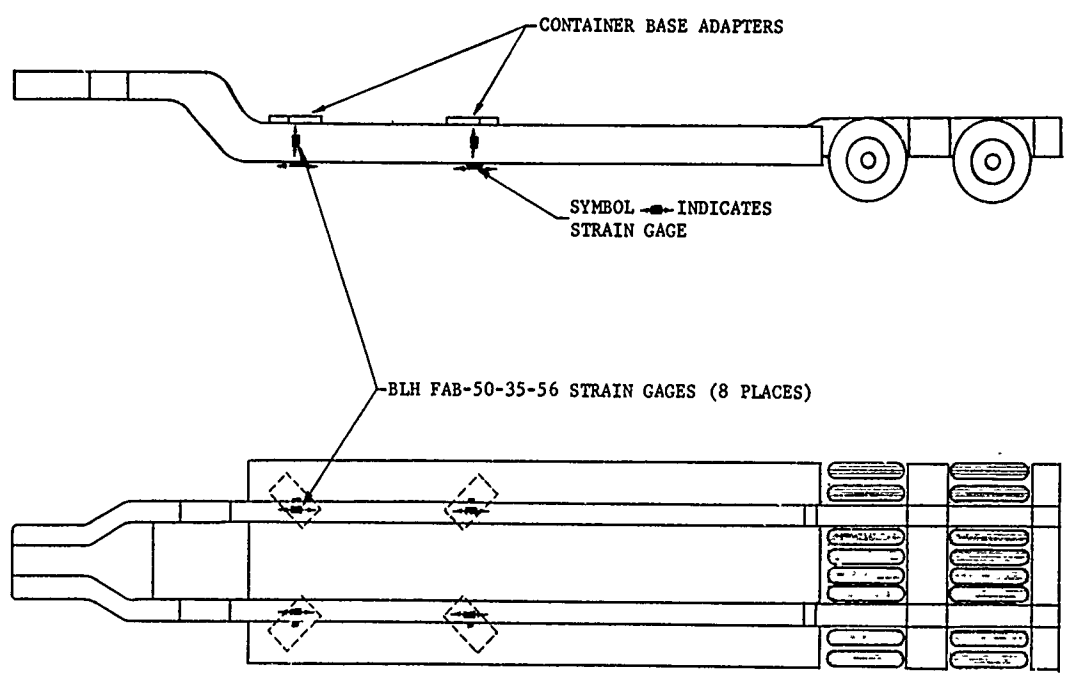
Fig. 4. Location of strain gages on trailer

92
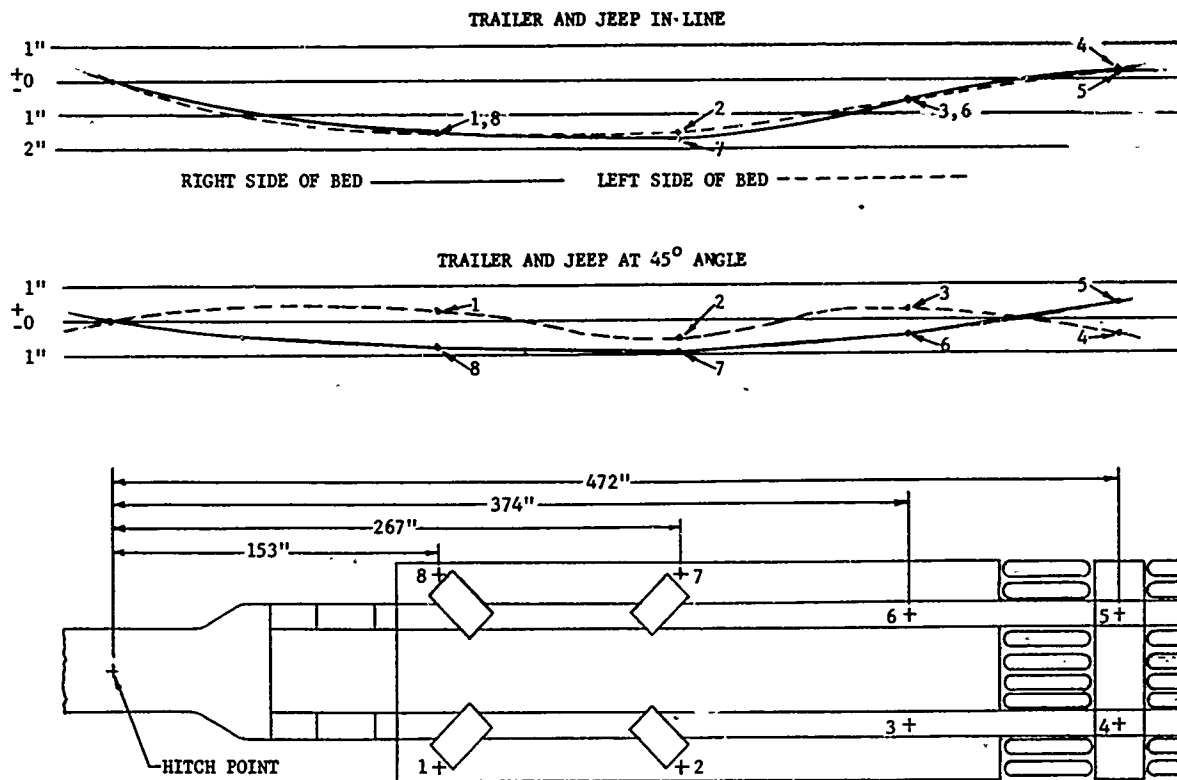
Fig. 5. Trailer bed deflection

TABLE 2
Trailer Bed Deflection

Point on Trailer Bed	Deflection, in.	
	Jeep Trailer in Line	Jeep at 45-Degree Angle to Trailer
1	-1.50	0.30
2	-1.64	-0.51
3	-0.58	0.29
4	0.24	-0.42
5	0.34	-0.80
6	-0.58	-0.94
7	-1.53	-0.45
8	-1.49	0.43

during lifting of the right rear corner of the trailer bed to 4 1/2 in. with the trailer attached and jackknifed to a 45-degree angle to the tractor. Readings were 0.00208 in./in. compression on the segment case and 0.00563 in./in. tension on the container base.

The greatest overall strain occurred at the top weld of the segment case, 105 degrees from top dead center (TDC). The greatest strain on the container base was in the vertical axis 225 degrees from TDC.

As a rule, strains on the segment case increased when the trailer bed was lifted; however, there was a decrease noted in two areas on the side of the segment case farthest from the lifted corner of the trailer bed. These two areas were near the bottom weld 195 to 285 degrees from TDC and near the top weld 165 to 225 degrees from TDC.

Conclusions — During normal handling, strains and accelerations on the segment were less than half of the allowable limits; however,

strain was expected to be greater during the actual highway movement test. The recorded data indicated that strains on the trailer bed and the container base were greater than that on the segment case, but these strains were not critical. Use of the universal fifth wheel between the trailer and the jeep dolly will result in less strain of the segment, container base, trailer, and hitch point because of the design of this type of fifth wheel.

Highway Transportation Test — 400 Miles

The purpose of this test was to demonstrate the feasibility of transporting live solid rocket motor segments from UTC, Development Center (near San Jose, California) to Edwards Air Force Base, over approximately 440 miles of highway. Data collected during this test were used to develop an acceptable method of transporting live segments via highway.

Objectives of the test were to: (a) demonstrate the feasibility of transporting a live SRM segment and associated AGE by means of standard commercial heavy duty equipment, (b) to monitor and record the environmental effects to which the SRM would be subjected during the test, and (c) demonstrate the capability of the

SRM/AGE package with the transporter and the transportation route.

Special permits issued by the California State Division of Highways permitted the test load to travel between sunrise and sunset, Monday through Friday. The route followed was established by a previous road survey which considered road characteristics, capacity of structures, terrain traversed, and other items pertinent to stability and safe travel of the load. The route selected was authorized as an "explosive route" for Program 624A loads by the State of California Fire Marshal. Approved stops located away from large towns or densely populated areas were authorized for overnight layovers. The composition of road test convoy was as shown in Fig. 6. The data acquisition system operated continuously during the load movement, and one hour before and after each day's travel, to obtain data on the varying wind conditions and their effect on the temperature of the segment.

Composition of the Test Load — The test load consisted of a live propellant segment (Class "B" explosive), associated AGE (container assembly, TCU, and DEGS), special trailer interfaces to accept the load, and a data acquisition system. Locations of the load, AGE and data acquisition system are shown in Fig. 7. TCU was
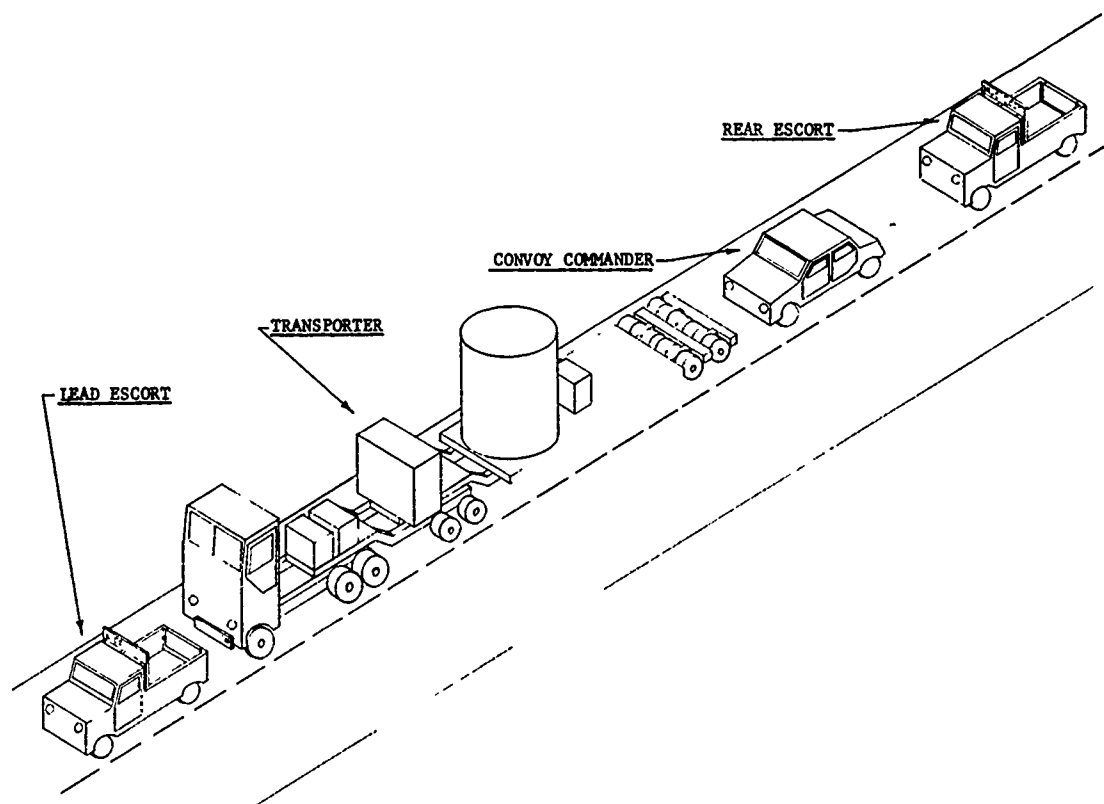
Fig. 6. Road test convoy

94
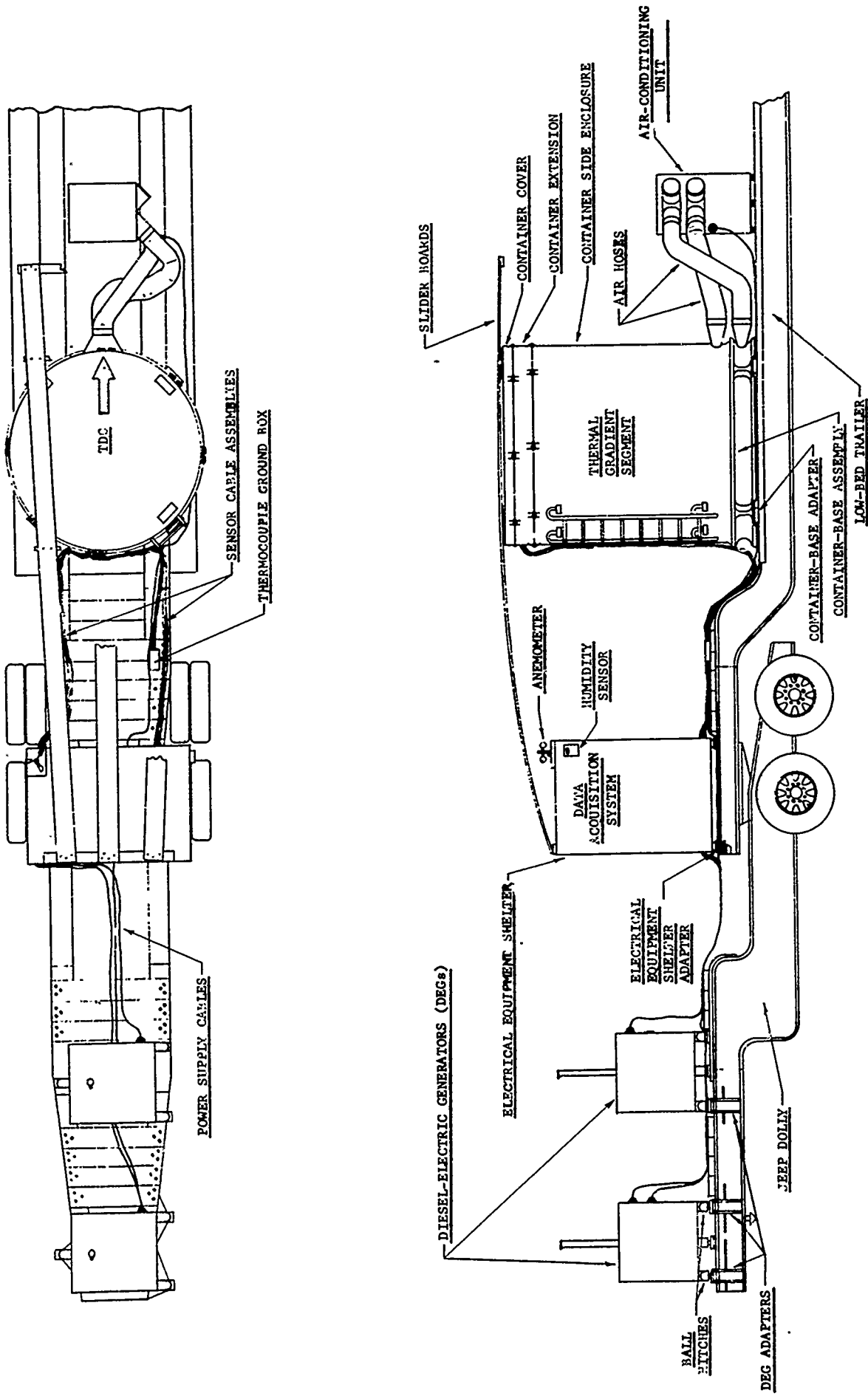
Fig. 7. Transporter loading configuration

95

Fig. 8. Loaded transporter

mounted on the trailer bed aft of the load, and the data acquisition system was installed in a shelter mounted on the trailer gooseneck. Sliding boards were placed over the electrical shelter and load to enable the transporter to clear low wires and branches. The loaded transporter (Fig. 8) weighed approximately 160,000 lb. gross, and its loaded maximum

dimensions were an 80-ft. length, 11-ft. 4-in. width, and 17-ft. 5-in. height. Trailer clearance from ground was 11 3/4 in.

Instrumentation — The total of 117 thermocouples were used. Thirty-six of these were previously cast into the segment grain, and the remainder were located as shown in Figs. 9 and 10. Twelve accelerometers were used, with 11 mounted on the segment handling rings, located as shown in Fig. 11. Twelve strain gages were mounted near the bottom weld of the segment case, all in a vertical axis as shown in Fig. 12. Two humidity sensors were used. One was located over the core of the segment and the other, an anemometer, was located on the electrical equipment shelter.

Results — Representative zero to peak accelerations and force frequencies were recorded for each major segment of the route, as well as those experienced by inducing a deliberate stop on an incline. A sample of such recordings is given in Table 3.

Tests were also conducted to determine the natural frequency of the loaded trailer. These data, which were obtained by driving the loaded trailer over 4-in. blocks, indicated that the loaded trailer had a natural frequency of 1.95 cps and that shock was mitigated between the trailer bed and the bore of the segment by a factor of approximately 3.0. Table 4 reflects these data. A trailer deflection test indicated the maximum degree of trailer deflection under weight of the container assembly was 2.70. Figure 13 provides a point by point breakdown of the trailer deflection measurements and plot.

Conclusions — Maximum acceleration during the road test were less than 1/5 of the

TABLE 3
Representative Zero-to-Peak Accelerations and Forcing
Frequencies from UTCDC to Mendota

Route Area	Acceleration (g)	Forcing Frequency (cps)
UTC Development Center main gate	0.20 - 0.31	2-3
San Felipe Road and Silver Creek Road	0.20	2-3
King Road, Aborn Road, and Loupe Avenue triangle	0.29 - 0.38	2-6
U. S. Highway 101	0.10 - 0.15	2-3
Pacheco Pass	0.20 - 0.25	2-3
San Luis Dam construction site	0.20 - 0.25	2-6
Entering Los Banos	0.20 - 0.25	2-5
Dos Palos railroad tracks	0.20 - 0.40	2.5-3
Entering Mendota	0.20 - 0.25	2-3
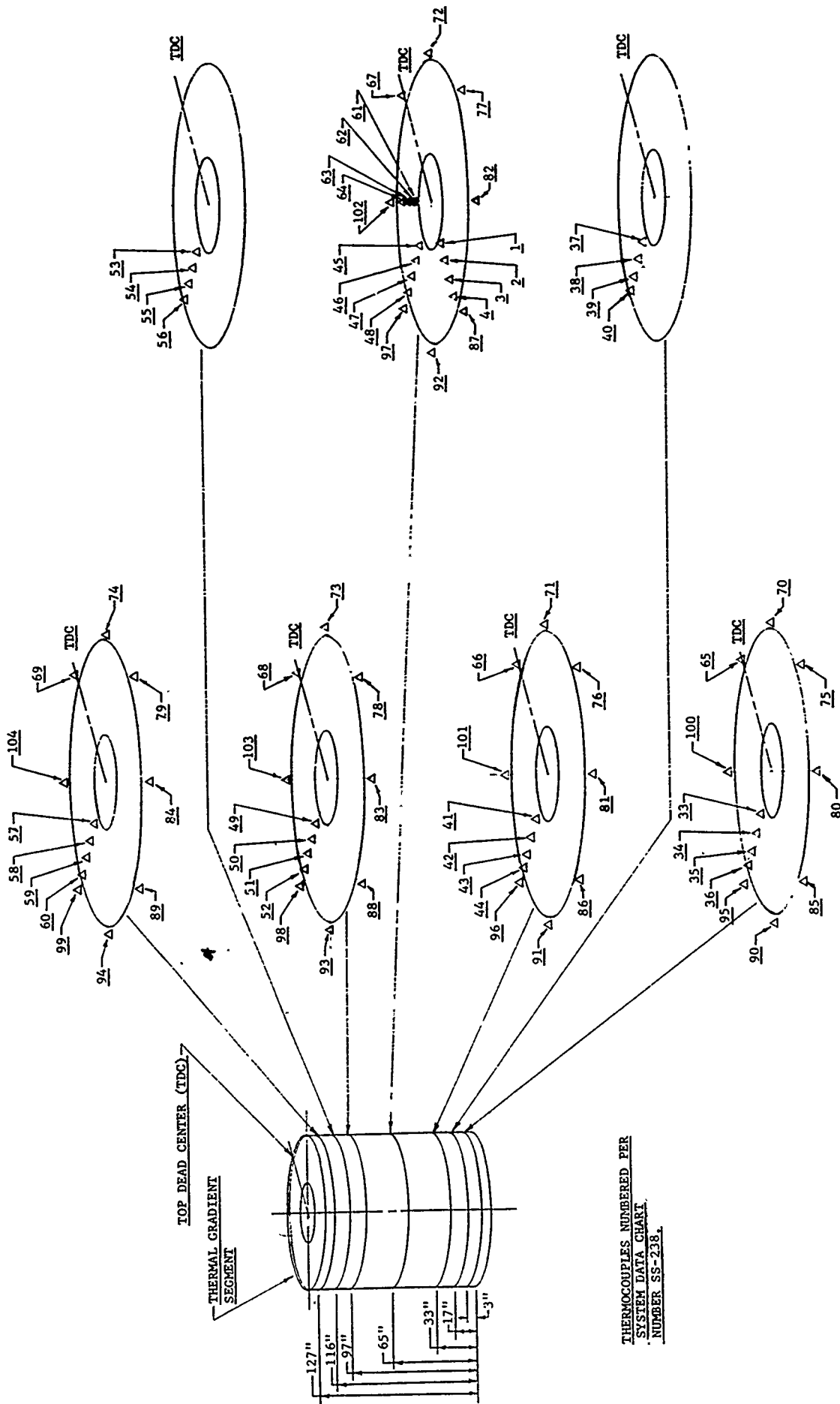
Fig. 9. Thermocouple locations
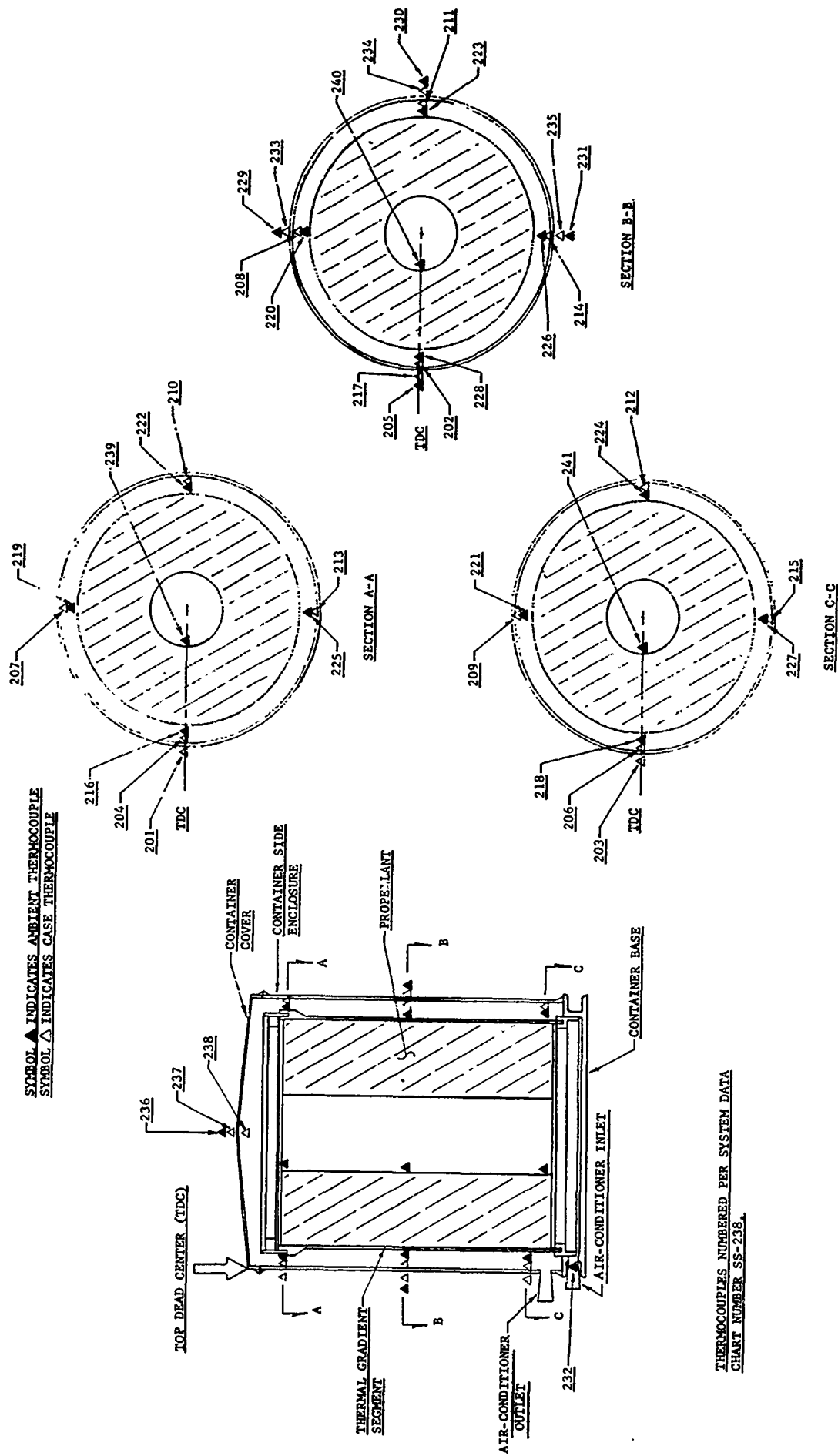
Fig. 10. Ambient thermocouple locations

SYMBOL ▲ INDICATES AMBIENT THERMOCOUPLE
SYMBOL △ INDICATES CASE THERMOCOUPLE

SECTION A-A

SECTION B-B

SECTION C-C

CONTAINER COVER
CONTAINER SIDE ENCLOSURE
PROPELLANT
CONTAINER BASE

TOP DEAD CENTER (TDC)

THERMAL GRADIENT SEGMENT

AIR-CONDITIONER OUTLET

AIR-CONDITIONER INLET

THERMOCOUPLES NUMBERED PER SYSTEM DATA
CHART NUMBER SS-238.

98

TABLE 4
Natural Frequency Test of Loaded Trailer
(4-in. Block Test)

Accelerometer	Location	Acceleration (g)	Response Frequency (cps)
A5 - Y axis	Trailer bed	0.36	1.97
A6 - Y axis	Segment top	0.3	1.97
A9 - Y axis	Container base	0.95	1.95
A10 - Y axis	Segment bore	0.28	1.97
A11 - Y axis	Segment bore	0.3	1.94
A12 - Y axis	Trailer bed	0.95	1.95

maximum allowable 3 g. Measured strain on the segment and the case were insignificant. Examination indicated that the propellant was not broken or cracked, and there was no failure of the bond between the propellant and liner. The shipping package was compatible with the transporter and the established transportation route, and road hazards such as narrow roadway, low wires, over-hanging tree branches, and road dips were minor and not critical.

It was concluded that on this type of load, the standard fifth wheel has a distinct advantage over universal fifth wheel. The standard fifth

Fig. 11. Accelerometer locations

99

HYDRODYNAMICS A22-56100
HUMIDITY SENSOR

CABLE ASSEMBLY LEADS TO
DATA ACQUISITION SYSTEM

TOP DEAD CENTER

PROPELLANT

BOTTOM WELD

TWELVE BLH FAB 50-35-56 STRAIN
GAGES EQUALLY SPACED AND PLACED
APPROXIMATELY 1 INCH FROM THE
BOTTOM WELD

SYMBOL ⭣ INDICATES
STRAIN GAGE
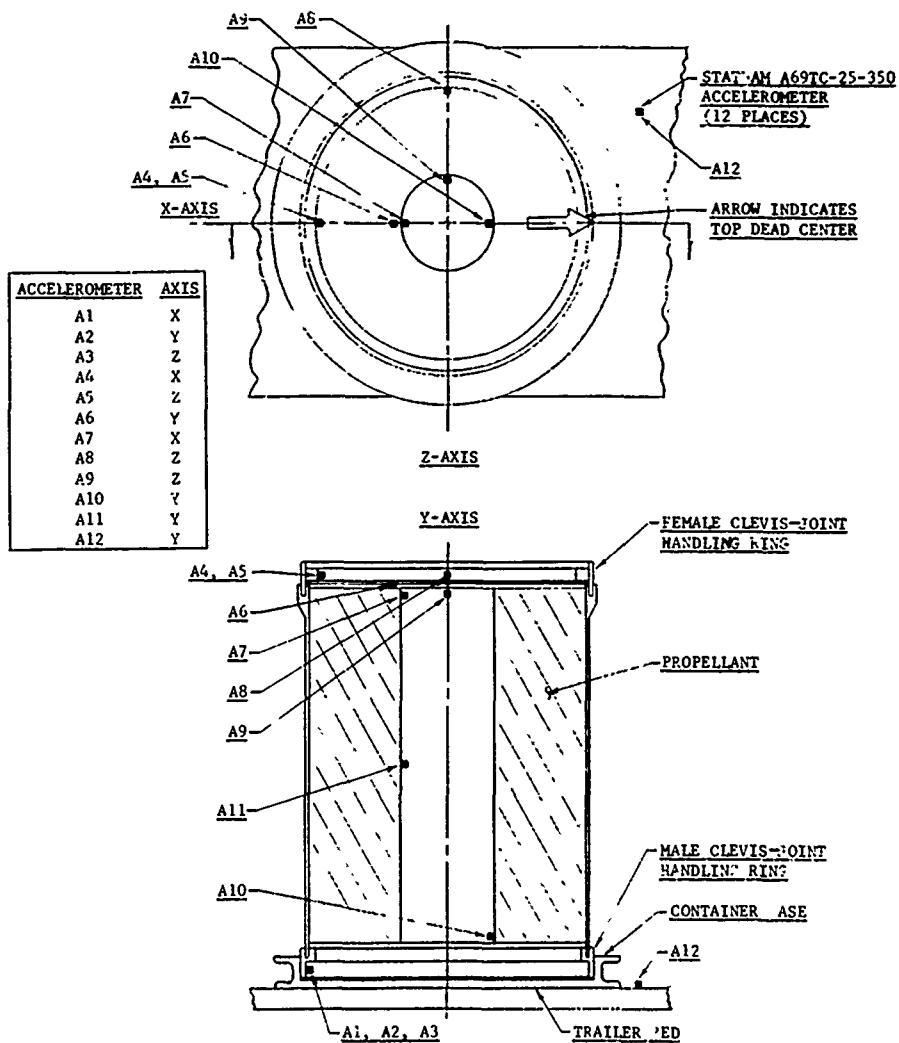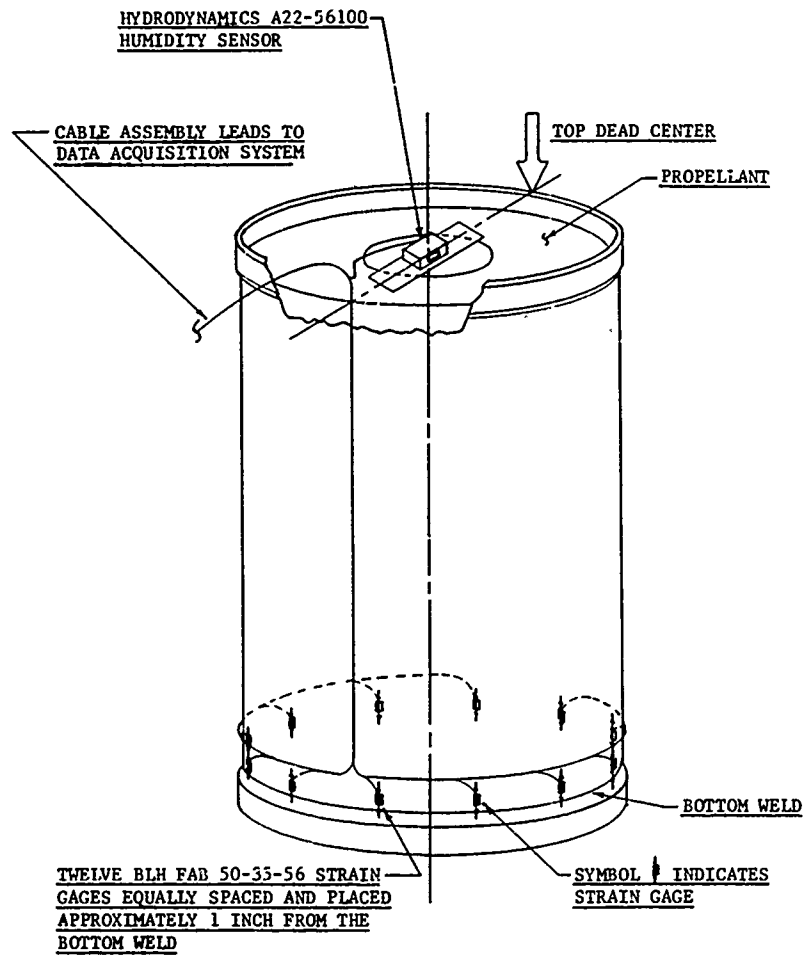
Fig. 12. Strain gage and humidity sensor locations

HITCH POINT

CONTAINER BASE ADAPTER (4 PLACES)

0.88 IN. DEFLECTION

2.60 IN. DEFLECTION

2.70 IN. DEFLECTION

0.60 IN. DEFLECTION

0 IN.
2 IN.
4 IN.
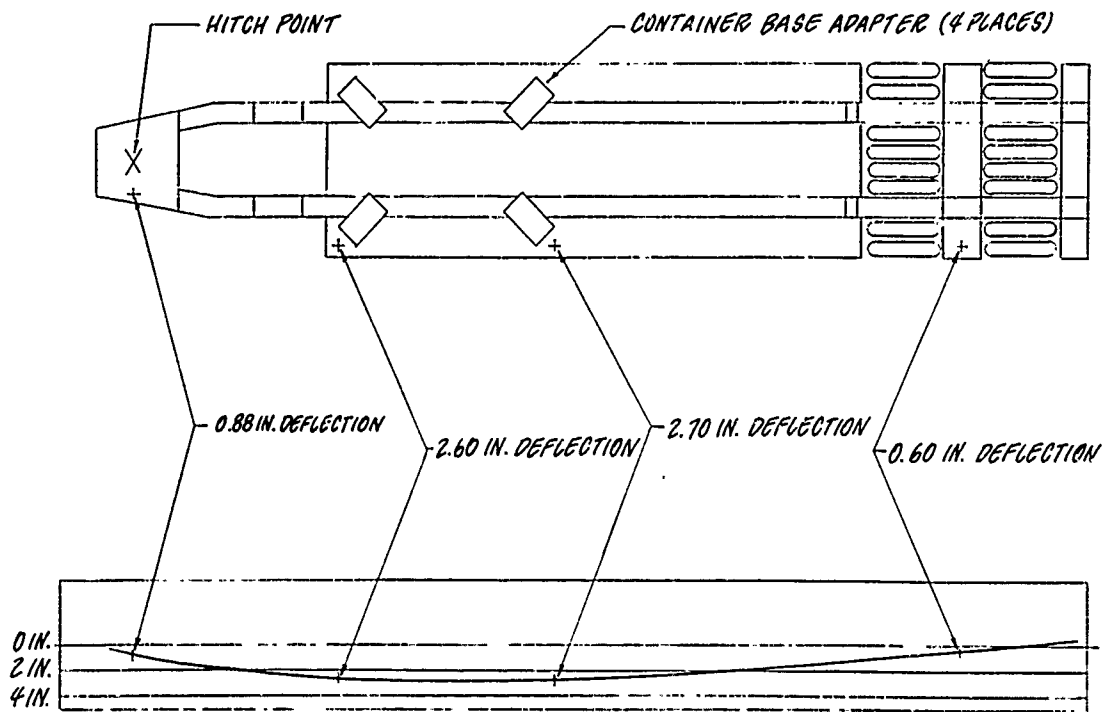
Fig. 13. Trailer deflection measurements and plot

100

wheel held the loaded trailer in line with the tractor and jeep dolly on superelevations, whereas the universal fifth wheel allowed the trailer to travel and "lean" on steep superelevations.

Railcar Impact Test

The purpose of this test was to demonstrate the effect of couplings at various speeds on the special 100-ton capacity hydracushion railcar and on a test load consisting of an inert SRM segment and a simulated segment. Test objectives were: (a) to demonstrate (in part) the transportability of SRM components by rail, (b) to demonstrate the accelerations to which the SRM components and AGE would be subjected when the special car was impacted at varying speeds, and (c) to prove the adequacy of design of the car deck interfaces securing the shipment to the car.

The reports, recommendations, and conclusions accumulated as a result of the impact test were to be used to finalize an acceptable method of transporting live components by rail to the Eastern Test Range (ETR). The test was also to be witnessed by an American Association of Railroads (AAR) Bureau of Explosive representative who could recommend that special Interstate Commercial Commission (ICC) permits could be issued approving the proposed method of shipment if results were satisfactory. Due to the considerable movement volume projected (each shipment consisting of 14 cars per shipment carrying about one million pounds of explosives plus 300,000 lb. of AGE), the railroads and the ICC were anxious to have proof that the shipment method and mode of transport would be safe and compatible, with regular freight train service operations.

A general layout of the railcar impact test is shown in Fig. 14. Equipment furnished by the rail carrier consisted of: (a) 100-ton capacity 20-in. travel hydracushion underframe freight car equipped with special interfaces for Program 624A shipments; (b) five empty railcars to be used as buffers; (c) one switch engine; (d) 200 ft of reasonably level track; and (e) electric timers, stop watches, and track torpedoes.

The test configuration consisted of: (a) the data acquisition system mounted on a truck connected by cabling to the instrumentation and DEGS on the freight car; (b) inert segment, weighing 82,000 lb, 11 ft 4 in. diameter, 13 ft 8 in. high, mounted in AGE container and secured to the freight car bed on the interfacing

mounting pads provided; (c) simulated segment filled with sand, weighing 85,000 lb weight, 11 ft 4 in. in diameter, 13 ft 8 in. high, mounted in AGE container base and secured to freight car bed on the interface mounting pad; (d) air conditioner mounted on the bed of the railcar powered by the DEGS with air conditioner hoses leading to the test shipment; (e) two DEGS secured to mounting plates provided on bed of the railcar (one DEG furnished power for the shipment environment system and a second set furnished power to the data acquisition system); and (f) shock recorders and accelerometers mounted in their routine shipping positions on the inert container base. Figures 15 and 16 illustrate the test setup.

Test instrumentation consisted in part of two accelographs, each with 8-channel capacity. These accelographs and two AGE shock recorders were used to record the impact accelerations. Sensor illustration consisted of 14 accelerometers located as shown in Fig. 14. Five accelerometers were mounted on the railcar and nine on the segment, handling ring, and shipping container base.

Pre-Test Procedures — The railroad crew was briefed on the test procedures. Five empty buffer cars were placed at the far end of the 200-ft track, with brakes set and couplers extended. The test car was placed between the switch engine and buffer cars. Track torpedoes and electric timer switches were placed on the test track for use in computing test car's speed of traveling.

Test Procedures — Test runs consisted of accelerating the test car with a switch engine to a speed approximating a previously designated speed, releasing the car from the switch engine, and allowing it to roll into the five buffer cars. After each run, the draft gear was extended on the buffer cars and the brakes were reset. A complete inspection of segments, railcar interfaces, and AGE were conducted after each test run.

The first series of tests were run with the test car fully loaded, as shown in Fig. 17. Total track weight of the test item was 247,800 lb. In this series of tests, the car was impacted on the A end at 5.50, 5.65, 7.50 and 10.30 mph. Then the B end of the car was impacted at 9.70 mph.

On completion of the first series of tests, the simulated segment and container base were removed from the car for a second series run. Total weight of this new configuration was 162,000 lb. During the second series, the car was

101

Fig. 14. Accelerometer locations, railcar impact test
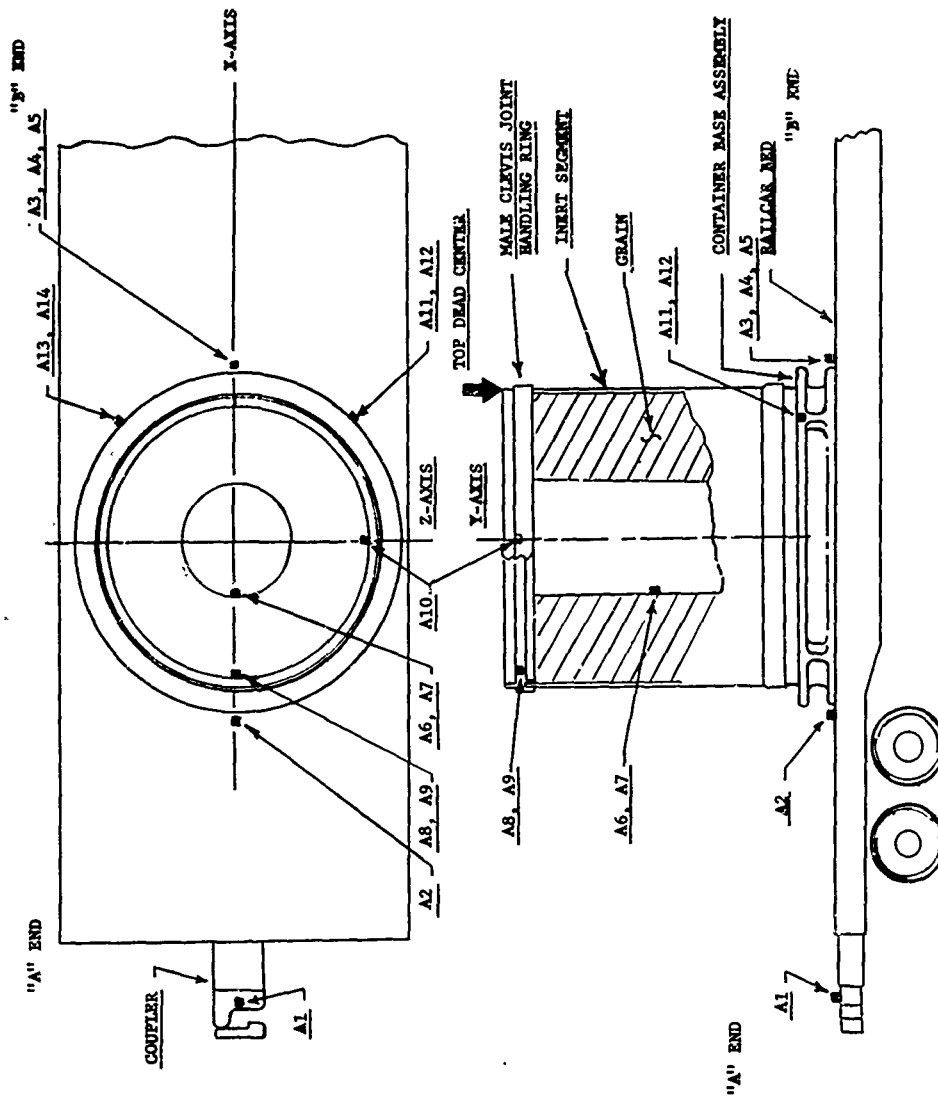
Accelerometer Number	Location From TDC	Placement
A1	X - 180°	Coupler
A2	Y - 180°	Bed, next to case
A3	Z - 0°	Bed, next to case
A4	X - 0°	Bed, next to case
A5	Y - 0°	Bed, next to case
A6	X - 180°	Grain, inner radius, midplane
A7	Y - 180°	Grain, inner radius, midplane
A8	X - 180°	Male clevis joint handling ring
A9	Y - 180°	Male clevis joint handling ring
A10	Z - 90°	Male clevis joint handling ring
A11	Y - 45°	Container base
A12	X - 45°	Container base
A13	Y - 315°	Container base (AGE shock recorder)
A14	X - 315°	Container base (AGE shock recorder)

SYMBOL ■ INDICATES ACCELEROMETER MOUNT

SYMBOL □ INDICATES HIDDEN ACCELEROMETER MOUNT

Fig. 15. Railcar impact test setup,
side view

impacted on the A end at 5.26, 7.32, and 8.45
mph. The B end of the car was then impacted
at 6.11, 7.50, and 9.70 mph. On completion of
the second series of the tests, a third series
was run with only the diesel engine generator
on the car. Test item track weight for this
configuration was 69,400 lb. During this third
series of tests, the car was impacted on the A
end at 5.00, 7.89, and 10 mph. The B end was
not impacted.

Draft gear sill travel was measured for all
test runs. Buffer car movement along the track
as a result of impacts was measured for the
first and second series of runs.

Fig. 16. Railcar impact test setup,
end view

Results — Rail impact accelerations result-
ing from the test were as given in Table 5 for
accelerometers A2 through A12. No accelera-
tions over the maximum tolerance of 3 g, with
the exception of accelerometer A1 located on
the railcar coupler, which sustained a load of
25 g, occurred on the first test run. This ac-
celerometer was damaged beyond use and was
removed for the remainder of the test. Highest
accelerations obtained from the test were in
the X axis, 2.27 g; in the Y axis, 2.90 g; and in
the Z axis, 0.94 g. Highest impact speed was
10.30 mph.

The AGE shock recorders monitoring ac-
celerometers A13 and A14 registered no ac-
celerations of 3 g or over.

Maximum draft gear sill travel was 18.5 in.
at an impact speed of 10.30 mph. Maximum
buffer car movement along the track was 192
in. at an impact speed of 9.70 mph. Table 6
summarizes rail impact test sill travel and buf-
fer car movement.

Conclusion — Accelerations encountered were
below the maximum allowable accelerations
of 3 g. Propellant grain and container base ac-
cumulations were less than 2 g, and in the ma-
jority of runs less than 1 g. Results of test runs
when converted to impact forces compare favor-
ably with the results of a hydracushion car of the
impact test plotted in Fig. 45.41 in the Shock and
Vibration Handbook (1).

The railcar impacts had no visible effects
on the railcar, interfaces, aerospace ground
equipment, and attachment fittings. It was con-
cluded that a special car and the method of
securing the AGE to the railcar are adequate to
sustain normal impacts which result from nor-
mal railcar humping operations. Based on test
results, special ICC permit was issued to cover
Program 624A shipments by the tested method
and transporter mode.

Transcontinental Rail Test

The purpose of the test was to accumulate
data and provide information to establish the
parameters for Program 624A standard rail-
road transportation system procedures re-
quired for delivery of SRM components from
UTC, Coyote, California, to ETR, Florida.

Objectives of the test were to: (a) prove
that SRM segments can be safely transported by
rail; (b) to determine the characteristics of vi-
bration and acceleration of the SRM segment,
forward closure, associated AGE and the special

103
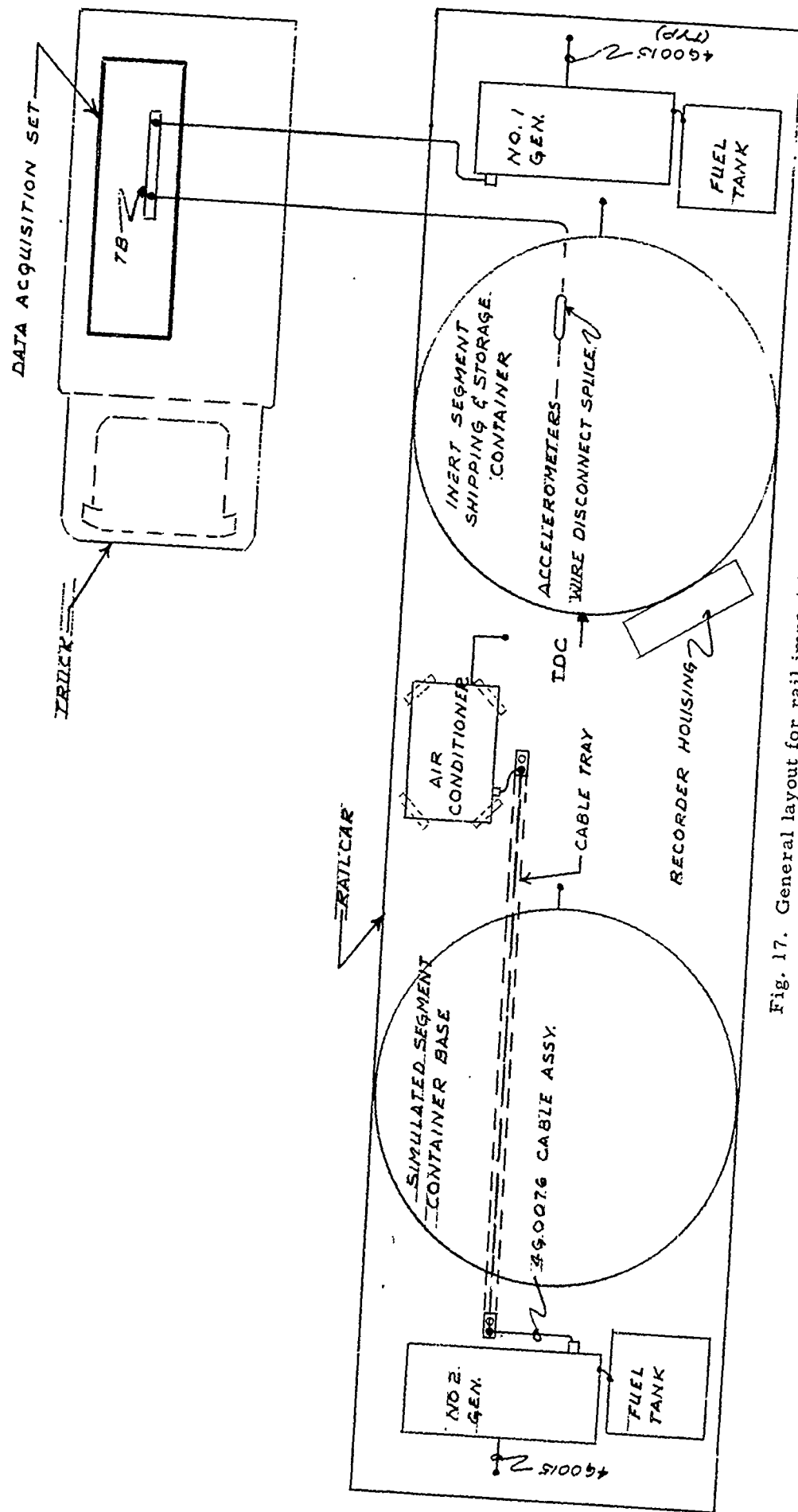
Fig. 17. General layout for rail impact test

104

TABLE 5
Rail Impact Test Accelerations

	Impact Speed (mph)	Car End	Accelerometer (g)										
			A2-Y	A3-Z	A4-X	A5-Y	A6-X	A7-Y	A8-X	A9-Y	A10-Z	A11-X	A12-X
First Test Series	5.50	A	2.32	0.14	0.70	0.50	0.38	0.30	0.20	0.31	0.19	0.19	0.43
	5.65	A	1.60	0.27	0.89	0.38	0.31	0.25	0.46	0.21	0.09	0.29	0.25
	7.50	A	2.12	0.29	1.21	0.53	0.41	0.23	0.61	0.21	0.12	0.24	0.17
	10.30	A	2.00	0.29	2.11	0.96	0.72	0.60	0.72	0.28	0.09	0.52	0.56
	9.70	B	2.32	0.49	2.27	1.29	1.00	0.62	1.34	0.36	0.17	0.45	0.40
Second Test Series	6.11	B	2.59	0.22	0.64	0.32	0.70	0.32	0.07	0.52	0.35	0.50	0.08
	7.50	B	2.55	0.23	1.39	0.69	1.00	0.86	1.21	0.82	0.94	0.96	1.85
	9.70	B	2.70	0.39	1.41	0.67	1.20	0.81	1.82	0.72	0.47	0.48	1.14
	8.45	A	2.80	0.29	1.59	0.40	0.60	0.61	1.09	0.72	0.71	0.59	0.78
	5.26	A	2.25	0.12	0.67	0.39	0.51	0.20	0.15	0.31	0.19	0.24	0.25
	7.32	A	2.90	0.22	1.13	0.25	0.72	0.15	0.91	0.26	0.19	0.38	0.57
Third Test Series	5.00	A	0.75	0.33	1.14	0.61							
	7.89	A	1.48	0.41	1.98	0.38							
	10.00	A	1.27	0.59	1.88	0.59							

TABLE 6
Rail Impact Test Sill Travel and Buffer Car Movement

	Impact Speed (mph)	Car End	Sill Travel (in.)	Buffer Car Movement (in.)
First Test Series	5.50	A	14	36
	5.65	A	14-1/8	51
	7.50	A	16-1/2	89
	10.30	A	18-1/2	180
	9.70	B	18	192
Second Test Series	6.11	B	9-1/4	36
	7.50	B	11-9/16	58
	9.70	B	15-7/8	101
	8.45	A	15-1/16	76
	5.26	A	11-1/4	36-1/2
	7.32	A	15	50
Third Test Series	5.00	A	6-5/16	
	7.89	A	10-1/16	
	10.00	A	10-7/8	

100-ton capacity hydracushion flatcar during transport; (c) establish availability of rail system facilities and services for the cross-country transport of SRM components; (d) verify the reliability of the environmental control system in maintaining the temperature and humidity environments within acceptable tolerance during rail transport; (e) verify the accuracy of the AGE recorders during rail shipment; and (f) verify the car interface compatibility between the railcar and AGE.

Special transcontinental routes, as shown in Fig. 18, capable of accepting the excessive weight of car with lading (approximately 200,000 lb) and load dimensional clearance of 17 ft 1 in. in height and 11 ft 4 in. in width had been previously established. A railcar humping test previously conducted had verified that the lading would not be exposed to shock during normal rail service handlings which would be in excess of 3-g tolerances allowed. This test was required to verify that the shock and vibration

105

Fig. 18. Rail route map
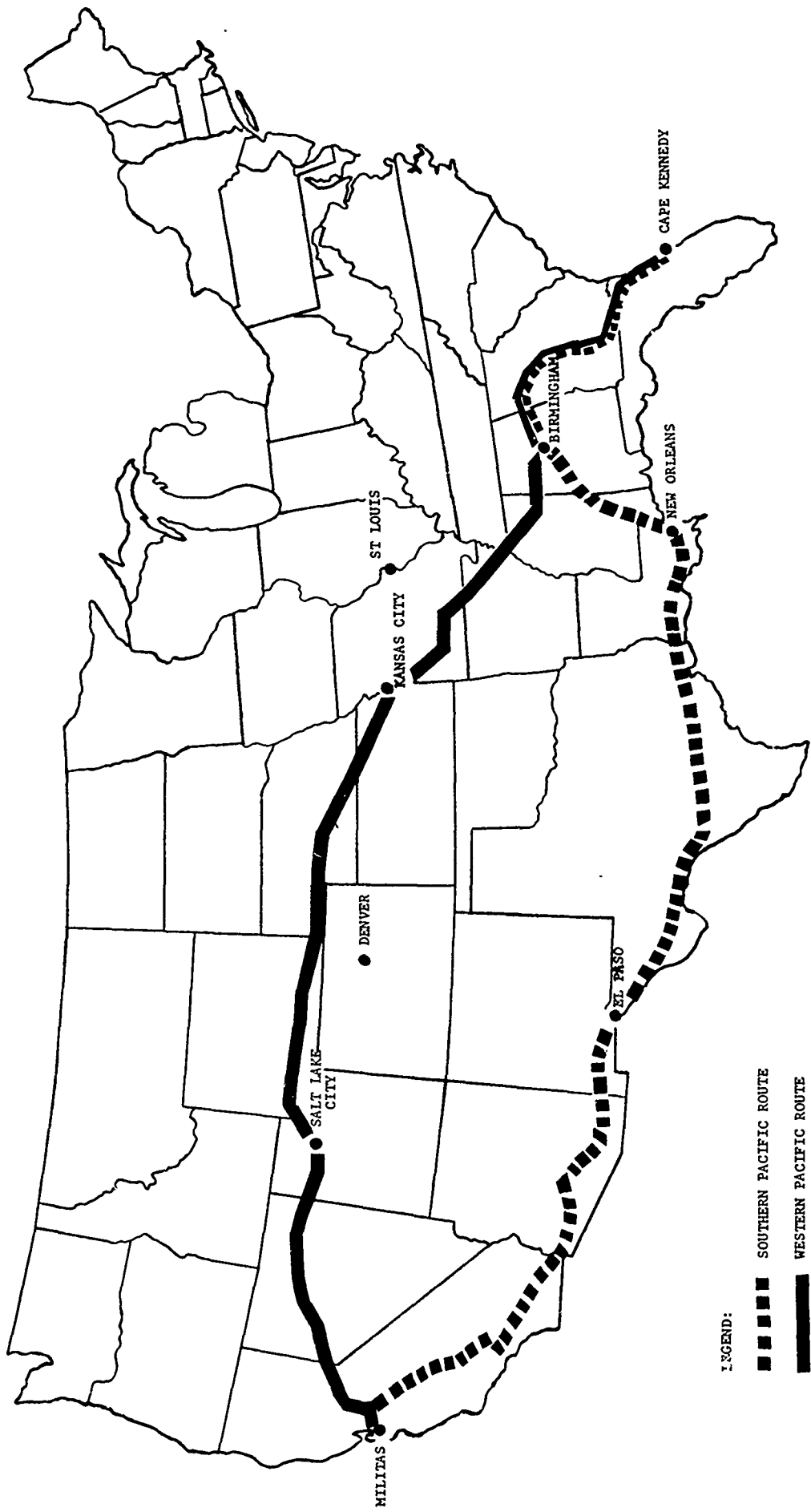
LEGEND:

SOUTHERN PACIFIC ROUTE

WESTERN PACIFIC ROUTE

tolerances would not be exceeded during actual cross-country travel over the selected routes, when shipments were moving in regularly scheduled freight train service. Since the characteristics of the track, trackbed, and terrain traversed, as well as traveling conditions encountered, would have a bearing on the test results, rail track profiles secured from each of the railroads involved in the 6,000-mile round trip route were analyzed, to establish those portions of the track over which testing and data accumulation were to occur. In analyzing the rail track profiles and establishing test locations, consideration was given to such items as track weight, condition of roadbed, travel over structures, travel through classification yards, grades, and curving track, so that in the final analysis conditions representative of all of the routes' characteristics would be included in the test.

Twelve test phases were established with mile posts and stations reflected on the test plan to control the start and stop of monitoring for each phase. Test plan for the phase covering New Orleans, Louisiana, to Meridian, Alabama, is reproduced in Fig. 19. While the test train was enroute, the location of the test car within the train was varied to determine the effect of such changes, especially the "whip" effects experienced at the end of a long train, as well as effects of slack, run-out, and shock.

Test load transporting equipment consisted of: (a) 100-ton capacity hydracushion railcar, interfaced for carriage of Program 624A components; (b) a 70-ft long railroad baggage car to house the data acquisition system; and (c) a personnel railcar to accommodate the test crew, AAR Bureau of Explosives representative, and Government Agency representative.

The test load consisted of: (a) a live SRM segment, weighing 97,000 lb, 11 ft 4 in. in diameter and 13 ft 8 in. high, and forward closure weighing 58,500 lb, 11 ft 4 in. in diameter and 13 ft 8 in. high, in containers which included monitoring instruments to sense and record
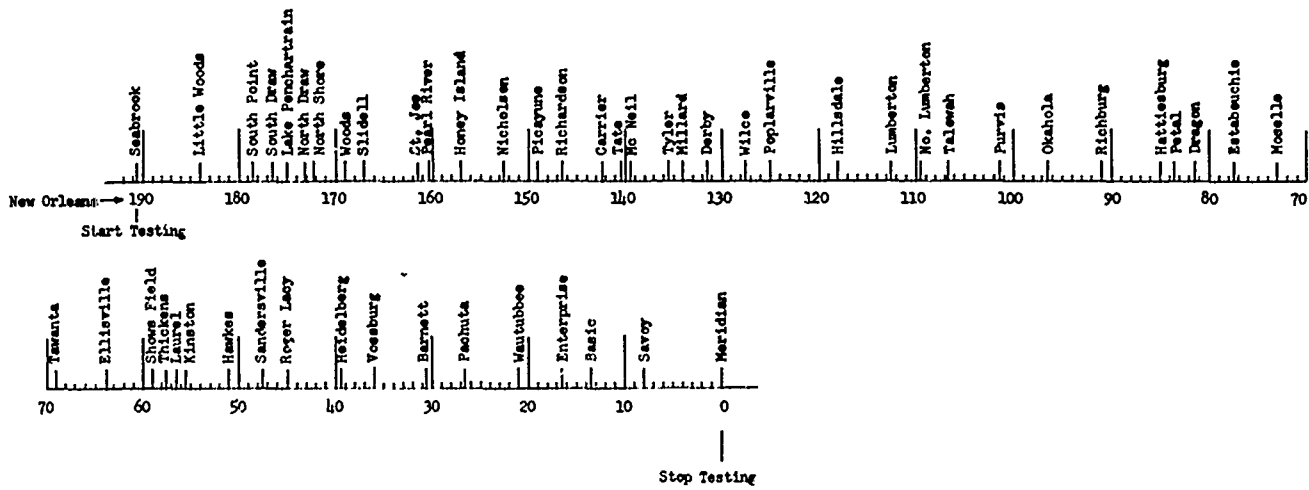
Fig. 19. Test plan -- phase III -- Southern Railway System --
Seabrook, La. to Meridian, Miss.
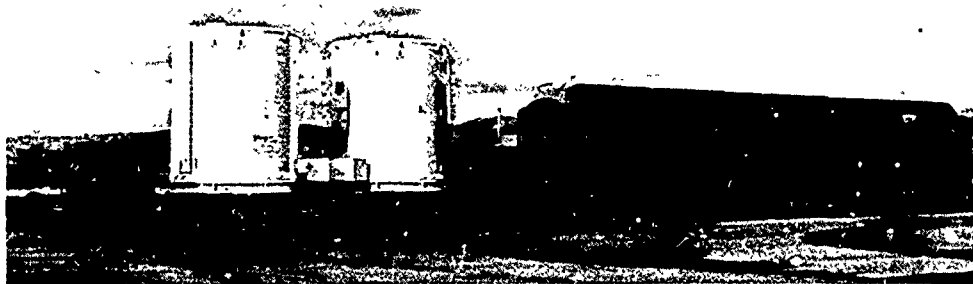
Fig. 20. Transcontinental rail test setup

107

temperature, vibrations and accelerations; and (b) AGE consisting of a TCU linked by air ducts to test shipments and a diesel engine generator power unit. The data acquisition car and test load are illustrated in Fig. 20.

The data acquisition system was installed in the baggage car and coupled, as shown in Fig. 21, to the test car. The system was calibrated immediately before start of phase I test and thereafter as required. Eighty-one thermocouples were installed as shown in Fig. 21. Forty-eight were installed on the segment container side enclosure, 24 to measure air temperatures and 24 to measure surface temperatures. The rest were distributed, as shown in Fig. 22, to measure surface and air temperatures on the segment case, segment core, handling ring, container cover and container base. Eighteen accelerometers were used, as shown in Figs. 21 and 23, with five installed on the segment, two on the forward closure, two on the igniter case, four on container bases, four on the flatcar bed, and one on the bend car coupler. One anemometer was installed on the baggage car.

Test Operations — The test cars proceeded from the origin railhead near San Jose, California, to Los Angeles by special train making three braking stops at speeds of 15, 25, and 35 mph on route. From Los Angeles to Jacksonville, Florida, via the Southern Route, and return to San Jose via the Northern Route, the test train was moved in regular freight train service and normal operating schedules.

Instrumentation records made were cross-referenced as follows: (a) oscillograph acceleration records with train speed tapes, geographic location, time and mile posts; and (b) Bristol recorder temperature records with oscillograph records of wind direction, wind velocity, train speed, geographic location, time and mile post.

Temperature data were obtained to determine the external and internal heat absorbed by the segment container. A directional vane and anemometer were used to correlate heat transfer with wind velocity and direction. Vibration and shock data were recorded to reflect the degree of shock and vibration encountered during the test phases, under the varying ranges of physical road bed, train speeds, and terrain conditions anticipated by study of rail track profiles.

At each stop and railroad division point, the following car interfaces were impacted by the test crew: (a) shipping containers to freight car, (b) air duct hoses to container and air conditioner, (c) diesel engine generator to freight car, and (d) air conditioner to freight car.

Results — The highest acceleration recorded were caused by inherent slack built into the coupling system of each car. While the slack per car is small, the total slack for an entire train can be quite large and produce a "whip" effect, especially noticeable when traversing rolling terrain and during dynamic braking. During the test, train lengths varied from 16 cars with a total weight of 193 tons to 185 cars with a total weight of 8,946 tons. By adding the slack produced per coupler, the engine would travel a distance of 61 ft 8 in. to move the last car of the 185-car train; therefore, the fewer cars in the train, the less time required for the engine to accelerate, with a lower resulting shock to a car at the end of the train, such as SRM component cars. Track and roadbed conditions were minor factors because of speed restrictions imposed on the trains by the respective common carriers over areas of adverse road conditions.

The maximum accelerations recorded were 13 g on the test flatcar coupler in the X axis, 1.8 g on the test flatcar bed in the Y axis, and 1.8 g on the SRM components in the X axis. There were no accelerations over 3 g in any axis, with the exception of those imposed on the test flatcar coupler. Test flatcar and SRM component sway, as reduced from Z axis accelerometer data, occurred more frequently in rail yard and switch yard movements at low speeds, as opposed to mainline movement. The frequency range of the three orthogonal axes was 2 to 100 cps. The fundamental frequency of the axis was for the Z axis, 2 to 7 cps; for the X axis, 5 to 10 cps; and for the Y axis, 5 to 20 cps. In addition, a frequency of 40 to 100 cps was imposed on the basic forcing frequencies. These imposed frequencies resulted in a complex frequency pattern. Tables 7 and 8 are two samples of the twelve test phases recorded, indicating maximum accelerations and frequencies imposed on the test items during the trip.

The SRM component grain temperatures were held between 60° and 70°F throughout the trip, within allowable limits of 60° to 90°F. Ambient temperatures ranged from 26° to 82°F. Weather conditions included rain, snow, and wind. AGE humidity recorders, which indicated relative humidity of 70 percent during loading (in the rain) at origin railhead, slowly dropped while moving enroute across country, and recorded 40 percent in the closure container and 30 percent in the segment container on arrival at Jacksonville, Florida.

108

ACCELEROMETER NUMBER	PLACEMENT	LOCATION FROM TDC
A1	Flatcar Coupler "B" end	X-N.A.
A2	Flatbed, next to Segment Container	Y-180
A3	Flatbed, next to Segment Container	Z-0
A4	Flatbed, next to Segment Container	X-0
A5	Flatbed, next to Segment Container	Y-0
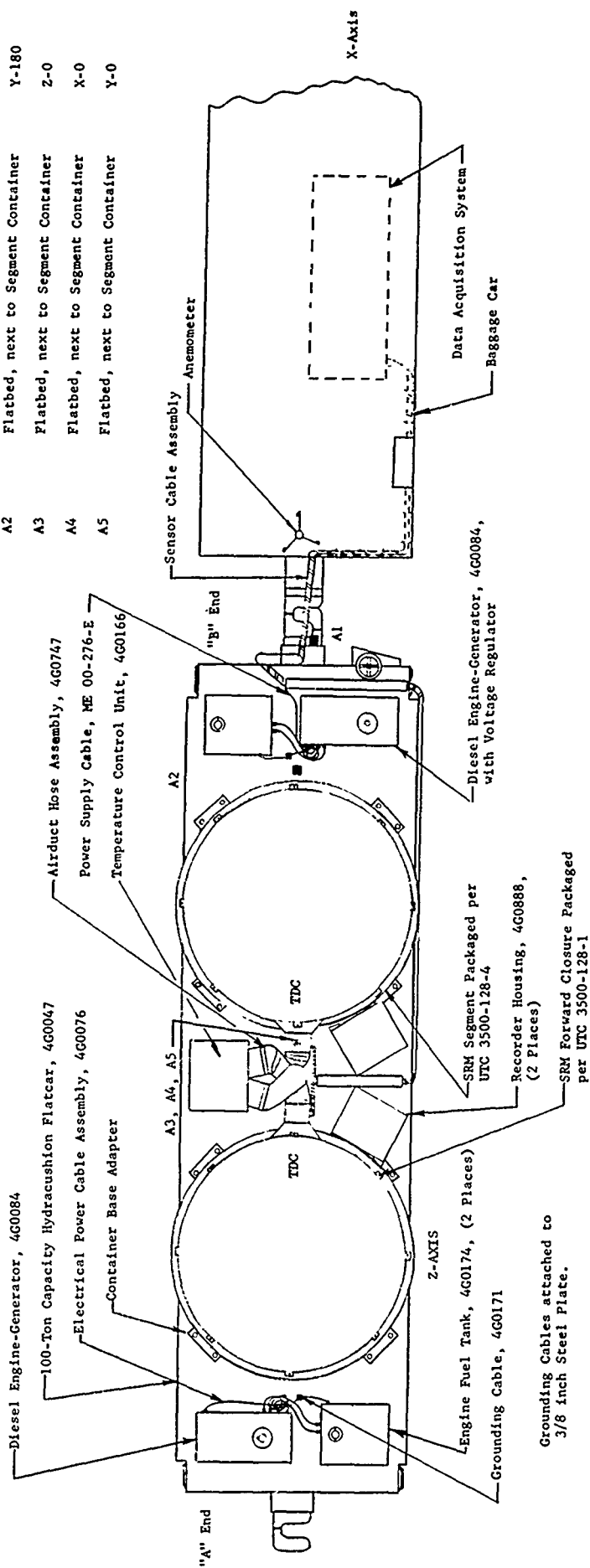
Fig. 21. Transcontinental rail test setup and flatcar accelerometer locations
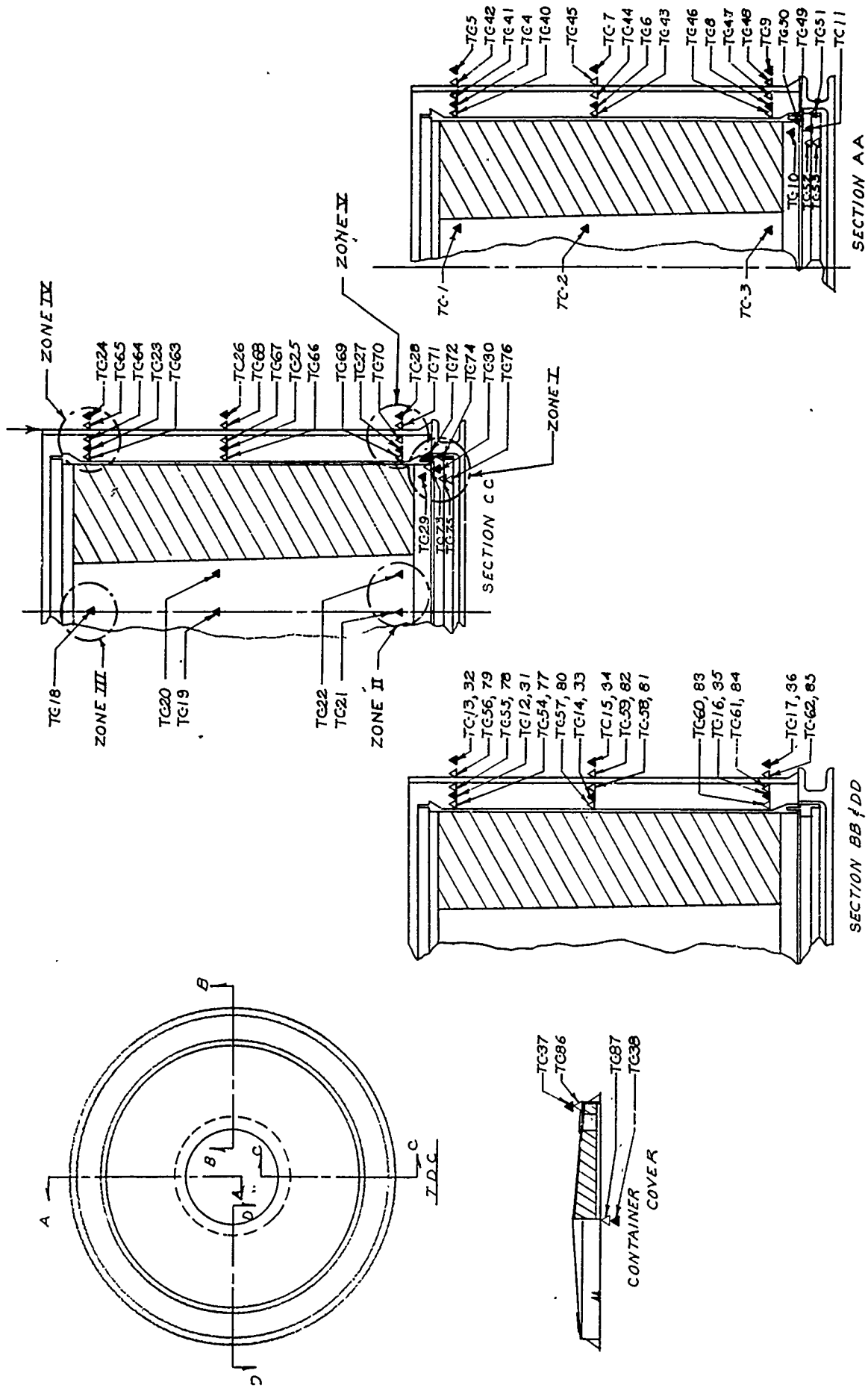
Fig. 22. Thermocouple locations

110

Accelerometer Number	Placement	Location from TDC
A10	Segment Hoist Fixture	Z - 90°
A11	Igniter R-P2	X - 0°
A12	Igniter R-P2	Y - 0°
A13	Fwd. Closure Ring	X - 180°
A14	Fwd. Closure Ring	Y - 180°

SEGMENT S/N 101025

Accelerometer Number	Placement	Location from TDC
A6	Grain Midplane	X - 0°
A7	Grain Midplane	X - 0°
A8	Segment Hoist Fixture	X - 0°
A9	Segment Hoist Fixture	X - 0°

FORWARD CLOSURE S/N 2406

Y AXIS Vertical
X AXIS Longitudinal
Z AXIS Transverse
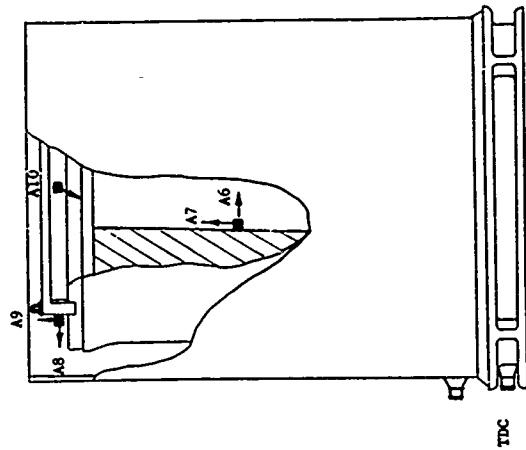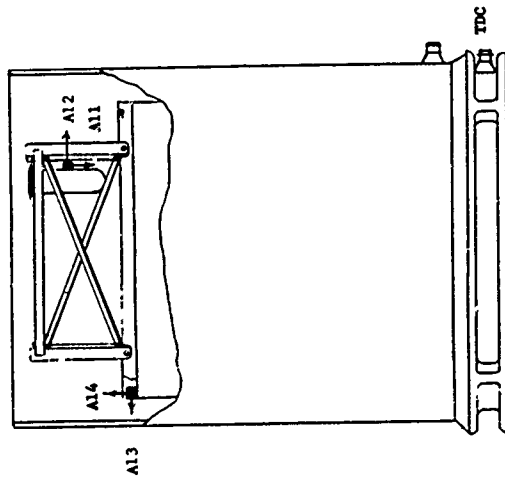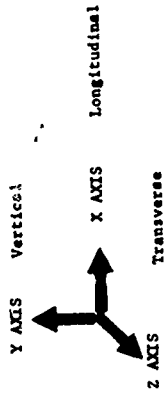
Fig. 23. SRM component accelerometer locations

TABLE 7
Test Phase VI

Acceleration Location	Maximum Response		Remarks
	Amplitude (g)	Frequency (cps)	
A1-X Coupler 0°	6.10	Shock	Test phase conducted between Kansas City, Missouri and Gibbon, Nebraska.
A2-Y Flatbed 180°	1.80	5-10	
A3-Z Flatbed 0°	0.23	10-15	
A4-X Flatbed 0°	0.26	2-6	Flat terrain. Train speed, 70 mph.
A5-Y Flatbed 0°	0.37	5-10	Little or no slack action.
A6-X Grain Midplane 180°	0.27	8-10	Average train speed during test phase — 47 mph.
A7-Y Grain Midplane 180°	0.36	3-8	
A8-X Segment Case, Top 180°	0.19	10-15	
A9-Y Segment, Case, Top 180°	1.40	3-5	
A10-Z Segment Case, Top 90°	0.34	4-8	
A11-Y Igniter	1.20	3-6	
A12-X Igniter	1.10	2-4	
A13-Y Forward-Closure Adapter Ring 180°	0.50	5-12	
A14-X Forward-Closure Adapter Ring 180°	0.70	10-15	

The anemometer indicated that winds caused by the train movement were 18 to 22 mph less than actual train speed. This condition was caused by a partial vacuum created by the trains when moving at mainline speed. The wind appeared to have little effect on component conditioning.

Conclusion — The maximum accelerations received by the SRM components were less than 2 g, as compared with the maximum allowable of 3 g. The greatest accelerations were attained during the slack action of the train, which could be severe enough to break coupler parts on the runouts or buckle center sills on runins. The most common cause of slack action noted was the manner in which the train engineer handled the braking system. The dynamic braking system, rather than the entire train system, was used by many engineers. An example of engineer control was seen between Birmingham, Alabama, and Jacksonville, Florida. On the trip east, the ride was the best encountered to that point. On the return trip over the same track, the slack action was so severe during braking and runouts that numerous components of the personnel car were loosened from their mountings and required repair. At times, it was impossible to stand or walk in the car without being thrown to the floor.

The SRM components and AGE were compatible with the transporter and transportation routes. Interfaces between the rail flatcar and AGE were compatible.

112

TABLE 8
Test Phase IX

Acceleration Location	Maximum Response		Remarks
	Amplitude (g)	Frequency (cps)	
A1-X Coupler 0°	3.40	Shock	Test phase conducted between Salt Lake City, Utah and Wells, Nevada.
A2-Y Flatbed 180°	0.15	5-15	
A3-Z Flatbed 0°	0.25	2-3	6 in. to 8 in. snow storm. Long grades with numerous tunnels.
A4-X Flatbed 0°	0.20	5-10	
A5-Y Flatbed 0°	1.10	5-20	Maximum train speed during this phase was 50 mph.
A6-X Grain Midplane 180°	0.20	3-5	
A7-Y Grain Midplane 180°	Bad. Cal.		Average train speed during test, 29 mph.
A8-X Segment Case, Top 180°	0.20	3-7	
A9-Y Segment Case, Top 180°	0.80	10-15	
A10-Z Segment Case, Top 90°	0.20	2-3	
A11-Y Igniter	0.90	4-8	
A12-X Igniter	0.10	2-3	
A13-Y Forward-Closure Adapter Ring 180°	0.20	5-15	
A14-X Forward-Closure Adapter Ring 180°	0.40	5-10	

TEST PROGRAM CONCLUSIONS

Test results indicate that the special rail and highway transporters, containers, AGE and environment systems fulfilled the requirements of the Program 624A (Titan III-C) Program. Either rail or highway transport system will provide protection of the SRM components against all normal transportation environments and assure that the maximum allowable 3-g shock, 50 percent humidity, and 60° to 90° F temperature range will not be exceeded. Results also illustrate that the common carrier industry range of equipment includes equipment of standard make which can be modified to accept shipments satisfactorily of excess weight, dimension, and sensitive nature. Thus, these test results can lead to the fulfillment of the need of both the purchaser and supplier of missile and space-age equipment to substitute transport systems composed of combinations of modified standard components, common to industry and readily available in the market, for systems requiring individual design and special fabrication at the cost of considerable time and money.

REFERENCE

1. Sergei G. Guins, "Shock and Vibration in Road and Rail Vehicles, Part II, Rail Vehicles," Shock and Vibration Handbook, edited by Cyril M. Harris and Charles E. Crede (McGraw-Hill, New York) 1960, pp. 45-21

*   *   *

DYNAMIC ENVIRONMENT OF M-113 ARMORED
PERSONNEL CARRIER

G. M. Pomonik and N. G. Tinling
Hughes Aircraft Company
Culver City, California

A measurement program was conducted to determine the shock and vibration environment of the TOW weapon system installation in the M-113 armored personnel carrier. Data were obtained over a range of vehicle speeds and road conditions and at various vehicle locations to provide general information on the M-113 dynamic environment. Vibration data are presented for vehicle speeds between 5 and 35 mph on both dirt and asphalt roads. Data for significant conditions is presented as acceleration spectral density and amplitude distributions. The broadband results are summarized as functions of vehicle speed and measurement location. Shock data were obtained for vehicle speeds from 7 to 13 mph over wooden ramps on a dirt and asphalt Munson course. Shock spectra of the most severe data are presented. The results are summarized as functions of vehicle speed and measurement location.

INTRODUCTION

A measurement program was conducted to determine the shock and vibration environment of the TOW weapon system installation in the M-113 armored personnel carrier. Data were obtained over a range of vehicle speeds and road conditions and at various vehicle locations to provide general information on the M-113 dynamic environment.

The M-113 armored personnel carrier (Fig. 1) is a high-production multipurpose vehicle. Its proposed uses include mortar carrier, command post, communications center armored cargo carrier, and special purpose weapon carrier for applications such as the TOW weapon system. This report and those listed in the references provide preliminary design information for future equipment installations in the M-113.

The shock and vibration environment produced by M-113 motion has received attention by various agencies (1-5). The results obtained provided a guideline for a more detailed investigation of critical conditions. In summary, previous tests indicate that:

1. The most severe vibration is obtained on a level paved road; and

2. The most severe shock occurs when the suspension bottoms.

These conclusions were arrived at after comprehensive testing under a variety of vehicle maneuvers and road conditions.

Based on these findings, the test was conducted to provide an abundance of acceleration data for conditions of (a) high speed on both concrete and dirt roads, and (b) suspension bottoming.

DETAILS OF TEST

Most of the vibration tests were conducted at the test track of the Food Machinery and Chemical Corp. (FMC), San Jose, California, manufacturers of the vehicle. The shock tests were conducted on a Munson track at the Hughes Aircraft Company Fullerton facility in California.

M-113 vehicle serial number F892 was used in the San Jose tests. This vehicle was used previously for general testing by FMC and had an accumulated hull mileage of 14,500 miles. The tracks on this vehicle were worn. The M-113 used at Fullerton was a relatively new vehicle with tracks in very good condition.
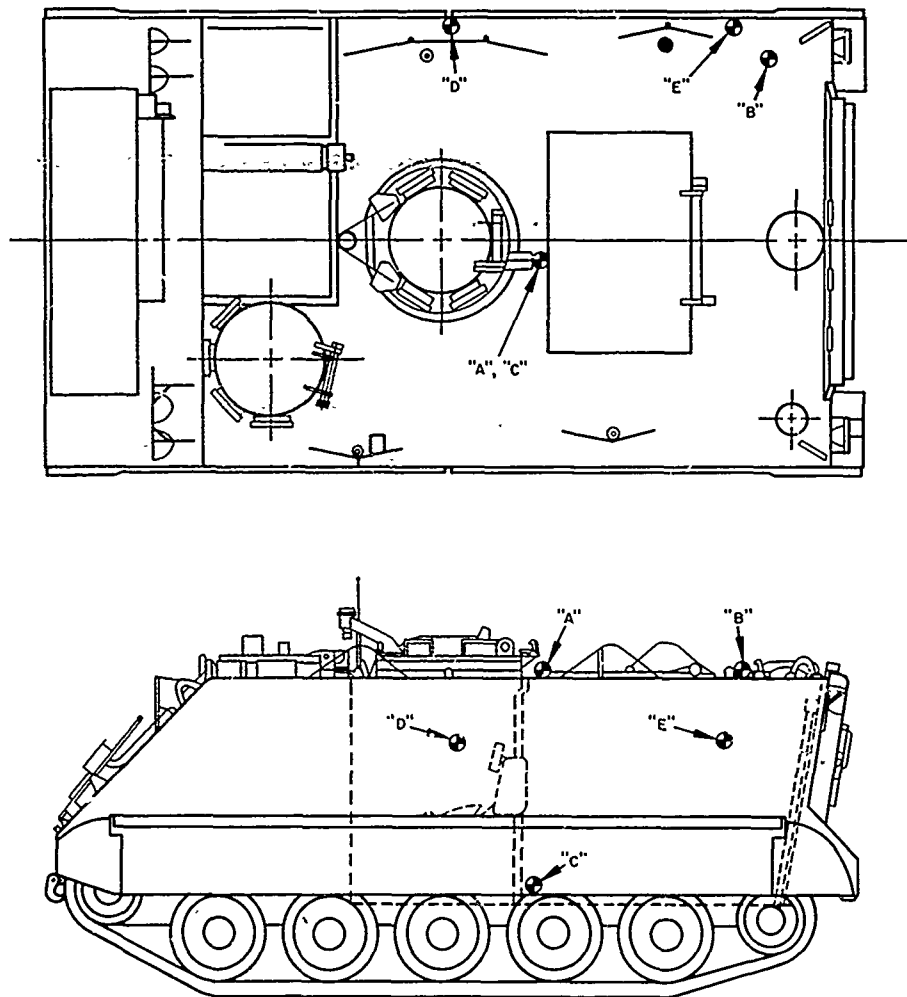
Fig. 1. Accelerometer locations

Instrumentation

Figure 1 shows the accelerometer locations for both tests. Piezoelectric accelerometers were used for the vibration tests, and strain gage accelerometers for the shock test. Block diagrams for the instrumentation are shown in Figs. 2 and 3. All instrumentation was carried on the M-113 during the FMC tests. At Fullerton, an instrumentation truck was driven next to the M-113 during the tests.

Measurement Conditions

In the vibration tests, measurements were made on a concrete and dirt track at speeds of 5, 10, 15, 20, 25, 27 (maximum on dirt), 30, and 34 mph (maximum on paved road).

The shock test was performed on a Munson course containing wooden ramps as shown in Fig. 4. Tests were run at vehicle speeds of 7, 9, 11, and 13 mph on the shock course. The suspension system bottomed at 13 mph while going over ramps spaced 14 ft apart. In addition, vibration data were recorded while traveling over an asphalt surface at 20, 25, and 30 mph.

VIBRATION TEST RESULTS

Broadband acceleration levels for all measurement locations are presented in Fig. 5. Acceleration spectral densities of selected data points are shown in Fig. 6. Included are spectra for the most severe vibration for all locations, for vertical accelerations at position B for a range of road speeds, and for position A on a road test of a new vehicle. Amplitude densities of certain narrowband data are presented in Fig. 7.

The vibration produced by vehicle motion—specifically by the track engagement with the ground—has many strong features. As might be expected, the vibration levels increase with

116
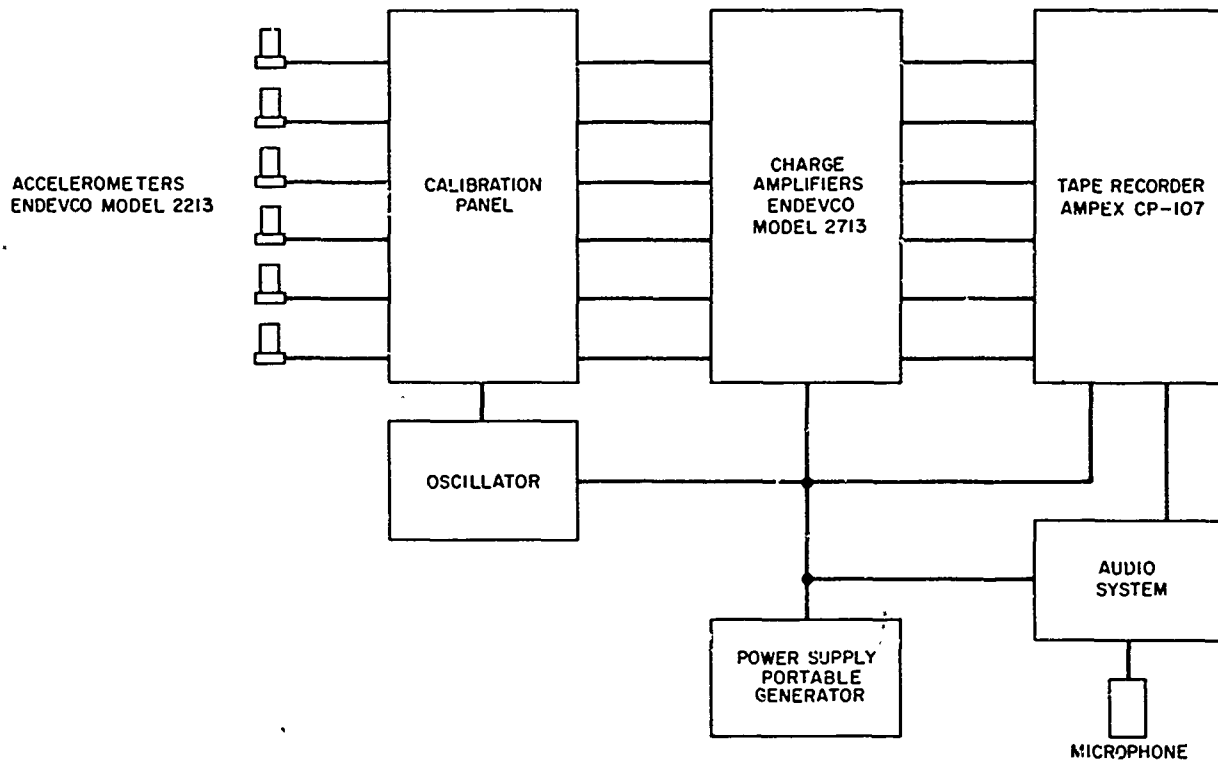
Fig. 2. Instrumentation, vibration test at FMC Corp.
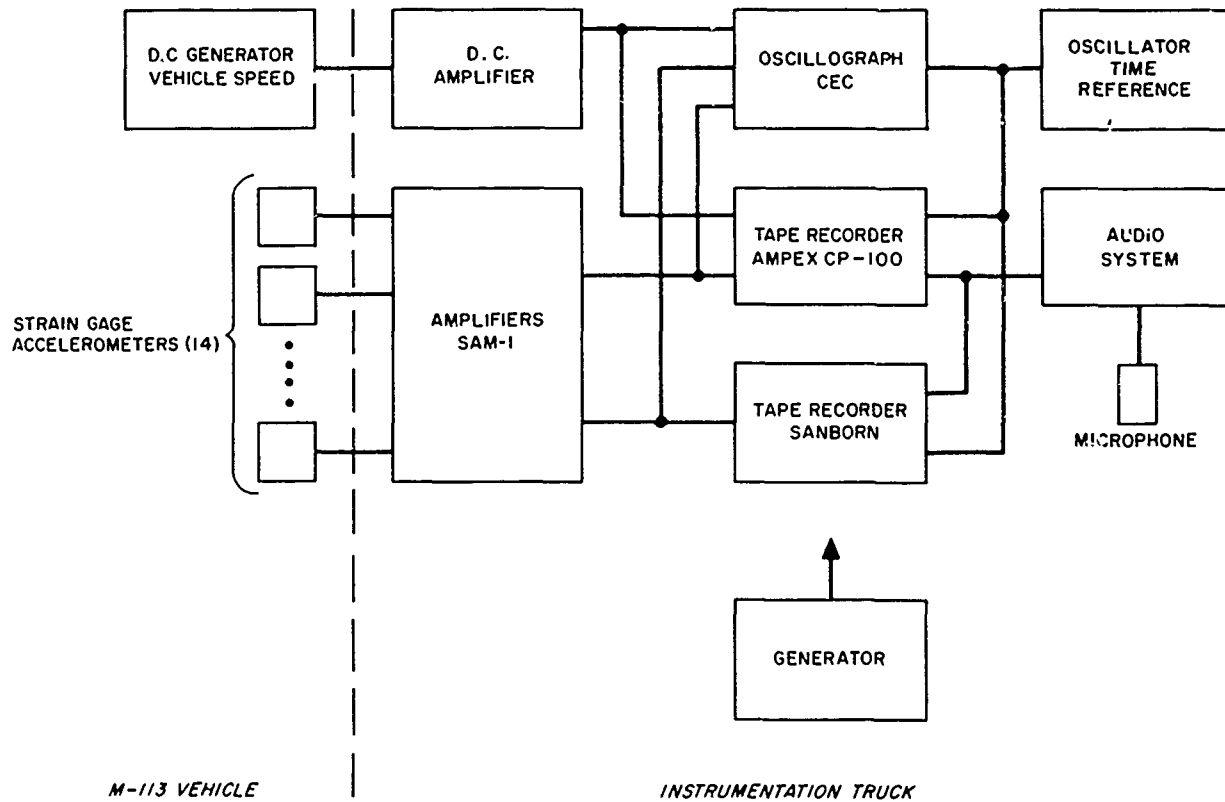
Fig. 3. Instrumentation, shock and vibration tests at Fullerton

117
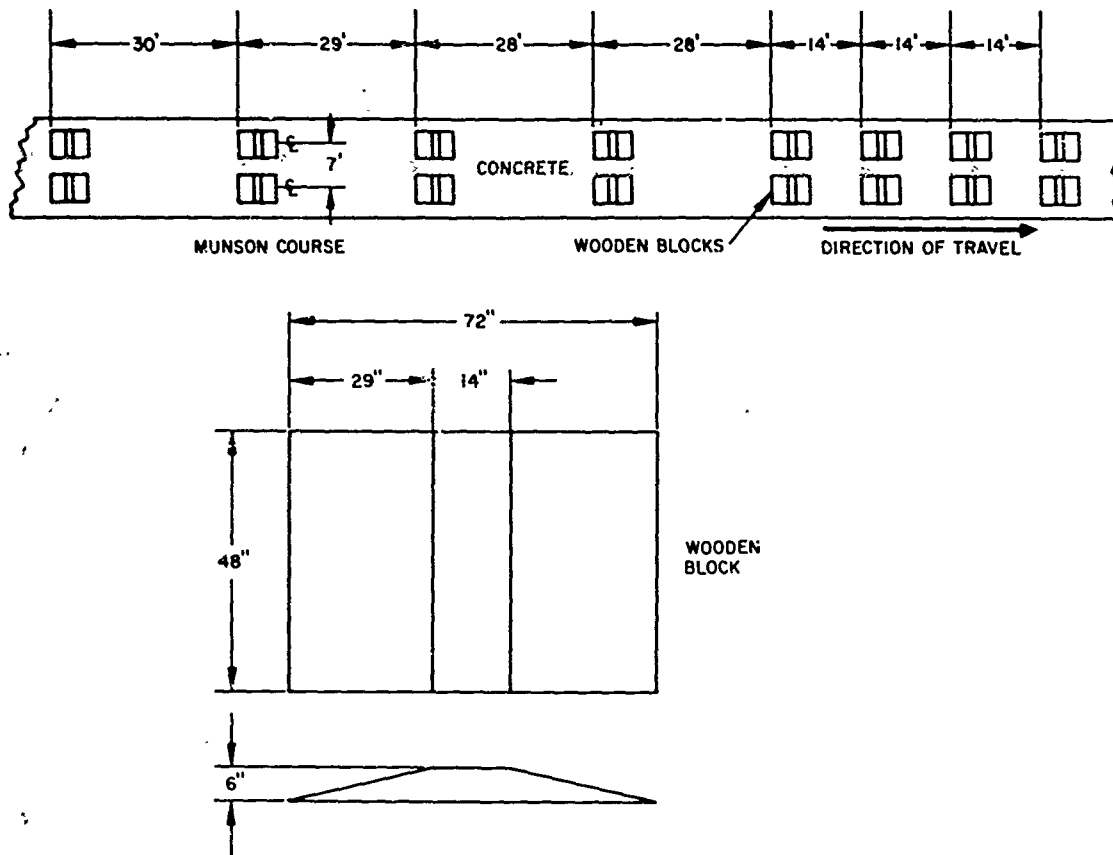
Fig. 4. Size and location of wooden ramps used in shock tests

vehicle speed. There were exceptions to this rule as the measurements made on the vehicle deck and floor reveal (positions B and C). These locations exhibit their highest vibration levels at 29 mph. Otherwise, the levels are proportional to the velocity. At almost all conditions, the longitudinal vibration was lowest. The vertical and lateral vibration showed equal prominence, depending on the location. Positions A, B, and C exhibit higher levels in the vertical direction; positions D and E had higher levels in the lateral direction. Postions A, B, and C were located on structure that was stiffest in the lateral and longitudinal directions, and positions D and E were on structure that was stiffest in the vertical and longitudinal direction. Examination of the vibration spectra reveal that there is significant high-frequency content in the data in the vertical direction for positions A, B, and C and in the lateral direction for positions D and E.

Another significant feature of the vibration is the appearance of a strong spectral peak at the tread engagement frequency. This frequency is equal to the velocity divided by the tread length. Because of the strong excitation associated with this frequency, its characteristics must be understood. The spectral peak appeared in all of the data in varying magnitudes, usually of higher value at higher speeds. The amplitude distribution of the spike revealed that in the vertical direction it was strongly sinusoidal. Above 25 mph in the other directions, it tended to be only slightly sinusoidal. At lower speeds and on dirt tracks it appeared to be nearly Gaussian in all directions.

A comparison of the vibration data taken on a used vehicle with that taken on a new vehicle reveal that the levels are slightly greater on the former. Acceleration spectral densities for position A were computed from data taken on a new vehicle during the Fullerton shock tests. Because of high-frequency response limitation of the accelerometers used during this test, the broadband acceleration levels cannot be directly compared to the levels reported for the used vehicle. However, examination of the spectra reveals that, in most instances, the level of the tread frequency spike is lower for the new vehicle.

SHOCK TEST RESULTS

The shocks which occurred during suspension bottoming as the vehicle rode over the

118
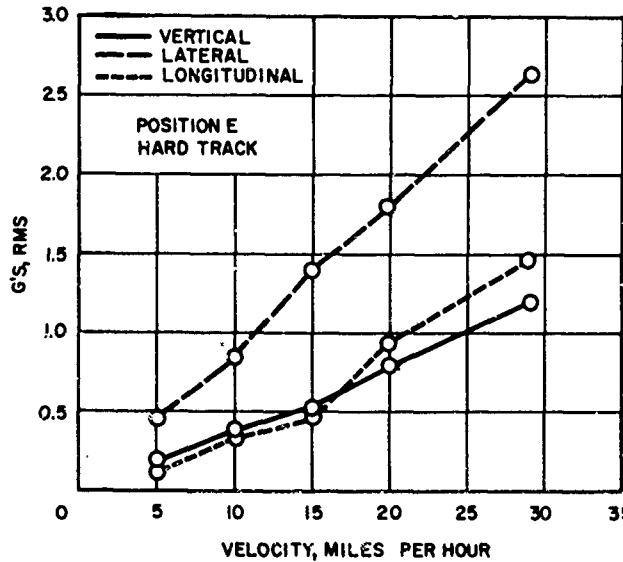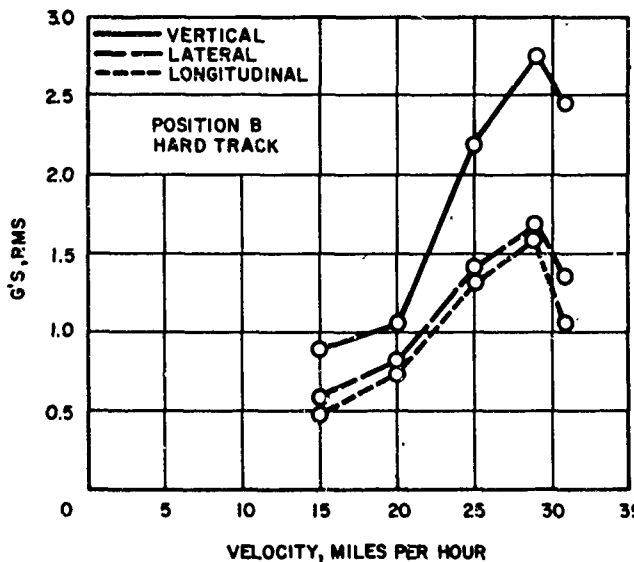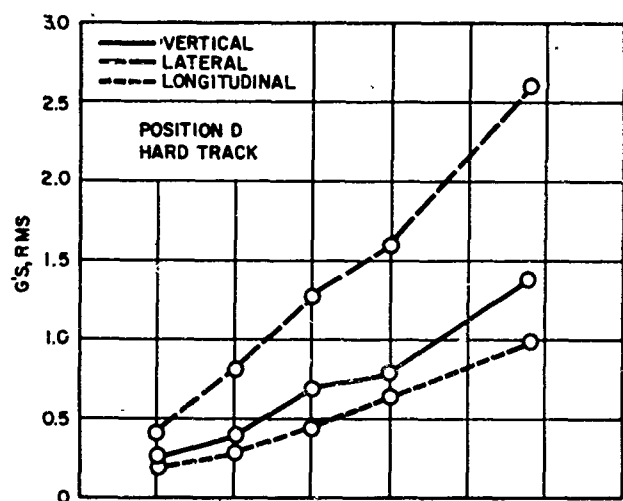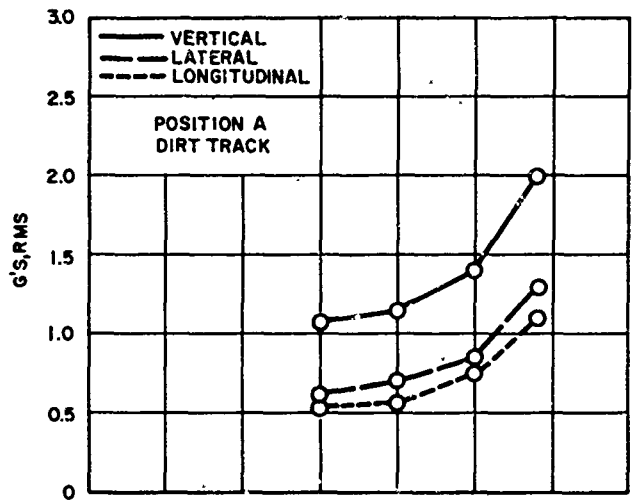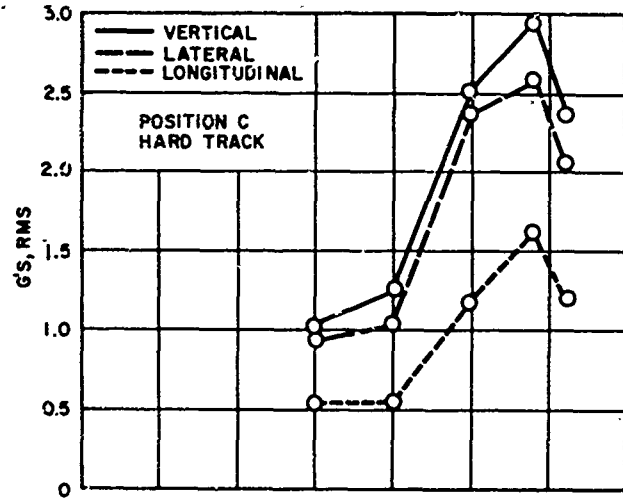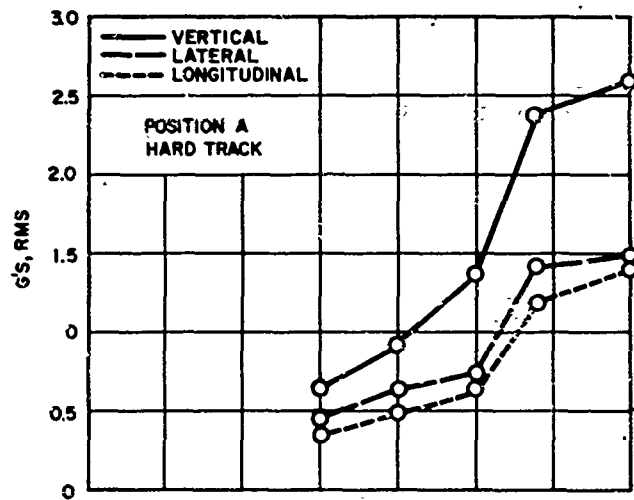
Fig. 5. Acceleration vs velocity, all measurement locations

119
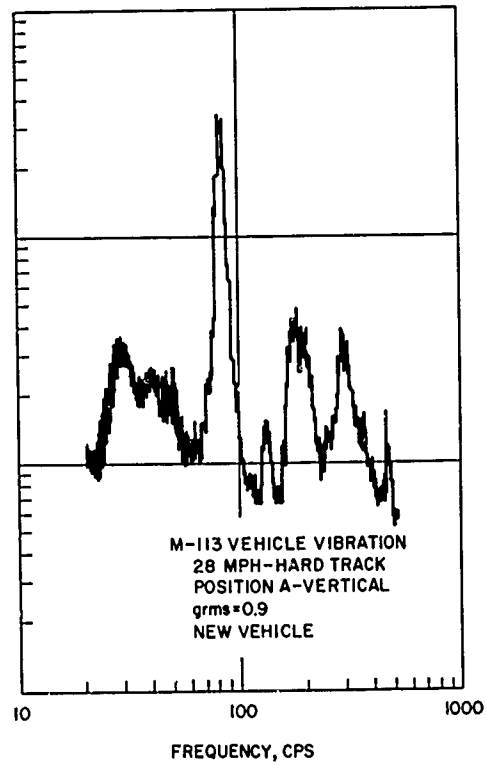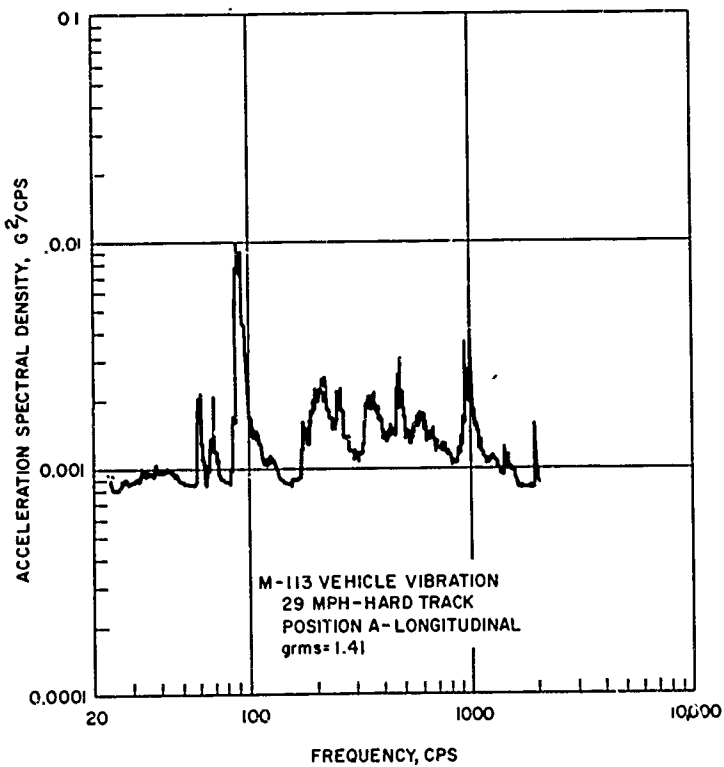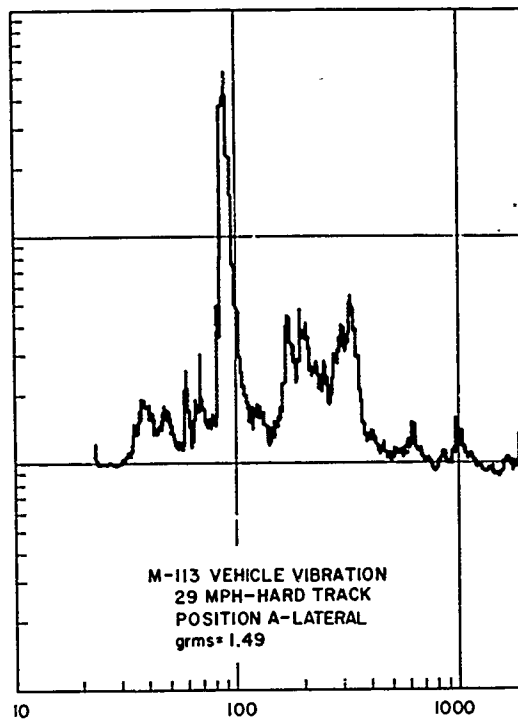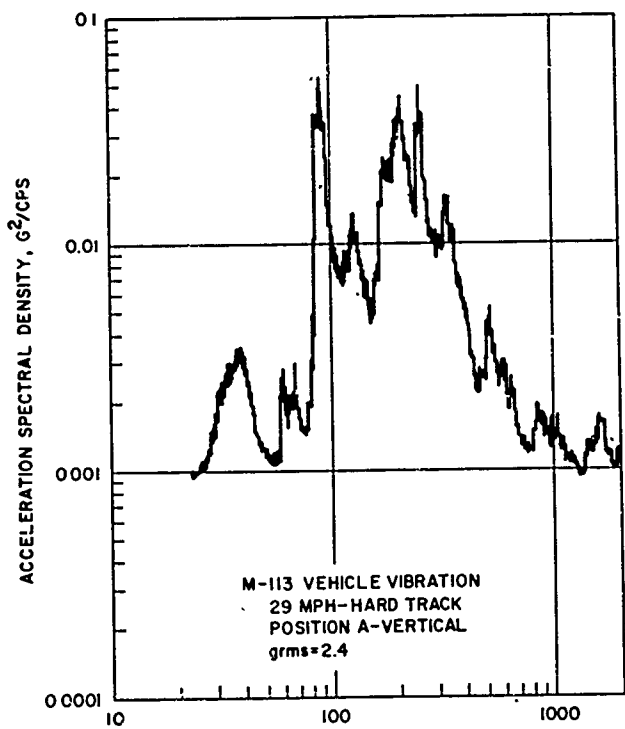
Fig. 6. Acceleration spectral densities, selected data points

Fig. 6. Acceleration spectral densities, selected data points (Cont'd.)
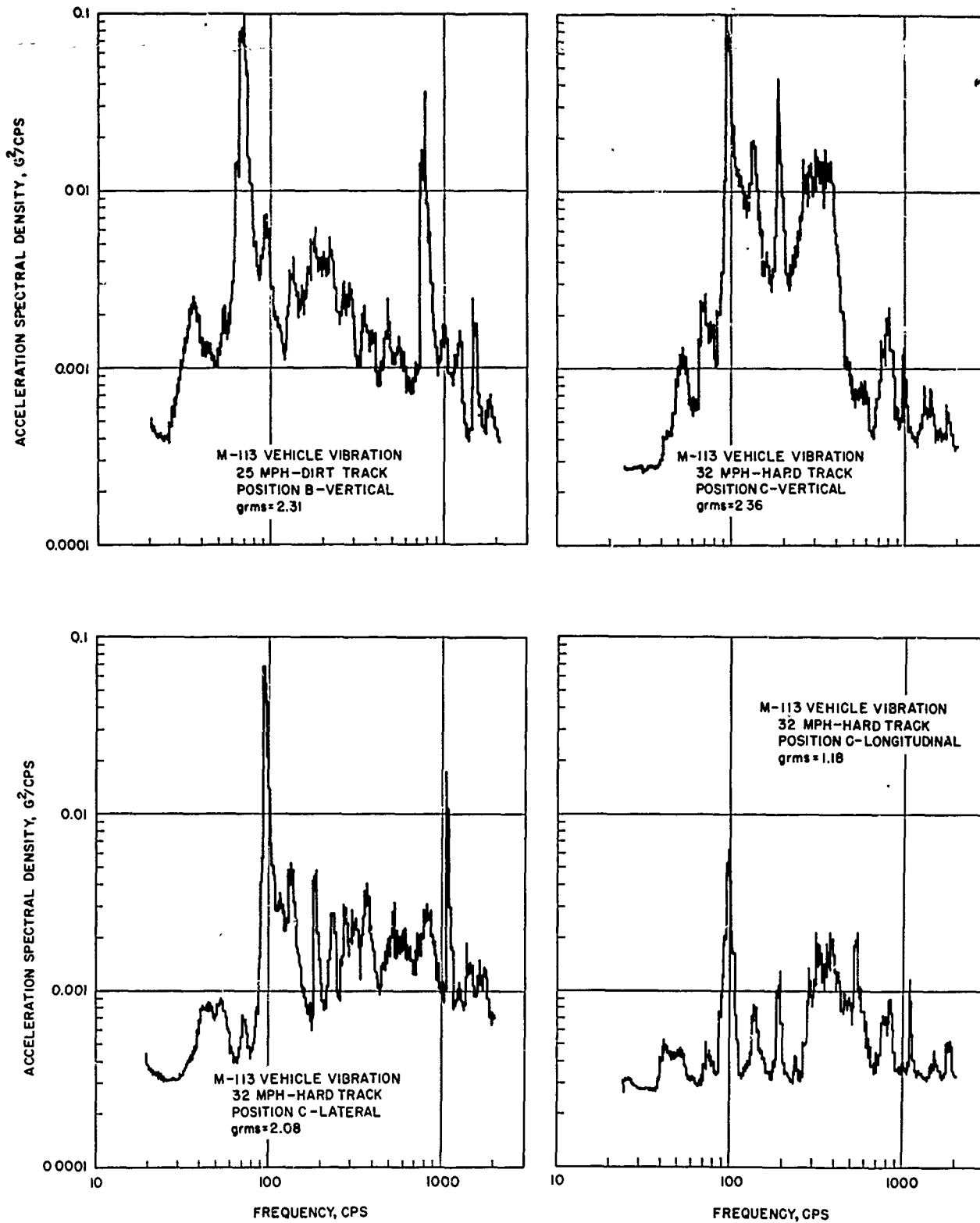
121

Fig. 6. Acceleration spectral densities, selected data points (Cont'd.)

122
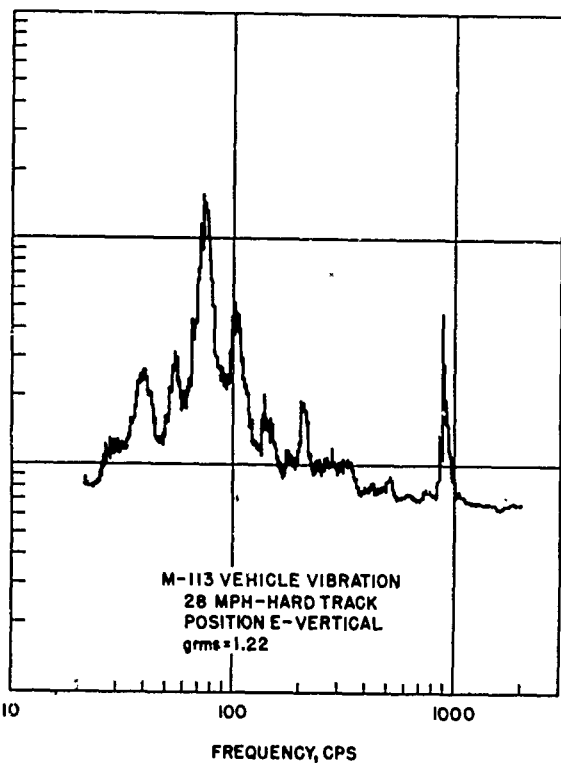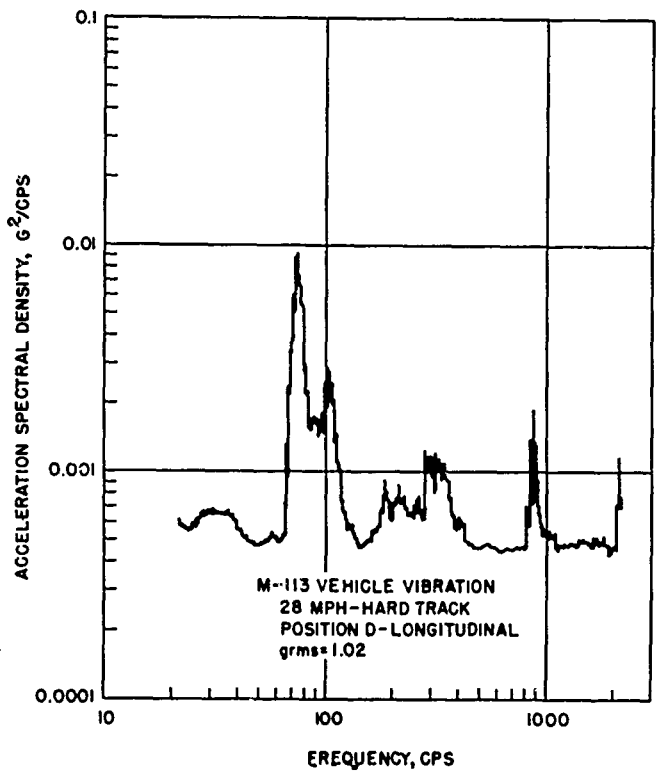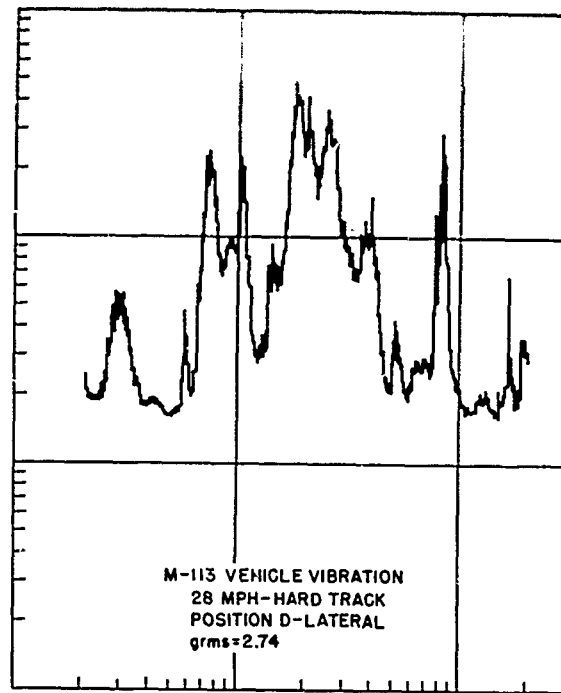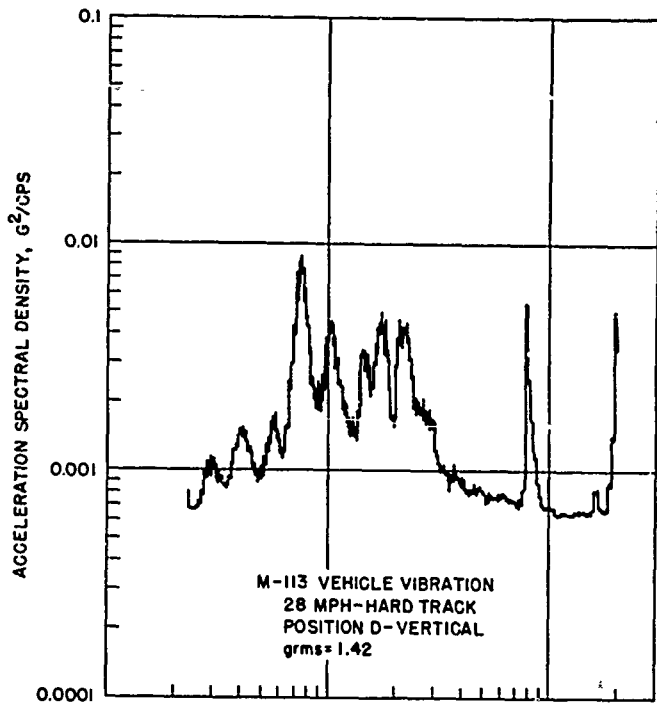
Fig. 6. Acceleration spectral densities, selected data points (Cont'd.)
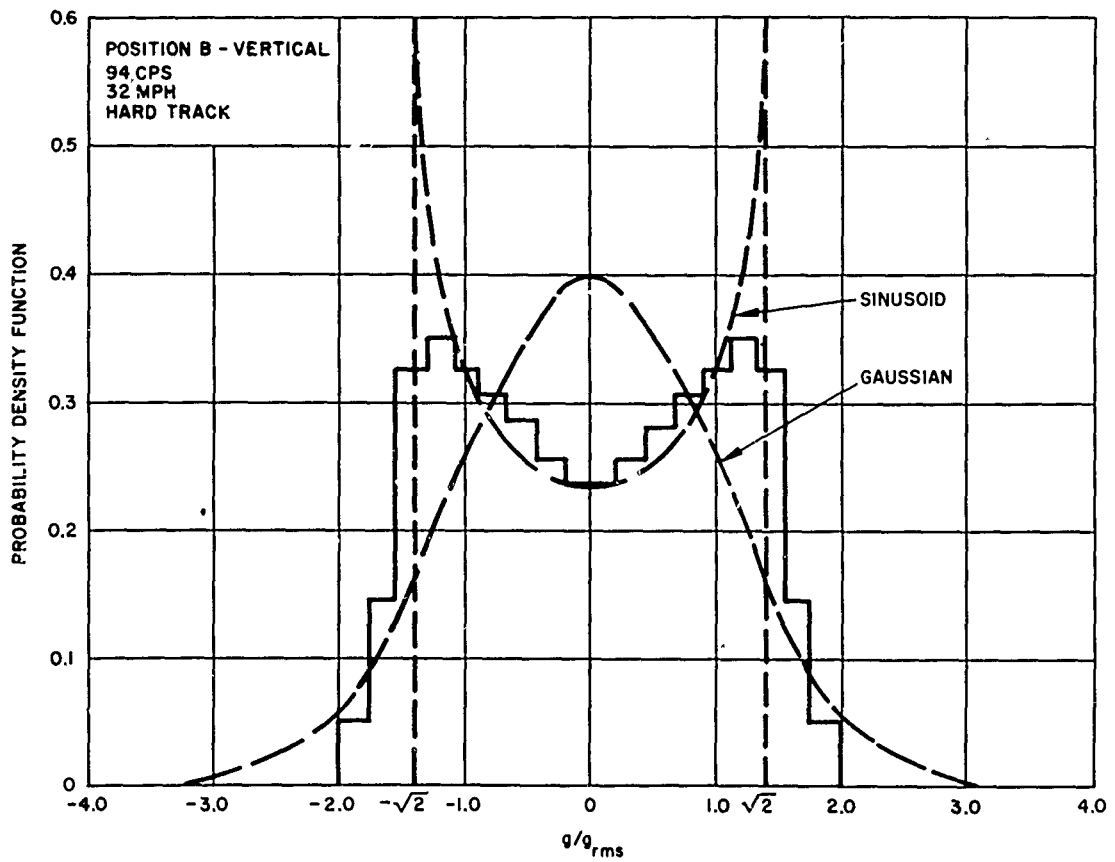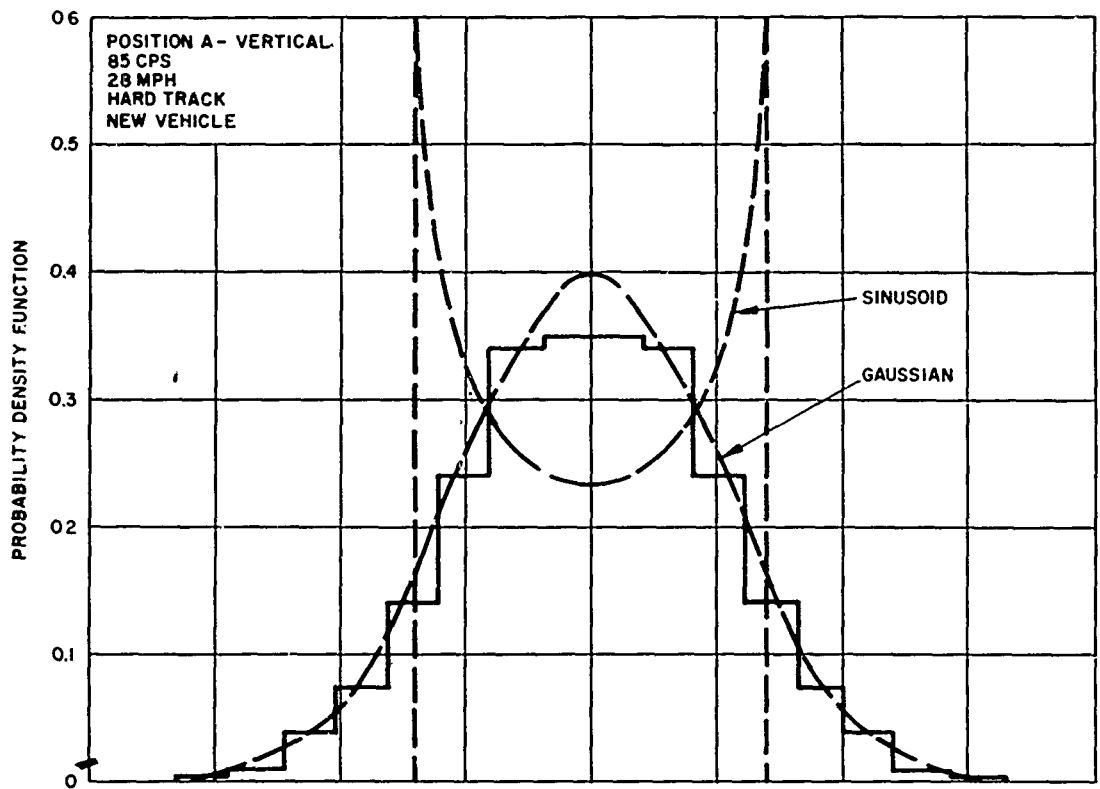
Fig. 7. Amplitude densities

Munson course are less predictable than the vibration environment. Shock levels did increase with velocity, with the highest levels recorded at 13 mph. Generally, the shocks recorded from test to test represented the same velocity change with different combinations of duration and level. The highest shock level measured was 32 g and had a pulse duration less than 2 ms. Longer duration shocks had correspondingly lower levels. As in the vibration tests, measurements on the floor and deck of the vehicle had levels which were highest in the vertical direction, and measurements made on the side wall had their highest levels in the lateral direction. Shock spectra of some typical pulses are shown in Fig. 8.

CONCLUSIONS

As the results show, the vibration of the M-113 vehicle is significant. Important characteristics which can be concluded from the test are:

1. Generally, the vibration levels are proportional to vehicle speed;

2. The vibration levels are of comparable magnitude in all directions;

3. At all speeds, the vibration has a broad frequency spectrum and a strong peak at the tread frequency;

4. The spectrum at frequencies other than the tread frequency has a Gaussian distribution; and

5. At high vehicle speeds, the tread frequency spike was strongly sinusoidal.

The level and pulse duration of the shocks which occurred during suspension bottoming varied from location to location and test to test and, therefore, cannot be predicted with accuracy. However, significant levels were measured in all directions.

REFERENCES

1. V. A. Eddington, "Road Shock and Vibration Test of Armored Personnel Carrier M-113 (Vehicle Response Investigation for Mauler Weapon System)," Aberdeen Proving Ground, Rept. DPS-391, Dec. 1961

2. R. P. Lenert, "Noise and Vibration Test of M-113 Armored Personnel Carrier with Standard and Short Pitch Track," Aberdeen Proving Ground, Rept. DPS/PTA-166, Sept. 1962

3. "Vibration and Shock Environments in Vehicles of the Airborne Multipurpose Family,"

Food Machinery and Chemical Corp., San Jose, Calif., Rept. ORD 619, Dec. 27, 1960

4. "Vibration and Shock on the XM474E2 F1 Missile Equipment Carrier," Food Machinery and Chemical Corp., San Jose, Calif., Rept. ORD 621, Jan. 25, 1961

5. "APC M-113 Full Vibration Induced by Engine Operation with Vehicle Stationary," Food Machinery and Chemical Corp., San Jose, Calif., Rept. ORD 557, Jan. 25, 1960

Appendix

NOTES ON DATA ANALYSIS

ACCELERATION SPECTRAL DENSITY

A swept filter analysis was used with the analysis system consisting of a Spectral Dynamics SD101A for the analyzer and a Balantine true rms meter for the detector. The following were the analysis parameters: filter bandwidth, 5 cps; loop length, 10 seconds; sweep time (20-2000 cps), 15 minutes; and averaging time constant, 3 seconds.

AMPLITUDE DENSITY

In performing the amplitude density analysis the data are passed through a broadband filter (half-power points at 17.5 and 7000 cps) to a 1/10-octave bandwidth filter. The filtered data are fed to a bank of 10 amplitude discriminators. These discriminators are biased in equal increments of full scale, and the time that the instantaneous amplitude of the data is within each of these discriminators is determined. These
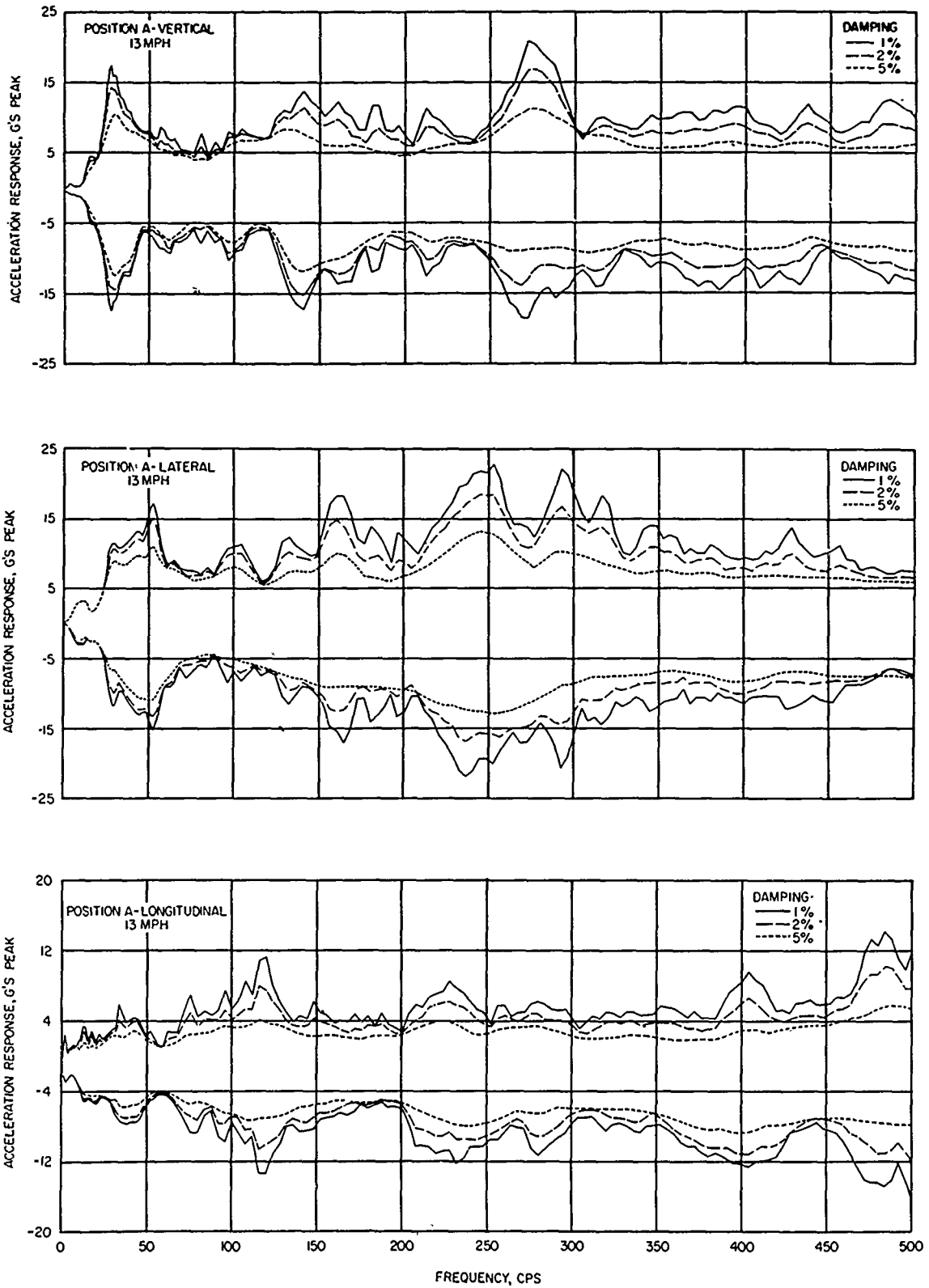
Fig. 8. Shock spectra, typical pulses
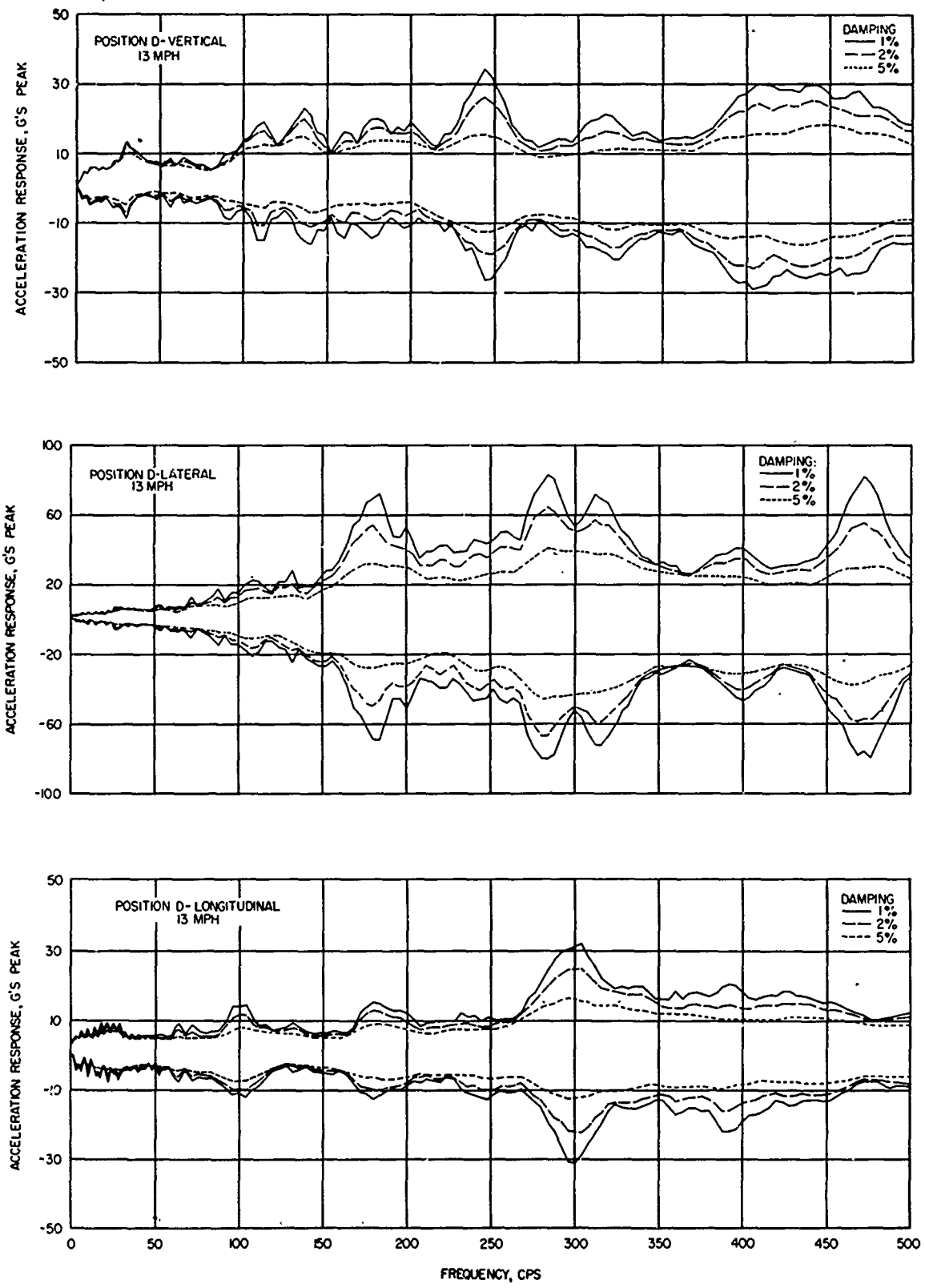
Fig. 8. Shock spectra, typical pulses (Cont'd).

times, divided by the total analysis time, are normalized with respect to the amplitude of the equal discriminator increments. The amplitude increments are previously normalized with respect to rms value of the data. Therefore, the area under the amplitude density curve equals the probability that the instantaneous value of the data is within the amplitude limits of that area.

SHOCK SPECTRA

The signal from the magnetic tape recording of the acceleration is fed into a series of electrical analogs of lightly damped, single degree of freedom systems. The peak negative and positive outputs from each of these analogs is the response used to plot the spectrum. The damping values used in the analysis were 1, 2, and 5 percent of critical damping. These result in amplification factors (Q) of 50, 25, and 10, respectively.

DISCUSSION

Mr. Scott (Sandia Corp.): What was the load inside the M-113 during these tests?

Mr. Tinling: It was loaded with a dummy of the weapon system that was going to be installed.

Mr. Scott: Was it heavily loaded, lightly loaded, or practically empty?

Mr. Tinling: I do not know how to classify it.

Mr. Forkois (U.S. Naval Research Laboratory): What was the phenomenon connected with the shock inputs?

Mr. Tinling: When the vehicle was driven over the wooden ramp the suspension would bottom and there would be an input velocity change.

Mr. Forkois: This is what I suspected. Do you know approximately the g value attained?

Mr. Tinling: It varied quite a bit. A maximum level of 32 g of about 2 ms duration was observed. Most levels were lower—10 to 15 g with 5 to 8 ms duration.

Mr. Marshall (Aeronutronic Division): What was the relation between the bed measurement and the deck measurement in terms of vibration level?

Mr. Tinling: Fairly similar.

*   *   *

128

INTERPRETATION AND APPLICATION OF SPECIFICATION
REQUIREMENTS THAT SIMULATE VIBRATION RESPONSES
OF EQUIPMENT BEING SHIPPED BY COMMON CARRIER

James E. Rice
Goodyear Aerospace Corporaticn
Akron, Ohio

The object of this paper is to encourage investigations which will show that vibration resonance dwell test requirements that simulate loads related to transportation by common carrier are not realistic for certain conditions. It is felt that the test frequency ranges and g inputs are too high for items weighing 1000 lb or more. Of the various criteria currently used to establish transportation load criteria, MIL-STD-810 was chosen for discussion, since it clearly displays the problem.

By examination of the dynamic characteristics of the common carriers, it can be shown that steady state vibration loads at values large enough to cause damage are not present at frequencies greater than 30 cps for items weighing 1000 lb. It is felt that the criteria as now presented can encourage poor designs and introduce unnecessary costs of producing military hardware for the weight range considered.

INTRODUCTION

A currently accepted standard used by government agencies and industry is MIL-STD-810. It is felt that the criteria governing vibration testing to simulate shipment by common carrier can be interpreted in such a manner that poor designs are encouraged and good designs will be penalized by increased costs which are felt to be unnecessary. Since the Department of Defense is making a determined effort to reduce unnecessary costs, every avenue should be explored so long as reliability is not jeopardized. Also, any interpretation that could encourage poor design must be carefully studied.

To bring the problem into focus as quickly as possible, the following questions must be raised:

1. What is the problem?

2. Why is it a problem?

3. What are the consequences of the interpretation to be discussed?

4. Will analysis or measured data support the viewpoint to be expressed in this paper?

5. What is the purpose of introducing the problem at this symposium, rather than directly contacting the Aeronautical Systems Division, Wright-Patterson Air Force Base, Ohio?

WHAT IS THE PROBLEM?

A situation frequently encountered is that personnel who are not dynamics specialists have the responsibility of monitoring contracts or awarding contracts, either in government agencies or as prime contractors. Their guide must be the current standards. The criteria that reduce input frequency with increasing weight do not provide guidance to show that 1000-lb objects will respond dynamically in a far different manner than 400-lb objects. Figure 514-8 of MIL-STD-810 (1) permits a decrease in test frequency with weight, but for items weighing 300 lb or more, the upper frequency level is 50 cps. Should this be so for a 1000-lb item or a 5000-lb item? Figure 514-8 does not discriminate, and nontechnical monitors can only assume that 50 cps is the cutoff limit. It is felt that this upper frequency cutoff should be reduced to 30 cps for items weighing 1000 lb or more.

The design problem is the resonance dwell requirement of 1/2 hour at each of four natural frequencies for each of three axes with an input as large as 5 g. Generally speaking, large complex consoles, such as ground support equipment, will respond at the same resonance frequency in each of the three axes, due to coupled modes, so it is not uncommon to subject the equipment to 1-1/2 hours of resonance at 50 cps with a 5-g input and a 25-g output. Only those who have had the experience of seeing this response for a 1000-lb console, loaded with heavy pumps, chassis on slides, dials, gages, and mazes of hydraulic tubing, can appreciate the severity of such an environment. The concrete floor shudders, and 130 db of acoustic noise is generated by the radiating sheet metal side panels of the console.

WHY IS THIS A PROBLEM?

The problem created by specifying such high g levels at such high frequencies (1) is that the development costs to design a structure to withstand the loads are substantial. Also, it is usually not possible to buy "off-the-shelf" equipment that has been qualified to vibration levels greater than 15 g, so the cost of requalification must be borne. This involves large sums of money.

WHAT ARE THE CONSEQUENCES
OF THE INTERPRETATION
TO BE DISCUSSED?

A serious consequence can be the designers' response to the requirement. If the primary structure has four natural frequencies less than 26 cps, the specified vibration input levels are ±1.3 g. Even with an amplification factor of 5, the induced vibration level on components is only ±6.5 g for the resonance dwell periods. This simplifies the procurement problem for component assemblies. Also it is much simpler and less expensive to design a large structure with natural frequencies less than 26 cps than to design the structure to have no natural frequencies below 50 cps (to avoid resonance dwells). Some agencies define a resonance as a dynamic response with a Q = 2. This means if the primary structure had a lowest natural frequency of 60 cps, and was fairly well damped, a Q = 2 could be experienced at 50 cps because of the broad response curve, thus necessitating a resonance dwell.

It will be shown later that the steady state forces from common carriers that excite shipped items at their resonance frequencies

are contained in frequencies below 26 cps for a 1000-lb object, so the soft structure could continually be excited at resonance in service, whereas a stiff structure would not. This encourages poor design. Obviously, those aware of the input frequencies keep the structural natural frequencies above 26 cps, but with the resulting penalties in cost.

WILL ANALYSIS OR MEASURED
DATA SUPPORT THE VIEWPOINT
EXPRESSED IN THIS PAPER?

Newton's law, $F = ma$, requires a steady state alternating force of 5000 lb to induce a 5-g response for a 1000-lb object. Also, action equals reaction, so the item being shipped will apply these loads to the carrier. The common carriers do not supply such large steady state forces at frequencies above 30 cps. Shocks can induce a high-frequency shock spectrum on equipment being shipped, but these are decaying transients and do not justify resonance dwells for such long periods with a 5000-lb input. If shock spectrum response is the problem, we should require proper shock testing in place of resonance dwells at high g inputs.

A number of excellent papers have been presented at recent Shock and Vibration Symposia which show that both the input g levels and the cut-off frequencies are questionably high when 1000-lb objects are being shipped. Two papers presented at the 31st Shock and Vibration Symposium describe investigations to establish dynamic loads in cargo airplanes and trucks. In the test reported in the first paper (2), pickup's were placed on a 1000-lb bomb and on structure adjacent to the bomb. No response greater than 0.5 g was measured on the bomb at frequencies greater than 30 cps. The pickups on adjacent structure responded at ±1 g at frequencies up to 500 cps. This ±1 g merely reflected the fact that light-weight structure will respond at high frequencies but with little force. The second paper (3) described an analysis of data to try to correlate the vibration requirement of MIL-E-4970 by test. The tested item under consideration was a heavy refrigeration unit. The conclusions reached were that even over the severe Munson Road course, the maximum value at any one frequency did not exceed 1.1 g, and even the 3 sigma values did not exceed 2.5 g. The requirements of MIL-E-4970 Procedure VI are almost identical to MIL-STD-810 for the common carrier vibration test.

The tests at Aberdeen Proving Ground and many similar tests show that a truck responds with a steady state vibration input at one of two

natural frequencies which are the "sprung weight" which varies from 1 to 5 cps and the "unsprung weight" (or wheel hop) which varies from 12 to 17 cps (4). Since the road surface is best described by power spectral density (PSD) measurements (5), the truck responds only at these two natural frequency ranges, as is characteristic of response of dynamic systems to PSD inputs. The Munson Road course excites the same frequencies. There is a third frequency range, the body natural frequencies, for trucks from 60 to 120 cps. These frequencies have been measured, but the force to excite 1000-lb objects is not present. Usually the input forces at these high frequencies are shock-induced transients with little power to drive heavy items.

Steady state vibration inputs from ships and trains are at frequencies less than 30 cps. As previously stated, the dynamic characteristics of all common carriers that could cause failure from steady state inputs occur at frequencies less than 30 cps.

The Shock and Vibration Handbook (4, pp. 45-29, 45-30) indicates that the steady state vibration input of trains is in the frequency range less than 10 cps with a maximum steady state input of 1.3 g. The vibration input common to ships is shown in Fig. 46.2 (4, p. 46-4) and is 0.3 g at frequencies less than 20 cps.

There is little doubt that shock loads are experienced by items being transported by trains and trucks. The shock loads from trains are due to humping and cargo shifting resulting from sudden velocity changes. The large accelerations experienced by items being shipped by trucks can be either shocks due to chuckholes or bumps in the road, which cause the shock struts to bottom, or to the vibration loads occurring 1 percent of the time. Aberdeen Proving Ground places the measured accelerations on trucks into three categories: single maximum acceleration, accelerations exceeded 1 percent of the time, and rms accelerations.

It is felt that the damage experienced by lading is due to these large loads whether they be clearly defined as the single maximum shock or accelerations experienced 1 percent of the time in trucks. Either of these can induce high-frequency response on the carrier or in the shipped item. After the high-frequency components are separated from the major pulse (3), the signature of the damaging frequencies can

be more readily identified. Also, if further testing is conducted on trucks and trains, in which both the response of the shipped item and nearby structure is measured, the cutoff frequencies can be established for trucks and trains as they were for airplanes (2). With this information, it is felt that test requirements to simulate shipment by common carrier can be examined to see if the present requirements should be changed.

The use of shipping containers has not been discussed so far. If properly designed, they are an excellent solution to the transportation problem. Special shock mitigating rail cars are also very effective.

WHAT IS THE PURPOSE OF PRESENTING THIS PROBLEM AT THIS SYMPOSIUM INSTEAD OF CONTACTING ASD DIRECTLY?

The answer is as simple as this: it is a serious responsibility to change a specification or standard, and personnel with this responsibility need sufficient facts and agreement from experts to warrant a change. The attendees of this Symposium represent experienced dynamicists, familiar with all aspects of the problem, and heads of government agencies that perform testing that can show the needed facts and provide expert interpretation of the data. In addition, those who disagree with the basic premise of the paper will present other viewpoints which should be considered. It is hoped that sufficient interest has been generated to initiate such healthy discussion, so that studies can be initiated to clarify areas of disagreement.

It is not the purpose of this discussion to criticize MIL-STD-810, which represents an advancement in a most difficult field. Junker (6) made the following statement at the 31st Symposium which is very appropriate to the problem: "It is essential that constant surveillance and liaison across the vast Military-Contractor effort be maintained so that MIL-STD-810 can be kept up to date. If, through the use of this Standard, deficiencies are noted or if new criteria and methodology are developed for which there is a general need, it is suggested that recommendations be made for upgrading the Standard."

It is with this thought in mind that this paper is presented.

REFERENCES

1. MIL-STD-810A, "Military Standard Environmental Test Methods for Aerospace and Ground Equipment," June 1965, pp. 514-2, 514-11

2. C. E. Thomas and P. G. Bolds, "Effects of Weight on the Frequency and Amplitude of Vibration Test Items," Bulletin No. 31, Part II, March 1963, p. 221

3. R. D. Baily and J. W. Apgar, "Preparation and Analysis of Munson Road-Test Tapes for Laboratory Vibration Tests," Bulletin No. 31, Part II, March 1963, p. 64

4. C. M. Harris and C. E. Crede, "Shock and Vibration Handbook" (McGraw-Hill, New York), 1961, Vol. 3, Ch 45

5. J. R. Harvey and R. A. Wursche, "Roughness Measurements and Missile System Response Evaluation for Highway Environment," 35th Symposium, October 1965

6. Virgil J. Junker, "Environmental Testing Standardization Via MIL-STD-810 Environmental Test Methods for Aerospace and Ground Equipment," Bulletin No. 31, Part II, March 1963, p. 36

DISCUSSION

Mr. Schell (Air Force Flight Dynamics Laboratory): Although it is not clear in the specification, it was never intended that the vibration test requirement of MIL-STD-810 be applied to equipment weighing more than 1000 lb.

Mr. Rice: It is true that people who monitor programs frequently do not intend that the test be extended to these weights. I know this is true because I have talked to Mr. Thomas and Mr. Earls and others at Wright-Patterson Air Force Base. There are people, however, who interpret the specification as allowing its application out to 1000, 2000, or even 5000 lb. It is for these people that I wish a definition.

Mr. Schell: I wish that we could write a perfect specification, but I do not know of anybody who has managed to do this yet. As these points come up we try to take care of them. This might be a point that we can take care of in the present revision for tri-service coordination on the document. In my opinion, MIL-STD-810 ought to be divided into weight categories, such as 1 lb, 1-10 lb, 10-50 lb, 50-100 lb and so on, for dynamics testing purposes. Since we are limited, however, in money and

people, we just do not have enough time to devote to these things. If you have some good suggestions we will be glad to try and incorporate them. As far as the test levels in the document are concerned, they are based on environmental measurements. At that time we did not have any impedance techniques and I do not think impedance techniques today are well enough developed to apply to this problem. If there are some who disagree with me, I would like to hear their arguments.

Mr. Rice: Thank you, Mr. Schell; I am so happy to hear your comments. I do not want to fall into the category of those who merely criticize. I only want to help. I have had to ship many big objects, and I want to try to pass on the experience I have had. It confuses my most learned friends when they do not have the measured data in their grasp. There is something in the system that vexes and frustrates me a great deal. If I know that a specification must be changed and can get to my counterpart I could change it in one day. But there is a rule that you must spend $50,000 and 3 months to prove that God and Newton are wrong, and then they will talk to you. (Applause.)

*　　*　　*

SHOCK AND VIBRATION ISOLATION

NEAR-OPTIMUM SHOCK MOUNTS FOR PROTECTING
EQUIPMENT FROM ACCELERATION PULSES

Ralph E. Blake
Lockheed Missiles and Space Company
Sunnyvale, California

In this theoretical study, the properties of a mount are defined by the dynamic force-deflection curve. To relate mount properties to strength required in equipment, an "index of severity" is developed from the normal-mode theory of structural response. The best mount is the one which minimizes the index of severity of the shock transmitted to the equipment.

The mount force-deflection curve was fixed except for three shape parameters. The problem of finding the optimum set of parameters was then programmed for a computer. Computer input consists of the disturbing shock pulse, the maximum allowed mount deflection, and some assumptions as to expected dynamic properties of the equipment. The resulting solution is "near-optimum" in that the shape was constrained except for three parameters and typical properties of the equipment were assumed. However, comparison with a theoretical lower bound on the index of severity suggests that there is not room left for great improvement.

Shape parameters, indices of severity, and shock severity spectra are reported for several cases. Shock severity spectra are similar to shock spectra but are modified to give more emphasis to vibratory response in equipment.

The extent to which assumptions can be relaxed to deal with similar problems of interest has to be examined. The shock disturbance was assumed to be a pulse, without reversal of sign. No modeling of human comfort or injury criteria was included. Mount deflection was assumed to be limited by system design problems, but trade-offs of space, weight, cost, reliability, etc., involved in system optimization were not introduced.

INTRODUCTION

A shock mount is a flexible nonlinear device used to reduce the damaging effects on an equipment of a shock or impact. It achieves this by trading space to reduce the force necessary to accommodate the equipment motion to the base motion. Mounts now in use can be found in an endless variety of design concepts, materials, and applications. They include rubber pads and bumpers, metal springs, air and hydraulic springs and shock absorbers, friction brakes, yielding and buckling elements, plastic foam, crushable honeycomb, rubberized hair, and nylon line. Sources of shock include blast from explosions, parachute drops, accidental drops of shipments, lunar landing, aircraft landing, freight car humping, and bumpy roads. With so many alternatives, the question arises as to whether one mount design is better than another.

More than 10 years ago, this question was attacked directly at the Naval Research Laboratory by testing mounts with a special apparatus on the Navy shock machines (1). Figure 1a shows dynamic load-deflection curves obtained for four mount types, and Fig. 1b shows

133
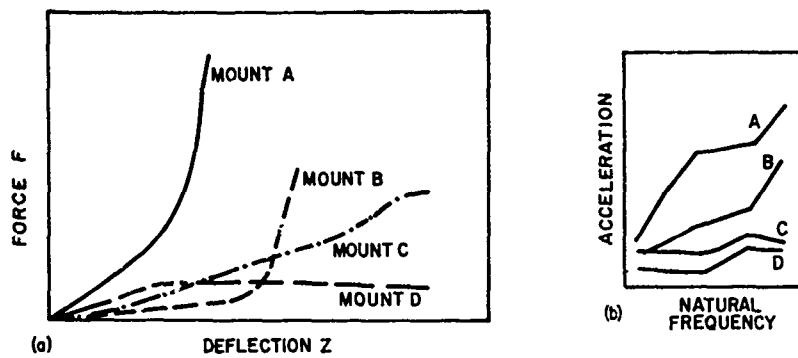
Fig. 1. Force-deflection curves and shock spectra
from Navy shock machine

the corresponding shock spectra of the motion of masses supported on the mounts. Mounts A and B were overloaded and showed force peaks due to bottoming, Mount C was fairly linear, and Mount D produced a constant force over much of its deflection. Judging these mounts by their shock spectra, Mount D was the best. But why was it best? Would it be possible for some other force-deflection curve to produce an even lower spectrum? What is the best possible mount load-deflection curve?

About a year ago, we started a study at Lockheed for the Air Force Ballistic Systems Division to define the potential benefits of shock-mounting equipment. The results to be reported concern a theoretical investigation to define the best possible load-deflection curve for a mount and the severity of shock transmitted. The design of hardware to approximate the ideal will not be discussed here; a complete report is given in Ref. (2).

First, the theoretical situation and parameters of the shock input and the mount are described. Then normal mode theory is employed to justify a new quantitative measure for the severity of shock transmitted to equipment. This "index of severity" is a weighted average of a modified shock spectrum which takes account of structural "tuning" effects in the equipment. Next, the relation of some possible mount characteristics to the index of severity is investigated. On the basis of these results, some key mount parameters were selected and a computer program set up. The computer finds the combinations of parameters which minimize the index of severity for a given input shock. Some optimum load-deflection curves and their corresponding severities are shown and compared with a theoretical limit on the possible protection.

NOMENCLATURE

a_o Acceleration of rigid box caused by constant-force mount

c/c_c Fraction of critical damping

d Geometric progression ratio in index computation

F Mount force

f_n Frequency in cps of nth normal mode

g Acceleration of gravity

I Index of shock severity

J Static influence coefficient

k,K Spring stiffnesses

ℓ,L Lengths

m,M Masses

P Force on base

P_1,P_2,P_3 Parameters of mount force-deflection curve

q "Shock-resonance" or "tuning" factor in index

r Any response of a linear elastic structure

R_n Normal-mode participation factor

S Maximum deflection of shock mount

S_o Displacement of base at time T_o

134

t	Time
T	Time of maximum deflection S
T_o	T of constant-force mount
V_n	Vibratory response factor of nth normal mode
v	Velocity of base at time T
$X, \dot{X}, \ddot{X}$	Displacement, velocity, acceleration of base
$Y, \dot{Y}, \ddot{Y}, \dddot{Y}$	Displacement, velocity, acceleration, and jerk of box
Z	Deflection of shock mount
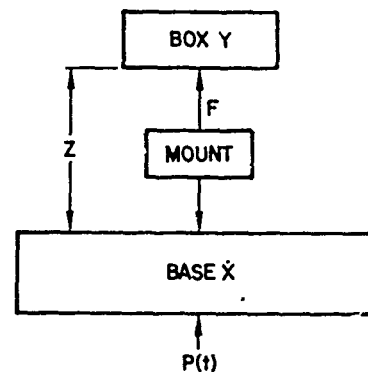
Fig. 2. Forces and motions in shock mount problem

INPUT SHOCK AND ASSUMPTIONS

All shock motions and forces will be assumed to be parallel to one direction. This does not seem to be a serious restriction; the notation is much simpler and most cases are essentially one directional.

Figure 2 shows an equipment "box" attached to a "base" by a mount. Some exciting force $P(t)$ causes an acceleration $\ddot{X}(t)$ of the base. It will be assumed that the force $F(t)$ exerted by the mount has no effect on $\ddot{X}(t)$. Furthermore, the box will be assumed to be rigid only for the purpose of describing the changes in mount height $Z(t)$. These assumptions could be relaxed somewhat by assigning local flexibilities of the box and base to the mount and by considering the effect of box mass on the rigid-body motion of the base. But the general problem of including mechanical impedances of the systems is not dealt with here. Thus, the mount must be far more flexible and deform much further than the structures. It is also expected that a flexible mount will help to justify the assumptions by having a minimum tendency to excite or transmit structural vibrations.

The base motion $\ddot{X}(t)$ is an acceleration pulse; that is, it has one sign and does not reverse or oscillate. Although it may be possible to deal with some oscillation, as in the case of the Navy shock machines, this has not been explored; the study by Eubanks (3) appears to bar us from handling the most general cases. Thus, earthquake shocks are excluded but impacts, drops, blast pulses, etc., are included.

An acceleration which does not change sign causes a continuously increasing velocity. Thus, in Fig. 3, the acceleration $\ddot{X}(t)$ corresponds to the velocity $\dot{X}(t)$.
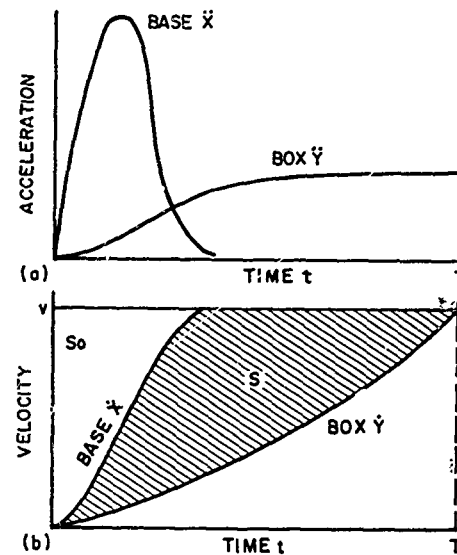
Fig. 3. Acceleration and velocity histories of box and base

SHOCK MOUNT PARAMETERS

Figure 3 also shows rigid-body acceleration $\ddot{Y}(t)$ and velocity $\dot{Y}(t)$ time histories that a box might have as the result of the force $F(t)$ of the mount. The deflection of the mount is the integral of the difference in the two velocities,

$$Z(t) = \int_0^t (\dot{X} - \dot{Y})dt . \qquad (1)$$

At time T, the two velocities are equal and the maximum deflection S occurs. Since it will be seen that the severity of shock to the box can be reduced indefinitely if S can be increased indefinitely, S is an important parameter.

In most designs, S cannot be increased without penalty in space, weight, cost, etc., so the optimum mount will be the one which makes the best use of an allowed deflection, S, to minimize the shock effects of $F(t)$ for a given input $\ddot{X}(t)$. Since the weight, reliability, cost and space for possible mount hardware designs will be different, the mount characteristics may not be optimum from a broader system viewpoint. In this first attempt, such system trade-off problems will be omitted.

After meeting its obligation to bring the box velocity up to that of the base without exceeding S, the mount force is still subject to some requirements. But these are usually minor and can be met without exceeding the strength required of the box up to time T. Hence, the basic problem is to find the box motion $\dot{Y}(t)$ up to the time T (when $\dot{Y} = \dot{X}$ and $Z = S$), such that the chance of damaging the box is a minimum. Given $\dot{Y}(t)$, it is a simple matter to plot force F versus deflection Z.

INDEX OF SHOCK SEVERITY

To pick out the best $\dot{Y}(t)$ curve from the infinite number which satisfy the space requirement, some criterion for preferring one to another is required. The criterion of minimum peak acceleration $|\ddot{Y}(t)|_{max}$ is overly simple and leads one straight to a constant-force mount. This mount produces severe vibrations of the box due to the initial step discontinuity, as will be seen later.

The shock spectrum was used for the Navy shock mount evaluation (1). This takes vibration, as well as a peak acceleration, into account, but it will be shown that a modification to increase the relative importance of vibration will be desirable.

The problem to be considered here is not that a specific box has been designed and tested and all of the needed dynamic characteristics and conditions when failure occurs are known. This is a rare situation. Instead, we must consider a whole population of possible box characteristics and ask for a mount having the highest probability of protecting a randomly selected equipment from failure. This would then be the best standard mount to try when an exhaustive tailoring to the box peculiarities is not worthwhile. Such custom-fitting can improve on the standard mount, but not very much, as will be shown later. Thus, the mount has been called "near-optimum" because it could be improved on when details of the box and systems trade-offs become known. But it will be an optimum

solution in the mathematical sense, since this does not require that the assumptions be the best possible approximation to reality.

The next task is to set up a general mathematical model to represent the response of the majority of equipments. This model is tentative, allowing for adjustment to suit improved information on typical box characteristics and also to see how sensitive the answer is to errors in assumptions.

The basic assumption is that the box has distributed mass with linear elastic springs up to the point of failure. With the further assumption that damping is small, viscous, and uniformly distributed, it can be asserted that the response of the box to the force $F(t)$ is described by the normal-mode theory. The assumption of linear behavior is reasonable for most structures up to the point of buckling, yielding, brittle fracture, slipping of friction bonds, etc. Although there are some exceptions, the great majority of failures can be related to the exceeding of some critical mechanical quantity such as force, stress, strain, and displacement. Many of these failures are preceded by elastic linear behavior of the box structure, as in the fracture of brittle materials, opening of relays, contact or arcing of electrical elements, permanent set, slippage of mechanical joints, and collision of adjacent parts. In the cases of fracture after plastic deformation and elastic buckling, the region of the box involved in the failure will be nonlinear, while the remainder is elastic. In the cases of fatigue and gyro drift, failure is due to an accumulation of effects. However, fatigue is not important, since only about 10 oscillations occur in response to shock, and gyros are special cases. For plastic deformations and elastic buckling, the conservative assumption can be made (as in static stress analysis) that the start of nonlinearity is synonymous with failure. Thus, it is considered that an assumption that the box is linear and elastic up to the point of failure will be sufficiently realistic for practically all cases of interest.

The assumption of linear behavior is, of course, the starting point of the well-known normal-mode theory of structural response (3, 4). In the appendix, normal-mode theory is used to show that the response of any of the quantities (force, stress, relative displacement, strain, or acceleration) at any point in the box is related in the disturbing force $F(t)$ by an equation of the form

$$r(t) = \ddot{Y}(t) \sum_{n=1}^{\infty} R_n - \sum_{n=1}^{\infty} R_n V_n(f_n, t), \quad (2)$$

136

where, with small damping,

$$V_n(f_n, t) = \int_0^t \left(\frac{d\ddot{Y}}{d\tau}\right) e^{-c/c_c\, 2\pi f_n(t-\tau)}$$

$$\times \cos 2\pi f_n(t - \tau)d\tau \, ,$$

and $\ddot{Y}(t)$ is the acceleration that the force would have produced if the box were rigid, $r(t)$ is the response quantity in the proper dimensions, and f_n, c/c_c and R_n are determined by the details of the box structure and the locations where r is observed and F is applied.

As seen in the appendix, R_n is very difficult to compute, even when a box design is available. But the problem at hand is to consider how to change the mount to minimize the peak value of $r(t)$. In Eq. (2) the values of R_n are unknown but fixed by the box design; $\ddot{Y}(t)$ is due to the mount force and can be manipulated by the mount design. The approach to be used here is to ask what shape of $\ddot{Y}(t)$ would be best for minimizing response in the box. Minimum response is considered to be synonymous with the minimum strength requirement for the average box, maximum chance of a given box surviving, or maximum shock severity that can be withstood.

According to Eq. (2), the response at some t is made up of terms directly proportional to $\ddot{Y}(t)$ and terms in which the variations of $\ddot{Y}$ have an integrated effect. Examination of the integral V shows that whenever $\ddot{Y}(t)$ is not varying (that is, $(d\ddot{Y}/dt) = 0$), the integral is simply a damped sinusoidal vibration at the frequency f_n. Thus, if one waits a sufficiently long time after $\ddot{Y}(t)$ becomes constant, the oscillations will decay to zero and

$$r(t) = \ddot{Y}(t) \sum_{n=1}^{\infty} R_n = J \ddot{Y}(t) \, . \tag{3}$$

Actually, it is unnecessary to use normal-mode theory to compute the $r(t)$ of Eq. (3). The stress distribution does not vary with time and could be computed by the methods of static stress analysis. J is just an influence coefficient. Thus, we shall call $\ddot{Y}(t)$ J the "static response" and each term of the right-hand series of Eq. (2) the "vibratory response of the nth mode."

Since, in general, the terms in Eq. (2) reach maxima at different times and the R_n are not known, it cannot be proved in an absolute sense that some curve $\ddot{Y}_1(t)$ is better than $\ddot{Y}_2(t)$. But

we can regard a particular box design and its R_n values as a random sample from the population of all possible designs, and we can reasonably prefer $Y_1(t)$ to $Y_2(t)$ if it is probable that $(r_1)_{max}$ will be less than $(r_2)_{max}$ for a box selected at random. Random selection means simply that the box was chosen without reference to its actual values of R_n and f_n.

The next problem is to muster all the information possible concerning the various possible values of f_n and R_n. The assumptions selected here represent our judgment and can be revised to suit. Little can be said about how the natural frequencies are scattered over the frequency spectrum above the fundamental (lowest) natural frequency, but it is generally true that a box is fairly compact and rigid. Thus, it could be assumed that the box has no natural frequencies below 100 cps; or to be precise, natural frequencies below 100 cps are considered very improbable. Since the results will be dimensionless, the lowest natural frequency, f_1, need not be selected until more is known of the box.

As one looks at successively higher natural frequencies, it should be reasonable to anticipate some trend in the value of R_n and the probability that a frequency range will be associated with failure. Since the lower natural frequencies generally involve flexure of the chassis structure, whereas failure to function involves some component, the typical natural frequencies of components are considered to be more significant. On the basis of very limited and unsystematic data, we anticipate that the range 100 to 500 cps is most important, 500 to 1000 cps is next, and over 1000 cps is least important. A weighting scheme was selected which gave diminishing value to vibratory terms from 100 to 1000 cps and no weight above 1000 cps. The final result is not expected to be very sensitive to the weighting scheme because vibration values tend to rise or fall together as $\ddot{Y}(t)$ is changed and good $\ddot{Y}(t)$ shapes cause relatively little vibration above 1000 cps.

Finally, we come to the question of whether static or vibratory terms are more important. A common assumption is to consider that a mount producing the lowest peak value of $\ddot{Y}(t)$ is the best (3, 6, 7); vibratory response is ignored. This assumption has been disproved by studies of the simple two-mass model of a box shown in Fig. 4. Since the box has only one natural frequency, Eq. (2) reduced to

$$r(t) = R_1 \{\ddot{Y}(t) - V_1(f, t)\} \, , \tag{4}$$

and $\ddot{Y}(t)$ and the integral, V, will have equal weight. A plot of the peak values of the term in

137
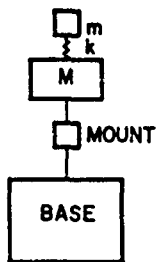
Fig. 4. Two-mass box
on shock mount

brackets as a function of natural frequency (e.g., Fig. 1) is known as a "shock spectrum." Studies of various possible mounts have shown that shock spectrum values less than twice the peak value of $\ddot{Y}(t)$ are easily achieved, provided the natural frequency f_n is well above the frequency dominating the vibration of the box on the mount. Several possible mounts give a vibratory component in Eq. (2) of less than 10 percent.

However, a slightly more complex model is sufficient to show that Eq. (4) is misleading and that vibratory components deserve more weight. The three-mass system in Fig. 5 has two oscillatory modes, so the response of spring k will be

$$r(t) = \ddot{Y}(t)(R_1 + R_2) - R_1 V_1(f_1, t) - R_2 V_2(f_2, t) . \quad (5)$$

Now, it happens that the R's may be either plus or minus in sign; for load in the spring, k, one is plus and the other minus. The signs of the oscillatory terms tend to alternate with time so that they can add together with the same sign even though R_1 and R_2 are subtracted in the static term. It is easy to see that, for any number of degrees of freedom greater than the one represented in Fig. 4, the vibratory terms can overwhelm the static term.
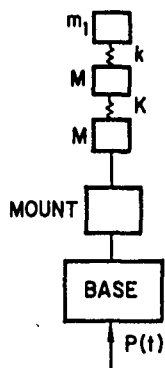
Fig. 5. Three-mass box
on shock mount

The relative importance of static and vibration response was indicated in Ref. (8). The factors R_1 and R_2 for the three-mass system

depended on the ratio m/M and the ratio of frequencies (the ratio $\sqrt{k/m}$ to $\sqrt{2k/m}$). The largest R_n values occurred when the frequencies were equal and the upper part of the system was said to be "tuned" to the lower system. When tuning existed, the small mass had a "shock resonance" with the large system. The ratio of peak load in spring to the peak of static load was calculated for the case of a step-force input. This ratio depended on the mass ratio $m/2M$ and the system percent of critical damping c/c_c, as shown in Fig. 6. The factor for a two-mass analysis $(k = \infty)$ would be 2 or less.
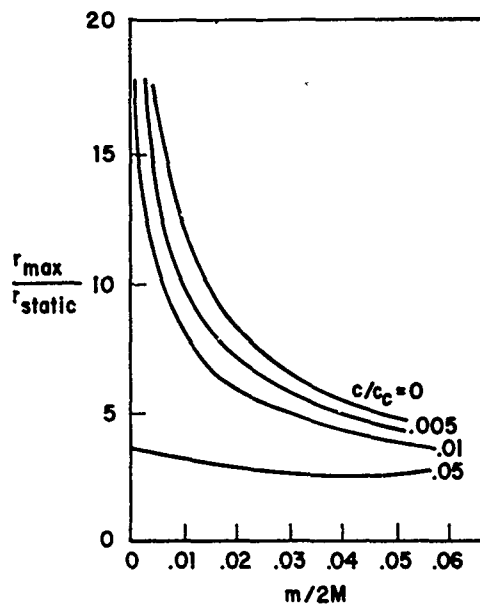
Fig. 6. Shock response amplification by structural tuning

Another illustration of this phenomenon is a rod subjected to an axial step force at one end (Fig. 7). It is well known that a step wave of force propagates along the rod with unchanged magnitude; that is, at a point distance ℓ from the far end, the force is $F(\ell) = F$. The static force is obviously $F\,\ell/L$, so that the ratio of actual force to the static component is L/ℓ.
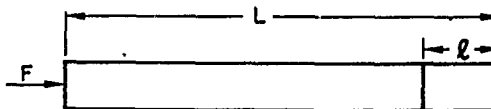
Fig. 7. Rod subjected to
axial step force

Both the rod and the tuned three-mass system are special cases which are not typical of

138

actual structure. It was also shown in Ref. (9) that the high response due to tuning occurred in a system of 20 masses, when the small system was tuned to a mode of vibration of the large one. Even so, tuning is not a typical situation; it requires the accidental matching of natural frequencies. On the other hand, failure of equipment is not a typical situation and it is plausible to suggest that tuning is a common cause of failure. Unfortunately, evidence for or against this hypothesis is lacking.

We have indicated that the shock spectrum is an unsatisfactory index of shock severity because it gives equal weight to the static and vibratory components of response. The vibratory component should have greater emphasis; this can be provided by a factor q in

$$r(t) = \sum_{n=1}^{\infty} R_n \{ \ddot{Y}(t) + q V_n(f_n, t) \} . \qquad (6)$$

There is little to indicate the most suitable value of q to be used in the comparison of possible shock mounts. For the present, provision is being made in the computer analysis for various values of q.

In using Eq. (6) as a basis for comparing shock mount $\ddot{Y}(t)$ curves, we have already decided to give weight to the possible R_n and f_n values by making all R_n's equal but concentrating f_n's toward 100 cps. Thus, as our index I reflecting the severity of $\ddot{Y}(t)$ curve, we have selected

$$I = \frac{1}{b} \sum_{n=1}^{b} \left| \ddot{Y}(t) + q V_n(f_n, t) \right|_{max} , \qquad (7)$$

with

$$f_n = 100, 100d, 100d^2, \ldots, 100d^{b-1} \text{ cps} ,$$

and

$$q = 1, 5, \text{ or } 10 .$$

The geometric progression of f_n with factor d was also selected to avoid coinciding with the set of peaks and valleys that occur in many spectra at uniform intervals of f_n.

In view of the many assumptions and approximations necessary to reach a numerical index of severity, the index should be used only to suggest $\ddot{Y}(t)$ curves that deserve further attention. These curves must be tested and examined to assure that they satisfy the thinking on which the index was based, nonmathematical

criteria must be added, and judgment and common sense must be applied to arrive at final recommendations. It is considered better to use approximations and judgment with a realistic model of the situation than to achieve mathematical precision through an over-simplified model.

CONSTANT-FORCE MOUNT

The mount which exerts a constant force from time 0 to T provides a valuable basis for comparison of other mounts. Figure 8 compares the constant-force mount (dotted) with another $\ddot{Y}(t)$ having the same deflection S. The shaded area is zero so the dotted curve must somewhere have higher slope (acceleration) than the constant-force line. It follows that any mount with the same deflection must have a higher peak acceleration than the constant-force mount. Furthermore, since any index of severity exceeds the peak acceleration, the constant-force acceleration is the lower bound of the index for all possible mounts.
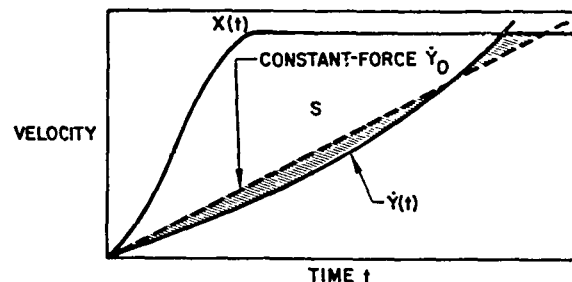
Fig. 8. Constant-force mount minimizes peak acceleration

The index of severity for a constant force F_o applied to a box of mass m is simply

$$I_o = \frac{F_o}{m} (1 + q) = a_o (1 + q) . \qquad (8)$$

Thus, limits on the index for any mount can be set by the step-force result. The index cannot be lower than a_o and need not be higher than I_o. Since the constant-force case is so easily calculated, it enables one to make quick analyses which are accurate enough for many purposes.

SOME BETTER MOUNTS

In seeking the optimum shape of $\ddot{Y}(t)$ curve, one is looking for an infinite number of points or parameters. This number could be cut down if

139

we expressed $\ddot{Y}(t)$ by a Fourier series and ignored frequencies above some limit, such as 1000 cps. This still leaves many more parameters than the two or three which would be suitable for computer optimization. So the approach used was to study some candidate $\ddot{Y}(t)$ curves by hand calculations as a guide to the selection of the $\ddot{Y}(t)$ curve, with two or three undefined parameters to be tried on the computer. Again, the result will be less than optimum, but we can use judgment to try again—unless comparison with the constant-force mount suggests that there would be little profit in going further.

The strong vibratory response of the constant force appears to be due to the step discontinuity at the beginning, which is a spike on a $\ddot{Y}(t)$ plot. Because of the resemblance of the integral of Eq. (2) to the Fourier coefficient, it appears that lower vibratory response would be obtained by making $\ddot{Y}(t)$ a smooth shape of some duration. This move, of course, increases the peak acceleration. So the problem is to find a shape which is the best compromise.

Three more shapes are shown in Fig. 9. Each has a time parameter, τ, which had to be selected to get the best index. To do this it was assumed that the input was a very short-duration acceleration pulse and caused a net velocity change of 10 fps and S was 1 in.

SHAPE	CURVE	NORMALIZED INDEX OF SEVERITY
CONSTANT FORCE		1.00+1.00q
LINEAR RAMP		1.16+0.19q
EXPONENTIAL RISE		1.12+0.13q
VERSED SINE		1.23+0.10q
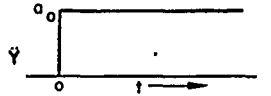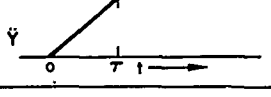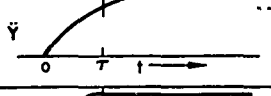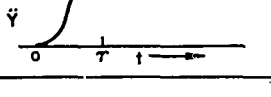
Fig. 9. Indices of severity for some acceleration-time shapes

The indices of severity were normalized by dividing by the constant-force value of a_o, which was simply $v^2/2S$. Thus, the linear ramp had a 16 percent higher peak acceleration than the constant force, but it produced only 19 percent of the vibration. The exponential rise was better

in both peak force and vibration, while the versed sine produced the least oscillation. The versed sine had the highest peak acceleration, apparently because it rose too slowly at the beginning.

COMPUTER OPTIMIZATION
  PROGRAM

On the basis of the preliminary studies, it appeared that some compromise between the exponential and versed-sine shapes might be best. The load-deflection curve of Fig. 10 was selected with the three parameters, P_1, P_2, and P_3. The curve is made up of two segments of parabolas and a straight line. The slope is zero at $Z = 0$, and from P_2 up, it has no discontinuities. Since P_1 and P_2 are not necessarily less than S, considerable variation of shape is possible, as shown in Fig. 11.
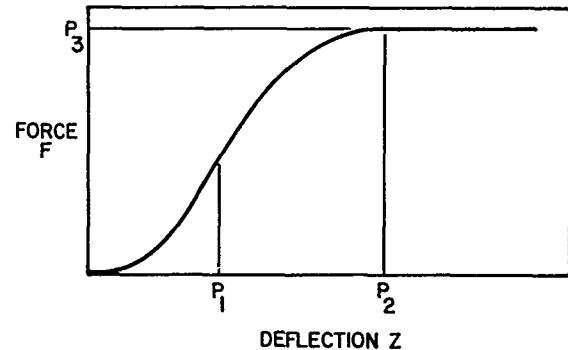
Fig. 10. Shape parameters of force-deflection curves
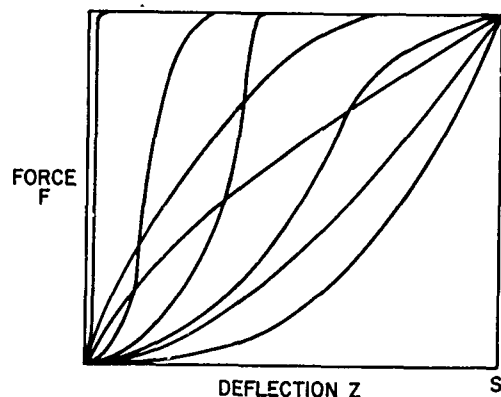
Fig. 11. Shapes permitted by parameters

A block diagram of the present computer program is shown in Fig. 12. Inputs for the program include:

140

INPUT DATA

Weight Factor
Range of Frequencies

Base Acceleration

Initial Shock Mount
Parameters

Allowable Deflection

OUTPUT DATA
Optimum Values of:

Shock Mount
Parameters

Shock Mount Force
Time Curve

Severity Spectrum
and Index

RESPONSE CALCULATION

Response Acceleration

SEVERITY SPECTRUM & SEVERITY INDEX

Shock Mount Deflection

Revised Shock Mount Parameters

OPTIMIZATION PROGRAM

Fig. 12. Flow diagram of computer optimization

1. The acceleration-time history of the base, $\ddot{X}(t)$;

2. The mount deflection, S;

3. The vibratory response tuning factor, q;

4. Vibratory damping factor, c/c_c; and

5. Natural frequencies and weighing factor for computing severity index, f_n and d.

The program operates by computing a severity index for an initial set of mount parameters. It then moves in a series of steps toward sets of parameters producing lower severity indices. When it can find no better set, it stops and the last set is the optimum.

To aid in understanding the result and to allow the study of sensitivity of the result, the program also prints out the severity spectrum for the optimum or any other mount characteristic of interest.

PRELIMINARY OPTIMIZATION
RESULTS

The computer program has not been in operation long enough to explore all of the possibilities of interest, but results have been obtained for some interesting cases. The first studies were of very short duration pulses so that only the resulting change in velocity, $v = \ddot{X}(t)$, was significant. This step-velocity change is the most important shock input, and

it will be shown later that the results can apply to many longer duration pulse shapes.

By plotting points for dimensionless parameters, the number of computer runs can be minimized. The inputs to the computer are v, S, f, c/c_c, and the f_n's. The f_n's are defined by the lowest frequency f_1 and the geometric progression factor d. Outputs of interest include the optimum parameters P_1, P_2 and P_3, the index of severity $I(q)$, and the shock severity spectrum $I(f_n,q)$. Results will be given in terms of the dimensionless parameters P_1/S, P_2/S, $P_3 2S/v^2$, $I 2S/v^2$, $4f_n S/v$, q, d, and c/c_c.

The combinations $v^2/2S$ and $v/2S$ were chosen because they are, respectively, the acceleration and the time T_o for a constant-force mount. Thus $I 2S/v^2$ will be between 1 and $1+q$, as was shown earlier. The range of the frequency parameter $4f_1 S/v$ is limited at present to values somewhat above 1 so that the vibratory response at the lowest frequency f_1 will reach a peak prior to T_o. This limitation also insures that mode deflections will be small compared to mount deflections.

Figure 13 shows the input conditions, optimum parameters and indices for the velocity-change shocks studied to date. The trend is toward a higher severity parameter (I/a_o) with lower frequency parameters; this was to be expected. But the shape parameters $(P_2/S$ and $P_3/a_o)$ reached a maximum in the middle of the frequency range. It is easy to see that large frequency parameters should have a near-constant force as optimum. Only a small ramp

141
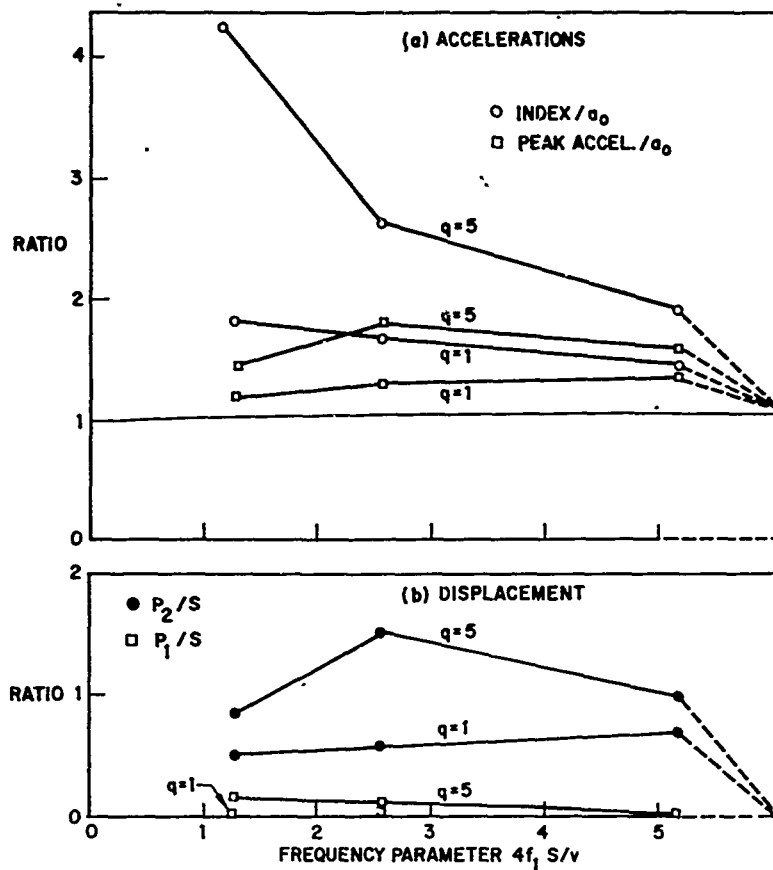
Fig. 13. Optimum indices and peak accelerations

(P_2/S) would be needed to avoid vibratory disturbance of the relatively high frequency modes. Hence, the index approaches 1 as $4f_1 S/v$ approaches infinity. But as $4f_1 S/v$ gets smaller, the mount shape reaches a limit on the concession in peak acceleration that is worthwhile. For low values of $4f_1 S/v$ the shape again tends towards the constant force. Values for $4f_1 S/v$ less than 1 are not indicated because this would require definition of the mount characteristics beyond T.

For the "shock resonance" factor $q = 5$, the mount shape tends to avoid vibrations at the expense of peak acceleration; that is, P_2/S and P_3/a_0 are higher. P_1/S is greater than 0, unlike the $q = 1$ result.

SHOCK SEVERITY SPECTRA

Plots of shock severity spectra for the six velocity-change cases studied are shown in Fig. 14. These curves all show a rather simple trend with the magnitude of vibrations being relatively small at higher frequencies. The index is always lower than the low frequency end of the spectrum and higher at the other end. The correctness of this depends on how the

probability of causing a failure varies with amplitude and frequency of the spectrum. Since data for the probability distribution will be very hard to gather, a more promising approach is to study the sensitivity of the optimum to error in probabilities. This is planned for the near future.

SENSITIVITY OF OPTIMA
TO ASSUMPTIONS

Preliminary indications are that the severity index is not very sensitive to the shape factors or the assumption as to q, the tuning factor. As the computer moved toward the optimum shape, the index did not vary much for quite large ranges of P_2 and P_3.

Furthermore, the optimum shape for $q = 5$ was almost as good as the optimum for $q = 1$, if q were actually 1. The reverse was also true. Hence, errors in q had little effect on the index in the range $q = 1$ to 5. Although the index did not vary much, the shape did, suggesting that the index is not sensitive to details of shape.

The difference between the indices obtained and the lower limit a_0 suggests that it

142
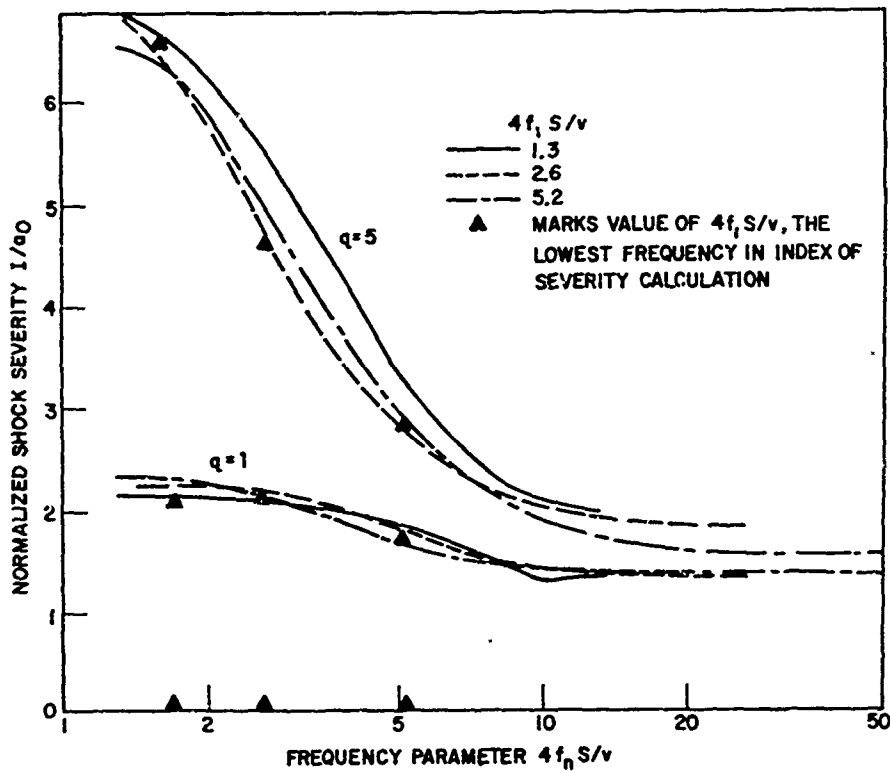
Fig. 14. Shock severity spectra of optimum mounts

would seldom be worthwhile to tailor a mount exactly to suit a given box.

OTHER INPUT PULSE SHAPES

The results for velocity-step shocks can be extended to a large class of acceleration pulses without using the optimization program. The base motion $\dot{X}$ in Fig. 3 has reached a constant value, v, prior to the maximum mount deflection, S, occurring at T. The box motion $\dot{Y}$ would have produced a mount deflection of $(S + S_o)$ if the input had been a velocity step v. It is not difficult to prove that if $\dot{Y}$ is the optimum box motion for the velocity step v and displacement $(S + S_o)$, it is also optimum for $\dot{X}$ and S.

Suppose the optimum $\dot{Y}$ for v and $(S + S_o)$ were used as the first trial solution to the computer for the inputs $\dot{X}(t)$ and S. The computer would try alternative curves near $\dot{Y}$ and find that they had higher indices—because the same alternatives were tried and found higher in the original optimization. Thus, if $\dot{X}$ is not so oddly shaped as to allow two optima, y is optimum for $\dot{X}$. It is required that $\ddot{X}$ be zero in the neighborhood of T.

To find a load-deflection curve of the optimum mount, one must compute, $Z(t) = (X - Y)$ and plot it against simultaneous values of $\ddot{Y}$.

It is evident that a velocity step is the most severe shape of input motion. More gradual velocity changes, in effect, allow the mount a "free" increase in deflection, S_o. This, of course, allows a reduction in severity index.

LONG-DURATION INPUT PULSES

For acceleration pulses which have not reached zero by the time of peak mount deflection T, the above theorem does not apply. The theorem can be modified to say that a $\dot{Y}$ will be an optimum for all input $\dot{X}$ curves having the same slope at T and appropriate deflection. But to be useful, optimum solutions would be needed for a variety of slopes.

For the present, it seems more practical to perform the computer optimization for each (long-duration) input pulse of interest. This has been done for a half-sine shape and an exponential decay pulse.

143

OPTIMIZATION FOR OTHER REQUIREMENTS

The cases studied thus far are only a beginning of those which are of practical interest. No change would be needed to consider other acceleration pulse shapes; the step acceleration would be of general interest. Definition of the mount force after time τ would be needed to consider lower natural frequencies.

The given deflection condition could be replaced by a more sophisticated weight-cost-penalty criterion related to a system's effectiveness trade-offs.

Finally, consideration could be given to including some modeling of human comfort or injury criteria in a severity index.

REFERENCES

1. J. P. Walsh and R. E. Blake, Mechanical Engineering, 77:3, March 1955

2. "Hardening Technology Studies Report (U)," LMSC B130200, Vol. IV (SRD), 30 Sept. 1965

3. R. A. Eubanks, Shock and Vibration Bulletin, No. 34, Part 3 (Dept. of Defense) Dec 1964, p. 157

4. J. W. S. Rayleigh, The Theory of Sound, 2nd Ed. (Dover, New York), 1945

5. J. J. O'Hara and P. J. Cunniff, "Elements of Normal Mode Theory," NRL Report 6002, Nov. 15, 1963

6. A. B. Burns, "Guide for the Selection and Application of Shock Mounts for Shipboard Equipment," American Machine and Foundry Co. Greenwich, Conn., 1961

7. L. A. Schmidt, Jr., and R. L. Fox, "Synthesis of a Simple Shock Isolator," NASA CR-55, June 1964

8. R. E. Blake and T. R. Ringstrom, Shock and Vibration Bulletin, No. 28, Part IV (Dept. of Defense), Aug. 1950, p. 15

Appendix

NORMAL MODE-THEORY OF STRUCTURAL RESPONSE

Since mathematical derivations of the normal-mode theory are given in several texts, they are not repeated here. The required assumptions are stated, and the usual results of the theory are given. Various terms in the equation are explained and examined. It is shown that the expressions for stress, strain, deflection, and acceleration are all of the form given by Eq. (2).

The theory concerns the response of any shape of linear elastic structure to any disturbance whose variation with time is given. The structure has distributed mass, damping, and elastic (spring) elements. The system of elastic elements could be described by stating the stiffness of all the springs or by a set of influence coefficients, but deflections must be small enough that this description is sufficient. Damping is viscous and must be distributed in the same manner in a fixed ratio to the spring

system or the mass system. There are no limitations to the distribution of exciting forces over the structure, their direction, or their manner of variation with time. Excitation by arbitrary motions, which any parts of the structure must follow are also included. Of course, there are practical limits to the degree of complexity of a situation which can be handled, but they are not due to a limitation of theory.

The linearity of the system makes it possible to use the principle of superposition. The response of the structure resulting from application of a force at one point at one instant of time is independent of response to other forces; thus, one need only add (superpose) the effects of individual forces to obtain the total response. If $r_{ij}(t-\tau)$ is the response at time t at point i on the structure due to a unit force at point j which acted for the time interval τ to $\tau + d\tau$, then the response to many forces $F_k(\tau)$ is

$$r_i(t) = \sum_k \int_0^t F_k(\tau)\, r_{ik}(t-\tau)d\tau . \quad (A-1)$$

The response usually derived is the deflection, the distance that the point on the structure has moved from the point it would have occupied if no forces had been applied. A complete description of the deflection of all mass points on the structure requires the statement of as many numbers as the system has degrees of freedom ν. All real structures have distributed mass and thus $\nu = \infty$. For analysis, structures are often represented by point masses, each able to move in three dimensions. The number of degrees of freedom is then three times the number of masses, and there will be ν values of i in Eq. (A-1).

It has been found that a structure will vibrate after all disturbing forces are removed in certain special patterns called normal modes and at certain frequencies called natural frequencies. Any arbitrary deflection of the structure can be represented as the sum of normal modes of suitable amplitude—in close analogy to the representation of any arbitrary function by a Fourier series. The advantage is the same; a satisfactory approximation can be obtained in fewer terms than the number of degrees of freedom. Thus, we have said that if ϕ_{in} defines the shape of the nth normal mode, the most general motion possible in the absence of disturbances is

$$r_i(t) = \sum_n A_n \phi_{in}\, e^{-c/c_c\, 2\pi f_n t} \sin(2\pi f_n t + \theta).$$

The A_n's may have any value; in fact, all A_n's may be zero except one and the structure will vibrate at a single frequency. Methods of computing mode shapes ϕ_{in} and their corresponding natural frequencies f_n are given in the references.

The solution for $r_{ij}(t-\tau)$, the so-called indicial admittance, following an impulsive disturbance, turns out to be (for small damping)

$$r_{ij}(t-\tau) = \sum_n \frac{\phi_{jn}\phi_{in}}{2\pi f_n \sum_\ell M_\ell \phi_{\ell n}^2}\, e^{-c/c_c\, 2\pi f_n(t-\tau)}$$
$$\times \sin 2\pi f_n(t-\tau), \quad (A-2)$$

where M_ℓ is the mass associated with the deflection $\phi_{\ell n}$; therefore,

$$r_i(t) = \sum_{n,k} \left[\frac{\phi_{kn}\phi_{in}}{\Sigma M_\ell \phi_{\ell n}^2}\right] \frac{1}{2\pi f_n} \int_0^t F_k(\tau)\, e^{-c/c_c\, 2\pi f_n(t-\tau)}$$

$$\times \sin 2\pi f_n(t-\tau)d\tau. \quad (A-3)$$

The corresponding equation for disturbing motions is omitted, since it is not needed for this report.

Damage is not associated directly with deflection, but it may be due to excessive strain or relative motion between two parts, that is, with $[r_i(t) - r_j(t)]$. When Eq. (A-1) is used to find this expression, the result is similar to Eq. (A-3) except that ϕ_{in} is replaced by $[\phi_{in} - \phi_{jn}]$ and, of course, $r_i(t)$ is replaced by $[r_i(t) - r_j(t)]$. Since stress and internal forces are proportional to strain and relative deflection, a similar result is obtained for them.

Forces can also be calculated from the accelerations of masses. The expression for acceleration is the same as Eq. (A-3) except that $2\pi f_n$ is in the numerator.

The integral of Eq. (A-3) can be expressed in two parts:

$$\frac{1}{2\pi f_n} \int F_k(\tau)\, e^{-c/c_c\, 2\pi f_n(t-\tau)} \sin 2\pi f_n(t-\tau)d\tau$$

$$= \frac{F_k(t)}{(2\pi f_n)^2} - \frac{1}{(2\pi f_n)^2}\int_0^t \left(\frac{dF_k}{d\tau}\right) e^{-c/c_c\, 2\pi f_n(t-\tau)}$$

$$\times \cos 2\pi f_n(t-\tau)d\tau. \quad (A-4)$$

Letting

$$\left[\frac{\phi_{kn}\phi_{in}}{(2\pi f_n)^2\, \Sigma M_\ell \phi_{\ell n}^2}\right] \equiv R_{kin}, \quad (A-5)$$

and

$$\int \left(\frac{dF_k}{d\tau}\right) e^{-c/c_c\, 2\pi f_n(t-\tau)} \cos 2\pi f_n(t-\tau)d\tau$$

$$\equiv V_n(f_n, t), \quad (A-6)$$

the form used in Eq. (2) is obtained.

145

DISCUSSION

Mr. Snyder (General Dynamics/Electric Boat): Are you planning to compare your analytical data eventually with experimental data, or have you done this in your efforts to determine the optimum design for a mount to put under some of your chassis, boxes, and so on?

Mr. Blake: Not in the immediate future. We would like to do that eventually when we have some ideas of what hardware would be best to use as a mount.

Mr. Snyder: Will these data eventually be available?

Mr. Blake: Yes, if we get the information I am sure it will be available. If it is done for the Air Force it will be in our reports to them, of course.

Mr. Johnson (K. W. Johnson & Co.): Are your data based on a single force deflection curve of a single pad, cushion or resilient element?

Mr. Blake: Yes, in this case the problem was in one dimension. There is one shock mount and all parts move in one dimension.

Mr. Johnson: Does your method apply to mounts presently being developed with some medium for a low-frequency vibration mount, then leading into a stiffer system for shock cushioning? Will your method apply to this type of mount?

Mr. Blake: You mean could we put in series, for example, a soft element then a stiff element?

Mr. Johnson: Yes.

Mr. Blake: At this point, we do not care how one achieves the force time history that we find to be optimum.

*   *   *

SHOCK ATTENUATION USING PASSIVE ELEMENTS

V. H. Neubert and D. L. Pyke
Pennsylvania State University
University Park, Pennsylvania
and
D. F. Poeth
HRB-Singer Corporation
State College, Pennsylvania

In ships or other vehicles, it may be desirable to add mass or passive dynamic absorbers to protect mounted equipment from shock inputs. Also, the equipment itself will act as a dynamic absorber with respect to motion of its base, as is known from the shock spectral dip phenomena. Studies were carried out to investigate the magnitude of the effect of using masses, compared with masses on springs, as passive absorbers. Also, a nonlinear absorber was studied where the mass was supported by a bolt with relatively low preloads so that separation of the mass from the base could easily occur in one direction only.

Response of a thin free-free bar of circular cross-section is compared with that of the same bar with masses or mass and spring combinations attached at the end opposite the struck end. Masses alone may be quite effective in reducing amplitude of motion at the attachment point, but amplitude at other points may be increased. Using the same mass on a spring as a passive dynamic absorber may be more or less effective than using the mass by itself, depending on the spectrum of the input pulse and the effect of the absorber on the system mobility.

For the second system, a disc was attached to a short, thick steel cylinder using a single preloaded bolt, simulating in ships the use of holddown bolts to attach equipment bedplates to foundations. By measuring bolt strain and base acceleration a fairly clear physical picture of the motion occurring was obtained. While the disc is in contact with the base cylinder it has the ability to act as a high-frequency dynamic absorber. During separation or partial separation, it suddenly becomes a low-frequency system consisting of a mass supported primarily by a bolt. The usual shock spectrum of base motion indicated some absorber-type action at low frequencies. A special shock spectrum, calculated from base accelerations during intervals of separation compared with a spectrum from accelerations during contact, indicated to some extent the directional variation of the base motion.

INTRODUCTION

The attenuating effect of passive dynamic absorbers in systems experiencing steady sinusoidal vibrations has been thoroughly discussed in the literature. Den Hartog (1,2) presented the classic case of an absorber attached to a base mass and spring system. Neubert (3) considered a uniform bar having one or two absorbers tuned to attenuate steady vibrations. Optimum tuning and optimum damping on displacement and velocity or mobility curves was emphasized. It was also demonstrated that in some cases, use of mass only may be more desirable than adding both a mass and spring to form a dynamic absorber.

In this paper, examples are presented to demonstrate the effect of adding masses or dynamic absorbers to attenuate transient vibrations.

Two different systems were used in the experiments. One was essentially a one-dimensional bar, 30 in. long by 3/8 in. in diameter, to which either masses or mass and spring combinations were attached as shown in Fig. 1. The other system is called a cylinder

147

and was 13 7/16 in. long by 6 in. in diameter. A mass was attached to the cylinder by a single preloaded bolt as shown in the bottom of Fig. 1. The transient force was applied by using strikers as indicated by the dotted lines. The effect of the addition of passive elements on maximum displacements at the point of attachment of the elements is discussed.
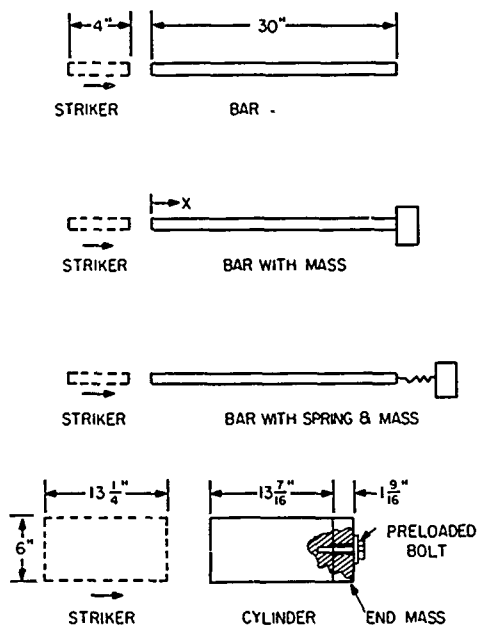
Fig. 1. Systems studied

Primarily, experimental results are presented for the cylinder, which is much more complex than the bar. For the bar, both experimental and analytical results were obtained and agreement between the predicted and measured values was excellent (4).

THEORETICAL BACKGROUND FOR MOBILITY OF THIN BARS

To introduce notation, some of the theoretical relationships for the thin bar is first reviewed. To predict the transient response of the thin bar with end attachments, the one-dimensional wave equation may be applied. Two types of solutions are discussed: one based on the use of normal modes of free vibration, and the other based on the use of appropriate mobilities and the Fourier transform relationship between mobility and transient response. Each method has some advantage in helping to visualize the physical behavior and both approaches are outlined briefly.

For the thin bar, u is the particle displacement and x is the position along the bar measured from the struck end. If E is Young's modulus, ρ the mass density and $a^2 = E/\rho$, the wave equation in one dimension is

$$a^2 \frac{\partial^2 u}{\partial x^2} = \frac{\partial^2 u}{\partial t^2} .$$ (1)

To investigate mobility, the form of the solution for steady sinusoidal vibrations is

$$u(x,t) = \left(B \cos \frac{\omega x}{a} + C \sin \frac{\omega x}{a} \right) e^{j \omega t} .$$ (2)

Here B and C are constants determined from boundary conditions. If the area of the free-free bar is A and the force $f e^{j \omega t}$ is applied at $x = 0$, the boundary conditions are

$$AE \frac{\partial u}{\partial x} (0,t) = -f e^{j \omega t}$$

and (3)

$$AE \frac{\partial u}{\partial x} (\ell,t) = 0 .$$

Evaluating the constants B and C in Eq. (2) based on Eq. (3) and differentiating with respect to time, we obtain the particle velocity

$$\dot{u}(x,t) = - \frac{j f e^{j \omega t}}{A \rho a} \left[\frac{\cos \frac{\omega}{a} (\ell - x)}{\sin \frac{\omega \ell}{a}} \right] .$$ (4)

Mobility M_{ij} is defined as the velocity at i due to a force at j. If position 1 is defined to be at $x = 0$ and position 2 at $x = \ell$, then

$$M'_{11} = \frac{\dot{u}(0,t)}{f e^{j \omega t}}$$

and (5)

$$M'_{21} = \frac{\dot{u}(\ell,t)}{f e^{j \omega t}} .$$

Primes are added here to distinguish from mobilities of combined systems.

Then from Eq. (4), using $\omega \ell / a = p$,

$$M'_{11} = - \frac{j}{A \rho a} \frac{\cos p}{\sin p}$$ (6)

and

$$M'_{21} = - \frac{j}{A \rho a} \frac{1}{\sin p} .$$ (7)

148

The M'_{11} and M'_{21} are shown by dotted lines in Figs. 2 and 3.

If the bar has a dynamic absorber attached at position 2, the mobilities of the combination are

$$M_{11} = M'_{11} - \frac{(M'_{21})^2}{M'_{22} + M'_{33}} \qquad (8)$$

and

$$M_{21} = M'_{21} - \frac{M'_{22} M'_{21}}{M'_{22} + M'_{33}} . \qquad (9)$$

The mobility M'_{33} is the mobility of the dynamic absorber driven at the base of the spring or, if k is the stiffness of the absorber spring and m the absorber mass,

$$M'_{33} = \frac{-\frac{jk}{\omega} + j\omega m}{-\frac{jk}{\omega} j\omega m} \qquad (10)$$

or

$$M'_{33} = -\frac{j}{A\rho a} \frac{1 - \frac{p^2}{p_n^2}}{\beta p} . \qquad (11)$$

Here $\beta = m/A\rho\ell$ is the ratio of the absorber mass to total bar mass and $p_n = \omega_n \ell/a$ is a
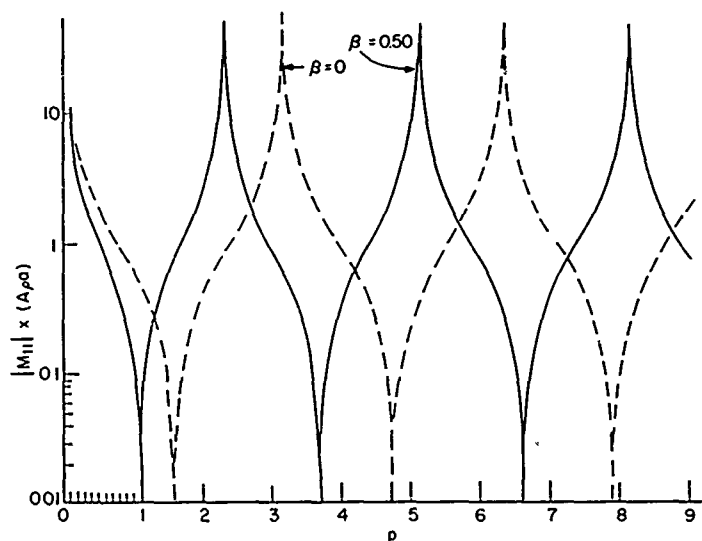
(a)
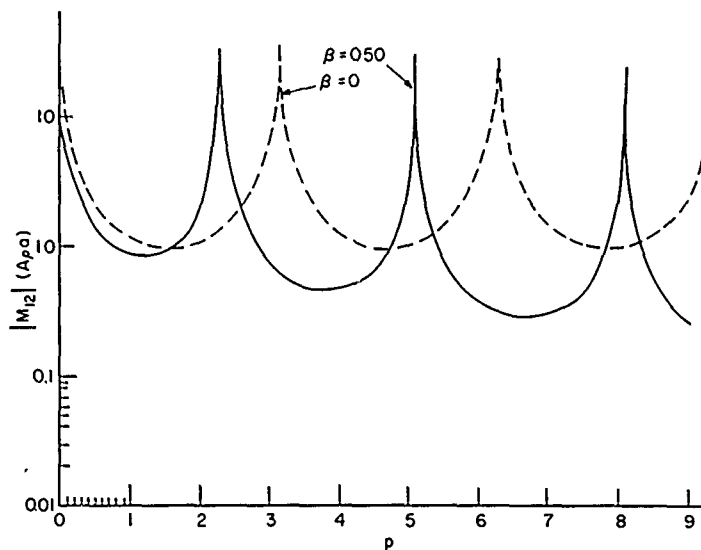
(b)

Fig. 2. Point and transfer mobility for free-free bar ($\beta = 0$) and bar with concentrated mass at $x = \ell$ ($\beta = 0.50$)

149
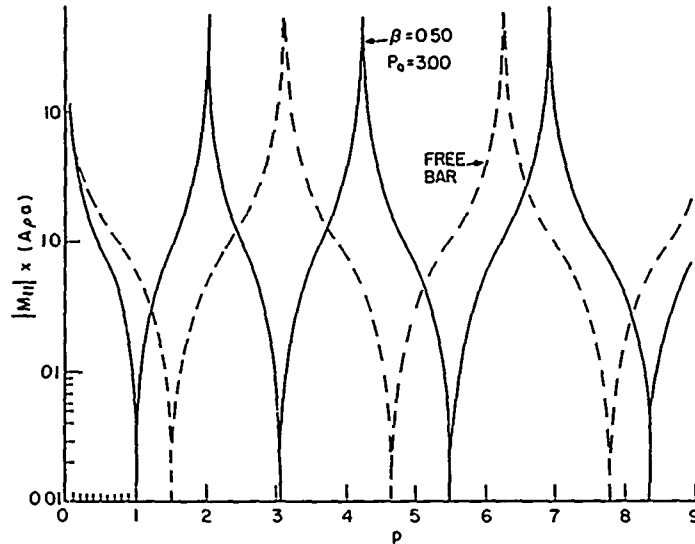
(a)
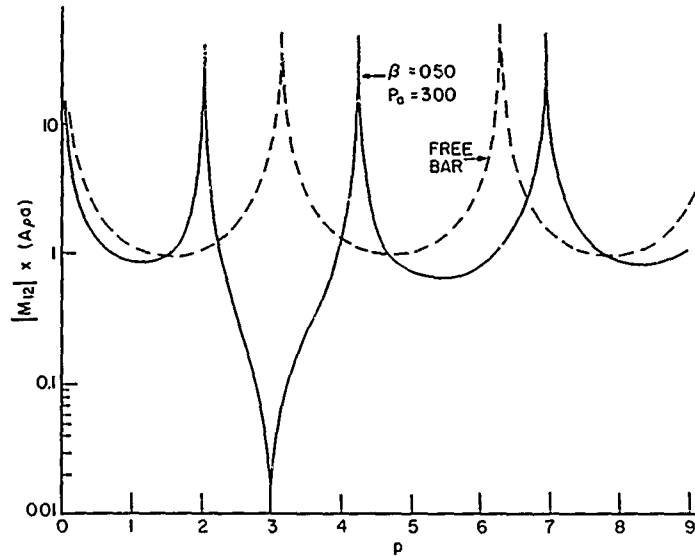
(b)

Fig. 3. Point and transfer mobility for free-free bar ($\beta = 0$) and bar with dynamic absorber at $x = \ell$ ($\beta = 0.50$)

nondimensional natural frequency. From Eqs. (6) and (7) it is obvious that resonances occur at $p = p_n = n\pi$ or $\omega_n = n\pi a/\ell$ for the free-free bar.

For the combination indicated by Eq. (8) or (9), the resonances will occur at $M_{22}' + M_{33}' = 0$. Since $M_{22}' = M_{11}'$, the frequency Eq. (12) is obtained by adding Eqs. (6) and (11) and cancelling some constants:

$$\tan p = \frac{\beta p}{\dfrac{p^2}{p_n^2} - 1} . \tag{12}$$

If the absorber spring is very stiff, $p_n \to \infty$ and the resulting frequency equation is, for the bar with a rigid mass attached at $x = \ell$,

$$\tan p = -\beta p . \tag{13}$$

If the end mass is zero, $\beta = 0$ and the frequency equation for the free-free bar is

$$\sin p = 0 . \tag{14}$$

If the mobility is known, the transient response may be obtained from

150

$$v_i(t) = \frac{1}{2\pi} \int_{-\infty}^{\infty} e^{j\omega t} M_{ij}(\omega) \, F_j(\omega) d\omega. \quad (15)$$

The numerical evaluation of Eq. (15) is possible. Here $F(\omega)$ is the Fourier transform of the actual forcing function.

The pressure pulse applied to the bar may be deduced from the strain record at $x = \ell/2$ in Fig. 4. The first negative pulse is assumed to represent the shape of the input pressure supplied by the impact of the striker bar. This pulse was used in a numerical analysis as transient input to the bar at $x = 0$ with the dotted line in Fig. 4 showing the resulting predicted strain at $x = \ell/2$. The case shown in Fig. 4 is for $\beta = 0.62$ and $p_a = (k/m)^{1/2} \ell/a = 1.575$ where p_a is the nondimensional natural frequency of the absorber.
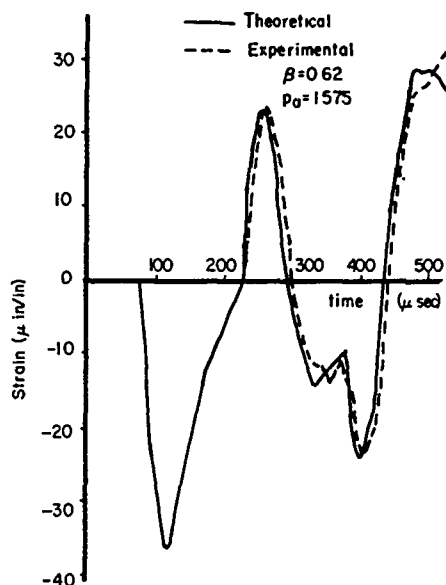
Fig. 4. Strain vs time at $x = \ell/2$ for bar with dynamic absorber at $x = \ell$ ($\beta = 0.62$, $p_a = 1.575$)

The input force is not exactly a half-sine wave. If it were a half-sine wave of frequency ω_f, the Fourier transform $F_j(\omega)$ of the input would have a broad spectrum of input primarily from $\omega = 0$ to $\omega = 3\omega_f$ (5). For a half-sine wave of 150 μsec duration, the first frequency cutoff would correspond to $p = 9$ for the bar studied.

In Fig. 2 the solid curves represent mobility of a bar with a mass rigidly attached at $x = \ell$ and $\beta = 0.50$. As expected, the resonant or natural frequencies are less than those for the free-free bar. The magnitude of transfer mobility is significantly decreased.

In Fig. 3 typical mobility curves are shown for a dynamic absorber attached at $x = \ell$. Here $\beta = 0.50$ and $p_a = 3.00$ is the nondimensional natural frequency of the absorber. The point mobility curve shows the usual attenuation range near $p = 3.00$, with an additional resonance appearing. Again the transfer mobility shows a decrease in amplitude.

Although Eq. (12) indicates that knowledge of $M_{ij}(\omega)$ and $F_j(\omega)$ will aid in anticipating transient response, it is also helpful to investigate the normal mode solution.

NORMAL MODE SOLUTION

The normal mode solution for a bar free at $x = 0$ and having attachments at $x = \ell$ is of the form

$$u(x,t) = \sum_{n=0}^{\infty} \cos \frac{\omega_n x}{a} q_n(t)$$

$$= \sum_{n=0}^{\infty} \cos \frac{p_n x}{\ell} q_n(t). \quad (16)$$

The p_n are the natural frequencies determined for various cases from Eqs. (12), (13) or (14). The mode shape is $\cos(p_n x/\ell)$ for each case.

If the kinetic and potential energies are written for the various cases in terms of the q coordinates and Lagrange's equations are used, then the decoupled equations will be

$$M_n \ddot{q}_n + M_n \omega_n^2 q_n = Q_n \qquad n > 0$$
$$M_o \ddot{q}_o = Q_o \qquad n = 0. \quad (17)$$

For all cases, for a force $F(t)$ acting at $x = 0$,

$$Q_n = F(t).$$

For the general case (4) of a bar of mass $m_b = A\rho\ell$, with an absorber at $x = \ell$,

$$M_n = \frac{m_b}{2} + \frac{m}{2} \frac{k(k + \omega_n^2 m)}{(k - \omega_n^2 m)^2} \cos^2 \frac{\omega_n \ell}{a} \qquad n > 0. \quad (18)$$

If k is very large, M_n for a bar with an end mass only is

$$M_n = \frac{m_b}{2} + \frac{m}{2} \cos^2 \frac{\omega_n \ell}{a} \qquad n > 0 . \qquad (19)$$

Also, if $m = 0$, the value for a free-free bar is

$$M_n = \frac{m_b}{2} \qquad n > 0 . \qquad (20)$$

For $n = 0$, for all cases, $M_o = m_b + m$ and $p_n = 0$.

A general form of Eq. (17) is

$$M_n \ddot{q}_n + M_n \omega_n^2 q_n = F(t) \quad n > 0. \qquad (21)$$

If $F(t)$ were a steady sinusoidal force $F(t) = f e^{j\omega t}$ the response is obtained by substituting the solution of Eq. (21) into Eq. (16) or

$$u(x, t) = \sum_{n=1}^{\infty} \cos \frac{p_n x}{\ell} \frac{f e^{j\omega t}}{M_n(\omega_n^2 - \omega^2)}$$

$$- \frac{f e^{j\omega t}}{(m_b + m) \omega^2} . \qquad (22)$$

If $F(t)$ is a half-sine wave,

$$\begin{cases} F(t) = f_f \sin \omega_f(t) & 0 \le t \le \frac{\pi}{\omega_f} \\ \\ F(t) = 0 & t \ge \frac{\pi}{\omega_f} . \end{cases}$$

In this case, the solution for elastic displacements is

$$u(x, t) = \sum_{n=1}^{\infty} \frac{f_f}{M_n(\omega_n^2 - \omega_f^2)} \left(\cos \frac{p_n x}{\ell} \right)$$

$$\times \left(\sin \omega_f t - \frac{\omega_f}{\omega_n} \sin \omega_n t \right) \quad 0 \le t \le \frac{\pi}{\omega_f} \quad (23)$$

and

$$u(x, t) = \sum_{n=1}^{\infty} \frac{f_f}{M_n(\omega_n^2 - \omega_f^2)} \left(\cos \frac{p_n x}{\ell} \right)$$

$$\times \left[\left(-\frac{\omega_f}{\omega_n} \sin \frac{\pi \omega_n}{\omega_f} \right) \sin \omega_n \left(t - \frac{\pi}{\omega_f} \right) \right.$$

$$\left. - \left(1 + \cos \frac{\pi \omega_n}{\omega_f} \right) \cos \omega_n \left(t - \frac{\pi}{\omega_f} \right) \right] \quad t \ge \frac{\pi}{\omega_f}. \quad (24)$$

The actual prediction of response for the cases presented was carried out using a normal mode analysis. For the greatest possible accuracy, the input force-time curve was approximated by a series of step functions, and the response obtained as the total response to these step-function inputs. In this summation process much of the physical understanding of the problem is lost. On the other hand, the input may be approximated to some extent by a half-sine wave. Thus, Eqs. (23) and (24) at least show qualitatively the parameters involved. Obviously a modal effective mass term may be identified as

$$M_n \Big/ \left[\left(\cos \frac{p_n h}{\ell} \right) \left(\cos \frac{p_n x}{\ell} \right) \right]$$

where h is the position of the force and x the position at which displacement is measured. In this case $h = 0$ so the effective mass is

$$M_n \Big/ \cos \frac{p_n x}{\ell} .$$

The impedance curves and Eqs. (19) and (20) show that M_n decreases when the concentrated mass is added to the tip. The other important parameter is ω_f / ω_n. For a pulse of 150 μsec duration, $p_f = \omega_f \ell / a$ is about 3.14. A decrease in ω_n particularly for the first mode results in an increase in modal amplitude, even though M_n increases slightly.

TRANSIENT RESPONSE OF BAR WITH END ATTACHMENTS

From the preceding discussion it is obvious that the transient response may be predicted using calculated or measured mechanical mobility. This approach has been discussed in detail by Belsheim and Young (6). In the present example of a simple bar, a traveling wave solution could also be obtained. A normal mode solution was actually used with ten modes summed to predict elastic displacement to within 1 percent and 100 modes summed to predict strain.

In Fig. 4, the calculated strain at $x = \ell/2$ is compared with the measured strain. The applied pressure pulse applied at $x = 0$ was assumed to be the same shape as the first negative strain pulse which appears on Fig. 4 beginning at 80 μsec and ending at 230 μsec. The magnitude of the applied pressure pulse was taken as Young's modulus E times the strain magnitude of the first pulse. The comparison of measured and calculated strain in Fig. 4 is typical of many presented in Ref. (4), confirming the validity of the analytical approach used.

For this study, the maximum elastic displacements were calculated along the bar for various cases using the same input as in Fig. 4. Some results for maximum elastic displacement are shown in Fig. 5 for a mass rigidly attached to the bar at $x = \ell = 30$ in. The dotted line in Fig. 5 shows the maximum elastic displacements for a free-free bar where $\beta = 0$. These displacements generally do not occur at the same instant of time. Other values of β were considered as shown. Addition of concentrated mass causes considerable reduction in displacements at the attachment point. However, the amplitude at the drive point is increased. This may be anticipated to some extent by observing that

$$u(x,t) = \sum_{n=1}^{\infty} \cos \frac{p_n x}{\ell} q_n(t)$$

for the elastic modes. The modal amplitudes at $x = 0$ and $x = \ell$ will only be equal in magnitude when $p_n = n\pi$, or when the bar is free-free. Addition of mass causes the values of p_n to decrease, which causes nodal points to shift to the right on the bar.
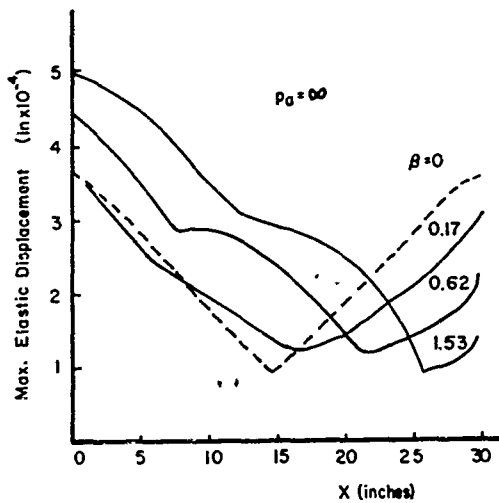
Fig. 5. Maximum elastic displacement for bar with concentrated mass at $x = \ell$ and various values of β

Results for a bar with a dynamic absorber at $x = \ell$ with frequency $p_a = 1.575$ are shown in Fig. 6. The same values of β were considered. Comparison of Fig. 6 with Fig. 5 indicates that addition of the absorber may or may not be more beneficial than using the mass by itself. This is confirmed in Fig. 7 where, for $\beta = 1.53$, maximum displacements are plotted for several values of p_a. With respect to attenuation at

$x = \ell$, the value of $p_a = 1.575$ is of particular interest because the first mode node is at $x = \ell$. Other cases would certainly be of interest in addition to those examples considered here.
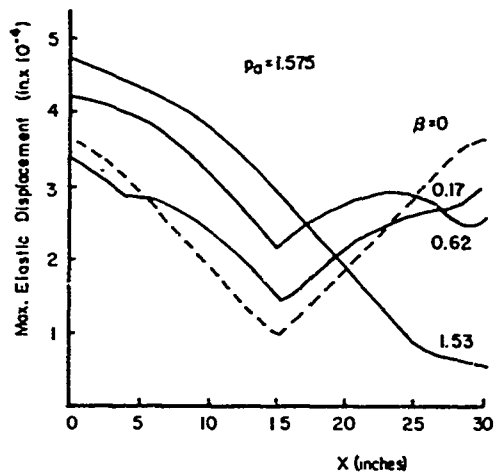
Fig. 6. Maximum elastic displacement for bar with dynamic absorber at $x = \ell$ and various values of β, with $p_a = 1.575$
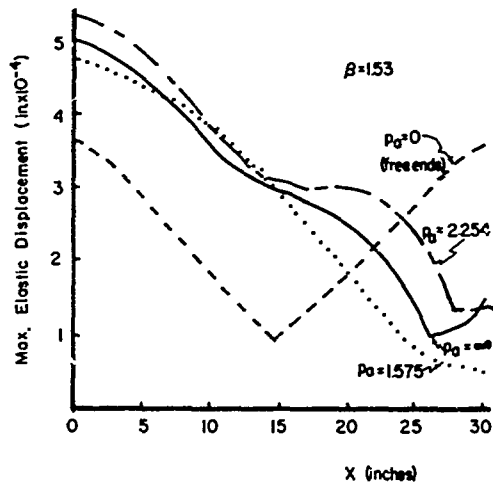
Fig. 7. Maximum elastic displacements for bar with dynamic absorber at $x = \ell$ and various values of p_a, with $\beta = 1.53$

CYLINDER WITH NONLINEAR ATTACHMENT

The cylinder having the end mass attached by a preloaded bolt is shown in Fig. 1. The gage length of the bolt was 1 1/8 in. on a section machined to a diameter equal to the root thread diameter of 0.185 in. The area of the bolt section was 0.0269 sq in. In the photograph (Fig. 8) strain in the bolt is recorded as the

153

lower trace in each pair of traces. The upper trace is the record of acceleration near a point on the axis of the cylinder at which the bolt was attached. The accelerometer was mounted in a small recessed hole. Details of instrumentation are given in Ref. 7 or 8.
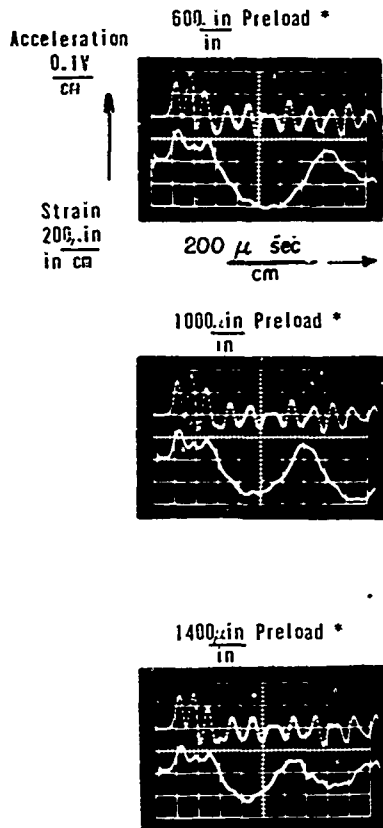
Fig. 8. Oscilloscope records of base acceleration and bolt strain vs time for various initial bolt preloads

Preload strains in the bolt of 600, 1000 and 1400 μin./in. were used for the cases of Fig. 8. If $E = 10.1 \times 10^6$ psi, the preload stress for a strain of 1400 μin./in. on the bolt was about 14,000 psi or a total force of about 38 lb. The percent of contact of the end mass and the cylinder is not known, but if the contact area were 10 sq in., the pressure would have been only about 4 psi. Thus, the contact area could support practically no superimposed tensile strain and it might be assumed that separation of the end mass from the cylinder would occur at tensile strains greater than about 0.1 μin./in. In the cylinder the first strain pulse is compressive, but it is then reflected as a tensile pulse. Thus, it might be assumed that there is separation of the end mass from the cylinder each time the strain becomes negative. It is observed that the negative swings are nearly half-sine waves. As the preload is increased, the length of these half-sine waves decreases. This indicates that the separation may not be complete and the stiffness of the contact region is variable, rather than simply being equal to the bolt stiffness during separation.

For the present study, it is of particular interest to investigate the effect of motion of the end mass on the base motion. Base velocity (Fig. 9) was obtained by integrating the acceleration. The effect of preload, as shown in Fig. 9, is that higher preloads tend to result in decreased base velocity during the early time interval before the first apparent separation.

In Fig. 10, the shock spectra associated with base motion for two different preloads are shown. The higher amplitudes of Fig. 9 are associated with lower frequency components. The change in magnitude at about 800 cps indicates that some absorbed action is taking place.
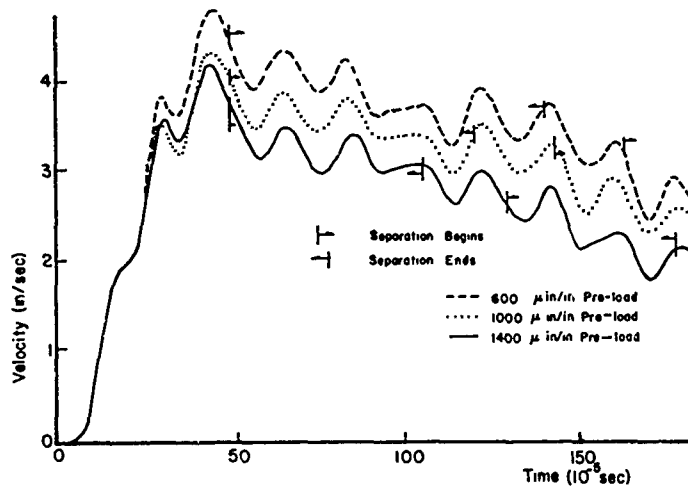
Fig. 9. Base velocity vs time for various bolt preloads

154
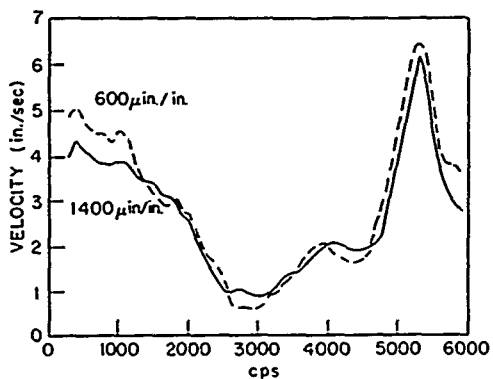
Fig. 10. Velocity spectrum for
two different bolt preloads

For the 600 μin./in. preload, the maximum
negative shock spectral velocities are compared
with maximum positive velocities in Fig. 11.
They are practically the same except at frequen-
cies near 3000 cps.

In Fig. 12, the initial shock spectrum is
compared with the residual spectrum. The
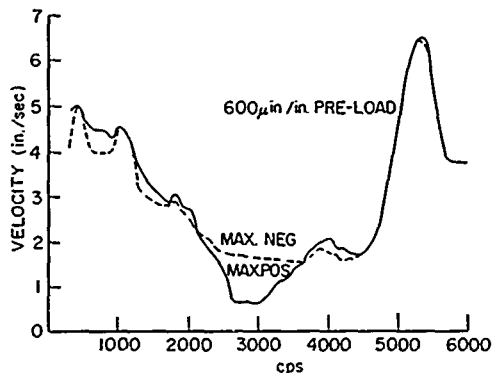
Fig. 11. Spectra of maximum nega-
tive and maximum positive velocities
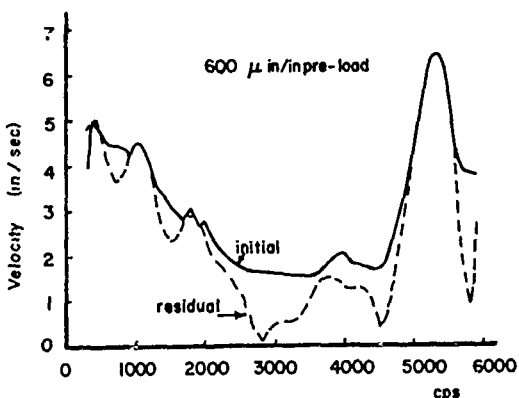
Fig. 12. Initial velocity spectrum
and residual spectrum

"residual" spectrum was obtained by assuming
for calculations that the base acceleration was
zero at the end of the oscilloscope records of
Fig. 8.

Finally, an effort was made to determine a
spectrum sensitive to the highly directive nature
of the system. This was done by calculating one
residual spectrum using as inputs the base ac-
celerations during intervals of contact. A sec-
ond residual spectrum was calculated using the
base accelerations occurring during intervals
of separation. This has some mathematical
justification for linear systems based on the
Duhamel integral. The resulting spectra are
shown in Fig. 13. It is interesting to note that
during contact the low frequencies dominate and
during separation the higher frequency compo-
nents contribute most to the spectrum.
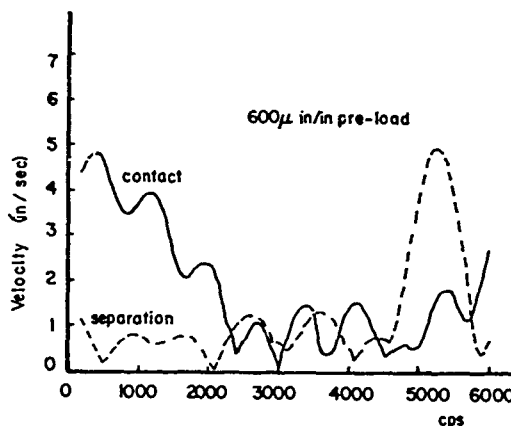
Fig. 13. Velocity spectrum calcu-
lated from base accelerations meas-
ured during contact and from base
accelerations measured during sep-
aration

The accelerometer outputs were filtered
using a low-pass filter with a cutoff of 8500
cps. Initially a 2000-cps filter was tried, but it
was found that this eliminated much of the es-
sential information regarding base acceleration.
In Ref. 8, emphasis is placed on relating bolt
strain to acceleration measured at the base and
on the end mass.

SUMMARY AND CONCLUSIONS

The results show that, for an input pulse
having a broad frequency spectrum, concen-
trated mass may be added to attenuate vibra-
tions at a certain point. The effect of mass has
been known and accounted for in many shock
spectra. The fact that using the same mass on

155

a dynamic absorber may be more or less useful than the mass by itself is of particular interest. Thus, a machine having a certain dominant frequency with respect to shock response may be protected by having a system nearby having a similar dominant frequency. This suggests also that consideration might be given to having items with similar fixed base resonances mounted in the same area in a vehicle.

No consideration has been given here to increase in stress due to hard spots created by adding structure locally. Of course, additional mass or dynamic absorbers could be distributed over an area rather than placing one large mass or absorber at a particular spot.

Knowledge of the effect of the addition of passive elements on the point or transfer mobility is sufficient to predict resulting transient response. Visual inspection of the change in the mobility curve is generally not sufficient to decide on an optimum frequency for an absorber, because $F(\omega)$, the Fourier transform of the transient input, and $e^{j\omega t}$ are also involved. Thus, each case must be calculated. However, even for complex elastic systems, calculation of transient response is readily performed using a digital computer.

The cylinder carrying the mass attached by a preloaded bolt simulates equipment bolted to a subbase. In the laboratory apparatus used, measurement of the dynamic strain in the bolt furnished the most useful information regarding behavior of the system during shock loading. Traces presented clearly indicate that the strain during separation has primarily a low-frequency content, and higher frequencies dominate during periods when the mass is in contact with the base. This was difficult to detect in the usual shock spectra calculated using the base acceleration as input. It did appear in shock spectra (Fig. 13) calculated by using base acceleration during contact as one input and base acceleration during separation as a separate input. The separation appears to have been only partial separation probably because of elastic deformation of the surface of the end mass which contacted the base cylinder.

No signals due to sharp impacts were noted in accelerometer or strain records. These might have been expected if the mass banged against the base. This may be another sign that separation did not occur instantaneously, but rather a more continuous reduction in the area of contact occurred.

The problem arises as to how acceleration data may be processed to detect that preloads have been exceeded during shock motions. If sharp separation occurs, the machine on the bolts as springs will represent a low-frequency system compared to the situation where the machine bedplate is in contact with the foundation. On a usual shock spectrum, a dip caused by the motion during the outswing may be cancelled by motion which occurs during contact. Due to the simplicity of the system used in the present studies, special shock spectra were calculated from base motion which emphasize the directivity of the base motion. As a general procedure, accelerations measured on the machine itself may be useful. Information regarding strains in bolts is probably the most essential in determining that the desired preload exists and in understanding response during shock motions.

ACKNOWLEDGMENT

REFERENCES

1. J. P. Den Hartog and J. Ormondroyd, Trans. ASME 50, 9 (1928)

2. J. P. Den Hartog, Mechanical Vibrations (McGraw-Hill, New York), 1954

3. V. H. Neubert, J. Acoust. Soc. Am. 36, 673 (1964)

4. D. L. Pyke, "Investigation of One-Dimensional Elastic Waves with Compound Reflection Conditions," Masters Thesis, Pennsylvania State University, Dept. of Engineering Mechanics, Sept. 1965

5. S. Rubin, "Concepts in Shock Data Analysis," in C. E. Crede Shock and Vibration Handbook, Vol. 2 (C. M. Harris and C. E. Crede, Ed.) (McGraw-Hill, New York), 1961

6. R. O. Belsheim and J. W. Young, Jr., "Mechanical Impedance as a Tool for Shock or Vibration Analysis," U.S. Naval Research Laboratory, NRL Rept 5409, Feb. 15, 1960

7. D. F. Poeth, "Response to Shock Loading of a Mass Supported by a Pre-Loaded Spring," Masters Thesis, Pennsylvania State

University, Dept. of Engineering Mechanics, March 1965

8. V. H. Neubert and D. F. Poeth, "Shock Response of a Pre-Loaded Connection," Office of Naval Research Contract No. Nonr-656 (28)(x), Interim Rept. No. 3, Feb. 1965

*　　*　　*

157

INVESTIGATION OF THE VIBRATION
DAMPING PROPERTIES OF VISCOELASTIC
MATERIALS USING A DELAY ANGLE TECHNIQUE

Saul A. Eller and Levi Cohen
U. S. Naval Applied Science Laboratory
Brooklyn, New York 11251

The vibration damping properties of 1/4-, 1/2-, and 2-in. thicknesses of ML-D2 and a urethane viscoelastic damping material were studied in the frequency range of 150 to 11,000 cps by disc and beam methods, which measured the rate of vibration decay in the steel substrates onto which the materials were adhered. Results were expressed in terms of percent of critical damping of the material. In addition, the materials were investigated by a novel delay angle technique which measured acceleration ratio, velocity of sound, and delay angle over a frequency range of 50 to 10,000 cps. High vibration damping occurred at those frequencies where there were resonances in the thickness-wise direction, as indicated by high acceleration ratio values, confirming the work done by another investigator in this field. The ML-D2 material had better vibration damping properties than the urethane material at frequencies above 1,300 cps, whereas the reverse was true at lower frequencies. Analysis of the data obtained by the delay angle technique indicated that a frequency is reached at which only those portions of the material which are in contact with, or adjacent to, the substrate are vibrating, and thus absorbing energy. This is one explanation why vibration damping at all frequencies is not proportional to the thickness of the material.

INTRODUCTION

The Navy has been conducting extensive research programs to reduce ship noise and to minimize its effects by the following methods: (a) elimination of the causes of vibration in ship's components, (b) isolation of sensitive equipment (e.g., sonar) from noise sources, and (c) absorption of vibrational energy by adhering energy-absorbing materials to bulkheads of compartments, particularly those in the vicinity of sonar equipment.

This paper concerns an investigation into the physical properties of viscoelastic materials used to absorb vibrational energy. The use of these materials has been so successful that more than 3 million square feet of ML-D2, a viscoelastic vibration damping material, have been installed to date by the Navy in the Fleet Rehabilitation and Modernization Program (1).

The use of viscoelastic materials for damping vibrations is understandable because, as noted by Ruzicka (2), these materials have a specific damping energy several hundred times that of typical structural materials.

Although satisfactory viscoelastic materials have been developed, there is comparatively little fundamental information regarding the manner in which viscoelastic materials absorb vibrational energy and the frequency range in which they exhibit optimum damping properties. Some investigators attribute vibration damping to tension and compression forces parallel to the surface of the material, whereas other investigators attribute damping to forces in the thickness-wise direction.

The effectiveness of damping materials can be indicated by percent c/c_c (percent of critical damping), the percentage of damping required for a nonoscillatory return to original conditions. This may be determined by either the disc or beam methods, described below.

Both of these methods have the disadvantage of requiring a new setup for each discrete frequency at which the damping of the material is

determined. In addition, the quantity of material and the time required are relatively high.

The delay angle technique to be described rates damping materials in terms of "acceleration ratio" (gain in acceleration in traversing through the material). At high acceleration ratios, the material is absorbing more energy and, therefore, is a better damping material. Only one small specimen of each thickness is required for the entire frequency range of interest.

VISCOELASTIC MATERIALS

The viscoelastic materials studied were ML-D2 and NASL-D101 urethane material which were developed and formulated by T. Ramos of the U. S. Naval Applied Science Laboratory. These materials can be cured at room temperature; their compositions are given in Table 1. Samples in thicknesses of 1/4, 1/2 and 1 in. were studied with the disc method and the delay angle technique, whereas only a 2-in. thickness of material was studied with the beam method.

VIBRATION DECAY MEASUREMENTS USING DISC AND BEAM METHODS

The disc method, described by Kallas and Rufolo (3), makes use of a coated steel disc suspended at its center. The disc is given a sharp impact and its vibration is measured

with an accelerometer. Damping is calculated in terms of the percent of critical damping of the system. When a mechanical system of mass m, damping c, and flexibility k is subjected to an impact force, the response y or a point on the mass at time t after the impacts is given by

$$m \frac{d^2y}{dt^2} + c \frac{dy}{dt} + ky = 0 . \tag{1}$$

The solution of this equation is given in the appendix for reference, and leads to

$$c = \frac{Dm}{4.34} , \tag{2}$$

where D is the decay rate in decibels per second, and to

$$c_c = 4\pi m f_o , \tag{3}$$

where

c_c = the minimum damping for nonoscillatory return (critical damping), and

$f_o = (1/2\pi) \sqrt{k/m}$ is the natural frequency.

Combining Eqs. (2) and (3), we get

$$\frac{c}{c_c} = \frac{Dm}{4.34} \times \frac{1}{4\pi m f_o} = 0.0183 \frac{D}{f_o}$$

or

TABLE 1
Composition of ML-D2 and NASL-D101 Urethane Vibration Damping Materials

Component	Function	Parts by Weight	Order of Mixing
(a) ML-D2 (sp gr = 0.73)			
Halowax 4004	Flame regardant	42	1
Epon 828	Co-reactant	20	2
Versamid 115	Co-reactant	100	3
DMP-30	Hardener	5	4
Antimony trioxide	Flame retardant	14	5
Aluminum oxide (80 mesh, loose grains)	Filler	400	6
(b) NASL-D101 (sp gr = 1.54)			
Chlorinated paraffin	Plasticizer and flame retardant	55	1
Polyol	Chain extender	25	2
Urethane prepolymer	Reactant	100	3
Ottawa River sand	Filler	80	4
Organotin	Catalyst	30	5

$$\% \frac{c}{c_c} = 1.83 \frac{D}{f_o} . \tag{4}$$

The method takes into consideration the inherent damping in the steel disc onto which the viscoelastic material is adhered by subtracting the vibration decay due to the steel disc from that of the composite system. Therefore, the

$$\% \frac{c}{c_c} \text{ (of the material)} = \frac{1.83}{f_o} (D_o - D_B), \tag{5}$$

where

D_o = damping rate of coated disc, db/sec;

D_B = damping rate of bare disc, db/sec; and

f_o = natural frequency, cps.

A more detailed development of the disc method is given by Timoshenko (4). Another analytical study of the vibrating disc which discusses the geometrical relationship to frequency response has been presented by House and Kritz (5).

Tests on each thickness of material were made on a series of 3/8-in. thick discs which measured 8, 6, 4, 3 1/2 and 3 in. in diameter and had bare disc natural frequencies of 1750, 3500, 7000, 9000, and 11,000 cps, respectively. The specimens covered only one face of the disc, as shown in the setup for this method (Fig. 1).

The beam method was similar to the disc method, except that a 45 1/2-in. by 3-in. piece of viscoelastic material was adhered to a steel beam, 47 in. long by 3 in. wide by 1 3/4 in. thick. The beam was suspended at its midpoint and driven by a small shaker to vibrate at a number of resonant frequencies. A view of the setup for the beam method is shown in Fig. 2. When resonance was attained, the shaker was shut off and the time rate of decay of the vibration of the beam was determined using electronic equipment and calculations similar to those used for the disc method.

APPARATUS USED FOR DELAY ANGLE TECHNIQUE

The delay angle technique was designed to determine the effect of thickness-wise (longitudinal) tension and compression forces on the damping properties of viscoelastic materials.

Figure 3 shows a specimen mounted on a specimen plate, with holder and accelerometers attached. Figure 4 is a view of the specimen mounted on an electrodynamic shaker, and Fig. 5 is a schematic of the apparatus. As shown

Fig. 1. Setup for disc method
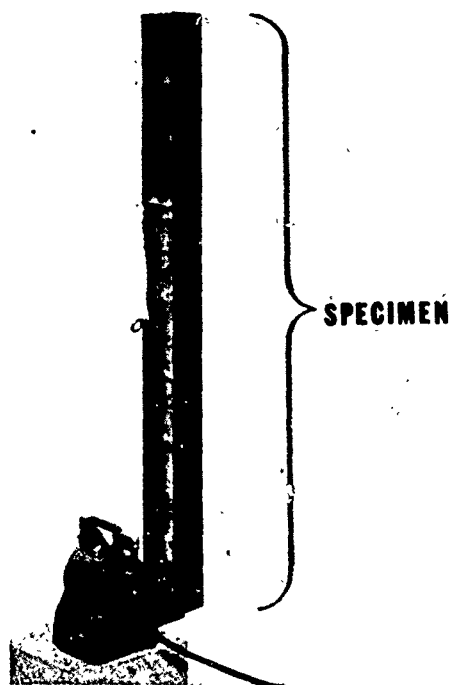
Fig. 2. Beam and shaker

161
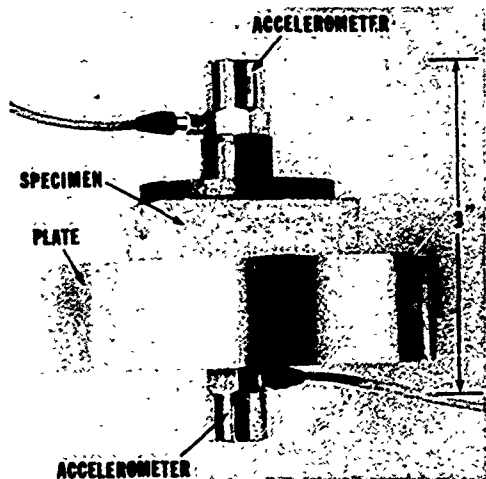
Fig. 3. Specimen assembled for
delay angle technique

Fig. 5. Schematic for delay
angle technique

Fig. 4. Specimen on
shaker for delay angle
technique

in Fig. 5, the specimen which measures 2 in. by
2 in. by the desired thickness is adhered with
an epoxy adhesive to the 1-in. thick 4-in. diam-
eter steel specimen plate bolted to the shaker.

An accelerometer holder is adhered with
epoxy adhesive to the upper surface of the
specimen, and the upper accelerometer is
bolted to the holder. The lower accelerometer
is bolted to the undersurface of the specimen
plate. Both accelerometers are on the center-
line of the apparatus. The upper accelerometer
thus measures motion of the specimen plate
after the motion traverses the specimen, where-
as the lower accelerometer measures motion of
the specimen plate directly.

The lower (or input) accelerometer is used
to maintain the shaker at a constant sinusoidal
acceleration level of 10 g over the frequency
range of 50 to 10,000 cps. The accelerometer
outputs are connected to a phase angle meter
which is used to measure the delay angle, or
time required, for a wave to traverse the speci-
men. Acceleration ratio is measured directly
on the true-rms voltmeter by scaling the upper
accelerometer output to 1.0 when the directly
measured gain is 1.0. This occurs at low fre-
quencies. In addition, the accelerometer out-
puts are connected to a dual beam oscilloscope
to permit comparison of the wave shapes and
their phase relationship in a Lissajous figure.

PROCEDURE USING DELAY
ANGLE TECHNIQUE

Initially, acceleration ratio and delay angle
were measured over the frequency range of 50
to 10,000 cps for a specimen consisting only of
a double layer of epoxy adhesive. The acceler-
ation ratio remained essentially 1.0 at all fre-
quencies for this specimen, and no corrections
were made in subsequent runs. However, there
was an appreciable error in delay angle, and
the values of delay angle obtained in this test
were subtracted from the values obtained with
the viscoelastic materials to correct for errors
introduced by instrumentation and epoxy adhes-
ive layers.

To reduce errors at high frequencies, where
the absolute amplitudes of vibration were in the

162
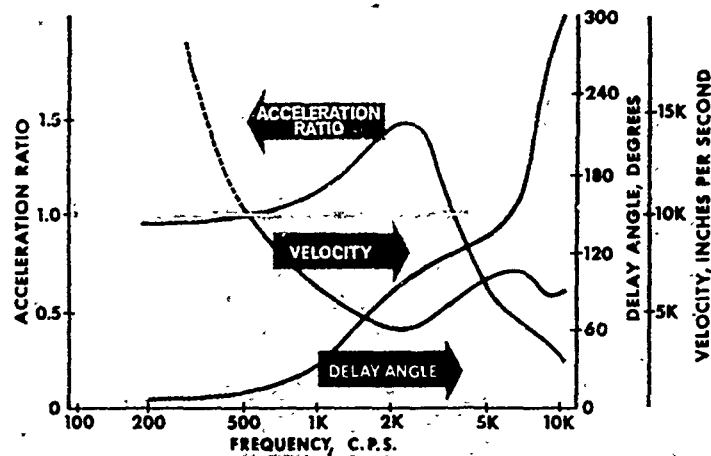
Fig. 6. Typical acceleration ratio, velocity and
delay angle in 1/2-in. thick ML-D2

order of microinches, the accelerometers were
mounted with a torque of 20 lb-in. on polished
and oiled surfaces.

Normally, readings of acceleration ratio
and delay angle were taken at 50, 100, 200, and
500 cps and thereafter at 500-cps increments
to 10,000 cps. Readings were also taken of
resonance frequencies and of frequencies at
which acceleration ratio passed through 1.0 or
the delay angle passed through multiples of 90
degrees.

RESULTS AND ANALYSIS

Typical results of acceleration ratio and
delay angle obtained on a viscoelastic material
are shown in Fig. 6. The acceleration ratio had
a value close to 1 at low frequencies, rose with
increase in frequency to a maximum at resonance,
and then fell off with further increase in frequency.
An acceleration ratio of 1 indicated that the mo-
tion of the specimen plate was transmitted through
the specimen without amplification or reduction.
An acceleration.ratio greater than 1 indicated
amplification of motion and, hence, resonance
in the specimen; a ratio less than 1 indicated
that the upper portions of the specimen were
vibrating at an amplitude less than that of the
plate. (In sinusoidal vibration, displacement
ratio equals acceleration ratio.)

The delay angle was zero at low frequency,
increased rapidly to reach 90 degrees at close
to the resonance frequency, and then continued
to rise with further increase in frequency.

The velocity of the vibratory wave through
the material is also shown in Fig. 6. The velocity
was calculated by

$$V = \frac{360 \ fT}{\theta} , \qquad (6)$$

where

V = velocity through the material, in./sec;

f = frequency of vibration, cps;

T = thickness of the material, in.; and

θ = delay angle, degrees.

As seen on the graphs, the minimum velocity of
the vibratory wave occurred when the accelera-
tion ratio was a maximum.

Examination of the Lissajous figures and of
the shifted waves indicated that both the upper
and lower accelerometers were vibrating at the
same frequency throughout the entire frequency
range, and that there was no apparent harmonic
distortion.

In Fig. 7, the acceleration ratio (delay angle
technique) and percent c/c_c (disc and beam
methods) obtained on 1/4-, 1/2-, and 1- and 2-in.
thicknesses of ML-D2 are shown. The acceler-
ation ratio curves obtained for the different
thicknesses of ML-D2 are similar to the typical
acceleration ratio curve shown in Fig. 6. The
peak value of acceleration ratio occurs at pro-
gressively lower frequencies as the thickness of
the specimen increases: 5000 cps for 1/4 in.,
2100 cps for 1/2 in. and 1900 cps for 1 in. The
percent c/c_c curves also exhibit a similar trend,
as the values of percent c/c_c increase to a maxi-
mum and then fall off with further increase in
frequency. In addition, the maximum value of
percent c/c_c occurs at a lower frequency as the
thickness increases: 9000 cps for 1/4 in., 7000

163
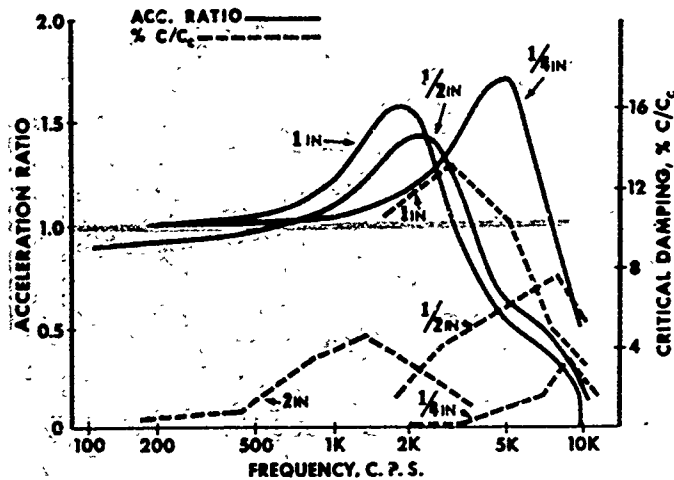
Fig. 7. Acceleration ratio and percent c/c_c of ML-D2

cps for 1/2 in., 3500 cps for 1 in., and 1300 cps for 2 in. Furthermore, the peak value of percent c/c_c for a 2-in. thickness occurs at approximately the frequency that could be predicted from examination of the acceleration ratio curves.

At frequencies below 7000 cps, the percent c/c_c is dependent on thickness of material, whereas above 7000 cps this relationship does not hold; 1/2-in. thick ML-D2 has a higher percent c/c_c than 1-in. material; at frequencies above 9000 cps, there is comparatively little difference between the percent c/c_c obtained on 1/4-, 1/2-, and 1-in. thick specimens. At these frequencies, the vibrations are apparently occurring so rapidly that only those portions of the specimen that are close to the metal

substrate are vibrating and thus absorbing energy. The upper portions of the specimen are vibrating at an amplitude much less than that of the substrate, as indicated by the low acceleration ratio obtained at these frequencies.

In Fig. 8, the acceleration ratio and percent c/c_c obtained on 1/4-, 1/2-, 1- and 2-in. thicknesses of the urethane material are shown. The shape of the acceleration ratio curves are similar to those obtained with ML-D2. In addition, the peak values of acceleration ratio occur at progressively lower frequencies as the thickness of the specimen increases: 850 cps for 1/4-in., 630 cps for 1/2-in., and 270 cps for 1-in. thickness. At frequencies above 2000 cps, the acceleration ratio is very low and there is not much difference between the acceleration ratio obtained on 1/4-, 1/2- and 1-in.
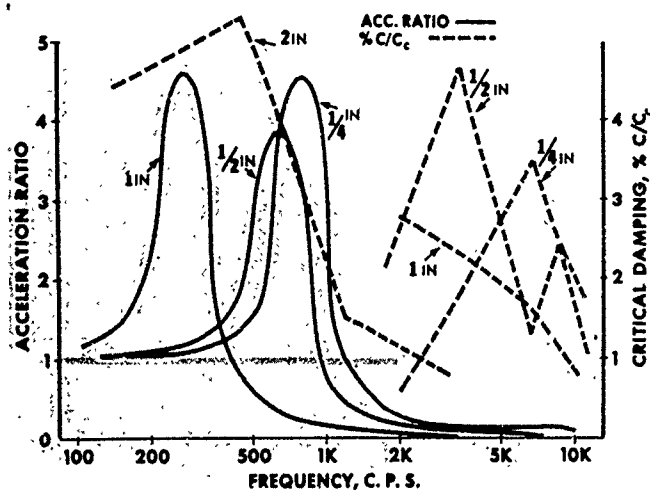
Fig. 8. Acceleration ratio and percent c/c_c of NASL-D101 urethane vibration damping material

thicknesses. Above 2000 cps, the percent c/c_c is rather low (peak value of 4.8 percent compared to 13 percent for ML-D2), and there is comparatively little difference in percent c/c_c of the different thicknesses. The acceleration ratio curves indicate that the urethane material would have high vibration damping at frequencies below 1000 cps. This is confirmed by the peak value of percent c/c_c of 5 percent obtained by the beam method at 450 cps on 2-in. thick material. Examination of the percent c/c_c curves also indicates that at frequencies above 5000 cps a 1/4-in. thickness of material has a higher percent c/c_c than 1/2- and 1-in. thicknesses of material. Above 5000 cps it should also be noted that the acceleration ratio is low, and there is little difference due to thickness of specimen. Apparently, at these frequencies, only the layers of material at and adjacent to the metal substrate are absorbing energy. Furthermore, the non-vibrating portions may be inhibiting motion of the specimen and thereby reducing energy absorption.

COMPARISON OF ML-D2 AND NASL-D101 URETHANE MATERIALS

As shown in Figs. 7 and 8, the ML-D2 material has better vibration damping properties than the urethane material at frequencies above 1300 cps, whereas the reverse occurs below 1300 cps. Furthermore, high acceleration ratios, i.e., greater than 1.0, occur over a broader frequency range for ML-D2 than for the urethane material. The narrowness of the frequency range, wherein the urethane has high acceleration ratios and consequently good vibration damping properties, may be due to the uniform size and weight of the Ottawa River sand particles used for the filler.

DISCUSSION

There is an apparent disparity between the conditions under which viscoelastic materials are tested with the delay angle technique and those encountered by the materials in service. For example:

1. There is the added mass of the accelerometer holder and the accelerometer (total weight = 84.2 gm) adhered to the normally unadhered surface of the specimen.

2. The specimen is vibrated sinusoidally at a constant 10 g with swept single frequency, whereas in service, the material vibrates simultaneously at a large number of unknown accelerations and frequencies.

However, despite these differences, the frequency ranges in which the materials have high acceleration ratio values show good qualitative correlation with the frequency ranges in which they have good vibration damping properties. The correlation between the two parameters (acceleration ratio and percent c/c_c) improves with increase in thickness of the materials. Apparently, as the mass of the specimen is increased, the effect of the added mass of the accelerometer and holder is decreased.

A viscoelastic material absorbs vibrational energy because of the hysteresis effect. As noted by Van Santen (6), the area beneath one cycle of the hysteresis loop $\pi p_o x_o \sin \phi$, and the work per unit time converted into heat by the damping is

$$\frac{p_o \dot{x}_o}{2} \sin \phi,$$

where

p_o = maximum force acting on the material,

x_o = maximum deformation produced by the force p_o,

ϕ = angle that the deformation lags the force, and

$\dot{x}_o$ = maximum velocity of the material.

The work converted into heat by the material cannot be calculated from the above equation, since the force, velocity, and lag angle for each portion of the vibrating material are unknown. However, with all other factors equal, the greater the velocity of the material, the greater the energy absorption and, hence, vibration damping. This is consistent with the observation reported herein, that at frequencies where the acceleration ratio and, hence, velocity ratio of the material was high, the percent c/c_c was correspondingly high.

As noted in the introduction, some investigators attribute vibration damping to tension and compression forces parallel to the surface of the material, whereas other investigators attribute damping to forces in the thickness-wise direction. The investigation reported herein indicates that damping is due to forces in the thickness-wise direction of materials which have particles of filler in a viscoelastic matrix and have a thickness greater than 1/4 in. Furthermore, this investigation indicates that optimum damping occurs at frequencies where there are resonances in the thickness-wise direction. That damping in thick layers of

viscoelastic material may be attributed to resonances in the thickness-wise direction is substantiated by Bolt, Beranek, and Newman (7), who note that damping increases, apparently due to a resonance phenomenon, have been observed in viscoelastic layers, where previous theories did not predict damping peaks. Furthermore, Bolt, Beranek, and Newman (7) conclude that thickness-wise wave motion is relatively soft and thick viscoelastic layers may be primarily responsible for the damping behavior of plates to which the viscoelastic layers are attached.

The various methods of rating the damping properties of materials are not directly comparable. The most common indicator, percent of critical damping, is not an intrinsic characteristic of the material but is dependent on both the method used and the actual geometry within a method. For example, use of discs of identical resonant frequencies but differing in diameter and thickness would lead to different values of percent c/c_c. At best, any method commonly used allows the individual investigator to rank materials.

Most methods lead to the same ranking, i.e., results are qualitative. What is needed, of course, is a material parameter which would be independent of the geometry and would characterize the damping properties of the material. The delay angle technique offers a method for determining the behavior of vibrating viscoelastic materials which is independent of substrate geometry.

CONCLUSIONS

The delay angle technique developed in this investigation is a tool which can be used to study viscoelastic materials over a continuous frequency range of 50 to 10,000 cps. This technique has been used to determine the frequency ranges in which different thicknesses of two types of viscoelastic materials have optimum vibration damping properties. The technique has advantageous features in that acceleration ratio and, hence, resonances in the material can be determined on a relatively small specimen over the desired frequency range within one hour. It can also be used to measure the velocity of sound in viscoelastic materials vibrating at or close to their resonance frequency. It has a disadvantage in that the mass of the accelerometer and holder influence the frequency at which maximum damping occurs. However, this influence is reduced as the thickness of the specimen is increased.

The delay angle technique has shown that vibration damping of 1/4- to 2-in. thick viscoelastic materials at frequencies from 50 to 10,000 cps is due to resonances in the thickness-wise direction. Additionally, analysis of the data obtained using this technique explains why vibration damping at all frequencies is not proportional to the thickness of material. The delay angle technique can be easily automated.

ACKNOWLEDGMENT

REFERENCES

1. MIL-P-22581 (SHIPS) "Plastic Sheet, Vibration Damping, Type ML-D2," Aug. 1960

2. J. E. Ruzicka, "Damping Structural Resonances Using Viscoelastic Sheer Damping Mechanisms, Part 1," ASME Paper No. 60-WA-73

3. D. H. Kallas and A. Rufolo, "Damping of Hulls by Use of Viscoelastic Materials," U.S. Naval Academy, 1961

4. S. Timoshenko, Vibration Problems in Engineering (D. Van Nostrand Co., New York), 1937

5. House and Kritz, "An Analytic Study of the Vibrating Free Disk," Presented at National Ultrasonic Symposium, Stanford U., California, Aug. 1959

6. G. W. Van Santen, Introduction to Mechanical Vibrations (MacMillan, New York), 1958, pp. 184-187

7. Bolt, Beranek, and Newman, Inc., Rept. 938, June 1962

The general solution of

$$m\frac{d^2y}{dt^2} + c\frac{dy}{dt} + ky = 0 \qquad (A-1)$$

is that of a sinusoidal curve of constantly decreasing amplitude, shown below,
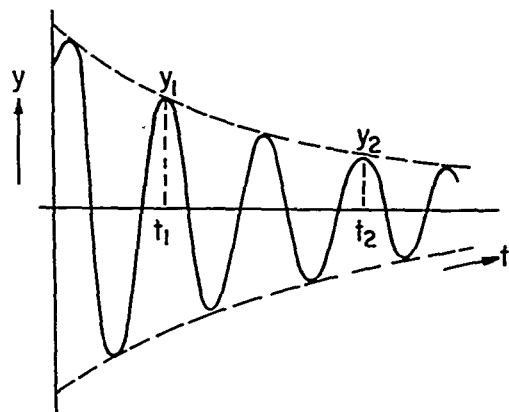
whose equation is

$$y = e^{-\frac{c}{2m}t}(A\sin \omega t + B\cos \omega t), \qquad (A-2)$$

where A and B are constants and ω is the angular frequency.

$$\omega = \sqrt{\frac{c^2 - 4mk}{4m^2}}. \qquad (A-3)$$

When c approaches 0,

$$|\omega| \equiv \sqrt{\frac{k}{m}}. \qquad (A-4)$$

ω is equal to $2\pi f$, where f is the frequency of vibration of the system.

To calculate the magnitude of the damping c, two points y_1 and y_2 are selected on the envelope of the sinusoidal curve, so that ωt_1 and ωt_2 equal 90 degrees. Substitution of these values in Eq. (A-2) yields:

$$y_1 = Ae^{-\frac{c}{2m}t_1} \qquad (A-5)$$

and

$$y_2 = Ae^{-\frac{c}{2m}t_2}. \qquad (A-5)$$

Dividing y_1 by y_2, we have

$$\frac{y_1}{y_2} = \frac{Ae^{-\frac{c}{2m}t_1}}{Ae^{-\frac{c}{2m}t_2}} = e^{-\frac{c}{2m}(t_1-t_2)} = e^{\frac{c}{2m}(t_2-t_1)} \qquad (A-6)$$

or

$$\log_e\left(\frac{y_1}{y_2}\right) = \frac{c}{2m}(t_2-t_1). \qquad (A-7)$$

The relationship between y_1 and y_2 may be expressed in decibels by

$$20\log_{10}\left(\frac{y_1}{y_2}\right) = d \text{ (decibels)}. \qquad (A-8)$$

Since the falloff of amplitude from y_1 to y_2 occurs in a time period $\Delta t = (t_2-t_1)$ seconds, the decay rate, in decibels per second, is

$$D = \frac{20\log_{10}\left(\frac{y_1}{y_2}\right)}{(t_2-t_1)}. \qquad (A-9)$$

The number of vibration cycles n which can occur during this time period is

$$n = f(t_2-t_1). \qquad (A-10)$$

Therefore,

$$(t_2-t_1) = \frac{n}{f},$$

or

$$D = \frac{20\log_{10}\left(\frac{y_1}{y_2}\right)}{n/f}. \qquad (A-11)$$

Substituting this into Eq. (A-7) yields:

$$\log_e\left(\frac{y_1}{y_2}\right) = \frac{c}{2m}(t_2-t_1) = \frac{c}{2m}\left(\frac{n}{f}\right),$$

$$\qquad (A-12)$$

$$2.303\log_{10}\left(\frac{y_1}{y_2}\right) = \frac{c}{2m}\left(\frac{n}{f}\right),$$

$$\frac{\log_{10}\left(\frac{y_1}{y_2}\right)}{n/f} = \frac{c}{2m} \times \frac{1}{2.303} = \frac{D}{20}, \qquad \text{(A-13)}$$

$$D = 20\,\frac{c}{2m} \times \frac{1}{2.303} = 4.34\,\frac{c}{m}, \qquad \text{(A-14)}$$

or

$$c = \frac{Dm}{4.34}. \qquad \text{(A-15)}$$

If the damping c for this system is assumed to be small relative to m and k, the natural frequency is given by

$$f_o = \frac{1}{2\pi}\sqrt{\frac{k}{m}}. \qquad \text{(A-16)}$$

The damping effectiveness of materials can be reported in terms of the critical damping c_c. For this condition, ω is 0 and occurs when

$$\sqrt{c_c^2 - 4mk} = 0$$

or $\qquad\qquad\qquad\qquad$ (A-17)

$$c_c^2 = 4mk.$$

Since measurements are made at the natural frequency f_o

$$k = 4\pi^2 f_o^2 m. \qquad \text{(A-18)}$$

Combination of Eqs. (A-17) and (A-18) gives

$$c_c^2 = 4m(4\pi^2 f_o^2 m), \qquad \text{(A-19)}$$

from which

$$c_c = 2m(2\pi f_o). \qquad \text{(A-20)}$$

Dividing the value of c by c_c we get

$$\frac{c}{c_c} = \frac{Dm}{4.34} \times \frac{1}{2m \times 2\pi f_o}$$

$$= \frac{1}{4.34 \times 4 \times \pi f_o} = 0.0183\,\frac{D}{f_o}, \qquad \text{(A-21)}$$

or

$$\%\,\frac{c}{c_c} \approx 1.83\,\frac{D}{f_o}. \qquad \text{(A-22)}$$

DISCUSSION

Mr. Melnick (TRG Inc.): Has any concern been given to the proximity of welding to these joints? Has a test been run or has field information shown that this material will stand up after welding within a foot or within inches of it?

Mr. Eller: You mean after the material is applied, can you weld?

Mr. Melnick: Nearby at least.

Mr. Eller: No tests have been made but it would be best to weld first if possible.

Mr. Melnick: You constantly have alterations to ships during drydocking.

Mr. Eller: You can remove the material and replace it. Since we have worked with the ML-D2 that I have described in this paper, a sprayable form of the material has become available. It can be sprayed in place after you weld.

Voice: What kind of elastic moduli to these materials have?

Mr. Eller: They are relatively soft, softer than rubbers. We have not measured it, but I estimate about 8000 psi.

*　　　*　　　*

ENERGY ABSORPTION BY DYNAMIC CRUSHING*

C. V. David
General Atomic Division, General Dynamics Corporation,
Special Nuclear Effects Laboratory
San Diego, California

The dissipation of energy by crushing a structure is well known. If the crushing process is slow, the energy absorbed corresponds to the static crushing force times the amount of crushing. If the load is applied instantaneously and exceeds appreciably the static crushing reaction, a smashing process occurs and the specific energy absorption of the system increases. In this case, the reaction of the structure is considerably altered. The investigation of the dynamic behavior of such a crushable structure is described.

Honeycomblike cores, 6 in. long, 12 in. in diameter, and of 0.008-in. thick stainless steel corrugated sheets, were assembled between two steel plates 1 in. and 1/4 in. thick. The 1/4-in. thick plate was accelerated to 600 to 700 fps and smashed and crushed the core against the 1-in. plate. Accelerometers mounted on the back of the 1-in. plate measured the reaction from the core against this plate. Similar samples were crushed statically, and the dynamic and static specific energies were compared. For the plate velocities investigated, an improvement by a factor of 2 to 3 of dynamic loading over static loading was obtained.

INTRODUCTION

The dissipation of energy by crushing specially designed structures (such as honeycomblike cores) has been used for several years, and off-the-shelf items are available commercially. The crushing characteristics of such structures have been extensively studied experimentally and analytically (1). But in all cases, the crushing of the core takes place on a time scale such that local buckling of the cell walls can occur ahead of the crushing plate. This produces a uniform crushing pattern along the core length until bottoming-out is reached. If, on the contrary, the crushing plate moves appreciably faster than the rate at which local buckling can propagate, a different process takes place and the core metal is smashed into shavings. This process produces two effects: the energy dissipated per unit weight of core increases, and the time history of the reaction transmitted to the supporting structure is altered.

The use of high-strength steel cores for a dynamic application has been considered for cases where the crushing plate might have initial velocities of 500 to 1000 fps. Therefore, a test program was initiated at General Atomic to investigate the behavior of realistic designs. Objectives were (a) to ascertain whether (and to what extent) the specific energy dissipation of a crushable core is higher under rapid loading conditions than it is under static, or slow-crushing, conditions; (b) to ascertain the behavior of the core in the vicinity of the primary impact plate after the impulse is delivered to the plate; (c) to obtain information on the reaction of the core against the supporting structure as a function of time, since it was believed that the relatively constant force that existed during static crushing tests would not exist under dynamic loading; and (d) to demonstrate the ability of the system to function under actual dynamic conditions.

To achieve these objectives, it was decided to test scaled-down models of the full-size crushable-core system. In these tests, the primary impact plate was to be given sufficient impulse to obtain realistic dynamic test conditions. The results could then be compared with results from a static crushing test. The energy source to deliver the proper impulse to the plate would be developed from data already available

from high-explosive (HE) testing techniques. The experimental program was thus divided into the development of the energy source, the dynamic crushing tests, and the static crushing tests.

The source development and dynamic crushing tests were carried out at the General Atomic Green Farm Test Site (2). At the HE test facilities available at the site it is possible to recover plates weighing several hundred pounds and moving at a velocity of a few hundred feet per second without damage to the plate from ground impact (2). A number of plates were accelerated to velocities of 600 to 900 fps. Following these experiments, three dynamic tests of quarter-scale core assemblies were made. Each assembly consisted of a 1/4-in. steel plate brazed to a crushable core that was bonded to a 1-in. thick steel plate. Instrumentation consisted of two accelerometers mounted on the 1-in. plate and a high-speed motion picture camera from which the velocity and orientation of the moving assembly could be ascertained. In the static tests, a core assembly was crushed on a Baldwin compression test machine.

MODEL DESIGN

The models were designed to provide quick preliminary results that could be used to predict whether the full-size system design was sound and what could be expected from a known configuration. The choice of materials was limited, since they had to be immediately available and have properties compatible with the available manufacturing and assembly processes. The following combination of materials was selected:

Core: AM-355 CRT-XH stainless steel, 0.008 in. thick and having a strength of about 150,000 psi yield after brazing at 1250°F (total core weight of approximately 4 lb); and

Plate: USS T1 for both the 1/4- and 1-in. plates, having a strength of about 100,000 psi yield.

The original plans called for both plates and the core to be brazed at a maximum temperature of 1250°F. But since the large mismatch in thickness between the core wall and the 1-in. plate was incompatible with an acceptable braze, the 1-in. plate was bonded to the core with an adhesive. The parts were all built according to the drawing in Fig. 1.

The 1-in. plate used as a back support for the assembly simulates the inertia of a large solid mass. With this plate attached to the core, the energy dissipated in the core is about 82 percent of the absolute kinetic energy of the 1/4-in. plate. Two eyebolts were mounted on the 1-in. plate to allow the assembly to be installed for the dynamic tests, as shown in Fig. 2.

Provisions were made for mounting two accelerometers on the back of the 1-in. plate to record the force transmitted by the core to the plate during the crushing process as a function of time. Since the energy dissipation capability of the core would have been too large if the core had completely covered the area of the plate, the core density was effectively decreased by making six radial openings, as illustrated in Fig. 1. A total of five assemblies were built: three were tested dynamically, one was tested statically, and the fifth was kept as a spare. An assembled model is shown in Fig. 3.

ENERGY SOURCE DEVELOPMENT

A series of ten experiments was performed to determine what combination of sheet HE and polyurethane foam damper would give the required impulse. In these experiments, 12-in. diameter plates, 1/4 in. thick, were mounted inside a heavy steel ring which acted as a barrier and positioning device. The energy source, which consisted of circular sheets of HE and polyurethane foam, was placed in contact with the 1/4-in. plate and flush with one side of the steel ring. The foam was positioned between the HE and the plate to modify the impulse delivered to the plate. Combinations of three foam densities, two foam thicknesses, and two HE weights were used. The plate velocities were measured from films taken by a Fastax camera which viewed the first 20 ft of plate travel. The test results are given in Table 1.

Since the accuracy of the results is estimated to be only within about 10 percent, one can conclude from Table 1 that the total amount of foam (thickness times density) is almost immaterial and that the magnitude of the plate velocity is determined primarily by the amount of HE used. One obtains, roughly, 680 fps with A-3 and 900 fps with A-4.

For a given amount of HE, the pressure peaks developed against the plate should increase for decreasing amounts of foam. These pressure peaks have not been measured but should be in the 25- to 50-kbar range for the 0.25-in., 2-lb/ft^3, A-3 combination of Table 1. The 1/4-in. plate used for this test did not exhibit any spallation. Only a slight dishing was noticeable.

170
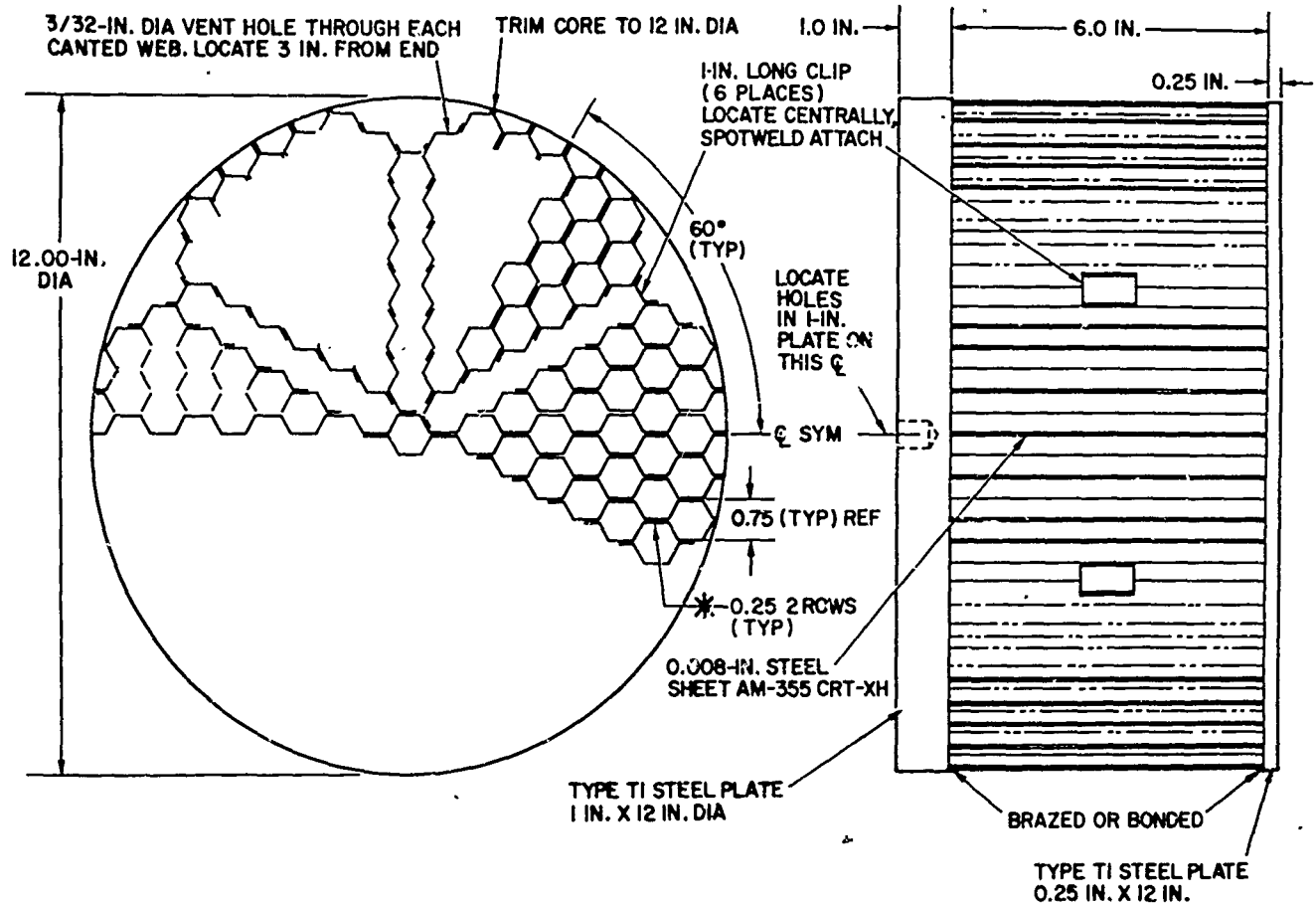
Fig. 1. Test model design layout

TABLE 1
Velocity (Impulse) Measurements

Foam Configuration		HE*	Plate Velocity at 12 Ft (fps)	Plate Velocity at 6 Ft (fps)	Estimated Initial Plate Velocity (fps)
Thickness (in.)	Density (lb/ft³)				
0.5	2	A-3	585	605	630
0.5	2	A-4	830	860	900
0.5	4	A-3	655	---	700
0.5	4	A-4	865	---	920
0.25	2	A-3	670	680	700
0.25	2	A-4	840	860	800
0.25	4	A-3	605	640	600
0.25	4	A-4	815	895	950
0.25	10	A-3	630	---	660
0.25	10	A-4	820	---	860

*A-3 and A-4 represent sheet HE containing 3 and 4 gm/in.² of HE, respectively.

(a)

(b)
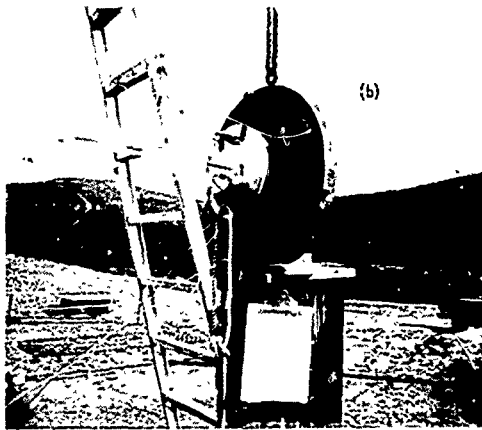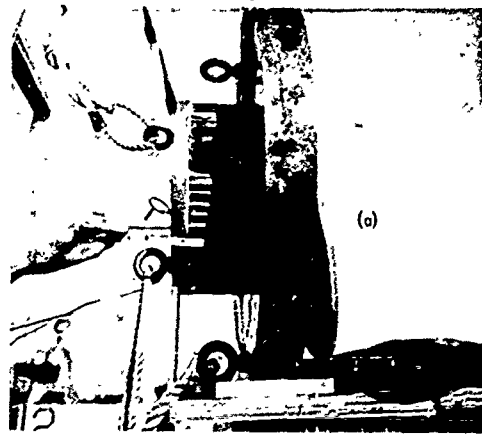
Fig. 2. Crushable sample installed
for dynamic testing
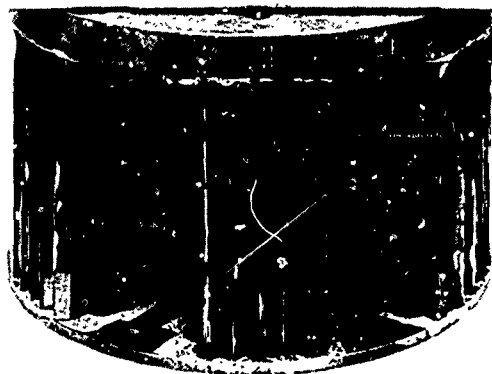
Fig. 3. Crushable sample

DYNAMIC CRUSHING TESTS

For the full-size application contemplated, a plate velocity of 630 fps was fairly realistic, so this velocity was chosen for the crushable sample dynamic tests. An HE-polyurethane foam configuration of sheet A-3 and 0.5-in. thick, 2-lb/ft^3 foam slab was adopted. The energy source and the test sample were installed in a manner similar to that described for the source development tests.

Three samples were tested: two were slightly precrushed and one was not. The precrushing was performed in such a way that the core was crushed about 0.25 in. at the juncture with the 1-in. plate.

Non-Precrushed Test Sample

This first test was only partly successful because of difficulties with high frequency oscillations in the accelerometer signals. As a result of this experiment, the accelerometer signals in the remaining two experiments were filtered to attenuate the high frequency components.

This experiment showed that the 1/4 in. plate separated from the core at an early time, probably at the time at which the plate stopped crushing the core. The motion picture film revealed that the 1/4-in. plate actually recoiled from the 1-in.-plate-core assembly. Apparently, an appreciable amount of energy was stored elastically in the core at the end of the crushing process. After separation, the 1-in. plate had a velocity of 120 ft/sec and the 1/4-in. plate a velocity of 96 ft/sec.

The test sample is shown in Fig. 4. The crushing of the core is quite different from that usually obtained in static tests. It is seen to have occurred primarily on the end to which the 1/4-in. plate was attached. The core metal is not crushed per se but is smashed into chips, which are pressed together against the 1/4-in. plate. There appears to be no real crushing except for half a convolution next to the smashed portion. The remaining part of the core was intact. The smashed length of core was about 3.5 in. The complete destruction of the integrity of that part of the core next to the 1/4-in. plate during the smashing process explains why the 1/4-in. plate could not remain attached to the core.

First Precrushed Test Sample

Since the core of the non-precrushed test sample (Fig. 4) did not develop the expected crushing pattern at the 1-in. plate connection and, therefore, probably created much higher crushing force peaks than were expected, it was

172

decided to precrush all cores at the 1-in. plate connection. The dynamic behavior of the core was considerably altered by the precrushing, as revealed by Fig. 5.
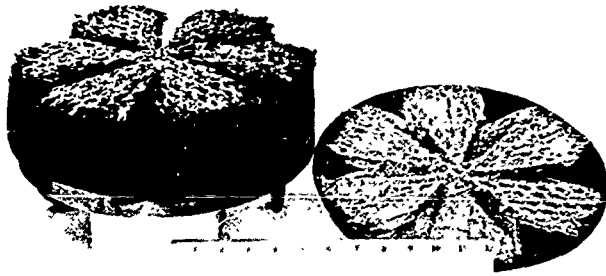
Fig. 4. Non-precrushed test sample after dynamic test

Fig. 5. First precrushed test sample after dynamic test

After testing, the core was found to be smashed at the 1/4-in.-plate end and also crushed at the 1-in.-plate end. The crushing stroke was about 4.25 in. long, which was 0.75 in. longer than that measured for the previous test. The magnitude of the 1-in.-plate acceleration, as indicated by the two accelerometers, was larger than anticipated. The one good accelerometer signal record did not include the peak acceleration, although it can be estimated. This signal is shown in Fig. 6. Records of the signal from the other accelerometer indicate that it apparently sensed about twice the acceleration measured by the first accelerometer. A difference in the two accelerometer indications was also observed in the third dynamic

test, but it has not been resolved. It appears that the calibrations of one or both of the accelerometers had changed from their original values, but the tight scheduling of this task did not permit a recalculation to be performed. It has thus been tacitly assumed that while the absolute values of the acceleration signals are questionable, the shapes of the acceleration versus time records are correct.
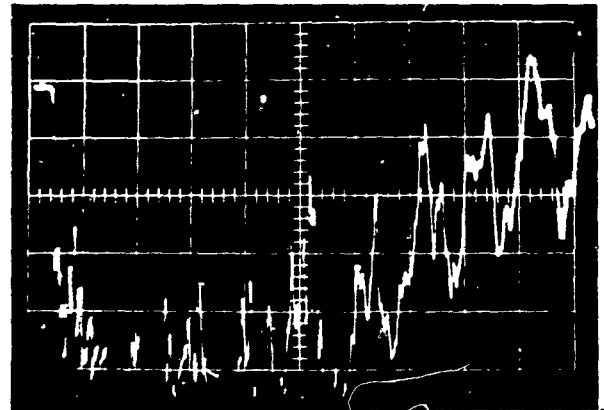
Fig. 6. Accelerometer signal, acceleration vs time (second dynamic test): vertical scale = 1000 g/cm (positive downward); horizontal scale = 0.2 ms/ cm starting at time of detonation (each division along scales = 1 cm)

The average maximum acceleration indicated in Fig. 6 is about 6000 g and is, therefore, more than twice that expected (2500 g). But the duration of the signal was, as predicted, about 2.3 ms. The 1/4-in. plate again separated from the core. The following velocities were measured from the recording film: 1/4-in. plate, 150 fps; 1-in. plate and attached core, 110 fps.

Second Precrushed Test Sample

In this test, good records of the accelerometer signals were obtained. Figure 7 shows the signal from one of the accelerometers, illustrating the shape of the acceleration versus time curve. It is noted that the signal shows a peak acceleration which is quite high compared to the average value. Prior to this test, the precrushing of the core of this sample was observed to be azimuthally unsymmetrical; i.e., the core was not completely precrushed around the entire perimeter. One would, therefore, expect a rather high peak acceleration corresponding to the force transmitted to the 1-in. plate before initiation of the crushing action.

173

This interpretation is borne out by the fact that in the first precrushed test, the core of the assembly was observed to be rather uniformly precrushed and the acceleration signal of Fig. 6 did not appear to have very high peaks.
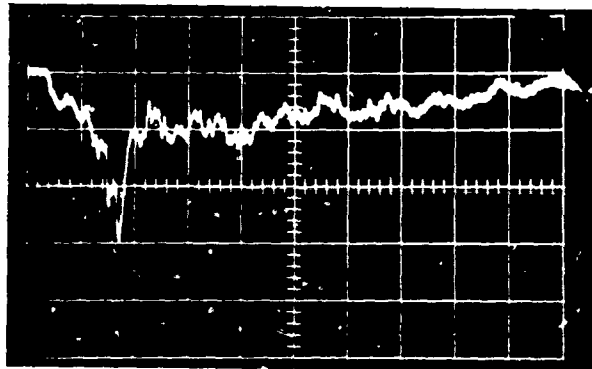
Fig. 7. Accelerometer signal, acceleration vs time (third dynamic test): vertical scale = 5000 g/cm (positive downward); horizontal scale = 0.2 ms/cm starting at time of detonation (each division along scales = 1 cm)

Again, the 1/4-in. plate separated from the core, and the following velocities were measured: 1/4-in. plate, 125 fps; 1-in. plate and core, 105 fps.

Two photographs of the test sample are shown in Fig. 8. The top of the 1-in. plate with the accelerometers still connected is also shown.

Figure 9 shows the three dynamic-test samples after the experiments for comparison with the sample before test. The 1/4-in. plate is also presented to show the plate edge bending caused by the uneven support of the core.

STATIC CRUSHING

The fourth sample was crushed at a very slow rate (1 in./min) on a Baldwin compression test machine to determine the static crushing characteristics of the core. The crushing process was stopped when the 1/4-in. plate bottomed out. The crushing force was recorded versus displacement, and the results are presented in Fig. 10. A force of 72,300 lb was required to initiate the crushing, and a constant force of 61,000 lb was sufficient to continue it. The initial length of the core was about 6-in. and the crushing travel was about 4.4 in., indicating that about three-fourths of the core length is available for a compression stroke.
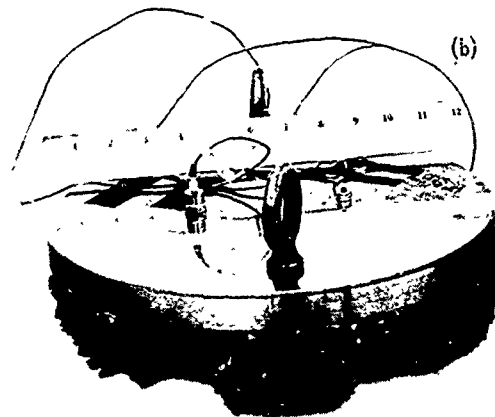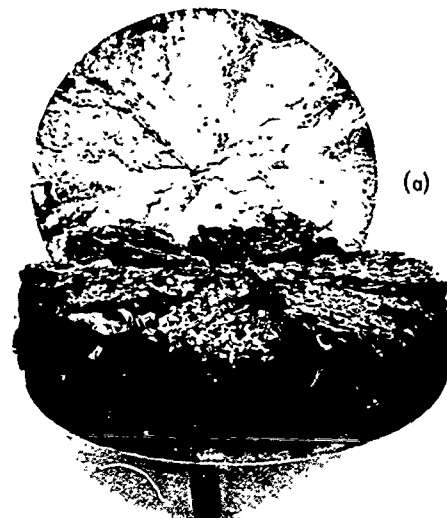
Fig. 8. Second precrushed test sample after dynamic test
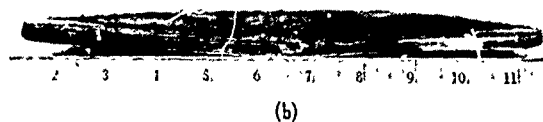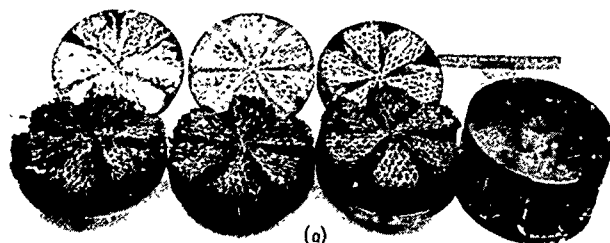
Fig. 9. Dynamic test samples before and after test

The crushing force was quite constant, except for some irregularities corresponding to each local buckling convolution along the core length. The main disturbance, indicated by the

174
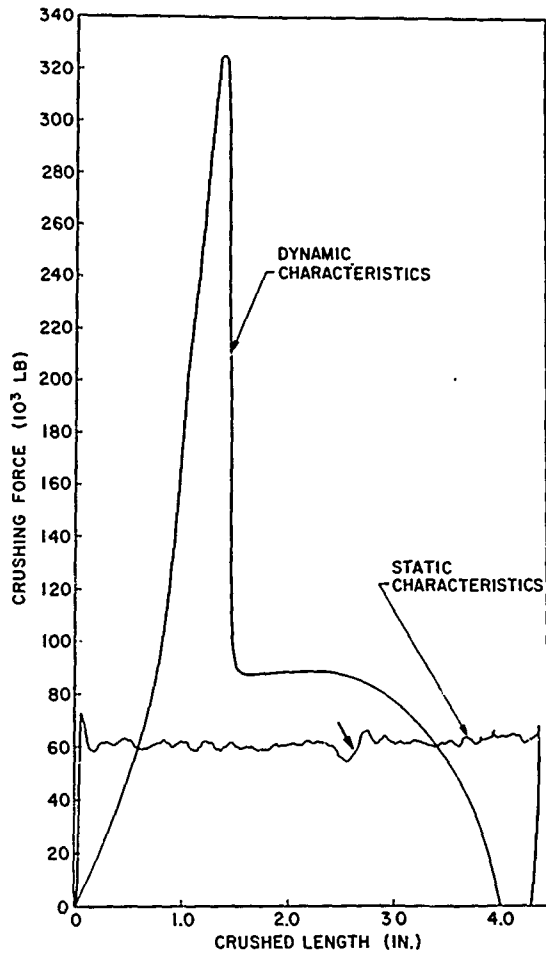
Fig. 10. Crushing force vs core length

Fig. 11. Precrushed test sample before and after static testing

arrow in Fig. 10, was caused by the 1-in. spacer clip shown in Fig. 1. The bottoming-out is indicated by the beginning of a sharp rise of the force curve.

The total energy dissipated by the crushing was $61,000 \times 4.4/12 = 22,400$ ft-lb, and since the core weighed about 4 lb, the energy dissipated per pound of core material was $22,400/4 = 5,600$ ft-lb/lb. Since the core wall thickness was 0.008 in. and the material yield about 150,000 psi, one can predict an energy dissipation capability for an optimum cell wall thickness of 0.030 in. and 300 series maraging steel of about $5,600 \times 300,000/150,000 \times (0.030/0.008)^{0.7} = 28,400$ ft-lb/lb.

The static test sample before and after crushing is shown in Fig. 11. One readily notices the difference between this crushing pattern and that obtained in the dynamic tests.

DISCUSSION OF RESULTS

Although it would have been desirable to perform more dynamic tests and to resolve the difficulties encountered with the accelerometers, the brief period allotted for this task permitted only the execution of the few tests just described. These tests did yield a considerable amount of information, however.

Influence of Precrushing

If the core is not precrushed, and especially if both ends of the core are restrained (brazed or bonded to plates), the onset of local buckling, which is required for crushing, occurs at a much higher load than the static crushing force. Furthermore, if the load is applied very rapidly and for a very short time, it is doubtful that the core will buckle even locally; in this case, loads up to and above its static compression strength might be transmitted. This would result in too high loads on the support structure. This loading peak phenomenon is evident in Fig. 7. One advantage, of course, is that all the energy goes into smashing the core, which is a much more efficient way to dissipate energy, as will be shown later. For instance, the same amount of kinetic energy was dissipated in the non-precrushed test sample as in the second precrushed test sample, but in the non-precrushed sample it took only 3.5 in. of core (with smashing and negligible crushing) as compared to 5.5 in. of core (with smashing and appreciable crushing) for the precrushed model.

175

The precrushing, therefore, plays two roles:

1. It reduces the early peak load to tolerable levels; and

2. It filters out some of the compression stress-wave effects initiated by the early-time smashing of the core and tends to eliminate high-frequency, high-amplitude vibrations.

The disadvantage of precrushing is that it decreases the efficiency of the energy dissipation process, since part of the energy is used for crushing the core at the connection to the suport structure.

The physical interaction during the dynamic crushing of a precrushed core assembly appears to be as follows:

1. The core end attached to the moving plate is smashed and a compression stress wave is transmitted to the core wall. This stress wave, trapped in the core, accelerates the unsmashed part of the core until it has reached the velocity of the moving plate. Some crushing of the core probably occurs near the 1-in. plate during this process.

2. When the core and the 1/4-in. plate have the same velocity, the core is crushed against the 1-in. plate.

3. The end result is a core half smashed and half crushed, as depicted in Figs. 5 and 8. The smashing is similar to that shown in Fig. 4, and the crushing is similar to that obtained during the static test (Fig. 11).

Velocity Measurement

To evaluate the energy dissipation of the core in the dynamic tests, it is necessary to determine what energy is actually imparted to the primary impact plates in each of the tests. This can be determined if the "initial" velocity of the plate is known. Although the initial velocity of the plate was nominally 630 fps based on the results of the energy source development test previously discussed, it was necessary to ascertain what the velocities in the dynamic tests actually were. Data taken from the motion picture films of the moving assembly yielded the late-time velocities of the 1-in. plate with attached core and the 1/4-in. plate. This information, given in Table 2, when inserted in the equation for conservation of momentum, gave the actual initial velocities of the 1/4-in. plates, which are also presented in Table 2.

TABLE 2
Typical Plate Velocities

Dynamic Test	Late-Time Velocity of 1-in. Plate with Attached Core (fps)	Late-Time Velocity of 1/4-in. Plate (fps)	Calculated "Initial" Velocity of 1/4-in. Plate (fps)
1	120	96	683
2	150	110	784
3	120	105	668

All of the calculated initial velocities are higher than the expected 630 fps, probably because the interaction time between the plate and HE source was greater owing to the slow movement of the more massive plate-core assembly as compared to a plate alone.

Energy Dissipation

The difference between the initial and final kinetic energies of the core assembly is the energy dissipated in the core. By using the conservation of momentum equation, this kinetic energy dissipation can be expressed by

$$E_k = \frac{1}{2} \frac{W_p}{g} V_p^2 \left(1 - \frac{W_p}{W_t}\right), \qquad (1)$$

where W_p is the weight of the primary impact plate (i.e., the 1/4-in. plate), W_t is the weight of the total assembly, and V_p is the initial velocity of the 1/4-in. plate. As $W_p = 8$ lb and $W_t = \sim 44$ lb, the energy dissipations E_k in the three dynamic tests are 48,000 lb-ft for the first assembly, 63,000 lb-ft for the second assembly, and 46,000 lb-ft for the third assembly.

Since about 4 in. of the 6-in. core were smashed for the first assembly (no crushing), the specific energy dissipation of this 4-lb core was $48,000/4 \times 6/4 = 18,000$ lb-ft/lb. For the second and third assemblies, the energy dissipation was 15,400 lb-ft/lb and 11,800 lb-ft/lb, respectively. These figures indicate (a) that the smashing action dissipated almost 220 percent more energy than the static crushing; and (b) that for the plate velocities considered and the core-to-plate weight ratio used, a combination of smashing and crushing yields up to 175 and 112 percent more energy dissipation than static crushing. As a first approximation, then,

176

one can assume that for the plate velocity and the core density-to-plate weight ratio used in these tests, the dynamic crushing yields up to twice the specific energy dissipation of the static crushing.

Core Reaction Against the Support Structure

Two disturbing factors appeared during the dynamic tests: the existence of high-frequency oscillatory acceleration and the presence of high-magnitude acceleration spike, as shown in Fig. 7. Although the spike is of short duration and might disappear if an adequate amount of precrushing were present, the high-frequency oscillation would probably remain. It may correspond to the small oscillations exhibited by the static crushing force, magnified many times because of the influence of the time element on buckling. The influence of this oscillatory force on the response of the support structure should be investigated.

Also, it appears that the smashing-crushing of the core does not result in a constant force as does the slow application of the load during the static tests. For instance, an approximate evaluation of the average reaction of the core against the 1-in. plate versus core crushing stroke is shown in Fig. 10. This does not compare well with the static crushing force. It appears that after the peak force is reached, the uncrushed core has accelerated enough that the crushing against the 1-in. plate takes place and produces a constant-level force comparable to but slightly higher than the static crushing load.

Smashing-Crushing Energy

The dynamic response curve of Fig. 10 was obtained from corrected readings given by the accelerometer signal. The amplitude of the signal was corrected so that the time integral of the acceleration,

$$\int_0^{t_f} a(t)\, dt ,$$

was equal to the 1-in.-plate velocity as measured by the motion picture film. In the case of the third dynamic test, for example, this would be

$$k \int_0^{t_f} a(t)\, dt = 125 \text{ fps.} \qquad (2)$$

where k is the correction factor and $a(t)$ is the 1-in. plate acceleration given by the scope trace of Fig. 7. The step integration of this curve gave $k = 0.59$ for $t_f = 2.2$ ms, which was when the acceleration dropped to zero.

Since the total amount of crushing in the third dynamic test is known to have been 4 in., the relative distance between the two plates, expressed in terms of the initial velocity and normalized acceleration, can be set equal to 4 in.:

$$V_0 t_f - k \iint_0^{t_f} a(t)\, dt^2 - k \iint_0^{t_f} a'(t)\, dt^2 = 4 \text{ in.} \qquad (3)$$

Here, the 1/4-in. plate is assumed to receive an acceleration $a'(t)$, related to $a(t)$ by the mass ratio of the two plates. Thus,

$$\frac{a'(t)}{a(t)} \cong 4 .$$

The results obtained were used to plot the dynamic response curve of Fig. 10.

One can then integrate the dynamic test curve of Fig. 10 to obtain the work done by the core reacting against the 1-in. plate. It is

$$\omega = \iint_0^{x_f} F(x)\, dx , \qquad (4)$$

where $F(x)$ is the curve just discussed and $x_f = 4$ in. This yields $\omega = 30,500$ lb-ft. But since the core has a mass (equal to about one-half that of the 1/4-in. plate), by inertia it reacts against the 1/4-in. plate with a higher force than $F(x)$. The core can be considered as a lumped mass between two springs. In this case, part of the 1/4-in.-plate kinetic energy is trapped in oscillations within the core and does not contribute to the reaction against the 1-in. plate. A similar study indicates that 25 to 30 percent of the 1/4-in.-plate kinetic energy could have been dissipated in the core only to accelerate it. Therefore, the total energy absorbed by the core could be $30,500/(0.75 \text{ to } 0.70) \cong$ 40,600 to 43,700 lb-ft. These numbers compare reasonably well with the 45,000 lb-ft calculated as the kinetic energy of the plate.

CONCLUSIONS

The experimental program described in this paper yielded very interesting results:

1. The specific energy dissipation achievable by honeycomb core smashing can be two to three times as high as that obtainable by crushing. This smashing occurs if the smashed end moves at high velocities (a few hundred feet per second).

2. The precrushing of the core at the support attachment affects noticeably the amount of specific energy dissipation (up to one-third) and the core reaction against the support.

3. The smashing process completely destroys the core connection to the moving plate. The latter always recoils after the interaction is completed.

4. For a "one-shot" application, the energy dissipation capability of such crushable structures is extremely high and could lead to very compact and light systems.

5. Considerable work would still be required to determine more accurately the influence of the plate velocity on the smashing process, of precrushing, of the core cell configuration, and of the core material. The present investigation was only intended to probe this new area and constitutes a spot check of the problem.

ACKNOWLEDGMENT

The author wishes to acknowledge the contribution to this work of Ronald E. Rinehart, who supervised the HE testing and performed some of the analytical work.

REFERENCES

1. R. K. McFarland, Jr., "A Limited Analysis of the Collapse of Hexagonal Cell Structures Under Axial Load," Jet Propulsion Laboratory Tech. Rept. 32-186, Dec. 1, 1961

2. "Technical Summary Report, Nuclear Pulse Propulsion Project, Vol. IV, Experimental Structure Response (U)," Air Force Systems Command Rept. RTD-TDR-63-3006, July 1963

* * *

DRY FRICTION DAMPING WITH FORCE
PROPORTIONAL TO DISPLACEMENT

Leon Wallerstein, Jr.
Lord Manufacturing Company
Erie, Pennsylvania

Conventional (constant force) friction dampers have certain shortcomings which inhibit their use in vibration isolation systems. Among them are a potential for infinite resonance amplitude, a limitation on force isolation, the creation of static off-center conditions, and the introduction of harmonics not necessarily in the environment. If the friction force is made proportional to displacement, these deficiencies disappear or become unimportant, and exceptional vibration isolation can be realized. One form of such a damper is shown which exhibits both an elastic stiffness and a friction gradient for which expressions are given. The friction gradient is two-valued and depends on the relative signs of displacement and velocity; its dual nature shows clearly in force-displacement tests. Self-centering is assured when the elastic gradient exceeds the minimum friction gradient. Analog computer solutions for a single degree of freedom system are given as transmissibility-frequency curves for several damping ratios. The decay rate at high frequencies is 12 db/octave, equal to that of an undamped system. Resonance transmissibility depends only on the ratio of friction gradient to elastic gradient; it is (analytically) independent of input amplitude, as confirmed by model tests.

INTRODUCTION

Most vibration isolation systems incorporate some form of damping, among them dry, sliding friction which has a number of attractive properties. It also introduces problems which militate against its use. Our purpose is to show how a modification of this common damper form can yield uncommonly good results.

What attracts us to friction dampers is that they are relatively simple, have no leakage problems, and are quite insensitive to changes in temperature, frequency, and strain amplitude. This cannot be said of fluid dampers and of many elastomers. On the other hand, conventional (constant force) friction dampers have these shortcomings: (a) relatively high transmission of vibration in the normal "isolating" range, (b) the characteristic of infinite resonance when input exceeds a critical value (1), (c) the creation of static offset, and (d) the introduction of harmonics not necessarily in the environment. This is a formidable list of defects, but they disappear or become unimportant, and exceptional vibration isolation results, if the damper is so designed that friction force is proportional to displacement. The force is, of course, directed against velocity, and when such a damper is made to execute harmonic oscillations, it generates the wave form shown in Fig. 1.

DESCRIPTION OF A DISPLACEMENT-PROPORTIONED (DP) DAMPER

Form and Force-Displacement Properties

The single degree of freedom system of Fig. 2 shows one configuration such a damper might take. At static equilibrium the damper spring k_d is unstressed; displacement in either direction creates a proportional tension in k_d and a corresponding force on the sliding surfaces.

Thus, a friction gradient (A) is established. Its dimensions are like those of an elastic gradient or stiffness, e.g., pounds per inch, and it has two values, given by

$$\frac{A_1}{k_d} = \frac{4\mu \tan \alpha (1 + \tan^2\alpha)}{(1 - \mu \tan \alpha)}, \qquad (1)$$

179

when x and $\dot{x}$ are of like sign, and

$$\frac{A_2}{k_d} = \frac{4\mu \tan\alpha(1 + \tan^2\alpha)}{(1 + \mu \tan\alpha)} . \qquad (2)$$

when x and $\dot{x}$ are of unlike sign.
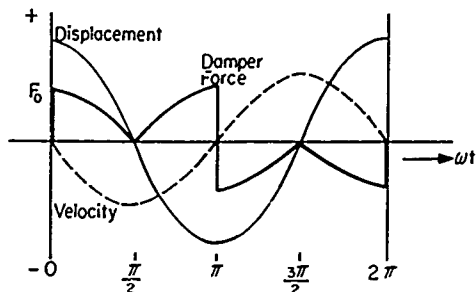
Fig. 1. Wave form, displacement-
proportioned (DP) damper
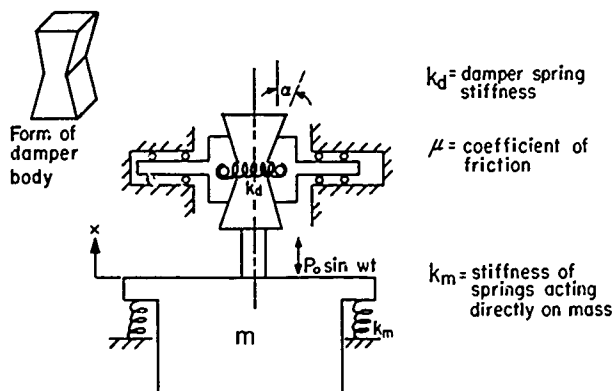
Fig. 2. Single degree of freedom
system with DP friction damper

The elastic stiffness of the system is given by

$$K = k_e + k_m , \qquad (3)$$

where

$$k_e = 4k_d \tan^2\alpha . \qquad (4)$$

is an elastic stiffness due to the damper, and k_m is the stiffness of springs acting directly on mass (m).

Figure 3 is the result of tests on the model shown in Fig. 4, and demonstrates clearly the two-valued nature [Eqs. (1) and (2)] of the friction gradient. For increasing displacement (x and $\dot{x}$ alike), the slope is $K + A_1$, and for
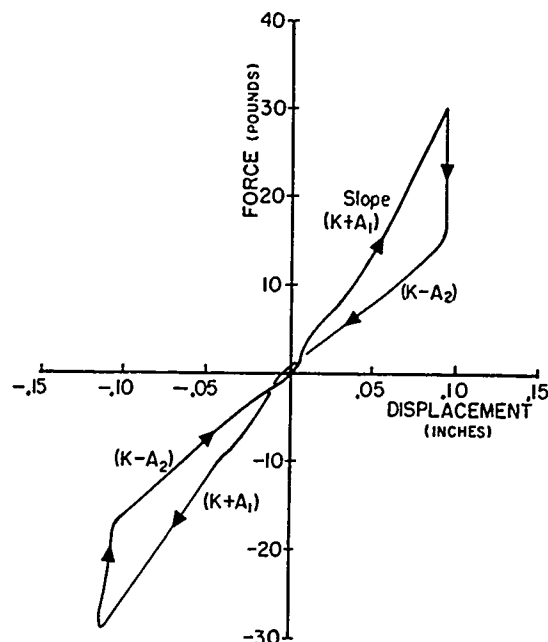
Fig. 3. Force-displacement
curve for model of Fig. 4

decreasing displacement, it is $K - A_2$. The measured slopes correspond well with calculated values, being respectively 280 lb/in. and 279 lb/in. for $(K + A_1)$, and 168 and 149 lb/in. for $(K - A_2)$.

Returnability

Self-centering of the system is assured if the spring gradient exceeds the minimum friction gradient; i.e., if $K > A_2$.

Harmonic Composition

Figure 5 and Table 1 show coefficients for the Fourier series which represents both the square wave and the DP damper force-time relation; i.e.,

$$f(t) = \Sigma F_n \sin \omega_n t , \qquad (5)$$

where $n = 1, 3, 5, \ldots$. We are interested primarily in the first order since it is only this component which contributes to damping (2). For the conventional damper, the coefficient is $4F_0/\pi$, compared to $2F_0/\pi$ for the DP damper, and the former might, superficially, be considered more "efficient." In addition, its third harmonic is smaller, so it generates less spurious vibration.

These advantages are more apparent than real; at high frequencies, where displacements

180
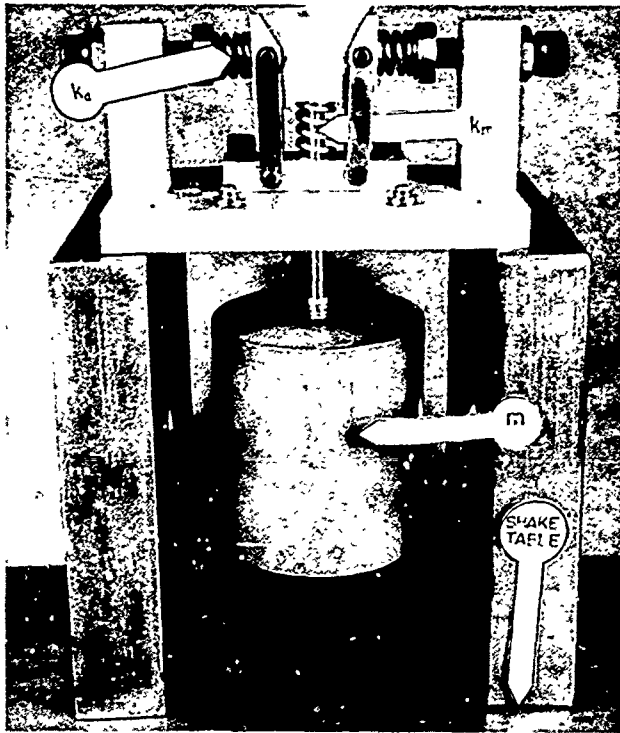
Fig. 4. DP damper test model
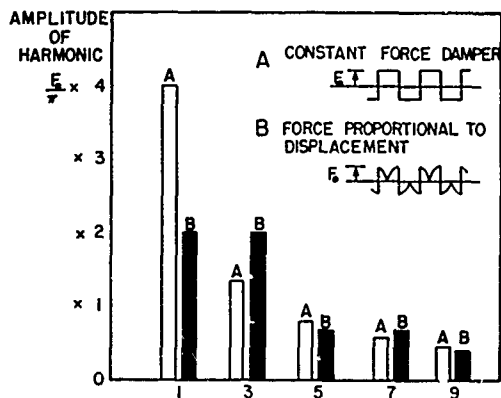
Fig. 5. Harmonic composition
of damper force

TABLE 1
Coefficients of Harmonic Components

Damper	1	3	5	7	9
Square wave	$\dfrac{4F_0}{\pi}$	$\dfrac{4F_0}{3\pi}$	$\dfrac{4F_0}{5\pi}$	$\dfrac{4F_0}{7\pi}$	$\dfrac{4F_0}{9\pi}$ ...
Displacement-proportioned	$\dfrac{2F_0}{\pi}$	$\dfrac{2F_0}{\pi}$	$\dfrac{2F_0}{3\pi}$	$\dfrac{2F_0}{3\pi}$	$\dfrac{2F_0}{5\pi}$ ...

are generally small, the conventional damper continues to transmit large forces and, therefore, degrades the isolation system. By contrast, the DP damper generates large force when it is needed and small force when it is not; this quite outweighs its less favorable harmonic structure.

SYSTEM CHARACTERISTICS

Equation of Motion and Solutions

From Fig. 2, we derive

$$m\ddot{x} + A \frac{\dot{x}}{|\dot{x}|} |x| + Kx = P_o \sin \omega t . \qquad (6)$$

The damping term is proportional to displacement by virtue of $|x|$ and has the sign of velocity due to $\dot{x}/|\dot{x}|$. The value of A can be taken as $1/2(A_1 + A_2)$ with very little error. Solutions, by analog computation, are shown in Fig. 6 for the range $A/K = 0.1$ to 0.5. The transmissibility at each frequency is the ratio of peak transmitted force to peak excitation force taken from oscillograph time-force histories, such as in Figs. 7 and 8. Thus, true transmissibility is represented, despite nonlinearity of the damper. Equivalent (same f_n and T_{res}) viscous-damped systems are shown for comparison. For DP damping, high-frequency transmissibility decreases at a rate of 12 db/octave, equal to that of an undamped system. The rate for viscous damping is 6 db/octave. Conventional friction damping produces constant transmissibility (of at least $\pi/4$ in magnitude), since both transmitted (friction) force F and excitation force P_o are unchanged with frequency. The high transmissibility level results from the fact that $F/P_o = \pi/4$ to avoid infinite resonance amplitude (1,2).

Wave Form

The damper is a nonlinear element, and distorted responses can be expected even though sinusoidal inputs are applied. Figure 9 shows all force components within the system for a typical condition, $A/K = 0.3$ and resonance operation. The damper force closely matches the idealized form of Fig. 1. The body motion, however, having the form of Kx, is nearly sinusoidal; therefore, we justify the assumption leading to Eqs. (8) and (9), which follow.

181

Fig. 6. Frequency ratio

Fig. 7. Instantaneous transmitted force for various damping ratios

Fig. 8. Instantaneous transmitted force for various damping ratios

Resonance Transmissibility (T_{res})

Since m executes harmonic motion, we can equate the work input by harmonic force P_o to the work extracted by the damper force to determine the displacement amplitude at resonance, X_{res}. The only component of damper force capable of extracting energy (2) is the first harmonic $2F_o/\pi$, so that we can write

$$\pi P_o X_{res} = \pi (2F_o/\pi) X_{res} = 2AX_{res}^2 . \qquad (7)$$

By dividing by K and setting $X_{st} = P_o/K$, we have

$$T_{res} = \frac{X_{res}}{X_{st}} = \frac{\pi}{2A/K} . \qquad (8)$$

For a system excited by sinusoidal motion of the support with displacement amplitude a_o, we can approximate a force-excited system by setting $P_o = m\omega_n^2 a_o$. Substituting in Eq. (7) and noting that $\omega_n^2 = K/m$, we again have

$$T_{res} = \frac{X_{res}}{a_o} = \frac{\pi}{2A/K} . \qquad (9)$$
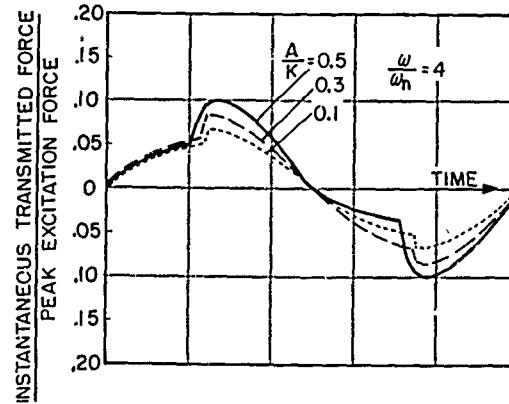
Thus, for either force of motion excitation, resonance transmissibility depends only on A/K. It is unaffected by input amplitude or frequency. Calculated values are compared with analog and physical model results in Table 2.

It is interesting to note the relation among DP, viscous, and hysteresis (rubber-like) damping with respect to resonance transmissibility:

$$T_{res} = \frac{\pi}{2A/K} = \frac{1}{2c/c_c} = \frac{1}{G''/G'} . \qquad (10)$$

182
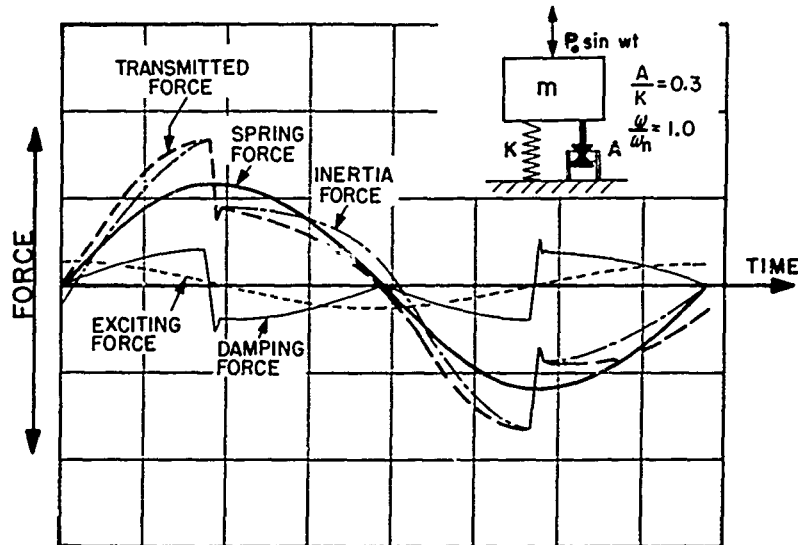
Fig. 9. Force components at resonance in a single degree of freedom system with DP friction damping

TABLE 2
Resonance Transmissibility

A/K	By Eq. (8) or Eq. (9)	By Analog Computer	By Model at Inputs (s.a.)		
			0.005 In.	0.010 In.	0.020 In.
0.1	15.7	11.2	—	—	—
0.3	5.3	4.1	6.20	6.25	6.45
0.5	3.1	2.5	—	—	—

In this, c and c_c are, of course, actual and critical damping for the viscous system; G'' and G' are damping and elastic components of the "rubber" modulus.

Model Tests

Static force-displacement curves, from the model shown in Fig. 4, have already been discussed. Vibration tests through the resonance range at three different inputs are shown by Fig. 10 and confirm that resonance transmissibility depends only on the value of A/K. Transmissibility vs frequency to 500 cps is recorded in Fig. 11, the input being taken from a typical specification, MIL-E-005272B, Procedure 1. Comparison with the computer-derived curves of Fig. 6 shows some degradation in isolation qualities at high frequency. Two factors appear to be responsible for this: (a) intercoil resonance of the springs, and (b) coupling of
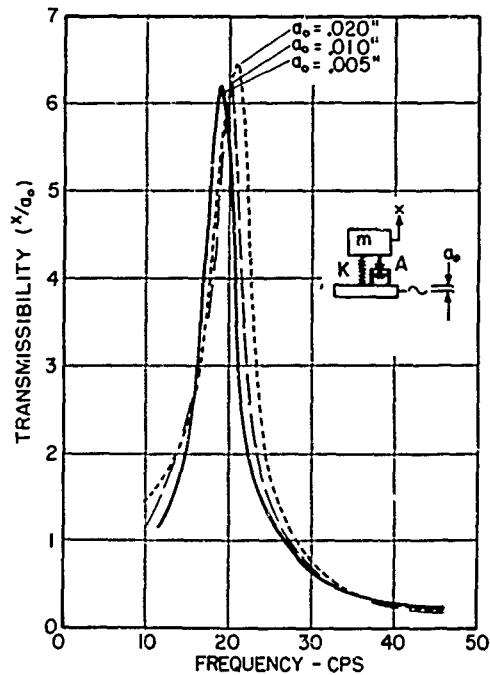
Fig. 10. Effect of input on DP damped model

vertical forces on the mass (m) with lateral acceleration forces on the damper shoes. The latter occurs as the damper passes through its neutral point, where vibration velocity is maximum. The shoes, which are approaching each other, suddenly start separating, and the velocity change is associated with high horizontal acceleration. The resulting force depends on mass of the shoes, but whatever its magnitude, a vertical component appears on the mounted mass because of the damper face. Minimum

183
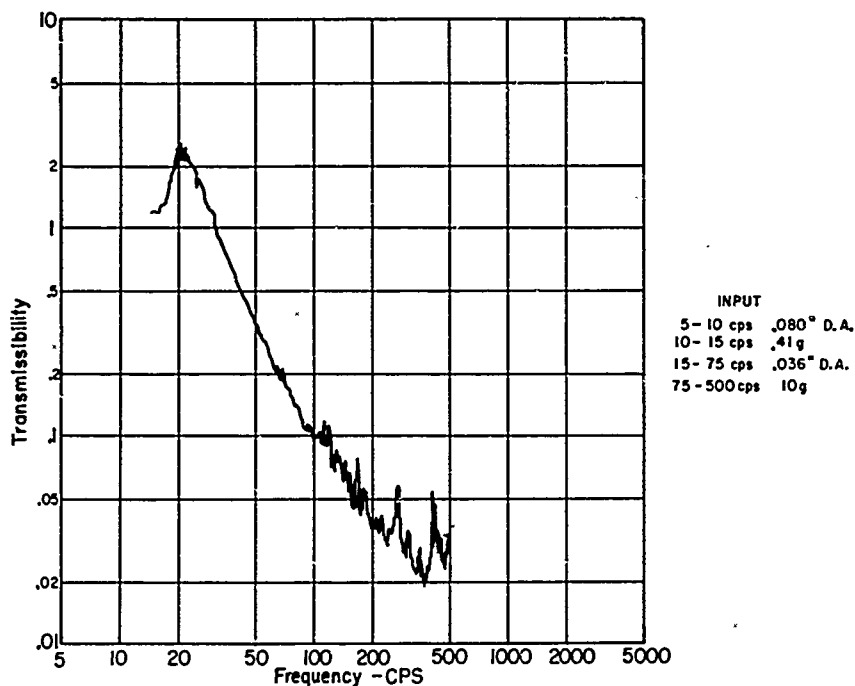
Fig. 11. High-frequency transmissibility of DP damped model

weight elements are, therefore, important in this particular DP damper configuration.

Other Forms

Displacement-proportioned damping can be realized in a variety of ways, only one of which has been shown. Figure 12 is another. Here is a uniaxial or biaxial isolator, in which the supported body rests on rollers or balls, spaced apart by a retainer. Spring restraint on the retainer causes it to rub against the balls or rollers with increasing force as displacement progresses, obviously a DP damper characteristic.

In closing, we should note that DP damping is not the only form in which dry friction can be used to advantage. Some of the problems of

the conventional, constant force damper can be relieved, for example, by lost-motion designs in which the damping is inactive for small displacements. Another technique uses the damper in series with a spring (3). These expedients are effective if the vibration inputs conform closely to that for which they are designed. Displacement-proportioned damping, on the other hand, is not critical in this respect; it is predictable in performance and appears to merit attention by the designer of vibration isolation systems.

ACKNOWLEDGMENTS

Sincere thanks are due William T. Polak and Shankerappa Hulsoor for analog computer studies, and to Mrs. William J. Mellow for preparation of the drawings of this report.

REFERENCES

1. G. W. Painter, "Dry-Friction Damped Isolators," Product Engineering (1959)

2. J. P. Den Hartog, Mechanical Vibrations, 4th ed. (McGraw-Hill, New York), 1956, pp. 12-20, 373-377

3. C. M. Harris and C. E. Crede, Shock and Vibration Handbook, Vol. 2 (McGraw-Hill, New York), 1961, pp. 30-12 to 30-16

184
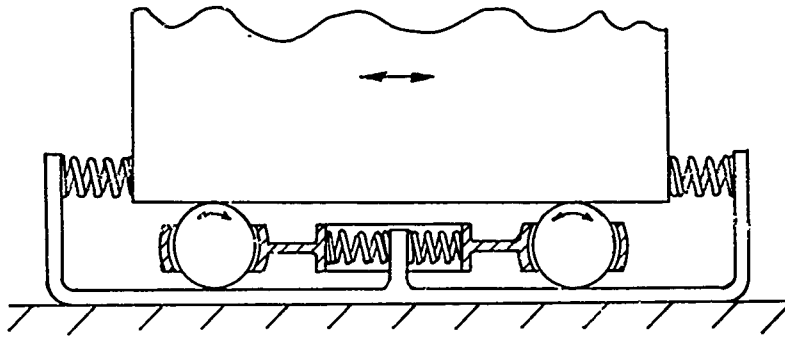
Fig. 12. Another form of DP damping --
friction between balls and retainer in-
creases in proportion to displacement

DISCUSSION

Mr. Mahaffey (LTV Astronautics): Were your surfaces metal to metal in this damper?

Mr. Wallerstein: No, they were not. They had a protective coating. There are a great variety of coatings that can be used, depending on the environment in which you are operating.

Mr. Mahaffey: Is this friction-damping force affected by humidity and various kinds of impurities?

Mr. Wallerstein: We have made a number of studies, not so much in connection with this but with another program; we have found a variety of coatings and films which are pretty good. For example, we have one that will operate at 500°F for 1000 hours under vibratory conditions and is still pretty good. If the conditions are known, a coating that will protect the surface can be found.

*   *   *

RESPONSE OF RESILIENT MOUNTS UNDER SHOCK LOADING

E. A. Thornton and R. D. Short
Underwater Explosions Research Division
David Taylor Model Basin
Portsmouth, Virginia

Experimental and theoretical studies of the type 5M10,000-H rubber resilient mount assembly consisting of a compression and shear mount and snubber were conducted to determine its performance under shock loading. In the experimental study, the mount assembly (supporting a rigid test mass) was installed on the Floating Shock Platform and subjected to a series of five shock tests. In the theoretical study, a simple mathematical model combining springs and dashpots was used to represent the response of the mounts under vertical shock loading. Dynamic force-deflection curves, obtained from the experimental and theoretical data, showed good agreement. The studies demonstrated that the viscous effects of rubber play a significant role under shock loading. Thus, the conclusion was that the behavior of resilient mounts for shipboard installations cannot be based on static tests alone.

INTRODUCTION

Resilient mounting systems are used on modern Naval ships to reduce the structure-borne noise introduced by machinery items. To meet noise isolation requirements, the mounting systems are generally made of natural rubber, have relatively low static spring constants, and produce natural frequencies from about 5 to 25 cps at rated loads. Since the low mount stiffness permits large excursions during ship maneuvers and shock motions, snubbers are included as an integral part of the mounting system.

The need for understanding the performance of resilient mount behavior under shock loading has become increasingly important as the shock requirements for Naval ships have increased. Several questions concerning the performance of resilient mounts under shock loading have arisen. One of the most important questions concerns the shock mitigation characteristics of the mounts, since the dynamic characteristics of rubber have been found to have an important role when subjected to shock loading.

As a part of the Navy's shock-hardening program, a number of resiliently mounted items have been shock tested on the Floating Shock Platform (FSP) (1). When possible, the David Taylor Model Basin (DTMB) has studied the performance of these mounting systems to gain insight into the performance of the mounts under dynamic conditions. The information gained from the evaluation of the test results on one mount, the 5M10,000-H resilient mounting system, showed that the dynamic behavior of the mounts differed significantly from that based on static tests. The study of data from these tests indicated the need for controlled experiments, since the equipment motions obscured many of the details of the dynamic behavior of the mounts.

In this paper, experimental and theoretical investigations of the performance of the 5M10,000-H mounting system under shock loading will be briefly described. A more comprehensive coverage of the details of these investigations is contained in a recent report (2).

EXPERIMENTAL PROCEDURE

Tests of resiliently mounted equipment on the FSP had shown the need for a rigid, concentrated mass for an accurate study of the mount behavior under shock. To fulfill this requirement, a test mass was constructed that consisted of a rectangular steel box filled with 16,000 lb of lead. The weight was supported on the FSP by two 5M10,000-H resilient mounts. Each of the 5M10,000-H mounts consists of: (a) a compression mount to support the major portion of the static vertical load, (b) a shear mount to stabilize the static load with respect

to lateral motion and support part of the vertical load, and (c) upper and lower snubbers to restrict vertical and lateral excursions under dynamic conditions. Figure 1 is a view of the test fixture installed on the FSP. The shear and compression mounts were installed in a symmetrical arrangement to maintain static stability; only one of each is visible in Fig. 1. Each of the snubbers shown has a clearance under static conditions of 5/16 in.

The inner bottom of the FSP and the test mass were instrumented with a number of velocity meters, accelerometers, and deflection gages to record the shock response. Some of these instruments can be seen in Fig. 1. A series of five shock tests similar to the routine FSP tests were conducted.

SHOCK RESPONSE OF TEST MASS

Instrumentation histories indicated that the shock response of the mass consisted essentially of a vertical translation. In each test, the motion of the mass was controlled by the influence of the snubber engagements. The records show that shear and compression mounts have negligible influence on dynamic behavior. The engagement of the snubbers is clearly demonstrated by periods of sharp acceleration and deceleration of the mass. During periods of snubber disengagement, the mass moves with

constant velocity. These facts are clearly evident from the typical velocity and acceleration histories of the mass shown in Figs. 2 and 3. A typical relative deflection history of the mass is shown in Fig. 4.

DYNAMIC FORCE-DEFLECTION CURVES

The relationships between the dynamic forces transmitted by the mounts and the accompanying deflections are of basic interest in the design of new, more effective mounting systems. In addition, these results are necessary for the dynamic analysis of equipment supported by systems using resilient mounts of the present type. To meet these needs, dynamic force-deflection curves were derived for the first compression and expansion of the upper snubber of the 5M10,000-H mounts. The force-deflection curves were found by calculating the instantaneous force transmitted by the mounts from the average acceleration histories (Fig. 3) of the mass. The corresponding mount deflection was then read from an average deflection history (Fig. 4). Force-deflection curves were obtained in this way for each test. Two typical results are compared with the static force-deflection curve in Fig. 5.

Comparison of the dynamic and static force-deflection curves reveals a number of
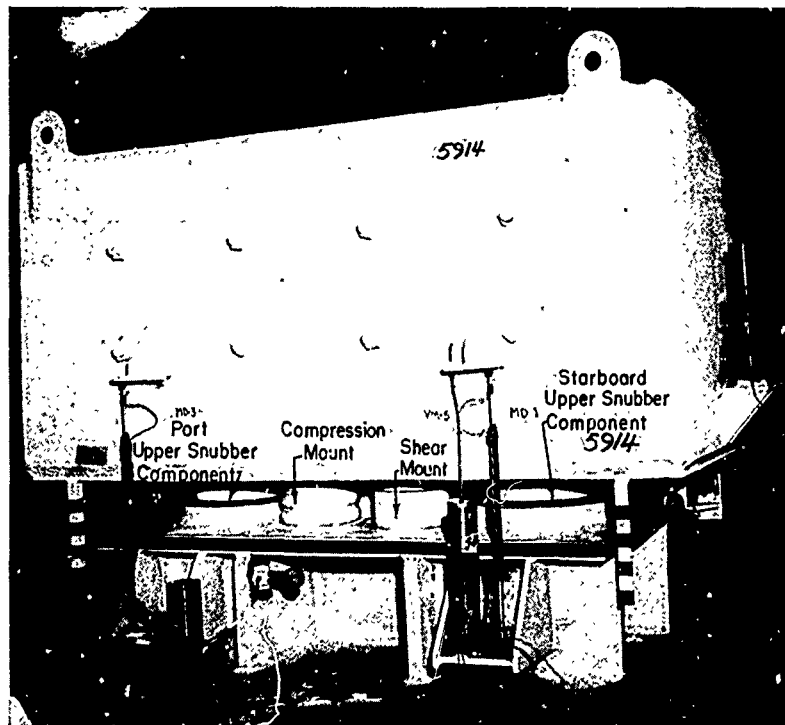
Fig. 1. Mount components in completed test fixture

188
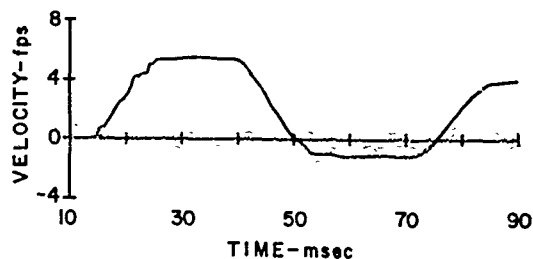
Fig. 2. Typical velocity history of mass
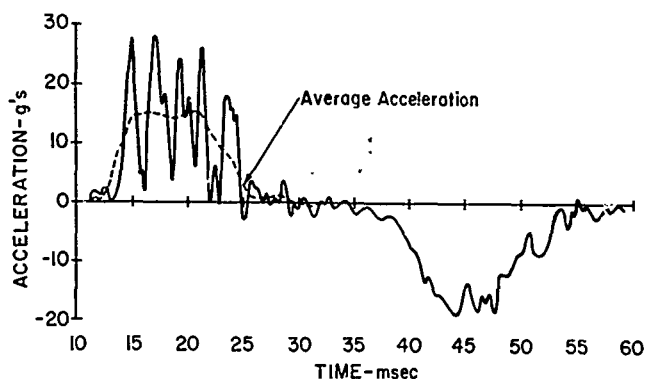
Fig. 3. Typical acceleration history of mass
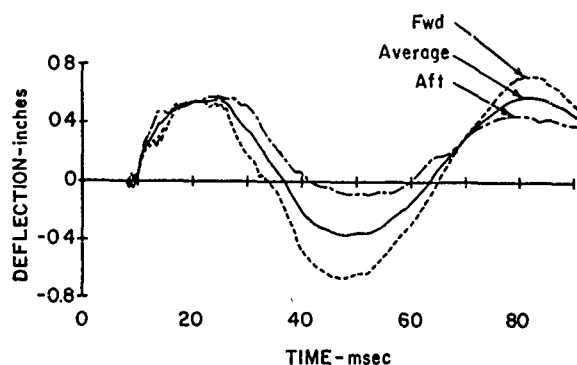
Fig. 4. Typical vertical deflection histories

Fig. 5. Experimental dynamic force vs deflection curves for two tests

For the range of tests considered, the maximum force and maximum deflection were found to increase linearly with increasing attack severity. This relation is shown in Figs. 6 and 7 where the maximum forces and maximum deflection experienced by the mounts is plotted versus shock factor.

$$\text{Shock factor} = \frac{\sqrt{W}}{R} \; \frac{1 + \sin \theta}{Z}, \qquad (1)$$

where

W = the charge weight in pounds of TNT,

R = the slant range, and

θ = the angle between R and the horizontal.

The dynamic force-deflection curves also show a large amount of energy absorption which indicated that significant damping is present in the mounts.

THEORETICAL ANALYSIS OF
RESILIENT MOUNT RESPONSE

The mechanics of deformation of rubber are significantly different from the linear, elastic behavior of metallic structures to which most engineers are accustomed. One of the distinctive characteristics of rubber is the role of viscous effects in its response to dynamic loads. This important role of viscosity has led

significant differences. The static force-deflection curve is characterized by force increases with increasing deflection as the deflection approaches a nearly vertical asymptote. This asymptote is approached at relatively low levels of force and essentially establishes that the maximum deflection is independent of the applied force. For the dynamic force-deflection curves, on the other hand, the maximum deflection and maximum force vary with the input velocity. Therefore, the force-deflection behavior is specified by a family of curves which is a function of the loading rate (attack severity).

189

Fig. 6. Maximum force vs shock factor
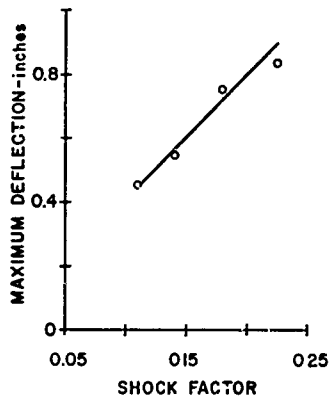
Fig. 7. Maximum deflection vs shock factor

a number of writers to represent the behavior of rubber by mathematical models using various mechanical systems consisting of combinations of springs and dashpots. For the present study, the model shown in Fig. 8 was selected to represent the behavior. Other mathematically equivalent models could have been used to give the same results.

The 5M10,000-H resilient mounts were represented by two parallel systems similar to Fig. 8, one for the compression and shear
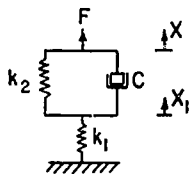
Fig. 8. Mathematical model of resilient mount

mounts and one for the snubber. The snubber, of course, has a clearance under static conditions so that it will not engage until the relative deflection has decreased by this amount. The complete mathematical representation for vertical loading is shown in Fig. 9.
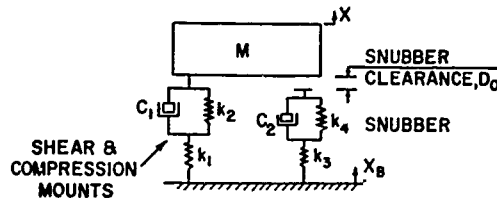
Fig. 9. Mathematical model of 5M10,000-H resilient mount

Two of the constants, K_2 and K_4, were found from static force-deflection curves. The other constants were obtained from experimental test results. One test was selected for this purpose and the shock input motion was represented analytically as shown in Fig. 10. The system of Fig. 9 was then programmed on an analog computer and the quantities K_1, K_3, C_1, and C_2 were adjusted to obtain the best fit for the measured acceleration, velocity, and displacement histories of the mass. The values found for the constants are as follows: k_1 = 65 kips/in., k_2 = 10 kips/in., k_3 = 758 kips/in., k_4 = 40 kips/in., c_1 = 1.8 kips-sec/in., c_2 = 4.71 kips-sec/in., M = 248 slugs, and D_o = 5/16 in. The system

LEGEND
----- Measured Velocity
——— $v = 12(1 - 42t) - 2.25 \sin \dfrac{2\pi t}{0.020}$
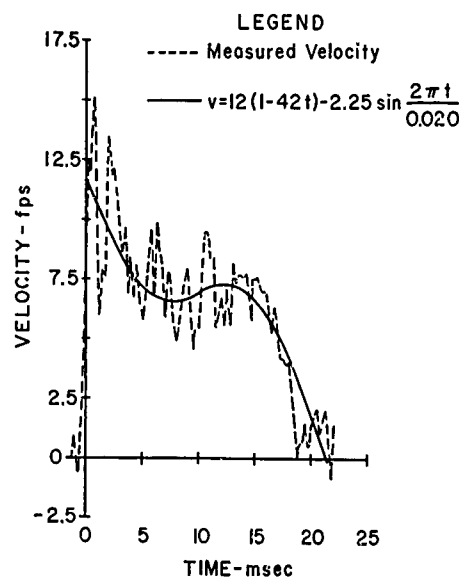
Fig. 10. Average base velocity histories

190

with these constants was then applied to the remainder of the tests using analytical representations for the base motion in each case. Theoretical dynamic force-deflection curves were obtained in this way for each test. Two such curves, together with the experimental data of Fig. 5, are shown in Fig. 11. In general, the agreement with experimental results was good. The maximum error in the worst case was less than 11 percent of the maximum value of the variable.

CONCLUSIONS

Investigations of the behavior of the 5M10,000-H resilient mount assembly under vertical shock loading has provided considerable insight into its behavior under dynamic conditions. Furthermore, it has been demonstrated that the behavior of this mount under shock cannot be based on static tests alone, since the viscous effects of rubber play a significant role under shock loading. Because of this fact, the dynamic characteristics must be used in calculation of the response of supported equipment under shock conditions. The action of the 5M10,000-H mount under vertical shock load was also found to be adequately described
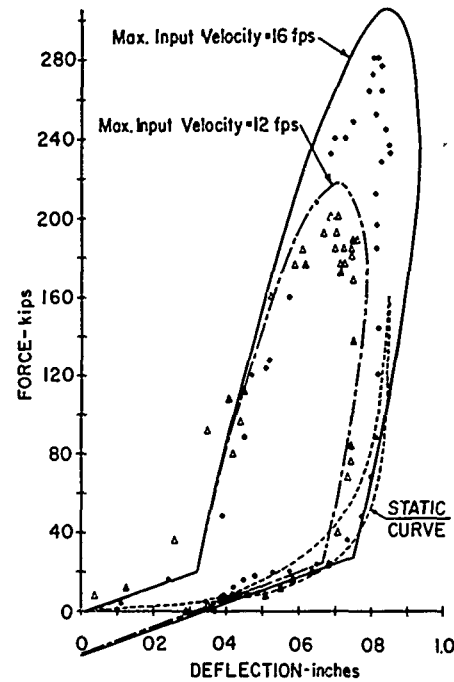
Fig. 11. Force-deflection curves for two tests

by a mathematical model consisting of parallel systems of two springs and a dashpot.

REFERENCES

1. J. K. Fleming and R. E. Oliver, "An Explosion Shock-Testing Method for Shipboard Equipment," Shock, Vibration and Associated Environments Bull. No. 29, Part I, March 1961, pp. 12-18

2. Earl A. Thornton, Robert D. Short, Jr., and Ramon R. Walker, "Response of 5M10,000-H Resilient Mounts Under Shock Loading," DTMB Rept. 1899, Jan. 1965

DISCUSSION

Mr. Levin (Bureau of Ships): I do not think that you nor I would want to leave the impression that the 10,000-lb mount that you showed is the only Navy mount that we have. For the sake of illustration, would you refer to one of our mounts with a lower load rating and show that the purposes of snubbing, compression, and shear could be taken care of in these other mounts, too?

Mr. Short: I am not an expert on all types of Navy mounts. I do know of a few others which are of somewhat different design. There are some very close to these. I am not familiar with any that have a continuous loading without the gap, if this is what you have in mind.

Mr. Levin: There are mounts with sufficient characteristics to take care of the forces, the shears, and the compression that you mentioned.

Mr. Short: Right. The point was not that this mount is not any good. The response of these mounts to shock cannot be determined from the static characteristics, even the very small deflection characteristics alone. There is no intention to say that this is the only Navy mount, or that all Navy mounts look like this in different sizes.

Mr. Hall (Edgerton, Germeshausen & Grier): Have you considered air mounts?

Mr. Short: No. To date we have looked at only two mounts. We are just getting started in our program. This is the first mount. There is another which is similar to this, except that it is a conical-shaped rubber mount. We have considered nothing but rubber mounts to date. We would be interested in any information you may have on air mounts.

191

A NEW APPROACH TO PACKAGE CUSHIONING DESIGN

Gordon S. Mustin
Special Projects Consultants, Inc.
Washington, D.C.

Dynamic shock absorption data for 16 different nonlinear cushioning materials were analyzed. It was found that the shock isolation information needed by the designer could be reduced to two curves for each material, plus a general envelope curve applicable to all of the materials. This finding, which is consistent with theory, represents an improvement over current use of an acceleration vs static stress curve for each thickness and for each drop height. As a result of this finding, the remaining challenges of nonlinear isolator technology can now be attacked. Among the most important of these are variations in isolator shape, temperature effects, viscoelastic behavior, and configurations with more than one degree of freedom.

INTRODUCTION

The problem of using a package cushioning material as a shock isolator has generated considerable interest for a number of years. The need for logical design techniques has been intensified by the ever-increasing volume of delicate, costly items which must be shipped with demonstrable reliability. In a purely technical sense, package cushioning materials generate interest because they are a special case of the nonlinear isolator with distributed mass and elasticity.

None of the existing known theoretical approaches has proven satisfactory in practice. On the other hand, the practical expedients which have been adopted lack clear relation to theory and, worse, do not provide concise engineering design data.

Figure 1, taken from Humbert and Hanlon (1), is typical of the current method of presenting cushioning material properties. The popularity of using a family of acceleration vs static stress curves is attested by the appearance of this approach in the literature (2-5).

It is obvious that Fig. 1 has several drawbacks for the designer. Among the most pertinent are:

1. The material properties are merely being sampled. This is true no matter how many acceleration vs static stress curves may be drawn.

2. When seeking an optimum solution to a specific problem, the designer must consult a great many curve families. At best, this operation is tedious. At worst, the designer can never be sure of achieving his goal.

3. Unless, by chance, the solution falls along one of the existing plotted lines, the designer must perform at least one interpolation, the latter largely by intuition.

This paper describes a method which will eliminate some of these defects.

NOMENCLATURE

A Surface area of cushion, sq in.

a,b Constants defined in Eq. (17)

c,d Constants defined in Eq. (18)

D Operator symbol denoting first derivative of function immediately following

D^{-1} Operator symbol denoting integral of function immediately following

G Peak acceleration divided by acceleration of gravity

G_o Optimum peak acceleration ratio

h Height of drop, in.

193
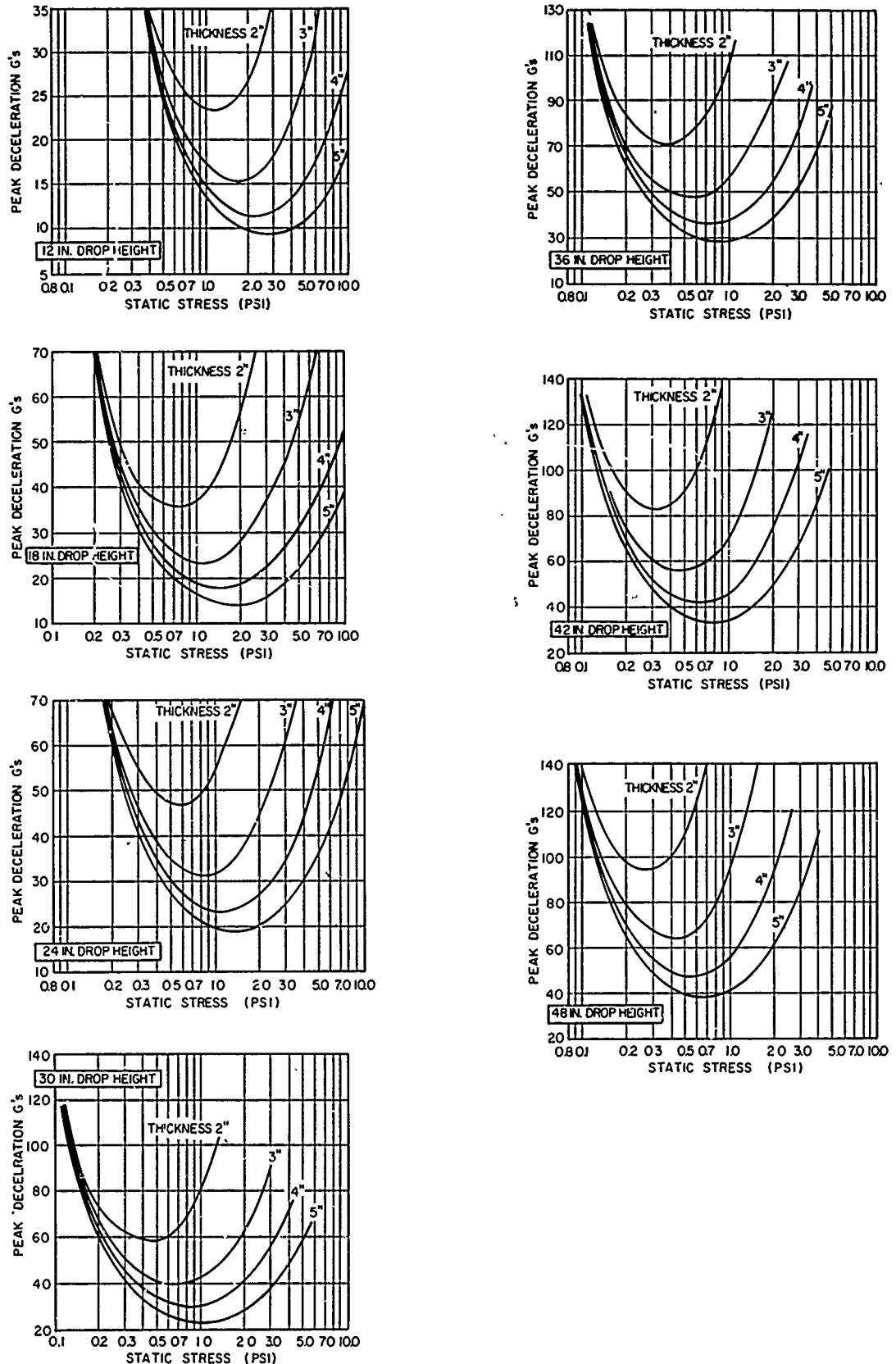
Fig. 1. Dynamic data on polyethylene foam (1)

194

J Ratio of peak stress developed to energy per unit volume absorbed by a cushioning material

J_o Optimum value of J

T Cushion thickness, in.

W Weight of cushioned article, lb

ϵ Strain, in. deflection/in. thickness

ϵ_o Optimum strain

μ Coefficient of friction

ρ Set of parameters affecting dynamic stress-strain relationship

σ Stress, psi

σ_m Maximum stress developed in any particular drop

σ_o Optimum stress

σ_s Static stress

σ_s' Optimum static stress

BACKGROUND

Let the dynamic stress-strain characteristics of a cushioning material be represented by a continuous function

$$\sigma = f(\epsilon, \rho) \qquad 0 \le \epsilon \le 1.0 , \qquad (1)$$

where

σ = stress, force per unit area;

ϵ = strain, in. deflection/in. thickness;

ρ = set of parameters, as yet undefined, which affect the stress-strain relationship; and

f( ) = function of the statements contained in ( ).

Since the function is continuous within limits, both the first derivative and the integral exist, or

$$D\sigma = \frac{\partial}{\partial \epsilon} [f(\epsilon, \rho)], \qquad (2)$$

$$D^{-1}\sigma = \int_0^\epsilon [f(\epsilon, \rho)] \, d\epsilon . \qquad (3)$$

Let the cushioning material be cut into a flat pad with surface area A and thickness T. Support on this pad a weight, W, in such a fashion that the static stress σ_s (σ_s = W/A) is uniform. Drop the assembly flatwise onto a rigid surface from the height h.

Following the line originally taken by Mindlin (6), while ignoring air resistance and restricting attention to peak values, we have

$$D^{-1}\sigma_m = \sigma_s \left(\frac{h}{T} + \epsilon\right) . \qquad (4)$$

It is evident that

$$\sigma_m = \sigma_s G , \qquad (5)$$

where G is peak acceleration divided by the acceleration of gravity. Substituting this relation into Eq. (4) and rearranging terms, we have

$$G = J \left(\frac{h}{T} + \epsilon\right) , \qquad (6)$$

where the symbol J, first used by Janssen (7), is the ratio of peak stress developed to the energy per unit volume absorbed by the material at that stress; i.e., $J = \sigma_m / D^{-1}\sigma_m$.

Normally, h is considerably larger than T and ϵ is everywhere less than 1.0 by definition. On this basis, we may write, with good accuracy,

$$G = J \frac{h}{T} . \qquad (7)$$

Obviously, for fixed G and h, T is minimized as J is minimized. The set J can be minimized either when the set has minima when ϵ reaches its maximum set of values or when there is some other distinct set of minima. These latter minima exist provided there be real, nontrivial, solutions in ϵ_o to

$$D\sigma_o(D^{-1}\sigma_o) - \sigma_o^2 = 0 . \qquad (8)$$

Equation (8) is the first derivative of $J(DJ)$ set equal to zero and simplified. For J to be a minimum, it is also necessary for the second derivative to be positive. These conditions being met, there is a nonempty set, J_o,

195

which gives minimum thickness for each value assumed by the parameter ρ.

Yurenka and Giacobine (8) investigated tangent, algebraic and logarithmic elasticities with $\rho = 1.0$. The value of J_o for tangent elasticity duplicated the result previously found by Mindlin (6).

If ϵ_o exists, Eq. (1) states that there corresponds a set of optimum dynamic stresses σ_o. Hence, from Eq. (5), there also exists a set of optimum static stresses. The optimum static stress σ'_s is determined from Eq. (4), and may be expressed with good accuracy as

$$\sigma'_s = \frac{T}{h} \times D^{-1}\sigma_o . \qquad (9)$$

All problems in package cushion design, or the more general problem of nonlinear shock isolator design, may be reduced to the essentials of solving Eq. (6) or (7) for minimum thickness and Eq. (9) for corresponding optimum static stress. In actual practice, however, this is not easy to do. One of the main reasons for this difficulty is that ρ is rarely, if ever, equal to 1.0 or to any other constant. As a result, J_o is not a unique number but, rather, a set of numbers. The practical difficulty of determining ρ, and how the dynamic stress-strain relationship is affected thereby, may be considered one of the prime reasons for lack of progress since the use of $G - \sigma_s$ curves was introduced in 1957 (9).

In 1961 and 1962, however, Soper and Dove (10,11) showed that one could write

$$J = f\left(\frac{\sigma_o h}{T}, \ \frac{h}{T}, \ \mu\right) \qquad (10)$$

where μ is the coefficient of friction. This special scaling law is considered valid, provided the mass of the cushioning is much less than the mass of the cushioned article, the peak acceleration is much greater than the acceleration of gravity, and the local stress states in the cushion are dependent only on time, the angle at which the stress is applied, and the specific variables indicated in Eq. (10). These investigators then listed the following nonexclusive configurations which appear to satisfy the last condition:

1. Material thickness everywhere very small relative to the dimensions of the cushioned component, and no slippage at one or both material surfaces;

2. Flat, uniform cushion, laterally confined or possessing negligible Poisson effect; and

3. Flat, uniform cushion, and lubricated surfaces.

Almost all previous work on cushioning material properties has been concentrated on plane cushions meeting either criterion 2 or 3. In these cases, the coefficient of friction does not enter and Eq. (10) may be written

$$J = f\left(\frac{\sigma_s h}{T}, \ \frac{h}{T}\right) . \qquad (11)$$

It is clear, then, that we may consider $f(h/T)$ to be equivalent to $f(\rho)$.

Plots of J vs energy per unit volume for a selected number of values of h/T will result in considerable reduction in the total number of curves required. In view of the definition of J given in Eq. (7), however, required thickness would appear as a component of the ordinate, of the abscissa, and of each curve in the family, As a result, the designer would have to approach the solution by successive approximations, and the improvement, from his standpoint, does not meet the simplicity criterion, even though relationship of the plots to theory is better than heretofore.

A SOLUTION FOR DESIGNERS

By definition, the optimum point on a J curve is the minimum value assumed by J. This point has an optimum energy per unit volume. Hence, for each value of h/T, dividing actual J by J_o will result in

$$\frac{J}{J_o} = \frac{G}{G_o} = \left.\frac{\sigma_s}{\sigma'_s}\right|_{h/T} = \text{a constant}. \qquad (12)$$

On the basis of Eq. (12), 16 different materials were analyzed. Data were taken from the literature (2-5). Even though different sources were used, the data were combined unless it was apparent that they stemmed from a common source. The envelope of results is shown in Fig. 2.

Most of the materials developed, effectively, a single curve independent of the parameter h/T, but the rubberized hairs did not. While an interesting topic for investigation, this area was not pursued in the face of the finding that all curves practically coincide in the stress

196
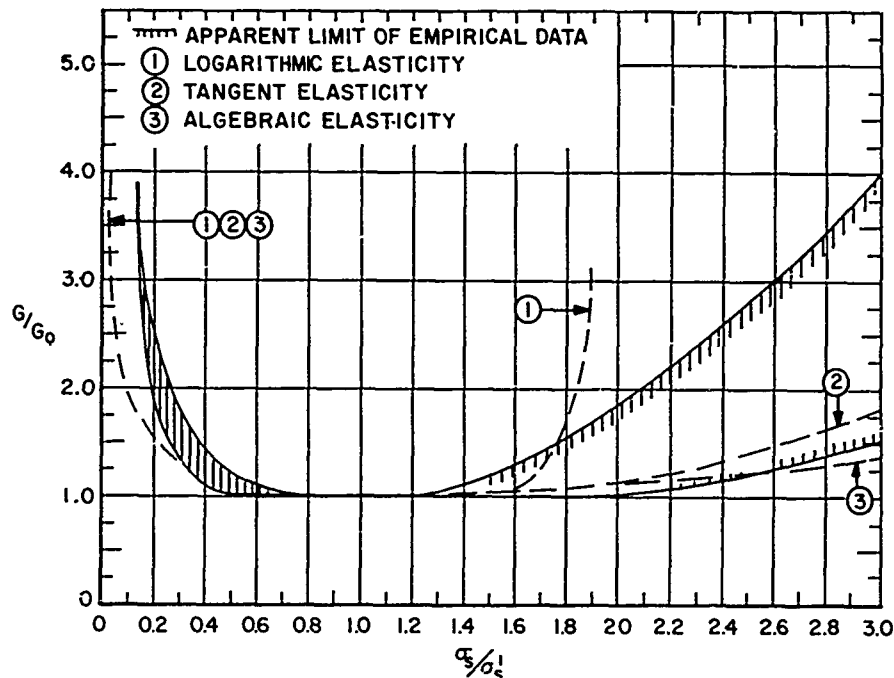
Fig. 2. Envelope of acceleration stress curves

ratio region 0.4 to 1.5 and are flat between 0.7 and 1.3.

In effect, then, Fig. 2 demonstrates that wide static stress variation from optimum can occur without significant effect on peak acceleration. Some time ago, it was shown (12) that, for a given thickness and area, wide variation in material stiffness was possible. The two findings, taken together, indicate that the designer has wide latitude both in selecting materials and in detailing the design. As a minimum, Fig. 2 may be taken as establishing reasonably wide limits on the accuracy with which G_o and σ_s' must be determined for any given material.

Figure 2 is only usable if values for G_o and σ_s' can be found. We turn, therefore, to solving this aspect of the problem. Both solutions are found with the aid of the Soper and Dove relation, Eq. (11).

From the definition of J given in Eq. (6), we have in Eq. (11) the energy per unit volume absorbed by the material as the numerator on the left-hand side and the energy per unit volume imposed on the material on the right-hand side. It appears reasonable, therefore, that we might write

$$\sigma_o = f\left(\frac{\sigma_s' h}{T}, \frac{h}{T}\right). \tag{13}$$

Because of Eq. (5), we now have σ_s' on both sides. Hence, we divide through by σ_s', arriving at

$$G_o = f\left(\frac{h}{T}\right). \tag{14}$$

Substitute for J its equivalent taken from Eq. (7). Dividing both sides by energy per unit volume, we have

$$\frac{G_o T^2}{\sigma_s' h^2} = f\left(\frac{h}{T}\right), \tag{15}$$

which may be further simplified and written as

$$\sigma_s' = f\left(G_o \frac{h}{T}\right). \tag{16}$$

Logically then, we proceed to seeking empirical relations giving substance to Eqs. (15) and (16).

Using the principle of least squares, satisfactory fits of the data for 16 materials can be found by writing Eq. (14) explicitly as

$$G_o = a\left(\frac{h}{T}\right) + b. \tag{17}$$

Values of the constants a and b are given in Table 1. This table also contains computed

197

TABLE 1
Solutions to the Acceleration Equation

Material No.	No. of Data Points	a	b	Standard Deviation	Computed χ^2	Max. χ^2 (P = 0.99)[a]	Corr. Coeff.	Computed (t)	Min. t (P = 0.99)[b]
1	16	3.65	-2.53	2.50	3.620	5.229	0.9853	22.912	2.977
2	19	2.73	2.91	2.14	4.440	7.012	0.9512	14.318	2.898
3	27	2.85	2.71	2.75	7.321	12.198	0.9650	20.025	2.787
4	22	3.98	3.46	1.50	1.424	8.897	0.9983	76.646	2.845
5	26	3.13	-4.61	2.32	10.069	11.524	0.9923	40.749	2.797
6	16	4.67	-9.43	2.58	2.551	5.229	0.9904	28.105	2.977
7	16	2.79	3.74	1.67	1.464	5.229	0.9887	25.941	2.977
8	16	3.72	6.83	1.18	0.600	5.229	0.9968	47.781	2.977
9	28	3.64	0.44	3.50	9.267	12.879	0.9726	22.910	2.779
10	28	3.95	0.25	0.87	0.826	12.879	0.9992	126.823	2.779
11	16	2.37	4.31	2.18	0.310	5.229	0.9813	19.077	2.977
12	8	3.10	13.14	2.96	2.006	2.167[c]	0.9456	8.475	3.707
13	12	3.25	-4.02	2.70	2.220	3.053	0.9788	16.434	3.169
14	7	3.12	6.26	1.78	1.279	1.635[c]	0.9880	15.477	4.032
15	15	4.88	-0.35	1.31	1.123	4.660	0.9965	44.131	3.012
16	21	4.51	1.20	3.52	5.719	8.260	0.9916	34.673	2.861
17	20	4.52	0.68	2.00	2.080	7.633	0.9956	46.067	2.878
18	56	4.54	1.03	2.62	9.536	27.012	0.9934	65.221	2.67
19	78	4.26	2.47	3.11	16.909	43.054	0.9915	68.036	2.64

[a]From R. A. Fisher, "Statistical Methods for Research Workers."
[b]From G. W. Snedecor, "Calculation and Interpretation of Analysis of Variance and Co-Variance," Collegiate Press, Ames, Iowa, 1934.
[c]This value of χ^2 is for P = 0.95.

values of the standard deviation of the regression line, the χ-squared statistic, and a computed value of t for use in Student's t-test. The fit to the available data is sufficiently reliable for design purposes.

Note that 19 materials are identified in Table 1. Materials 15, 16 and 17 are three different densities of polystyrene foam. Forest Products Laboratory data (4) concerning the same materials were combined as a single material and are shown in line 4 of the table. To satisfy curiosity, data for materials 15, 16 and 17 are combined in 18 and all of 18 and 4 are combined in 19. Although the various regression lines do differ, no estimate of the significance of these differences is attempted here.

Working primarily with high energy absorptive materials, Soper and Dove (10) found that J_o tended to become constant and postulated this tendency as a characteristic of many cushioning materials. Equation (17) is an expression for the variation of the elements of J_o. Dividing both sides by h/T we have J_o equal to a constant plus b divided by h/T. Where b is small, J_o may be considered a constant for all practical purposes, even at the low values of h/T used here. In any case, tendency for J_o to become constant is confirmed by these results.

Turning now to relation Eq. (16), the same 16 materials provide a satisfactory least squares fit to the explicit equation

$$\sigma'_s = c \left(G_o \frac{h}{T} \right)^d . \qquad (18)$$

Values of the constants c and d are shown in Table 2, which also contains the standard deviation and the χ-squared statistic. Previous remarks concerning materials 4 and 15 through 19 apply.

Equations (17) and (18) are plotted for material 10 in Fig. 3.

TABLE 2
Solutions to the Static Stress Equation

Material No.	No. of Data Points	c	d	Standard Deviation	Computed x^2	Max. x^2 $(P = 0.99)$[a]
1	16	0.80	-0.23	0.025	0.035	5.229
2	19	0.35	-0.41	0.016	0.065	7.012
3	27	0.21	-0.26	0.017	0.106	12.198
4	22	6.81	-0.40	0.070	0.134	8.897
5	26	0.37	-0.13	0.052	0.297	11.524
6	16	0.41	-0.12	0.038	0.097	5.229
7	16	0.11	-0.18	0.009	0.028	5.229
8	16	0.20	-0.23	0.017	0.072	5.229
9	28	0.72	-0.43	0.011	0.032	12.879
10	28	11.86	-0.48	0.190	0.754	12.879
11	16	0.091	-0.15	0.009	0.030	5.229
12	8	0.069	-0.18	0.004	0.005	1.239
13	12	1.00	-0.23	0.022	0.019	3.053
14	7	0.31	-0.36	0.016	0.023	0.872
15	15	3.54	-0.31	0.101	0.157	4.660
16	21	4.76	-0.32	0.196	1.088	8.260
17	20	3.72	-0.29	0.137	0.417	7.633
18	56	3.68	-0.29	0.164	1.843	27.012
19	78	4.36	-0.32	0.156	2.240	43.054

[a]From Fisher's tables.

DESIGN EXAMPLE

Suppose that a 50-lb object is to be dropped 24 in. with a maximum allowable acceleration of 30 g. Entering the graph with $G_o = 30$, we find h/T is 7.5. Thickness for a 24-in. drop height is 3.2 in. The corresponding value of $G_o h/T$ is 225 for which the indicated optimum static stress is 0.91 psi. From this the required area is 55 sq in.

Because meeting a requirement for exactly 3.2 in. of thickness may prove awkward in practice, several other thickness options are examined in Table 3. Note that a surface area of 50 sq in. and a thickness of 3 in. results in a maximum acceleration of 32 g. Given the usual uncertainty concerning maximum acceleration permissible in package design situations, and making due allowance for shock mitigating effects of the outer container, this combination provides minimum cushion volume for the particular conditions with this material.

Note that, in Fig. 3, the variable $G_o h/T$ must be formed from the first regression line. Attempts should not be made to work backwards in the static stress line.

IMPLICATIONS

The results obtained are essentially empirical and, therefore, generalizing could be questionable. Nevertheless, it seems clearly established that three simple curves can be substituted for an infinite continuum of curves, inadequately, and redundantly, sampled by some 28 curves as exemplified by Fig. 1.

As a result of this conclusion, it appears that the available handbooks and design data (2-4) should be revised to reflect the results obtained here. Further, the basic test method specification (13) should be revised to the extent of changing the method of reporting the results obtained.

The military specification for cushioning materials (14) should be revised to abandon an awkward classification of materials based on performance of a limited number of thicknesses at a single drop height.

With the foregoing suggested changes in existing approaches out of the way, let us turn to some of the more obvious limitations of the approach taken in this paper. These limitations

TABLE 3
Variations in Cushion Thickness and Area[a]

Parameter Calculated	Value			
A. Original computations:				
1. Cushion thickness, in.	3.00	3.20	3.25	3.50
2. h/T for 24-in. drop	8.0	7.50	7.38	6.86
3. Indicated G_o for step 2 h/T	32	30	29	27
4. Steps 2×3 to give $G_o h/T$	256	225	214	185
5. σ'_s corresponding to step 4 value	0.89	0.91	0.93	1.00
6. Area required for 50-lb wt, sq in.	56.2	55.0	53.7	50.0
B. Effect of setting area at 60 sq in.:				
1. Static stress ratio	1.07	1.09	1.12	1.20
2. Probable acceleration, from Fig. 2	32	30	29	27.5
C. Effect of setting area at 50 sq in.:				
1. Static stress ratio	0.89	0.91	0.93	1.00
2. Probable acceleration	32	30	29	27
D. Comparative cushion volumes:				
1. Volume from A	169	176	174	175
2. Volume from B	180	192	195	210
3. Volume from C	150	160	162	175

[a]Material No. 10, 24-in. drop, 50-lb weight, 30 g design goal.

are relatively few in number, but they are substantive:

1. Secondary data, processed for publication, were used for the curve matches found here. Future work should be done with original data now that an approach is indicated. In any case, however, reduction in the total quantity of data required to describe a material for preliminary design purposes should be possible.

2. Most of the data were obtained using constant surface area cushions in which the thickness was varied. While acceptable matches were found, even with 6-in. thick materials in the sample, there is no guarantee that such thicknesses do not represent a significant variable.

3. Many of the materials are open-celled plastics. Hence, ability of air to escape might very well affect the results obtained with a specific design. The previous limitation is thus partially restated here. Also open to question is what will result when the sides of the cushion are partially or totally sealed, a problem explored in preliminary fashion by Gigliotti (15). Objections 2 and 3 can be

restated as an intuitive disquiet resulting from ignoring the theory of models when there is insufficient experimental evidence that it is safe to do so with these materials.

4. Each sample analyzed was a flat cushion in the shape of a rectangular parallelepiped. Other shapes should be investigated. Soper and Dove (10,16) have shown that numerical shape factors can be found, at least for hemispherical systems. For one particular material, not analyzed in this paper, this factor was found to be 0.81.

5. These results are limited to single degree of freedom systems. Obviously, multiple degrees of freedom, such as are found in rotational drop tests, introduce new problems which remain to be investigated.

6. All of these data are for room temperature conditions. It is well known that most elastomeric materials are sensitive to wide temperature changes. Temperature variation data usable in package design are limited, although the curves developed by Schuler (17) have merit. Useful data should be more readily attainable by concentrating on the optimum points of the J curves.

$$G_0 = 3.95\left(\frac{h}{T}\right) \pm 25 \quad \text{STD DEV} = .87 \quad \text{CORR COEFF} = .999$$

$$\sigma_s^! = 11.86 \left(G_0 \frac{h}{T}\right)^{-48} \quad \text{STD DEV} = .19.$$
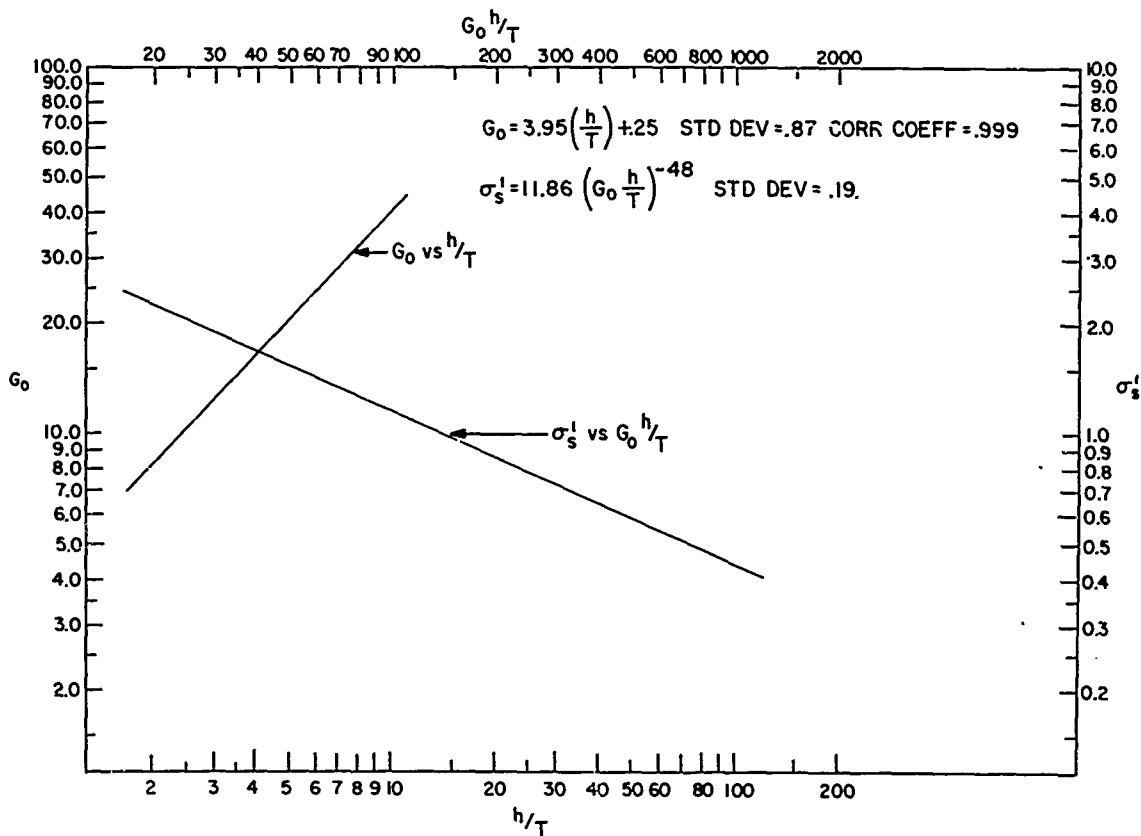
Fig. 3. Design curves for material 10

7. All of the materials exhibit time sensitivity in their dynamic stress-strain relationships. While the use of empirical curves is a helpful way around this dilemma, such usage does not give a clear picture of total performance sufficient to predict behavior beyond the limits of the experimental data. Since these materials are also temperature sensitive, it would appear necessary to determine their viscoelastic behavior. Burgess (18) has shown how the complex dynamic modulus can be converted to mechanical impedance and the latter techniques used for response prediction. At present, this would seem the direction that package cushioning research should take.

All of the foregoing constitute gaps which remain in our knowledge of the behavior of nonlinear isolators. It is hoped that the simplified design technique developed in this paper will permit investigators to accept the challenges posed by these gaps.

ACKNOWLEDGMENT

REFERENCES

1. W. E. Humbert and R. G. Hanlon, Package Engineering, April 1962

2. P. E. Franklin and M. T. Hatae, Ch. 41, Shock and Vibration Handbook (C. M. Harris and C. E. Crede, Eds.) (McGraw-Hill, New York), 1961

3. M. E. Gigliotti, "Design Criteria for Plastic Package Cushioning Materials," Plastic Rept. No. 4, Dec. 1961

4. MIL-HDBK-304, Package Cushioning Design Handbook, 25 Nov. 1964

5. R. K. Stern, Modern Packaging (Dec. 1959)

6. R. D. Mindlin, Bell System Tech. J., 24: 353 (July-Oct. 1945)

7. R. R. Janssen, "A Method for the Proper Selection of a Package Cushion Material and Its Dimensions," North American Aviation Rept. NA-51-1004, 1952

8. S. Yurenka and C. R. Giacobine, "The Selection of Package Dimensions Based on Optimum Cushion Factors," Douglas Aircraft Co. Testing Div. Rept. No. Dev-2128, July 1956

9. O. S. Kerstner, "General Principles of Package Design; Part I — Cushioning," Northrop Aircraft Rept. No. NAI-57-187, Feb. 1957

10. W. G. Soper and R. C. Dove, "Data Presentation for Cushioning Materials," Paper No. 27-4, 17th Annual Tech. Conf., Soc. of Plastics Engrs., Jan. 1961

11. W. G. Soper and R. C. Dove, J. Appl. Mech., 263 (June 1962)

12. G. S. Mustin, Shock and Vibration Bull. No. 28, Pt. 4, p. 79, 1960

13. ASTM Method D 1372-55, 1955

14. Military Specification MIL-C-26861

15. M. E. Gigliotti, Modern Packaging (Sept. 1960)

16. W. G. Soper and R. C. Dove, Shock and Vibration Bull. No. 28, Pt. 4, p. 65, 1960

17. S. C. Schuler, "Recent British Developments in Package Cushioning and the Design of an Impact Testing Machine and a Dynamic Tester," Royal Radar Establishment Memo No. 1712, 1960

18. J. C. Burgess, WADD Tech. Rept. 60-671, Oct. 1960

DISCUSSION

Mr. Zell (Picatinny Arsenal): I have had a peripheral acquaintanceship with the development of some of the problems that Gordon has indicated. I feel that there was a certain polemical air in the paper, which I think is unfortunate. In some of the approaches used, the people who were involved were generally well aware of the many existing limitations, but felt that these limitations should have been tackled to provide some order where there was chaos. I do not feel that the work of Forest Products Laboratory in assembling the Packaging Handbook should be denigrated. Although the rationalization of the data presented here is an extremely valuable approach toward simplification of the problem, I think that we should be careful in the parameters which we use to rationalize. The validity of any basic design approach is strengthened when the parameters are those which bear immediate relationship to the problem at hand. I think that nondimensional parameters should reflect something that is intrinsic to the nature of the material itself. The factor j, that was mentioned, which has been known in the development of the literature as cushion factor, is actually a shape factor. Thus, it is basically a general characterization of the nature of the stress-strain material, whether the j is static or dynamic. I think that this is one parameter that should appear in the basic presentation. Before we go off half-cocked and try to digest the voluminous data admittedly present, we should give some judicious consideration to finding rationalized parameters that have immediate application to the problem. For example, the cushion factor or the shape factor could be inverted and characterized as efficiency. This has direct significance to the engineer. I have not had time to digest this entire paper, but I am not convinced that the parameters which would seem to provide the best rationalization are necessarily the ones that we should put foremost into the minds of the people using these materials. I think this bears some discussion.

Mr. Mustin: In any investigation one usually finds himself with a set of numbers. After these data have been run through the computer and the results analyzed, it may appear that it could have been done better in another way. Now the first curve, g vs h/t, is actually, and is so identified in the written paper, a plot of the variation of the elements of the cushion factor, or Janson's j. In deriving the second curve, σ'_s as a function of optimum acceleration times h/t, I was at liberty, but did not realize it at the time, to have plotted it as a function of h/gt, which is j^{-1}, or the efficiency factor that you mentioned. I still stand on the proposition that we are able to substitute two straight lines for a multiplicity of lines.

* * *

OPTIMAL SHOCK ISOLATION SYNTHESIS

T. Liber and E. Sevin
IIT Research Institute
Chicago, Illinois

The problem of optimum shock isolator synthesis, in the sense of
minimizing the relative isolator displacement for a prescribed level of
input acceleration attenuation, has been formulated and solved for
single degree of freedom systems. The methods of dynamic program-
ming and linear programming are found applicable to a discrete ver-
sion of the problem; the latter technique was more efficient. The opti-
mal isolator is active, possessing the characteristics of "bang-bang"
control. Results of optimal isolator performance are obtained for four
types of input shock wave forms. These results, expressed as a rela-
tionship between limiting values of relative isolator displacement and
mass acceleration, permit direct determination of the margin for im-
provement existing between the optimal and any specified candidate
isolator design. The dependence of the optimal isolator performance
on the detail of the isolator function and the input shock wave form is
discussed.

INTRODUCTION

Generally speaking, the function of shock
isolation is to attenuate the motion environment
transmitted from a base structure to its inte-
rior components. Often the principal design
requirement is to reduce peak transmitted ac-
celerations to tolerable levels; this is accom-
plished by some form of relatively low-
frequency mechanical system interposed be-
tween the base structure and the interior
component. Besides achieving a specified level
of acceleration attenuation, the designer also
may be required to limit relative velocity and
displacement and to accomplish all this at low
cost and high reliability. Obvious counterparts
to this problem exist in the design of elec-
tronic, pneumatic, and hydraulic systems
subject to severe external excitations.

While the designer may seek to achieve an
isolator whose performance is optimum within
a set of imposed constraints (few of which may
be expressed in quantitative terms), practical
considerations often serve to restrict his atten-
tion to a very limited number of candidate iso-
lator concepts. This being the case, it is un-
likely that his final solution will be optimum in
any general sense. Perhaps of greater impor-
tance is the fact that the designer remains ig-
norant of the extent to which the performance
of his system approximates that of the optimum.
Thus, while he can generally assume that

improvement is possible, he almost never
knows whether the margin for improvement
makes further consideration practically
worthwhile.

The path to improved design methodology
would appear to lie in the direction of general
synthesis techniques, whose power have been
amply demonstrated in control theory and cer-
tain structural design problems. The practi-
cality of such an approach for shock isolator
design is the subject of this paper. While the
discussion henceforth could proceed along
strictly mathematical lines, we prefer to estab-
lish a setting within the context of a highly
practical design situation. This will be the de-
sign of shock isolation systems applicable to
protective construction, a problem area of in-
creasing importance in the development of
hardened military facilities, such as under-
ground missile launch sites and command and
control centers. Our results, of course, are by
no means limited to these applications.

Shock isolation systems for underground
facility application usually must satisfy two
main operational requirements, aside from cost
and reliability. Firstly, the interior components
to be isolated from the effects of the blast-
induced shock environment incident on the con-
taining structure are mostly acceleration sensi-
tive, so high levels of acceleration attenuation
must be achieved at any expense. This inevitably

leads to low-frequency isolation systems, which produce comparatively large displacements of the isolated component relative to its containing structure. Often the interior dimensions of the structure (e.g., missile silo) are controlled by the "rattlespace" requirement for shock-isolated components. As the overall facility cost generally is a rather sensitive function of structure volume, the practical desire to reduce rattlespace is clear. Therefore, reduction of the rattlespace requirement is the second principal design consideration.

In this context the general isolator design problem can be expressed in the following manner: "Out of the totality of possible isolator concepts, select one which (for a given input) achieves a specified level of acceleration attenuation and provides the minimum rattlespace."

This would appear to be the most simple and direct formulation of the design problem and, frankly, it has puzzled us for some time that the designer does not instinctively think in such terms. There is, of course, no doubt that he traditionally does not approach the design problem in this way, and the mere fact that he may not be able to discern the solution seems a wholly inadequate excuse; if he cannot, there are many who can. In this paper we develop the solution to precisely this problem for single degree of freedom systems and compare the optimum performance with that of conventional isolator designs. It should come as no surprise that there can be considerable room for performance improvement over conventional designs. Insofar as the solution techniques are concerned, they do not appear to be limited to the kinematically simple systems considered, and we would look to numerous developments along these lines.

PROBLEM FORMULATION

Equation of Motion

The single degree of freedom system considered is shown in Fig. 1a. The "isolator" g is

interposed between the mass (element to be isolated) and the movable base which is subject to the prescribed shock excitation $y(t)$. The displacement of the mass is denoted by z, measured relative to a fixed frame of reference. The displacement of the mass relative to the base is denoted by x, where $x = z - y$.

The equation of motion for unit mass is

$$\ddot{z} + g = 0 . \qquad (1)$$

The initial conditions will be taken as*

$$z(0) = \dot{z}(0) = 0 . \qquad (2)$$

The kinematic conditions are

$$z = x + y ,$$

$$\dot{z} = \dot{x} + \dot{y} , \qquad (3)$$

$$\ddot{z} = \ddot{x} + \ddot{y} .$$

We will require that the input acceleration $\ddot{y}(t)$ and input displacement $y(t)$ be bounded in the time interval of interest. (It is not necessary that $y(t)$ be bounded beyond the time of interest, since the base could subsequently undergo a uniform velocity.) While it does not affect the formulation of the problem, we will subsequently restrict attention to inputs which ultimately return the base to rest; i.e., either $\dot{y}(t) = 0$ for all $t > T$; T finite, or $\dot{y}(t) = 0$ as $t \to \infty$.

The above equations may be considered a nondimensional formulation, where the dimensional quantities are as follows:

$$z = \bar{z}/D_o , \quad x = \bar{x}/D_o , \quad y = \bar{y}/D_o ;$$

$$t = \bar{t} \sqrt{\frac{k_o}{mD_o}} ;$$

---

*The analysis easily can be extended to the more general case of $\dot{z}(0) = $ constant.

(a.) SHOCK ISOLATOR
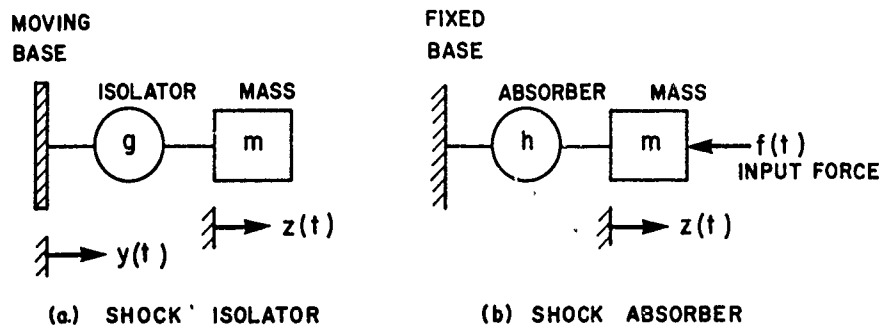
(b) SHOCK ABSORBER

Fig. 1. Single degree of freedom shock isolator and absorber model

204

and

$$g = \bar{g}/k_o \, .$$

In these relations, the "barred" quantities are of physical dimension; m is the mass, and D_o and k_o are the scale factors for the input shock and the isolator function, respectively. The dimensional forms of Eqs. (1), (2), and (3) are

$$m\bar{z}'' + k_o g = 0 \, ,$$

$$\bar{z}(0) = \bar{z}'(0) = 0 \, ,$$

and

$$\bar{z} = \bar{x} + \bar{y}(\bar{t}) \, ,$$

where the primes denote differentiation with respect to real time $\bar{t}$. The nondimensional notation will be used throughout the paper.

Definition of Optimum Isolator

We consider that the optimal isolator is the isolator function g having the property that, for a prescribed shock input $y(t)$, either (a) the maximum relative displacement of the mass does not exceed a prescribed bound and the maximum absolute acceleration of the mass is minimized, or (b) the maximum absolute acceleration does not exceed a prescribed bound and the maximum relative displacement is minimized. In more precise terms, we desire to find the function g such that either

$$\max_{[t]} |x| \leq D \, , \text{ a constant} \, ,$$

and

$$\max_{[t]} |\ddot{z}| = \text{a minimum} \, ,$$

(4a)

or

$$\max_{[t]} |\ddot{z}| \leq A \, , \text{ a constant} \, ,$$

and

$$\max_{[t]} |x| = \text{a minimum} \, .$$

(4b)

In each case, z is the solution of Eqs. (1) and (2), x is given by Eq. (3), and the input function $y(t)$ is prescribed in the interval $0 \leq t < T$. In addition, we require all velocities and displacements to be continuous. The formulation is intended to admit bounded discontinuities in the accelerations.

It can be shown (1,2) that these two formulations are reciprocal in the sense that either leads to the same min-max values. In other words, if the solution to Eq. (4a) with prescribed

D yields a $g*$ and min-max $|\ddot{z}| = A$, then the solution to Eq. (4b) with A prescribed and the same g^* will yield min-max $|x| = D$. Therefore, we may use A and D to denote either bounds on the prescribed mass acceleration or isolator displacement, or their respective min-max values associated with $g*$.

The desired function $g*$ will be referred to as the "optimum isolator" for the prescribed input since its response as characterized by maximum mass acceleration and relative displacement (rattlespace) is the best possible. The relationship thereby established between the lower bounds on relative displacement D and absolute acceleration A will be referred to as the "optimal (isolator) performance" for the prescribed input.

Characterization of Optimal Isolator

We have not yet indicated a specific functional dependence of the optimal isolator, and there would appear to be several choices available. It might seem most natural to seek a representation of g in terms of the (relative) state variables x and $\dot{x}$; that is, $g = g(x, \dot{x})$. Another choice might be to introduce a set of control variables u_1, or inspection of Eq. (1) might suggest seeking g as an explicit function of time; i.e., $g = g(t)$.

It is easily shown that an a priori assumption of the form $g = g(x, \dot{x})$ does not lead to a well set problem; that is, a unique solution for the optimum isolator possessing this form cannot be obtained. This result may be demonstrated either through an analytical argument within the context of the calculus of variations (2), or by means of the following heuristic argument.

Assume that the desired optimum isolator has been found in the form $g = g*(x, \dot{x})$. This may be represented by a surface in the $(x, \dot{x}, g)$ space as shown in Fig. 2. Associated with $g*$, the optimal response is given by $x = x*(t)$ and $\dot{x} = \dot{x}*(t)$, which corresponds to some curve C, in the $(x, \dot{x})$ plane (phase plane) of Fig. 2, as shown. Now $g*$ may be thought of as an explicit function of time since

$$g*(x, \dot{x}) = g*[x*(t), \dot{x}*(t)] = G*(t) \, .$$

The function $G*(t)$ represents a curve in the $(x, \dot{x}, g)$ space which is the intersection of a right cylinder erected on C with the $g*$ surface. But as nothing has been said concerning the explicit functional form of $g(x, \dot{x})$, there may be many such surfaces containing $G*(t)$; e.g., $G(t)$
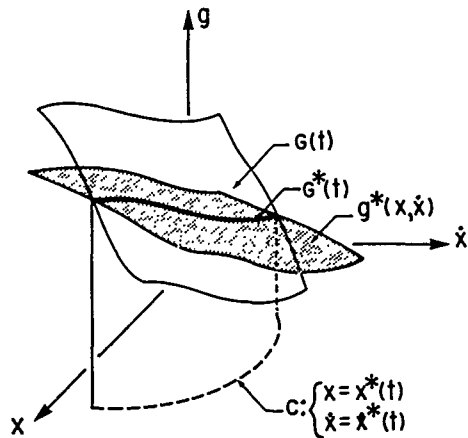
Fig. 2. Characterization of
optimum isolator

as shown in Fig. 2. Hence, there cannot be a unique expression for $g*$. It will be noted that this argument does not really depend on the specific form of the optimization problem as given by Eqs. (4a) or (4b). The situation is different of course as one further constrains the class of isolator functions under consideration, such as by introducing a set of control variables or by selecting an explicit functional form for g. However, it does not suit our purposes to do so at this time. As a result we must be content to seek the optimal isolator as an explicit function of time, which we will continue to call $g*(t)$. The implications of this from the point of view of practical isolator design will be considered in a later section.

The question remains as to the uniqueness of $g*(t)$. It is clear that for times much beyond that at which the min-max values are achieved, $g*(t)$ might not be unique, since any form of $g(t)$ is acceptable which subsequently does not violate the constraints of the problem. Indeed, it is easily demonstrated that a unique $g*(t)$ does not exist over a general time interval of interest, T. However, all $g*(t)$ which yield the same pair of min-max values, A and D, possess unique characteristics (e.g., constant force increments) over certain subintervals of T. The location and length of these subintervals depend on A or D, the input function $y(t)$, and the initial conditions on $z(t)$. Specific examples of this "quasi-unique" character of $g*(t)$ will be given in the section on results.

Optimum Shock Absorber,
    An Analogous Problem

Another physical problem of essentially the same analytical form as the shock isolator

is that of the shock absorber depicted in Fig. 1b. Here the absorber h is interposed between the mass and a fixed base. The mass is subject to a prescribed force, and the performance requirements generally relate to the mass acceleration $\ddot{z}$, the transmitted force h and/or the mass displacement z. An analogous formulation to that of Eq. (4) then results from finding the absorber function h, which has the property that, for a prescribed force input $f(t)$;

$$\max_{[t]} h \leq H , \text{ a constant} ,$$

and

$$\max_{[t]} \ddot{z} = \text{a minimum} ,$$

where z is the solution of $m\ddot{z} + h = f(t)$ and $z(0) = \dot{z}(0) = 0$ in a prescribed interval of time; z and $\dot{z}$ must be continuous and $\ddot{z}$ must be f-bounded. Of course, other formulations are possible, such as those imposing bounds on displacement and velocity.

The solution to the problem stated is considerably more straightforward than the isolator problem and is reported in Ref. (2). We will not concern ourselves here further with the optimum shock absorber problem.

Limiting Situations

The problem formulated in Eqs. (4a) or (4b) admit of two obvious limiting situations. Consider a prescribed input $y(t)$ and let

$$\max_{[t]} |y| = D_y ,$$

and

$$\max_{[t]} |\ddot{y}| = A_y .$$

Then, with reference to Eq. (4a), if we permit $D = D_y$, min-max $|\ddot{z}| = 0$ which is achieved with $g* = 0$, i.e., an "infinitely soft" isolator, or a constant force spring if gravity effects are to be included in Eq. (1). On the other hand, with reference to Eq. (4b), if $A = A_y$, min-max $|x| = 0$, which implies $g* = \infty$, i.e., a "rigid isolator." Thus, as is perfectly obvious, the required rattlespace approaches the maximum input displacement as the level of acceleration attenuation increases, and, conversely, the transmitted acceleration approaches the maximum input acceleration as the rattlespace requirement tends to zero. Our interest lies in isolator performance between these practical bounds. It may be observed, however, that nonoptimal systems easily can exceed these

206

bounds. For example, if the rigid isolator were thought to be a very stiff, but undamped, linearly elastic element, the transmitted acceleration could be twice as great as the maximum input acceleration, even in a nonresonant situation. Similarly, a low-frequency oscillatory pulse could cause a very soft elastic system to undergo excursions far greater than the maximum input displacement.

Input Considerations

The problem formulation requires only that the input displacement and acceleration be bounded. Otherwise the solution techniques are not influenced by the particular form of the input.

The work reported herein was motivated by application to the shock isolation of equipment within hardened military installations; hence, we were concerned with input wave forms related to ground shock motions induced by high explosive and nuclear detonations. Results have been obtained for four specific velocity pulses whose characteristic forms are shown in Fig. 3.
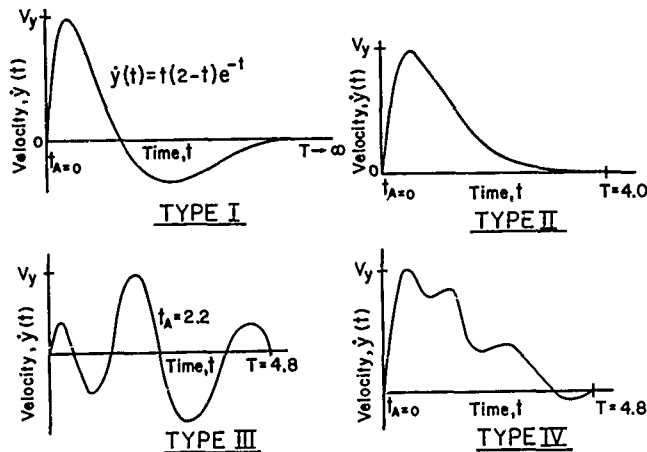
Fig. 3. Input velocity wave form

The Type I input is given by

$$\dot{y}(t) = t(2-t) e^{-t} \quad \text{for} \quad t \geq 0 ,$$

which is derived from $y(t) = t^2 e^{-t}$. It is seen that $y(t) \to 0$, $\dot{y}(t) \to 0$ as $t \to \infty$ and $\ddot{y}$ is bounded and everywhere continuous. The other three velocity wave forms were prescribed as tabular functions and in each case the base returns to a rest position in finite time. The nondimensional wave form parameters are summarized in Table 1.

TABLE 1
Wave Form Characteristics[a]

Type	Duration T	Maximum Values			
		D_y	V_y	A_y	t_A
I	∞	0.5414	0.4612	2.000	0
II	4.0	0.6812	0.4620	1.425	0
III	4.8	0.1614	0.2970	1.020	2.2
IV	4.8	0.8092	0.4630	1.430	0

[a] Max $|y| = D_y$,
Max $|\dot{y}| = V_y$, and
Max $|\ddot{y}| = A_y = \ddot{y}(t_A)$.

Reference Systems

For purposes of comparison with the optimum isolator, we have chosen a damped linear oscillator subject to the same inputs. That is, the reference passive system corresponds to g in Eq. (1) of the (nondimensional) form

$$g(x, \dot{x}) = c\dot{x} + kx .$$

In each case, we have selected the damping and spring rate coefficients which best satisfy the performance constraints given by Eq. (4). Having selected g in this form, we no longer are dealing with the optimal problem, but merely the selection of c and k such that $\max |x|$ takes on its minimum value for prescribed bounds on $|\ddot{z}|$. This could be termed the problem of the optimal linear isolator.

Also, for comparison purposes, we have determined the response of the undamped linear oscillator ($c = 0$) subject to the same inputs. Here, there is no consideration of "optimum," since the response is a unique function of the oscillator frequency.

SOLUTION TECHNIQUES

Available Approaches

During the course of our work, we have identified four separate approaches, each of different degrees of efficiency. These are documented in Refs. (1 and 2) and will be mentioned only briefly here. One of the methods was used to generate most of the results presented, and this approach will be discussed in somewhat greater detail.

The optimal isolator problem would appear to have its natural setting within the framework of the calculus of variations. In fact, our

problem can be identified as a "Mayer Problem," and it is possible to show that it is sufficient that the desired solution $g*(t)$ be either piecewise constant or $g*(t) = -\ddot{y}(t)$ over certain subintervals of time. While this approach discloses a "bang-bang" type of control, it does not yet yield a convenient method of finding either the bounding (min-max) values or the complete details of the optimum isolator function.

The fact that the optimum isolator consists partly of constant force increments suggested a graphical procedure for constructing $g*(t)$. This method is particularly convenient where the initial force increment is the min-max value.

The method of dynamic programming (3) provides a general solution technique whose disadvantage is a relatively major computing effort. This approach requires the problem to be expressed in discrete, rather than continuous, form and leads to the following functional equation:

$$\phi_i(z_i, \dot{z}_i, D) = \min_{[a_i]}\text{-}\max \left[a_i, \phi_{i+1}(z_{i+1}, \dot{z}_{i+1}, D) \right],$$

(5)

where

a_i = assumed constant value of $\ddot{z}$ during the ith time interval; i.e., $(i-1)\Delta t \leq t < i\Delta t$ for $i = 1, 2, \ldots, n$,

$\dot{z}_{i+1}$ = value of $\dot{z}$ at beginning of $(i+1)$st interval (end of ith interval) = $\dot{z}_i + a_i\Delta t$,

z_{i+1} = value of z at beginning of $(i+1)$st interval = $z_i + \dot{z}_i\Delta t + 1/2\, a_i(\Delta t)^2$, and

ϕ_i = minimum value of $\max |a_j|$ for $i \leq j < n+1$ such that $|x_j| = |z_j - y_j| \leq D$ for $i \leq j < n+1$.

The calculation is started by observing that $\phi_{n+1} = 0$ for permissible values of z_{n+1}, and application of Eq. (5) then yields a table of values of ϕ_n. In this fashion Eq. (5) is used as a recurrence relation until ultimately ϕ_1 is calculated. For the stated initial conditions of interest, Eq. (2), the desired min-max value of acceleration is seen to be

$$A = \min\text{-}\max |\ddot{z}| = \phi_1(0,0;D).$$

The function $g*(t)$ is obtained from the table of values of a_i, which are found during application of Eq. (5). This requires a second computational pass, since the appropriate values of a_i are not recognizable until the a_1 corresponding to $\phi_1(0,0;D)$ is determined.

A computational program using this scheme was written for the IBM 7094 computer, and results were obtained for a few values of D with $y(t) = t^2 e^{-t}$ (Type I input). Results of acceptable accuracy were obtained, but only at the expense of dealing with fairly large tables of the ϕ_i. It required approximately 12 minutes of computer time to calculate $\phi_1(0,0;D)$ for each value of the displacement-bound D. While this program did not provide for calculation of $g*(t)$, a somewhat lesser time would be required for the additional calculations.

Linear Programming

The method of linear programming was found to be the most efficient of the techniques investigated. The major achievement, if it may be called that, lay in recognizing that the problem possessed a linear programming formulation. While by way of hindsight, such a formulation indeed is seen to be obvious, we must confess that it took some time for this to occur to us.

As in the method of dynamic programming, we first pose a discrete version of the problem. The total time interval of interest is divided into n subintervals of length Δt. The acceleration $\ddot{z}$ is assumed to be constant over each subinterval; i.e.,

$$\ddot{z}(t) = a_i, \text{ a constant for } (i-1)\, \Delta t \leq t < i\Delta t;$$
$$i = 1, 2, \ldots, n. \quad (6)$$

Denote the value of z at the beginning of the ith interval by z_i, and similarly for the other quantities of interest. Thus, $z_i = z[(i-1)\Delta t]$; etc. The initial conditions of Eq. (2) then become

$$z_1 = \dot{z}_1 = 0. \quad (7)$$

The motion $z(t)$ now is completely determined by the set of numbers a_i and the initial conditions of Eq. (7). We seek that particular set of a_i having the property that

$$|z_i - y_i| \leq D; \quad i = 1, 2, \ldots, n,$$

and

$$\max |a_i| = \text{a minimum}.$$

(8)

That indeed this is a problem of linear programming is shown in the following derivations.

Equation (6) has as its solution

$$\dot{z}_{i+1} = \dot{z}_i + a_i\Delta t$$

$$z_{i+1} = z_i + \dot{z}_i\Delta t + 1/2a_i(\Delta t)^2 \quad \text{for } i = 1, 2, \ldots, n,$$

208

with $z_1 = \dot{z}_1 = 0$. A general term for z_{i+1} involving only the a_i can be shown by induction to be:

$$z_{i+1} = \frac{(\Delta t)^2}{2} \sum_{j=1}^{i} [2(i-j)+1] a_j; \quad i = 1,2,\ldots,n. \tag{9}$$

As a consequence of Eqs. (8) and (9), the a_i must satisfy the following set of $2n$ linear inequalities:

$$\frac{(\Delta t)^2}{2} \sum_{j=1}^{i} [2(i-j)+1] a_j \geq y_{i+1} - D$$

$$\frac{(\Delta t)^2}{2} \sum_{j=1}^{i} [2(i-j)+1] a_j \geq y_{i+1} + D \tag{10}$$

$$\text{for } i = 1,2,\ldots,n.$$

Introduce the quantity ϕ and require that

$$\text{and} \quad \left.\begin{array}{c} a_i \leq \phi \\ \\ a_i \geq -\phi \end{array}\right\} \quad \text{for } i = 1,2,\ldots,n. \tag{11}$$

As Eq. (11) is equivalent to setting $\phi = \max |a_i|$, we may take ϕ to be a linear objective function which we seek to minimize, subject to the constraints of Eq. (10). This essentially completes the linear programming formulation. To put it more in terms of standard linear programming language, we may introduce the slack variable s_i defined by $s_i = \phi - a_i$.

Then Eqs. (10) and (11) become

$$\sum_{j=1}^{i} [2(i-j)+1] s_i - i^2\phi - D\left(\frac{2}{\Delta t^2}\right) \leq -y_{i+1}\left(\frac{2}{\Delta t^2}\right) \tag{12}$$

$$\sum_{j=1}^{i} [2(i-j)+1] s_i - i^2\phi + D\left(\frac{2}{\Delta t^2}\right) \geq -y_{i+1}\left(\frac{2}{\Delta t^2}\right)$$

$$2\phi - s_i \geq 0$$

for $i = 1, 2, \ldots, n$. Our linear programming problem, finally, is to minimize ϕ subject to the $3n$ linear inequalities of Eq. (12). (The first of Eq. (11) implies $s_i > 0$. This need not be stated in Eq. (12), since it may be considered an implied condition in a linear programming problem.)

We have adapted a standard linear program routine for the IBM 7094 to the present problem. The solution time for each value of D and $n = 50$ is about one minute. Output consists of ϕ and the set of a_i which, by Eq. (1), provides the

desired optimal isolator function $g*(t)$. All results presented herein were obtained by this means.

RESULTS

Optimum Isolator Performance

The numerical results characterizing the performance of the optimal isolator for each of the four wave forms considered (Fig. 3) are shown in Figs. 4, 5, 6 and 7 as the curves labeled "Optimum Isolator." Also shown in these figures is the performance of the reference passive isolators, i.e., the optimum damped linear oscillator and the undamped oscillator. The performance of the latter is shown only in part, since otherwise the acceleration scale would have been compressed considerably. The complete performance curve for the undamped isolator is shown in shock spectral form for two of the inputs in Figs. 10 and 11.
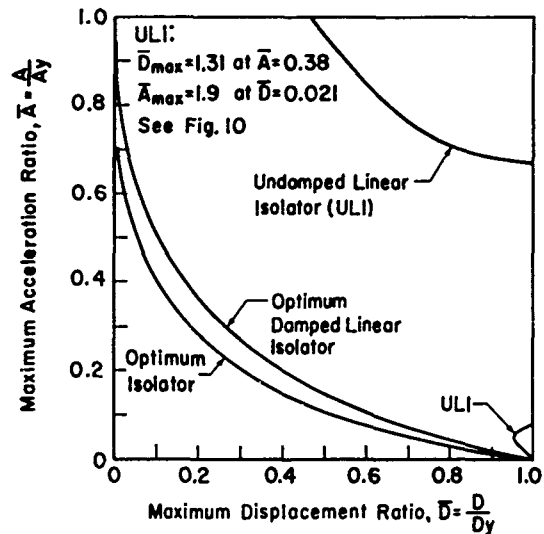
Fig. 4. Tradeoff limit diagram,
Type I input

The results are portrayed as plots of the min-max values of relative displacement D and absolute acceleration A, normalized by the maximum values of the respective input displacement D_y and acceleration A_y. We have termed these tradeoff limit (TL) curves and diagrams for fairly obvious reasons. It will be noted that TL-ratios are independent of the nondimensional scale factors. As was discussed earlier, in the section on limiting situations, the curves necessarily pass through the points $\bar{D} = D/D_y = 1$, $\bar{A} = A/A_y = 0$, and $\bar{D} = 0$,
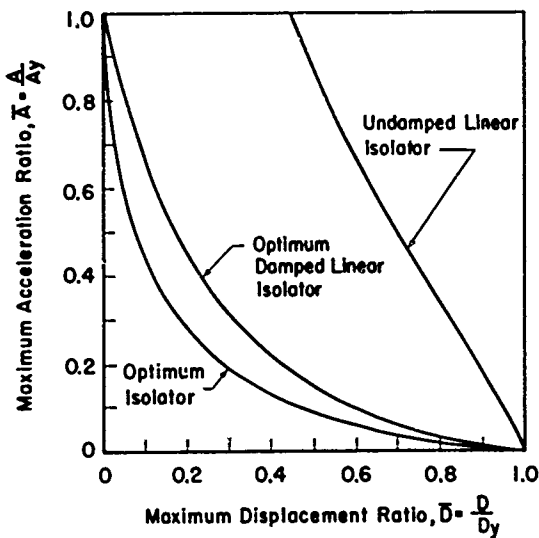
Fig. 5. Tradeoff limit diagram,
Type II input
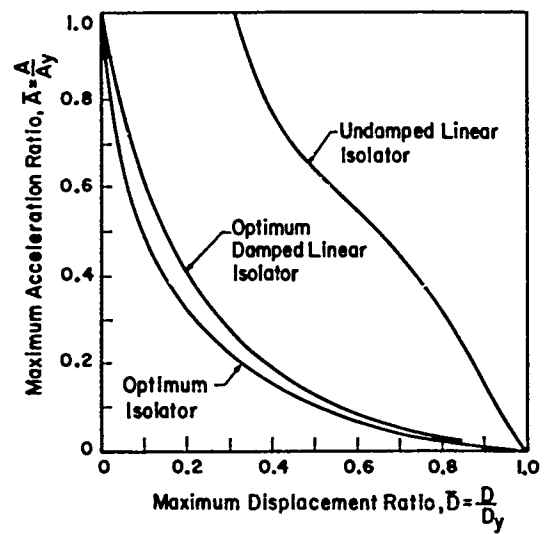
Fig. 7. Tradeoff limit diagram,
Type IV input
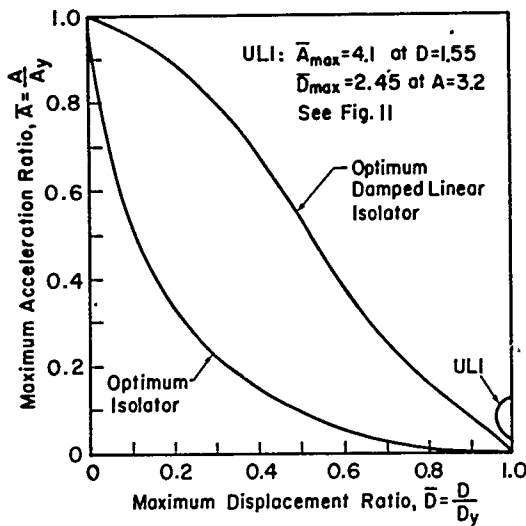
Fig. 6. Tradeoff limit diagram,
Type III input

$\overline{A} = 1$. Each point on the optimum isolator curve $(\overline{D}, \overline{A})$ corresponds to a particular isolator "design," having the property that its (nondimensional) maximum transmitted acceleration is $\overline{A}A_y$, and its (nondimensional) maximum relative displacement (= $\overline{D}D_y$) is the least possible, or, correspondingly, that its maximum relative displacement is $\overline{D}D_y$, and its maximum transmitted acceleration (= $\overline{A}A_y$) is the least possible. The significance of these results to practical isolator design is discussed later.

Optimum Isolator Function

The optimum isolator function $g*(t)$ is known to consist in part of piecewise constant

force increments, as was discussed in the section on available approaches. We also know that a unique characterization of $g*(t)$ is not possible once the min-max values have been achieved. This situation is seen clearly in Figs. 8 and 9 which pertain to the particular solution for Type I input and a displacement bound of $D = 0.1$.

Figure 8 shows the time variation of the relative displacement x. The solid curve up to $t = 5$ (point C) is plotted directly from the output
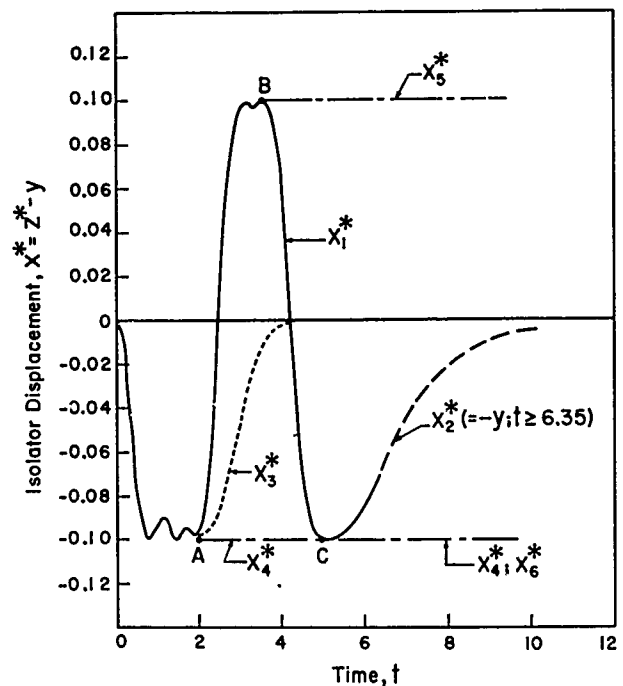
Fig. 8. Optimum isolator displacement

210

Fig. 9. Optimum isolator function

in Fig. 9. The input acceleration $\ddot{y}(t)$ is shown in Fig. 9 for comparison purposes.

For times $t > 1.88$, a variety of solutions for $g*(t)$ are possible, several of which are shown in Fig. 9. The dashed curve labeled g_2^* is to be viewed as a continuation of $g_1^*(t)$ for $t > 5$. Thus,

$$g_2^*(t) = \begin{cases} g_1^*(t) & 0 \le t < 5 \\ 0.055 & 5 \le t < 6.35 \\ 0 & t \ge 6.35 . \end{cases}$$

This function has the effect of bringing the mass to rest at $t = 6.35$ so that at later times, $x*(t) = -y(t)$, as shown by the dashed curve in Fig. 8.

Another possibility, $g_3^*(t)$, is an extension of $g_1^*(t)$ for $t > 1.88$, and is represented by the dash-dot curve g_3^* in Fig. 9, where

$$g_3^*(t) = \begin{cases} g_1^*(t) & 0 \le t < 1.88 \\ -\ddot{y}(t) & 1.88 \le t < 2 \\ -0.075 & 2 \le t < 4.07 \\ -\ddot{y}(t) & t \ge 4.07 . \end{cases}$$

This function has the effect of causing the mass to execute the same motion as the base for $t \ge 4.07$, so that $x* = 0$ beyond this time, as shown in Fig. 8. Other possibilities might include letting $g*(t) = -\ddot{y}(t)$ beyond the time at which $x*$ assumes a bound value. Such times are indicated by points A, B, and C in Fig. 8, where $x_4^* = -0.1$ for $t \ge 2$, $x_5^* = 0.1$ for $t \ge 3.6$, $x_6^* = -0.1$ for $t \ge 5$.

of the linear programming solution which terminated at this time. At later times the relative displacement would continue to oscillate between the bounds ±0.1, despite the fact that the min-max acceleration A occurs initially, this being in the nature of the linear programming formulation.

The isolator function corresponding to this solution is shown as the solid curve, labeled g_1^*, in Fig. 9 up to $t = 5$. The min-max acceleration A = 0.59 persists in the interval $0 < t < 0.75$, at which time the displacement bound is reached. The relative displacement maintains the bound value in the interval $0.75 < t < 1.88$, and then another constant acceleration increment occurs. During the time that $x* = D = 0.1$, we have $\dot{x}* = 0$ and, hence, $g*(t) = -\ddot{y}(t)$. The oscillatory behavior of $x*(t)$ during $0.75 < t < 1.88$ (Fig. 8) results from the inability of the linear programming solution to completely represent $\ddot{y}(t)$ by constant acceleration increments during this interval; the approximation, of course, improves as the time increment, Δt, is reduced. Inasmuch as the actual behavior is known, it was not considered necessary to improve the numerical solution further. The function $g_1^*(t)$ is represented as being identically equal to $\ddot{y}(t)$

DISCUSSION

Three types of questions would appear to interest the shock isolation system designer during the initial phases of his design:

1. What is the margin of improvement offered by the optimal system over some other candidate design?

2. How dependent is the optimal (or near-optimal) isolator performance on the details of the optimal isolator function?

3. How dependent is the optimal isolator performance, and the associated isolator function, on the details of the shock input?

The present results pertain specifically to the first question and permit several inferences

211

to be drawn concerning the third. The matter of isolator function sensitivity can only be guessed at for the present.

With regard to margin of improvement, it is clear that the tradeoff limit curves of Figs. 4 through 7 provide precisely this information. It may be well, however, to show a specific example. Figure 10 shows a conventional shock spectrum for an undamped linear isolator subject to the Type I input. (The numerical values pertain to the nondimensional form of the isolator and input; thus, while the values of frequencies in cycles per second and acceleration in g units indicated on the figure appear unrealistic, they do pertain to practical situations of isolator design for protective construction application. As noted earlier, the normalized form of acceleration and relative displacement performance are independent of the nondimensional scale factors.)

undamped system results in an enhancement, rather than an attenuation, of the input displacement for this input and acceleration (frequency) level. In marked contrast, by means of the optimum isolator* the rattlespace requirement can be reduced to $D = 0.17$ (Fig. 10, point 2) for the same level of acceleration attenuation. This corresponds to a relative displacement attenuation of $\bar{D} = 0.31$, or a percentage improvement of $[(1.3-0.31)/0.31](100) = 320$, which is a factor of three better than that of the undamped system. The only way in which an undamped isolator could meet the rattlespace requirement of $\bar{D} = 0.31$ would be by transmitting an acceleration about 10 percent in excess of the input level (Fig. 10, $\bar{A} = 1.1$, point 3).

The viscously damped linear isolator offers considerable improvement over the undamped system, as can be seen from Fig. 4. Thus, for $\bar{A} = 0.2$, $\bar{D} = 0.4$, which is only about 29 percent
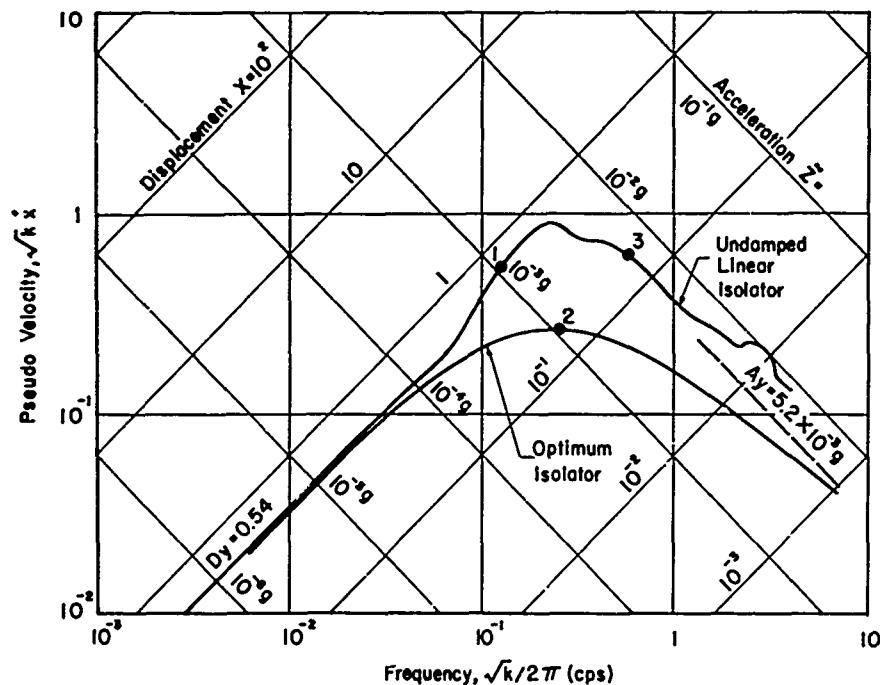
Fig. 10. Optimum and undamped linear isolator
shock spectra, Type I input

Assume that it is desired to reduce the peak transmitted acceleration to 20 percent of the input value. From Table 1, $A_y = 2$, so that in the units of Fig. 10, the desired (nondimensional) acceleration level, A, is $0.2 \times 2/386 = 0.001$ g. If the undamped system of Fig. 10 were to be used as the isolator, the required rattlespace would be $D = 0.7$ (Fig. 10, point 1). This corresponds to a relative displacement attenuation of $\bar{D} = 0.7/0.54 = 1.3$. Thus, the

less effective than the optimum isolator at this level of acceleration attenuation. The margin of improvement becomes relatively less dramatic at increasing levels of acceleration

---

*Neither the frequency nor pseudovelocity scales of the shock spectrum have any significance for the optimum isolator. Rather, the curve merely expresses the appropriate relationship between displacement and acceleration.

212

attenuation, i.e., for extremely "soft" systems. Referring again to Fig. 10, for $\bar{A} = 0.05$, A = 0.00026 g, and the rattlespace requirements for the undamped and optimum isolator differ only by about 10 percent. As is evident in Figs. 6 and 11, the relative inefficiency of the undamped isolator can be greater at all acceleration levels for inputs of a predominant oscillatory nature such as Type III.

We consider now the extent to which the present results contribute to an understanding of the dependence of optimal performance on the input wave forms. Figure 12 is a composite plot of the tradeoff limit curves for the four wave forms considered. (The additional curve in this figure will be discussed later.) Figure 13 is a similar plot for the undamped and optimally damped linear systems. The relatively
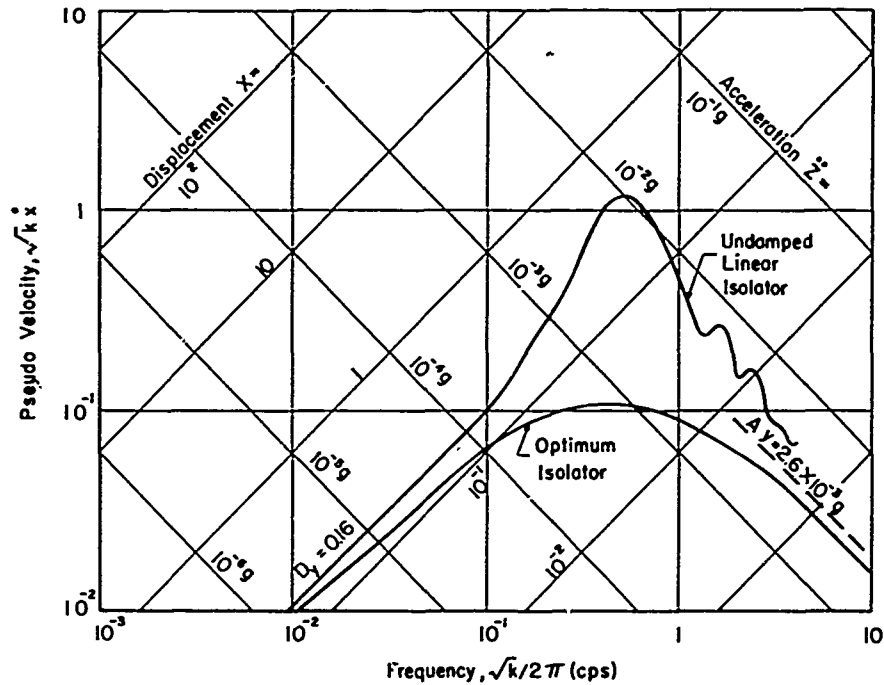
Fig. 11. Optimum and undamped linear isolator shock spectra, Type II input

Generally, then, comparison of isolator system performance, either relative to the optimum or to a more arbitrary standard, is conveniently handled by means of the tradeoff limit diagrams of Figs. 4 through 7. The differences in abscissae between a candidate system and the optimal at prescribed levels of acceleration attenuation is a direct measure of the margin for improvement in rattlespace performance. It also suggests a meaningful way of assigning some sort of performance index to candidate systems. It should be emphasized that combinations of acceleration and relative displacement attenuation levels, which lie in the region between the coordinate axes and the optimal curve, are not physically attainable for the input shock under consideration. That is to say, no isolation concept exists whose performance falls into this region. Such information can be of considerable help to the designer if he should be confronted with unachievable performance criteria.
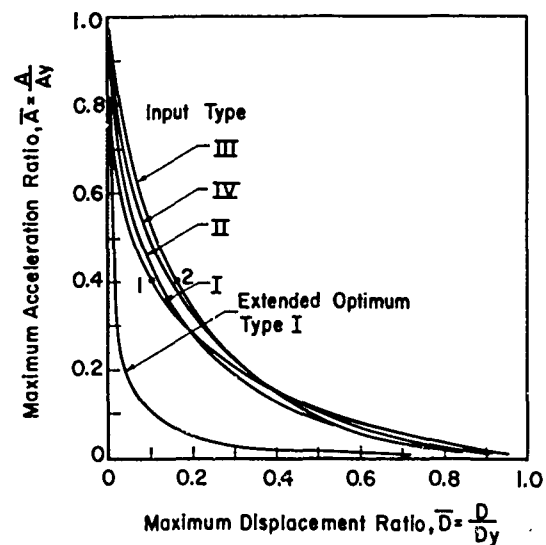
Fig. 12. Influence of input wave form on tradeoff limit curves for optimum isolator

213

small spread of the four curves in Fig. 12 indicates that the optimum isolator performance is relatively insensitive to major variations in the input parameters. As these wave forms are both characteristically different and realistic for certain applications, this result is promising from the design point of view. It must be emphasized, however, that no claim is made to the effect that the performance of an optimum isolator is insensitive to the input, but only that the optimum performance, for each of the inputs considered, do not differ by much. The distinction can be important, as will be described.
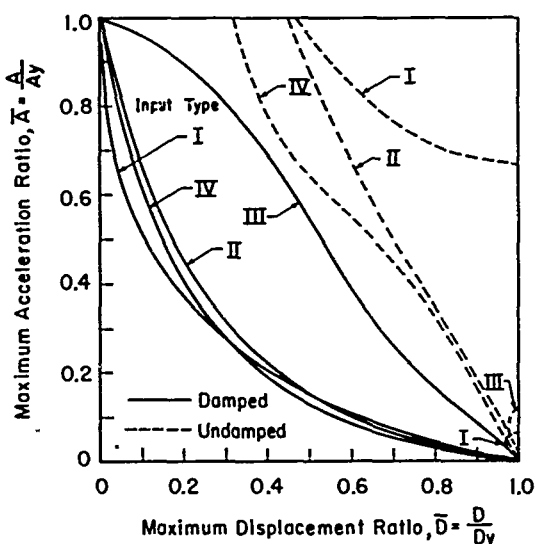
Fig. 13. Influence of input wave form on tradeoff limit curves for undamped and optimum damped linear isolators

Consider some point on one of the curves of Fig. 12, e.g., point 1 for the Type I input. This point, as does every point on the curve, represents the performance of an optimum isolator designed for the indicated level of acceleration and displacement attenuation. If this particular isolator were subject to the Type III input, its performance would plot as some point to the right of curve III; in general, it would not lie on the curve. A point on curve III having the same acceleration attenuation as the first isolator (point 2) would be optimal for wave form III but would be a different isolator than the first. In this example, just where the first isolator would plot on Fig. 12 is not known; all that can be said is that for prescribed acceleration attenuation, point 2 represents a lower bound on the relative displacement performance of the point 1 isolator when subject to Type III input. In this sense, any two of the curves in Fig. 12 may be viewed reciprocally as lower

bounds to the performance sensitivity for the associated inputs. Additional study is required to determine the actual sensitivities.

It should be noted that the distinction between general system performance and specific isolator performance becomes unimportant when the optimal system is intended solely as the basis of performance rating or margin for improvement. Here, one would be quite satisfied to know that the optimal relationship between acceleration and relative displacement attenuation is insensitive to input details, without regard to the sensitivities of particular designs. The present results suggest this to be the case in practical situations, but additional inputs should be considered in a systematic manner.

It is certain, of course, that inputs do exist for which the optimum performance curve must differ appreciably from those shown in Fig. 12. A particular example is discussed below. An extreme case is one in which the input exhibits a small positive velocity for long times after the maximum acceleration response is achieved. Here the maximum input displacement, D_y, can be arbitrarily large, so that the optimal performance curve must approach the coordinate axes, regardless of the values of A and D. This suggests the pragmatic view that input sensitivity be considered for variations in input wave forms about some nominal form, rather than for extreme wave forms unlikely to occur in a given design situation.

So far the optimal isolator has been assumed to start from conditions of rest at the time of arrival of the input shock (Eq. (2)). It is of interest to relax this condition and consider the isolator performance, which is optimal with respect to Eq. (4) and the totality of admissible initial conditions. Since, on physical grounds, the isolator must start from rest at some time, e.g., t_i, this extended problem is identical to the original one, except that the solution is obtained over the interval $t_i \leq t < T$. If we retain the original origin of time, $t_i < 0$, and Eq. (2) is replaced by $z(t_i) = \dot{z}(t_i) = 0$. The desired solution, termed the extended optimum, is shown in Fig. 12 for the Type I input. The improvement over the previous optimal solutions clearly is significant over much of the range of acceleration attenuation.

The concept of the extended optimum, that is, an isolator which is warned of what is to come and able to take appropriate action before the fact, is not inconsistent with the optimum isolator just considered. That, too, was anticipatory in nature and, hence, an active isolation

214

system. However, the extended optimum is not generally as realistic a standard of isolator performance, since it applies only to pre-actuated systems.

We have not as yet obtained specific data concerning the dependency of the optimum performance on the details of the isolator function. Such understanding, of course, is mandatory before serious consideration can be given to specific hardware designs. It must suffice for present to suggest that the optimal performance may not be critically dependent on the isolator function and, in fact, may be rather insensitive to these details. This guess is based on two observations. First, the damped linear isolator was seen to approximate modestly well the optimum performance, despite the fact that its time response is markedly dissimilar to that of the optimal isolator (Fig. 9). Secondly, the graphical argument presented earlier in support

of the non-uniqueness of the optimal isolator function (Fig. 2) seems to make plausible the contention that many classes of isolators can be adapted to approximate reasonably well the desired response function. Clearly, additional study of this aspect is required.

ACKNOWLEDGMENTS

REFERENCES

1. "Optimal Shock Isolation Synthesis," IIT Research Inst. Final Rept. M6084, July 1965; to be published as Air Force Weapons Lab. Rept. WL TR 65-82

2. "Optimum Shock Isolator and Absorber Design Techniques," IIT Research Inst. Final Rept. M6078, April 1965

3. R. Bellman, "Dynamic Programming" (Princeton University Press, Princeton, N.J:), 1957

DISCUSSION

Mr. O'Hearne (Martin Co.): Would you comment on the adaptability of this method for a much larger class of inputs, say a stochastic input?

Dr. Sevin: It would be extremely interesting to look at this approach for an input which is described as a random function. We have not done that yet, but we plan to. To be sure, we have considered only a limited number of inputs and in many instances, one looks at the response to a superposition of a number of inputs. It is interesting, I think, to observe that the very nature of the optimal solution permits one to use superposition. The system may be subject to four different inputs which may occur randomly or, at least, in an unspecified way with time. Generally one would have to consider a superposition of all possibilities. The very nature of the optimal solution implies a trial of each one independently. The best performance for any one of the four would be optimal for any combination of the four. I think that is an interesting observation.

- Mr. O'Hearne: I made the comment because it seemed, in a way, a shame to do such elegant analysis for specified inputs where, in the general situation, one finds they are usually quite arbitrary. ..

Dr. Sevin: Yes, I agree with you. To be sure we seldom know inputs. There is another potential for analysis which is quite different than that which I have mentioned. Consider a system that is optimized with respect to some inputs. Use that optimal solution to pose the mathematical problem of specifying a class of inputs which varies about the one for which the optimal was found. In a general way, these should have certain properties that define them as a family of inputs. Then seek to determine the bounds to the response and the uncertainty in the response of the optimal to a class of inputs. I am pretty sure that problem can be solved.

Mr. O'Hearne: That is very interesting, thank you.

* * *

VIBRATION ISOLATION THROUGH
PNEUMATIC SPRING AND DAMPING

Russel L. Hall
Edgerton, Germeshausen & Grier, Inc.
Las Vegas, Nevada

This paper concerns the passive isolation of harmful shock and vibrations as applied to a relatively large package containing fragile data acquisition equipment. The shock isolator consisted of a lightweight cylinder containing compressed air and a piston which is fully extended at steady state. The air cylinder isolator functions as zero deflection support, spring and damper. Electronic simulation indicated that the air cylinder isolator will more effectively isolate single shock pulses than will other conventional systems.

NOMENCLATURE

M_y Package mass, lb_m

M_y Isolator mass, lb_m

B Linear damping coefficient, $lb_f/ft/sec$

K Spring force, lb_f (nonlinear); spring rate, lb_f/ft (linear)

y Package displacement, ft

x Isolator displacement, ft

z Input displacement, ft

F Force, lb_f

t Time, sec

A_p Piston head area, sq in.

A_s Piston stem area, sq in.

A_d Damper port area, sq in.

k Ratio of specific heat of air, 1.45

g Gravitational constant, 32.2 lb_m ft/lb_f sec^2

ρ Air density, lb_m/cu ft

Y_a Isentropic expansion factor

R Air specific gas constant, 53.36 lb_f ft/lb_m °R

$\alpha, \beta, \gamma,$ C_1, C_2, C_3 Solution constants which depend on problem initial conditions

ω Forcing frequency, radians/sec

P Pressure, lb_f/sq in.

T Temperature, °R

V Volume, cu in.

m Air mass, lb_m

$\dot{m}$ Air flow, lb_m/sec

$\dot{m}_s$ Sonic air flow, lb_m/sec

A_t Venturi throat area, sq in.

v Specific volume, cu ft/lb_m

a, b Real and imaginary parts of a differential equation root

e Natural log base, 2.718

Q Heat, BTU

C_p Specific heat at constant pressure

C_v Specific heat at constant volume

C Coefficient of flow discharge

D Diameter, in.

ϕ Adiabatic expansion factor

INTRODUCTION

This analysis was performed to determine a method of shock isolation for excitations originating through the base of a system. The package of interest resembled a large commercial trailer (Fig. 1) and was designed to be temporarily located at ground level in areas subjected to severe jolting earth movements. Efficient isolation through the air spring damper appeared to require that the nonlinearities associated with the air spring offset the nonlinearities associated with the air damper.
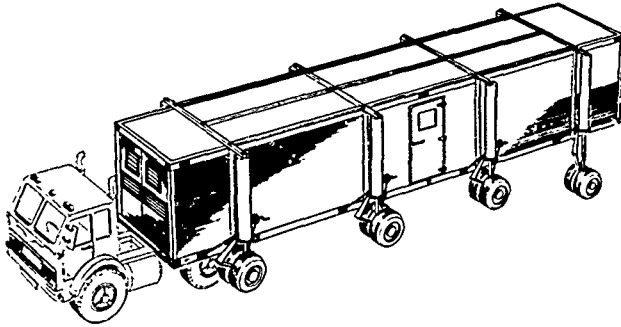
Fig. 1. High resolution trailer
in mobile position

The trailer body, wheels, and air spring damper support were imagined as passive elements arranged as shown in Fig. 2. Linear nodal force balance equations may be written, describing one degree of freedom and lumping all vibration control into one isolator:
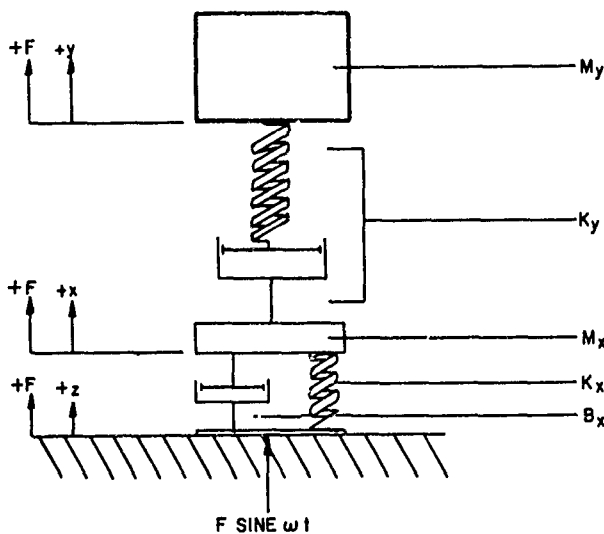
Fig. 2. Isolation through
air spring and damper

$$M_y \ddot{y} = K_y - M_y G , \qquad (1)$$

$$M_x \ddot{x} = B_x(\dot{z} - \dot{x}) + K_x(z - x) - K_y$$
$$- M_x g - A_d(P_1 - P_2). \qquad (2)$$

K_y was simulated as a nonlinear force. All throttling processes were assumed isentropic. Construction materials were assumed to be rigid with the exception of the pneumatic tires. The system was recognized as a nonautonomous system, i.e., a system whose properties are affected by the independent variable, time.

Air damping control was designed to operate in open loop control fashion with fixed unidirectional orifices in the piston head. Air friction was imagined as a thermodynamic irreversibility causing a temperature increase in the throttled air. This damping inefficiency was not included in the electronic analog problem simulation due to the estimated negligible effect on overall system response. Air damping was adjusted so as to isolate most effectively shock pulses in a predetermined range.

INVESTIGATION

Mathematical techniques were used to study the response of the configurated single mass linear system. The package acceleration profile, it was postulated, would be a measure of the isolator efficiency. Three isolator configurations were investigated using linear differential equations having constant coefficients. Figures 3, 4, and 5 represent these systems and their associated acceleration profiles for perturbations noted.

The given specifications required a 40,000 lb_m to be shock isolated from a single strong earth movement. It was required that the package acceleration profile be described by the minimum absolute value for any reasonable isolator. The Electronic Associates, Inc., TR-48 Analog Computer was subsequently used to describe a more detailed multiple mass system employing the pneumatic spring damper. Linear differential equations having nonlinear coefficients were programmed for the electronic computer simulation. Figure 6 illustrates the TR-48 Computer in operation.

Figure 3 illustrates a (air) spring mass system response and typical package acceleration profile after the system was subjected to some predetermined free fall height. The (air) spring was assumed to have zero deflection at steady state:

218
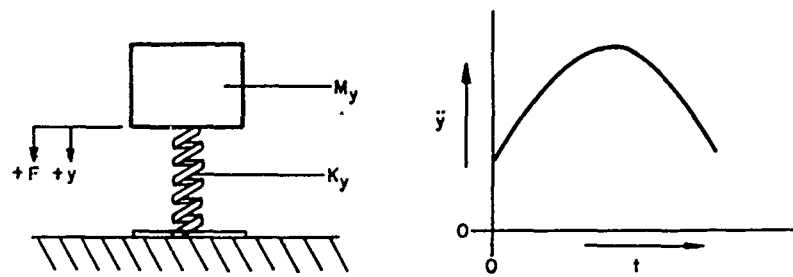
Fig. 3. Isolation through a linear spring
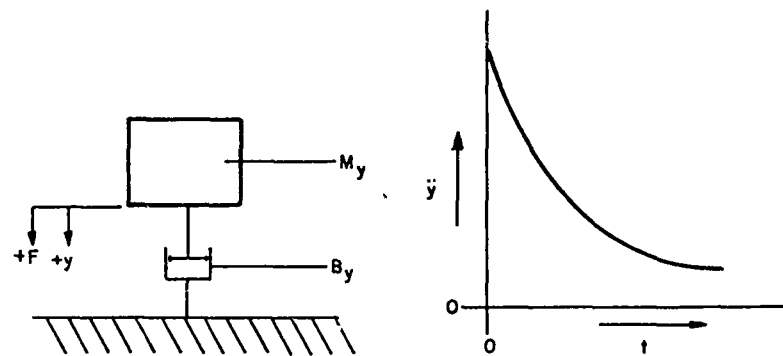
Fig. 4. Isolation through a viscous damper
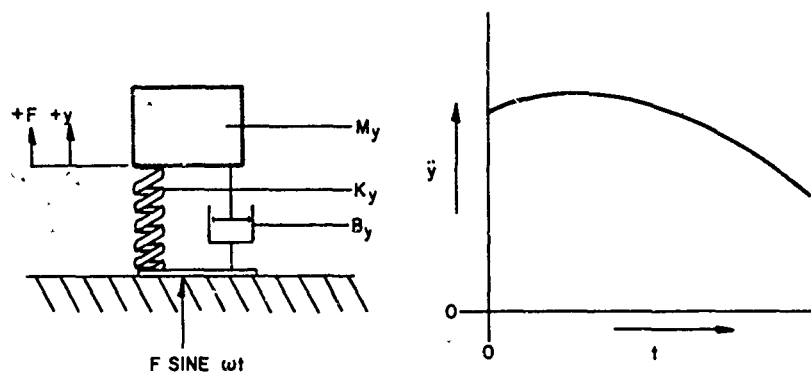
Fig. 5. Isolation through linear spring
and viscous damper

$$M\ddot{y} = Mg - (F + K\dot{y}) , \qquad (3)$$

$$\ddot{y} = -\frac{K}{M} C_1 \sin\left(\sqrt{\frac{K}{M}} + \alpha\right) . \qquad (4)$$

The values of C_1 and α were determined using problem initial conditions.

Figure 4 illustrates a damper mass system response and typical package acceleration profile after the system was subjected, again, to some predetermined free fall height. Since there is no restoring force in this system, it

was assumed that the package would come to a full stop within the single damper stroke:

$$M\ddot{y} = Mg - B\dot{y} , \qquad (5)$$

$$\ddot{y} = -\frac{B}{M} C_1 e \exp -\frac{B}{M} t . \qquad (6)$$

The value of C_1 was determined using problem initial conditions.

The package acceleration profiles derived from Figs. 3 and 4 were considered inefficient

219
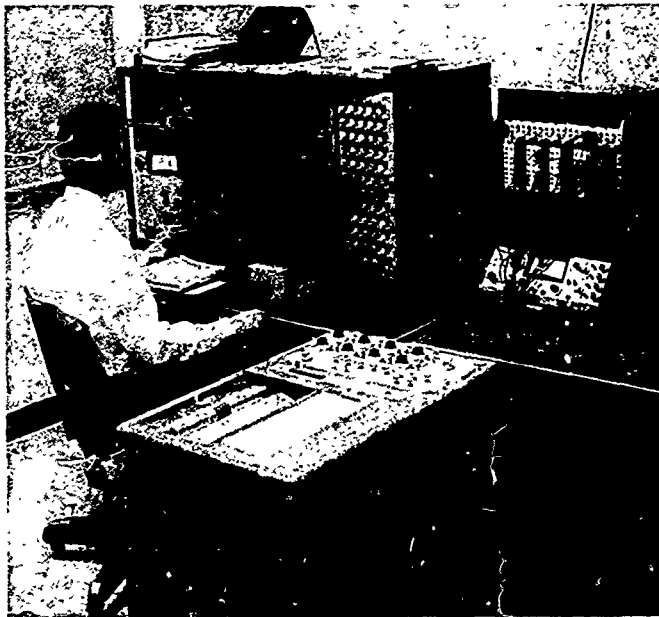
Fig. 6. Analog computer

with regard to the type of isolator used. Figure 5 illustrates the passive elements previously described arranged in parallel to form still another type of isolator. It was assumed that the package base would at no time be separated from the forcing input function. A sinusoidal perturbation was used:

$$M\ddot{y} = (F - Mg) + B(\dot{x} - \dot{y}) + K(x \sin \omega t - y) ,$$

$$y = - C_1 e^{at} b^2 \sin(bt + \alpha) + 2aC_1 e^{at} b \cos(bt + \alpha)$$

$$+ a^2 C_1 e^{at} \sin(bt + \alpha) - \omega^2 C_2 \sin(\omega t + \beta)$$

$$- \omega^2 C_3 \sin(\omega t + \gamma) . \tag{8}$$

The values of C_1, C_2, C_3, α, β, and γ were determined using problem initial conditions.

The acceleration profile described in Fig. 5 was set aside in search of a more efficient isolator.

Logic gave use to the previously investigated spring and damper elements arranged in series. It was imagined that an air cylinder piston combination would physically provide the series configuration desired. Figure 7 illustrates the hardware design of this type of isolator. Functionally, the piston stem provides zero static deflection spring support and the piston head provides bidirectional damping.

As a prelude to the above study, the nonlinearities associated with a (air) spring mass system were studied. Figure 8 illustrates the typical force displacement relationship derived from pure air spring isolation. Analysis was performed according to the familiar isentropic relationship, for a perfect gas, $P = P_o(v_o/v) \exp k$.

For purposes of comparison, time history tapes were made from an electronic analog simulation of the air spring mass system. Figure 9 illustrates the response of the package described above when forced by a single positive sinusoidal pulse having a 4-ft amplitude. The pulse time durations were varied stepwise from 1.43 to 0.21 sec. Figure 10 illustrates the typical (air) spring mass magnification factor as curve ①.

The air cylinder piston configuration previously discussed forms an (air) spring damper. Equations (1) and (2) describe a two-node (mass) system incorporating an (air) spring damper. The following relationships were incorporated into the electronic analog model to describe (air) spring damper nonlinearities:

$$K = A_p P_1 - (A_p - A_s) P_2 , \tag{9}$$

$$P_1 = \frac{m_1 R T_1}{V_1} , \tag{10}$$

$$P_2 = \frac{m_2 R T_2}{V_2} , \tag{11}$$

$$m_1 = m_o - m_2, \tag{12}$$

$$m_2 = \int_0^t \dot{m} \, dt , \tag{13}$$

220

Fig. 7. Wheel strut design

1. CYLINDER ASS'Y
2. SCISSORS TOP HALF
3. SCISSORS LOWER HALF
4. AXLE ASSEMBLY
5. UPPER SHAFT
6. LOWER SHAFT
7. FLAT WASHER
8. COTTER PIN
9. HEX SOCKET SHOLDER SCREW
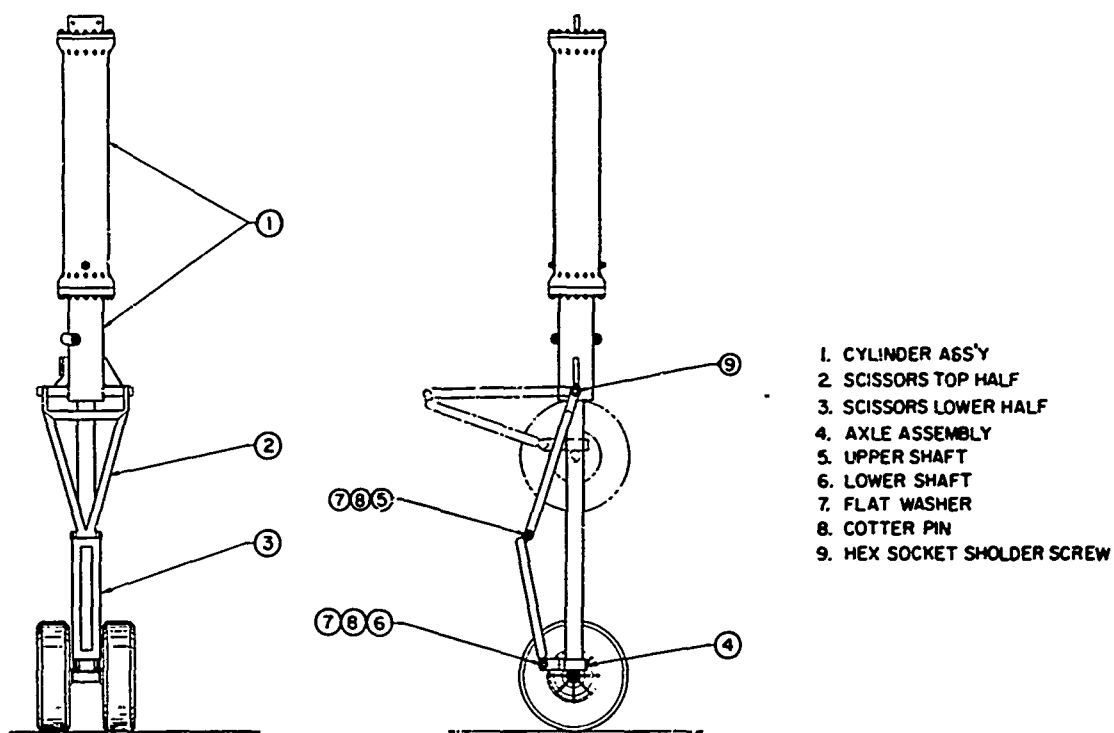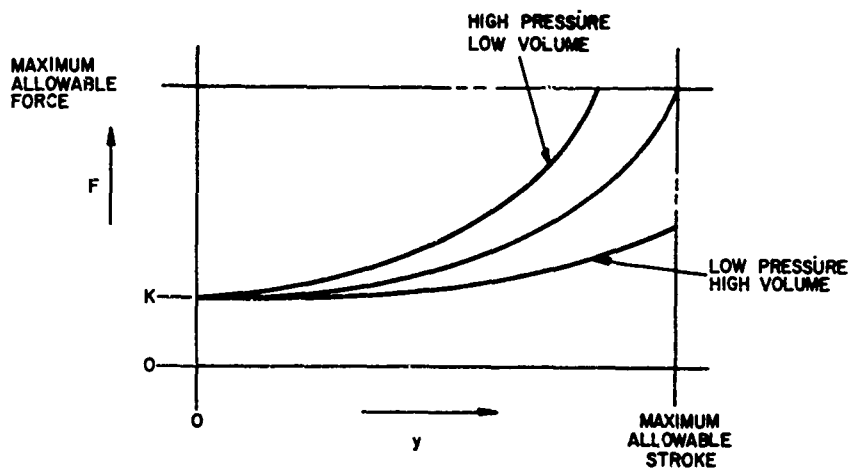
Fig. 8. Typical air spring rate

$$V_1 = V_o - A_p(x - y) ,\tag{14}$$

$$V_2 = (A_p - A_s)(x - y) ,\tag{15}$$

$$T_1 = T_o\left(\frac{P_1}{P_o}\right)^{\frac{k-1}{k}} ,\tag{16}$$

$$T_2 = T_o\left(\frac{P_2}{P_o}\right)^{\frac{k-1}{k}} ,\tag{17}$$

and from Obert (1)

$$\dot{m} = 0.525\,C\,Y_a\,\phi D^2\,[\rho_1(P_1 - P_2)] .\tag{18}$$

The air flow $\dot{m}$ was limited at sonic velocity using the following relationship:

$$\dot{m}_s = \rho A(kgRT) .\tag{19}$$

It was recognized that a pneumatic damping inefficiency does exist for the thermodynamically isentropic throttling process which

221
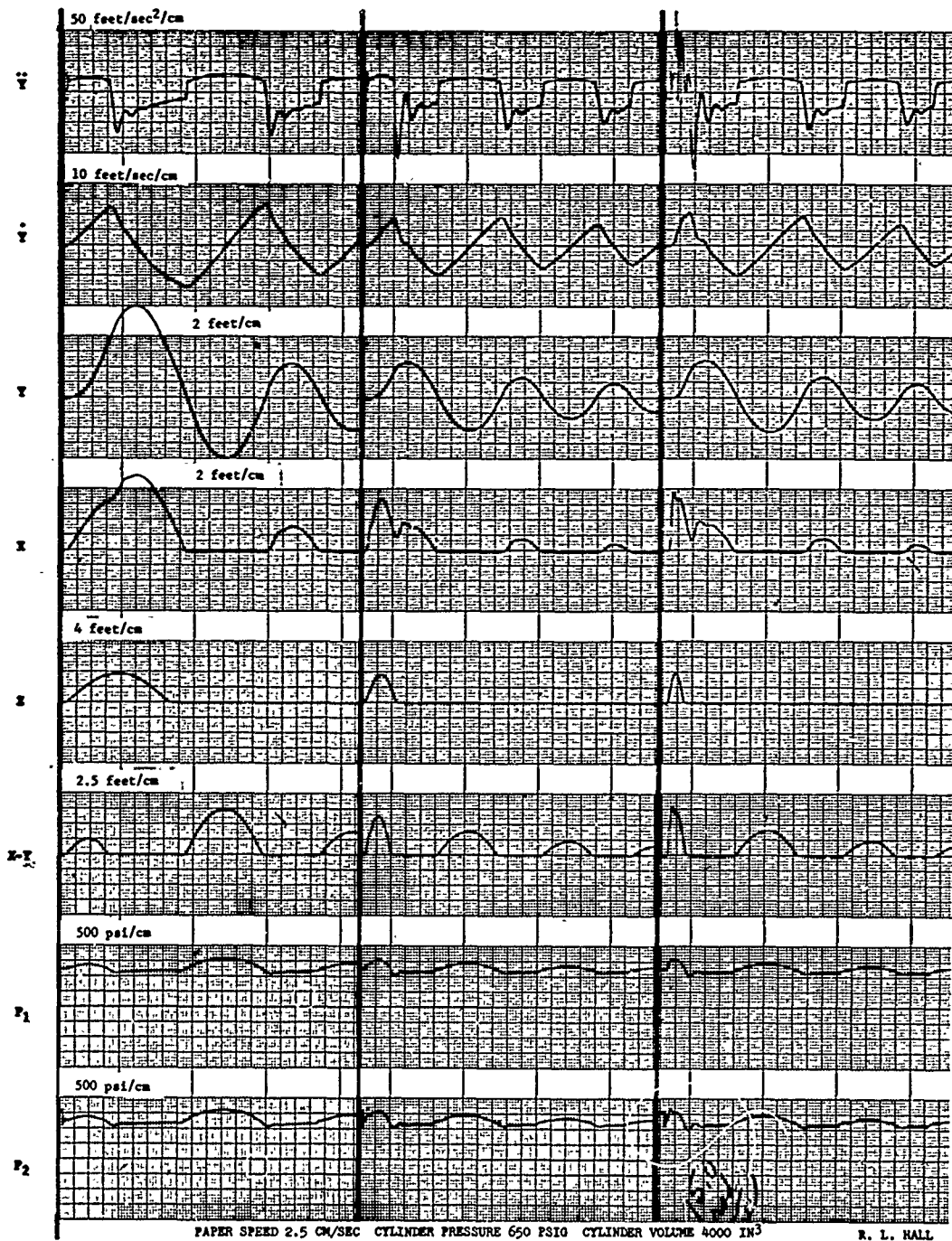
Fig. 9. Response of air spring mass system
to single positive sine pulse

was assumed. This irreversibility was esti-
mated to be insignificant in the overall problem
and was derived as

$$Q = \dot{m}\left\{\left[\frac{R(T_2 - T_1)}{1 - k}\right] - \left[C_v(T_1 - T_2)\right]\right\} \quad . \quad (20)$$

The effects of system damping were stud-
ied by flowing air from one side of the piston
head to the other as the piston moved relative
to the encompassing air cylinder. System

modeling revealed that the series air spring
damper isolation compares favorably with the
conventional parallel linear spring damper iso-
lation when responding to forcing frequencies
below the system natural frequency. At higher
frequencies, the air damper appeared to be less
effective because of the compression of the air
spring. For the above to be true, the piston
head area (air damper) should be designed as
small as possible. Figure 11 illustrates the
response of a system isolated from the base

222
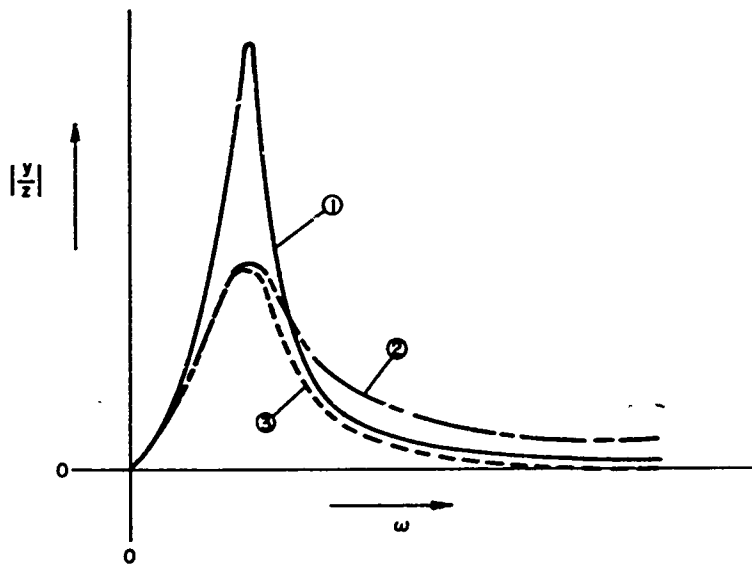
Fig. 10. Comparison of system
response magnification factors

forcing through an (air) spring damper as described above.

Particular attention was focused on the package acceleration profile and the amplitude displacement for perturbation in the system natural frequency range. Figure 10 shows a typical air spring damper mass magnification factor as curve ③. Curve ② indicates the typical linear spring damper in a parallel isolator configuration previously discussed.

System responses of the air spring damper isolator were investigated at higher frequencies. Figure 12 illustrates a sine wave perturbation having a frequency of 8.8 cps and an amplitude of ±0.5 ft. It was noted that the system had just approached an unstable condition. Figure 13 shows the same system after a damper had been placed between the package mass and wheels of 200 lb_f/ft/sec.

REFERENCE

1. E. F. Obert, Thermodynamics (McGraw-Hill, New York), 1948, pp. 130-153

BIBLIOGRAPHY

Doebelin, E. O., "Dynamic Analysis and Feedback Control" (McGraw-Hill, New York), 1962, pp. 26-57, 76-152

Olson, F. E., "Vibration Isolation Study H Computer Simulation," EG&G Memo., Aug. 6, 1965.

Thomson, W. T., "Vibration Theory and Applications" (Prentice Hall), 1965, pp. 130-153
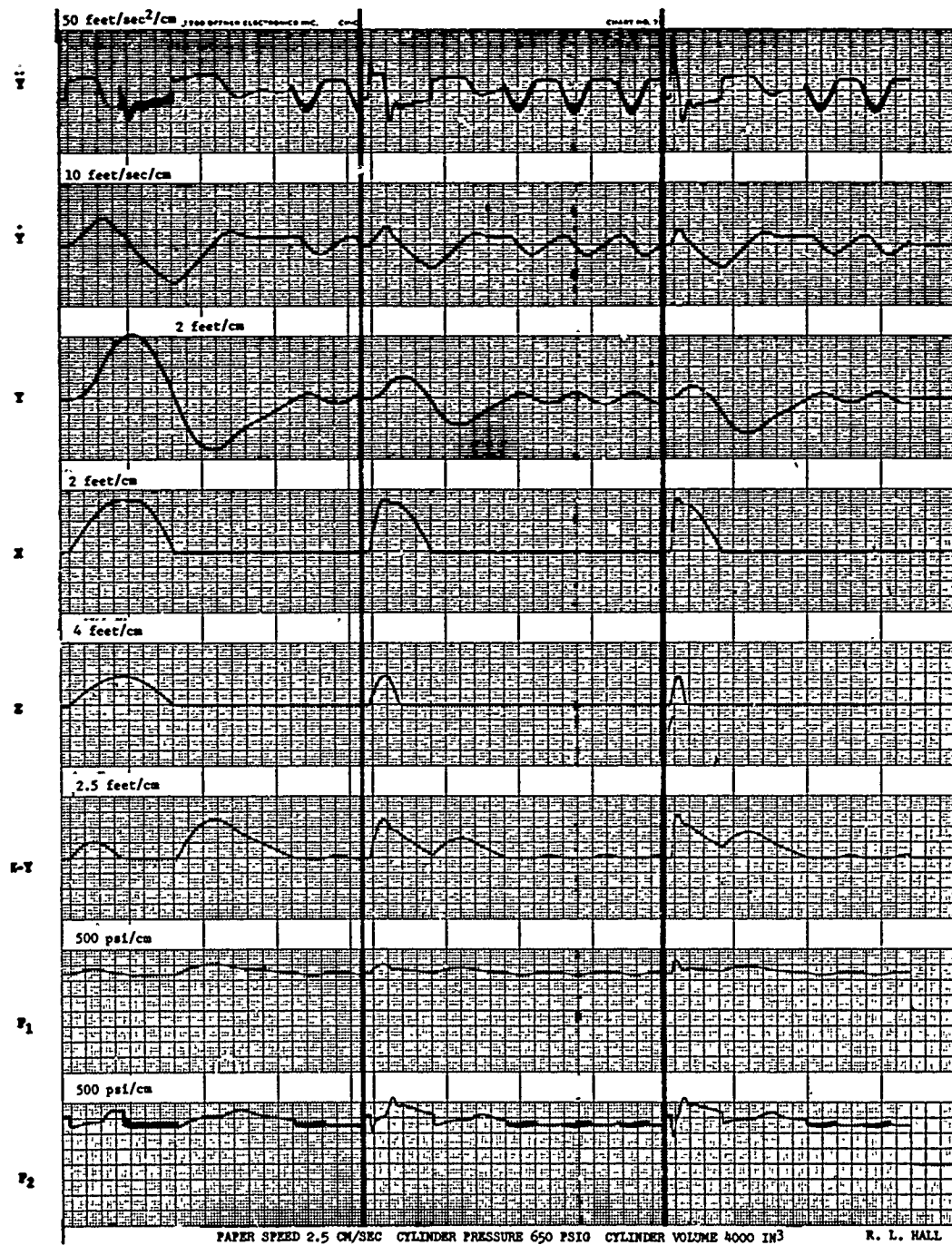
Fig. 11. Response of air spring mass damper
system to single positive sine pulse

224
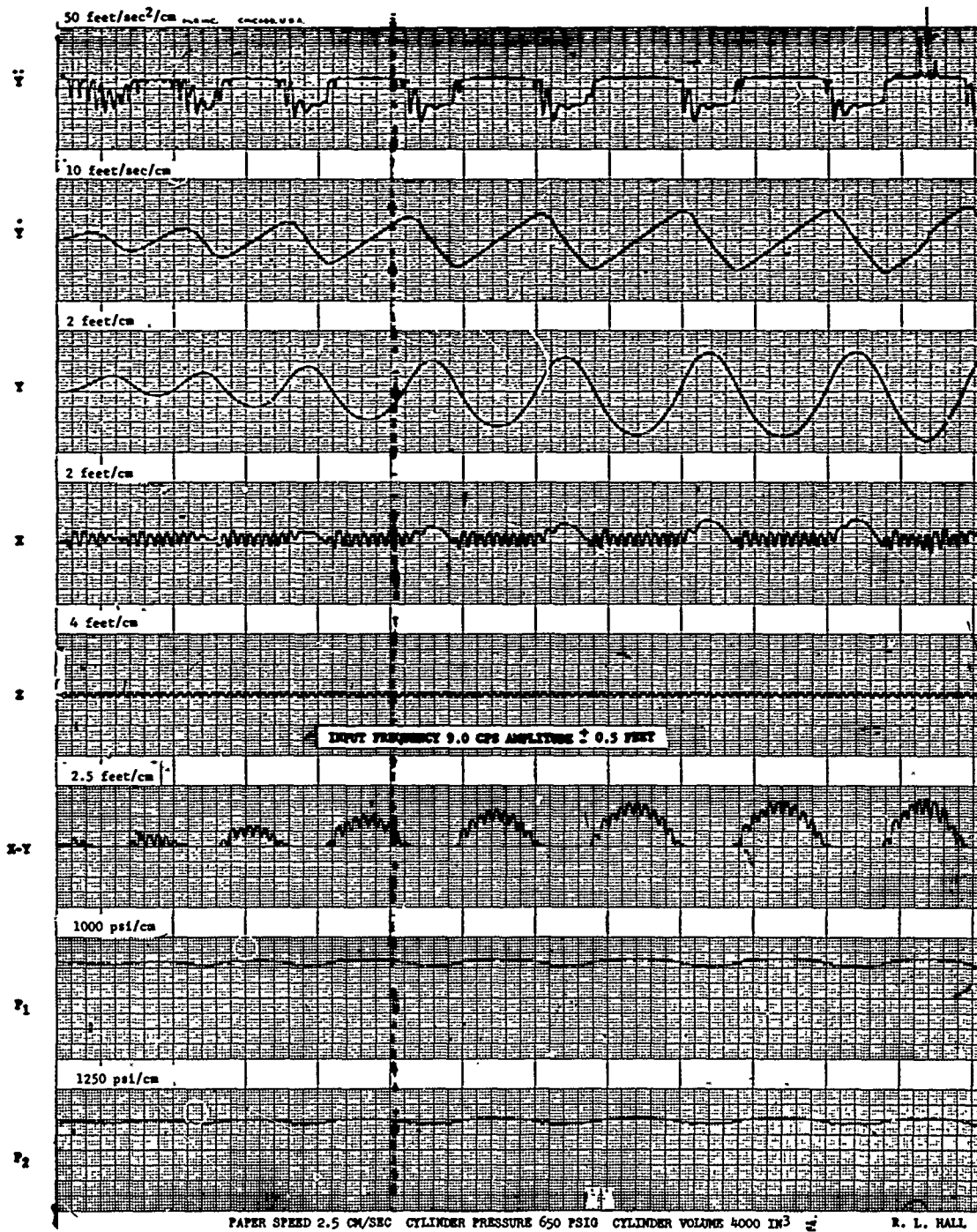
Fig. 12. Response of air spring mass damper system
for higher sinusoidal forcing frequencies
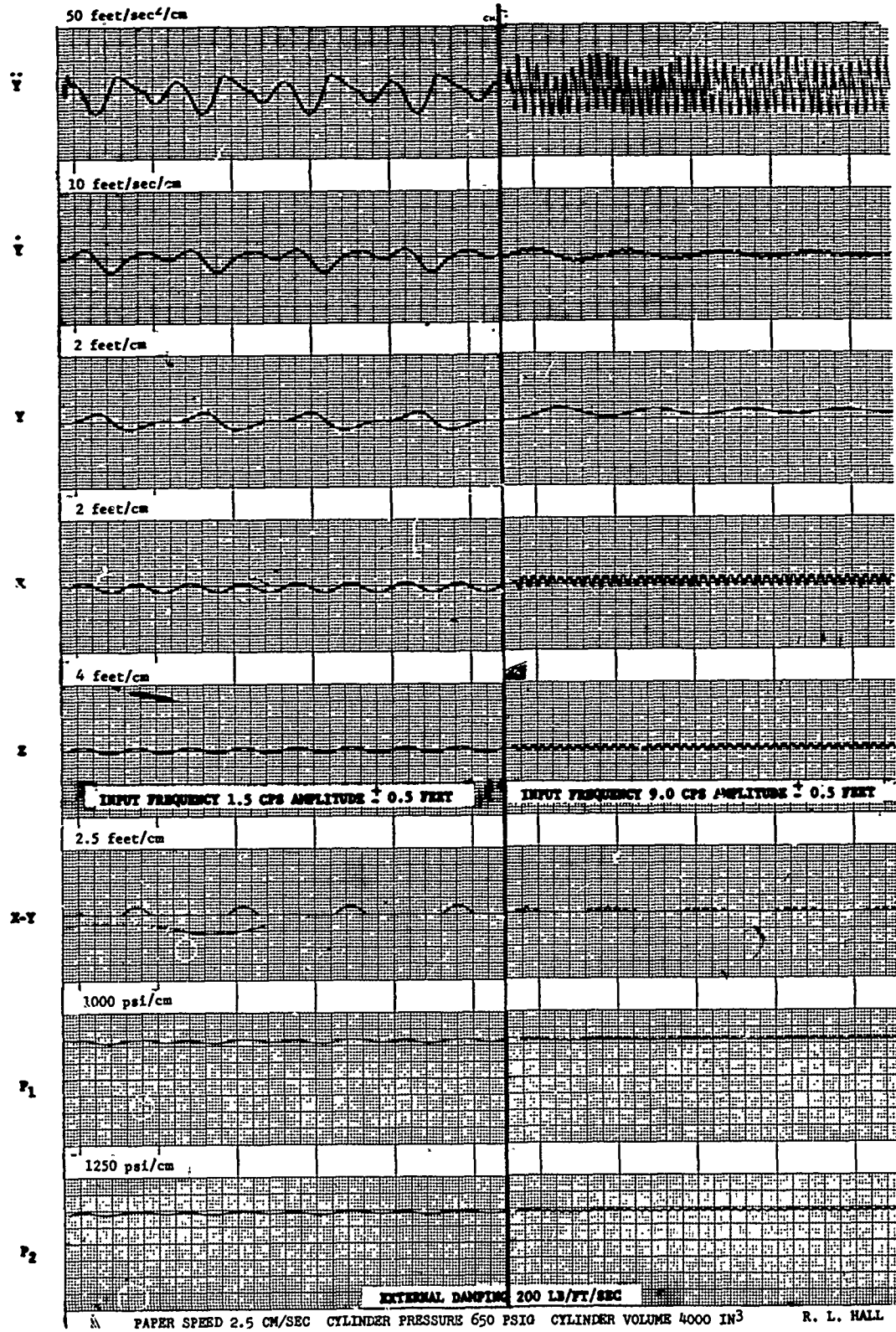
Fig. 13. Effect of external viscous damper

*   *   *

DESIGN AND ADVANTAGES OF A TWO-STAGE MOUNTING
SYSTEM FOR MAJOR MACHINES IN SHIP'S ENGINE ROOM

Robert M. Gorman
General Dynamics/Electric Boat Division
Groton, Connecticut

Approximately 100 tons of low-speed machinery had to be isolated in a surface ship's engine room. Standard single-stage mounting systems with sufficient attenuation characteristics would not have the rigidity to withstand the ship's rolling and slamming. It was decided, therefore, to use a two-stage mounting system incorporating a massive subbase on which all the machines would be isolation-mounted. The subbase would, in turn, be isolation-mounted to the ship's hull.

An analytical comparison of one- and two-stage systems was made on the basis of attenuation and stability characteristics. A general transmissibility equation for the two-stage system was derived. Force transmissibility was analytically determined for a large range of mount damping, mount stiffness, and subbase weight. Results include a set of parametric curves. Hull impedance, obtained from experimental measurements on a similar hull, was included in the system's mathematical model.

Four major machines were on the subbase. These and the subbase itself were considered rigid masses to simplify determining all the mounting system's natural frequencies. Each element was given six degrees of freedom and the resulting 30 natural frequencies were found using Electric Boat's standard structures program.

INTRODUCTION

Effective vibration isolation of heavy machinery having rotational frequencies less than 30 cps is a difficult problem. One method that may be used is a two-stage mounting system, consisting of isolation mounting machines on a rigid massive subbase which, in turn, is mounted on the ship's hull. The added weight, space, and cost requirements are counterbalanced by an isolation system that is far more effective than the standard one-stage type.

The particular case investigated here involved isolating two 80,000-lb and two 17,000-lb diesel generators. The large diesels run at 12 cps and the smaller diesels at 20 cps. The ship has an extremely severe radiated noise requirement which calls for all equipment to meet a sea state 2 waterborne noise level at 20 ft. This means the isolation system for the large diesels has to reduce the fundamental unbalance forces by a factor of 1/625 or 56 db. To meet this requirement, the standard springs used in a one-stage isolation system would have a natural

frequency of 1/2 cps, a static deflection of approximately 40 in., and a stiffness of only 2000 lb/in. Clearly this system would be too flimsy to expose to the rolling and slamming experienced on surface ships.

NOMENCLATURE

A   Constant of proportionality, in.

B   Constant of proportionality, in.

c   Damping coefficient, lb-in./sec

e   Base of natural logarithm system

f   Frequency, cps

F   Force, lb

j $\sqrt{-1}$

k   Stiffness, lb/in.

m   Mass, lb-sec^2/in.

ω Radian frequency, rad/sec

ω_{xy} $\sqrt{k_x/m_y}$, rad/sec

t   Time, sec

T·   Transmissibility

x   Displacement (vertical), in.

$\ddot{x}$ Acceleration (vertical), in./sec^2

ANALYTICAL COMPARISON OF ONE- AND TWO-STAGE MOUNTING SYSTEMS

One-Stage System

This basic system is shown in Fig. 1. For simplicity, damping has been ignored. The basic equation of motion for the system is

$$m_1\ddot{x}_1 + k_1 x_1 = F \sin \omega t . \qquad (1)$$

F sin ωt
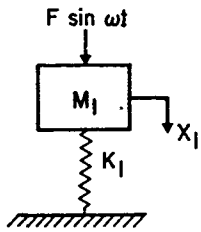
Fig. 1. One-stage mounting system

Transmissibility is defined as the ratio of the force output of the system to the force input:

$$T = \frac{F_{out}}{F_{in}} = \frac{k_1 x_1}{F \sin \omega t} = \frac{k_1 x_1}{m_1\ddot{x}_1 + k_1 x_1} . \qquad (2)$$

The displacement, x_1, will be of the form $x_1 = Ae^{j\omega t}$; hence, $\ddot{x}_1 = -A\omega^2 e^{j\omega t}$. Substituting these values of x_1 and $\ddot{x}_1$ into Eq. (2) gives

$$T = \frac{kAe^{j\omega t}}{-mA\omega^2 e^{j\omega t} + kAe^{j\omega t}} . \qquad (3)$$

Letting $k_1/m_1 = \omega_{11}^2$ and simplifying Eq. (3) gives

$$T = \frac{1}{1 - \left(\frac{\omega}{\omega_{11}}\right)^2} . \qquad (4)$$

This transmissibility is plotted versus frequency in Fig. 2. Note that at frequencies above resonance, the curve has a negative slope of 40 db/decade.

Two-Stage Systems

Figure 3 shows a schematic of a two-stage mounting system. As before, damping is ignored and motion is considered in only the vertical direction. Equations of motion for this system are

$$m_1\ddot{x}_1 + k_1(x_1 - x_2) = F \sin \omega t \qquad (5)$$

and

$$m_2\ddot{x}_2 + k_1(x_2 - x_1) + k_2 x_2 = 0. \qquad (6)$$

As before, transmissibility is defined as force output divided by input, or

$$T· = \frac{k_2 x_2}{F \sin \omega t} = \frac{k_2 x_2}{m_1\ddot{x}_1 + k_1(x_1 - x_2)} . \qquad (7)$$

The displacements and accelerations will be of the form $x_1 = Ae^{j\omega t}$, $\ddot{x}_1 = -A\omega^2 e^{j\omega t}$, $x_2 = Be^{j\omega t}$, and $\ddot{x}_2 = -B\omega^2 e^{j\omega t}$. Substituting these into Eq. (6) yields

$$A = \left[\frac{k_1 + k_2 - m_2\omega^2}{k_1}\right]B . \qquad (8)$$

If the displacements and accelerations, along with the ratio of A/B, are substituted into Eq. (7), the following equation is found:

$$T = \frac{1}{\frac{m_1 m_2}{k_1 k_2}\omega^4 - \left(\frac{m_1 k_1 + m_1 k_2 + k_1 m_2}{k_1 k_2}\right)\omega^2 + 1} . \qquad (9)$$

Now, letting $k_1/m_1 = \omega_{11}^2$, $k_2/m_1 = \omega_{21}^2$, $k_1/m_2 = \omega_{12}^2$, and $k_2/m_2 = \omega_{22}^2$, Eq. (9) becomes

$$T = \frac{1}{\frac{\omega^4}{\omega_{11}^2 \omega_{22}^2} - \left(\frac{\omega^2}{\omega_{21}^2} + \frac{\omega^2}{\omega_{11}^2} + \frac{\omega^2}{\omega_{22}^2}\right) + 1} . \qquad (10)$$

Transmissibility versus frequency is plotted in Fig. 4. There are two resonances in this curve. Between them the transmissibility falls off at 40 db/decade as it did in the single-stage system. Above the second resonance, however, the transmissibility decreases at 80 db/decade.
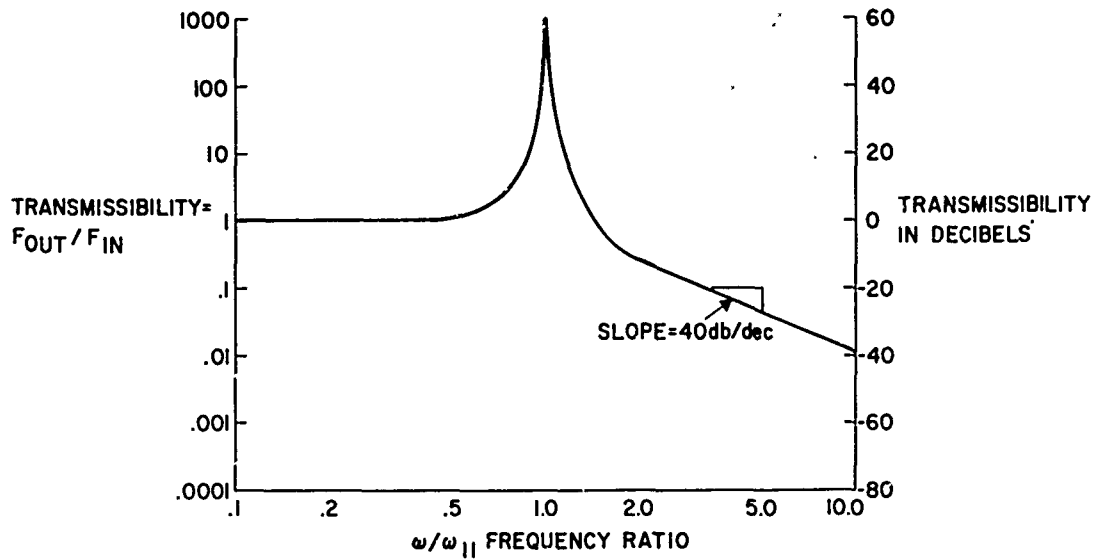
Fig. 2. Transmissibility of one-stage mounting system
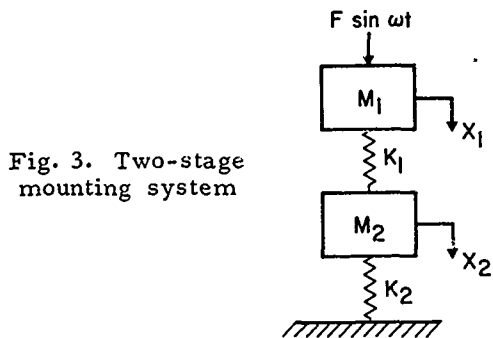
Fig. 3. Two-stage mounting system

It is here that the great value of the two-stage system is felt.

DESIGN OF A TWO-STAGE ISOLATION SYSTEM

As mentioned in the introduction, four large machines were to be isolated. It was decided to mount them all on a common subbase. Figure 5 is a schematic of the machines on the subbase.
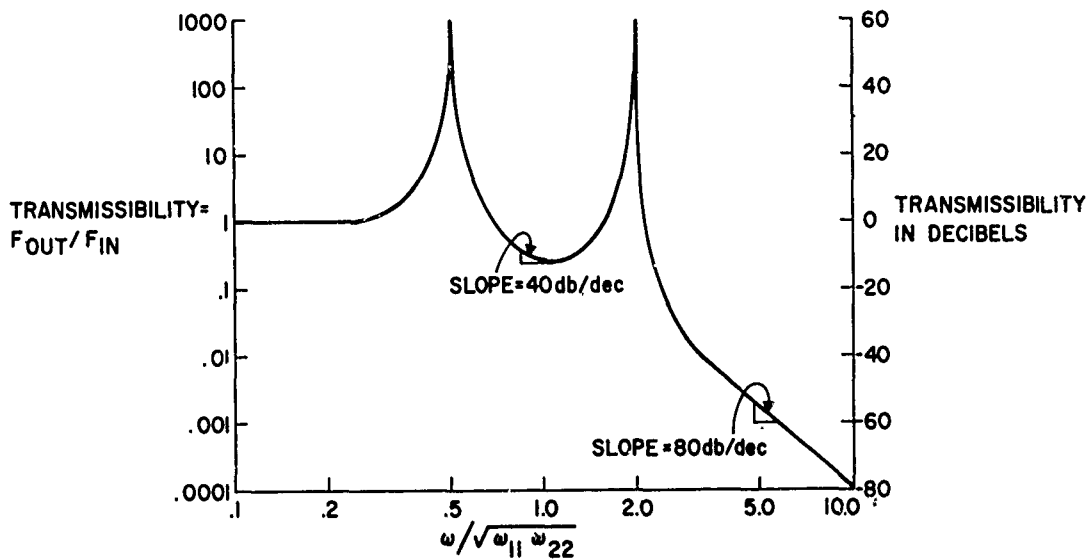
Fig. 4. Transmissibility of two-stage mounting system
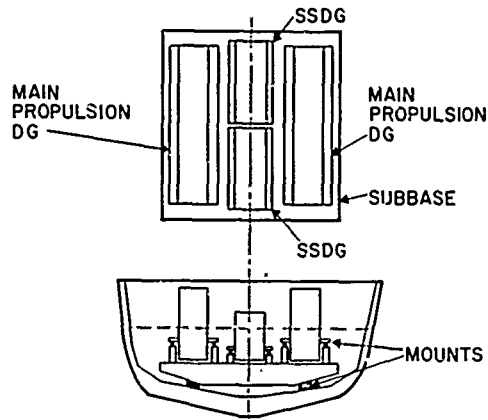
Fig. 5. Proposed subbase and main
machinery configuration

The ship's service diesel generators (SSDG) are mounted in line, fore and aft; while the larger, main propulsion diesel generators (MPDG) are mounted outboard of them. Table 1 gives the weights and fundamental rotational frequencies.

TABLE 1

Name	No. of Units	Weight/Unit (lb)	Fundamental Rotational Frequency (cps)
SSDG	2	17,000	20
MPDG	2	80,000	12

SUBBASE MASS

For the good of the ship, minimizing the weight of the subbase is of prime importance. Unfortunately, this is in direct conflict with the optimization of the attenuation and stability characteristics of the system. As will be shown, a low subbase weight, or more correctly, low ratio of subbase weight to machine weight, raises the second natural frequency to a prohibitively high value and lowers the first one to too low a value.

It was desirable to have the two vertical natural frequencies equal to 2 and 5 cps. The following can then be stated (Fig. 5):

1. The machine weight is fixed at 80,000 lb.

2. The machine mounts are to be such that $\omega_{11}/2\pi = \sqrt{k_1/m_1} = 2$ cps, therefore, $k_1 = 25,000$ lb/in.

3. $\omega_{22}/2\pi = \sqrt{k_2/m_2} = 5$ cps.

By use of these steps, the denominator of Eq. (10) can be solved for the two-system resonances which can be plotted as a function of m_2/m_1. This is done in Fig. 6.
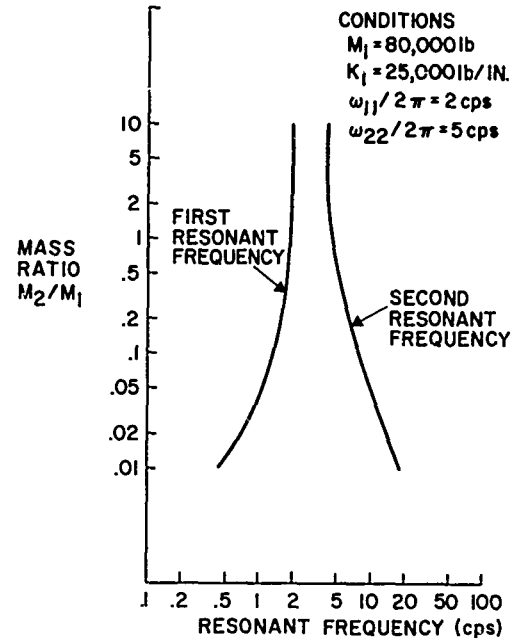
Fig. 6. Dependence of resonant
frequency on mass ratio

In choosing the optimum mass ratio for our application, two major factors had to be considered. First, the system's total attenuation is affected most severely by the position of the second resonance. This resonance should be as close to 5 cps as possible. Second, the stability of the system is largely determined by the lower resonance. The lower this resonance is, the more unstable the total system becomes. Therefore, the lower resonance should be as close to 2 cps as possible. Holding these two considerations in mind and remembering that the subbase weight must be minimized, we chose a mass ratio of 1 for the following reasons:

1. At mass ratios lower than 1, the second resonance increases quite rapidly. This lowers the attenuation of the system because it pushes this resonance closer to the machine rotational speed (12 cps).

2. At mass ratios lower than 1, the first resonances decrease quite rapidly. This means that the system is less stable and, therefore, more susceptible to injury due to rolling and slamming.

3. At mass ratios higher than 1, neither of the resonances get much closer to their asymptotic values of 2 and 5 cps. Therefore, any gain from a stability or attenuation standpoint would be marginal and not worth the increased weight.

Therefore, the subbase will weigh as much as the total weight of all the machines it supports. This figure is approximately 100 tons.

TRANSMISSIBILITY OF ACTUAL SYSTEM

Earlier in the paper, the equation governing transmissibility of the most fundamental two-stage system was found. The information that follows shows the transmissibility's dependence on mount damping, hull impedance, etc. A new, more complex mathematical model of the system was made and is shown in Fig. 7.

Fig. 7. Complex two-stage mounting system
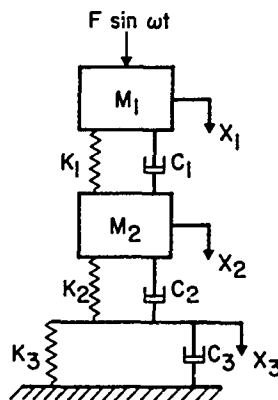
The hull impedance is represented as a spring (k_3) and dashpot (c_3) connected in parallel. This is obviously a very crude model of the actual hull. There is, however, good reason for this choice. Figure 8 is a plot of the impedance of a destroyer hull driving into a stiffener. Superimposed on this curve is our simplified system. One can see that this is a valid first-order approach to the real impedance; furthermore, since the actual hull impedance would be extremely impractical to model, it may be the best approach.

Another point that should be brought out is that the values of k and c obtained from Fig. 8 have to be increased since this curve only represents the impedance of one point, while our model has to have the total impedance into which the subbase mounts look.
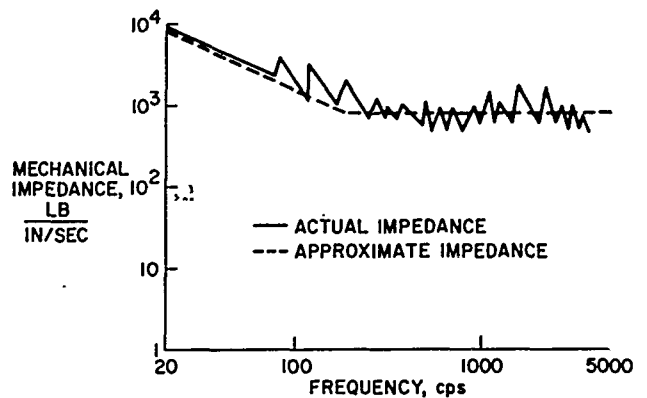
Fig. 8. Impedance of stiffener in destroyer hull in radial direction

Damping was considered in the two sets of mounts. The amount of damping was set at approximately 5 percent of critical. This is a typical figure for rubber mounts.

The model was programmed on Electric Boat Division's Pace TR-48 Analog Computer. Automatic repetitive operation and a large amount of on-line signal processing equipment was utilized to plot automatically the curves displayed in Figs. 9 through 13. This ancillary equipment proved very useful in making the complete parametric study presented in these graphs.

The values of the initial system parameters were as follows:

c_2 = 200 lb-sec/in.;

c_1 = 1500 lb-sec/in.;

k_2 = 500,000 lb/in.;

k_1 = 25,000 lb/in.;

m_2 = 518 lb-sec^2/in., or 200,000 lb;

m_1 = 207 lb-sec^2/in., or 80,000 lb;

c_3 = 15,000 lb-sec/in.; and

k_3 = 20,000,000 lb/in.

Of these eight parameters only the first five were varied since the machine weight and hull impedance were assumed to be constant.

Figure 9 shows the effect of various values of c_2, the damping in the subbase mounts. As

231
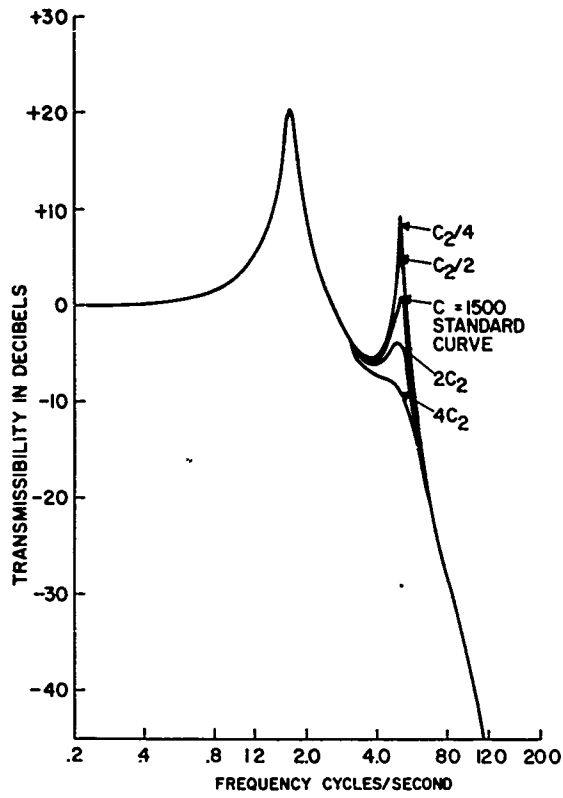
Fig. 9. Transmissibility vs driving
frequency for various values of c_2
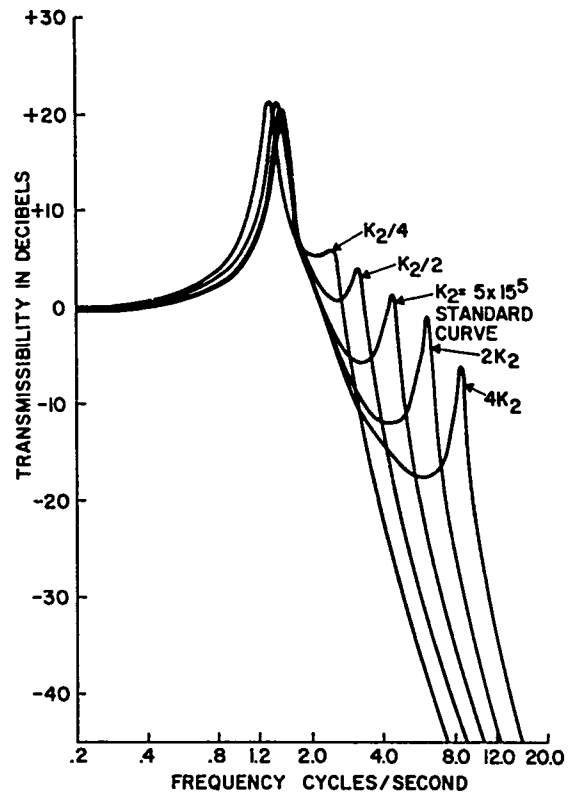
Fig. 11. Transmissibility vs driving
frequency for various values of k_2
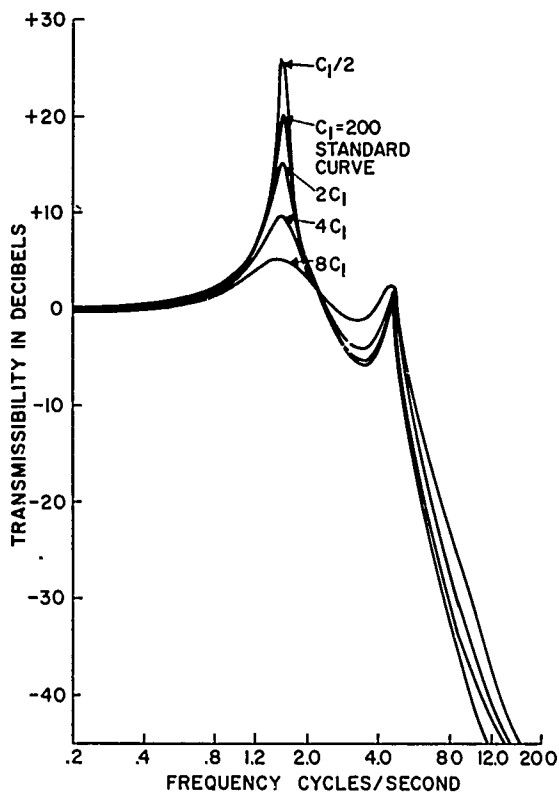
Fig. 10. Transmissibility vs driving
frequency for various values of c_1
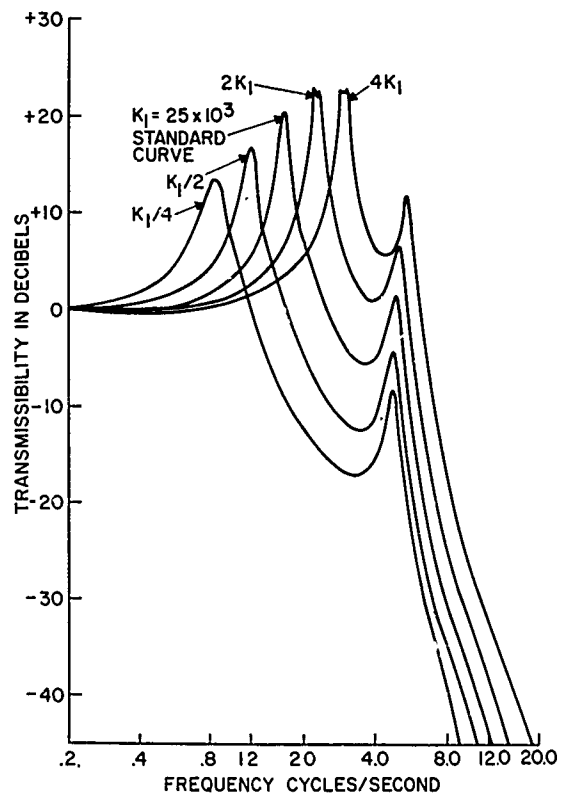
Fig. 12. Transmissibility vs driving
frequency for various values of k_1

232
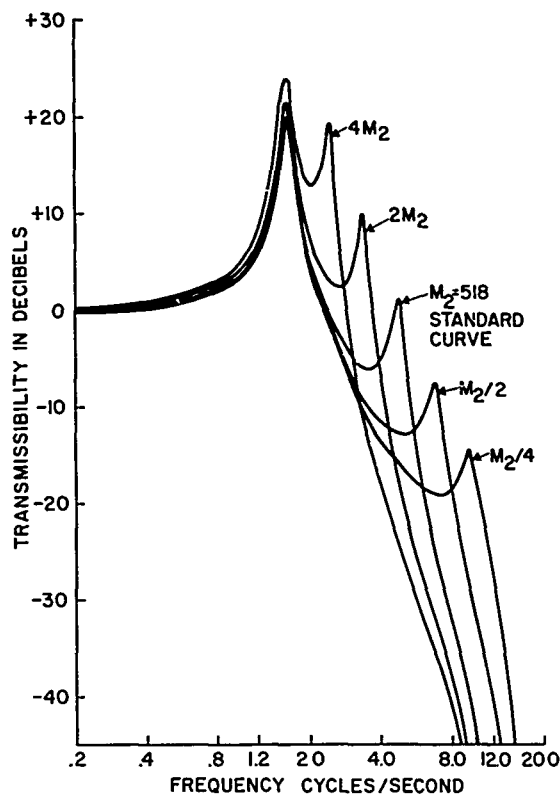
Fig. 13. Transmissibility vs driving
frequency for various values of m_2

expected, c_2 has very little effect on the height
of the first resonant peak. It does have a much
more pronounced effect on the second resonance.
This resonance would be practically eliminated
if 20 percent of critical damping $(4c_2)$ could be
incorporated in these mounts. It is more re-
markable that the attenuation above the second
resonance is not impaired by the added damping,
as it would be in a single-stage system.

Figure 10 shows the effect of various val-
ues of c_1, the damping in the machine mounts.
As expected, the first resonance height is al-
tered while that of the second resonance re-
mains fairly constant. Unlike Fig. 9, the slope
of the curve above the second resonance is de-
creased with increased damping. This decrease,
however, is not as large as would be expected.
Therefore, it can be concluded from Figs. 9 and
10 that damping in a two-stage system does not
have as adverse an effect on transmissibility
above resonance as it does in the one-stage
system. This is especially true when the sec-
ond resonance is damped.

Figures 11 and 12 show the effect of vary-
ing the two-mount stiffnesses. The transmissi-
bility at high frequencies is more sensitive to a
change in k_1 (Fig. 11) than k_2 (Fig. 12). It can
also be seen that the systems are effectively

decoupled because a change in k_1 shifts the
first resonances but not the second, and vice-
versa. In Fig. 12, the curves for $2k_1$ and $4k_1$
are clipped at the first resonant peak due to
limitations in the dynamic range of the computer.

Figure 13 shows the effect of varying the
subbase mass m_2. This, as expected, has the
opposite effect on transmissibility that varying
k_2 had. That is, an increase in m_2 decreases
the second resonance while a decrease in k_2
increases this resonance.

SYSTEM NATURAL FREQUENCIES

In the foregoing section, the force trans-
missibility has been found for two masses
translating in the vertical direction. It is as-
sumed that other transmitted forces or mo-
ments would be attenuated in the same manner
regardless of direction, rotation, or any com-
bination of these motions. The only restriction
is that the rigid body natural frequencies of the
system have to be appreciably below the lowest
forcing frequency (12 cps). It was, therefore,
decided to limit the highest natural frequency
to 6 cps.

A mathematical model of the system was
then made. To simplify closing the mount stiff-
nesses for the model, the five components were
assumed to be decoupled. The mounts used
were two-cycle mounts under the MPDG's,
three-cycle mounts under the SSDG's, and five-
cycle mounts under the subbase. Other assump-
tions made are listed below:

1. The damping in the mounts can be ig-
nored in determining natural frequencies;

2. The stiffness of mounts in the horizon-
tal plane is equal to the stiffness in the vertical
planes; and

3. The machines and subbase act as rigid
masses in the frequency range of interest (less
than 10 cps).

The system was analyzed in two steps.
First, the flexibility of each component's mount-
ing system was individually determined. This
enabled us to reduce the system shown in Fig.
14a to the one shown in 14b. When the five
components were thus treated, a mathematical
model of the whole system was made and is
shown in Fig. 15. Each spring now represents
the total flexibility of one machine's mounting
system and, therefore, has stiffness in all three
directions and three rotations. Each mass has six
degrees of freedom. The 30 natural frequencies

233

were determined using Electric Boat's standard structures program. These frequencies, given in Table 2, show that the highest natural frequency is 5.9 cps. This is considered acceptable for effective transmissibility.
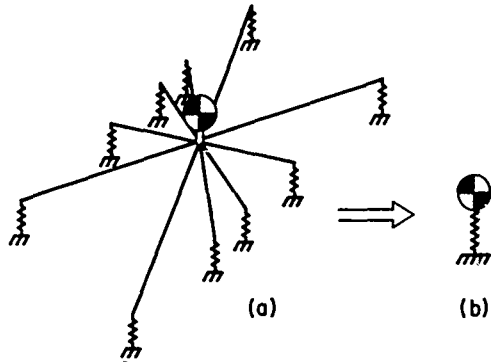
Fig. 14. Mathematical model of component
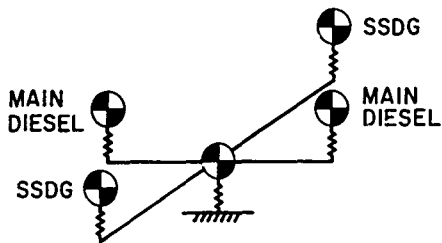
Fig. 15. Mathematical model of system

TABLE 2
Natural Frequencies of System

Mode	Frequencies (cps)	Mode	Frequencies (cps)
1	1.23	16	2.04
2	1.28	17	2.51
3	1.33	18	2.65
4	1.37	19	2.71
5	1.52	20	2.78
6	1.52	21	2.88
7	1.61	22	3.05
8	1.62	23	3.17
9	1.77	24	3.29
10	1.77	25	3.90
11	1.79	26	4.27
12	1.82	27	5.51
13	1.86	28	5.72
14	1.86	29	5.82
15	2.03	30	5.90

SUBBASE DESIGN

A subbase design is shown in Fig. 16. For this subbase to function properly, it must act as a rigid mass. Since this is physically impossible, an effort was made to maximize its first mode. The highest value we could obtain for the first natural frequency was 100 cps. To insure that this or other resonant peaks would not be too high, damping will be incorporated in the design of the subbase. Riveted construction will be used wherever possible, and all plating will be coated with a viscoelastic damping treatment.
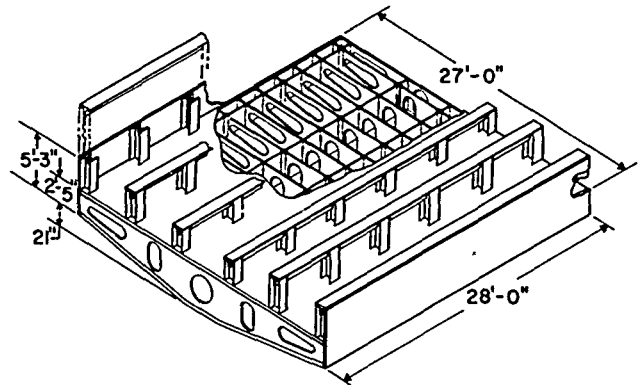
Fig. 14. Subbase

CONCLUSIONS

A two-stage system can be far superior to a one-stage system from the standpoint of force isolation and rigidity, because the transmissibility of a two-stage system above the second resonance is proportional to $1/\omega^4$ while in a one-stage system the maximum transmissibility is proportional to $1/\omega^2$. Therefore, a rigid two-stage system could be used to replace a flimsy one-stage system and still give superior isolation effectiveness. It should be remembered, however, that a two-stage design contributes a relatively large increase in weight to a system and, correspondingly, a large increase in cost.

ACKNOWLEDGMENTS

The author gratefully acknowledges the assistance given him by personnel in Electric Boat's Sound and Vibration Section, Applied Mechanics Section, Information Processing Section, and Creative Design Section. He is especially grateful to T. A. Champlin, Head of the Industrial Acoustics Group.

*   *   *

234

MODELING OF SPACECRAFT FOR

LOW-FREQUENCY NOISE REDUCTION

Richard H. Lyon, Robert E. Apfel, and Charles W. Dietrich
Bolt Beranek and Newman, Inc.
Cambridge, Massachusetts

The acoustic isolation or "noise reduction" (NR) of spacecraft struc-
tures over most of the frequency range can be computed and/or meas-
ured by methods that can be termed "conventional." The increased
interest in noise below 50 cps requires that extensions to these con-
ventional methods be made, both in analysis and experiment.

Conventional theory distinguishes between "mass law," or forced re-
sponse, and reradiation and transmission of sound by resonant motion.
The same considerations are appropriated to low-frequency NR. At
low frequencies, the forced motion is stiffness controlled and derivable
from "pressure vessel" analysis. The mechanical and acoustical res-
onances of the system modify this stiffness-controlled NR.

INTRODUCTION

There is an increasing interest in the low-frequency sound transmission behavior of spacecraft structures, because the larger boosters that are currently under development create an intense sound field with major components in the low-frequency regime below 50 to 100 cps (1). In addition, as these vehicles pass through the transonic and Max Q portions of their trajectory, they will experience additional large-amplitude low-frequency loadings (2). It is known that an excessive low-frequency acoustic and vibration environment can have undesirable psychoacoustic and physiological effects on man (3,4). Consequently, the ability of a spacecraft to shield the human passenger from these loads is of great concern.

The development of adequate techniques for predicting and measuring the low-frequency noise reduction (NR) afforded by the spacecraft structures forms a largely unexplored area of acoustic technology. The new Low Frequency Noise Facility at Langley Research Center (5) has been designed to allow the direct generation and measurement of acoustic signals of varying waveforms in the very low-frequency regime, and one of the tasks to which it can be put is the measurement of low-frequency NR. Spacecraft are expensive, however, and the schedule of their testing from final construction to their deployment as a vehicle is very rigorous and does not allow much time for explanatory studies

of structural response and sound transmission. For these and other reasons, it is desirable to have models available that display the same important acoustical and mechanical patterns of behavior that the "real thing" does.

If the model is to be significantly simpler and less expensive than the real item, then it is necessary to know what the important features of structural and acoustical behavior are in the actual spacecraft, insofar as low-frequency NR is concerned. This is so because we want not only to model the correct dynamics of the real system, but also to avoid introducing by our simplifications spurious effects that will reduce the utility of the experimental results on the model. An adequate theory of the behavior of structures at very low frequencies and the way that they transmit sound in this frequency regime is therefore required.

We begin by reviewing quickly the more or less classical approach to NR calculations in building structures. Although we can make very few direct applications of these calculations, there are at points certain similarities in the construction of the ideas that we want to point out. Following this review, we discuss a previous calculation of the NR provided by a rectangular box over a large range of frequencies. We then discuss some features of the NR of axisymmetric shells and indicate how these calculations relate to the low-frequency NR of the rectangular box. Finally, we discuss an effect

of the "double wall" construction of a current space vehicle on its acoustical behavior.

REVIEW OF "CLASSICAL" NR CALCULATIONS

In architectural acoustics, the NR provided by a structural wall depends on the so-called transmission loss of the wall and the acoustic absorption of the receiving space. The transmission loss of the wall is defined as (6, p. 324):

$$TL = 10 \log \Pi_{inc}/\Pi_{trans}, \qquad (1)$$

where Π_{inc} is the power incident on the wall and Π_{trans} is the power transmitted into the receiving room. The absorption properties of the receiving room are defined through its "room constant" R, which is given by (6, p. 312):

$$R = A_t \alpha (1 - \alpha)^{-1}, \qquad (2)$$

where A_t is the total surface area of the receiving room and α is its average absorption coefficient. In terms of these parameters and the area of the transmitting wall A_w, the NR, defined as the difference in sound pressure level in a reverberant field exterior to the room and that within the receiving room, is given by (6, p. 327):

$$NR = TL + 10 \log R/A_w. \qquad (3)$$

By putting the equation in this form, an attempt is made to separate the geometrical properties of the wall and the receiving space from the intrinsic properties of the wall. One can find the values of the transmission loss for various wall constructions in standard reference books (6, p. 329); these values, combined with geometrical and acoustical information on the receiving space, allow one to calculate the expected NR.

This argument assumes that the acoustic receiving space and the transmitting wall structure are both several acoustic wavelengths in size. Since these calculations are usually applied to predict NR over the range from a few hundred to a few thousand cps, such assumptions are appropriate. Also, at a few hundred cps, most wall structures have a flexural wavelength that is smaller than the acoustic wavelength (i.e., they are below their critical frequency), so the wall is also several bending wavelengths in size.

Since the room constant changes rather slowly with frequency, the frequency dependence of the noise reduction can usually be inferred

from the form of the transmission loss. A typical form for the transmission loss, in the region where the calculation by Eq. (3) is appropriate, is shown in Fig. 1 (7). The TL curve shown in Fig. 1 is fairly typical of a broad group of wall constructions. The most outstanding features are a notch in the curve at the critical frequency (the frequency at which the bending wavelength in the wall is equal to an acoustic wavelength in the medium), and the low-frequency asymptotic rise in TL at the rate of 6 db/octave.

The mass law dependence of the curve means that if a perfectly limp curtain were hung in place of the wall and if the curtain has the same mass/unit area as the wall, then it would provide the same NR as the actual wall. At first glance, this is rather surprising, because most walls have many resonances in this frequency region and one would expect them to increase the vibration levels of the wall to some value higher than that of the limp curtain. In fact, if one measures vibration levels on the wall during such an experiment, he will find that the vibration levels are usually higher than "limp wall" nonresonant vibration levels.

The reason that the transmission loss is governed by the lower amplitude "forced wave-nonresonant" portion of the vibration field is that its radiation efficiency is much higher than that of the resonant vibrations. Thus, the product of velocity amplitude and radiation efficiency is higher for the nonresonant transmission. Parenthetically, it should be noted that this is not always the case, and in some instances, the resonant vibrations may contribute to the sound transmission. This, in fact, is indicated in the lower part of the curve, where fluctuations around the mass law value arise due to modal resonances of the wall.

NR AT LOW FREQUENCIES

If we want to predict the NR of a spacecraft whose typical dimension is, for example, of the order of 10 ft, then the traditional approach as described in the previous section will be appropriate for frequencies above a few hundred cps. If we want to know the NR, i.e., the difference in sound pressure level within and outside the spacecraft in a frequency range from a few cps to approximately 50 cps, then clearly we must devise new techniques for its calculation. A clue to the procedure we might take is afforded by a previous calculation of the NR of a small box (8). The box was assumed to have a single flexible wall and five completely rigid walls. At higher frequencies, above the first few internal acoustic resonances of the box, one could
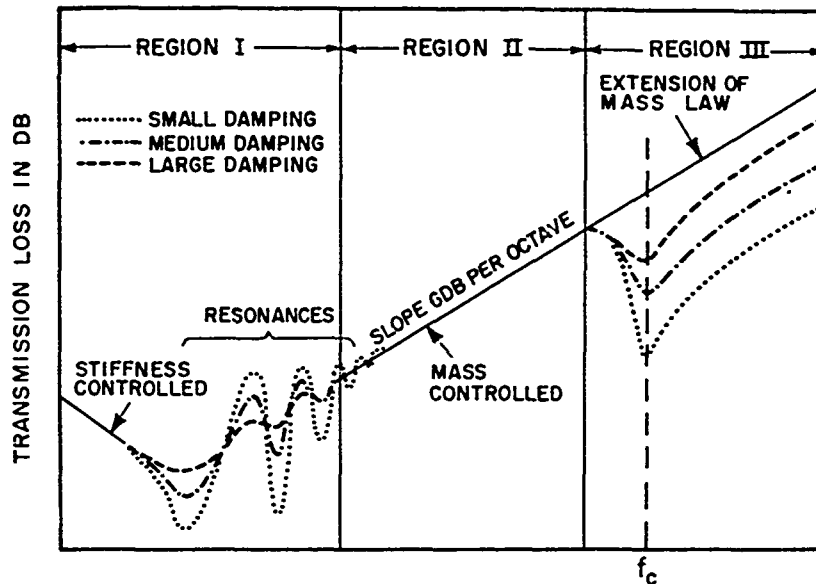
Fig. 1. Typical form of TL for structural wall

expect the traditional TL approach, as outlined in the previous section, to be appropriate. Below the frequency of the first acoustic resonance, the interior volume of the box becomes a compliance, but the flexible panel may continue to have resonant modes of vibration. The vibration of some of the panel modes produces a volume displacement into the box that results in increased internal pressure and a loss of NR. Finally, at frequencies below all structural resonances of the flexible panel and acoustic resonances of the contained volume, both the panel and the volume act as acoustic stiffnesses, and the NR achieved can be expressed in terms of their relative compliance. The NR curve computed for the box is shown in Fig. 2.

As an example, let us consider the axisymmetric spacecraft shown in Fig. 3. This spacecraft is made of sandwich panels having a core thickness of 3/5 in. with two facings of 8 mils each. A typical overall dimension of the vehicle is 10 ft. With these parameters we can estimate that the first flexural resonance of the skin will occur in the neighborhood of 5 cps and that the first internal acoustic resonance will occur at about 50 cps. The critical frequency of the sandwich shell is 500 cps.

The ring frequency, i.e., the frequency at which the major part of the shell will lose the stiffening effects of curvature, is about 7 kc. For a cylinder, the circumference becomes a longitudinal wavelength at this frequency. Clearly, if we are interested in frequencies up to about 50 cps, we would be concerned with the two lower frequency regions of Fig. 2 and

the high-frequency TL/NR calculations of Fig. 1 will not be of assistance to us. As far as modeling is concerned, this means that we should not have to pay particular attention to the absorptive properties of the interior space, since we are below the acoustic resonances of the contained volume, and that volume is behaving as an acoustic compliance.

EFFECTS OF AXISYMMETRIC
   GEOMETRY

Many of the space vehicles that have been designed have an axisymmetric geometry due to the inherent high strength-to-weight ratio that can be achieved with this shape. Let us attach a coordinate system s, ϕ to the shell, as shown in Fig. 3. The azimuthal angle is ϕ and, as we have noted, we assume that the geometry is invariant to rotations through this angle. The coordinate s is the distance along a line of constant ϕ from the lower pole of the shell to the upper pole. Due to the symmetry and periodicity requirements, we expect that displacements of the shell will have the dependence $\cos m\phi$, $\sin m\phi$. If $m = 0$, then motions of this type will not have a net volume displacement. For $m = 0$, there will be a net volume displacement and a consequent contribution to the internal acoustic pressure. The $m = 0$ "ring resonance" occurs, however, near the ring frequency of the shell which, as was pointed out above, occurs at about 7 kc. The lower order modes, therefore, that resonate in the 5- to 50-cps range will not have a net volume pumping contribution. This situation differs markedly from the rectangular box

237
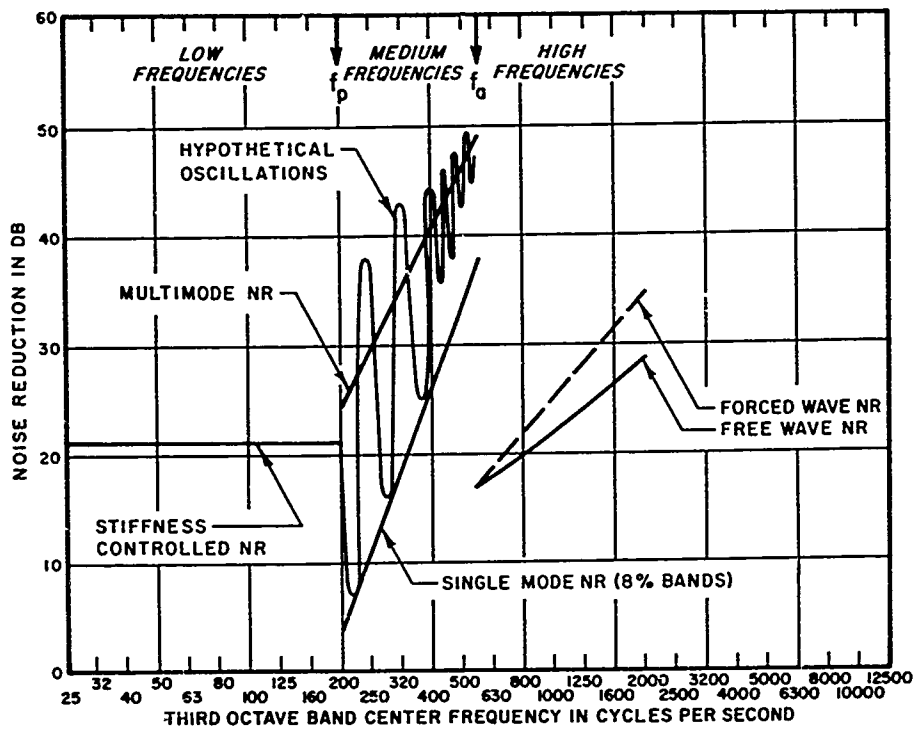
Fig. 2. Theoretical NR for supported 6-in. × 12-in. × 1/16-in.
aluminum panel covering rigid 6-in. deep enclosure
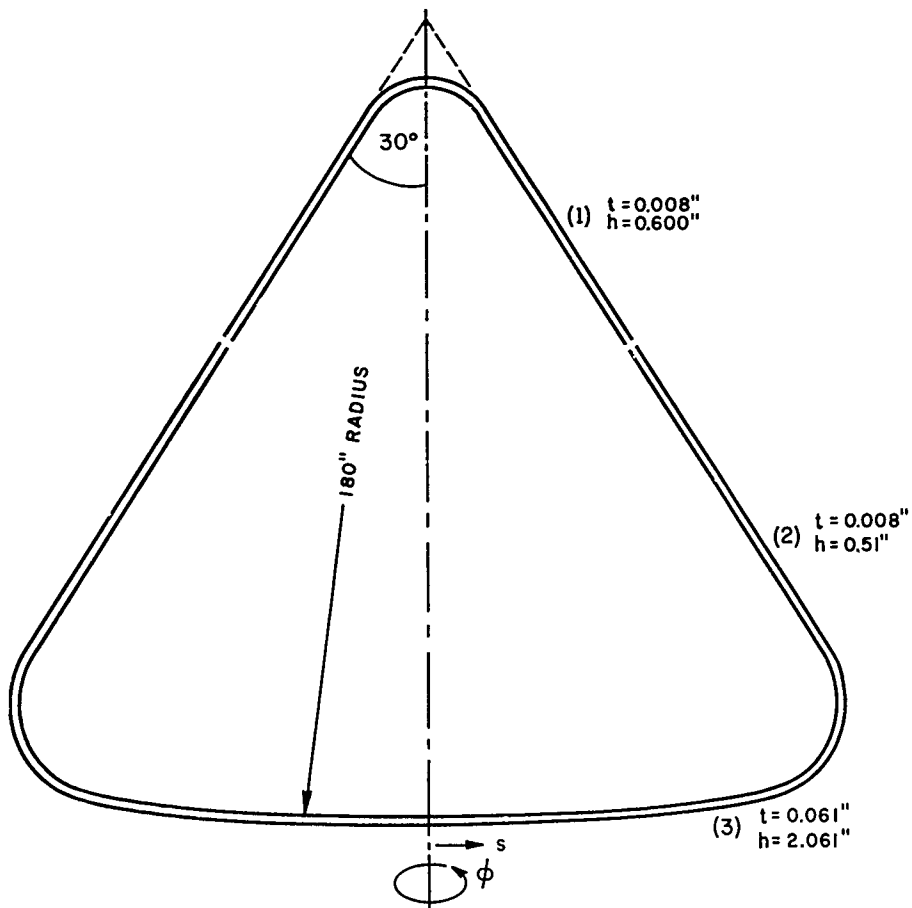
Fig. 3. Major structural sections of outer shell
(stainless steel sandwich)

238

calculation described earlier. We can expect, therefore, that the very low-frequency NR calculation will have its range of validity extended to higher frequencies, at least up to the first acoustic resonance of the interior volume. Consequently, in modeling the structure, it will be of primary importance to model its quasi-static compliance and to test experimentally whether the model in fact appears to be behaving as our theoretical notions suggest that it should.

We have a situation, therefore, that is reminiscent of the acoustic behavior of building walls. In a frequency region where there are many resonant modes of vibration, the sound transmission is governed by nonresonant motion. The main difference is that the building wall NR behavior is mass controlled, whereas the low-frequency NR of the space vehicle is stiffness controlled.

The acoustic compliance of the shell can be modeled by using a homogeneous sheet of metal if we know whether the shell is expected to resist deformation primarily by in-plane membrane stresses or whether deformation is controlled by its flexural rigidity. One way of evaluating this is to assume that the shell deformation is completely membrane controlled and then to apply flexural displacements at supporting edges to satisfy the boundary conditions. If the required flexural contribution propagates itself throughout the area of the shell, then at the very least, the flexural contribution must be considered in the compliance. The distance ℓ that the flexural effects propagate is given by (9):

$$\ell \approx (at_c)^{1/2}, \qquad (4)$$

where a is the radius of curvature of the shell, and t_c is the core thickness. For the shell of Fig. 3, this length is approximately 6 in. We conclude that the compliance is membrane controlled when the shell does not have appreciable structural discontinuities, such as longerons and other attachments. If the shell has flat segments, however, we can expect these sections to have an acoustic compliance that is controlled by their flexural rigidity.

A membrane compliance model of the steel shell in Fig. 3 would be a shell of the same overall dimensions but with a skin thickness of 16 mils. If the shell were made of aluminum, it would be 48 mils thick for the same membrane rigidity. It is clear that these much thinner shells would have many more flexural modes in the low-frequency range than the sandwich shells that they model. It is essential, therefore, to carry out experiments that will show

whether this model is adequate and what effects the slight structural irregularities always present might have on NR.

EXPERIMENTAL TESTS OF
SHELL NR

The steel shell shown in Fig. 3 is similar to the one used as the outer shell of the Apollo Command Module. The Command Module has an inner shell with an upper hatch cylinder that is approximately 30 in. in diameter and slightly longer than this in height. It is of aluminum sandwich construction with a core thickness of 1/4 in. and two facing sheets of 10 mils each. As a test of some of the ideas put forward in the previous sections, we have studied the NR of a 1/4-scale model of this hatch cylinder. The model is shown in Fig. 4 in its test chamber. It is approximately 7 in. in diameter and 7 in. long, and has an aluminum skin thickness of 5 mils. The two ends of the cylinder were fitted with 3/8-in. thick aluminum plates with a hole in one of the plates, so that the microphone can be inserted within the cylinder.
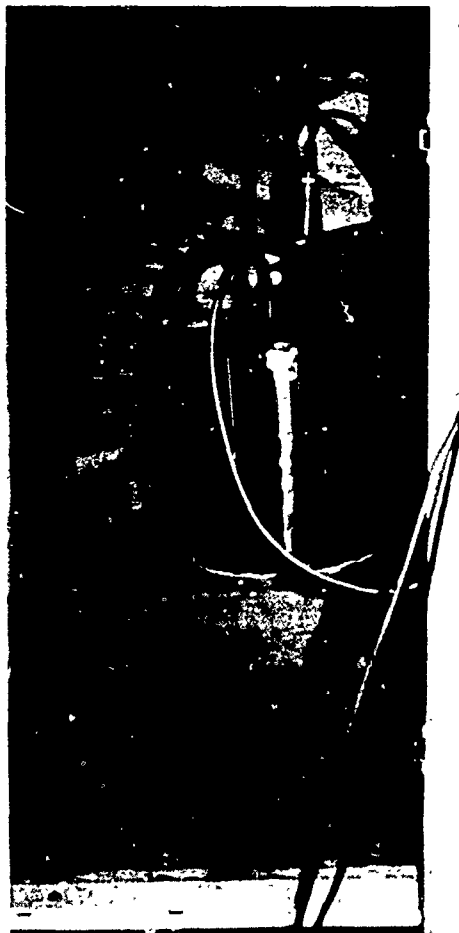
Fig. 4.   Scale model in
test chamber

239

The theoretical values of the shell compliance C_S and the compliance of the contained volume C_V are:

$$C_S = 5 \times 10^{-2} \text{ cu in./psi ,}$$

and　　　　　　　　　　　　　　　　　　　　　　　(5)

$$C_V = 15 \text{ cu in./psi .}$$

The noise reduction of this combination is given by

$$NR = 20 \log (C_V + C_S) C_S^{-1} \cong 50 \text{ db .} \quad (6)$$

Thus, the theoretical NR, assuming rigid end pieces, is 50 db, not a bad NR to be achieved by a piece of 5-mil aluminum foil. This NR is, in fact, so great that it is "short-circuited" by the 3/8-in. aluminum end plates. If we include their compliance in the calculation, we predict an NR of approximately 44 db.

If all dimensions of a structure are scaled by a factor of 1/4, the modeled structure will have the same dynamics as the full-sized structure when the frequency is 4 times as great as in the full-scale experiment. Thus, a range of 5 to 50 cps in full scale becomes a range of 20 to 200 cps in a 1/4-scale model study. The NR measured for the test cylinder is shown in Fig. 5. We note that the achieved NR does not exceed approximately 41 db.

Despite the lack of precise agreement between the calculation and the experimental results, the experiment does show the general adequacy of our model in two ways. First, the NR curve over the range of frequencies is rather smooth and does not display the existence of strong resonant modal contributions to the NR, despite the fact that our test cylinder has several hundred modes that resonate below 200 cps. The actual hatch structure, of course, would not have as many modes, since it is made of sandwich panels. Second, even though the value of 40 db is less than our predicted NR, it is still many times what one would expect if the shell were flexurally controlled. Nevertheless, other effects that we have not accounted for must be present and cause the 3-db discrepancy.

EFFECT OF ACOUSTIC
　RESONANCES ON NR

As we indicated previously, if the dimensions of the space vehicle are not too great, the major part of the low-frequency behavior of this space will be controlled by its acoustic compliance. This is true in general, but the particular double-shell configuration of the Command Module allows the possibility of resonances in the

acoustic space between the two shells. In the actual vehicle, this space is pretty well filled with thermal insulation and supporting gear for the mission, so acoustical resonances may not play a part in its noise transmission properties. On the other hand, a model of such a system may display resonances, and if so, we may wish to know how much sound transmission these contribute and what we should do to avoid them.

Unusually low-frequency acoustic resonances of the interspace between the two shells is made possible because of the long path length from one pole of this space to the other, as shown in Fig. 6. For the Command Module, this distance is approximately 18 ft. Theoretical analysis of the acoustics of such spaces indicates that we should expect an acoustic resonance when this path length is of the order of 1/2 wavelength, about 32 cps. A detailed analysis, using the Rayleigh-Ritz estimation procedure, gives a more precise value of this frequency at approximately 40 cps.

An experimental study of the existence of such resonances was made in a 1/10-scale model of this space with nearly rigid boundaries. The experimental value of the resonance frequency, scaled to full scale, was about 32 cps.

CONCLUSIONS

Theoretical and experimental analyses suggest that the major source of sound transmission at very low frequencies is the quasi-static volume displacement of the shell. This is particularly true for axisymmetric shells, since the great majority of modes resonating at low frequencies are not expected to have significant net volume displacements. The result of this is the maintenance of relatively large values of NR up to 50 cps or so.

This simple quasi-static picture of shell motion is complicated by the possibility of acoustical resonances of the interspace by double-shell structures. Some of these resonances can be driven by the membrane deflection of the shell and may cause low NR at a few selected frequencies. Operational space vehicles may avoid these effects, since the interspace volume is filled with thermal insulation and other equipment.

It should be emphasized that experimental analyses of NR (or any other mechanical-acoustical problem) should be looked on as more than a test of theory. The intelligent use of an experimental facility can be very effective in sorting out competing effects in vibration

240
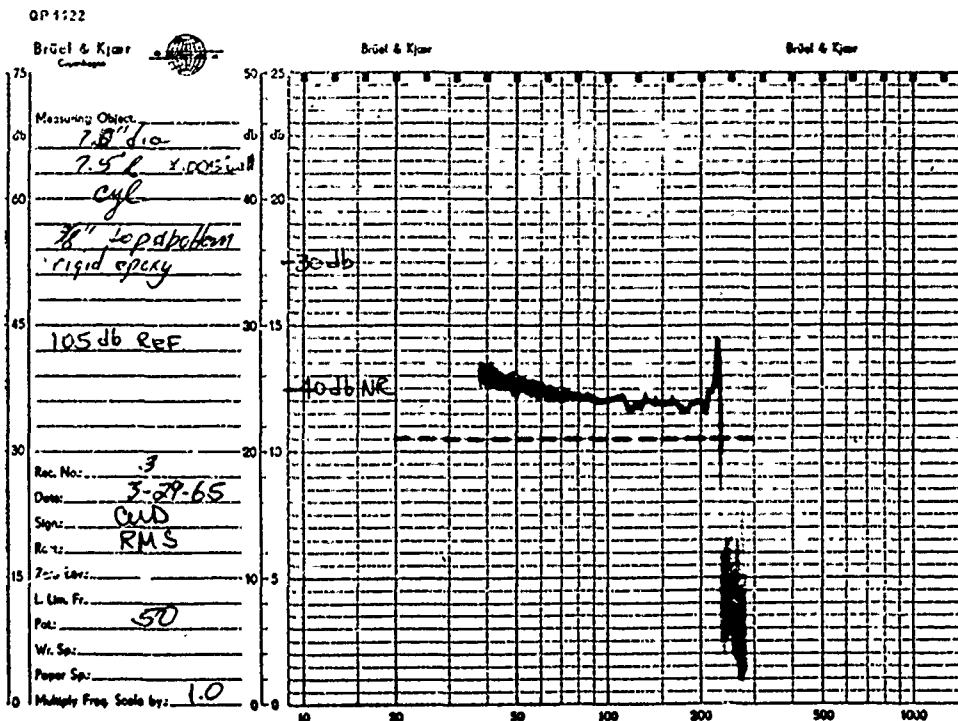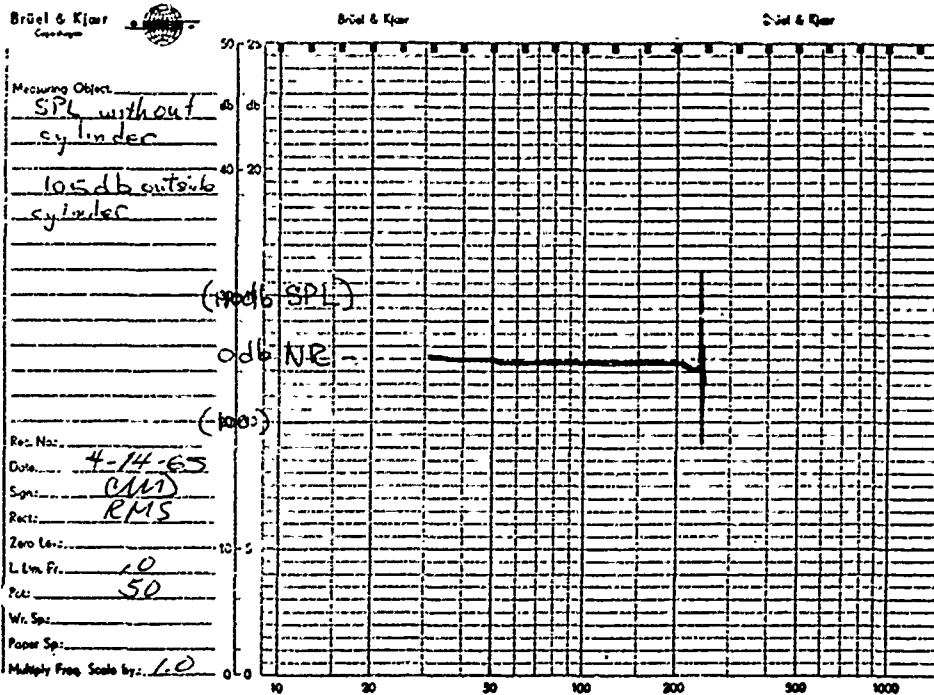
Fig. 5. NR data, 1/4-scale model
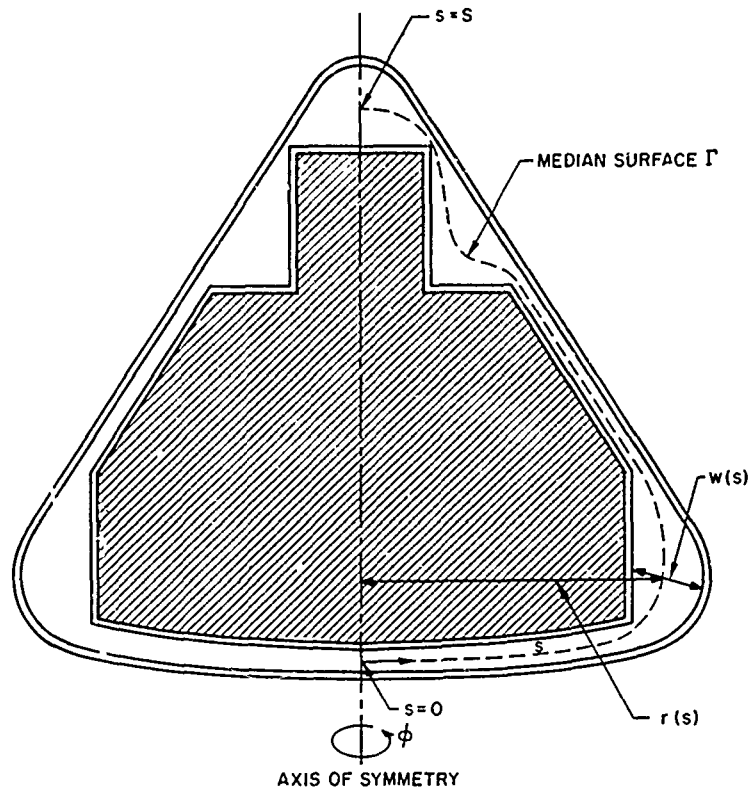
Fig. 6. Sketch of Command Module interspace

and sound transmission. Experiment, used in conjunction with theoretical analysis, can solve problems in sound transmission that either one alone cannot effectively or efficiently accomplish.

REFERENCES

1. F. M. Wiener, "Rocket Noise of Large Space Vehicles," 4th ICA Congress, Copenhagen, Denmark, Aug. 1962

2. H. H. Hubbard, D. A. Hilton, and W. H. Mayes, "Noise Considerations for Manned Reentry Vehicles," NASA TN D-450, Sept. 1960

3. D. E. Goldman and G. E. von Gierke, "Effects of Shock and Vibration on Man," Ch. 44 in Shock and Vibration Handbook, Vol. III (McGraw-Hill, New York), 1961

4. N. L. Carter and K. D. Kryter, "Masking of Pure Tones and Speech," J. Aud. Res. 2(1):66-98 (Jan. 1962)

5. P. M. Edge and W. H. Mayes, "Some Research Features and Capabilities of the Langley Low-Frequency Noise Facility," J. Acoust. Soc. Am. 37:1189(A) (1965)

6. L. L. Beranek, Acoustics (McGraw-Hill, New York), 1954

7. L. L. Beranek, "The Transmission and Radiation of Acoustic Waves by Solid Structures," in Noise Reduction (L. L. Beranek, Ed.) (McGraw-Hill, New York), 1960, p. 287

8. R. H. Lyon, "Noise Reduction of Rectangular Enclosures with One Flexible Wall," J. Acoust. Soc. Am. 35:1791-1797 (1963)

9. S. Timoshenko, Theory of Plates and Shells (McGraw-Hill, New York) 1954, p. 399 ff.

*   *   *

FLEXIBLE TOROIDAL SPRING CHARACTERISTICS*

C. V. David
General Atomic Division of General Dynamics Corporation
Special Nuclear Effects Laboratory
San Diego, California

Flexible toroidal springs have been investigated for an application including highly impulsive loading both on and off axis, and the results are reported. The present study was concerned with multitorus stacks and concentric multistack assemblies that operate as a unit. This arrangement, therefore, limits the torus mounting to clamping on the circle of tangency between the upper and lower tori and the plane of attachment. The torus spring can be submitted to four basic types of loading: compression-tension, bending, shear, and torsion. The characteristics of the spring are highly nonlinear, and exact solutions are almost impossible to calculate, especially for large deformations. Approximate analytical solutions were derived for three modes of loading: compression-tension, shear, and bending.

The torus-system characteristics for these three modes of deformation have been determined. The cross-coupling effects between the shear and bending modes and the structural characteristics of the torus wall are taken into account.

Several small experimental torus spring systems have been constructed and tested both statically and dynamically. Also, the equations of motion, restoring forces, and moments corresponding to the dynamic testing of a plate attached to a three-torus spring system were simulated on an analog computer. The results obtained have been compared and are found to be in good agreement.

INTRODUCTION

The problem of storing energy mechanically is growing more and more acute, since weight usually becomes more critical with the development of more advanced technologies. Large improvements in performance are constantly sought, often in cases where the environmental conditions are more severe. For instance, the need for a spring system that is light, extremely flexible, without moving parts, and requires no bulky connections arose several years ago. After a thorough investigation of various schemes, it became obvious that storing energy by compressing a gas inside a flexible-wall container was the best answer to the problems of weight and the severe shock loading conditions experienced at the connection between the loading mechanism and the spring. Maximum use of the volume available and uniform distribution of the load were also imperative. The design

finally evolved into concentric columns of stocked tori, pressurized and clamped at both ends. This system could operate in either tension or compression, as required.

To determine the dynamic response of such a system, a considerable amount of effort was needed since such a spring system had never been studied in detail. The information required was both analytical and technological. What were the restoring forces and moments developed by the system when subjected to large deformations? How much energy could be stored per unit weight? Could such a system be designed and built? What were its damping characteristics?

Answers to these questions were sought analytically and experimentally almost simultaneously. The results obtained by both methods

---

agree, and means are now available for calculating the response of toroidal springs to static or dynamic loading that are accurate enough that such a spring can be designed confidently, and the response of an existing system to given loads can also be calculated.

SYSTEM DESCRIPTION AND DISCUSSION

A torus spring can be used in a number of ways according to what characteristics and what type of mounting are desired. Figure 1 shows three ways a single torus could be utilized. In all cases, four modes of loading are possible, separately or combined: compression-tension, shear, bending, and torsion. In each case, the types of reactions developed by the torus are conditioned by the way the torus wall deforms. If it is assumed, as a first approximation, that the wall is infinitely flexible and does not stretch along the cross section, these reactions are proportional to the differential pressure (ΔP) across the torus wall. For a displacement ΔX of the load, $\Delta P = P_{(X)} - p$, where $P_{(X)} = P_0 \times f(\Delta X)$ is the absolute pressure inside the torus in the neutral position and p is the external pressure. $f(\Delta X)$ corresponds to the compression taking place inside the torus when it is deformed, since its volume then decreases. The maximum theoretical deformation of the torus system occurs when either the volume has become nil and reactions are infinite or a physical stop has been reached.

For the three cases of Fig. 1, this occurs when

$$\frac{\Delta X}{d} = \sqrt{\left(\frac{\pi}{2}\right)^2 - 1} \cong 1.21 ,$$

for case 1 and for pure axial deformation, in either direction. The reaction is then infinite. For case 2,

$$\frac{\Delta X}{d} = \left(\frac{\pi}{2} - 1\right) \cong 0.571 ,$$
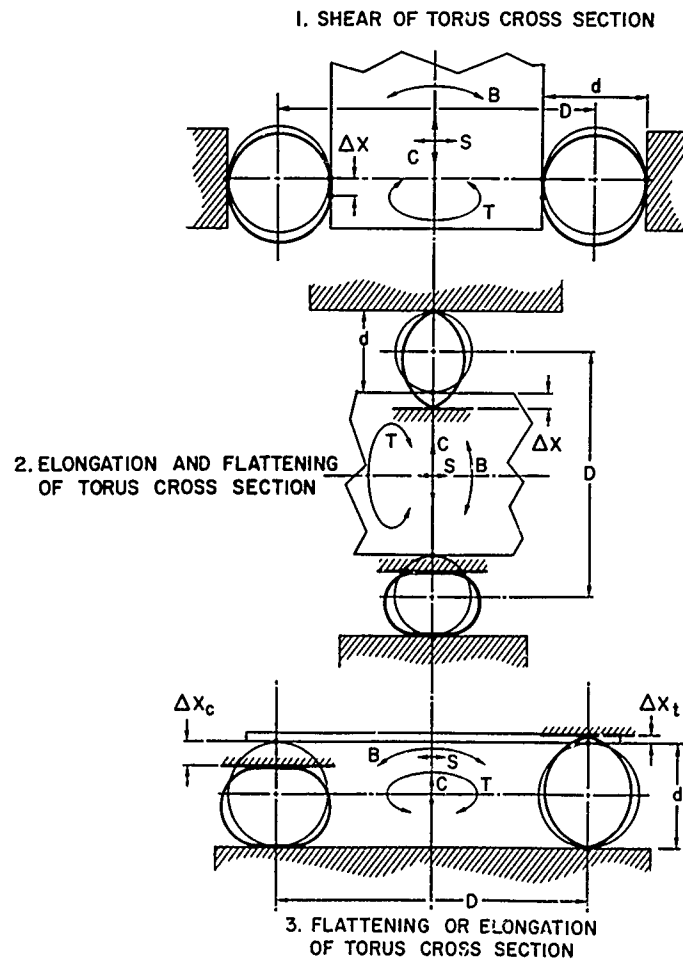
Fig. 1. Various uses of toroidal gas springs

244

when the upper section of the torus is completely stretched out, for instance. The vertical reaction of the system is still finite, since the volume has not decreased much. Finally,

$$\frac{\Delta X}{d} = 1 \quad \text{and} \quad \frac{\Delta X}{d} = \left(\frac{\pi}{2} - 1\right) \cong 0.571 ,$$

for case 3 in compression and tension, respectively. In both instances, the torus reaction is infinite. Cases 1 and 2 exhibit a symmetry in the loading mode, but case 3 does not. In all cases, each single torus section could be replaced by a multitorus-multistack assembly if so desired.

For the application investigated at General Atomic, the use of toroidal springs was limited to case 3, which was the only case that was extensively studied. Also, the torsion mode was not considered, since there was no foreseeable loading in this mode. Figure 2 shows a typical torus system assembly that can be considered as a model. It will be assumed that the pressure outside the tori is either constant or nil; in other words, $p_1 = p_2 = p_3$ at all times. Assuming that the base is rigid and fixed, the loads are applied through a loading plate. The torus internal volumes are sealed and practically no gas can flow in or out.

When the loading plate position changes, the torus cross sections deform and restoring forces and moments are developed. Figure 3 presents the simple case of axial plate displacement. In the compression case, the torus cross section flattens out and the volume inside the torus decreases, causing $P_{(X)}$ to increase. The reaction $F_{(X)}$ against the plate is then $2\pi [P_{(X)} - p] cD$. If tension is applied to the torus cross section, the walls assume a lens shape and the hoop tension developed in the torus walls produces a reaction opposing $F_{(X)}$, with $F_{(X)}$ increasing with ΔX. If shear is applied to the torus stack in either tension or compression, the lack of symmetry of the deformed torus cross section creates a restoring side force. If a tilting motion is superimposed on either of the other
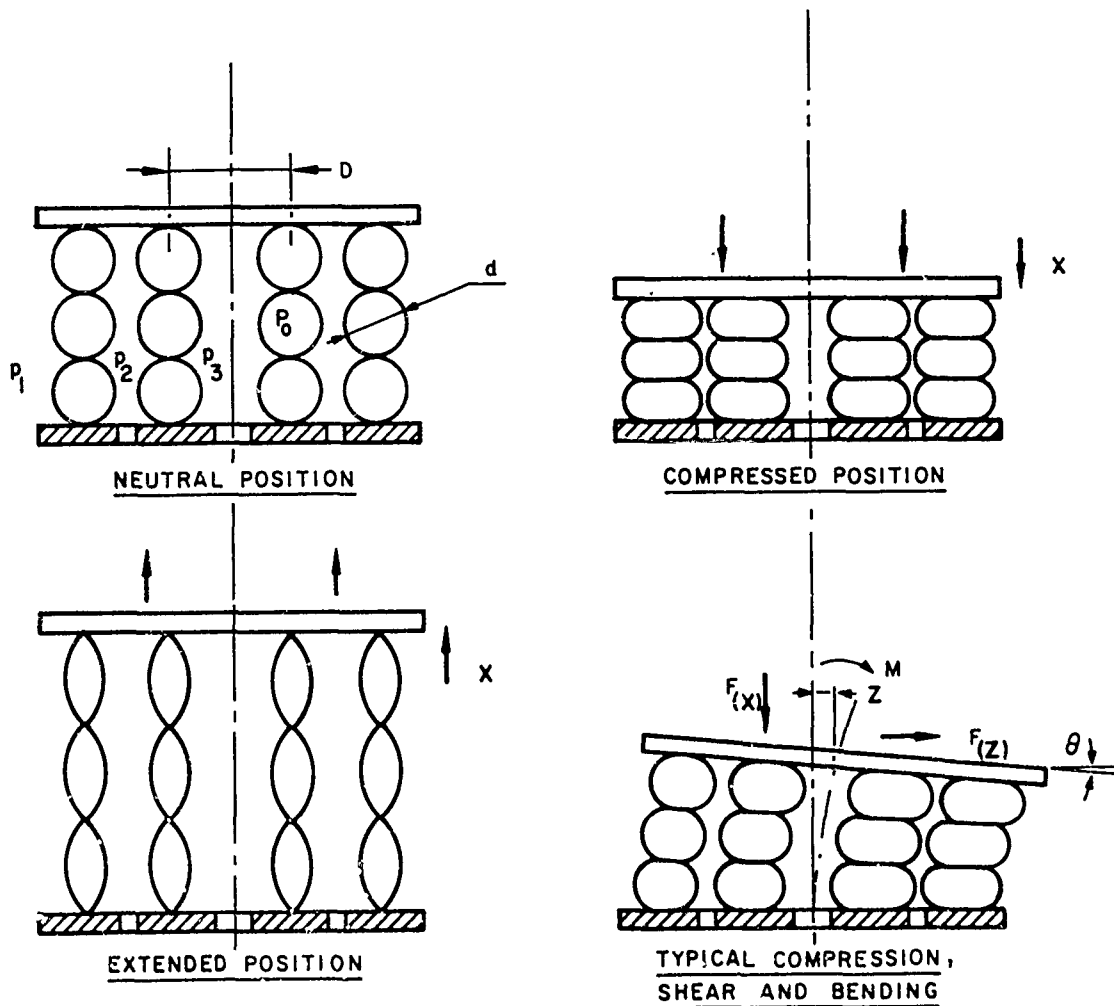
Fig. 2. Toroidal gas spring operation

245
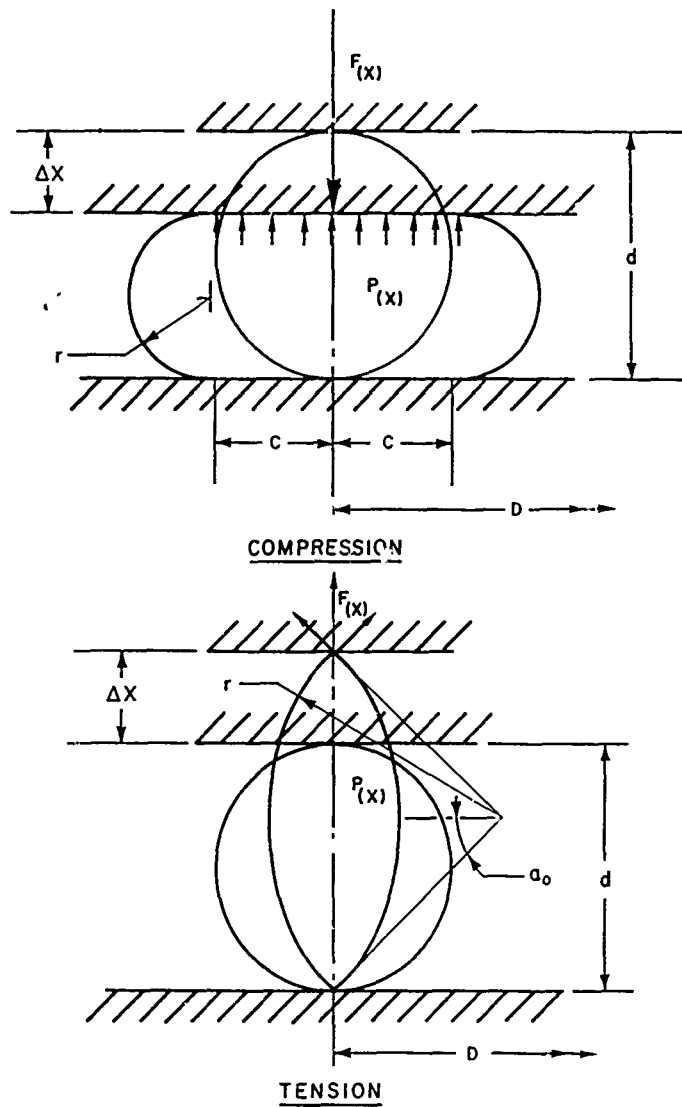
Fig. 3. Torus cross-section deformation in
compression and tension

motion modes of the plate, it is easy to see how the differential flattening or elongation of the torus cross section will cause a restoring moment.

The object of this paper is to give means of calculating these restoring forces and moments when ΔX, d, and D are known for any number of tori in series and/or parallel that are inflated with a pressure P_0 in the neutral position and are made of a material of known characteristics.

RESTORING FORCES AND MOMENTS

A study reported in Ref. (1) yielded the basic equations defining the forces and the moments developed by a stack of tori. These are

expressed in terms of displacements for given applied loads and are as follows:

$$X = \frac{F_{(X)} nd'}{K_F} , \qquad (1)$$

$$\theta = \frac{M_{(\theta)} nd'}{K_M} + \frac{F_{(z)}(nd')^2}{2K_M} , \qquad (2)$$

$$Z = \frac{F_{(z)}(nd')^3}{3K_M} + \frac{F_{(z)} nd'}{K_V} + \frac{M_{(\theta)}(nd')^2}{2K_M} , \qquad (3)$$

where

$$K_F = \pi(P_{(X)} - p) d'DK_{NX} , \qquad (4)$$

$$K_M = \frac{\pi}{8} (P_{(X)} - p) d'D^3 K_{NX} , \qquad (5)$$

246

$$K_v = \frac{\pi}{2} d' D K_{qt}, \qquad (6)$$

and nd' is the average deformed length of the torus stack, n is the number of tori in one stack, and K_{NX} and K_{qt} are stiffness coefficients, defined later. An additional contributing term due to the shearing stiffness was neglected, since it is negligible compared with K_{qt}. The physical significance of most of the parameters given in these equations is shown in Fig. 3.

Equations (1) through (6) are based on the following simplifying assumptions:

1. The torus structure consists of a helically wound, geodesic fiber pattern.

2. Each individual torus is approximated by a ring of short cylindrical sections.

3. The deformation due to fiber stretching is negligible compared with those caused by changes in torus cross section.

4. Tilting and lateral motions are small compared with axial deformations.

5. Two ideal cases are considered where the fiber helix angle, β, is either variable, to keep a true geodesic pattern, or constant.

6. No circumferential constraint at the polar attachment circles of the tori is assumed to exist.

As a first approximation, if $P_0 \gg p$ and if the torus cross section does not vary considerably, one can find an equivalent pressure P_0' such that the value $P_{(x)} - p$ does not differ appreciably from $P_0' f(\Delta X/d)$ for any practical value of $\Delta X/d$. This pressure P_0' will be referred to as P_0 for simplification from now on, keeping in mind that P_0 is actually slightly higher than the gage pressure inside the torus in the neutral position. In vacuum, $p = 0$ and $P_0 \equiv P_0'$, of course. One can now express $P_{(x)}$ as $P_0 f(\Delta X/d)$, where $f(\Delta X/d)$ defines the polytropic compression of the gas inside the torus system.

Replacing K_F, K_M, and K_v by their respective values in Eqs. (1) through (3) and rearranging yields for a stack of n tori of diameter D_i,

$$X_{n_i} = \frac{n}{P_0 D_i} \times \frac{F_{(X)}}{\pi f \left(\frac{\Delta X}{d}\right) K_{NX}}, \qquad (7)$$

$$\theta_{n_i} = \frac{4nM_{(\theta)}}{P_0 D_i^3} \left[2 + \frac{F_{(z)}L}{M_{(\theta)}} \left(1 - \frac{\Delta X}{d}\right)\right] \frac{1}{\pi f \left(\frac{\Delta X}{d}\right) K_{NX}}, \qquad (8)$$

$$Z_{n_i} = \frac{nF_{(z)}}{P_0 D_i} \left\{ \left[\frac{L}{D_i} \left(1 - \frac{\Delta X}{d}\right)\right] \right.$$
$$\times \left[\frac{3M_{(\theta)}}{D_{i(z)}} + \frac{2L}{D_i}\left(1 - \frac{\Delta X}{d}\right)\right] \frac{4}{3\pi f \left(\frac{\Delta X}{d}\right) K_{NX}}$$
$$\left. + \frac{\sigma_0}{E \sin \beta_0 \sin \beta \cos \beta}\right\}, \qquad (9)$$

where σ_0 is the hoop stress in the torus wall and $L = nd$ (torus stack height in the neutral position), after rearrangement of K_{qt} as shown below. One must remember that $\Delta X > 0$ in compression and $\Delta X < 0$ in tension for the signs of Eqs. (8) and (9) to be correct.

Reference (1) gives

$$K_{qt} = \frac{4EA \sin \beta \cos \beta}{\Delta \ell}, \qquad (10)$$

where Δ is the torus cross section perimeter, ℓ is the length of a fiber between intersections (Fig. 4), E is the modulus of elasticity, and A is the fiber cross section. The number of fibers per inch of torus circumference is then

$$n' = \frac{1}{\ell \sin \beta} \qquad (11)$$

and

$$K_{qt} = \frac{4n'EA \sin^2\beta \cos \beta}{\Delta}, \qquad (12)$$

but $\Delta = \pi d$ and $n'A = t$, if t is the equivalent wall thickness of the torus structural material. Then,

$$K_{qt} = \frac{4Et \sin^2\beta \cos \beta}{\pi d}; \qquad (13)$$

t is related to the hoop stress, σ_0, in the torus wall in the neutral position by

$$2t\sigma_0 = P_0 d. \qquad (14)$$

Therefore,

WOUND FILAMENT CONFIGURATION

TYPICAL FORCE DIAGRAM
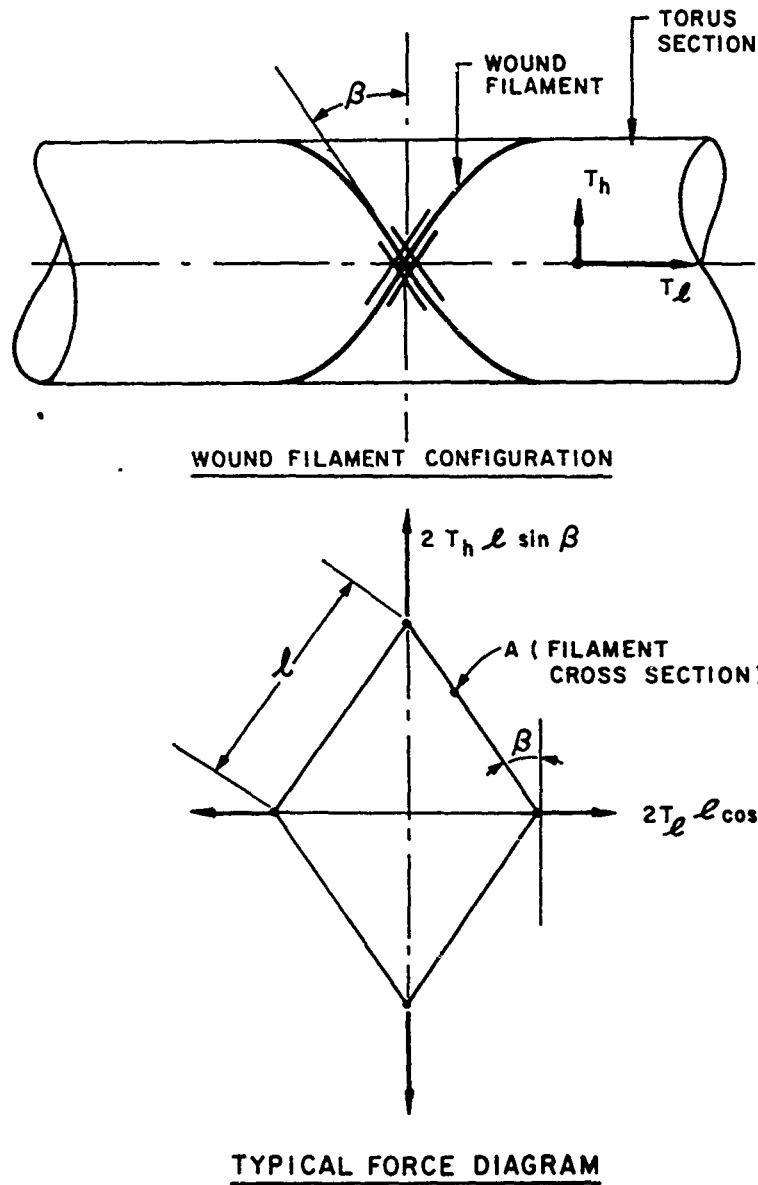
Fig. 4. Elementary diagram of forces
developed by structural fibers

$$K_{qt} = \frac{2EP_0 \, \sin^2\beta \, \cos\beta}{\pi\sigma_0} . \qquad (15)$$

K_{qt} is then only a function of the mechanical properties of the torus-wall structural material, and

$$K_{qt} = \frac{2E \, \sin^2\beta \, \cos\beta}{\pi\sigma_0} . \qquad (16)$$

For practical cases where D is independent of $\Delta X/d$ and does not vary, both n' and t should remain constant and

$$K_{qt} = \frac{2E \, \sin\beta_0 \, \sin\beta \, \cos\beta}{\pi\sigma_0} . \qquad (17)$$

The torus internal pressure was factored as shown in Eq. (9). The replacement of K_{qt} by its value in Eqs. (6) and (3) yields Eq. (9).

It is then possible to define a rigidity for the three types of possible motions (X, θ, and Z) in one plane for any torus stack of diameter D, if one divides Eq. (7) by $F_{(X)}$, Eq. (8) by $M_{(\theta)}$, and Eq. (9) by $F_{(Z)}$. Then, one can finally write

$$\frac{X}{F_{(X)}} = X_c = \frac{n}{P_0 D} \times X^* , \qquad (18)$$

$$\frac{\theta}{M_{(\theta)}} = \theta_c = \frac{n}{P_0 D^3} \times \theta^* , \qquad (19)$$

248

$$\frac{Z}{F_{(z)}} = Z_c = \frac{n}{P_0 D} \times Z^* , \qquad (20)$$

where

$$X^* = \frac{1}{\pi f \left(\frac{\Delta X}{d}\right) K_{NX}} , \qquad (21)$$

$$\theta^* = \frac{4}{\pi f \left(\frac{\Delta X}{d}\right) K_{NX}} \left[2 + \frac{F_{(z)} L}{M_{(\theta)}} \left(1 - \frac{\Delta X}{d} \right) \right], \qquad (22)$$

and

$$Z^* = \frac{4}{3\pi f \left(\frac{\Delta X}{d}\right) K_{NX}} \left\{ \frac{L}{D} \left(1 - \frac{\Delta X}{d} \right) \left[\frac{3M_{(\theta)}}{F_{(z)} D} + 2 \frac{L}{d} \left(1 - \frac{\Delta X}{d} \right) \right] \right\}$$

$$+ \frac{\sigma_0}{E \sin \beta_0 \sin \beta \cos \beta} . \qquad (23)$$

For a given structural material, defined by β, E, and σ_0, and a given aspect ratio L/D, one sees that for a fixed amount of axial compression or tension the torus-system rigidity coefficients X_c, θ_c, and Z_c are functions only of the torus-system size and configuration and the pressure inside the torus, since X^*, θ^*, and Z^* are dimensionless. It is then possible to calculate X_c, θ_c, and Z_c very easily for any value of $\Delta X/d$ if L/D and $M_{(\theta)}/F_{(z)}$ are defined. In other words it is straightforward to calculate the deformation of a given toroidal spring under known loads. But because of the cross-coupling between θ^* and Z^*, it is more difficult to determine the reactions of the same system when the deformations are known. One must define explicitly both $M_{(\theta)}$ and $F_{(z)}$ as functions of the deformations θ and Z.

It has been assumed that $f(\Delta X/d)$ and K_{NX} are independent of any other parameters. This can be easily shown for both tension and compression of the torus.

Compression

Assuming that the torus-wall stretching is negligible and referring to Fig. 3, one has

$$\frac{\pi r}{2c} = \frac{d - \Delta X}{\Delta X} , \qquad (24)$$

and assuming that the torus volume varies as the cross section (D remains constant),

$$\frac{V_0}{V_X} = \frac{\pi d^2}{4(2rc + \pi r^2)} . \qquad (25)$$

After substitution of Eq. (24) into Eq. (25) and rearrangement,

$$\frac{V_0}{V_X} = \frac{1}{1 - \left(\frac{\Delta X}{d}\right)^2} . \qquad (26)$$

For a polytropic compression of the gas inside, one has

$$P_{(X)} = P_0 \left(\frac{V_0}{V_X}\right)^\gamma = P_0 \left[\frac{1}{1 - \left(\frac{\Delta X}{d}\right)^2} \right]^\gamma \qquad (27)$$

and

$$f \left(\frac{\Delta X}{d}\right) = \left[\frac{1}{1 - \left(\frac{\Delta X}{d}\right)^2} \right]^\gamma . \qquad (28)$$

K_{NX} is defined as $dN_X/d(\Delta X)$ (1, Eq. (66)), where N_X is the axial loading on the torus per linear unit of length along its attachment to the loading plane per unit of pressure inside the torus and is given by

$$N_X = \frac{\pi}{2} \left[\frac{\frac{\cos \beta}{\cos \beta_0}}{1 + \frac{\pi r}{2c} \left(1 - \frac{\cos \beta}{\cos \beta_0} \right)} \right] \Delta X . \qquad (29)$$

Substituting Eq. (24) into Eq. (29) yields

$$N_X = \frac{\pi d}{2} \left[\frac{\frac{\cos \beta}{\cos \beta_0}}{1 + \left(\frac{d}{\Delta X} - 1\right) \left(1 - \frac{\cos \beta}{\cos \beta_0} \right)} \right] \frac{\Delta X}{d} , \qquad (30)$$

where N_X is again a function of $\Delta X/d$.

In the case of a filament-wound torus, which is truly isotensoidal in nature, in the neutral position the value of β_0 is well defined and equal to 35.3 degrees. But when the torus cross section deforms, the angle made by the filaments changes, since they are free to "pantograph," and β becomes a function of $\Delta X/d$, which makes the differentiation of Eq. (30) awkward analytically but easy to compute with digital-computer techniques. Therefore, for every value of $\Delta X/d$

249

and the corresponding value of β, a value of K_{NX} can be obtained.

β is given in Eq. (51) of Ref. (1) as

$$\beta = \tan^{-1} \sqrt{\frac{1}{2} \frac{1 + \frac{4c}{\pi r}}{1 + \frac{2c}{\pi r}}} \, . \qquad (31)$$

Substituting Eq. (24) into Eq. (31) again yields

$$\beta = \tan^{-1} \sqrt{\frac{1 + \frac{\Delta X}{d}}{2}} \, . \qquad (32)$$

The problem is entirely defined for this case.

Tension

With the same assumptions as are made above (Fig. 3), one sees that

$$\sin a_0 = \frac{2a_0}{\pi} \left(1 + \frac{\Delta X}{d} \right) . \qquad (33)$$

For every value of $\Delta X/d$, Eq. (33) can be solved and one gets a single meaningful value of a_0.

The same reasoning about the gas compression inside the torus system applies, and

$$f\left(\frac{\Delta X}{d}\right) = \left[\frac{2a_0}{\pi \left(1 - \frac{\sin 2a_0}{2a_0} \right)} \right]^\gamma . \qquad (34)$$

In this case, the relationship between β and a_0 is given by Eq. (61) of Ref. (1) and

$$\beta = \tan^{-1} \sqrt{\frac{1}{2} \left(1 - \frac{\sin a_0 \cos a_0}{a_0} \right)} \, . \qquad (35)$$

Therefore, β again becomes a function of $\Delta X/d$, and a solution is always possible for every value of $\Delta X/d$ between 1 and $\pi/2 - 1$ if the torus attachment to a flat plate driving the free end of the torus system is assumed rigid.

The value of N_X in this case (1) is

$$N_X = \left(\frac{\cos a_0}{\sin a_0 - \frac{2a_0}{\pi} \frac{\cos \beta_0}{\cos \beta}} \right) \Delta X . \qquad (36)$$

Multiple-Torus Stack System

If concentric stacks of multilayer tori are assembled together between two rigid planes, one has

$$F_t(X) = \Sigma F_{(X)} = \frac{P_0 X}{nX^*} \Sigma D_i , \qquad (37)$$

$$M_t(\theta) = \Sigma M_{(\theta)} = \frac{P_0 \theta}{n} \sum \frac{D_i^3}{\theta_i^*} , \qquad (38)$$

$$F_t(Z) = \Sigma F_{(Z)} = \frac{P_0 Z}{n} \sum \frac{D_i}{Z_i^*} , \qquad (39)$$

where θ_i^* and Z_i^* are functions of L/D_i and $M_{(\theta)}/F_{(Z)}D_i$ as shown by Eqs. (29) and (30). One should remember that this applies only if all tori have the same cross section in the neutral position.

Results

K_{NX} in compression and tension for variable and constant β is given as a function of $\Delta X/d$ in Fig. 5. The variations of β, $f(\Delta X/d)$, and a_0 (when applicable) with $\Delta X/d$ for the compression and tension cases are presented in Figs. 6 and 7, respectively. Figure 8 shows X^*. Because of the cross-coupling effects between θ^* and Z^*, these are not given in this paper but are available in Ref. 2, where L/D_i, $M_{(\theta)}/F_{(Z)}D_i$, σ_0, and E are used as parameters.

ENERGY STORAGE

The toroidal spring system described previously is best suited for axial loading, both in compression and in tension. The bending and shear loads applied are usually incidental and of much smaller magnitude than the compression and tension forces. Furthermore, because of the cross-coupling between the tilting and lateral motion modes, it would be impossible to integrate the force and moment equations to calculate the energy stored during the deformation of the torus stack. This cross-coupling effect between the axial motion mode and tilting and lateral modes was neglected and, therefore, the integration of Eq. (7) is straightforward and accurate enough as a first approximation for any values of θ and Z.

For a torus stack in compression, if one uses the value $K_{NX} = \pi/2$ one gets
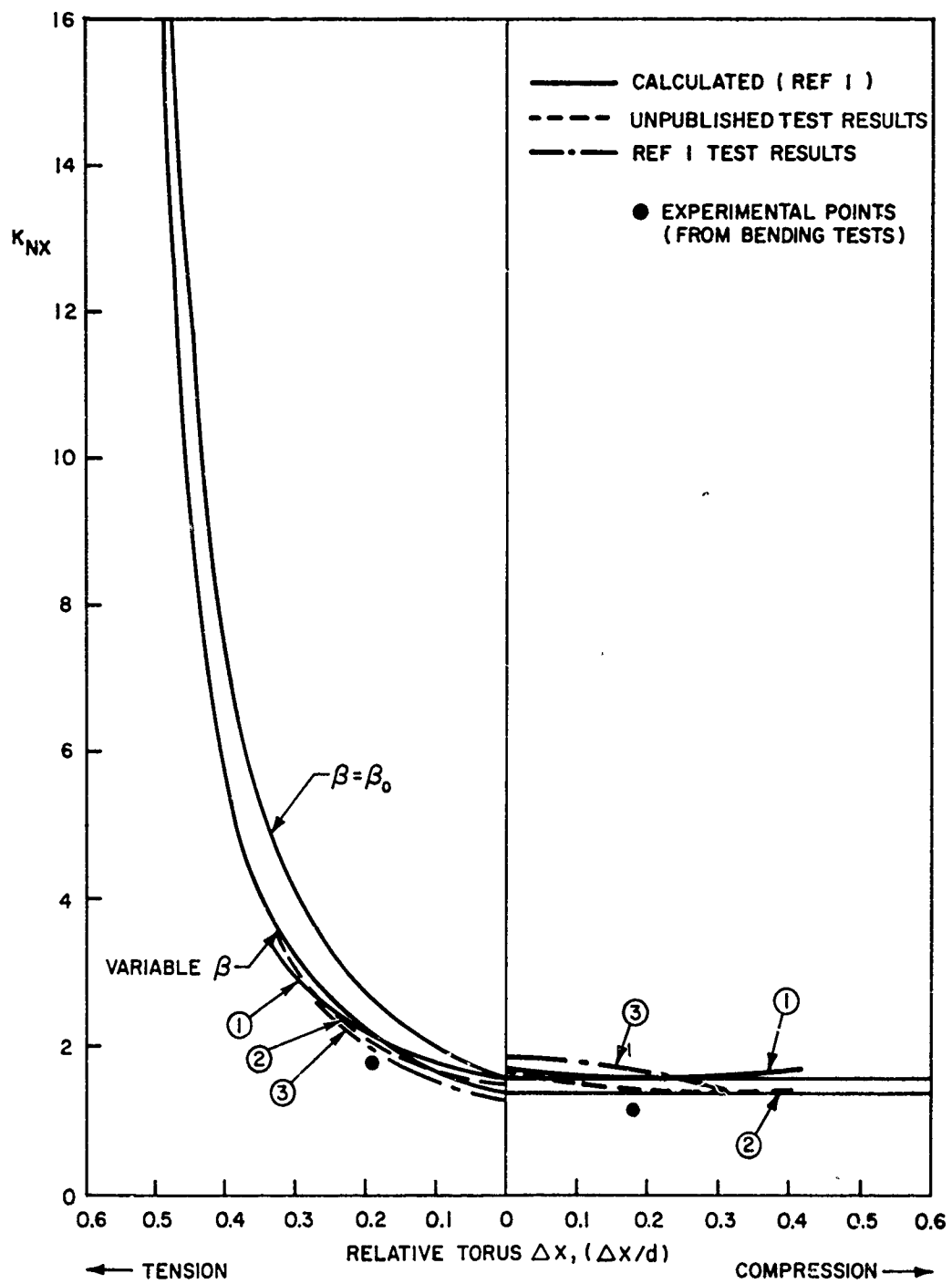
Fig. 5. Typical variation of K_{NX} as a function of $\Delta X/d$
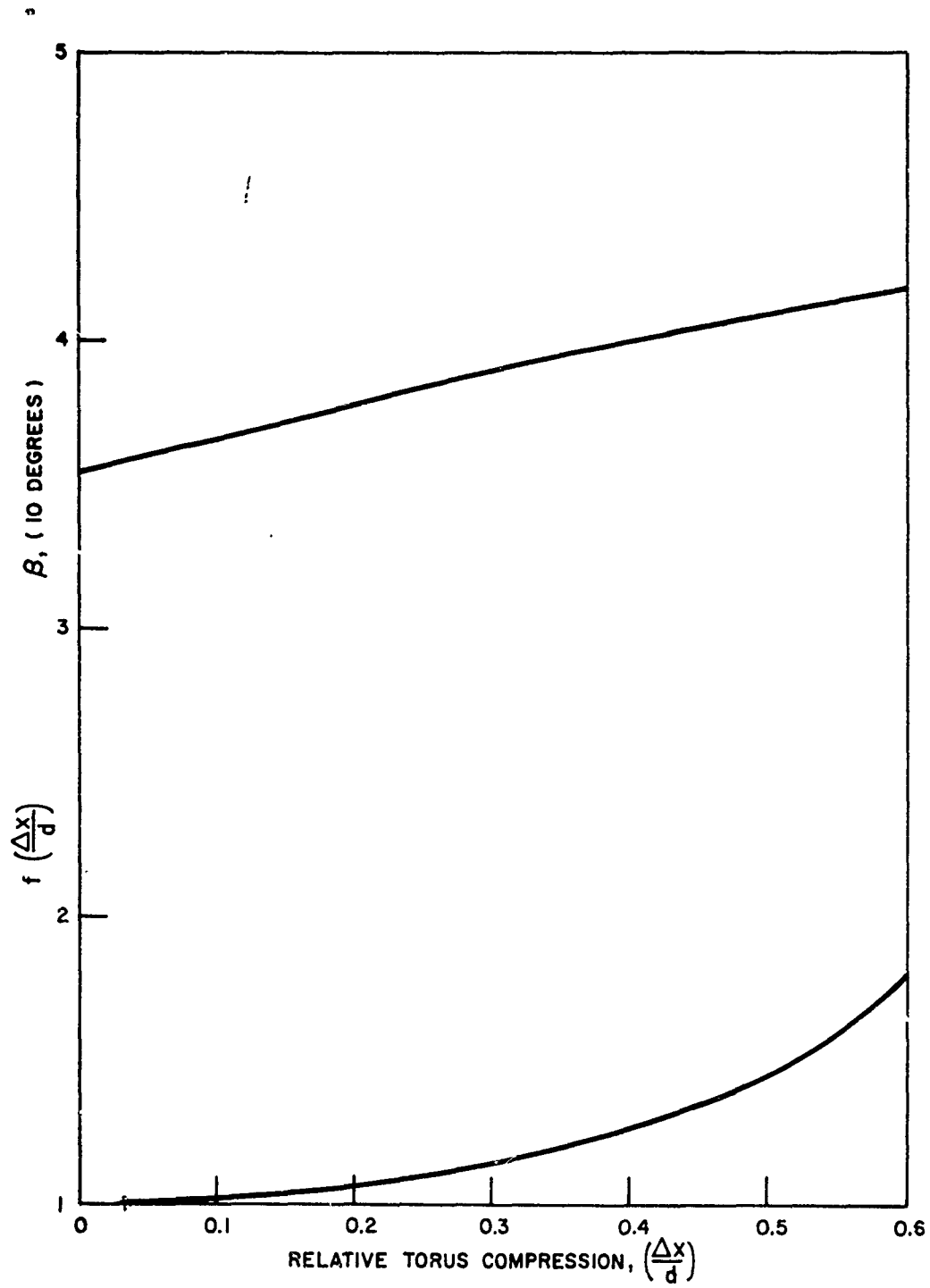
Fig. 6. Variation of β and $f(\Delta X/d)$ in compression
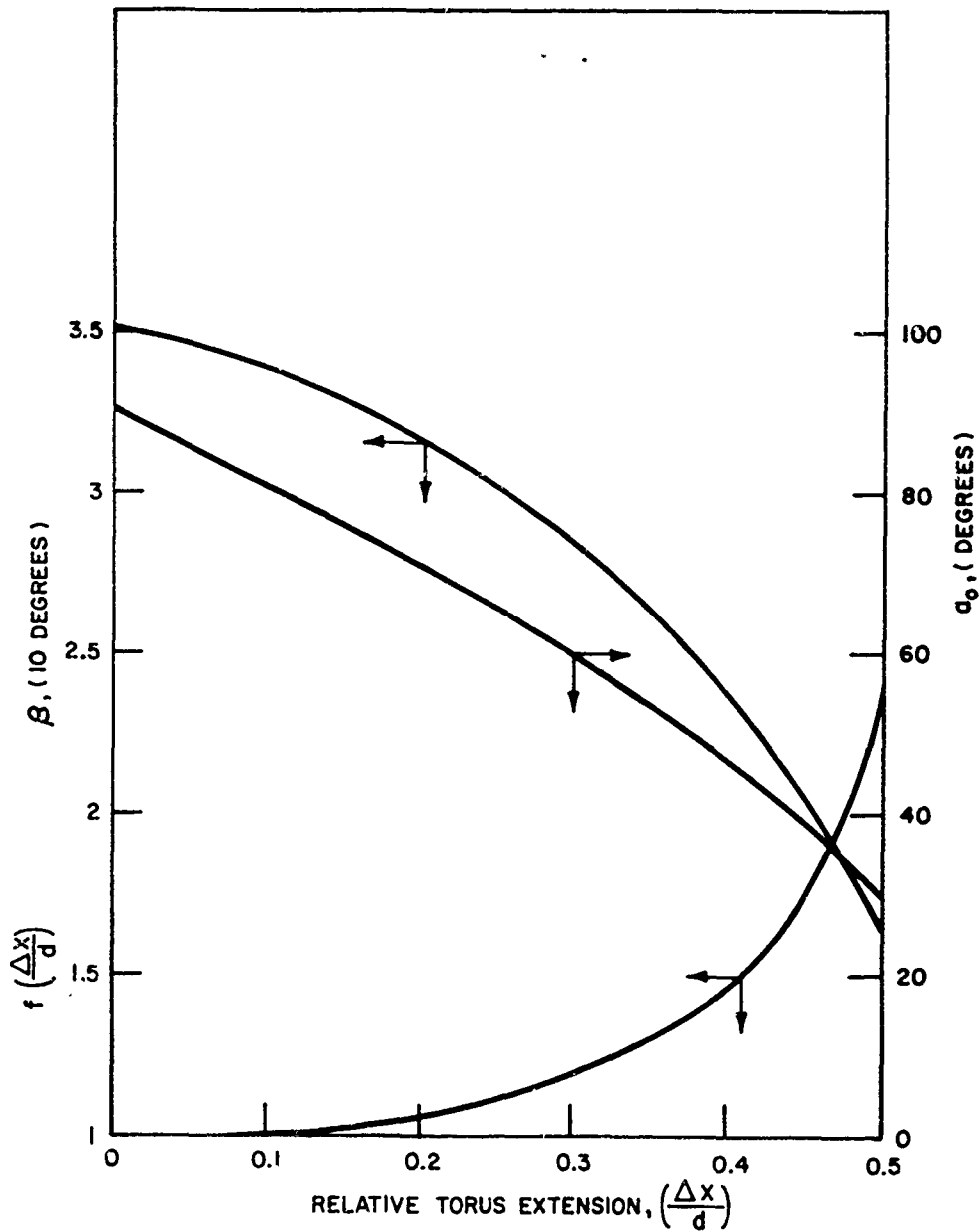
Fig. 7. Variation of β, a_0 and $f(\Delta X/d)$ in tension

$$F_{(X)} = \frac{\pi^2 P_0}{2n} D_i f\left(\frac{\Delta X}{d}\right) X_{n_i} . \qquad (40)$$

For each individual torus, using Eq. (28), one has

$$F_{(X)} = \frac{\pi^2}{2} \cdot P_0 dD \left[1 - \left(\frac{\Delta X}{d}\right)^2\right]^{-\gamma} \left(\frac{\Delta X}{d}\right) , \qquad (41)$$

since $X_{n_i} = n\Delta X$.

The integration of Eq. (41) between the neutral position and a compression ΔX for each torus yields

$$E_{(S)} = \frac{\pi^2}{1.6} P_0 d^2 D \left\{\left[1 - \left(\frac{\Delta X}{d}\right)^2\right]^{1-\gamma} - 1\right\} , \qquad (42)$$

where $E_{(S)}$ is the energy stored. This equation can be rewritten as

$$E_{(S)} = P_0 d^2 D E_c^* ,$$

where E_c^* is a dimensionless function of $\Delta X/d$. The value of E_c^* is shown in Fig. 9.

For the tension case the equations expressing K_{NX} and $f(\Delta X/d)$ are too complex for an analytical integration to be attempted, and Eq. (7)
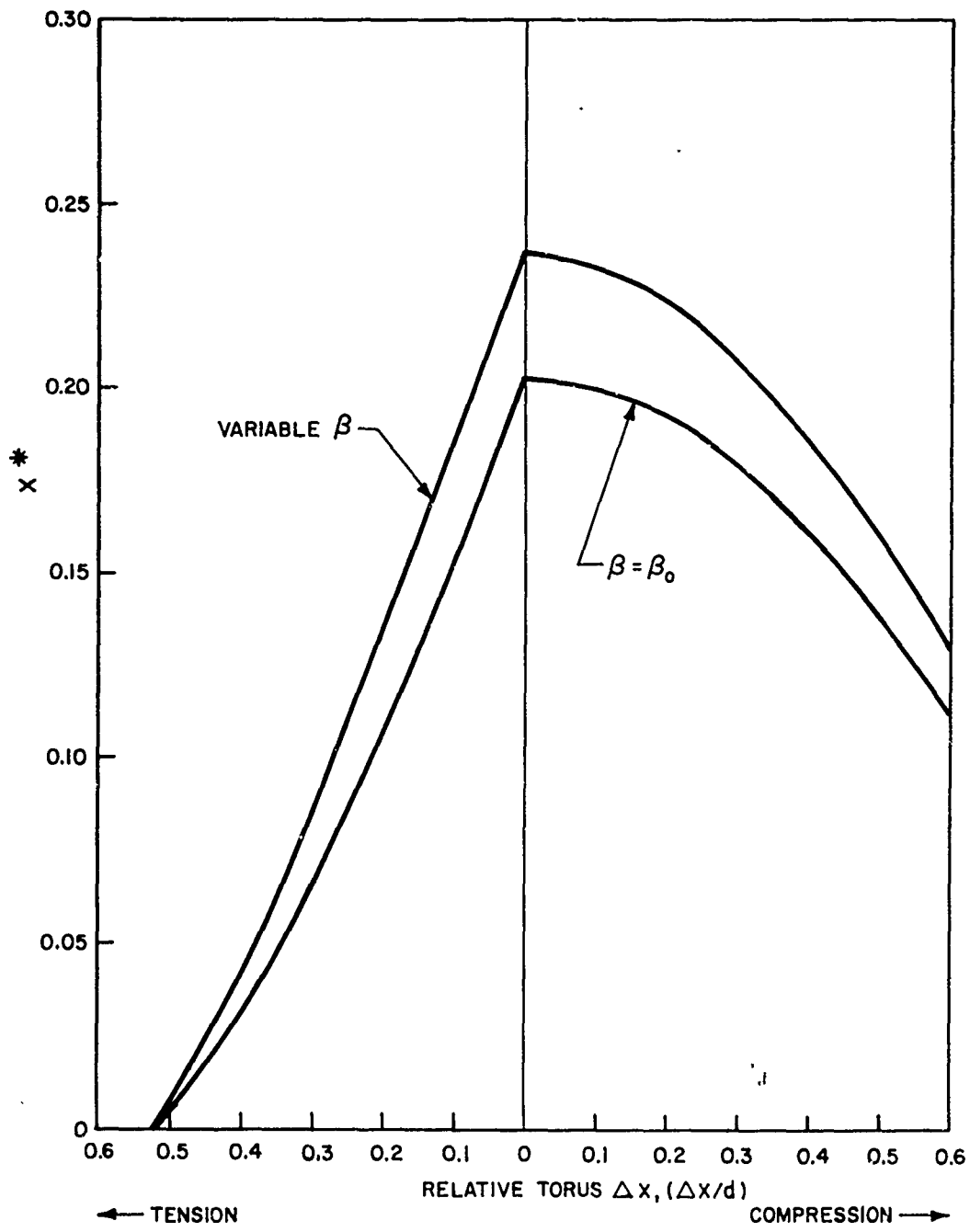
Fig. 8. Variation of X^* as a function of $\Delta X/d$
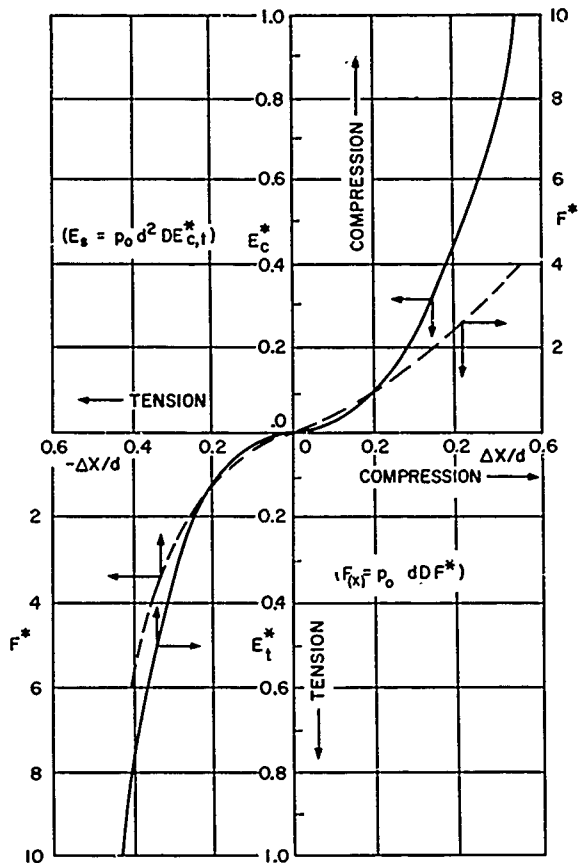
Fig. 9. E^* and F^* as functions of $\Delta X/d$

was integrated numerically. A result identical in form to Eq. (42) can be obtained:

$$E_{(S)} = P_0 d^2 D E_t^* . \tag{43}$$

A plot of E_t^* is also given in Fig. 9. We can easily see how the problem of designing a torus spring for a given energy storage requirement can be solved. On the other hand, for a given system configuration and axial deformation it is quite simple to calculate the energy stored in the gas spring. For a stack of n tori, $E_{(X)}$ should be multiplied by n.

Incidentally, Eq. (7) can also be written as

$$F_{(X)} = \pi P_0 \, dD \, f\left(\frac{\Delta X}{d}\right) K_{NX} \frac{\Delta X}{d} . \tag{44}$$

Again, one can express this equation as

$$F_{(X)} = P_0 \, dD \, F^* , \tag{45}$$

where F^* is a function of $\Delta X/d$. The number of tori in a stack is immaterial in this case, since they all develop the same reaction, and consideration of an individual torus of the stack

sufficies. F^* for compression and tension is also plotted in Fig. 9 for convenience if one does not wish to use the curves of Fig. 8.

These curves are sufficiently accurate for most practical engineering uses. Nevertheless, one should not forget that they are based on several assumptions that cannot be grossly violated indiscriminately.

EXPERIMENTAL RESULTS

Models of toroidal gas springs have been designed, built, and tested under both static and dynamic conditions. Experimental results were obtained and were compared with the characteristics calculated from Eqs. (25) through (39). Satisfactory agreement was established between the two conditions, although not as good as one might wish. This is mainly due to the fact that it is impossible to manufacture and install torus systems in the ideal way assumed for the analytical treatment. For instance, a discussion of β and of its significance might be useful at this time. As explained in the section on restoring forces and moments, β is the winding angle of the filament. When the torus is in compression or tension, its cross section deforms, but in all cases the free part of the torus wall (unrestrained) assumes a circular shape, and, if free to do so, the filaments will rearrange themselves so that they transmit only pure tension, and β will then adjust. At the limit of compression, then, one has $\beta = 45$ degrees, and at the limit of tension $\beta = 0$ (see Eqs. (32) and (35)). But two constraints are usually present in the system:

1. Shear reaction between the crossing filaments and between the filaments and the gastight inner shell (for instance, an inner tube); and

2. Shear reaction between the torus and its attachments to the end plates used for the compression and extension of the system.

If one assumes that these end plates are rigid (forcing the torus diameter, D, to remain constant), one can easily understand that in the tension case, for example, β cannot become zero at any time but actually remains almost constant. Therefore, practically, it would be more realistic to assume that β does not vary in tension. In compression the difference between the two assumptions is less important, and the actual characteristic is probably in between the two limits. Also, other arrangements of the structural filaments should be considered, such as knitting. In most practical cases, the

structural material must be bonded to a flexible shell to stabilize the filament mesh pattern. All these factors tend to make the torus wall overall structure behave quite differently from the idealized configuration assumed in the section on restoring forces and moments.

The lateral stiffness is also a function of the structural filament characteristics, working stress level, and modulus of elasticity. Therefore, three typical materials were investigated—nylon, Dacron, and steel wire—to determine whether this effect was significant. Table 1 gives values of σ_0 and E that were used for the calculations.

TABLE 1
σ_0 and E Values for Lateral
Stiffness Calculations

Material	σ_0 (10^3 psi)	E (10^6 psi)
Nylon	20	1
Dacron	20	5
Steel wire	100	30

As shown in Ref. (2), the influence of the structure is noticeable only for small values of L/D and also if $M_{(\theta)}/F_{(z)}D$ is small. This influence is more pronounced for high values of $\Delta X/d$. A small value of L/D corresponds to a very short torus stack and a small value of $M_{(\theta)}/F_{(z)}D$ to a small amount of bending; therefore, for a long and flexible stack of tori subjected to an appreciable bending deformation one can ignore the nature of the structural material of the torus wall. The curves of K_{NX} in tension and compression for constant and variable β given in Fig. 5 also point out that, as a first approximation, one could ignore the influence of β.

During the investigation, two types of torus systems were built: a three-torus stack made of nylon cloth wrapped and sewed around bicycle inner tubes, and two single tori made of Dacron filaments wound and knitted and locked on a thin-wall polyurethane inner tube. Both systems were tested statically and dynamically to determine their response to known loads, whether applied slowly or in an impulsive fashion. The test specimens, the testing procedures, and the test results are described at length elsewhere. These results were analyzed and reduced to a form that could be presented in Fig. 5.

Curve 1 corresponds to the nonstretchable wall case with a polytropic compression coefficient γ of 1.3 (see Eqs. (28) and (34)). Curve 2 represents experimental data obtained with the crudely built three-torus stack. Curve 3 was obtained by Astro Research Corporation (1) with a single torus. Finally, the values of K_{NX} calculated with $\beta = \beta_0$ and β variable are also given. Two typical values of K_{NX} are also indicated by a point. These two values were computed from a single-torus bending and rolling test reported in Ref. (1).

The values of K_{NX} are scattered appreciably in the range of $\Delta X/d$ investigated experimentally but are within the scatter bandwidth determined by the two assumptions $\beta = \beta_0$ and β variable, especially for compression. In tension, all the experimental values of K_{NX} depart from the results given in Eq. (36). Increasing values of $\Delta X/d$ correspond to increasing values of the tension developed at the torus-system attachments. Such attachments are quite difficult to make rigid and nonstretchable without affecting the torus behavior. This is not true for the compression case, which could explain why deformation of the attachment in tension would decrease the torus axial stiffness, as is observable in Fig. 5.

The single value of K_{NX} in compression, obtained from torus bending, also departs appreciably from the other experimental results. This, too, can be explained by the lack of rigidity of the torus attachment. The effect is more pronounced for a single-torus system than for a multitorus system. This would justify the lower values of K_{NX} given by curve 3 of Fig. 5 as compared with those given by curve 2.

Experimental results obtained with a single torus in shear (lateral rigidity) are given elsewhere. The lack of rigidity of the torus attachment is particularly obvious in this case, and the results presented are practically useless. They yield values of K_{NX} several times lower than those theoretically calculated.

For practical purposes, it is suggested that the two conditions that are best representative of a practical torus system behavior are for compression, $\beta = \text{constant} = \beta_0$, and for tension, β variable, unless additional experimental results for larger $\Delta X/d$ do not confirm the results already at hand.

Finally, an attempt was made to simulate the dynamic response of the three-torus system model on an analog computer with the use of a

mathematical model embodying the torus restoring force and moment equations derived earlier. The goal was to check whether the cross-coupling between the bending and shear deformation modes was adequately expressed by Eqs. (29) and (30). In the experiments, the torus system was compressed by a plate attached to it and accelerated by the explosion of an HE charge. In some cases the charge had been placed off-center to study the behavior of this spring concept under off-axis loads. This systematically caused a lateral oscillation of the plate that could not result from plate-charge shock wave interaction. The coefficients of the mathematical model equations, the amount of damping, and the initial conditions were calculated from the characteristics of the torus system model and also from the test results (static and dynamic). After some adjustment of the lateral stiffness coefficient, the curves of Fig. 10 were obtained. They compare well enough with the two experimental curves obtained elsewhere, especially since the latter were not reproducible to the same degree of accuracy from one test to another.
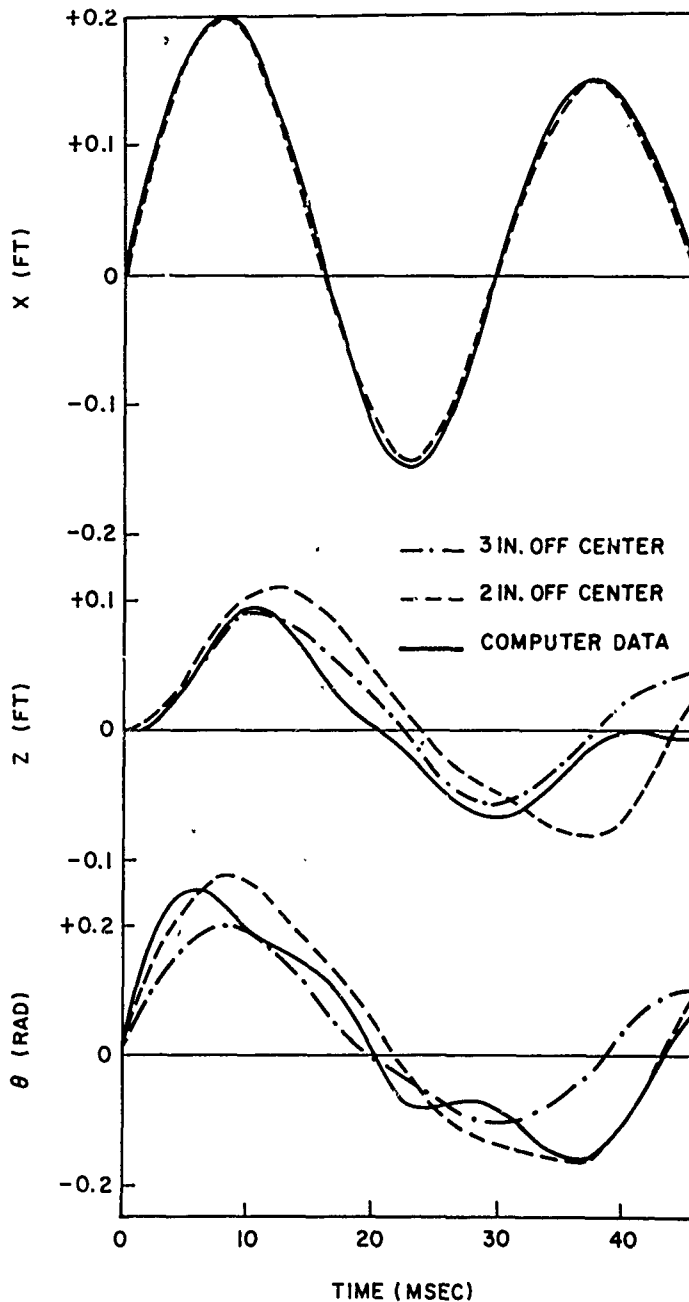
Fig. 10. Comparison of experimental and analytical dynamic characteristics of three-torus system

257

Numerous other dynamic tests conducted with a single torus clamped on a plate and equipped with a counterweight to simulate the axial loading by the inertia effect have also demonstrated that energy storage capacity and the forces developed in compression and tension agreed with the formulas given in this paper.

Finally, Fig. 11 presents a comparison between the calculated force characteristics of the three-torus system and the static test results. One sees that the agreement is excellent in tension but is somewhat lacking in compression. The system had been cycled 1000 times before the experimental curves were recorded. The amount of hysteresis is small.

phenomenon that would exist at early compression times of the torus if the plate were flat, as ideally contemplated. This snatching phenomenon is caused by the fact that the plate velocity increment V_p is larger than the vertical component of the wave velocity propagating along the torus wall and creates a release of the wall hoop tension, until this part of the wall is later snatched back into place. The shape of this clamping boss, of course, affects the torus characteristics and is an additional cause of error in the comparison of experimental results with analytical calculations.

Fig. 11. Comparison between experimental and analytical results for pure axial deformations

TYPICAL FLAT CLAMPING GROOVE

TYPICAL IDEALLY SHAPED CLAMPING BOSS
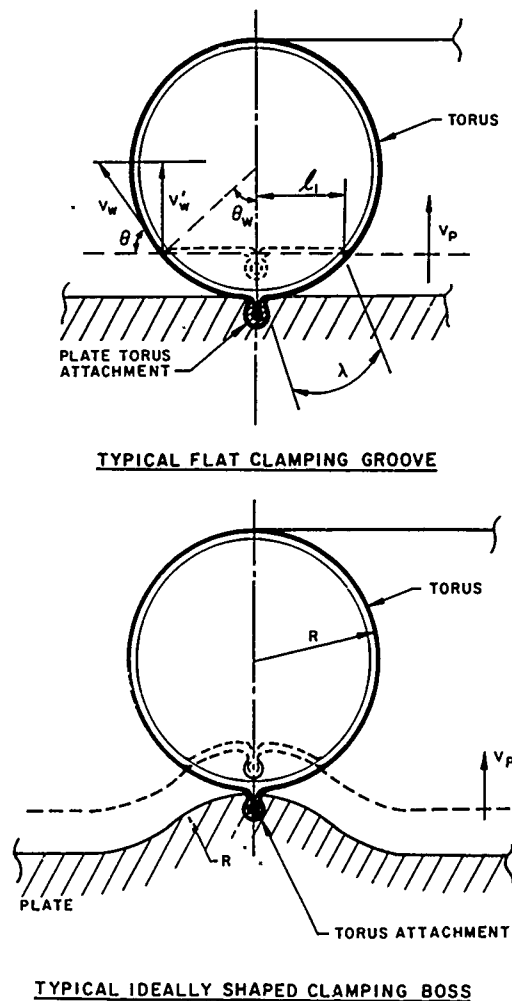
Fig. 12. Typical torus system attachment scheme

The problems of torus attachment to a plate subjected to repeated high-intensity shocks are very difficult to solve. A typical machined clamping boss, shown schematically in Fig. 12, was developed to be an integral part of the plate but also to eliminate the torus wall snatching

CONCLUSIONS AND RECOMMENDATIONS

Toroidal, flexible, gas-inflated, low-weight structures have proved to be excellent gas springs for special applications where no reaction is required in the neutral position and when

both compression and tension strokes are specified. This gas-spring configuration also permits rotation and side motion with resulting restoring forces so that operation is possible with six degrees of freedom. It is important, therefore, to be able to calculate the characteristics of such systems so that the designer may evaluate their performance when used within a more complex piece of equipment. They are particularly valuable in applications where shock loading is expected, since they can be made very flexible, even at their point of attachment. Although few applications have been considered so far because of their high cost due to the manufacturing complexity, torus systems should be investigated as possible gas springs whenever special requirements compatible with torus system characteristics have to be met.

Because of the complexity of the analysis of a system where both bending and side motions are involved, many simplifying assumptions have to be made to make the problem amenable to analytical treatment. The results obtained from such a study check relatively well with crude experimental data. Therefore,

it is believed that the results given in this paper are probably accurate enough for an approximate evaluation of the rigidity of a torus stack when used as a gas spring. It would be desirable to confirm these results with additional tests conducted with carefully constructed and rigidly attached multitorus stacks. Also, the influence of the type of construction, i.e., cloth or knitted filament, unidirectional or not, should be investigated further.

The experimental investigation should also include tests at higher values of $\Delta X/d$ than have yet been performed, especially for tension, since the discrepancy between theory and experiment seems greater in this case. The influence of the ratio D/d should be determined, since all experimental data so far have been obtained with D/d values of approximately 5 and 7.

In conclusion, a new analytical tool has been developed, but its limitations and range of applicability remain to be determined more accurately than has been possible until now. It is hoped that applications for this system will justify continued work in this area.

REFERENCES

1. Astro Research Corporation, "Structural Analysis of Torus Spring Assembly," General Atomic Informal Rept. GAMD-5148, March 1, 1965

2. C. V. David, "Axial and Lateral Rigidity of Pressurized Toroidal Filament Structures," General Atomic Informal Rept. GAMD-6061, Jan. 13, 1965

*　　*　　*

VIBRATION QUALIFICATION SPECIFICATION
FOR INERTIAL MEASURING UNITS

S. L. Burgwin
Honeywell, Inc., Aeronautical Division
St. Petersburg, Florida

Lack of understanding of the role of rectified torques in the performance of inertial measuring units (IMU) has contributed to a somewhat expensive misuse of military vibration specifications in the vibration qualification of IMU's. Difficulty arises from the usual addition that performance shall meet performance specifications at qualification vibration levels. This seemingly logical addition becomes illogical when the nature of rectified torques is considered.

Vibration levels for survival qualifications based on a limited sample are ordinarily about three times the maximum ambient operating levels to allow for material and piece part variation. Such levels become unrealistic and unnecessary for IMU performance qualification when the nature of rectified torque errors is considered.

Performance vibration errors in IMUs arise from rectified vibration torques, which are a function of acceleration squared. A factor of 3 in vibration level becomes a factor of 9 in performance vibration error. Few inertial systems can afford this margin in performance. The obvious solution is a separate vibration qualification specification for IMU performance.

The problem of rectified torques is discussed in this paper, and an approach to arriving at a more realistic specification is suggested. The discussion deals only with IMU's, but the same problems exist for any measuring instrument utilizing a moving element exposed to ambient vibration.

INTRODUCTION

It is convenient, in vibration testing, to use performance degradation as an indication of beginning failure. Vibration qualification tests, as now specified, generally follow this practice.

Measuring instruments with moving elements, utilizing torque rebalance in the measuring process, generally suffer performance degradation when subjected to vibration due to the generation of rectified torques. Such performance degradation is not an indication of beginning failure, and its use as such an indicator may result in failure of satisfactory equipment to meet vibration qualification specifications.

Discussion of the problem of rectified torques and an approach to a more satisfactory vibration qualification procedure is confined to the particular case of inertial measuring units (IMU), where the problem has apparently been most severe and has perhaps had the greatest attention. A searching investigation may uncover other devices and applications where the problem is also serious but has not been recognized.

QUALIFICATION SPECIFICATION PROGRAM

Inertial measuring units (for example, Fig. 1) of a particular design are qualified for operation in a vibration environment by subjecting a limited sample, usually consisting of one production IMU, to specified levels of single-axis vibration along each of the principal axes in turn and monitoring IMU performance. Failure to qualify results from failure of any mechanical or electrical component or from performance degradation to values outside of the specified performance limits for the IMU.
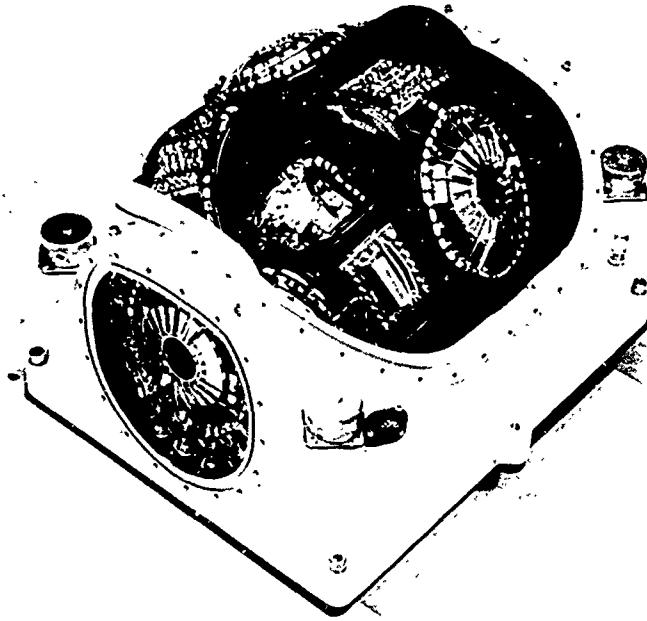
Fig. 1. Example of Honeywell IMU

The overall objective of the qualification test is to establish a high level of assurance that the IMU will survive and perform satisfactorily in the operating vibration environment.

Difficulties arise in specifying the test level of vibration for vibration qualification of an IMU. The level of environmental vibration to be expected at the IMU mounting point for a specific application usually cannot be precisely defined when the specification is written. Some allowance must be made for lack of precision in test simulation of the vibration environment. A further allowance must also be made for IMU material and manufacturing variation in qualification testing of a limited sample. In the absence of complete information in these areas, specified test levels of vibration, based on best judgment, often are an order of magnitude or more higher than the levels subsequently measured under operating conditions.

From the standpoint of survival, a safety factor of 3 (a test level of vibration that is three times operating level) can be justified, and in many cases, good arguments can be advanced for a safety factor as high as 10. The additional assurance of survival under operating conditions may well be worth the price of some overdesign.

The problems mentioned are not unique to vibration qualification of IMU's as regards

survival, but are in some measure common to vibration qualification of any equipment to be operated in a vibration environment. Present practices in vibration qualification appear quite successful in meeting the survival objective and, considering the state-of-the-art, probably cannot be greatly criticized.

Vibration qualification with respect to performance does, on the other hand, present problems unique to IMU's, or more generally to any instrument sensitive to spurious torques. Degradation of performance of an IMU in a vibration environment is not solely a survival problem, but is also dependent on the value of rectified error torques generated by the vibration. These torques are a function of the square of the vibration level and also depend on the direction of vibration. The directional dependence is such that rectified torques balance to a zero time average when the environmental vibration is completely random in direction, in space. Degradation of IMU performance in an operating environment can then be said to depend on the lack of space randomness of the vibration. Single-axis testing makes no allowance for space randomness and thus does not simulate the operational environment as regards rectified vibration torques; it tends to give much higher values of rectified torque than in the operational environment.

The vibration directional dependence of the rectified torques affect the results of the

262

single-axis vibration tests in another way. There are, in general, three directions of vibration in the IMU which produce no rectified torque. The location of these directions depends on cross-coupling in the IMU and may be close to the principal axes. Qualification vibration tests now normally specify single-axis vibration directed along each of the principal axes in turn. This procedure has justification for survival qualification but not for performance qualification. Should the zero rectified torque axes coincide with the principal axes and should the direction of vibration be actually along the principal axes, there would be no rectified torque or rectified torque problem, at least as concerns meeting the qualification specifications. There is probably little chance of such an occurrence, because the normal uncertainty of vibration direction in single-axis testing is about ±15 degrees.

The vibration directional dependence of the rectified vibration torques thus appears in qualification test results in two independent ways which may tend to nullify each other and mask both effects. In addition, the squared relationship between the rectified vibration torques and the test vibration levels makes the rectified torque problem extremely sensitive to the selection of "safety" factors, relating operating vibration levels to specified qualification test levels. The factors 3 to 10 justifiable for survival qualification become factors of 9 to 100 between the operating rectified vibration torques and those measured in the qualification tests at the higher specified vibration levels. Rectification torques are important enough in the performance of the IMU that a multiplying factor of 10 cannot be taken lightly, and this factor may cause failure to meet performance specifications.

Degradation of performance by rectified vibration torques is not a catastrophic type of failure. Furthermore, variation of the coefficients of these torques from unit to unit is subject to manufacturing control, so that it is difficult to justify safety factors of more than 50 percent of those suitable for survival qualification. Even performance qualification vibration levels of 50 percent of the vibration levels specified for survival qualification are by no means a complete answer to the rectified torque problem. The directional effects must also be considered.

No single vibration qualification test now available appears adequate to qualify both IMU survival and performance in one test, even with two separate test vibration levels. Present specifications appear adequate to qualify IMU survival, if the performance requirement is

modified. A new and different approach is needed for vibration qualification of IMU performance.

At present little or no precedent exists for a separate vibration qualification specification for IMU performance. All present vibration qualification specifications have been directed toward survival qualification, with performance qualification as more or less a "fallout" from the way of evaluating survival. Rectified torques have made this fallout something of a hazard to successful qualification.

Some discussion of the mechanisms of rectified torques are necessary before the requirements of a vibration qualification specification for IMU performance can be fully appreciated and a logical approach to such a specification considered.

RECTIFIED TORQUE MECHANISMS

In general, rectified torques result from simultaneous vibration at a given frequency in two of the six degrees of freedom of the body being vibrated.

Rectification arises from:

1. Anisoelasticity — unequal spring constants between the center of gravity and center of support along the three principal axes.

2. Coulomb or viscous material and structural damping (cylindrical torque) — vibration in two degrees of freedom, time-phased to produce a circular displacement of the cg with respect to the center of support, results in a constant torque proportional to the material and structural damping.

3. Anisoinertia — angular oscillation about two principal axes of unequal moments of inertia produces an average value of torque about the third axis (moment of inertia effect).

4. Spring geometry (coning) — angular oscillation about two principal axes also produces rectified motion about the third axis regardless of inertia, due to the noncommutation of Euler's angles.

5. Static unbalance (vibro-pendulous torque) — several combinations of translational and angular vibration can give rise to rectified torque when the cg is displaced from the center of support.

Almost any combination of vibration in two degrees of freedom, coupled with elastic anisotropy, asymmetric mass distribution, or plain material damping, can produce rectification torques.

Mathematically, any torque resulting from the product of sinusoidally varying terms will be a function of sine squared terms, which can be resolved into constant and double frequency components of torque.

The magnitude of rectified torques, in general, pose no threat to survival and are usually of importance only in the degradation of the performance of torque-sensitive instruments, such as gyros and accelerometers used in an IMU. This does not mean that the torques are always of small magnitude. Rectified torques have been observed of sufficient magnitude to override gimbal servomotors, in some instances, of low damped resonant excitation. (Torques of as much as 30 in.-oz have been observed in a 19-lb gimbaled platform.) The magnitude of the rectified torques are, in general, a function of mass squared and may be of interest in some applications outside the scope of this discussion. A better appreciation of the mechanisms and the problems involved can be gained by a brief discussion of one of the better

known types of rectified torque, the so-called "anisoelastic" torque.

The mechanism of anisoelastic torque may be appreciated by considering Figs. 2 and 3. In Fig. 2, a mass is supported within a ring by four springs. The springs in the horizontal axis have greater stiffness than those in the vertical axis. Dampers are shown to simulate material hysteresis damping. This diagram is a reasonable simulation of a gyro spin motor supported within a cylindrical floated gimbal or almost any simple mechanical gimbaled system. Figure 3 is a simplified view of Fig. 2.

In Fig. 3, displacement of cg, relative to the center of support (cs), due to vibration along the 45-degree axis, is represented by the dotted line between the two extreme displacements of the cg. Relative displacement between the cg and cs is not parallel to the vibration direction because of the difference in vertical and horizontal supporting spring constants. This displacement at low frequencies is small compared to the displacement of both cg and cs in inertial space. Therefore, the direction of the inertial force (F_m) is essentially parallel to the direction of vibration, and since it is directed through the center of mass, will have a lever arm about cs.
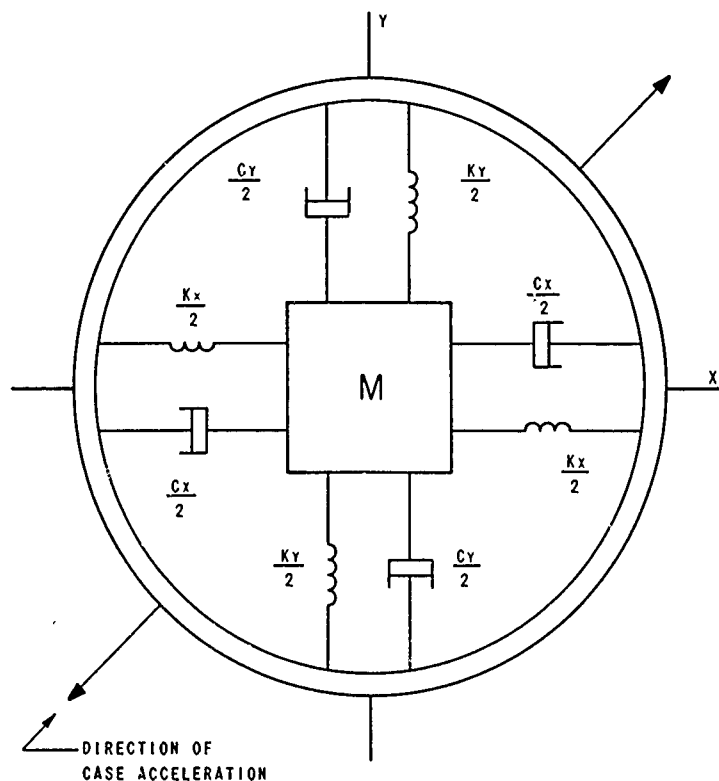
Fig. 2. Diagram of mass-spring-damper arrangement to illustrate anisoelastic torque
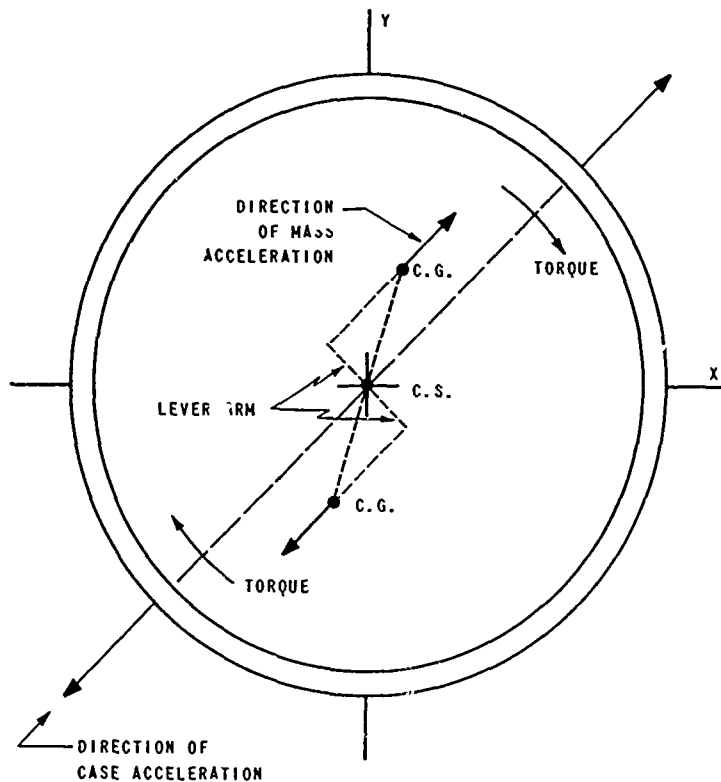
Fig. 3. Torque due to unequal spring constants

The resulting pulsating torque in this case is always clockwise and is a function of time, as shown in Fig. 4. The direction of this torque is such as to turn the mass and supporting structure until the axis with the lowest spring constant or maximum compliance is aligned with the direction of vibration.

The example is admittedly not exact, but serves to give some "feel" for the mechanism involved. Experimental models similar to the mechanism have been built and demonstrate the principle quite successfully.

The relationship between the rectified torque (T_{ave}), mass (M), and peak vibration acceleration (A) is given by the following equation:

$$T_{ave} = \frac{1}{2} M^2 A^2 \sin \theta \cos \theta$$

$$\times \left[\frac{1 - \frac{f^2}{f_x^2}}{K_x \left[\left(1 - \frac{f^2}{f_x^2} \right)^2 + B_x^2 \right]} - \frac{1 - \frac{f^2}{f_y^2}}{K_y \left[\left(1 - \frac{f^2}{f_y^2} \right)^2 + B_y^2 \right]} \right], \quad (1)$$

where

θ = angle between the vibration direction and the x axis,

f = vibration frequency,

f_x, f_y = natural frequencies along the x and y axes,

K_x, K_y = spring constants along the x and y axes, and

B_x, B_y = hysteresis damping constants along x and y axes = twice critical damping ratio.

When the vibration frequency is low relative to f_x and f_y, and B_x and B_y are small, Eq. (1) reduces essentially to the well-known equation

$$T_{ave} = \frac{1}{2} M^2 A^2 \sin \theta \cos \theta \left[\frac{1}{K_x} - \frac{1}{K_y} \right]. \quad (2)$$

The anisoelastic torque coefficient (E) is

$$E = \frac{T_{ave}}{A_{rms}^2} = M^2 \sin \theta \cos \theta \left[\frac{1}{K_x} - \frac{1}{K_y} \right]. \quad (3)$$

265
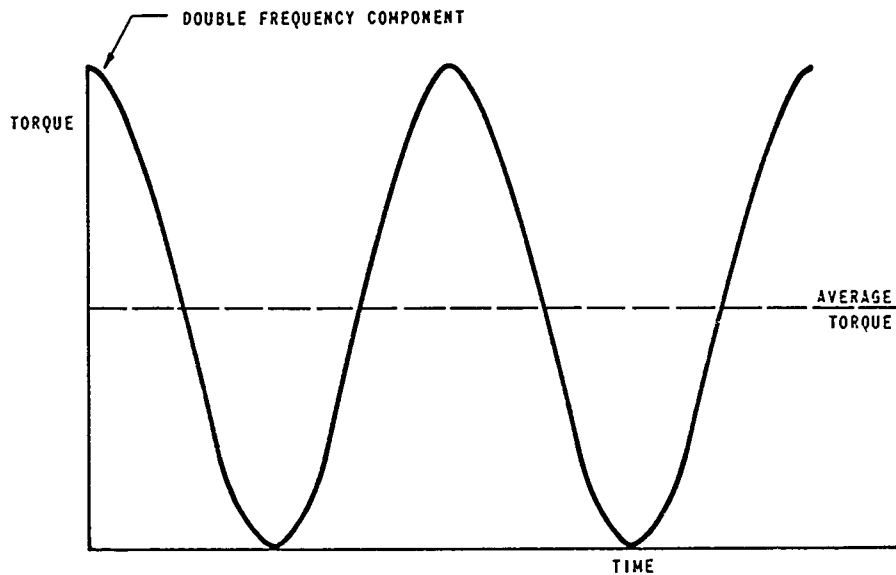
Fig. 4.   Time variation of anisoelastic torque of Fig. 3

A factor Z, related to transmissibility along the x and y axes, can be defined by the relationship

$$T_{ave} = EZ. \qquad (4)$$

Variation of Z with frequency is shown in Fig. 5. Only the low-frequency portion of this curve is of interest in the problem of vibration qualification of IMU's. The IMU performance degradation is largely a function of the rectified torques in gyros that can be designed so that the lowest resonant frequency is high enough to avoid much resonant rise in the test region. For example, Honeywell gyros are designed so that the lowest resonant frequency is well above 2,000 cps.

Equation 2 is the equation of most interest in the vibration qualification problem. It will be noted that a close match of x and y compliances $(1/K_x$ and $1/K_y)$ reduces the rectified torque. Practical limits in this direction have been reached in present gyro design so that additional factors of safety are difficult, if not impossible, to achieve.

Attention has already been directed to the squared relationship between the rectified torque and both mass and acceleration. The dependence of the rectified torque on the direction of vibration is of particular interest in the vibration qualification problem. The variation of rectified torque versus direction of vibration is shown in Fig. 6. Attention is directed to five characteristics important to the vibration qualification of performance problem:

1. The time average of the rectified torque is zero, if the direction of vibration is completely random.

2. Rectified torques are zero for direction of vibration along the principal axes.

3. Rectified torques vary ±50 percent of the maximum value for variation of vibration direction of ±15 degrees from the principal axes.

4. Rectified torques are maximum positive or negative in the 45-degree directions.

5. Rectified torques vary only ±7 percent for ±15 degrees variation from the 45-degree directions.

Other types of rectified torques mentioned earlier differ from the characteristics of the anisoelastic torque described. It is not within the scope of this discussion to cover each type in detail, but in general they are all functions of the square of the vibration level and are sensitive to direction of vibration. Variation of rectified torque with frequency is quite different for the other types of rectified torques, but the characteristics of interest in vibration qualification of performance are essentially similar to those listed for anisoelastic rectified torques.

A brief bibliography is given at the end of this discussion for those interested in a more detailed study of the various rectified torque mechanisms.

The characteristics discussed furnish a basis for a suggested approach to vibration qualification of IMU performance.

266
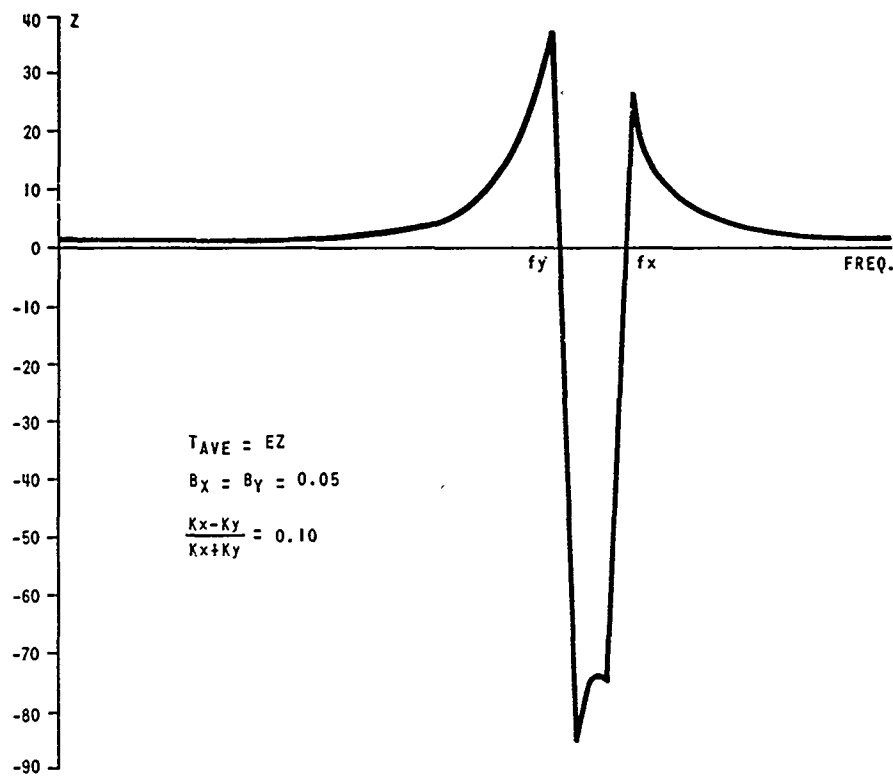
Fig. 5.   Variation of anisoelastic torque with vibration frequency

In the plot:

$$T_{AVE} = EZ$$

$$B_X = B_Y = 0.05$$

$$\frac{Kx-Ky}{Kx+Ky} = 0.10$$
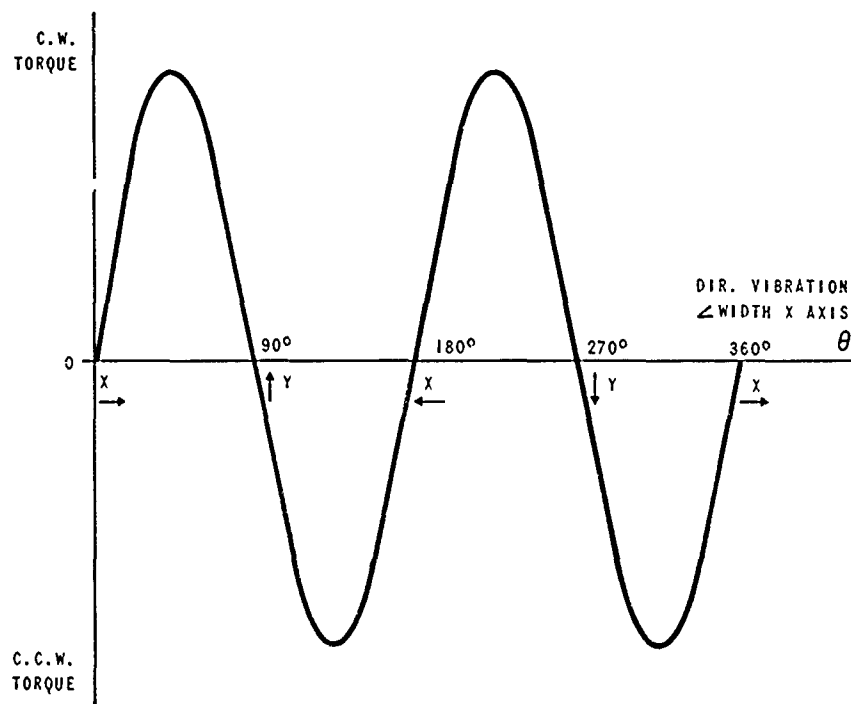
Fig. 6.   Anisoelastic torque vs direction of vibration, θ

QUALIFICATION SPECIFICATION
FOR IMU PERFORMANCE

It has been pointed out that present specifications for vibration qualification of IMUs would be relatively satisfactory from the survival standpoint, if the requirement of meeting performance at the high vibration test levels were modified. It is suggested that performance within specifications limits, after subjecting the test IMU to the specified vibration levels, is sufficient to monitor survival.

The performance degradation due to rectified torques, which are chiefly responsible for suggesting such a change, must be suitably measured and limited before complete vibration qualification is achieved. Performance qualification presents some difficult problems because of the two-axis nature of the rectified torques.

Information gathering and testing, as now practiced, are essentially single-axis processes. Simulation of a two-axis environment with single-axis tests at best involves some important approximations.

A suggested approach to the vibration qualification problem for IMU's is:

1. Utilize present vibration qualification procedures to qualify survival only, with the provision that performance meets specified values before and after vibration, but not necessarily during vibration — vibration specified along principal axes.

2. Generate separate specification for IMU performance with reduced vibration levels; the goal for these levels should be approximately 1.5 times the rms operation vibration level averaged over the duration of the mission.

3. Test vibration for performance qualification is to be directed along each in turn of the six face diagonals of the unit cube formed with the principal axes along the cube edges (Fig. 7). Performance is to be measured for each IMU principal axis for each of the vibration directions, a total of 18 values or six values per axis. Instead of the six face diagonals or 45-degree directions, it may be desirable to make a worst-axes search. It is anticipated that such a search will show the 45-degree axes to be close to the worst direction.

4. Specify two sets of performance limits: (a) a worst-case limit based on expected component performance and not mission performance; and (b) superposition limits to approximate IMU performance under three-axis vibration random in direction in space. A superposition limit for one IMU axis would be the algebraic sum of the six test values for that axis.

Justification for the reduced vibration levels of step 2 above is relatively simple. Catastrophic failure is a function of maximum stress. Survival, therefore, depends on peak vibration levels. IMU performance error (angular rate) depends on acceleration squared. IMU total navigation angle error depends on the integral of the performance rate error and, therefore, on the rms vibration level averaged over the acceleration versus time profile for the mission. Thus, vibration levels specified for qualifying survival may have little or no relationship to the values required to qualify IMU
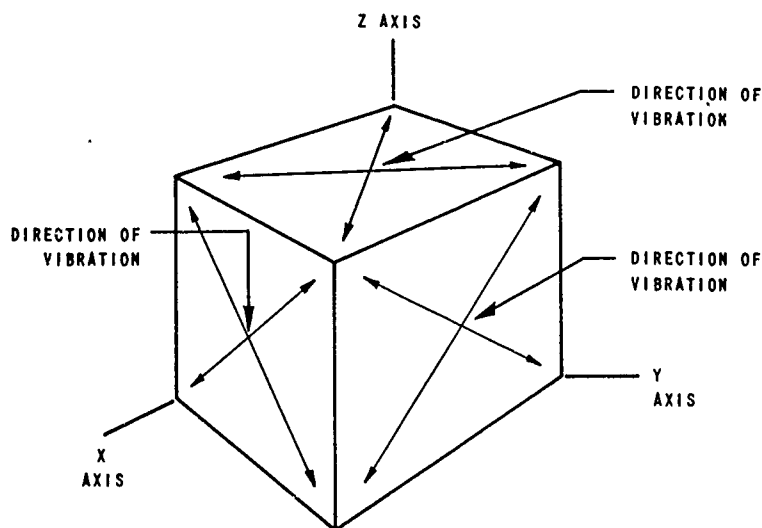
Fig. 7. Suggested vibration directions --
performance qualification

268

performance. Furthermore, a factor of safety of 3 suitable for survival testing can be reduced to 1.5 for performance qualification, because rectified torque coefficients are subject to closer manufacturing control than is ultimate strength of materials. It should be noted that the 1.5 safety factor (test vibration level 1.5 times operating level) covers a variation of 1.5 squared or 2.25 in rectified torque coefficients.

Justification of the 45-degree vibration direction is also relatively straightforward. Ideally, the vibration directions should be such as to give maximum rectified torques, that is, parallel to the face diagonals of the unit cube formed with the principal IMU axes along the cube edges. In practice, cross-coupling in the IMU shifts the maximum rectified torque axes away from the 45-degree directions, so that vibration in the specified 45-degree directions will produce less than maximum rectified torque. It might be argued that a search for the maximum rectified torque axes may perhaps be desirable. However, other test errors are such that variations of ±15 degrees from the maximum axis are tolerable and to be preferred over the greater complexity of a worst-axis search. It is suggested that specification of the 45-degree orientations of vibration testing is a practical choice.

Selection and justification of the suggested specification limiting values present some problems. The worst-case component limit, step 4a, must be based on the state-of-the-art and is designed merely to assure state-of-the-art or better components; it does not present a serious problem.

The superposition limit, step 4b, is more difficult to select and justify. It represents an attempt to simulate three-axis performance with six single-axis test values. The effort is handicapped by lack of information in two areas:

1. Space randomness, or rather lack of space randomness, in direction of the environmental vibration — the difference in power spectral density between the six 45-degree axes is of utmost importance in evaluating performance. Such data are not now available, probably because of a lack of awareness of its importance. Attention in gathering environmental data has been focused on requirements for survival evaluation where only the maximum power spectral density, regardless of direction in space, has significance.

2. Valid use of the superposition principle requires linearity of the mechanical characteristics of the test unit. Such information is also

meager, again due to lack of awareness of its importance.

It must be recognized that the value and usefulness of any performance qualification specification must necessarily be limited by such lack of information.

Some assumptions can be made that will give the suggested approach a degree of value and usefulness until better environmental and linearity data are available. Until this time, an assumption of complete space randomness of environmental vibration is the only practical assumption possible. This is not a safe assumption but some evidence indicates that it may be a relatively good assumption. For the purposes of performance qualification, it may turn out to be a very good assumption.

IMU performance under this assumption will be represented by the algebraic sum of the IMU drift rates about each principal IMU axis for the six directions of vibration. If the IMU were mechanically linear, the summation drift rate ideally would be zero. Actually the summation values would reflect testing uncertainty. The proposed test could turn out to be a good measure of the IMU nonlinearity within the limits of testing uncertainty. This may be the more important factor in evaluating IMU performance, particularly if the environmental vibration is nearly random in space-direction, as some meager evidence seems to indicate.

The concept of space randomness of vibration seems to be a difficult one for most engineers to accept. In general it can be said that the more complex the structure linking the forcing function to the measuring point, i.e., the greater the number of power paths, the more nearly random will be the vibration at the measuring point. The present practice of specifying one power spectral density curve for all axes tends to reflect a perhaps involuntary practical acceptance of the space randomness of vibration in existing structures. Perhaps the assumption of space randomness of vibration should be accepted until proven otherwise.

Completely realistic specification limits cannot be achieved without a knowledge of the environmental forcing function and the transfer function between the points of application and the mounting points of the device to be evaluated. The complexity of these functions inhibits progress in this direction. Engineering assumptions can be expected to be necessary for at least the immediate future.

CONCLUSION

The problem of unjustified rejection of torque sensitive instruments, such as IMU's, in present vibration qualification procedures because of performance degradation by rectified torques under unrealistic test conditions can be alleviated, if not completely solved, by evaluating performance and survival under separate qualification specifications.

The performance specification must be designed to take into account the characteristics of rectified torques described in this discussion, which include space randomness of the environmental vibration and nonlinear mechanical characteristics of the device under consideration.

An approach to a performance qualification specification for IMU's is discussed. It involves practical single-axis measurement of the effects of rectified torques and combines the results to simulate a three-axis environment. Admittedly, this approach is not ideal, but it may represent the most practical approach to the problem at the present state-of-the-art.

BIBLIOGRAPHY

Fernandez, M., and G. Macomber, Inertial Guidance Engineering (Prentice-Hall, New York), 1962, Appendices G, H, and I

Goodman, L. E., and A. R. Robinson, J. Appl. Mech. (June 1958)

Pitman, G. R., Jr., Inertial Guidance (John Wiley & Sons, New York), 1962, Ch. 3, pp. 79-91

Weinstock, H., "Specification for the Permissible Motions of a Platform for Performance Evaluation of Single-Degree-of-Freedom Inertial Gyroscopes," M.I.T. Instrument Laboratory Paper E-1267, Dec. 1962

*   *   *

EVALUATION OF A DESIGN FACTOR
APPROACH TO SPACE VEHICLE DESIGN
FOR RANDOM VIBRATION ENVIRONMENTS

D. E. Hines and D. A. Stewart
Douglas Aircraft Company, Inc.
Missile and Space Systems Division
Santa Monica, California

Structural fatigue induced by random vibration often sizes bracket
structures in modern aerospace vehicles. This document reports the
results of an experimental study conducted to evaluate a design factor
approach for application to the fatigue problem and to evaluate the de-
sign factor for cantilever beams.

INTRODUCTION AND SUMMARY

The study described in this document was
conducted to evaluate a technique for designing
space vehicles to withstand random vibration
environments by means of "design factors."
Using various design factors (K values), 140
cantilever beams with stress risers were de-
signed for the test. These were then tested to
failure in a specified random vibration environ-
ment. Since the beams were expected to have
different failure times (depending on the design
factor used), it was expected that a design fac-
tor could be isolated which would guarantee a
fatigue life suitable for space vehicle applica-
tions. For this study, the desired fatigue life
time was 10 min; however, data are included to
allow extrapolation to other fatigue lives.

When tested to the design level, the speci-
mens' fatigue lives ranged from 3×10^3 to
5×10^5 cycles. However, when the raw data
were analyzed, a considerable "scatter" was
observed. This was attributed to uncertainties
inherent in random data analysis, variations in
system damping from specimen to specimen,
variation of stress concentration factor, and
natural fatigue scatter.

Through the use of statistical techniques,
the scatter due to data reduction was greatly
reduced, leaving only that due to variation of
the materials. The design factor was then ex-
pressed in statistical form. The design factors
obtained experimentally were slightly lower

than those determined from an analysis based
on Miles' theory (1). The scatter in K values
was on the order of 20 percent for aluminum
specimens and 50 percent for steel specimens
(within 95 percent confidence limits). In both
cases, this scatter was deemed reasonable
considering the specimen materials and surface
finishes. Therefore, the general design factor
approach was shown to be feasible and the
method of defining the design factors was shown
to be acceptable.

Further data refinements, based on logical
assumptions as to the stress concentration fac-
tors at stresses approaching yield, were applied
to give useful random fatigue information to
supplement the limited quantity of data pub-
lished on this subject. In addition, sources of
structural damping were investigated, and semi-
quantitative agreement between experimental
data and the theory of Lazan (2) was obtained
for specimens with and without stress risers
when subjected to random excitation.

In summary then, the primary objectives
of this study were (a) to attempt to validate the
design factor approach, and (b) to determine
the constants for use in this design approach
based on random vibration fatigue tests of can-
tilever beams. Secondary objectives were (a)
to add to the existing body of experimental
random fatigue data, and (b) to identify (quali-
tatively and quantitatively) sources of uncer-
tainty in dynamic response problems.

NOMENCLATURE

b   Width (in.)

c/c_c Ratio of damping to critical damping

Q $1/2c/c_c$ = quality factor

E   Modulus of elasticity in tension (psi)

f_o Undamped natural frequency (cps)

ω_o $2\pi f_o$

F_{tu} Tensile ultimate stress (psi)

F_{ty} Tensile yield stress (psi)

F_{tw} Working stress (psi)

h   Thickness (in.)

I   Second moment of area (in.^{4})

K_{dyn} Dynamic load factor

$$K_{dyn} = \frac{1}{2c/c_c}$$

for sinusoidal loading;

$$K_{dyn} = \left(\frac{\pi f_o}{4c/c_c}\right)^{1/2}$$

for random loading

K   Design factor for random loading

K_s Design factor for sinusoidal loading

a   Constant from Miles' fatigue theory, chosen as 1 for this study

k_t Stress concentration factor for static loads in tension

k   Stress concentration factor for static loads in bending

k_f Stress concentration factor for fatigue

ℓ Length of beam (in.)

M   Bending moment (in.-lb)

PSD(f)   Power spectrum of random input (g^2/cps)

t   Averaging time used in data reduction

T   Time to failure

W   End weight (lb)

X   Tip deflection (in.)

$\ddot{X}$ Tip acceleration (in./sec^2)

ρ Density (lb/in.^{3})

σ_{eq} Equivalent stress (psi)

σ_o Static stress per unit load (psi/g)

σ_n Nominal stress at stress riser (psi)

σ_m $\sigma_n \times k_f$ (psi)

α Fatigue curve slope on log-log paper

ΔdB   Uncertainty in db at the 95 percent confidence level for power spectral analysis

Δf Frequency window utilized in data reduction

$\langle\ \rangle$ Indicates rms

DISCUSSION

There have been many studies of the fatigue characteristics of materials subjected to random vibrations and loads (3-15). However, the use of these data in design applications has been limited. It would be beneficial if structural design for random vibration environments could be reduced to a simple procedure, that is, if design factors could be developed which, when applied to static response calculations, would account for the dynamic characteristics of the system and the fatigue characteristics of the materials. Should such a simple procedure prove impractical due to the large number of variables and the uncertainty in determination of each variable, it might be advantageous to attempt a statistical approach to the problem similar to that used in estimation of space vehicle vibration environments.

In brief then, the purpose of this study was to evaluate a specific design technique for random vibration environments. This technique may be summarized by the equation

$$\sigma_{eq} = (K)(K_{dyn})\,\sigma_o\ (\text{load}) ,$$

where

$$\sigma_{eq} = \text{stress compared to } F_{tw};$$

272

F_{tw} = working stress which is ultimate over 1.4 yield or over 1.1, whichever is less;

K = design factor including fatigue properties of the material (F_{tw} over fatigue strength at the desired life);

K_{dyn} = dynamic load factor $(\pi/2) \, Qf \, |^{1/2}$ for random, Q for sinusoidal excitation;

σ_o = static stress for loads, such as those applied in vibration; and

$load$ = excitation force.

To evaluate the design approach implied by this equation, 140 beams were designed based on a dynamic stress analysis of the beams, an assumed damping, sinusoidal fatigue data and the random sinusoidal equivalence derived by Miles (1).

It should be emphasized that in this study, K and K_{dyn} are interdependent and cannot be separated. K can be used to determine a K_s value for sinusoidal input through division by Miles' equivalent stress factor.

The 140 specimen beams were designed and constructed of 2024-T4 aluminum or 4130 steel heat-treated to 140 to 160 ksi. The intended life of these specimens was about 3×10^4 cycles, corresponding to a 10-min life for a specimen resonant at 50 cps. The design of the specimens was varied to insure that the 3×10^4 cycle life was included and to provide useful fatigue information above and below this value. The actual test lives varied from 3×10^3 to 5×10^5 cycles.

The beams were instrumented to yield the acceleration input level, the acceleration response, and, in a few cases, the stress levels to determine the possible effect of modes higher than the first mode.

Instrumentation of the tip output accelerations fulfilled two purposes: (a) to allow an estimate of stress for each beam without relying on strain gage data, and (b) to evaluate the Q's of the individual beams.

The data were plotted in fatigue curve form utilizing the calculated stress per unit of tip acceleration and the measured tip acceleration levels. An excessive amount of scatter was observed. It was determined that this scatter was due to the following: (a) the rms tip response (which was the response of a very narrow

bandwidth resonator) being evaluated for a relatively short duration; (b) natural scatter in Q for a given beam configuration; (c) finite time for evaluating the input power spectral density (PSD); (d) variation in the stress concentration factor as a function of stress; (e) insufficient test duration; and (f) the narrow notches in the input spectrum at specimen resonance. Of these sources of scatter, item (e) requires further explanation. Assuming that fatigue accumulates according to Miner's hypothesis, the predicted fatigue life would be obtained if the proper number of peaks of various levels have occurred. This would require a test time on the order of, or greater than, that required to get an accurate value for the rms response. As is shown below, this time might be as long as 400 sec or 7.5 min for systems with Q's as high as those studied here. Any deviations from Miner's hypothesis increases the test time required to eliminate the uncertainties in this parameter. Since the average test time is only slightly greater than the minimum required (about 10 min), a moderate amount of scatter was introduced.

The data resulting from this study were then used to obtain the K values in three steps: (a) all uncertainty was incorporated in the K factor, (b) the effect of stress on the magnitude of stress concentrations factor was eliminated from K, and (c) the remaining scatter due to K and K_{dyn} was separated by making logical assumptions concerning the natural scatter in K as discussed in "Test Results and Analysis."

The experiment indicates that a K factor obtained analytically from Miles' theory gives values which correspond to the 80 to 90 percent confidence limits. Therefore, values obtained from Miles' theory are of the proper magnitude for design purposes. Table 1 presents K values using this theory. The proper K value for a specific design purpose will depend on the amount of information available concerning the problem at hand.

SPECIMEN CONFIGURATION

Two basic types of simple fatigue test specimen might have been used for this study. The first type consists of specimens without stress concentrations, and the second type incorporates stress concentrations. Each configuration had certain advantages and disadvantages, which are discussed in Appendix A.

To determine which type was to be used for this study, two sets of four specimens each were fabricated and tested to failure. One set

TABLE 1
Derived from Miles' Theory

Test	Aluminum 2024-T36	Aluminum 7075-T6	Magnesium AZ 31B-0	Stainless Steel 17 7 PH TH 1050	Beryllium S 200C
Tensile ultimate stress (psi)	70	78	32	180	70
Tensile yield stress (psi)	60	70	18	150	50
Working stress (psi)	50	55	16	130	45
Fatigue strength in $R = -1$ bending at					
10^4 cycles	48	49	23	115	24
10^5 cycles	37	37	20	104	23
10^6 cycles	29	26	17	83	22
K_s at					
10^4 cycles	1.04	1.02	0.70	1.13	1.88
10^5 cycles	1.35	1.35	0.80	1.25	1.96
10^6 cycles	1.73	1.92	0.94	1.57	2.00
Equivalent stress factor at					
10^4 cycles	2.2	2.1	2.6	3.0	2.9
10^5 cycles	–	–	–	–	3.6
10^6 cycles	–	–	–	–	5.6
K at					
10^4 cycles	2.28	2.14	1.82	3.39	5.45
10^5 cycles	2.97	2.84	2.08	3.75	7.05
10^6 cycles	3.80	4.03	2.44	4.71	11.22

had stress risers and the other did not. The specimens without the stress risers exhibited considerable nonlinear damping and a poorly defined failure point. The specimens with the stress risers exhibited only nominal nonlinear damping, and there was no difficulty in defining the failure point of these specimens. Therefore, the specimens containing the stress risers were chosen for the test.

The design and experiments performed on the specimens without the stress risers were parallel to those for the specimens with stress concentration factors. Therefore, details on these rejected specimens have been omitted from this report. Those tests did produce some interesting information, however, which is discussed in Appendix B. The remainder of this report is limited to discussion of specimens with stress risers.

The general configuration used in this study consisted of an end-weighted rectangular cantilevered bar containing two holes for stress risers. Such a specimen is shown in Fig. 1; Figs. 2 and 3 give fatigue curves for aluminum and steel specimens, respectively. The end-weighted bar permitted the stress per given input to be altered without changing the basic bar configuration. Therefore, many specimens
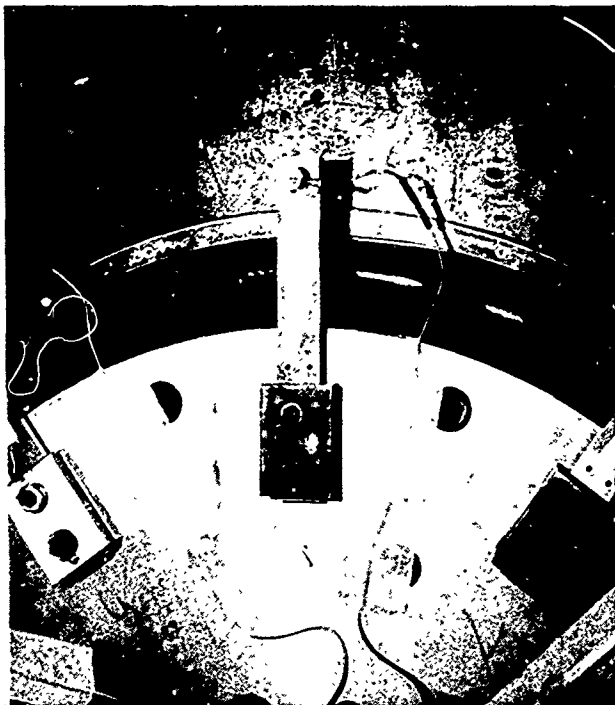
Fig. 1. Beam configuration
with stress risers

with varying expected fatigue lives could be fabricated of identical material and cut from the same sheet. This limited the scatter due to material composition and specimen thickness.

Specimen Sizing

Before the specimens could be sized, some basic parameters were to be defined. It was decided that the stress concentration holes would be 1/8-in. in diameter. To limit interaction between the stress pattern resulting from one hole and that of the second hole or from the edge of the bar, minimum separations were required. A 5-diameter separation between the hole centers and a 2-1/2-diameter separation between the hole centers and the beam edge were sufficient for this purpose. To meet these requirements, a beam 1-1/4 in. wide was required. In addition, it was decided to test four general beam configurations, two thicknesses of 2024-T4 aluminum and two thicknesses of 4130 steel heat-treated to 140 to 160 ksi. The test level was defined as 0.45 g^2/cps, and the average life was to be between 10^4 and 10^5 cycles to failure.

A preliminary set of specimens referred to as the "peg point" specimens was fabricated and tested to verify the analysis procedure. These specimens were designed using the fatigue analysis approach suggested by Miles, estimating damping as described in Appendix B, and then (by analysis) relating a K factor for both sinusoidal and random loading to each specimen. After the analysis was verified by these tests, the final design loads were defined
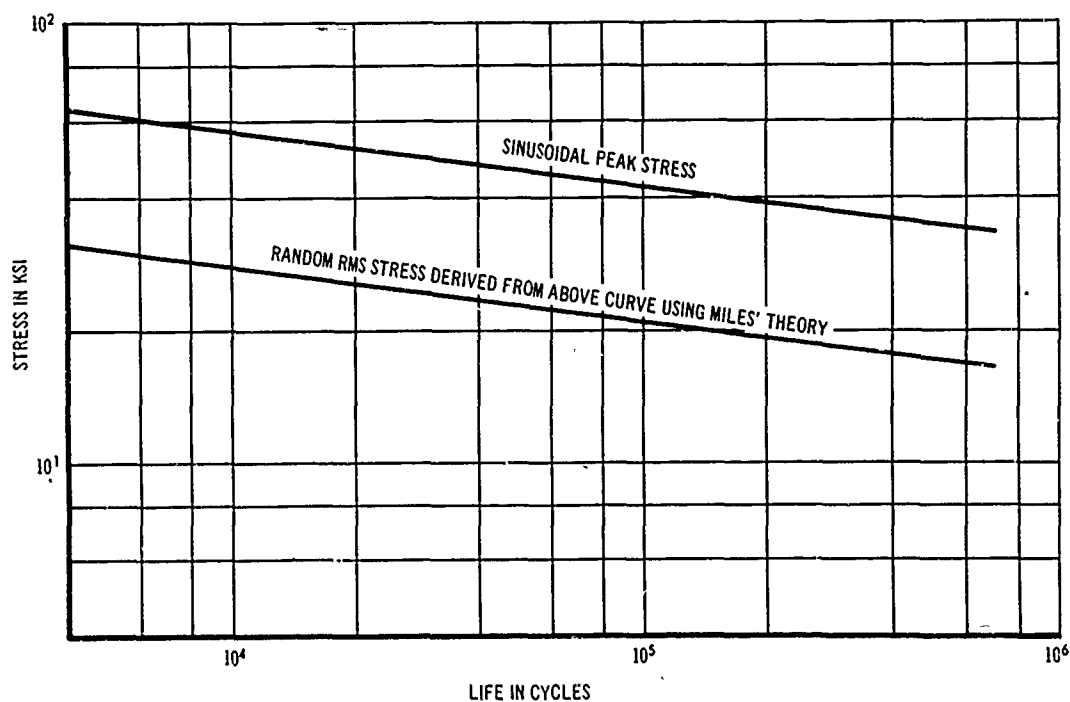
Fig. 2. Fatigue curves for 2024-T4 aluminum under bending
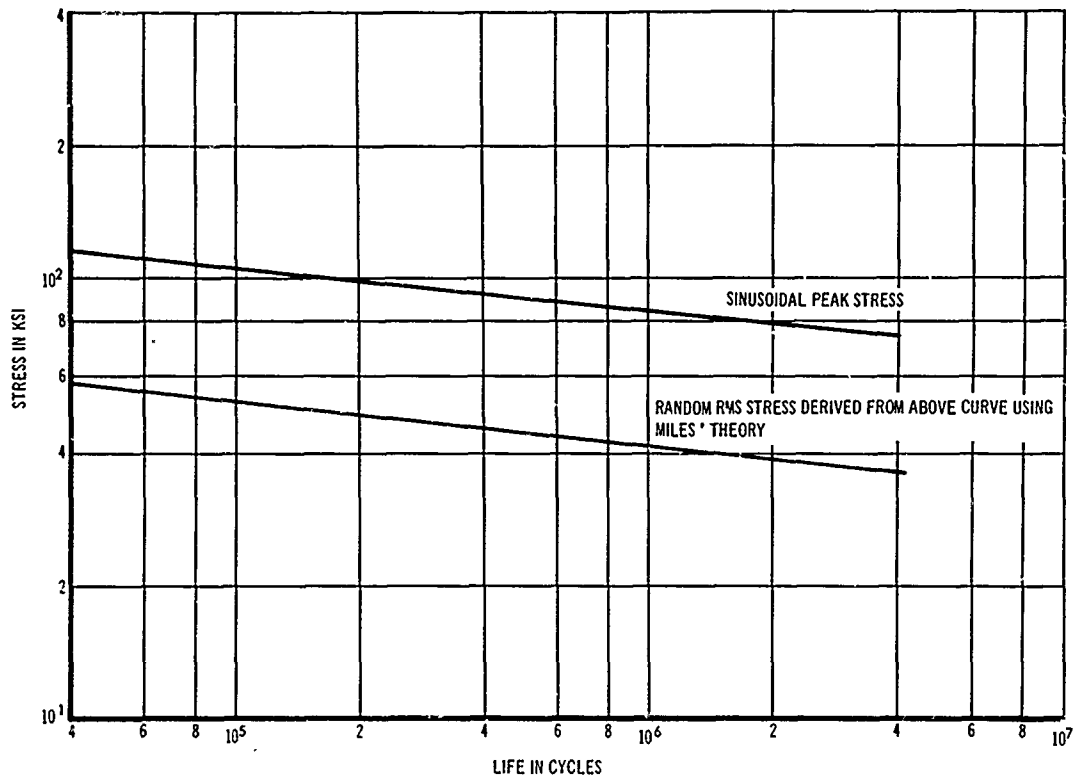
Fig. 3. Fatigue curves for 4130 steel hardened to 150 ksi

in a manner that would vary the K factor over a suitable range.

The design goals for the peg point specimens were that the specimens fatigue in 10 min when excited by a random loading of 0.45 g^2/cps and that the frequency be on the order of 50 cps. The general configuration of the specimens was chosen as end-loaded cantilever beams containing stress risers and excited at the beams' roots.

The preliminary design was obtained by using the desired life of 3×10^4 cycles (10 min for a 50-cps system) and utilizing the fatigue curves indicated in Figs. 2 and 3 to obtain nominal rms stress at the stress riser.

The stress concentration factors were established as discussed in Appendices C and D after the desired thicknesses of 1/8- and 1/4-in. beams were chosen. These factors are 1.47 and 1.57 for the 1/8- and 1/4-in. beams, respectively, for both the steel and aluminum specimens.

In addition, a frequency of 50 cps was chosen for the specimens, and Q was assumed to be 50 (based on material presented in Appendix B and in Refs. 1 and 3-8). This furnished sufficient information to obtain by simplified theory approximate values for the remaining undefined

parameters. The design was then refined using the more sophisticated approach discussed below.

In the more refined analysis, the Douglas version of the Mykelstad approach to modal properties was used to determine the natural frequencies and mode shapes for deflection and moment (normalized to 1 at the tip).

Using this information, the tip acceleration for a 1-in. tip displacement in the mode being considered can be obtained from

$$|\ddot{X}(g)| = \left\{ \omega_o^2 (1 \text{ in.})/386.4 \text{ in./sec}^2 \right\} g$$

or

$$|\ddot{X}(g)| = (\omega_o^2/386.4) \text{ in g's}.$$

The moment distribution obtained from the Mykelstad program can be used to obtain the nominal stress at the stress riser from

$$\sigma_o = \frac{MC}{I} = \frac{6M}{bh^2}.$$

Therefore, the stress per g of tip acceleration is given by

$$\frac{\sigma_o}{g} = \frac{6M(386.4)}{bh^2\omega^2}.$$

276

If random response is desired, the rms stress can be obtained from

$$\langle\sigma\rangle_n = \left[\frac{\pi}{2} Qf\ PSD(f)\right]^{1/2} \frac{\sigma_o}{g}$$

or

$$\langle\sigma\rangle_n = \left[\frac{Q}{4}\omega\ PSD(f)\right]^{1/2} \frac{6M \times 386.4}{bh^2\omega^2}$$

or

$$\frac{\langle\sigma\rangle_n}{(g^2/cps)^{1/2}} = \left(\frac{Q}{\omega^3}\right)^{1/2} \frac{3M \times 386.4}{bh^2}$$

$$= \left(\frac{Q}{f^3}\right)^{1/2} \times \frac{1.16 \times 10^3}{15.7} \frac{M}{bh^2} = 74\left(\frac{Q}{f^3}\right)^{1/2} \frac{M}{bh^2}.$$

For $h = 1/8$ in.,

$$\frac{\langle\sigma\rangle_n}{(g^2/cps)^{1/2}} = 4.74 \times 10^3 \frac{M}{b}\left(\frac{Q}{f^3}\right)^{1/2},$$

and for $h = 1/4$ in.,

$$\frac{\langle\sigma\rangle_n}{(g^2/cps)^{1/2}} = 1.18 \times 10^3 \frac{M}{b}\left(\frac{Q}{f^3}\right)^{1/2}.$$

The natural frequency and maximum stress including the concentration factors for each beam is given in Table 2, assuming $Q = 50$ for the configuration shown in Fig. 4. The test results from these specimens are included with those of the specimens for final analysis. The only result which should be noted here is the fatigue life for each specimen. These ranged from 1.6×10^4 to 4.2×10^4 cycles. These levels are sufficiently close to the desired levels to be used as a basis for the final specimen design.

TABLE 2
Frequencies and Nominal Stress for Peg
Point Specimens for 0.45 g^2/cps Input

Beam Description	f (cps)	Max $\langle\sigma\rangle$ per $(g^2/cps)^{1/2}$ (ksi)
1/8-in. steel	50.0	66
1/4-in. steel	50.6	76
1/8-in. aluminum	52.6	26.6
1/4-in. aluminum	53.3	30.2

Final Specimen Design

The final specimen designs were arrived at by a slightly different system than was used for the peg point specimens. The first mode shape for the beams used in this study is nearly independent of the end weight (m_b) for both displacement and moment. Therefore, for a given beam thickness, the stress at the critical section is dependent only on tip displacement. This results in the fact that the stress per given acceleration is proportional to the inverse of the frequency squared.

The tip acceleration is expressed as

$$\langle\ddot{X}\rangle = \left(\frac{\pi}{2} Qf\ PSD\right)^{1/2},$$

and, as stated above

$$\langle\sigma\rangle_n \propto \frac{\ddot{X}_{rms}}{f^2}.$$

Therefore,

$$\langle\sigma\rangle_n \propto \frac{1}{f^{3/2}},$$

but

$$f \propto \frac{1}{m_b^{1/2}},$$

so

$$\langle\sigma\rangle_n \propto = m_b^{3/4}.$$

The desired spread in σ_{rms} and, consequently, the K factor can be obtained by altering the end mass.

The end masses for the median test specimen were increased slightly to eliminate duplications, and the K's were established as 66, 77, 88, 100, 111, 125, and 132 percent of the median K. The mass variations required for these values are included in Table 3.

The nomenclature format which is used in this document to designate the beams is XX-XX. The first two places are A1, A2, S1, or S2, indicating 1/8- or 1/4-in. aluminum or 1/8- or 1/4-in. steel specimens, respectively. The second two places correspond to the end weight as indicated in Table 3. The order of increasing weight or stress is S1, R1, S2, R2, S3, R3, and S4.

DETAIL II
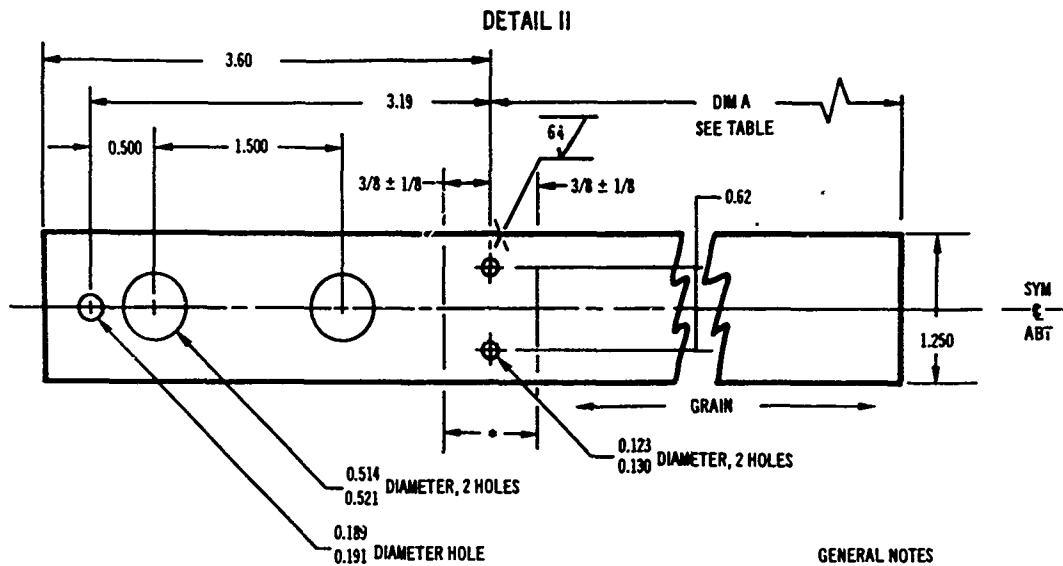
PART NO. | MATERIAL | THICKNESS (STK) | DM A
A1 | 2024-T4 ALUMINUM SHEET | 0.125 | 5.00
A2 | 2024-T4 ALUMINUM PLATE | 0.250 | 7.05
S1 | 4130 STEEL SHEET | 0.125 | 5.60
S2 | 4130 STEEL PLATE | 0.250 | 7.90

GENERAL NOTES
1. TOLERANCE
   2 PLACE DECIMAL ± 0.02
   3 PLACE DECIMAL ± 0.005
2. AREA MARKED * TO BE FREE OF SURFACE DEFECTS (VISIBLE)
3. HEAT TREAT S1 AND S2 TO 140-160 KSI BEFORE DRILLING.

Fig. 4. Beam configuration

TABLE 3
End Weights and Geometric Data for Final Beam Designs

Material	Designation	Length[a] (in.)	End Weight[b] (lb)						
			R1	R2	R3	S1	S2	S3	S4
Aluminum	K		1.35	1.8	2.25	0.57	0.76	0.96	1.15
	A1 (1/8)	5.00	0.127	0.187	0.252	0.108	0.161	0.215	0.262
	A2 (1/4)	7.05	0.368	0.527	0.710	0.305	0.455	0.607	0.710
Steel	K		1.65	2.2	2.75	0.70	0.93	1.16	1.4
	S1 (1/8)	5.60	0.272	0.400	0.540	0.232	0.344	0.460	0.560
	S2 (1/4)	7.90	0.78	1.12	1.52	0.265	0.97	1.30	1.58

[a]Measured from stress concentration holes to end of beam.
[b]Includes weight of last inch of beam and of accelerometer.

A more sophisticated analysis using the Mykelstad program was then performed, as previously discussed. The results of these analyses are included in the data reduction, but the changes are less than 2 percent and sufficiently small so as not to affect the design. It should be noted that the second mode stress response was always less than 5 percent of that in the fundamental mode.

TEST CONFIGURATIONS

The specimens were tested to failure in the Douglas test facility where the test equipment consisted of (a) the electrodynamic shaker and its support systems; (b) instrumentation, including strain gages and accelerometers; (c) recorders, both magnetic tape and oscillograph; and (d) data analysis equipment, both analog

278

and digital. Figure 5 is a block diagram of the data system. Instrumentation is shown in Fig. 6. All test equipment is listed in Table 4.

The specimens were mounted four at a time (or for final tests, ten at a time) on the C-100 shaker which has a rating of 12,400 force pounds. The shaker was driven by a 90-kva amplifier, and the system was equalized by an automatic equalizer. The original plan called for the use of peak-notch filters to refine the equalization, but they were not required.

The beams were instrumented with both accelerometers and strain gages. The accelerometers were mounted at the end of the beam and the strain gages were placed as shown in Fig. 7. Unfortunately, little strain gage information was obtained due to gage failure, adhesion, and calibration problems. Data from the accelerometers and strain gages were recorded on magnetic tape on an Ampex 14-channel tape recorder.

Power spectral density (PSD) plots (Fig. 8) and peak distributions were produced by the IBM 7094 computer (with Douglas computer program TD60), utilizing the taped information obtained from the Ampex recorder. The maximum dynamic range of the analysis is approximately 40 db. Resolution and accuracy tradeoff is in accordance with the relationship for the 90 percent confidence intervals as shown below:

$$\Delta dB^2 = \frac{200}{\Delta f \times t} \; .$$

TEST PROCEDURES

The tests on each set of beams were divided into three parts: equalization, sinusoidal sweep, and random testing.
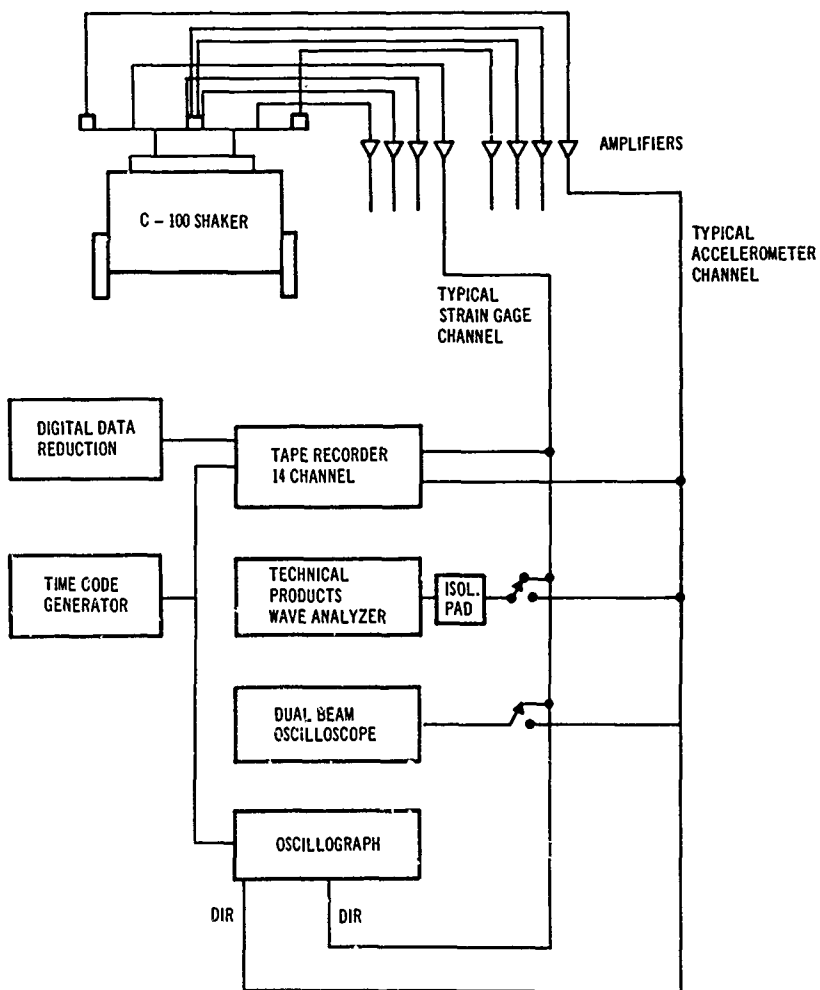
Fig. 5. Instrumentation block diagram
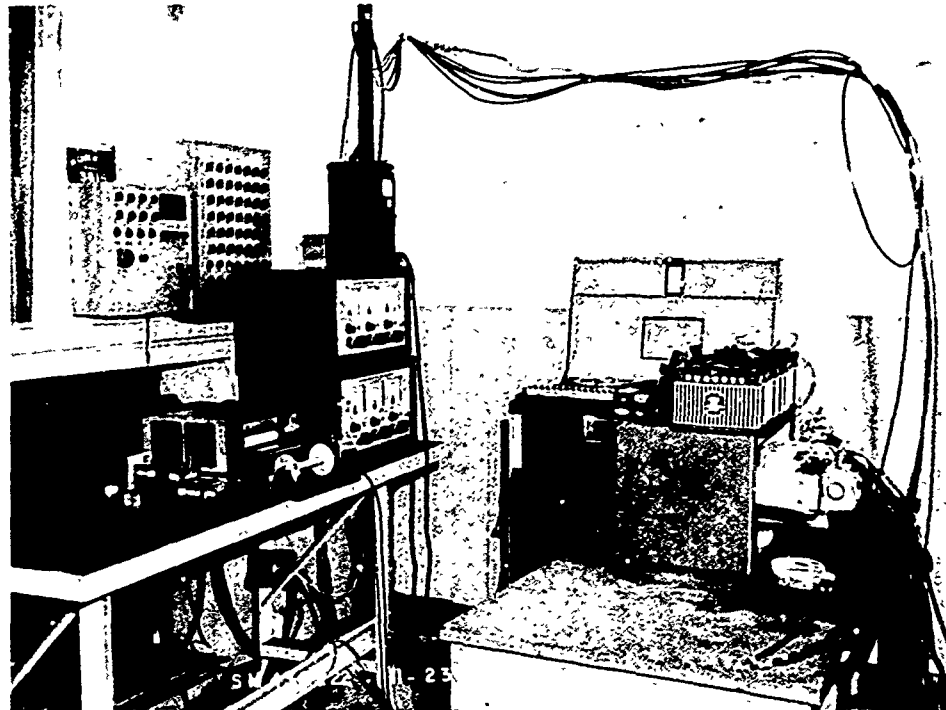
Fig. 6. Instrumentation

TABLE 4
Instrumentation

Quantity	Description	Model	Serial No.
1	Vibration — MB	C-100	III
1	Oscillator — Ling	Co-10	10977-22
1	Oscillator — Hewlett-Packard	202B	—
1	Servo Control Amplifier — Ling	S-10-B	—
1	True rms Voltmeter — Ballantine	320	—
1	Servo D&G Amplifier — Ling	S-12-D	—
1	Frequency Counter — Hewlett-Packard	5512A	634955
1	Oscilloscope — Tektronix	RM32	000203
1	Oscillograph — CEC	5-124-P4	3038
2	Dynamonitor — Endevco	2702, 2705	HA05, GA02
5	Accelerometers — Endevco	2215C	KA10, KA11, KA23, KA86, JB59
2	Strain Gages	A7-FBE-2	—
2	Strain Gages	A2217	—
1	Tape Recorder — P1	12114	105
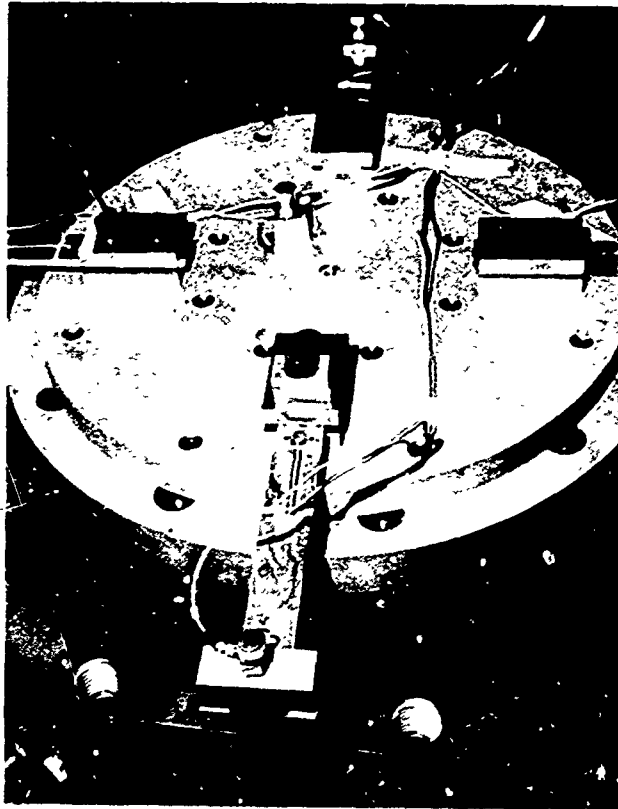
Fig. 7. Transducer configuration

(0.5 - CYCLE BANDWIDTH)
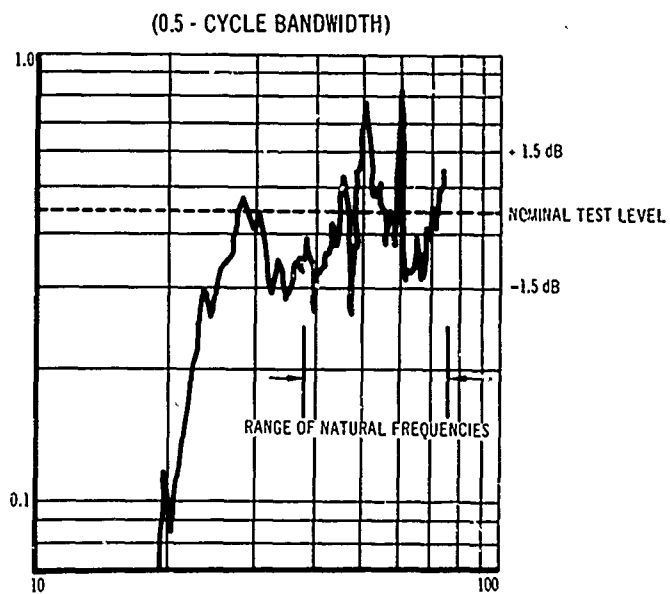
Fig. 8. Typical input power spectral density

Equalization

With four dissimilar beams mounted on the shaker, a random vibration input over a frequency range of 20 to 2000 cps was applied through an 80-channel automatic equalizer. The level of this random input was approximately 10 percent of the final rms random test level. The output of the control accelerometer, mounted in the center of the shaker head, was recorded on magnetic tape. From this tape, loops were cut and the data were reduced using a Technical Products wave analyzer. A PSD plot of the shaker output was obtained over two frequency ranges, 20 to 2000 cps and 20 to 200 cps. The filter bandwidths selected on the wave analyzer for these plots were 20 and 5 cps. These PSD's were then corrected for the frequency response characteristics of the tape recorder, and the corrected curves were checked to insure that the input level at the beam's first natural frequency was within ±1.5 db of the required input level. Representative PSD's of the input signal are shown in Figs. 9 and 10.

Sinusoidal Sweep

Four dissimilar beams were attached to the C-100 shaker in the vertical axis of vibration (normal to the specimen) and excited by a sinusoidal sweep from 20 to 1000 cps at a sweep rate of 1 octave/min. The level was 0.1 g O-P. The purpose of this sweep was to determine Q's and frequencies of resonance. It was found that a 1-octave/min sweep was too fast and did not allow the beams to build up to full amplitude at resonance. However, although the sweep rate was too high, it did allow localization of any major resonances in the beams. To determine frequencies of resonances accurately, the sweep was rerun with an input level of 0.1 g peak. The frequency range of the sweep was 30 to 60 cps and the sweep rate was 0.1 octave/min.

Random Tests

After the system had been equalized to within the limits described for the sinusoidal sweep, the random input was applied at the 0.45-g^2/cps design level. Accelerometers mounted at the tip of each beam, the control accelerometer, and the strain gages mounted at the stress concentration points on selected beams were monitored. The beams were tested to failure.

Several methods were considered for determining beam failure (change in tip response frequency), but none of these methods were accurate enough to be used as an on-line failure indicator. Consequently, it was decided to use the time when the beam actually separated as the failure point. During this part of the test, the shaker was stopped several times, either because of "dumping" of the shaker or because one of the beams had broken. Each time the shaker was stopped, the beams were inspected visually for fatigue cracks around the stress

NOTE: 20 – CPS FILTER BANDWIDTH
20 – 2,000 CPS
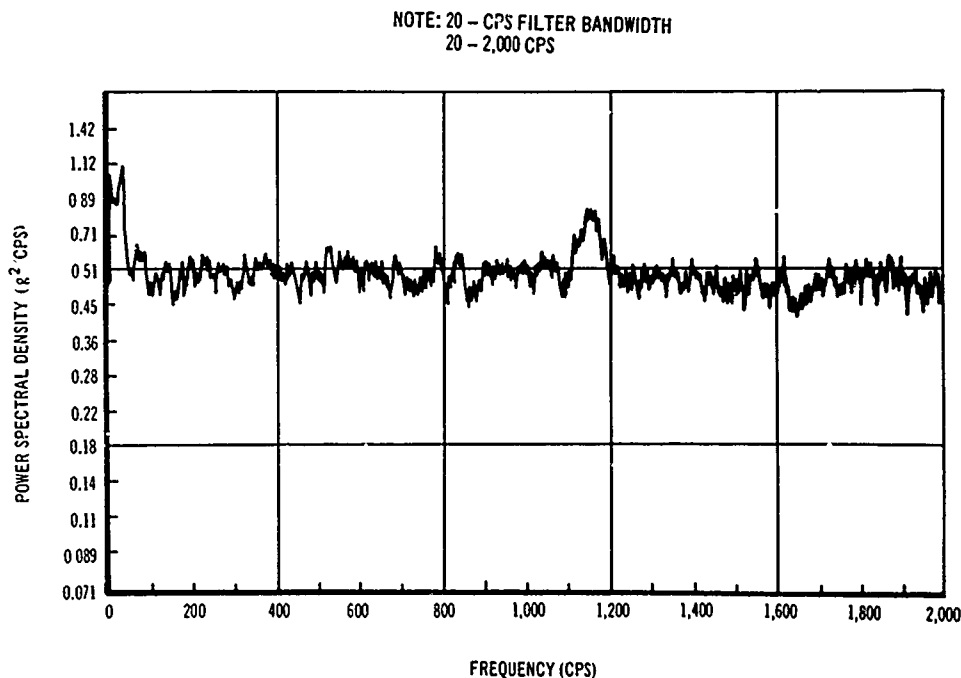
Fig. 9. Typical input PSD (20-2000 cps)

282
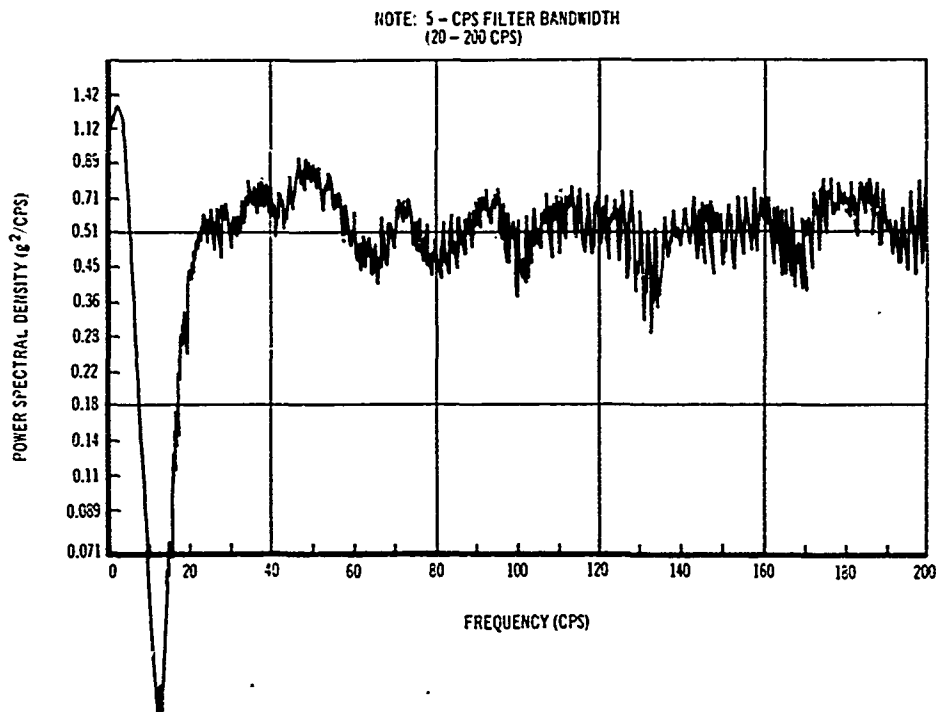
Fig. 10. Typical input PSD (20-200 cps)

concentration holes. The time interval from observation of a crack to complete failure never exceeded 20 percent of the total test time, thus supporting the method used to determine beam failure.

During the random vibration test, tape loops were cut for the production of analog PSD plots. The tape loops were cut at the beginning of each run to avoid any effects caused by cumulative fatigue damage.

TEST RESULTS AND ANALYSIS

The data resulting from this test are given in Tables 5 and 6. The data have been listed according to beam material and thickness. The parameters measured during the test were the individual specimen frequencies, the actual fatigue test input values, and the individual tip response of each specimen. The frequencies were obtained directly from the sinusoidal sweep data; however, some data reduction was required to obtain the input and tip response. The input PSD's were obtained by analyzing a 12-sec tape loop on the Technical Products analyzer using the 5-cps filter. This resulted

in a PSD which was then corrected for the tape recorder response. The values at each beam resonance are listed in the Table 5 under "PSD (in.)"

The g_{rms} value for the tip response was obtained from PSD's generated by the Technical Products analyzer using a 20-cps filter. When the resonant frequency fell in the 20-cps bandwidth of the analyzer, the measured level was predominately that of the resonant response. Therefore, the mean-square value of the tip response was 20 times the PSD value. The rms value was obtained by the equation

$$g_{rms} = PSD \ (g^2/cps) \times 20 \ cps^{1/2} .$$

A value for Q was then obtained using the standard equations for a single degree of freedom response to a random input. The moment at the stress riser per inch of tip displacement (M/in.) was calculated using the Myklestad program. These values are also listed in Tables 5 and 6. These values, the measured frequencies, and the rms tip accelerations were used to calculate the σ_n at the stress riser location for each specimen.

283

<div align="center">

TABLE 5
Aluminum Beam Data

</div>

Beam	Frequency	PSD (in.)	g_{rms}	M/in.	$\sigma_N \times 10^{-4}$	$\sigma_m \times 10^{-4}$	Q	N
(a) 1/8-In. Beam								
A1-S1 2	54	0.24	47	237	1.44	2.12	108.6	9×10^4
3	53.5	0.26	45	237	1.41	2.07	96.9	7.4
4	54.5	0.29	103	237	3.10	4.55	427.6	5.3
5	54.5	0.29	74	237	2.23	3.28	220.7	6.3
A1-R1 2	56	0.34	77	237	1.97	2.90	173.4	5.7
3	57	0.34	104	237	2.84	4.18	302.9	9.4
5	57	0.31	48	237	1.33	1.95	73.0	2.9×10^5
A1-S2 2	52	0.30	57	236	1.89	2.78	151.9	1.9×10^4
3	52	0.30	69	236	2.29	3.36	223.6	8.4
4	52	0.30	43	236	1.42	2.09	86.4	5.5
5	51.5	0.30	67	236	2.18	3.32	213.7	4.8
6	51.5	0.28	70	236	2.36	3.47	248.5	6.7
A1-R2 3	48	0.43	40	236	1.53	2.25	62.5	1.6
5	48	0.37	59	236	2.27	3.34	156.2	2.15
6	48.5	0.44	70	236	2.65	3.89	191.0	2.4
A1-S3 2	46	0.45	46	235	1.92	2.82	93.1	2.2
3	45	0.45	49	235	2.14	3.14	105.8	2.1
4	45.5	0.45	57	235	2.44	3.59	143.9	2.1
5	46	0.45	57	235	2.38	3.50	142.3	3.7
A1-R3 2	43	0.47	50	235	2.40	3.53	125.1	1.65
3	42.5	0.48	33	235	1.61	2.37	52.5	1.95
4	43	0.47	37	235	1.77	2.60	66.7	2.35
5	42.5	0.48	39	235	1.95	2.87	75.0	2
A1-S4 5	41.5	0.36	78	235	1.73	2.55	82.5	2.8
(b) 1/4-In. Beam								
A2-S1 2	59	0.33	44	927	1.10	1.73	47.2	6.3×10^4
3	58.5	0.31	38	927	0.96	1.51	35.9	2.4×10^5
4	58	0.31	75	927	1.95	3.06	154.3	7.5×10^4
5	58.5	0.33	114	927	2.90	4.55	330.0	3.4
A2-R1 3	53.5	0.29	62	924	1.89	2.97	163.0	2.3
4	53.5	0.29	62	924	1.89	2.97	161.3	5.5
5	53.5	0.24	45	924	1.37	2.15	105.0	6.2
A2-S2 2	49.5	0.30	52	922	1.83	2.87	144.3	1.5
4	48.5	0.31	48	922	1.79	2.81	123.5	2.8
5	49.5	0.31	40	922	1.41	2.21	80.4	2.5
6	49	0.29	61	922	2.20	3.45	207.3	1.45
A2-R2 2	45	0.30	28	920	1.22	1.92	54.5	6.1
3	45.5	0.30	28	920	1.17	1.83	50.8	1.7
4	45	0.30	45	920	1.90	2.99	132.5	1.75
6	45.5	0.30	42	920	1.79	2.81	116.7	1.2
A2-S3 2	42	0.29	36	918	1.75	2.74	105.9	1.45
3	42	0.48	45	918	2.23	3.50	106.3	4×10^3
4	42	0.48	59	918	2.90	4.56	177.7	2.2×10^4
5	42	0.48	38	918	1.85	2.91	72.8	1.5
6	42.5	0.48	31	918	1.49	2.34	47.5	1.4
A2-R3 2	39	0.46	43	917	2.45	3.85	111.4	3.9
3	39.5	0.36	35	917	1.96	3.07	94.8	6×10^3
4	39.5	0.47	42	917	2.32	3.65	103.8	4.4×10^4
6	39.5	0.36	51	917	2.83	4.44	201.1	4.9
A2-S4 4	40	0.36	28	917	1.48	2.32	57.3	4.5

TABLE 6
Steel Beam Data

Beam	Frequency	PSD (in.)	g_{rms}	M/in.	$\sigma_N \times 10^{-4}$	$\sigma_m \times 10^{-4}$	Q	N
(a) 1/8-In. Beam								
S1-S1 2	60.5	0.38	48	550	2.71	3.99	63.8	1.8×10^5
3	60.5	0.38	59	550	3.32	4.88	96.5	9×10^4
4	60.5	0.38	90	550	5.12	7.53	224.4	2×10^5
5	60.5	0.39	75	550	4.28	6.30	174.3	1.25
S1-R1 2	58.5	0.38	83	448	4.07	5.98	197.4	7.9×10^4
3	58.5	0.38	99	448	4.87	7.16	280.8	1.2×10^5
4	58	0.38	99	448	4.93	7.24	284.3	1.1
5	58.5	0.38	120	448	5.99	8.80	412.6	1.0
S1-S2 2	52	0.31	64	546	4.88	7.18	161.9	3.6×10^4
3	52.5	0.28	77	546	5.28	8.49	256.9	6.2
4	52.5	0.31	44	546	3.29	4.84	75.8	8.4
5	52	0.31	55	546	4.19	6.16	119.5	1.08×10^5
S1-R2 2	48.5	0.45	41	545	3.53	5.19	49.1	5.6×10^4
3	49	0.45	45	545	3.77	5.54	57.2	2.2
4	49	0.45	59	545	5.03	7.39	100.6	4.9
5.	48.5	0.38	55	545	4.79	7.04	114.6	3.3
6.	49	0.45	51	545	4.33	6.37	71.5	4.8
S1-S3 2	44.5	0.47	52	544	5.33	7.84	82.4	3.7
3	43	0.47	42	544	4.61	6.77	55.6	4.2
4	44	0.47	69	544	7.37	10.83	146.7	4
5	42.5	0.47	41	544	4.61	6.78	53.6	4.1
6	44.5	0.47	72	544	7.51	11.04	157.9	4.3
S1-R3 2	42.5	0.47	46	543	5.24	7.70	35.1	4.1
4	42	0.47	33	543	3.82	5.62	136.0	1.15×10^5
5	42.5	0.47	61	543	6.96	10.23	46.7	2.7×10^4
6	41	0.48	38	543	4.50	6.62	32.7	9
S1-S4 2	41.5	0.36	39	542	4.57	6.72	64.9	3.1
(b) 1/4-In. Beam								
S2-S1 2	78.5	0.42	65	2165	2.17	3.41	81.6	6.6×10^5
3	77.5	0.42	92	2165	3.13	4.92	165.6	5.1
S2-R1 2	54	0.30	41	2150	2.86	4.49	66.1	1.73
3	53.5	0.30	44	2150	3.11	4.89	76.8	1.31
4	53.5	0.28	55	2150	3.89	6.11	128.6	1.73
5	54	0.28	43	2150	2.98	4.68	77.9	1.9
S2-S2 2	51.5	0.31	37	2140	2.82	4.43	54.6	1.65
3	51.5	0.31	39	2140	2.98	4.68	60.7	1.4
4	52	0.29	52	2140	3.89	6.10	114.2	1.25
5	53	0.29	45	2140	3.24	5.09	83.9	1.4
6	52	0.29	53	2140	3.96	6.22	118.7	1.3
S2-R2 2	44	0.24	25	2135	2.63	4.13	37.7	1.5
3	46.5	0.38	22	2135	2.01	3.15	17.4	1.25
4	46.5	0.38	31	2135	2.87	4.50	34.6	9×10^4
5	45	0.27	26	2135	2.79	4.10	47.5	1.4×10^5
6	46.5	0.38	25	2135	2.30	3.61	23.4	1
S2-S3 2	42.5	0.38	32	2135	3.52	5.53	39.3	6.2×10^4
3	42.5	0.41	36	2135	4.06	6.38	47.4	1.1×10^5
4	41	0.47	28	2135	3.38	5.30	25.9	7.2×10^4
5	42.5	0.41	29	2135	3.26	5.12	30.7	9.4
6	43	0.41	31	2135	3.38	5.30	34.7	8
S2-R3 2	39	0.42	29	2125	2.49	5.91	32.7	9
4	38.5	0.38	32	2125	4.25	6.68	44.6	1.1×10^5
5	39.5	0.42	31	2125	4.00	6.28	36.9	9.4×10^4
6	39	0.42	24	2125	3.20	5.03	22.4	2×10^5
S2-S4 2	39	0.36	23	2125	3.03	4.76	24.0	7×10^4

The σ_m is the nominal stress multiplied by the stress concentration factor ($k_f = 1.47$ and 1.57 for the 1/8- and 1/4-in. beam, respectively) (Appendices C and D). The σ_m was then plotted as a function of N for the steel and aluminum. The aluminum data are presented in Fig. 11. The curve indicated considerable scatter. The parameters included in the data were natural frequency (f), calculated moment per unit tip displacement (M/in.), tip acceleration (g_{rms}), stress concentration factor (k_f), and failure time (T). Of these parameters, only k_f and g_{rms} could contain sufficient scatter to completely overshadow the natural fatigue scatter (10 to 20 percent) as indicated by the data.

The g_{rms} value resulted from measuring a random signal with an effective bandwidth much less than 1 cycle due to the high Q resonance of the system. Recalling the equation

$$\Delta dB^2 = \frac{200}{\Delta F \times T} ,$$

the accuracy of such levels must be low. To correct this, the tip acceleration levels must be related to some parameter which is more consistent than the g_{rms} value. The only possibility in this case is to utilize the expression $g_{rms} = (\pi/2) \times Q \times f \times PSD^{1/2}$. The value of f has been defined, and the value of $PSD^{1/2}$ is known to a much higher degree of accuracy than g_{rms}.

On the other hand, Q is a parameter which is difficult to obtain.

Assuming that Q is a constant for each material, the average of the Q's calculated by the expression given above reflects a reasonable value for Q of the specimen. If Q is, in fact, a constant and the input level and frequency were known precisely, a g_{rms} value predicted using the average Q would have the accuracy obtained from reducing a tape loop equal in time to the product of the number of specimens times the average time of each tape loop, or approximately 800 sec, which is sufficient time to obtain an accurate value of the rms value.

Other experimenters have found a great deal of scatter in Q. Although a portion of that scatter is due to experimental difficulties (Appendix E), the available information indicates that the above assumption is not correct. Therefore, the effects of this assumption must be examined. If Q does display some scatter, the above procedure will introduce this uncertainty into the g_{rms} data. That is, the above procedure largely eliminates an experimental error and introduces the natural scatter of one of the fundamental parameters, which is precisely the desired result. This correction has been applied to the data.

Relaxing the assumption that the stress concentration factor is independent of stress
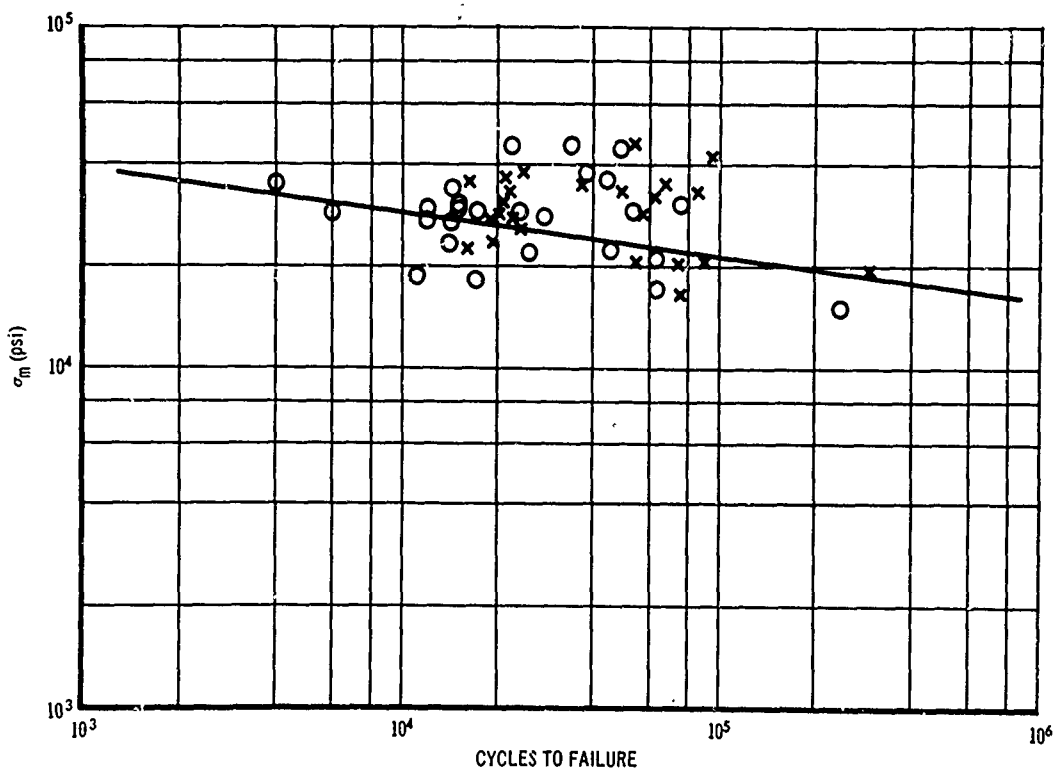
Fig. 11. Fatigue curve for aluminum including recorder correction only

levels results in values which are functions of the following parameters: (a) the fatigue characteristics of the metals tested, including uncertainties; (b) the natural scatter in Q and the effect of stress on this variable; (c) the effect of high stress on stress concentration factors; and (d) the uncertainties in input PSD, which include the notch effect due to shaker-specimen interaction and the test duration. Item (d) is inherent in this type of test and must be tolerated. The remaining scatter results from uncertainties in parameters which are included in the product of K and K_{dyn}. These data are shown in the form of random fatigue curves (Figs. 12 and 13) and as discussed below:

$$\langle\sigma\rangle_m = K K_{dyn} \sigma_o \text{ load}.$$

The factors of this equation can be evaluated three ways:

1. K_{dyn} and σ_o can be assumed to have no scatter so that all of the scatter can be combined into K;

2. σ_o can be corrected for stress amplitude effects, and the scatter can all be attributed to K; or

3. Assumptions can be made as to the amount of scatter in K, allowing the separation of scatter in K and K_{dyn}.

The first of these approaches has the advantage that it relieves the designer of scatter definition in K and σ_o. All that is required is nominal values for these parameters. The desired K can be obtained directly from Figs. 12 and 13 by taking the ratio of the working stress to the indicated fatigue curves. The results are shown in Figs. 14 and 15 as functions of number of cycles and of natural frequency, assuming a 10-min required life.

The sinusoidal K factor (K_s) can be obtained by dividing K by A, which is 2.04 for both specimen materials (1). For this reason, a K_c scale has been included in each figure. The correction for k_f was obtained as described below for the second approach.

The probability of a peak stress occurring in each $(1/2)\sigma$ increment was obtained assuming a Rayleigh distribution, and the mean stress in each band was assumed to be at the center of the band. Miner's accumulation was assumed, and it was also assumed that $\alpha = 6$.

The sum of the probabilities of occurrence in each band times the mean stress value for that band raised to the sixth power yields an approximate damage factor. If the calculated value of a given σ peak exceeds the yield strength of the material, then the actual stress for that value must be on the order of or less
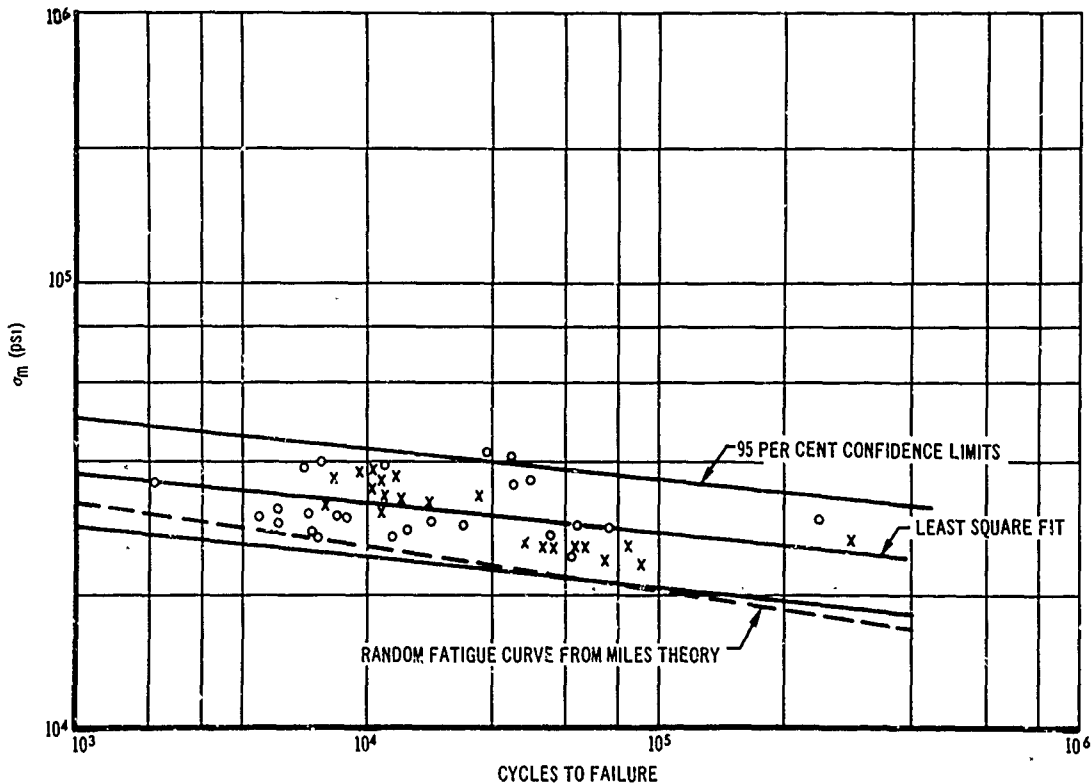
Fig. 12. Aluminum test data assuming $Q = 135$

287 .
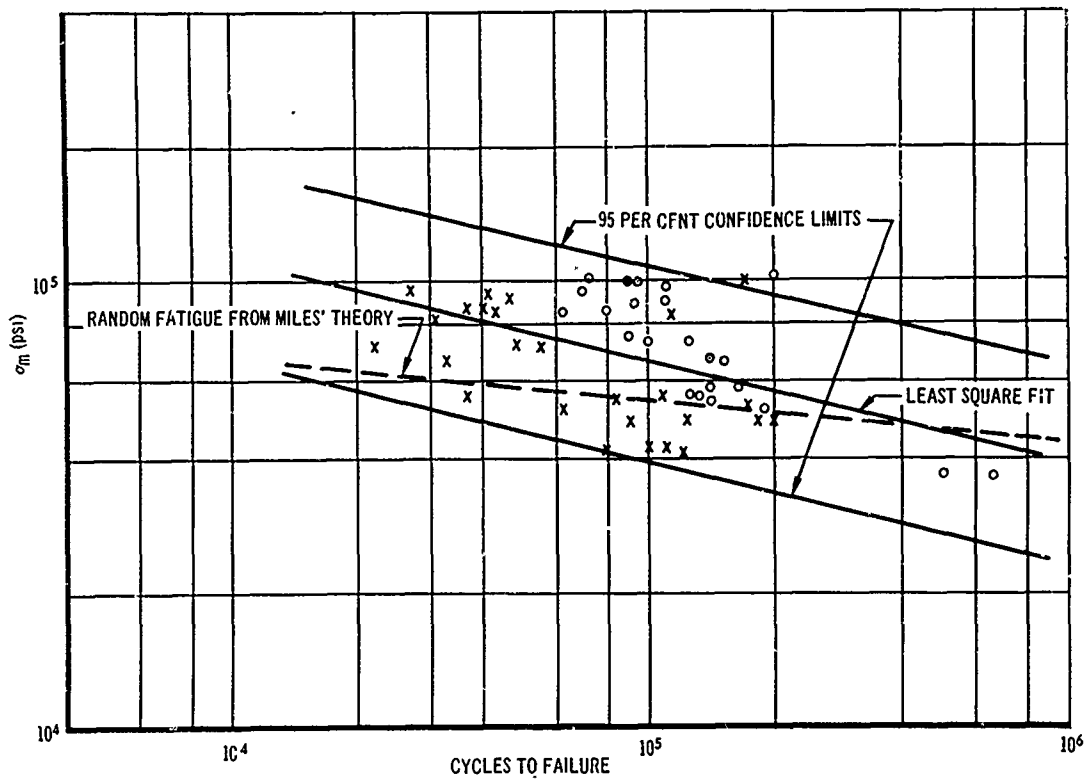
Fig. 13. Steel test data assuming Q = 95
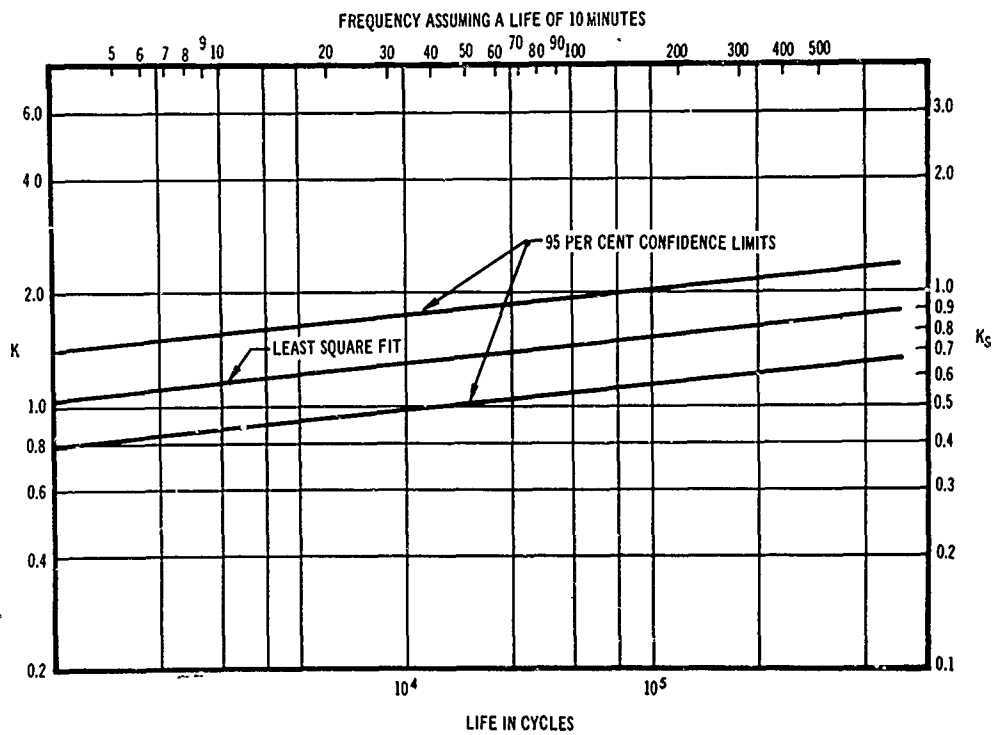
Fig. 14. Aluminum design factor (K)
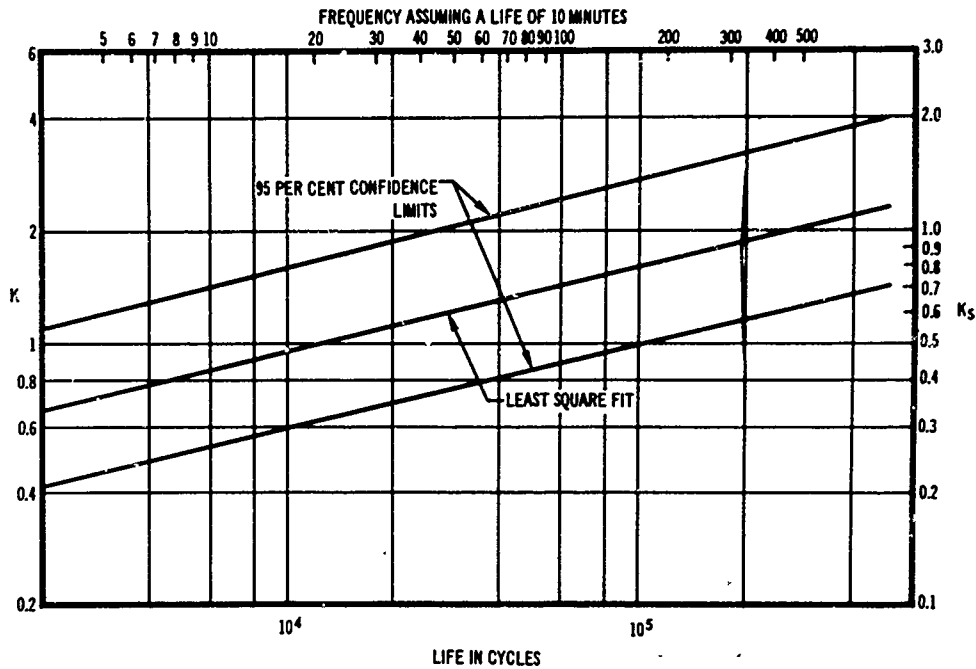
Fig. 15. Steel design factor (K).

than the yield strength. The relationship between yield and calculated rms stress values of 1, 1-1/2, 2, and 2-1/2 were chosen, and the probability of occurrence for stresses greater than yield were added to the band just below yield. The damage factor was calculated as discussed above, and the ratio of this factor to the factor obtained for low stress was obtained. This factor times the stress concentration factor of 1.5 is shown in Figs. 16 and 17.

Since the stress probably exceeds yield and the method of including the effect was conservative, the curves resulting from the above calculations have been shifted 20 percent to the right. This new curve was used to correct the data as shown in Figs. 18 and 19. The K and K_s factors obtained from these data are given in Figs. 20 and 21.

The third method mentioned above, i.e., separation of scatter, requires a review of the basic equation $\sigma_m = K K_{dyn}(\text{load}) \, \sigma_o$. The scatter in σ_o was due to k_f and is largely removed by the above correction. The scatter in K is limited to fatigue scatter only. In this type of test, the fatigue scatter should not exceed 15 percent for the 95 percent confidence levels (in stress) for smooth specimens like the aluminum and 20 to 25 percent for slightly rougher specimens similar to the steel specimens. The scatter in load is dependent on the accuracy of the measured input level. It is felt that the 95 percent confidence level uncertainty for this variable was from 10 to 15 percent. Using the

10 percent value to insure conservatism, the combined 95 percent confidence level uncertainty would be approximately 18 percent for aluminum. Therefore, the scatter in K_{dyn} is overshadowed by the scatter in K and in the forcing function measurement. The combined error for the load and K for steel is on the order of 25 percent. Therefore, the error in K_{dyn} is on the order of 40 percent.

A final word should be added concerning amplitude distributions obtained from the test data. Figure 22 shows an amplitude distribution typical of those obtained from tip accelerometer data. Note the agreement with the theoretical curve (Gaussian distribution) to 2-1/2 or 3σ. Figure 23, which is a distribution obtained from strain gage data, shows about the same agreement with the normal distribution. The magnitude of the multi-mode effect is indicated in Fig. 24, which is a PSD of the strain gage time history.

DISCUSSION OF K_{dyn} AND σ_o

The prediction of K_{dyn} and σ_o is an integral part of the design factor approach. The calculation of σ_o is straightforward except for the variation of the stress concentration factor under stress. Assuming that all of the uncertainties are in K, the stress concentration factor must be a dynamic factor (Appendix B). If the variation of k due to stress is eliminated from K, then it must be included in σ_o. This required prior knowledge of the environment and K_{dyn}.
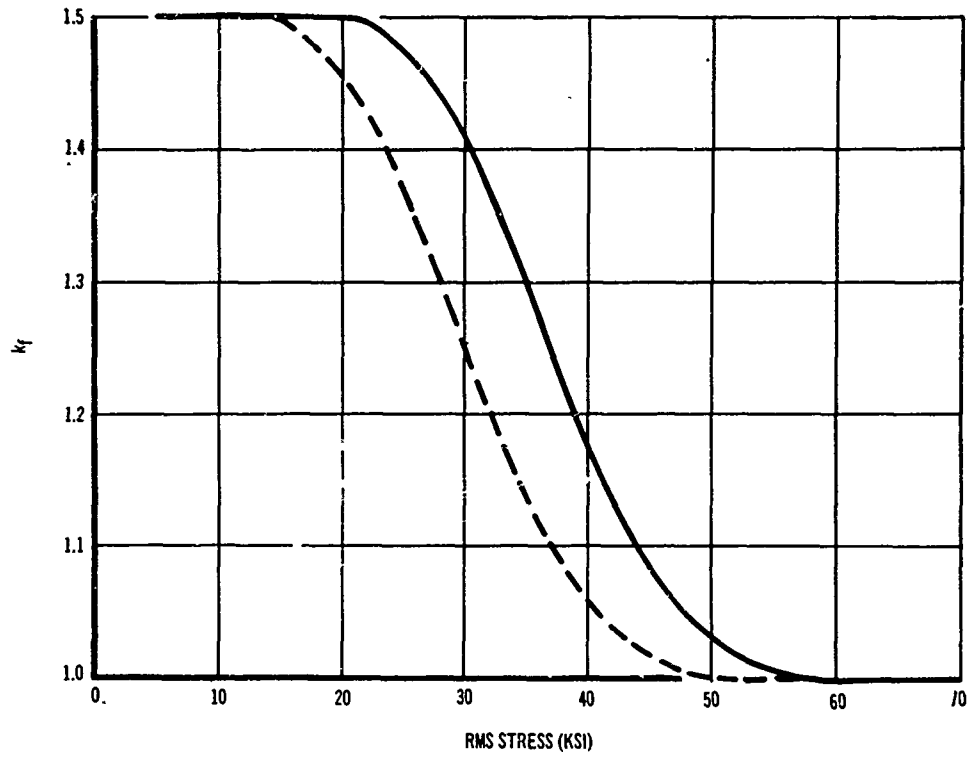
Fig. 16. Variation of k_f with stress above yield for aluminum
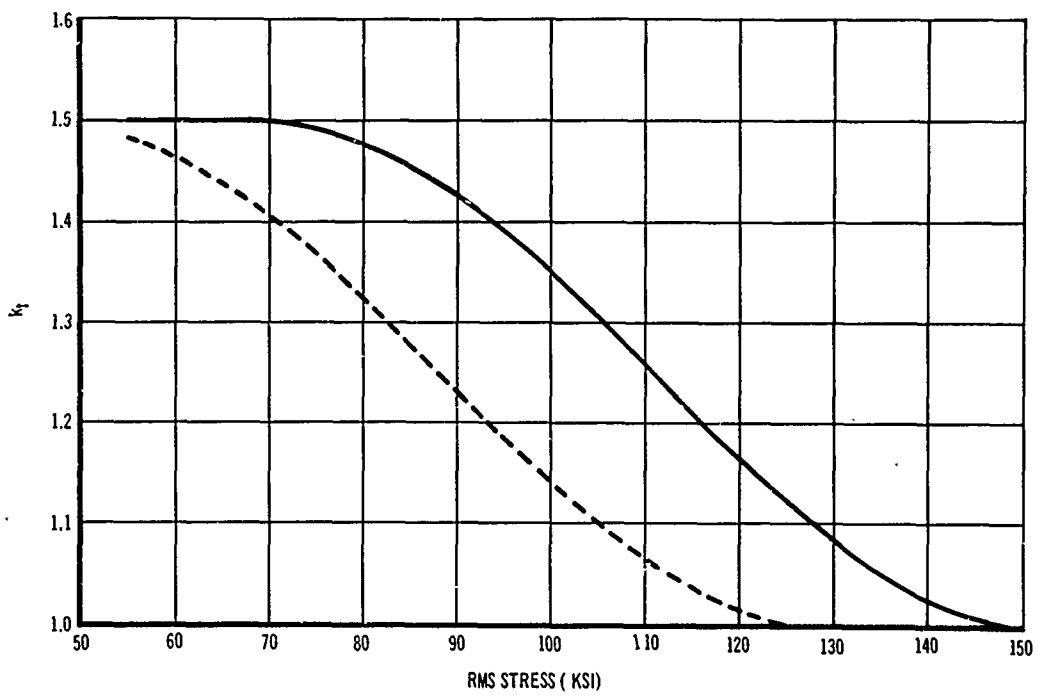
Fig. 17. Variation of k_f with stress above yield for steel

290
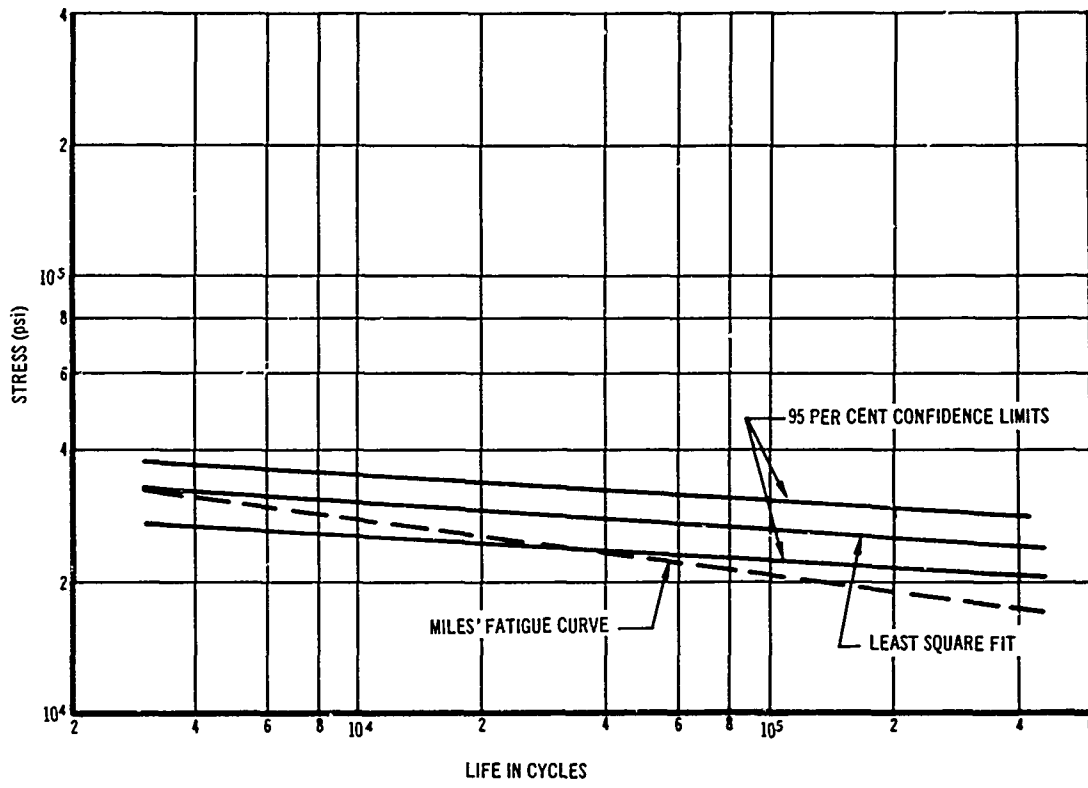
Fig. 18.   Aluminum test data including $\hat{k}_f$ correction
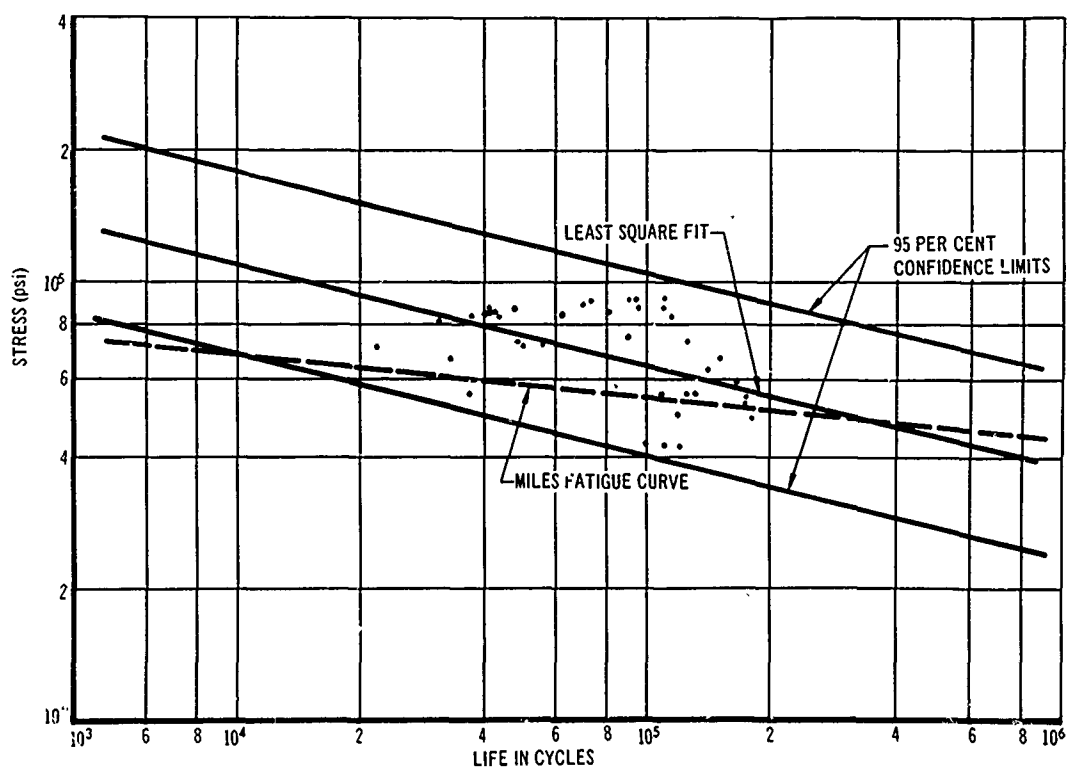
Fig. 19.   Steel test data including k_f correction
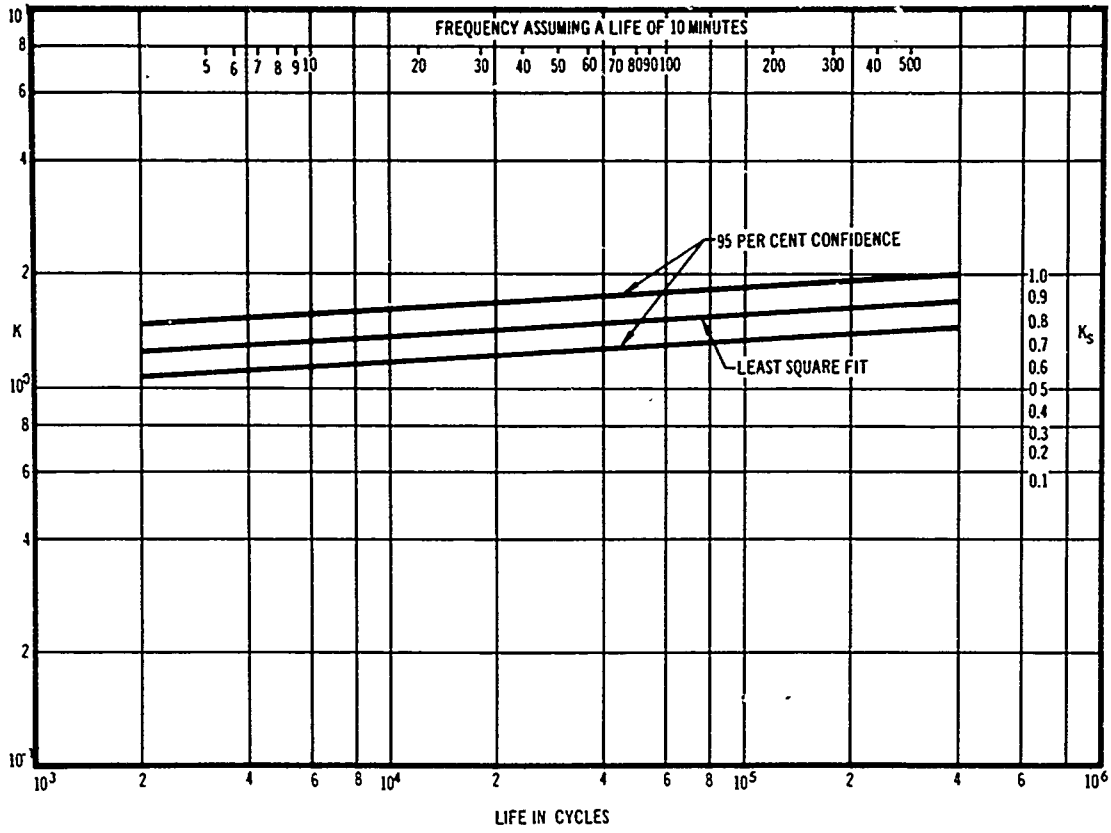
Fig. 20. Aluminum design factor K including k_f correction
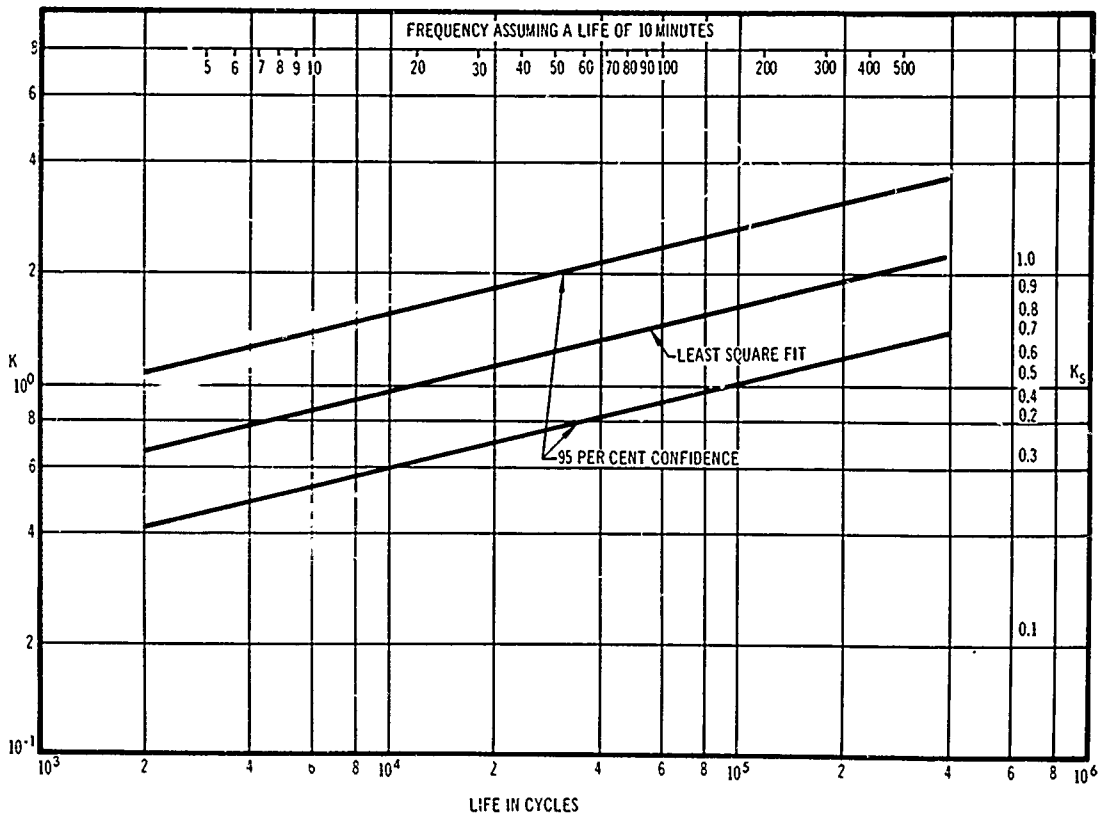
Fig. 21. Steel design factor K including k_f correction

292
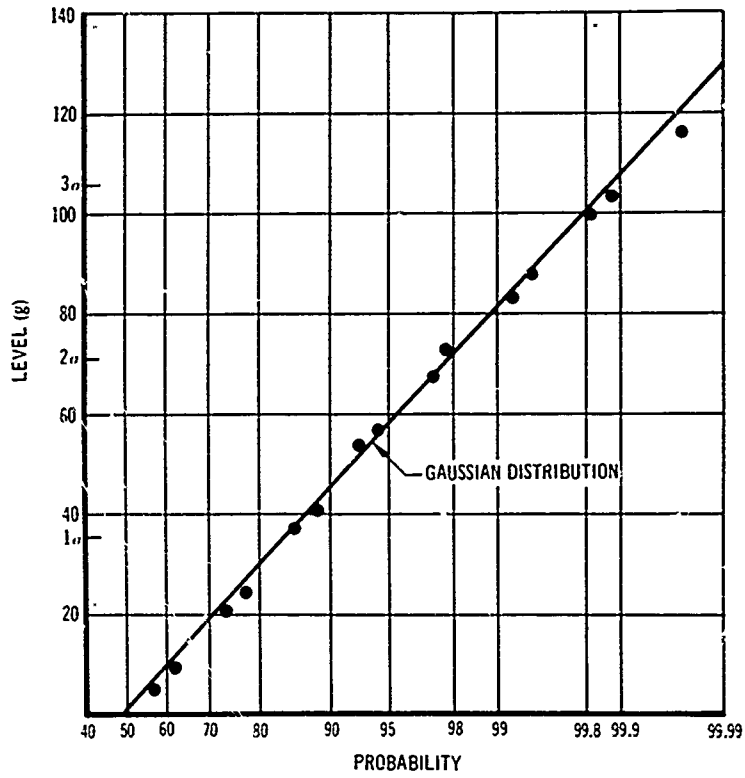
Fig. 22. Amplitude distribution
for 1/4-in. aluminum beam
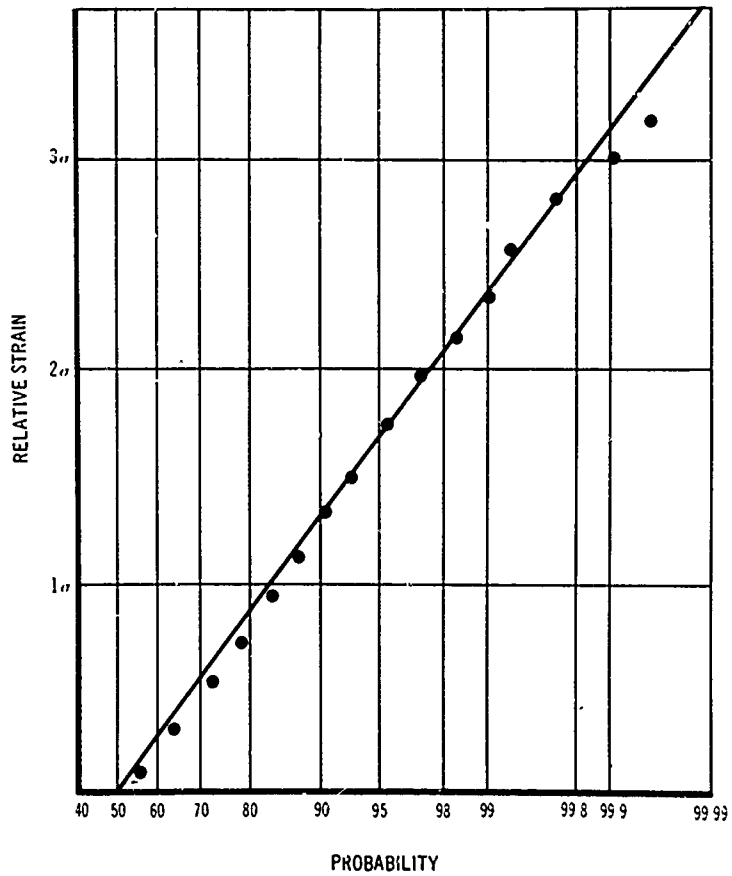
Fig. 23. Amplitude distribution
for strain gage measurements

293
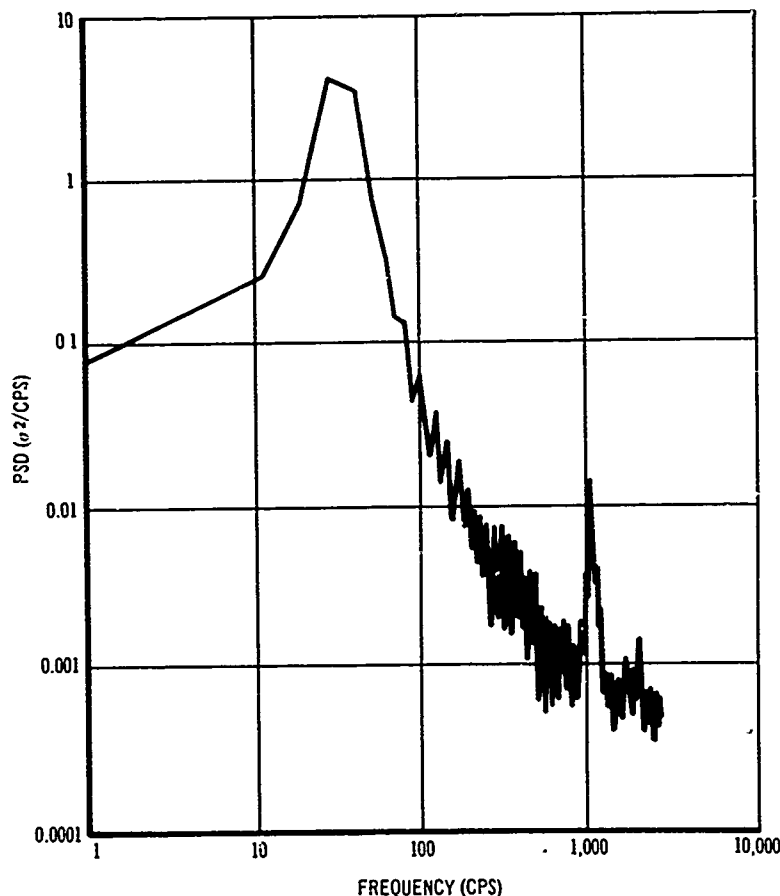
Fig. 24. Relative PSD for strain gage measurements

The deviations in K_{dyn} may or may not be included in the value of K_{dyn}. Regardless of where the deviation is included the mean value of K_{dyn} is obtained as shown below. The K_{dyn} for the random cases is

$$K_{dyn} = \left(\frac{\pi}{2} \cdot Qf\right)^{1/2} .$$

The K_{dyn} for the sinusoidal case requires more discussion.

The equivalent sine level must be derived from random data, and this derivation requires some knowledge of Q. If the Q of the system is used for the derivation of the sinusoidal load, then K_{dyn} for sine (K_{dynS}) equals Q. However, if the sinusoidal load was derived using a Q different from that of the specimen (Q'), then the levels will be higher by the factor of the square root of Q divided by Q'. Correcting this deviation in K_{dynS} yields

$$K_{dynS} = Q \left(\frac{Q'}{Q}\right)^{1/2} = (QQ')^{1/2} .$$

This equation is a general expression and in the case where $Q = Q'$ yields the first expression for K_{dynS}.

The scatter in K_{dyn} for both these cases is primarily due to the uncertainties in $Q^{1/2}$. This indicated that the uncertainty in Q for the aluminum specimens is much less than 20 percent and in steel is on the order of 100 percent for the 95 percent confidence limits. These values are less than those observed by other investigators for aluminum or steel.

CONCLUSIONS AND
RECOMMENDATIONS

These tests established the feasibility of utilizing equivalent static design factors in basic bracket design by postulating the required factors and then obtaining these factors through tests on simple cantilever beams.

The factors were obtained by direct measurement of the exciting force and the system's life. The required damping information was obtained by a statistical treatment of measured tip response. (However, the damping would be empirically estimated in an actual design application.) The information was then combined with the predicted stress information, and fatigue data were obtained. From these data, a fatigue factor (K) was obtained which included

294

only the scatter associated with the natural response and fatigue plus the uncertainty in defining the input levels. The K factor was then refined by eliminating the scatter due to various parameters. This resulted in three K factors, each of which would be of use, depending on the design application.

This same basic approach is applicable to actual structures, and the degree of tolerable scatter suggests the individual parameters which must be considered in each design.

Therefore, it is recommended that additional work be focused in the following general areas:

1. Better definition of damping, the scatter in damping, and the effect of stress levels on this parameter for the damping mechanisms encountered in bracket structures;

2. The effect of various common stress risers on both sinusoidal and random fatigue and the effect of stress amplitude on these parameters;

3. The definition (by test) of the static equivalent design factors for complex bracket systems; and

4. Combination of the above quantities into simple design charts to aid the designer.

ACKNOWLEDGMENTS

REFERENCES

1. J. W. Miles, "On Structural Fatigue Under Random Loading," J. Appl. Mech. (Nov. 1954)

2. B. J. Lazan, "Material and Interface Damping," in Handbook of Shock and Vibration (Crede and Harris, Eds.)

3. Research on Techniques of Establishing Random Type Fatigue Curves for Broad Band Sonic Loading, ASD-TDR-62-501, Oct. 1962

4. J. C. McClymonds et al., "Research of Techniques of Establishing Random Type Fatigue Curves," Douglas Aircraft Co. Rept. SM-30461, Nov. 1960

5. A. L. Eshleman et al., Structural Design for Acoustic Fatigue, ASD-TDR-63-820, Oct. 1963, Douglas Aircraft Co. Rept. LB-31354

6. C. Schjelderup, Accumulative Damage Caused by Random Loading, Douglas Aircraft Co. Tech. Paper LB-738, Jan. 1959

7. V. C. McIntosh and N. Granick, Experiments in Random Vibration, WADC TN 56-228

8. W. D. Trotter, "An Experimental Evaluation of Sinusoidal Substitutes for Random Vibration," Shock and Vibration Bull. 29, Pt. 4, p. 1 (June 1961)

9. B. M. Hall and L. T. Waterman, Correlation of Sinusoidal and Random Vibrations, Douglas Eng. Paper 1048

10. R. W. Fralich, Experimental Investigation of Effects of Random Loading on the Fatigue Life of Notched Cantilever Beams of 4130 Normalized Steel, NASA TND-663

11. Experimental Investigation of Effects of Random Loading on the Fatigue Life of Notched Cantilever Beam Specimens of 7075-T6 Aluminum Alloy, NASA Memorandum 4-12-59L

12. P. W. Smith, "Fatigue Tests of a Resonant Structure With Random Excitation," J. Acoust. Soc. Am. (Jan. 1963)

13. J. E. Foster, "Random-Sinusoidal Vibration Correlation Study," J. Environ. Sci., p. 6 (Aug. 1961)

14. L. W. Root, "Selection of Vibration Test Levels Using Fatigue Criteria," Shock and Vibration Bull. 34, Pt. 5, p. 55 (Feb. 1965)

15. A. K. Head and F. H. Hooke, Random Noise Fatigue Testing, Int. Conf. on Fatigue of Metals, I.M.E. and A.S.M.E., New York and London, Sept. 1956

BIBLIOGRAPHY

Aerospace Structural Metals Handbook, ASD-TDR-63-741, Dec. 1963

Crandall, S. H., Random Vibrations

Crede, C. E., "Failure Resulting from Vibration," in Vol. II of Random Vibration

Den Hartog, J. P., Mechanical Vibrations

Eshleman, A. L., J. D. Van Dyke, and P. M. Belcher, "A Procedure for Designing and Testing Aircraft Structure Loaded by Jet Engine Noise," Douglas Aircraft Co. Eng. Paper 693, March 1959

Fisher, E. G., "Theory of Equipment Design," in Handbook of Shock and Vibration (Crede and Harris, Eds.)

Granick, N., and J. E. Stern, "Material Damping of Aluminum by Resonance-Dwell Technique," Shock and Vibration Bull. 34, Pt. 5, p. 177 (Feb. 1965)

Grover, H. J., S. M. Bishop, and L. R. Jackson, "Fatigue Strengths of Aircraft Materials," NASA TN 3866, 1956

Illg, W., "Fatigue Tests on Notched and Unnotched Sheet Specimens of 2024-T3 and

7075-T6 Aluminum Alloys and of SAE 4130 Steel With Special Consideration of the Life Range 2 to 10,000 Cycles," NASA TN 3866, 1956

MacDuff, N. J., and R. P. Felgar, "Vibration Frequency Charts," Machine Design (Feb. 7, 1957)

McClymonds, J. C., "Sonic Fatigue Design Analyses," presented at Symposium on Fatigue of Aircraft Structures, Dayton, Ohio, Aug. 1959

Metallic Materials and Elements for Flight Vehicle Structures, MIL-HDBK-5, Aug. 1962

Norris, C. H., et al., Structural Design for Dynamic Loads

Peterson, R. E., WADC Tech. Rept. 59-507, Aug. 1959

Roark, R. J., Formulas for Stress and Strain

Timoshenko, S., Vibration Problems in Engineering

Vreeland, R. H., Douglas Aircraft Co. Strength Bull. No. 12 — Fatigue Manual, rev. Feb. 13, 1961

Appendix A

COMPARISON OF PLAIN AND NOTCHED SPECIMENS

It was originally decided that plain specimens (without stress risers) would be used in this test program. The two advantages of these specimens were that a variable k_f would be eliminated from the tests and since there would be local yielding near the failure point in any specimen (with an attendant modification of the distribution of peak stresses), use of a plain specimen would allow measurement of this effect with a strain gage at the critical section.

Prototype plain specimens were fabricated and tested with the results discussed in Appendix B. Based on the results of these tests, it was decided that the extreme nonlinearities observed with the plain specimens would complicate analysis of the test data, particularly since it was planned to correlate test results with a linear response and fatigue analysis. A further disadvantage of the plain specimens was that in

order to fail the specimens with the available shaker, the specimens would have to be fabricated of "weak" materials. Aluminum in the T-O condition and normalized steel were used, but it was recognized that these are not commonly used engineering materials, that their properties cannot be closely controlled, and that due to their ductility, they have the unusual property of a yield strength less than fatigue strength for the life range being studied.

New peg point specimens with two round holes for stress risers were then fabricated with the following advantages:

1. The stress concentration factors tended to reduce scatter in fatigue test results;

2. The double concentration factor doubled the number of possible crack initiation points,

296
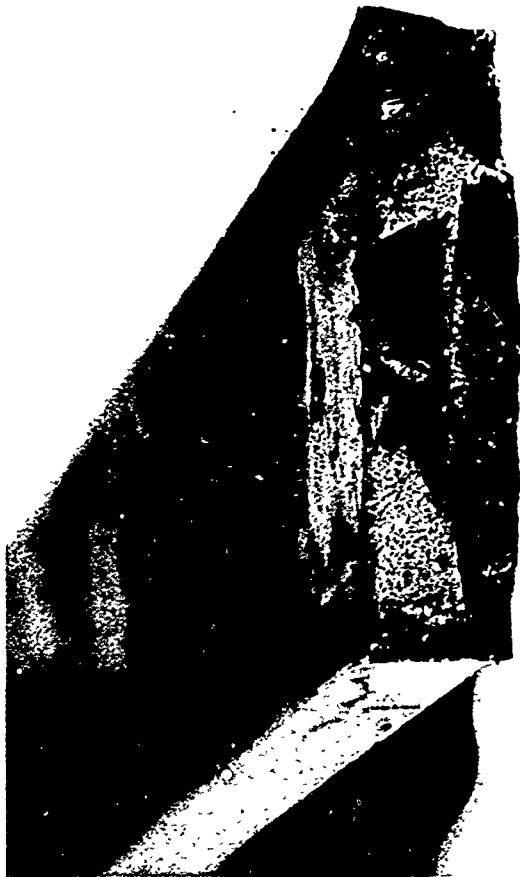
Fig. A-1. Plain specimens
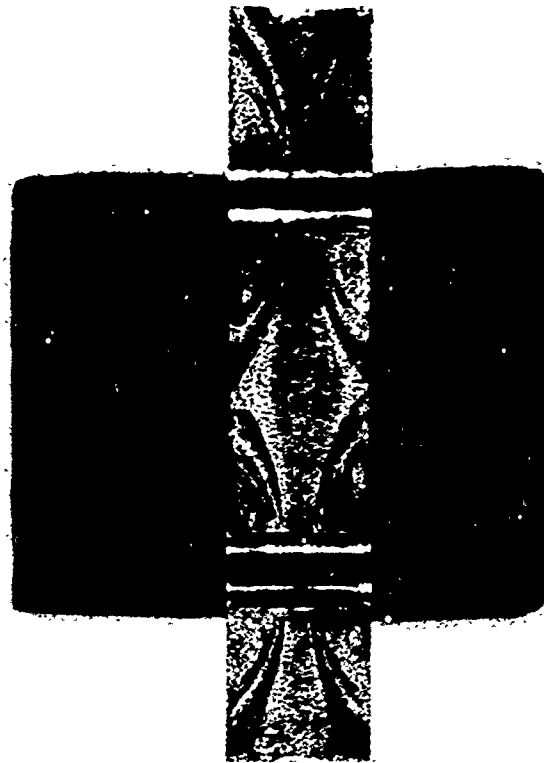
Fig. A-2. Specimen with stress concentrations

which tended to reduce scatter in the fatigue data;

3. Stress concentration factors are typical of actual bracket design; and

4. The stress concentration factor prevented the drastic reduction in Q observed in the former specimens at the fatigue stress point.

The irregularity of the failure process for the plain specimens is illustrated in Fig. A-1. Note that there are at least two out-of-plane crack nucleation points, thus causing a very irregular failure surface and considerable difficulty in defining failure. In Fig. A-2, which shows the failure surface for the specimen with the stress risers, note the regular crack growth from each of the crack nucleation points. In these specimens, general failure quickly followed formation of the first crack.

Appendix B

LINEARITY AND DAMPING CHARACTERISTICS OF SPECIMENS

Before initiating design and fabrication of the final specimens, preliminary tests were run on prototype specimens referred to as peg point specimens. It was hoped that these specimens would have life characteristics similar to the median of the final production specimens and that their dynamic and structural characteristics would be similar to a typical production specimen. Peg point specimens were originally fabricated without stress risers. Later it was decided that the final specimens should have stress risers. However, the results of the peg point specimen tests are still of considerable interest because of the insight they provided regarding structural damping and fatigue phenomena. The configuration of the first peg point

297
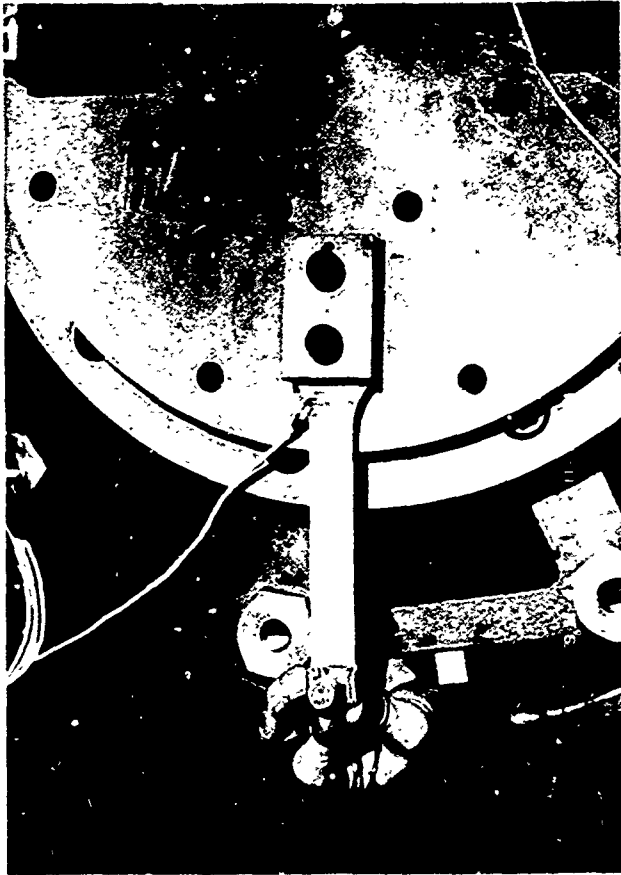
Fig. B-1. First peg point specimens

specimens is illustrated in Fig. B-1. When
these beams were vibrated to their design level,
several things were observed:

1. There was a sizable reduction in beam
response as fatigue was accumulated. This is
illustrated by Fig. B-2. This plot shows the
relative responses of a typical beam as failure
is approached, obtained from third-octave band
analyses of the response data. It represents
data from the beam end accelerometers which
have been plotted as a function of time before
failure.

2. Increases of input levels did not cause
the expected increases in tip response levels.
For example, a doubling of the input PSD value
at fatigue levels resulted in a 7 percent increase
for the 6-in. aluminum specimen. This indi-
cates a highly nonlinear Q in the test region.
This also indicates that the peak distribution
may be drastically altered.

Because of these effects, lives of the first peg
point specimens were far above design life.
Actually, levels four times higher than the de-
sign level were required to fail the beams.

An analysis of the damping characteristics
of the beams was then conducted to determine
if nonlinear damping was one of the causes of
the large discrepancy between the predicted
and measured failure levels. Originally, damp-
ing had been estimated from Trotter's data (8).
Prior to testing, damping of the specimens was
experimentally determined from resonant de-
cay tests. Finally, damping was again measured
in low-level sinusoidal sweeps. In every case,
Q was established to be between 65 and 130.
The design test level of approximately 0.2
g^2/cps was determined based on those esti-
mates of Q (the stress in the beam under ran-
dom excitation is proportional to Q). When in
actual test the failure level was established to
be closer to 2 g^2/cps than to the design level,
nonlinear damping was investigated as a possible
cause. Lazan (2) has shown that in the stress
range above the endurance limit, the damping
ratio is proportional to a high power of stress.

With this in mind, damping was again esti-
mated using the procedure suggested by Lazan
and available narrow band ($f = 0.2$ cps) power
spectral analyses. Tip-to-root amplification
ratios were used to determine damping during
the high-level (1.2 g^2/cps) tests.

Theoretical damping was calculated using
the following steps:

1. Estimate a "fatigue strength at 10^8 cy-
cles," σ_f for each material — 1.3×10^4 psi for
2024 aluminum and 4.7×10^4 for the 4031 steel.

2. Determine the stress (during the test, a
stress two times the rms stress was used).

3. Determine the specific damping energy,
D, from Lazan [(2), Fig. 36.17].

4. Determine the loss factor for a uniformly
loaded specimen from Eq. 36.14 of Ref. 2.

As a result of this analysis, it was decided to
use specimens with stress risers. There were
many advantages in this type of specimen (Ap-
pendix A). However, prior to fabricating the
new specimens, an analysis was conducted to
estimate the damping of the new specimens.
To eliminate any nonlinearities and also to pro-
duce sufficient response to fail the beams in a
reasonable time, Q's equal to at least 50 were
desired for the second set of peg point speci-
mens. An analysis confirmed that the Q's
would be in this range.

Figure B-3 shows the stress distribution
in the vicinity of a round hole in the tension side
of a plate and an analytical expression for this
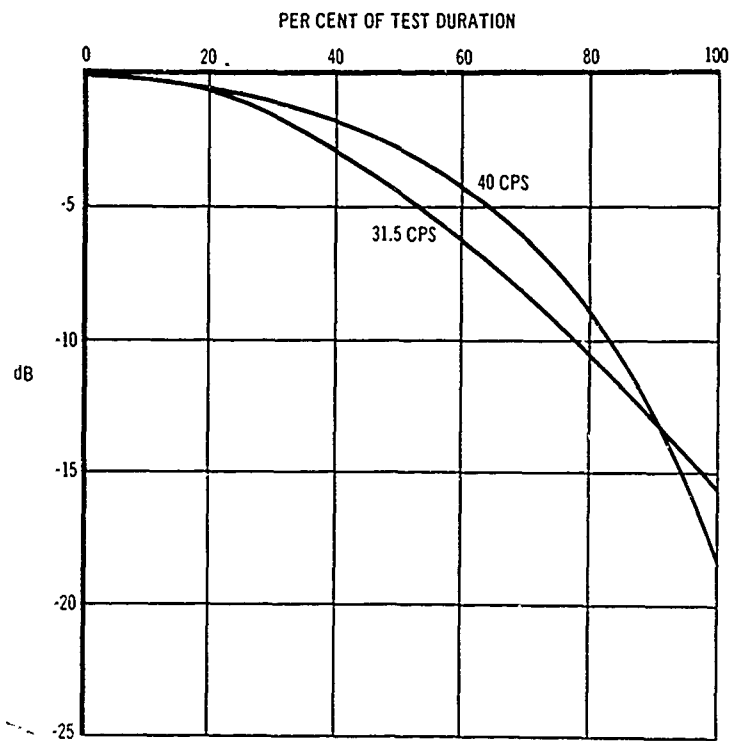
Fig. B-2. Reduction in rms acceleration
vs percentage of test duration

Fig. B-3. Stress distribution near
round hole in plate in tension
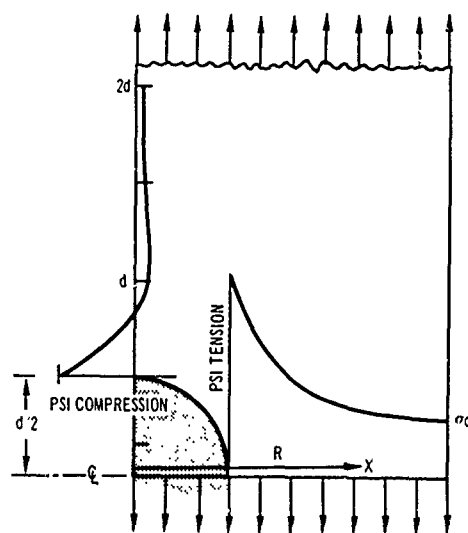
$$\sigma_R = \frac{\sigma_0}{2}\left(2 + \frac{d^2}{4R^2} + \frac{3}{16}\frac{d^4}{R^4}\right)^*$$

* TIMOSHENKO, S. ELEMENTS OF STRENGTH OF MATERIALS.
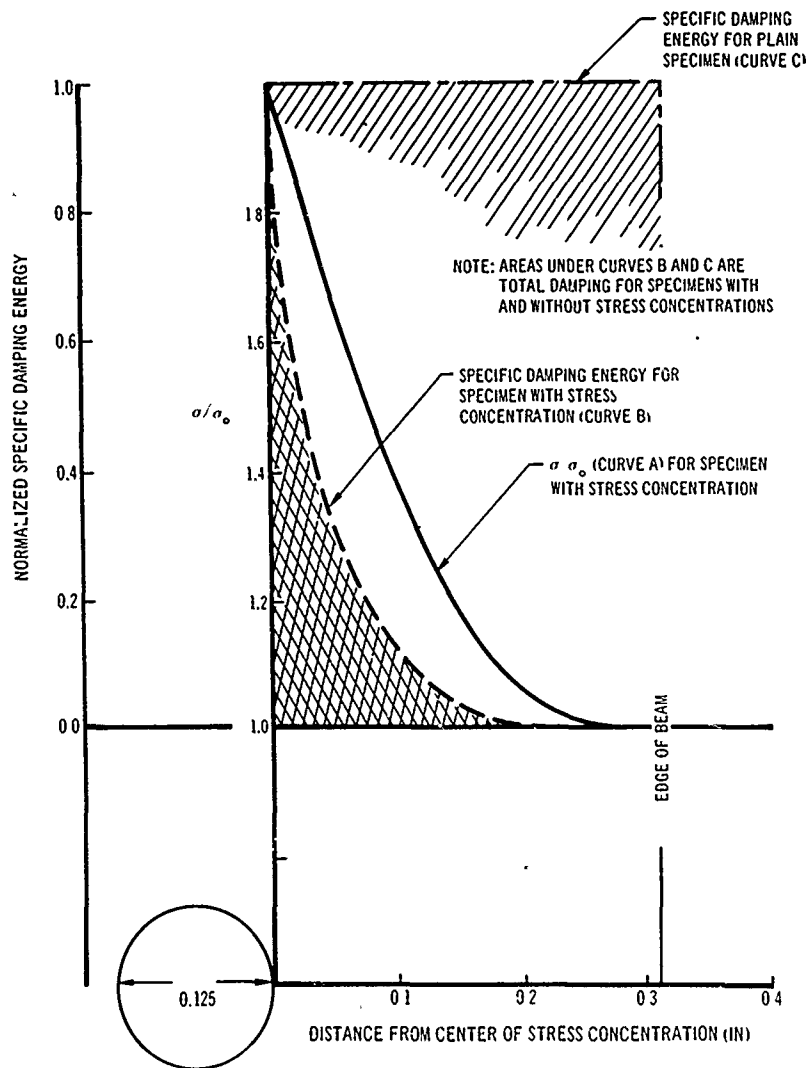
Fig. B-4. Comparison of damping energies of specimens with and without stress concentrations

distribution. Based on these data, the stress distribution was determined near each of the stress concentrations for the second peg point specimens. Note that the holes are sufficiently separated from each other and from the edge of the beam to minimize interactions (confirmed by the photoelastic analysis described in Appendix D).

With this stress distribution, the specific damping energy for each small volume of material in the vicinity of the holes could be determined from Ref. 2. At high stresses, this damping energy is proportional to the eighth power of stress. Damping energy is shown in Fig. B-4 (normalized to the values resulting from the stress at the failure point). The area under curve B is proportional to the total damping energy for the specimen with stress concentrations, and the entire area is proportional to the total damping energy for a plain specimen.

As the area ratio is at least 10:1, only one-tenth of the material damping in the plain specimens is expected in the specimens with stress concentrations. Q's should, therefore, be near the desired value of 50 when both material damping values and damping values from other sources are considered.

300

Appendix C

STRESS CONCENTRATION FACTORS

There is a sizable difference between static and fatigue stress concentration factors, k_t and k_f, respectively. An expression for this difference, presented by Peterson (C-1) and used by Smith (12) is

$$k_f = (k_t + \alpha/r)/(1 + \alpha/r) ,$$

where α is a material constant and r is the radius of the cut in the material. The α for both the steel and aluminum used in these tests was given by Peterson as 0.05. Therefore, the remaining task was to establish the static stress concentration in bending for the specimens.

The static stress concentration factors were obtained from Peterson in the following way. Since a good deal of the required information was to be obtained from tension curves and since the value in bending for a sheet with $a/h = 0$ corresponds to the tension case, the $a/h = 0$ was used as a standard where $a = 2r$ and h = thickness. The value of k_t for two holes in an infinite plate under tension normal to the line drawn between the hole centers is given by

$$k_{t_b} = \frac{\sigma_{max\,B}}{\sigma} \frac{(1 - a/b)}{(1 - a^2/b^2)} = 2.43 ,$$

$$k_{t_a} = \frac{\sigma_{max\,A}}{\sigma} = 3.02 .$$

The k_{t_b} factor should be correct; however, the k_{t_a} factor obviously must be changed to account for the edge condition.

The k_{t_a} factor for a hole the proper distance from the edge of an infinite plate is obtained as $k_{t_a} = 2.23$, which should be nearly correct for this case. Therefore, the following stress concentration values in tension were determined:

$$k_{t_a} = 2.23 ,$$

$$k_{t_b} = 2.43 .$$

These values can be corrected to the bending case by finding the given values of k_t on the $a/h = 0$ curve of Fig. 86 of Ref. C-1 and then dropping down to the proper a/h curve and reading the values. This results in values for plate thickness of 1/8 in. of

$$k_{t_a} = 1.67 ,$$

$$k_{t_b} = 1.84 ,$$

and for plate thickness of 1/4 in. of

$$k_{t_a} = 1.92 ,$$

$$k_{t_b} = 2.04 .$$

The maximum k_t is k_{t_b}; this is the only factor of interest, therefore, for correcting fatigue yield:

$$k_f = (1.84 + 0.05/0.0625)/(1 + 0.05/0.0625) = 1.47$$

for the 1/8-in. specimen and

$$k_f = (2.04 + 0.05/0.0625)/(1 + 0.05/0.0625) = 1.57$$

for the 1/4-in. specimen. These are the k_t values used in the design of the new peg point beams; they are reasonably close to the value determined experimentally by Smith (12).

REFERENCE

C-1. R. F. Peterson, Stress Concentration Design Factors

Appendix D

PHOTOELASTIC TEST RESULTS

A quantitative analysis of the stress distribution around the two stress concentration holes in one 6-in. aluminum beam under various static loads was performed both analytically and experimentally.

The experimental analysis utilized the birefringent coating technique. One side of the aluminum beam was coated with a layer (0.118-in. thick) of photoelastic plastic (Budd Instrument Company Type X.C.) (Fig. D-1).

301
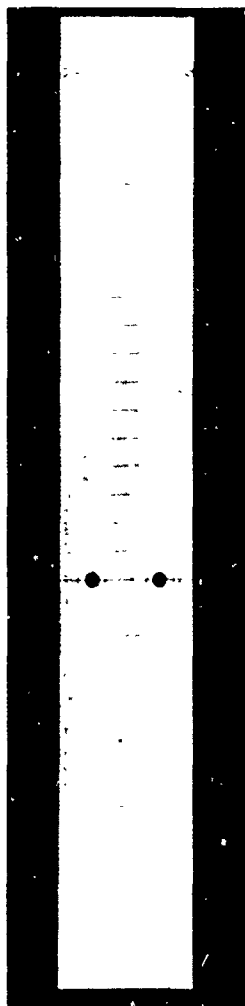
Fig. D-1. Specimen for photoelastic analysis

Fig. D-2. Test setup for photoelastic analysis

The beam was clamped at one end and illuminated with white polarized light. A known static load was applied to the other end, and the strained beam was viewed through a polariscope lens (Fig. D-2). Under this condition, the distribution of the actual strain in the beam was seen as a series of black and colored fringe patterns. Figure D-3 indicates the changes in the strain for different static loads. These photos also show that there was very little interaction between the stress concentration holes, even for large static loads. Average isochromatic fringe orders determined for various loads are plotted in Fig. D-4.

For more quantitative results, the magnitude and direction of the principal strains were determined, using the Budd Instrument Company large field polariscope (Type LF/Z-U). Data from this test follow:

1. Symbols:

k_t = stress concentration factor based on net section;

k_g = stress concentration factor based on gross section;

σ_{max} = maximum stress at hole edge;

σ_{net} = net section stress;

σ_{gross} = gross section stress;

I_{net} = net section moment of inertia;

I_{gross} = gross section moment of inertia;

M = moment;

c = distance from neutral axis to extreme outer fiber;

FO_{max} = average slope at hole edge; and

FO_{nom} = interpolated nominal slope between holes.

2. Equations:

$$k_t = \frac{\sigma_{max}}{\sigma_{net}} = \frac{\sigma_{max}}{\frac{Mc}{I_{net}}} = \frac{\sigma_{max} \, I_{net}}{Mc},$$

302

3 LB   6 LB   9 LB

12 LB   15 LB   18 LB
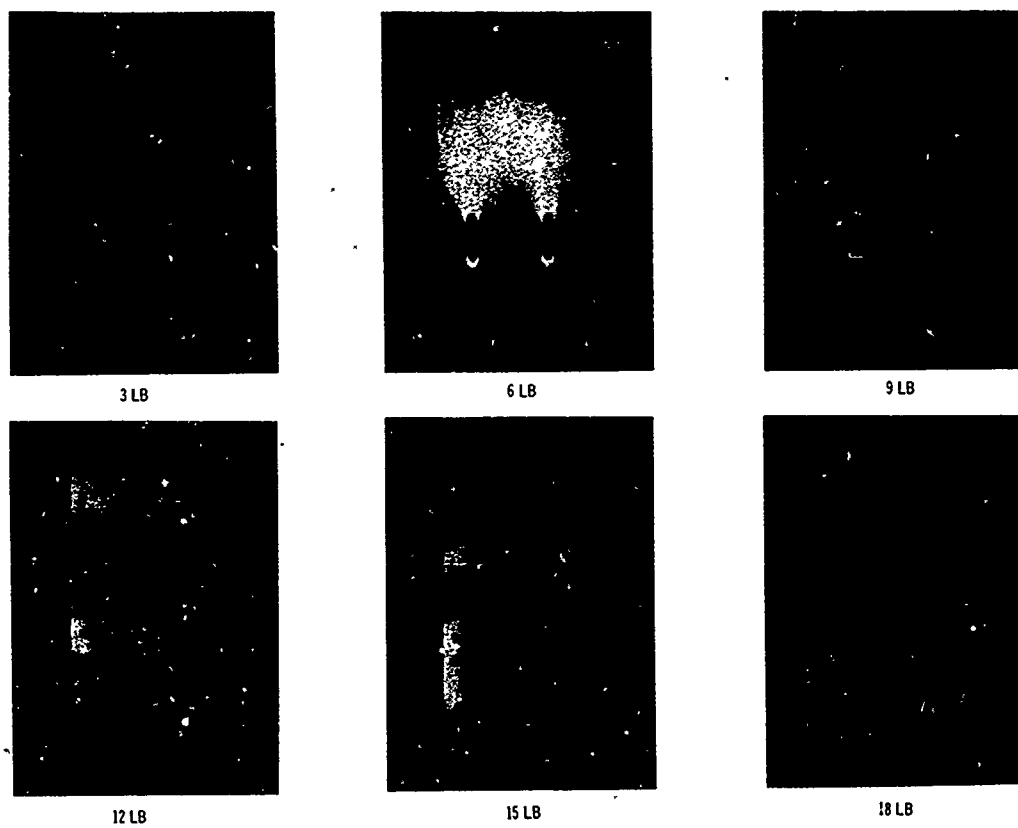
Fig. D-3. Fringe patterns showing stress distribution around holes
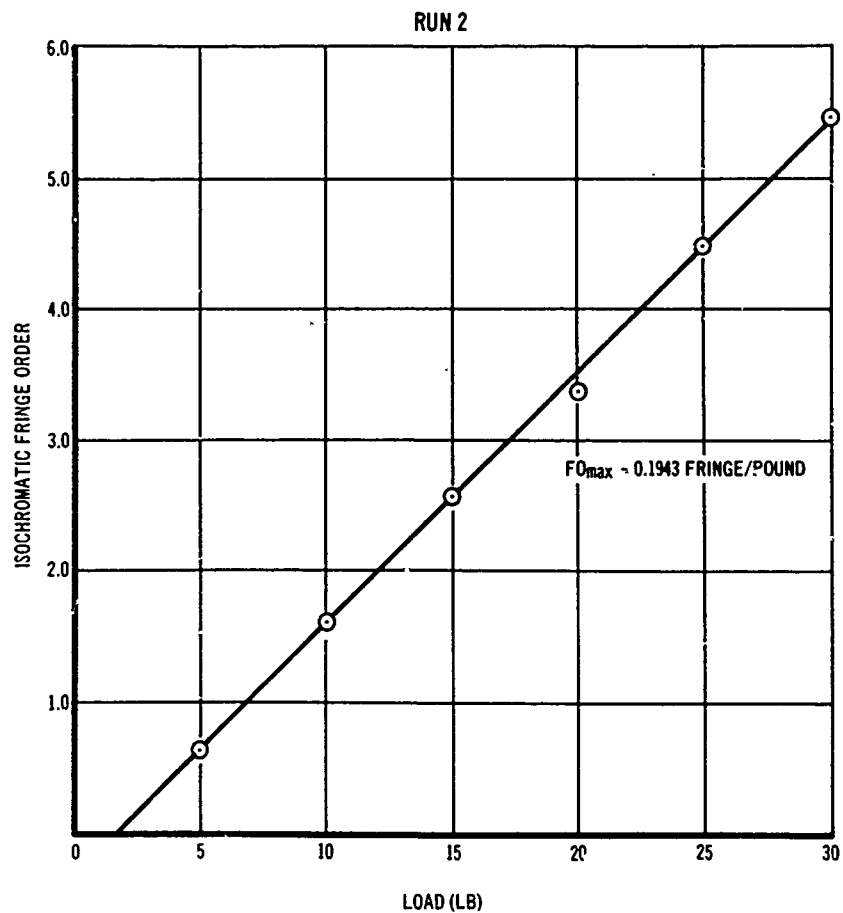
Fig. D-4. Average isochromatic fringe
order (FO) vs load at hole edge

$$k_g = \frac{\sigma_{max}}{\sigma_{gross}} = \frac{\sigma_{max}}{\frac{Mc}{I_{gross}}} = \frac{\sigma_{max} I_{gross}}{Mc} \ ,$$

$$\sigma_{max} = \frac{Mc \ k_g}{I_{gross}} \ ,$$

$$k_t = \frac{Mc \ k_g}{\frac{I_{gross}}{Mc}} \times I_{net} = k_g \times \frac{I_{net}}{I_{gross}} = \frac{FO_{max}}{FO_{nom}} \times \frac{I_{net}}{I_{gross}} \ .$$

3. Calculations:

First run $\quad k_t = \dfrac{0.188}{0.076} \times 0.8 = 1.98 \ ;$

Second run $\quad k_t = \dfrac{0.1943}{0.082} \times 0.8 = 1.90 \ ;$

$$k_t = 1.94 \pm 0.04 \ .$$

Appendix E

DIFFICULTIES IN MEASURING STRUCTURAL DAMPING

As the intent of this study was to evaluate techniques for designing for vibration environments, estimation and measurement of structural damping were of concern. Several techniques (listed below) were utilized at various times during the study, but all these techniques have fairly serious shortcomings — at least when dealing with lightly damped structures

where material damping predominates over other sources of damping.

The techniques for measuring damping which were studied included the following:

1. Resonance decay tests;

2. Sinusoidal sweep tests;

304

3. Random excitation — (a) Narrow band power spectral analysis, and (b) broadband power spectral analysis.

Decay tests at resonance and sinusoidal sweep tests present difficulties when dealing with material damping which is highly nonlinear, particularly when the stresses are above the endurance limit of the material. Obviously, to determine the damping in an actual application, comparable stresses must be achieved in testing. As an extreme example, on the first (plain) peg point specimens, Q's from low-level tests ranged from 65 to 130; under high-level random excitation, Q's ranged from 6 to 15. On the second peg point specimens, Q was determined as a function of input level for high-level sinusoidal sweeps. The results are shown in Fig. E-1. An additional difficulty with sinusoidal sweeps is that the sweep rate must be extremely slow to allow full response to be achieved in a lightly damped system. The slowest sweep rate commonly available in automated equipment is about 10 min/octave. A Q of 30 is the maximum that can accurately be measured with this sweep rate.

Even random excitation poses some difficulties. At high stresses, damping may increase as fatigue damage is accumulated. On the first peg point tests, response in one case decreased by nearly 20 db prior to failure. This agrees with Lazan's results (2). Even without this time dependence, however, there are two problems when dealing with high-Q systems:

1. Even with a massive shaker armature and relatively light specimen such as used in this study, a high-Q system may introduce a significant notch in the input spectra (Fig. 8).
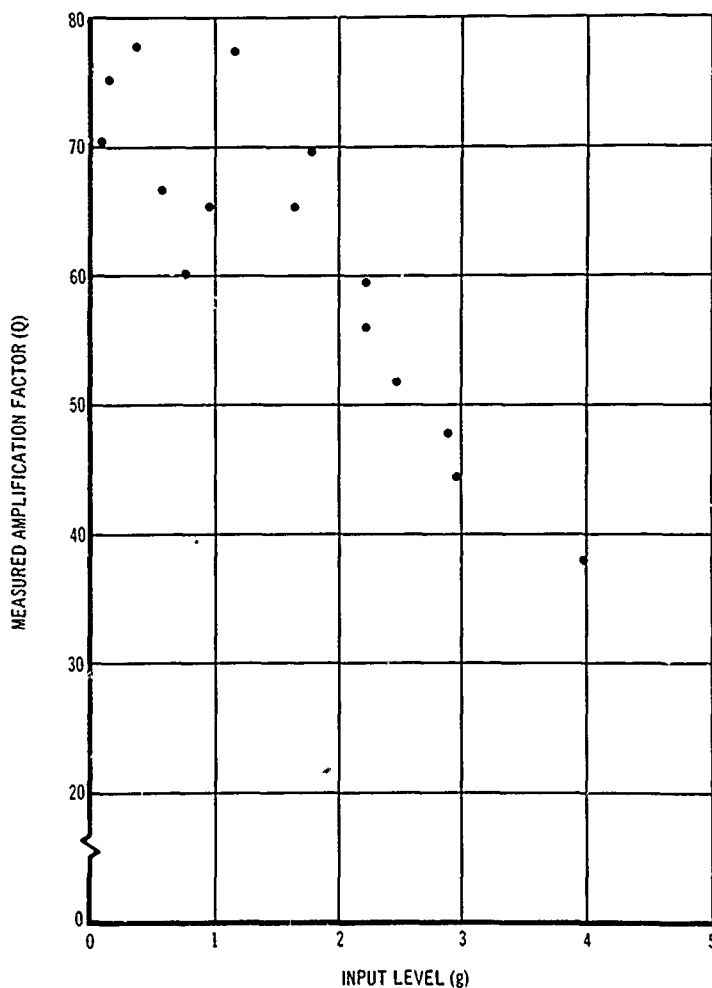
Fig. E-1. Measured Q as function of input level

2. If an attempt is made to correct this by comparing both input and response PSD's, an exceptionally long averaging time is required to obtain an accurate PSD. (This averaging time is controlled by the filter bandwidth or the resonant bandwidth, whichever is narrower, thus eliminating any possible time savings achieved by using wide filters.) For a system with $f_o = 50$ $Q = 100$, averaging time for 10 percent (1 db) accuracy with 90 percent confidence is 400 sec — a significant portion of the life of a specimen such as was tested during this study.

DISCUSSION

Mr. Gertel (Allied Research Assoc.): Did you make any attempt from your data to see if you could obtain a constant for summation of cycle ratios that are used in the cumulative fatigue damage calculations, or was that the factor k?

Mr. Hines: We included all of the fatigue information that we obtained experimentally in the k factor, and went no further than to try to define a k factor and the error or scatter in it.

Mr. Gertel: In the past work that has been done on cumulative fatigue using various damage concepts, the most popular being the linear or Miner's cumulative damage theory, the summation of cycle ratios is usually set equal to some constant factor for convenience. It would seem, perhaps, that this constant might be found from your experimental data for the particular sets that you did.

Mr. Hines: Possibly it could. One may be able to get some basic fatigue information from data such as this, but one has things introduced such as a stress concentration factor which is not as well defined as it could be. We were concerned with short-term life, such as is encountered in space missions. We were up fairly close to the knee in the fatigue curve. But Miles' approach using 1 for the k factor in the k alpha for the slope did yield a conservative value. It corresponded closely to the 90 percent confidence level of the data.

Mr. Root (Collins Radio Co.): I believe that Miles' analysis is based on the Palmgren-Miner summation. You have already shown this in one of the figures in comparison with the Miner summation.

Mr. Hines: I think he was more interested in the k alpha term where alpha is the reciprocal of the slope, in what k value should be used, and if it could be obtained from the data. The comparison I made was based on a k of 1, but we were at a bad place on the fatigue curve to make any real comparison. We did have other factors in it. I would not want to use that and say that you should use 2-1/2 or something else.

* * *

306

AN APPLICATION OF DECISION THEORY
TO A VIBRATION-FATIGUE PROBLEM

D. M. Aspinwall and R. E. Blake
Lockheed Missiles and Space Company
Sunnyvale, California

Statistical decision theory provides a model for the orderly considera-
tion and weighing of a number of diverse factors and pieces of evidence
which must be brought together in making a decision. As a realistic
example of such a procedure, we discuss the problem of whether a cer-
tain Polaris missile structure will have acceptable fatigue strength
throughout several years of exposure to submarine vibration.

Available choices are: (a) to increase the design strength, with a pen-
alty in weight and cost; (b) to accept the design as is and risk the de-
velopment of service failures in the future; or (c) to spend more money
on improving the data. The choice will depend on the relative values
(utilities) which the project leader and/or customer place on these al-
ternatives and on the risk of failures.

Since the discussion is aimed at a vibration engineer who specializes
in a technical field rather than in setting project goals, we emphasize
the problem of communicating his technical judgments in a form best
used by project management for making decisions. The vibration spe-
cialist would like to predict the probability of failure in service. But
this cannot be done with precision because the available data and theory
lack precision. This lack of precision is too large to ignore by using
nominal values or to envelope by use of conservative "worst" assump-
tions. Decision theory provides for estimating and keeping tabs on the
various sources of error.

The format required for this decision theory analysis is a probability
density of reliability. The essential elements in defining this curve
are the parameters of the probability distributions for load and
strength. A procedure for combining engineering judgments with ex-
perimental data on these important factors was used to develop the
probability density for reliability.

INTRODUCTION

Standardized specifications and tests for
resistance to shock and vibration are familiar
features of most military and space design
projects. They expedite the procurement,
screening, and passing of hundreds of hardware
designs with production-line efficiency. De-
signs which fail to pass can usually be changed
without too much trouble, or the test can be re-
vised to be more realistic for the specific hard-
ware and its anticipated environment. But oc-
casionally a problem comes up which is too
complicated, too important, and too expensive
to be disposed of in any easy fashion.

Such a dilemma was presented by the fail-
ure in fatigue of a major structural part of the
Polaris reentry system during a MIL-STD-167
vibration test. The test was known to be rather
conservative for application to a complete mis-
sile system, but preliminary analysis had sug-
gested that no problem would occur. Because
of schedule in the Polaris program, the part
had already been developed and used in several
ground and flight tests. A redesign would in-
volve scrapping much development time and
flight reliability data.

Thus the problem was to examine critically
all the environment and strength information

related to this part to decide whether redesign or acceptance would be the better course of action. The decision is, of course, the responsibility of the project management, since it depends on cost, effectiveness, and schedule tradeoffs of the missile system. It is the task of the shock and vibration engineer to provide the project with a clear and understandable picture of the technical side of the problem. This usually involves trying to convey the results of years of experience and study in a short interview. Theory is difficult enough to explain, but engineering judgment, intuition, and uncertainties are seldom communicated satisfactorily.

In the problem to be discussed here, a relatively new approach is used for presenting and assessing the shock and vibration picture. This is based on the premise that the project's real concern is with the risk of failure in service and the dependability of our information and predictions. They listen to our troubles about data, analysis, test simulation, and statistical variations only to get a feel for the dependability of our information and methods of handling it. Thus the aim of this study will be a prediction of the reliability that the part would have in service, and a description of the accuracy of the predictions.

The analysis follows the model provided by statistical decision theory. The theory simply shows how various facets of a problem can be handled separately and reduced to a common denominator, so that they can be fitted together logically and consistently. Decision theory is much like systems analysis and some aspects of game theory; it has been explained and discussed in several references (1-6). It differs from systems analysis in that it takes account of a very important but elusive factor in making a good decision: uncertainty. Uncertainty is a rather dirty word; it is generally taken for granted that no engineer with real talent is contaminated with it, and no engineer with real courage will admit to it in public. But it is always with us to some degree, and it usually costs money and effort to reduce that degree. Dealing intelligently with uncertainty consists of determining whether a prospective reduction in uncertainty is worth the effort. This too is a problem handled within the framework of decision theory. Decision theory is not discussed directly here; it is used. The purpose is to show by example how it differs from and improves on the alternative approaches.

PROJECT DESIGN PROBLEM

The fatigue sensitivity of the reentry system was due to some coincidences that became apparent after the development program was well along. The structure was found to resonate at a frequency generated by the submarine propeller, and the fatigue strength of the part was not quite adequate to pass the standard vibration tests. These facts would have been impossible to foresee by analyses; late discoveries of this type are one of the risks of a parallel-effort development schedule. The usual solution of increasing the strength of the part was made difficult by flight design and schedule requirements. To satisfy these requirements with a redesigned part would require a repetition of ground development and flight tests, or a decrease in confidence in flight reliability.

Another hope for a quick solution was to work out a substitute for MIL-STD-167 that would be more realistic for a Polaris missile in a Polaris submarine. Review of actual data indicates that this probably would have eliminated the difficulty if it were not for the resonant amplification. So the situation remained one of considerable uncertainty, with the uncertainties difficult and expensive to resolve.

Not only were there many technical uncertainties as to the vibration environment and fatigue strength, but also these quantities were highly variable statistically. Samples of data would not pin down the details of these statistical populations. They would only allow estimates to be made. It would not be meaningful to ask whether all or none of the parts would fail in service; one should ask for the probability of surviving, i.e., for the reliability.

The reliability of a missile system is one of the key parameters related to its military effectiveness. In general the cost/effectiveness of a system improves as the payload, range, and reliability increase, and as the cost and development time decrease. Since any decision concerning this part will have its small effect on several of these factors, the decision is a good one if its net result is to improve the cost/effectiveness. Evaluation of the relative worth of increments of cost, reliability, weight, etc., is the objective of systems analysis (5,7); judgment of whether the consequences of one course of action will be better than another is a function of project management. Decision theory provides a way to avoid putting the shock and vibration specialist on this unfamiliar ground by asking him whether he recommends that a part be redesigned. He should only be asked what is the risk of failure in service. The project should be asked how high a risk of failure would justify a redesign. Both should be asked how accurate their answer is, and what would be needed to improve it. If these answers do not make the choice an obvious one between

(a) acceptance of the design, (b) changing the design, or (c) gathering more information, decision theory provides a means for closer analysis.

The project engineer has the task of evaluating the alternative courses of action that might be taken and their influence on system goals. This can be very difficult, and system tradeoffs can be hard to discern after being converted into the artificial black-and-white language of contracts, requirements, and specifications. But the fact remains that the accuracy required of the shock and vibration engineer is limited by the accuracy with which the project knows what it should have. Both groups have to improve together, and it is not efficient for one to throw the burden of extreme accuracy onto the other. The remainder of this discussion concerns the task of the shock and vibration engineer: to assemble his information into a prediction of reliability and an assessment of its accuracy.

RELIABILITY

The information related to the reliability (probability that the part will not fail in service) falls naturally into two categories: (a) the load — factors in the external environment tending to produce failure; and (b) the strength — properties inherent in the structure tending to resist failure. The load L and the strength S can be expressed in the same units, with L as a measure of the applied environment and S as the magnitude of the environment required to cause failure of the structure. With these definitions, the reliability is simply the probability that a missile selected at random will have a value of S greater than the values of L which it experiences; that is, S > L, which is equivalent to

$$S - L > 0 \, ,$$
$$S/L > 1 \, ,$$
(1)

or

$$(\log S - \log L) > 0 \, .$$

The load and strength are independent statistical variables. The functions $(S-L)$, (S/L), and $(\log S - \log L)$ each have statistical distributions of a different form, but of course they each contain the same reliability prediction.

Just as the distributions above are composed of load and strength distributions, the loads and strengths in turn may be the resultant of several effects. Thus, the general problem of predicting reliability consists of predicting

the component distributions and then combining them. There are a number of approaches which can be applied, each with its advantages and each with its own degree of accuracy.

The principal stumbling block at this point is usually the uncertainty as to the form of a distribution (such as normal, log-normal, or Weibull). Occasionally, as in the case of fatigue strengths, there has been enough research to predict the mathematical form, or one may understand the causes of variation well enough to make a shrewd guess. In other cases, one may have little information and may follow the herd in assuming a normal distribution. In any case, there is a great danger of getting tangled in the intricate structure of mathematical statistics. Exquisite formulas and 8-place tables are often used, but they are no better than the basic assumptions behind them. It is more reasonable to use mathematical approximations in line with the accuracy of the rest of the decision analysis.

The mathematical procedures and computer program described in the Appendix were used in this study as the primary means of combining the distributions and formulating the reliability prediction. The program is based on the distributions being normal. In some instances, when it was known that the distribution was not normal, an equivalent normal distribution was substituted which best matched the actual distribution in the range of most significance to failure. Actually the natural logs of load and strengths were taken as normal. This avoids the embarrassing fact that normal distributions can include negative values, but strengths cannot. A check indicated no great difference between the results of assuming normal or log-normal distributions.

Some other approaches to calculating reliability have appeared in the literature. In one study, the mathematical distribution of S/L was worked out for the assumption that S and L are each normally distributed. In another report, a computer program was described which gives the distribution of any mathematical function of several parameters, when the distributions of the parameters are defined in any way.

The simplest approach to defining reliability, appropriate to a preliminary study, can be based on two theorems of statistics: (a) the mean of the sum (or difference) of two variables is the sum (or difference) of the means, and (b) the variance of the sum of two independent variables is the sum of the variances. One thus concerns himself with the means and variances of the distributions without regard for their distribution. On finding the mean and variance of

the combination by simple addition, one can find what the reliability would be if the combined distribution were normal. Combinations of prior knowledge and statistical data can also be made with approximate hand computations. These procedures were used in the early stages of the present study.

FACTORS AFFECTING
LOAD PREDICTION

The vibratory stresses and loads on the structural member of interest are proportional to the center-of-gravity acceleration of the body in the missile. This acceleration $\ddot{X}$ is the basic load variable and is affected by several other factors (Fig. 1).

The source of the vibration is in the propeller-blade interaction with the hull; these hydrodynamic forces will vary with speed, number of blades, etc. The vibration response of the hull, a combination of bending and torsional modes, will differ somewhat even for submarines of the same class. The response of the missile launch tube to the hull vibration will also be somewhat variable because of unintentional structural variations. The location of the launcher in the hull is also a random variable from the point of view of predicting where a given missile will be stowed. There will then be a transmissibility factor for the vibration response of the basic missile structure to the launcher. Finally there is a near-resonant amplification of $\ddot{X}$ from the basic missile structure.

Thus the acceleration could be expressed as the product of several factors:

$$\ddot{X} = P_1 T_{1n} T_{n2} T_{23} R, \qquad (2)$$

where P_1 is the resultant hydrodynamic force, T_{1n} is the hull transmission factor to the location of the nth launcher, T_{n2} is the transmission from the hull to the launcher, T_{23} is the transmission from launcher to basic missile structure, and R is the amplification factor from basic missile structure to $\ddot{X}$. To describe $\ddot{X}$ one must define the statistical distributions of all the terms on the right side of Eq. (2).

Data concerning submarine vibration is understandably scarce. One measurement has been reported of a basic missile structure vibration, that is, of the product $P_1 T_{1n} T_{n2} T_{23}$. The amplification factor R has been the subject of nine measurements, and two measurements have been made of $\ddot{X}$.

During the several years of operation which the missile is required to survive, the submarine will operate at a variety of propeller speeds. The only one of concern here is the one causing a frequency of 16.5 cps.

The remaining information needed is not in the form of "objective" numerical measurements. It is available only as "educated guesses" based on experience and/or theoretical analyses, and extrapolations based on assumptions (which are also educated guesses).

In using "subjective" assumptions and estimates, one has the problem of defining the
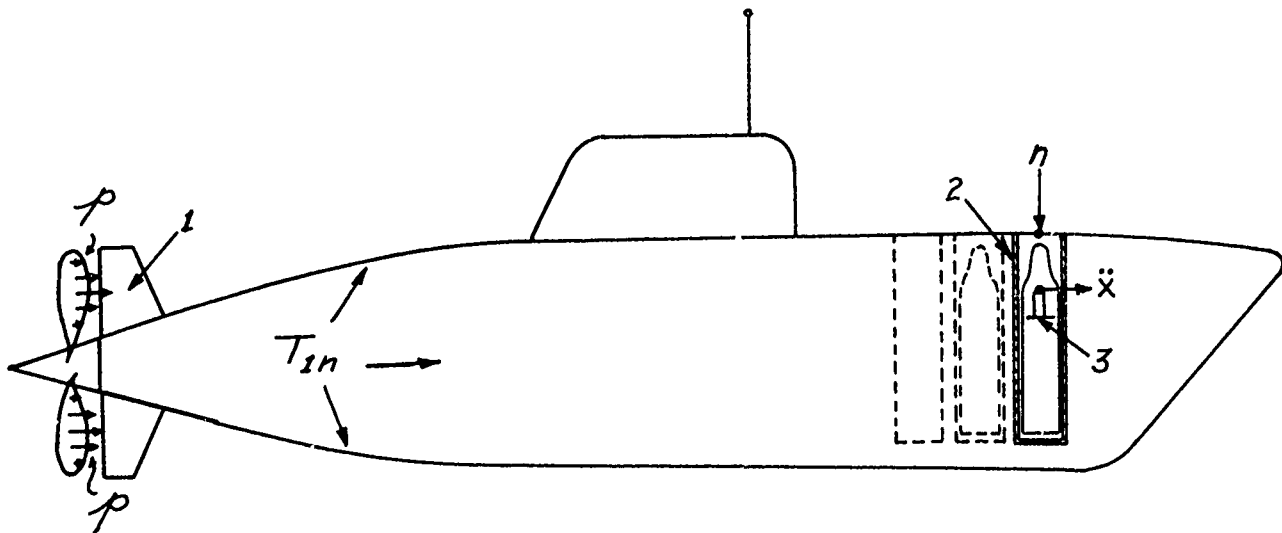
Fig. 1. Sketch of submarine and equipment

dependability and completeness of the source of information. This is analogous to the problem of using samples of data from a statistical population as a basis for predicting results of future sampling. The statistician makes a "reasonable" assumption of the type of statistical distribution, and then calculates "confidence levels" for various predictions. A confidence level is the probability that one has not been misled by a very small or unusual sample into making a false prediction.

The confidence method contains the implicit assumption that no relevant information is known except the numerical data and the type of distribution. This is an assumption more easily satisfied by a statistician than an engineering specialist with several years' experience. In engineering work, it is often necessary to combine statistical data, theoretical analyses, and subjective knowledge. To combine these quantitatively, the subjective knowledge will be expressed in probabilistic language suited to a combination, which will formally resemble Bayes' Rule of inverse probability (2). This does not require that subjective opinions "really are" statistical variables, although one could argue with considerable force that numerical predictions made by a population of people form a statistical population.

Although probability will be used to describe both the statistical fluctuation of uncontrolled variables and the dependability of information, the two will be kept separated and termed "probability" and "subjective probability," respectively. This distinction is important for deciding whether more information should be obtained.

ESTIMATES OF PARAMETERS

For convenience in predicting the statistical properties of $\ddot{X}$, we note that if a quantity is a statistical variable, its logarithm is also. In Eq. (1), $\ddot{X}$ is the product of several factors; so $\log \ddot{X}$ is the sum of the logs of the factors. So, representing the logs by lower-case symbols,

$$\log \ddot{X} = x = p_1 + t_{n1} + t_{n2} + t_{23} + r. \qquad (3)$$

Equation (3) contains several variables for which no separate information is available; therefore, probabilities will not be estimated for these variables individually, but only for their combined effect. The equation does indicate how complicated the expression for x is and warns the engineer that wide variations may be expected in data for the base vibrations and the body cg acceleration.

The problem of expressing the "subjective probabilities" about dependability of information is considered first. These subjective statements are made in the form of probability density functions for the means and variances of the important load and strength variables. The means and variances of load and strength variables are the descriptive parameters being estimated, rather than the loads and strengths themselves; subjective probabilities must, therefore, apply to the means and variances. Some probability density functions are defined by equations which contain several parameters, but only the mean and variance are needed to define a normal distribution, which is one reason for its wide application. For example, if the variable w has a normal distribution, then the probability density is:

$$f(w) = \frac{1}{\sqrt{2\pi}\,\sigma_w} e^{-\frac{1}{2}\left(\frac{w - \mu_w}{\sigma_w}\right)^2} \qquad (4)$$

and the required parameters are μ_w and σ_w.

Attention will now be focused on the probability distributions for the variables r and t, where $t = p_1 + t_{1n} + t_{n2} + t_{23}$. Subjective probabilities will first be derived for the means and variances of r and t; then these functions may be combined to give a subjective probability density for μ_x and σ_x. In this work, the probability functions for μ_r, μ_t, σ_r^2, and σ_t^2 are described by an equation similar to the normal probability distribution, and all parameters are independent. Then the probability functions for μ_x and σ_x^2 are also normal and

$$\mu_x = \mu_t + \mu_t \quad \text{and} \quad \sigma_x^2 = \sigma_r^2 + \sigma_t^2. \qquad (5)$$

The normal density function used to describe these parameters is not a theoretical necessity, but it is a convenient mathematical form where sums of variables are concerned.

Considerable data were available on the response factor, r, because this variable could be measured in ground tests of different reentry systems. Some typical amplification curves are shown in Fig. 2. The sample average and variance for r are $\bar{r} = 1.26$ and $s_r^2 = 0.0458$. Because these data do not define $\ddot{X}$, but just one of the factors, the results are used to make judgments about the subjective probability densities for μ_r and σ_r^2. The subjective probability densities can be used to describe past experience, analysis, or data interpretation. When data are directly applicable to the variable of interest, they can be incorporated directly into the subjective densities in a mathematical operation (see Appendix). When data

311
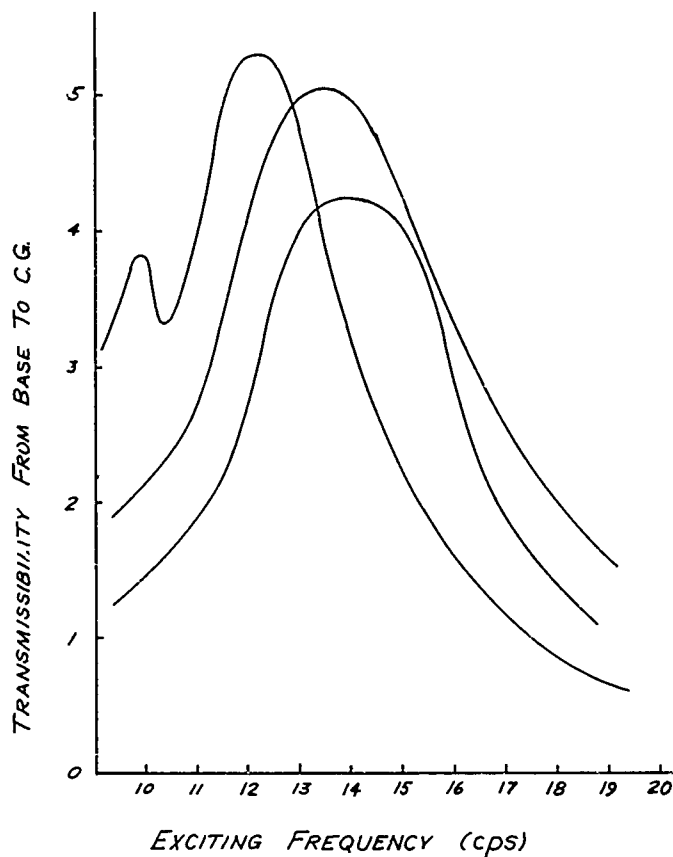
Fig. 2. Typical transmissibility curves for
the region of interest

must be related by judgment to the variables of
interest, a more intuitive approach must be used.

Tables of sampling distribution for nine
pieces of data were used to aid in this process.
These tables showed that $\bar{r}$ should vary within
1.26 ± 0.07 two-thirds of the time, and s_r^2
should vary within 0.0458 ± 0.03 two-thirds of
the time. Previous experience with amplifica-
tion factors indicates that the mean should be
somewhat higher, although with nine pieces of
data, the subjective probability should be tai-
lored to correspond closely to the sampling
distributions.

The Chi-square tables for sample vari-
ances, s^2, from a normal population give a
curve which plots like a log-normal distribu-
tion for higher values of s^2. The higher values
of s^2 are of more interest because they tend to
lower the reliability; so the standard deviation
of 0.03 for $f_1(s^2)$ was estimated from this Chi-
square plot on log-normal paper.

After taking all the information into account,
the following subjective probability density func-
tions* were adopted to describe μ_r and σ_r^2:

$$f_1(\mu_r) = e^{-\frac{1}{2}\left(\frac{\mu_r - 1.3}{1.0}\right)^2}, \qquad (6)$$

$$f_2(\sigma_r^2) = e^{-\frac{1}{2}\left(\frac{\sigma_r^2 - 0.05}{0.03}\right)^2}. \qquad (7)$$

Only one piece of data was available on the var-
iable t, the base acceleration for the system in
the submarine. The subjective probability den-
sities for the mean and variance of this vari-
able were based primarily on engineering judg-
ment. The functions chosen were

$$f_3(\mu_t) = e^{-\frac{1}{2}\left(\frac{\mu_t + 1.5}{0.5}\right)^2}, \qquad (8)$$

$$f_4(\sigma_t^2) = e^{-\frac{1}{2}\left(\frac{\sigma_t^2 - 0.1}{0.2}\right)^2}. \qquad (9)$$

Note that variances for the estimates of
both parameters are large; 0.5 is one-third of
1.5, the best estimate of μ_t, and 0.2 is twice as
large as 0.1, the best estimate of σ_t^2. These
large numbers are reflections of the complicated
origin of t and of the lack of data concerning t.

312

Our objective in deriving these subjective probabilities for μ_r, σ_r^2, μ_t, and σ_t^2 is to write similar equations for μ_x and σ_x^2. From Eq. (5) and the fact that the probability density for the sum of two normal variables is again normal, the following equations may be written:

$$f_5(\mu_x) = e^{-\frac{1}{2}\left(\frac{\mu_x - 1.3 + 1.5}{0.51}\right)^2}, \qquad (10)$$

$$f_6(\sigma_x^2) = e^{-\frac{1}{2}\left(\frac{\sigma_x^2 - 0.1 - 0.05}{0.202}\right)^2} \qquad (11)$$

With these subjective probabilities defined, actual data on $\ddot{X}$ may be considered.

Two pieces of data on $\ddot{X}$ were available. The values for $\ell_n \ddot{X}$ were -0.94 and -0.41. The sample average is

$$\bar{x} = -0.675, \qquad (12)$$

and the sample variance is

$$s_x^2 = 0.1406. \qquad (13)$$

All the information concerning the load variables is summarized in Eqs. (10) through (13) in a form which can be used in a computer program which will eventually be used to compute a probability density of reliability.

FACTORS AFFECTING STRENGTH PREDICTION

Although there were tests to failure on twelve full-scale pieces of hardware, the fatigue strengths remain subject to several uncertainties. To obtain results in a reasonable time, the tests were run at a higher-than-expected stress level. The test points shown on Fig. 3 must be extrapolated out to the vicinity of the 2.5 million cycles estimated for a full service life.

A further complication is that static stresses are added to the vibratory stresses. The static stresses are highly unpredictable, since they are caused by bolting together two parts which cannot be made to fit perfectly. Strain gages were used to measure stresses in a critical fillet region, but the experiments were handicapped by the shape and a complicated stress distribution.

To extrapolate the data of Fig. 3, the best method is to use the shape of a fatigue curve established by tests of laboratory specimens. Figure 4, copied from Ref. 8, shows that no single curve has been established. Even in tests of carefully made small specimens, fatigue strengths exhibit a large statistical scatter. One can anticipate even greater scatter in large production parts.

A study of some other fatigue curves showing the influence of static stress and stress
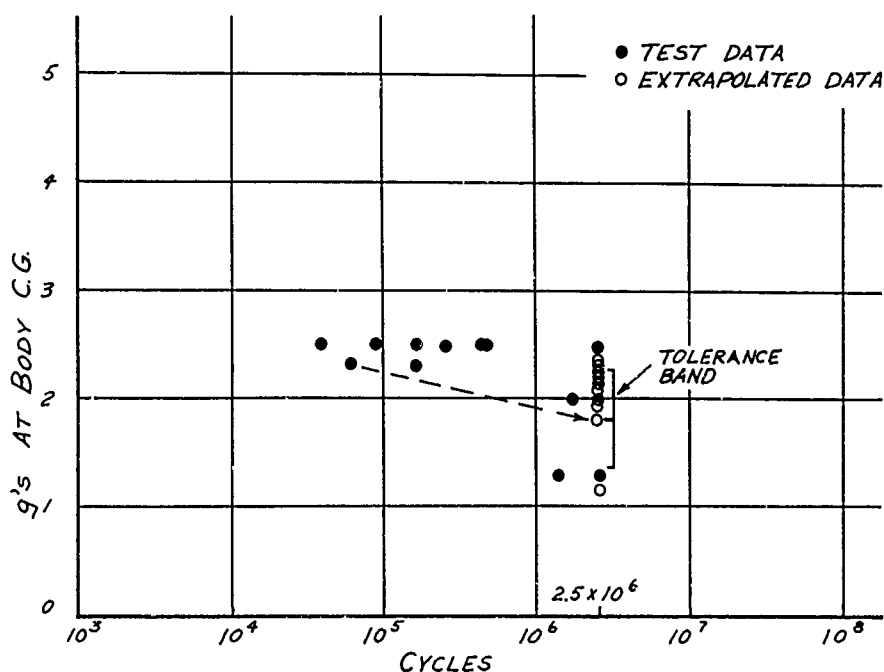
Fig. 3. Fatigue strength test data

313
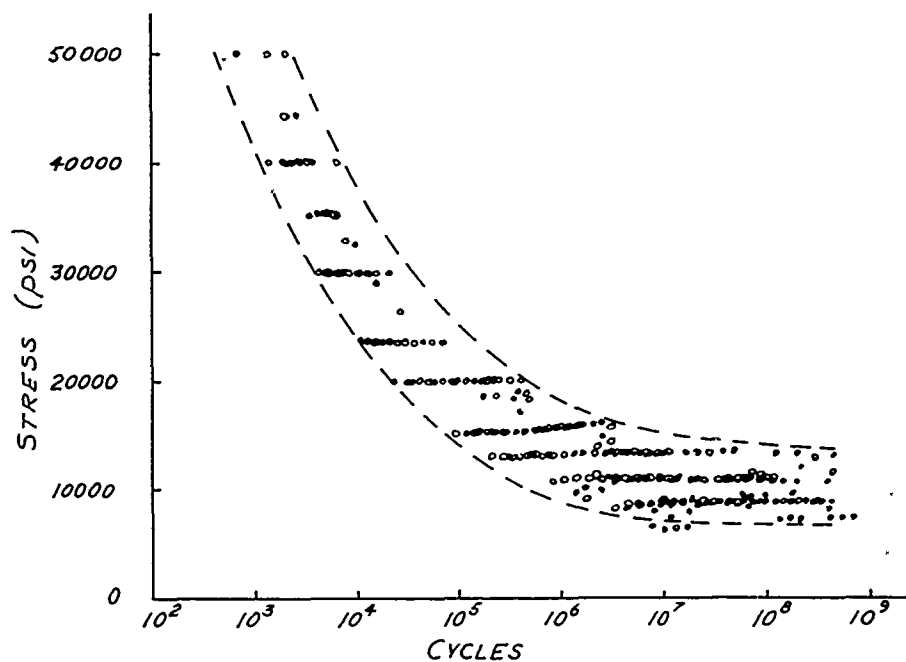
Fig. 4.   Fatigue data on notched aluminum specimens

concentration factors produced a very fortunate result. Although these factors had considerable influence on the magnitude of the fatigue strength, they had small effect on the shape of the extrapolation curve. Thus, the remaining problem was to select a nominal method of extrapolation and estimate its probable error. This was done by judgment based on the available curves. Figure 3 shows the extrapolation of only one of the points to its nominal value at 2.5 million cycles. The one-sigma tolerance band on the extrapolation is also shown.

The data were treated as if there were only 7 readings instead of 12. The reason for this is that the computer program as written did not provide for uncertainty as to the exact value of a test result. This uncertainty arose from the extrapolation problem; in other problems, it might be due to an inaccurate meter, etc. From judgment as to the extrapolation error and by consulting appropriate statistical tables, it appeared that using 7 instead of 12 readings would have the equivalent effect on the computer output. This subterfuge is, of course, not the most direct approach, but it was the shortest path around this unforeseen obstacle.

COMPUTED RESULT

The output of the computer is plotted on Fig. 5. The probability density of reliability is a highly skewed curve indicating that the actual reliability is numerically close to 1. One should not mistake the small numerical difference from

perfection for a insignificant difference. Each missile costs millions of dollars to build and deploy; a 1 percent chance of loss is equivalent to a very large sum of money.

MEANING OF THE RESULT

The output of Fig. 5 could be explored by integrating the curve and noting the percentage C of the area under the curve above various values of R. The value of C then is interpreted as a generalization of the statistical confidence idea; it is the probability that the data and experience used have led us to be correct when we say "the reliability exceeds R." Since the word probability has had various controversial uses and definitions, its meaning here can be summed up by the advice: "If our usage seems to stretch the meaning beyond your favorite definition, make your decision as if it did not." A fuller explanation is given in Refs. (1), (2), and (4).

The probability density of reliability sums up how much we know and do not know about the prospects of fatigue failures in service. If it seems too vague and inaccurate, it is because the information available is vague and inaccurate. The method of handling the information is intended to increase the vagueness to a lesser extent than any alternative. Many of the alternative methods give an appearance of precision by using a single number to replace a probability density, calling the average, the best estimate, the unbiased estimator, the maximum

314
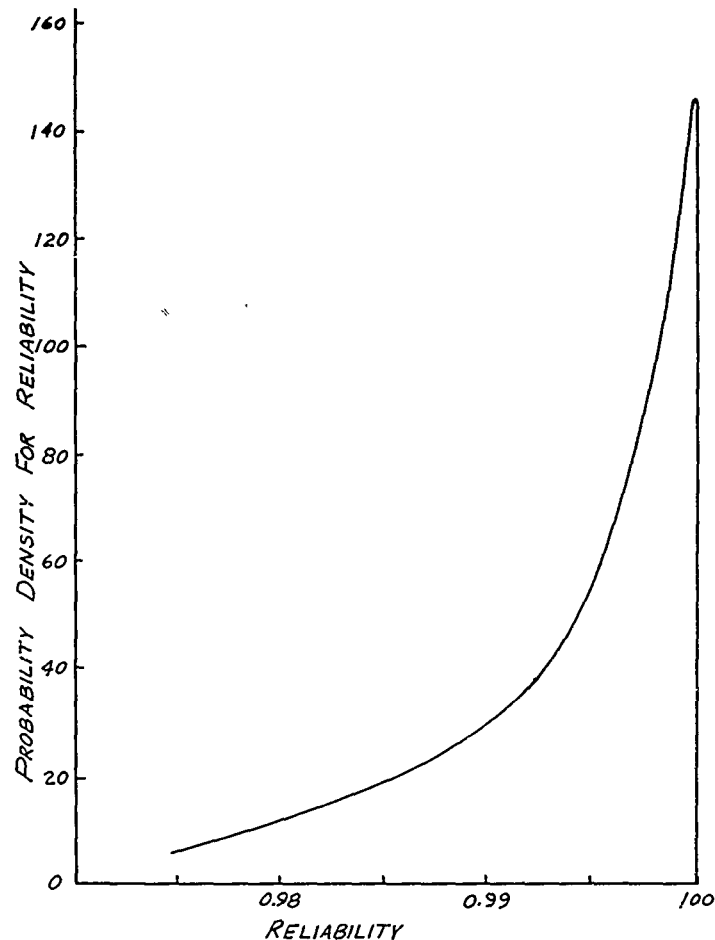
Fig. 5. Probability density of reliability

likelihood, a conservative value, the mode, etc., "the" value. In effect, one is being advised to make his decision as if he believed the single value to be correct. Decision theory puts the computation of an "equivalent-single-number" on a rational basis.

Since the various possible results (values of reliability) of using the design in service have such a wide range of importance to the system effectiveness, the most satisfactory evaluation consists of stating a numerical measure of worth (utility) as a function of the reliability. This is the procedure called for by decision theory. It enables one to compare alternative designs and to set a value on getting more information or data. It also permits one to replace the probability density of reliability by an equivalent reliability, that reliability which would have the same worth to the system as the "expected worth" of the set of uncertain reliabilities. This is much like the judgment that the value of a ticket to a certain raffle exceeds one dollar. One replaces the various prizes, their value to the bidder, and chances

of winning, by the judgment that the prospects are of greater value than the other uses that one might make of the dollar. The probability density curve is the best statement we can make from the available evidence of the project's chances of winning the various possible prizes or penalties, if it chooses to accept the design as is. The alternatives are to $\downarrow$ the cost of a redesign or pay the cost of better information.

If the above forms of presentation of results fail to interest the customer, one might abandon some of the subtleties and state the risk of failure of a single missile. If a missile fails in service because we failed to beef it up, it makes little difference whether the cause was an exceptional statistical aberration in the environment, the hardware, the data on which the design was based, or a mental aberration of an engineer. The first two relate to reliability; the latter two to confidence.

The average, or expected value, $E(R)$, of the reliability is obtained from the probability density of reliability $p_1(R)$ by the integral

315

$$E(R) = \int_0^1 Rp(R) \, dR. \qquad (14)$$

For Fig. 5, $E(R)$ is 99.3 percent. The risk of failure is thus $100 - 99.3 = 0.7$ percent, or 1 chance in 143. It must be repeated that this is a perfectly good statement of the risk that any single missile faces, but this risk is not quite what one should be interested in. If 1430 missiles were deployed, the $E(R)$ above would be the actual reliability, if we had perfect information, and we should expect 10 failures. Or there could also be a 0.7 percent chance that all would fail. These are not equivalent.

The expected reliability is the same as the equivalent reliability mentioned earlier, if one assumes the worth of the system is proportional to its reliability. Such an assumption is not likely to be valid over a wide range of values of reliability. But if one has narrowed the range of $p(R)$ sufficiently, $E(R)$ may be a useful expression of the result.

It is significant that the $p(R)$ curve (Fig. 5) is not symmetrical and the expected value of reliability (the mean) is lower than the 50 percent confidence value, 99.6 percent (the median). The difference expresses the price that we are paying for insufficient data. If the $p(R)$ curve gives us a 70 percent confidence that the reliability is in fact satisfactory, this means that there is a 70 percent chance that enough information to dispel our uncertainties would prove the design to be satisfactory as is. Lacking this proof, we must act as if the equivalent reliability is the true value.

As mentioned earlier, if one is dissatisfied with the uncertainty due to lack of precise and voluminous information, he is free to try to obtain more information, at a price. Decision theory provides a technique (1) for comparing the price of more information to its expected worth. When further investigation is not considered worth the price, one should then choose a course of action, accepting the residual risks and hedging against them if possible.

Although this problem originated some time ago in the Polaris Missile System and the setting has been preserved to make the discussion seem more realistic, the numerical values have been arbitrarily chosen and do not apply to any real missile system.

REFERENCES

1. H. Raiffa and R. Schlaifer, Applied Statistical Decision Theory (Harvard U. Press, Cambridge, Mass.) 1961

2. J. W. Pratt, H. Raiffa, and R. Schlaifer, J. Am. Stat. Assoc. (June 1964)

3. A. M. Mood and F. A. Graybill, Introduction to the Theory of Statistics (McGraw-Hill, New York) 1963

4. R. E. Blake, Shock and Vibration Bull. 31, Part 2, pp. 88-97, Oct. 1962

5. R. E. Blake, "Optimum Meteoroid Shielding of Spacecraft— An Application of Statistical Decision Theory," Lockheed Missiles and Space Co., Rept. SD/R-9, Aug. 24, 1964

6. D. M. Aspinwall, "Bayesian Statistics and Decision Theory in Engineering," Lockheed Missiles and Space Co., Rept. 801071, Nov. 13, 1961

7. C. J. Hitch and R. N. McKean, The Economics of Defense in the Nuclear Age (Harvard U. Press, Cambridge, Mass.), 1960

8. Metallic Materials and Elements for Flight Vehicle Structures, Dept. of Defense, Washington, D. C., MIL-HDBK-5, p. 3.3.1 (g), Aug. 1962

Appendix

MATHEMATICAL PROCEDURES

The computations which one might make to predict reliability will vary in cost and accuracy, depending on how efficiently one chooses his simplifying assumptions. In the example of this paper, it was decided to take advantage of a digital computer program prepared in 1963 for such problems by D. M. Aspinwall and J. E. McFeely of Lockheed Missiles and Space Company. This program provides the capability of performing the many computations, although requiring that all probability distributions be normal. One can evade this restriction to some extent by various subterfuges as discussed in the paper, such as letting the log of the variables be normally distributed.

Reliability can easily be computed for normal (or log-normal) distributions. If L is load and S is strength, then reliability is probability of survival and probability that $(S-L) > 0$. With each normal distribution defined by its mean μ and variance σ^2, the difference $(S-L)$ will be normal with mean $\mu_S - \mu_L$ and variance $\sigma_S^2 + \sigma_L^2$. The reliability is the area of the probability density of $S-L$ above zero; that is,

$$R = \int_0^\infty \frac{d(S-L)}{\sqrt{2\pi} \, (\sigma_S^2 + \sigma_L^2)^{1/2}} \, e^{-\frac{1}{2}\left[\frac{S-L-\mu_S-\mu_L}{(\sigma_S^2+\sigma_L^2)^{1/2}}\right]^2} . \quad \text{(A-1)}$$

The values of the four parameters would thus fix the value of reliability. But the parameters are not accurately known; their values can be predicted only by appropriate probability statements. The computer program calls for the subjective prediction of each parameter in the form of a normal distribution. Note that we are involved in normal distributions at two levels: (a) the statistical sampling distributions of loads and strengths defined by four parameters, and (b) the distributions of these parameters used to express the chance that a prediction that a parameter is in a certain numerical interval will be correct. There are, thus, eight subjective parameters to be selected; the means express a best estimate, and the variances express the probable error of the estimate.

In addition to one's subjective knowledge, there are experimental data on loads and strengths. These data can be summarized without loss of information by the estimators of the mean and variance of the data, $\bar{X}$ and s^2. The relation of such estimators to the mean and variance of the parent population is given in elementary statistics books; $\bar{X} - \mu$ is normal, and s^2/σ^2 is proportional to the Chi-square distribution. These distributions state the probability of observing a value of the estimator if the parameters of the population are known, whereas our concern is to predict the parameters from knowledge of the estimators. This problem of "inverse probability" has been solved by two different approaches: by Bayes' Theorem and by Fiducial Probability.

Although Bayes' Theorem has been accepted for certain classes of problems since it first appeared in 1763, it has been only recently that its use with subjective probabilities has been shown to be justified (2). Fiducial probability is substantially the same as the method of confidence intervals, in that the proofs are

very similar, and no subjective knowledge is required or provided for.

Since Bayes' Theorem can be used even when one's subjective knowledge is very slight, its result should then agree with that of fiducial probability. The most plausible way to express zero subjective knowledge of a parameter is by a constant probability density over the entire parameter range. This yields agreement with fiducial probability for μ but not for σ^2. This apparent disagreement can be resolved, if one considers that the choice of a linear scale for σ^2 is completely arbitrary. One could just as well have chosen some other function $f(\sigma^2)$ to express the spread of sample measurements. It turns out that $f(\sigma^2) = 1/\sigma^2$ will satisfy both approaches. A flat subjective distribution of $1/\sigma^2$ corresponds to an odd distribution of σ^2. But if one objects to the odd distribution of σ^2, he is claiming to have subjective knowledge of what σ^2 could reasonably be expected to be. Hence, he should use this knowledge to construct a better prediction.

The combination of subjective and statistical information is effected by Bayes' Theorem:

$$p(X) = \frac{p_a(X) \, P(\text{data}|X)}{N} , \quad \text{(A-2)}$$

where $p_a(X)$ is the subjective probability density of a parameter X, $P(\text{data}|X)$ is the probability of observing the estimator if X is given, N is a constant to satisfy the normalizing requirement that $p(X)$ integrate to $|$, and $p(X)$ is the resulting probability density of X. Then $p(X)$ is the product of two curves, as is illustrated in Fig. A-1 for the parameter σ_r^2. It is easy to see that if one of the peaks is broad compared to the other, the narrower peak will dominate the result. In such a case, the exact shape of the broad peak is not of much consequence.

With the eight parameters of the subjective probabilities and the four estimators of the load and strength parameters, the computer then calculates the probability density of reliability. The primary need for the computer is due to the fact that the four variables which define reliability must be considered simultaneously. Furthermore, the probabilities of the estimators $\bar{x}$ and s^2 are not independent. The probability distribution of $\bar{x}$ is normal with a variance, σ^2/n, where n is the number of samples. Since σ^2 is not known, the computation involves the joint probability distribution of $\bar{x}$ and s^2 for given pairs of μ and σ^2. This is best handled by the computer.

a) SUBJECTIVE PROBABILITY DENSITY FOR LOCATION OF ∇_r^2

b) PROBABILITY FUNCTION OF ∇_r^2, GIVEN S_r^2

c)

PROBABILITY DENSITY FOR ∇_r^2
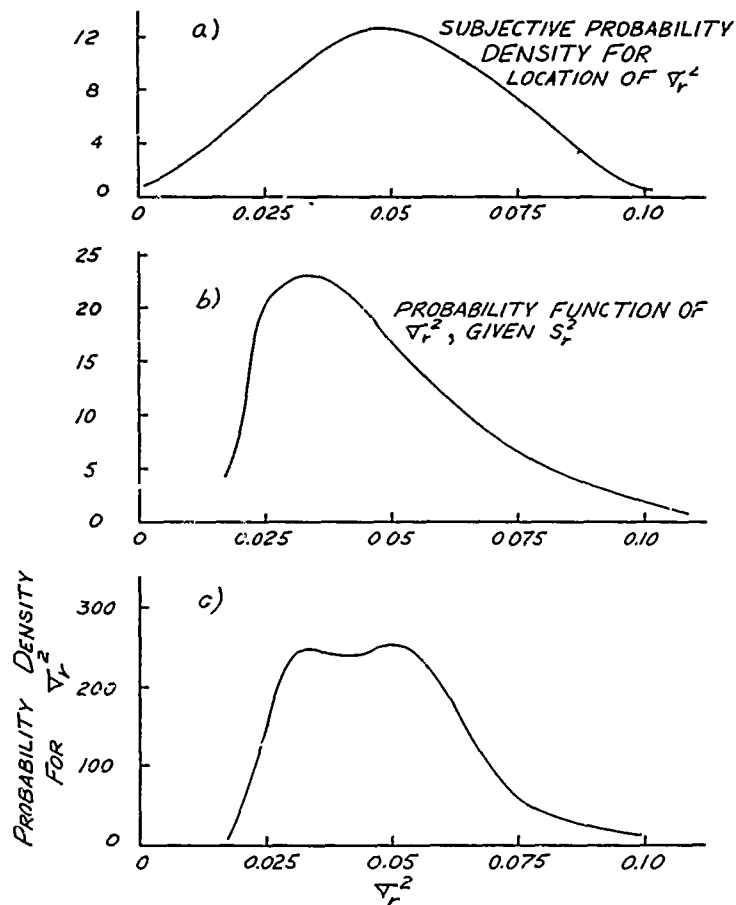
Fig. A-1. Development of probability density for σ_r^2

DISCUSSION

Mr. O'Hearne (Martin Co.): You said that you could be very arbitrary in selecting your a priori density function. It seems to me that you have taken this preselected density function, weighed the density actually experienced with that density function, and used the derived density. I think you would have to be prepared to defend your a priori judgment very strongly, whereas you seem to indicate that that would not be necessary.

Mr. Aspinwall: One has to defend that judgment just as one has to defend any engineering judgment. A good engineer will have a more accurate estimate of the parameter that I was discussing or any other parameter. He has to defend it against criticism, and I think it is everyone's duty to make the best estimate he can. What I meant to imply was that it is an individual matter. Your a priori density function may be different from mine, and no one can say I am right and you are wrong, or vice versa. The better engineer should have the better density function, but we can not tell who was right until we have flown the missiles to see whether or not they fail.

Mr. O'Hearne: It seems to me that when you mix what you actually experience with your preconceived notion, you are doing something a little subtle. I would not be arbitrary about it at all.

Mr. Aspinwall: I do not mean that it should be taken lightly. One has to do the best he can and use all of his experience and judgment. But one must plot a curve, and it must be stated in numerical form. In that sense, it is arbitrary.

Dr. Jaenke (AF Missile Development Center): Did you try to specify confidence levels for your estimates in this work? This might be an answer to the question which was just asked.

Mr. Aspinwall: No, we did not specify the standard confidence levels for each of these parameters because there were so many involved. The final response was the sum of the logs of these factors. Then with the load and strength with which we are concerned, the difference gives the reliability. We could specify confidence intervals for each variable, but I

318

think it is meaningless to try to specify standard confidences for the reliability. It is too complicated. The advantage of the decision theory approach is that the uncertainty in each variable can be included in each step, and the computer program yields the final probability density curve which combines all of them.

Dr. Jaenke: I was interested in your technique of combining a priori estimates with the experimental observations. In our activity we are using a similar approach in an entirely different area. It is again an area where statistical evaluation and estimation is involved, and it is quite surprising how much this combination of a priori and experimental investigation really helps in solving a problem.

Mr. Aspinwall: I agree. This is the heart of the technical presentation of data. I did not go into the utility function, but as far as estimating is concerned, I think this is the heart of the decision theory approach.

* * *

GENERAL SOILS MODEL FOR
SHOCK PROPAGATION STUDIES

C. X. C. F. Miranda
Department of Civil Engineering
University of Detroit
Detroit, Michigan
and
David C. Kraft
Department of Civil Engineering and Engineering Mechanics
· University of Dayton
Dayton, Ohio

A review is made of the currently accepted method for describing the one-dimensional stress-strain relationship for soils under shock loading. The implications of the currently accepted model for describing soil behavior are discussed with regard to its application to granular and cohesive soils. Based on experimental evidence presented, a new and more general model is proposed to represent the one-dimensional stress-strain relationship of all soils during locking behavior. The proposed model is a general one and can be used for shock propagation studies in soil media.

INTRODUCTION

The study of one-dimensional shock propagation phenomena in a nonlinear medium has, as its starting point, the one-dimensional stress-strain relationship for the soil. It is, therefore, necessary to formulate this relationship in such a manner that it reflects as nearly as possible the observed behavior of the soil, and yet not be so complicated that it hampers analytical evaluation of the shock propagation phenomena.

Recognizing this, several investigators (1, 2, 3) set out to develop such a relationship. In this context, two well-defined problems are at once evident. The first concerns the definition of what should be the correct procedure of obtaining experimentally the stress-strain curve; the currently accepted thinking on this subject seems to be the use of an oedometer (4). The second problem, with which this paper is primarily concerned, involves the selection of a mathematical model that would approximately describe the experimentally obtained curve. Results of both static and dynamic oedometer tests indicate that the stress-strain relationship is generally concave to the stress axis for both cohesive and cohesionless soils. Frequently, the initial portion of the curve exhibits an S-shaped behavior which is concave to the strain axis at comparatively low stress levels (2,4). From a practical standpoint of studying the shock wave propagation phenomena, it is necessary to define mathematically only that portion of the curve which is concave to the stress axis.

NOMENCLATURE

$A_0, A_1,$ Coefficients
$A_2 \ldots$

A_L, A_U Constant characteristics for stress-strain curve of the current model for loading and unloading phases

H_L Area under loading curve

H_U Area under the unloading curve

L   Subscript used to indicate loading

M_S Secant modulus

M_T Tangent modulus

U   Subscript used to indicate unloading

$a_L, b_L,$ Constant characteristics (nondimen-
a_U, b_U sional form equivalents) for stress-strain curve of proposed model

f   Nondimensionalized stress

321

n   Constant characteristic for stress-strain curve of current model

n_1, n_2 Constant characteristics of stress-strain curves for loading and unloading (current model)

p(t)   Impulse loading function

s   Normalized strain

s_0 Normalized residual strain

ϵ Strain

ϵ_{max} Maximum strain

ϵ_0 Residual strain

η Relative size of hysteresis loop

ρ_0 Density of medium

σ Stress

σ_L Stress during loading cycle

σ_{max} Maximum stress, also denoted by p_0

σ_U Stress during unloading cycle

MODEL CURRENTLY USED

The nonlinear hysteretic model first suggested by Hendron (5) has been used by other investigators (6,7). The details of this model are shown in Fig. 1. Also the mathematical
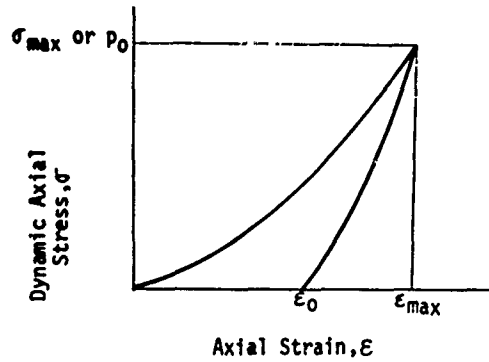

$$\sigma_L = A_L \, \epsilon^{n1}$$

$$\sigma_U = A_U \, (\epsilon - \epsilon_0)^{n2}$$
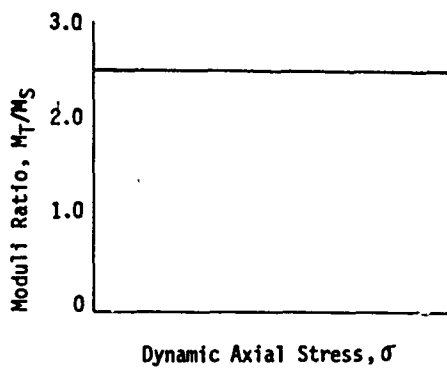
$$M_T/M_S = n_1 \text{ for loading}$$

$$M_T/M_S = n_2 \text{ for unloading}$$

Also: $n_1 = n_2 = n$
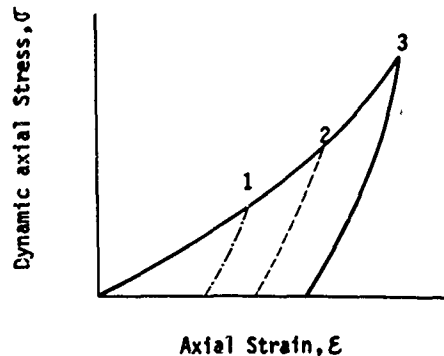
$$\eta = \epsilon_0/\epsilon_{max}]_1 = \epsilon_0/\epsilon_{max}]_2 = \epsilon_0/\epsilon_{max}]$$

Fig. 1. Model currently used

implications of the model are shown in the appendix. It is shown in this appendix that for the model in question the following relationships should hold:

1. The ratio M_T/M_S is independent of the stress level, where M_T is the tangent modulus at the stress σ, and M_S is the secant modulus at the same stress σ.

2. The relative size of the hysteresis loop, η, is given by

$$\eta = \epsilon_0/\epsilon_{max}, \qquad (1)$$

where ϵ_{max} is the strain occurring at $\sigma = \sigma_{max}$, and ϵ_0 is the residual strain on unloading at $\sigma = 0$.

As is indicated later, the implication that M_T/M_S is independent of the stress level obtains only in the case of sands. The second implication regarding the relative size of the hysteresis loop appears to be a rather restrictive relationship for all soils, and it may be difficult to find a theoretical basis for justifying such a relationship.

EXPERIMENTAL EVIDENCE FOR SANDS AND OTHER SOILS

Figure 2 presents results for a Minnesota sand (5). Figure 2a of this figure shows a typical stress-strain curve for this sand, while Fig. 2b suggests that the curve can be adequately described by an exponential form of the type of Eq. (A-1). Further, a plot of the variation of M_T/M_S, based on an analysis of the stress-strain relationship of Fig. 2a, and as shown in Fig. 2c, suggests that for this particular sand, the ratio of M_T/M_S, at least during the loading cycle, is very nearly independent of the stress level. Similar conclusions, for both the loading and the unloading cycles, could also be drawn for sands studied by other investigators (4,8). It could thus be said that the currently used model is a fairly good representation of the stress-strain curves for sands. In fact, the model was developed from data on sands.

However, a suggestion has been made (7) regarding the use of this model for studying wave propagation in all soils. Figures 3 to 5 present results of one-dimensional tests for three different soils, other than sands (9, 10 11). Figures 3b, 4b and 5b indicate that plots of stress versus strain on logarithmic paper do not yield straight lines, thereby indicating that an exponential curve is not an adequate representation. This is further confirmed by
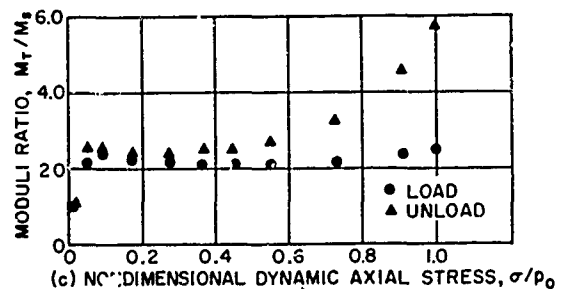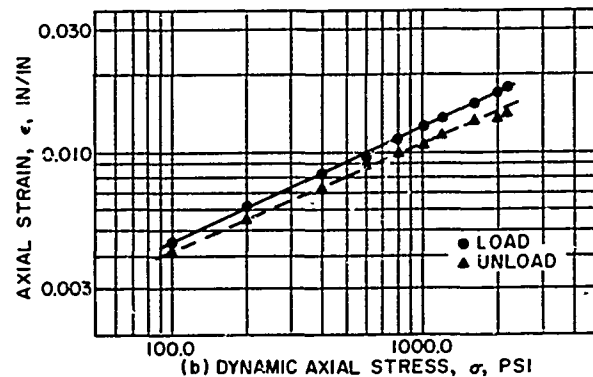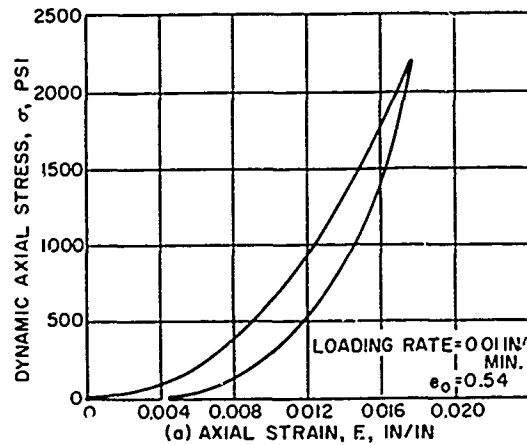
Fig. 2. Experimental data from Hendron for Minnesota sand

Figs. 3c, 4c, and 5c, which show that the variation of M_T/M_S is indeed a function of stress.

PROPOSED NEW MODEL

Since the variation of M_T/M_S is not independent of the stress level, one may in the most general form assume

$$\frac{M_T}{M_S} = A_0 + A_1\sigma + A_2\sigma^2 \ldots . \qquad (2)$$

But going back to Figs. 3 through 5, it can be seen that this expression can be, without much loss of accuracy, simplified to
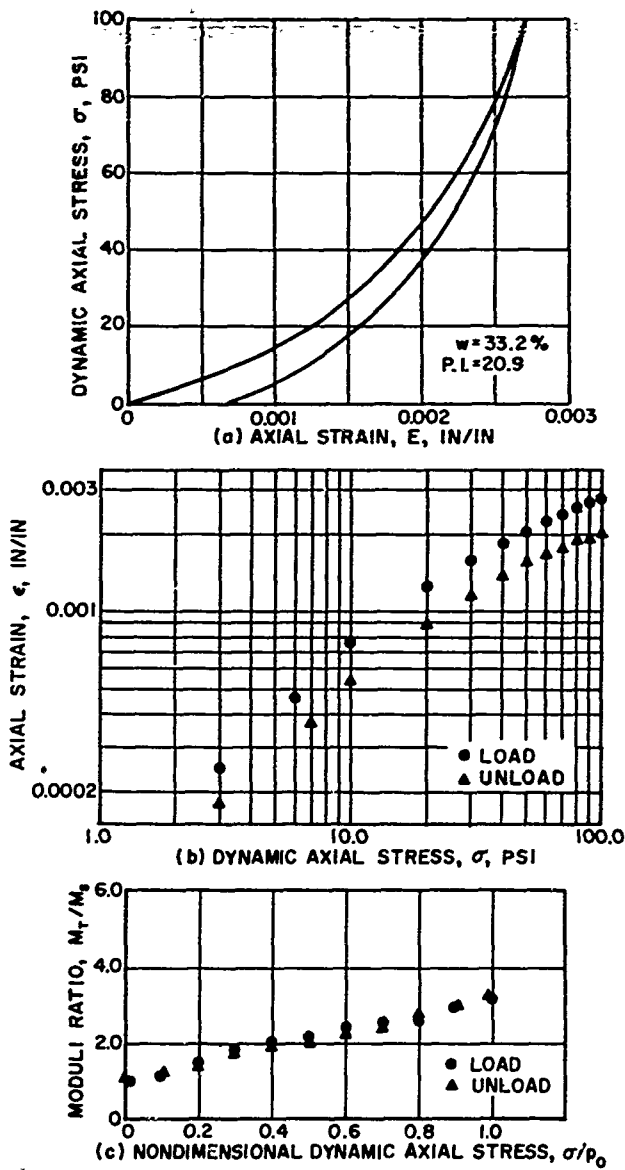
Fig. 3. Experimental data from Ginsburg
for Uetliberg clay

Fig. 4. Experimental data from Kane
for Goose Lake clay

$$\frac{M_T}{M_S} = A_0 + A_1 \sigma . \qquad (3)$$

In some cases it may be desirable to define the variation of M_T/M_S by two, or at best three, linear segments.

Now, recalling that

$$M_T = d\sigma/d\epsilon , \qquad (4)$$

and

$$M_S = \sigma/\epsilon , \qquad (5)$$

one gets

$$\frac{d\sigma/d\epsilon}{\sigma/\epsilon} = A_0 + A_1 \sigma . \qquad (6)$$

Further defining

$f = \sigma/\sigma_{max}$ = nondimensional stress,

$s = \epsilon/\epsilon_{max}$ = normalized strain, and

a_L, b_L = nondimensional equivalents of A_0 and A_1 for the loading cycle,

one obtains

324
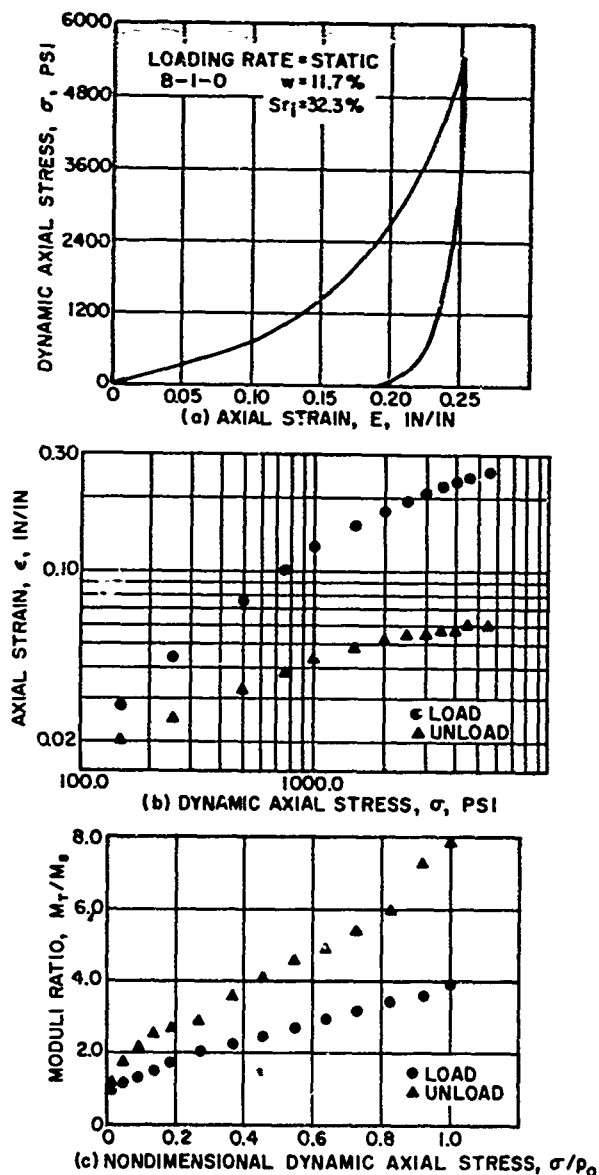
Fig. 5. Experimental data from Davisson for Playa silt

$$\frac{df/ds}{f/s} = a_L + b_L f , \qquad (7)$$

which on integration, subject to $f = 1.00$ when $s = 1.00$, yields

$$s = \left[\frac{(a_L + b_L)f}{a_L + b_L f}\right]^{1/a_L} . \qquad (8)$$

For the unloading portion of the curve the derivation remains essentially the same, with the only exceptions being that ϵ in Eq. (6) is to be replaced by $(\epsilon - \epsilon_0)$, and the integration is carried out subject to the $f = 1.00$ when $s = 1 - s_0$, leading eventually to

$$s - s_0 = \frac{1}{1 - s_0} \left[\frac{(a_U + b_U)f}{a_U + b_U f}\right]^{1/a_U} , \qquad (9)$$

where

$$s_0 = \frac{\epsilon_0}{\epsilon_{max}} .$$

Equations (8) and (9), then, define the proposed general model for all soils. The model is developed essentially from the experimental evidence that M_T/M_S is not generally independent of the stress level, but is, in most cases, of the form $A_0 + A_1\sigma$. The model can be used for extension of wave propagation and other studies from sands to other soils.

It is interesting to note that the following models can be generated from the proposed model by appropriate selection of the coefficients a and b and of the residual strain s_0:

1. Elastic nonhysteretic model;

2. Linear hysteretic model (12);

3. Model as used by Weidlinger and Matthews (6);

4. Linear form of the Weidlinger and Matthews (6) mode; and

5. Ideal locking model.

APPLICATION OF MODEL FOR SHOCK PROPAGATION STUDIES

The stress-strain relationship, as expressed by Eqs. (8) and (9), can be conveniently used for shock propagation studies. The model has been used by the authors (11) to study shock phenomena in a nonlinear medium using the same assumptions as were used by Weidlinger and Matthews (6). Taking into account these assumptions, Eqs. (8) and (9) become:

$$s = \left[\frac{(a_L + b_L)f}{a_L + b_L f}\right]^{1/a_l} , \qquad (10)$$

$$s = s_0 . \qquad (11)$$

The details of the development of the equations governing shock propagation phenomena are given elsewhere (11), and only the resultant equations are summarized below to demonstrate the applicability of the proposed model:

325

1. Shock velocity

$$\dot{z} = \left[\frac{P_0}{\rho_c \bar{\epsilon}_0}\right]^{1/2} \Bigg/ \left\langle \frac{f}{\left[\frac{(a_L + b_L)f}{a_L + b_L f}\right]^{1/a_L}}\right\rangle^{1/2} , \quad (12)$$

2. Shock location

$$z = \frac{1}{(\rho_0 \epsilon_0 P_0)^{1/2}(f)^{1/2}} \times \frac{\int_0^t p(t)\,dt}{\left[\frac{(a_L + b_L)f}{a_L + b_L f}\right]^{1/2a_L}} , \quad (13)$$

where ρ_0 is the density of medium and $p(t)$ is the loading function. Equations (12) and (13)

when reduced for the condition $b_L = 0.00$ (i.e. M_T/M_S = constant), can be shown to be identical to the equations of Weidlinger and Matthews (6).

CONCLUSIONS

The limitations of the currently used model have been discussed in the context of their possible use as a general soils model. Based on reported experimental evidence, it has been shown that the model is not adequate for this purpose.

The new model now proposed is in agreement with experimental evidence and lends itself to incorporation in shock wave propagation analysis in soils.

REFERENCES

1. R. V. Whitman, "Stress-Strain-Time Behavior of Soil In One Dimensional Compression," M.I.T., Dept. of Civil Eng., Res. Rept. R63-25, May 1963

2. M. T. Davisson, "Static and Dynamic Behavior of a Playa Silt in One-Dimension Compression," Kirkland AFB, New Mexico, TDR-63-3078, AFWL-TDR-63-3078, Sept. 1963

3. A. J. Hendron, Jr., "The Behavior of Sand in One-Dimensional Compression," Ph.D. Thesis, U. of Illinois, Urbana, 1963

4. R. V. Whitman, E. T. Miller, and P. J. Moore, J. Soil Mech. and Found. Div., ASCE (1964)

5. A. J. Hendron, Jr., "The Behavior of Sand In One-Dimensional Compression," Kirkland AFB, New Mexico, AFSWC-TDR-63-3089, Oct. 1963

6. P. Weidlinger and A. T. Matthews, "Shock and Reflection Phenomena In a Nonlinear Medium," presented at Ann. Structural Eng. Conf., ASCE, Oct. 1964

7. L. Seaman and R. V. Whitman, "Stress Propagation In Soils," Stanford Research Inst., Final Rept., Part IV, DASA 1266-4, June 1964

8. D. E. Calhoun, "Interim Report on Constrained Modulus Testing," unpub. rept., U. of New Mexico, Air Force Shock Tube Facility, 1964

9. T. Ginsburg, "Propagation of Shock Waves in the Ground," J. Structural Div., ASCE (Feb. 1964)

10. H. Kane et al., "A Study of the Behavior of a Clay Under Rapid and Dynamic Loading In the One-Dimensional and Triaxial Tests," Kirkland AFB, New Mexico, AFSWC-TDR-63-3116, Jan. 1963

11. D. C. Kraft, C. Miranda, and Delmar E. Calhoun, "Shock Propagation Phenomena in Nonlinear Media," submitted to Soil Mech. and Found. Div., ASCE, 1965

12. M. G. Salvadori, R. Skalok, and P. Weidlinger, "Waves and Shocks in Locking and Dissipative Media," J. Eng. Mech. Div., ASCE (April 1960)

Appendix

IMPLICATIONS OF CURRENTLY ACCEPTED MODEL

Referring to the loading cycle of Fig. 1, which is described by

$$\sigma_L = A_L \epsilon^{n_1}, \qquad (A\text{-}1)$$

one obtains the expressions for M_T and M_S as

$$M_T = \frac{d\sigma_L}{d\epsilon} = A_L n_1 \epsilon^{n_1 - 1}, \qquad (A\text{-}2)$$

$$M_S = \frac{\sigma_L}{\epsilon} = A_L \epsilon^{n_1 - 1}, \qquad (A\text{-}3)$$

leading to

$$\left. \frac{M_T}{M_S} \right|_L = n_1. \qquad (A\text{-}4)$$

This indicates that the ratio M_T/M_S is independent of the stress level. The same conclusion can be drawn from the unloading cycle described by

$$\sigma_U = A_U (\epsilon - \epsilon_0)^{n_2}, \qquad (A\text{-}5)$$

provided the secant modulus is defined with reference to the residual strain, ϵ_0, in which case

$$M_T = A_U n_2 (\epsilon - \epsilon_0)^{n_2 - 1}, \qquad (A\text{-}6)$$

$$M_S = A_U (\epsilon - \epsilon_0)^{n_2 - 1}, \qquad (A\text{-}7)$$

and

$$\left. \frac{M_T}{M_S} \right|_U = n_2. \qquad (A\text{-}8)$$

An assumption often made that the size of the hysteresis loop is independent of the maximum stress has been reported as coinciding with experimental evidence (5). This assumption leads to the conclusion that

$$n_1 = n_2 = n. \qquad (A\text{-}9)$$

Now, defining H_L as the area under the loading curve, and H_U as the area under the unloading curve, we have:

$$H_L = \int_0^{\epsilon_{max}} \sigma_L d\epsilon = \int_0^{\epsilon_{max}} A_L \epsilon^n d\epsilon = \frac{A_L}{n+1} \epsilon_{max}^{n+1}, \qquad (A\text{-}10)$$

and

$$H_U = \int_{\epsilon_0}^{\epsilon_{max}} \sigma_U d\epsilon = \int_{\epsilon_0}^{\epsilon_{max}} A_U (\epsilon - \epsilon_0)^n d\epsilon \qquad (A\text{-}11)$$

$$= \frac{A_U}{n+1} (\epsilon_{max} - \epsilon_0)^{n+1},$$

but

$$\sigma_{max} = A_L \epsilon_{max}^n = A_U (\epsilon_{max} - \epsilon_0)^n. \qquad (A\text{-}12)$$

Hence

$$H_L = \frac{1}{n+1} \epsilon_{max} \times \sigma_{max}, \qquad (A\text{-}13)$$

and

$$H_U = \frac{1}{n+1} (\epsilon_{max} - \epsilon_0) \times \sigma_{max}. \qquad (A\text{-}14)$$

Thus, the relative size of the hysteresis loop, η, becomes

$$\eta = \frac{H_L - H_U}{H_L}$$

$$= \frac{\dfrac{\epsilon_{max} \sigma_{max}}{n+1} - \dfrac{(\epsilon_{max} - \epsilon_0) \sigma_{max}}{n+1}}{\dfrac{\epsilon_{max} \sigma_{max}}{n+1}} \qquad (A\text{-}15)$$

$$= \frac{\epsilon_0}{\epsilon_{max}}.$$

Mr. Hall (Edgerton, Germeshausen & Grier): Has any testing been accomplished with a rock-type soil and, if so, is there any reason why your studies could not be applied to the same?

Dr. Kraft: No tests have been conducted on rock-type soil. The tests that we conducted while at the Air Force Shock Tube Facility were on a silt material. Everything presented in the paper was on either a sand, a silt, or a clay. There is no reason, however, why it can not be extended to a rock-type material. Generally speaking, the behavior for rocks might be very close to elastic behavior. There would be no question of going into greater detail as we have here for extreme variations in the stress-strain curve.

Dr. Sevin (IIT Research Institute): I respectfully suggest that your suggestion that this could possibly be a stress-strain relationship, applicable universally to all soils, is not really a valid one. I think there is much data which have not been quoted, which on one extreme suggest that perhaps the continuum model is not adequate for the representation of all soils. At the other extreme there is much data by Whitman, Selig and others which suggest we do not really know how to characterize soils in terms of such properties as densities and moisture content. These data indicate that a simple relationship, no matter how complex it might appear in equation form, could not treat the shock propagation problem in an adequate sense. First of all, the one-dimensional treatment is in question. In the real world where the one dimension goes down, we have a very prominant variation of the confined modulus. Even on a one-dimensional model with depth, the variation might be a factor of 10 in modulus within, say, the first 40 feet — or perhaps the next 100 to 200 feet. The work that Selig has published suggests that the loading, unloading and reloading-unloading behavior is not reproducible. If one attempts, however, to treat the stress-strain curves analytically on a load, unload, load, unload, repeated cycle, one can get reasonably close to the predominant characteristics. In summary, I would think that a model could not possibly be adequate for all soils in one dimension if it did not include the variation of the modulus, not only as a function of stress intensity, but as a function of position. It should also treat the load, unload, reload-unload characteristics. Again, the one-dimensional model itself has very serious limitations for real world applications.

Dr. Kraft: I will answer your question in three parts. First of all, it is true that we have assumed the medium to be a continuum. This is the assumption generally made, at least up to this point, in the studies that have been conducted. Secondly, with regard to your questioning the variations in density and moisture content which may occur with depth, this has been discussed, although not in great detail, in the other paper to which I referred. It was found that the variations in moisture content and density did not make a considerable amount of difference on the stress attenuation with depth. A range of moisture contents and densities were analyzed with respect to depth. Finally, you mentioned the problem of loading and unloading. A nuclear blast wave is a one-shot type of loading, not a continuing loading and unloading phenomenon. In truth, we are trying to study wave propagation with regard to hardened structures, in other words, the transmission of one blast wave to that hardened structure. So, I do not think that the loading and unloading phenomenon is particularly pertinent unless you have to go through a number of loading and unloading cycles to obtain soil properties which would reflect wave propagation. Does this answer your question?

Dr. Sevin: Partly. I would refer you to the Wilson-Sibley paper in an ASCE Journal of about 2 years ago. This reports a good deal of explosion data and laboratory tests reflecting the properties of real soils of various types from silts to a rock-like medium as a function of depth. These data show at least an order of magnitude change in the confined modulus with depth. Secondly, my reference to load, unload, reload was more in reference to strain rate reversals due to various possibilities such as reflections, loading, and unloading. I am not necessarily implying that you have to unload to the zero condition, reload up and so on. It was with reference to the blast phenomenon, of course,

Dr. Miranda: I want to stress one particular comment which Dr. Kraft has made, referring particularly to the variation of a and b with depth. The changes with depth can be reflected by the variation in the values of a and b with depth. Now a study of this type has been made and we have carried out an analysis to verify that, although there is variation in a and b, quantitatively it does not make very much difference in the variation of stress with depth. We have verified this by an actual calculation.

*　　*　　*